Transactions of the ASME®

Technical Editor, **T. H. OKIISHI (2003)**
Associate Technical Editors
Aeromechanical Interaction
R. E. KIELB (1999)
Gas Turbine (Review Chair)
D. BALLAL (2000)
Heat Transfer
M. G. DUNN (1999)
N. NIRMALEN (2000)
Turbomachinery
R. ABHARI (2002)
A. STRAZISAR (2000)

BOARD ON COMMUNICATIONS
Chairman and Vice-President
R. K. SHAH

OFFICERS OF THE ASME
President, **R. E. NICKELL**
Executive Director, **D. L. BELDEN**
Treasurer, **J. A. MASON**

PUBLISHING STAFF
Managing Director, Engineering
CHARLES W. BEARDSLEY
Director, Technical Publishing
PHILIP DI VIETRO
Managing Editor, Technical Publishing
CYNTHIA B. CLARK
Managing Editor, Transactions
CORNELIA MONAHAN
Production Coordinator
VALERIE WINTERS
Production Assistant
MARISOL ANDINO

Transactions of the ASME, Journal of Turbomachinery (ISSN 0889-504X) is published quarterly (Jan., Apr., July, Oct.) for $215.00 per year by The American Society of Mechanical Engineers, Three Park Avenue, New York, NY 10016. Periodicals postage paid at New York, NY and additional mailing offices. POSTMASTER: Send address changes to Transactions of the ASME, Journal of Turbomachinery, c/o THE AMERICAN SOCIETY OF MECHANICAL ENGINEERS, 22 Law Drive, Box 2300, Fairfield, NJ 07007-2300.
CHANGES OF ADDRESS must be received at Society headquarters seven weeks before they are to be effective. Please send old label and new address.
PRICES: To members, $40.00, annually; to nonmembers, $215.00.
To countries outside the United States and Canada, add $40.00 for surface postage and $60.00 for airmail postage.
STATEMENT from By-Laws. The Society shall not be responsible for statements or opinions advanced in papers or ... printed in its publications (B7.1, Par. 3).

INDEXED by Applied Mechanics Reviews and Engineering Information, Inc.
Canadian Goods & Services Tax Registration #126148048

Journal of Turbomachinery

Published Quarterly by The American Society of Mechanical Engineers

VOLUME 121 • NUMBER 3 • JULY 1999

TECHNICAL PAPERS

(Contents continued on p. 386)

This journal is printed on acid-free paper, which exceeds the ANSI Z39.48-1992 specification for permanence of paper and library materials. ♾™
♻ 85% recycled content, including 10% post-consumer fibers.

(Contents continued)

ANNOUNCEMENTS

Effect of Upstream Rotor Vortical Disturbances on the Time-Averaged Performance of Axial Compressor Stators: Part 1—Framework of Technical Approach and Wake–Stator Blade Interactions

T. V. Valkov
Shell International Gas Limited,
Shell Center,
London SE1 7NA United Kingdom

C. S. Tan
MIT Gas Turbine Laboratory,
Cambridge, MA 02139

In a two-part paper, key computed results from a set of first-of-a-kind numerical simulations on the unsteady interaction of axial compressor stators with upstream rotor wakes and tip leakage vortices are employed to elucidate their impact on the time-averaged performance of the stator. Detailed interrogation of the computed flowfield showed that for both wakes and tip leakage vortices, the impact of these mechanisms can be described on the same physical basis. Specifically, there are two generic mechanisms with significant influence on performance: reversible recovery of the energy in the wakes/tip vortices (beneficial) and the associated nontransitional boundary layer response (detrimental). In the presence of flow unsteadiness associated with rotor wakes and tip vortices, the efficiency of the stator under consideration is higher than that obtained using a mixed-out steady flow approximation. The effects of tip vortices and wakes are of comparable importance. The impact of stator interaction with upstream wakes and vortices depends on the following parameters: axial spacing, loading, and the frequency of wake fluctuations in the rotor frame. At reduced spacing, this impact becomes significant. The most important aspect of the tip vortex is the relative velocity defect and the associated relative total pressure defect, which is perceived by the stator in the same manner as a wake. In Part 1, the focus will be on the framework of technical approach, and the interaction of stator with the moving upstream rotor wakes.

1.0 Introduction and Technical Background

It has been shown experimentally that the performance of axial compressors depends on the axial spacing between blade rows. Smith (1970) reported a one-point efficiency gain and a two to four percent stage pressure rise increase in a low-speed research compressor, by reducing blade row spacing from 0.37 to 0.07 chords. Similar results were obtained later by Mikolajczak (1977). The unsteady flow associated with the interaction between moving and stationary blade rows is thought to be the most likely cause for these observations. A causal link between the performance and blade row interaction was put forward by Smith (1966) in his model of "wake recovery": For constant-density, inviscid flow, upstream wakes undergo an increase in length as they convect through the blade passage, so that Kelvin's theorem would suggest a corresponding decrease in velocity nonuniformity and thickness of the wake in inverse proportion to the increase in length; this results in a reversible conversion of some of the secondary kinetic energy in the wakes into pressure rise. This was subsequently demonstrated by the results from the unsteady two-dimensional inviscid simulations of Deregel and Tan (1996) and the two-dimensional analysis of Adamczyk (1996). However, a recent discussion by Smith (1996) indicates that reversible wake attenuation accounts for only 25 to 50 percent of the efficiency gains observed by Smith (1970).

1.1 Sources of Unsteadiness. Of the many types of unsteady rotor–stator interactions (Dorney and Sharma, 1996), only vortical interactions and their impact on time-averaged performance as measured in terms of stage adiabatic efficiency and pressure rise are considered here. Vortical interaction involves wakes and vortices shed from upstream blade rows; Fig. 1 provides an elucidation of these disturbances in the rotor relative frame, based on ensemble-averaged flow data. In general these can be of three types as delineated below:

1 Ensemble-averaged measurements of compressor rotor wakes (Stauter et al., 1991; Zierke and Okiishi, 1982) suggest that the wake profile can be characterized by a relative velocity defect and thickness. However, time-resolved data indicate that there may be substantial wake-to-wake variability, and the wake defect fluctuates in time (Kotidis and Epstein, 1991; Brookfield and Waitz, 1996).

2 Rotor tip leakage vortex is the principal flow nonuniformity in the tip region (Wisler, 1985; Storer and Cumpsty, 1991; Khalid, 1995; Nikolaou et al., 1996). For unshrouded blades, the tip leakage flow downstream of the rotor appears as a slowly swirling core of low-velocity fluid. The core, with a velocity defect a substantial fraction of the relative velocity and twice the leakage crossflow component, bears more similarity to a wake than to a

Contributed by the International Gas Turbine Institute and presented at the 43rd International Gas Turbine and Aeroengine Congress and Exhibition, Stockholm, Sweden, June 2–5, 1998. Manuscript received by the International Gas Turbine Institute February 1998. Paper No. 98-GT-312. Associate Technical Editor: R. E. Kielb.

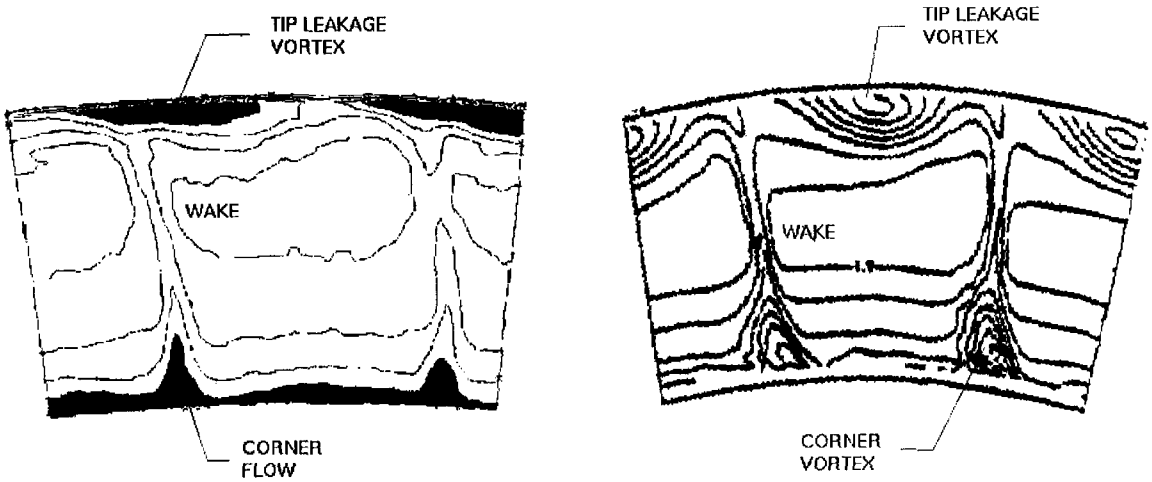

Fig. 1 Rotor wakes, tip leakage vortex, and corner vortices as indicated by ensemble-averaged relative velocity contours at compressor rotor exit. Left: Silkowski (1995). Right: from Nikolaou et al. (1966).

streamwise vortex (Fig. 1). As in wakes, the velocity components within the core can be expected to fluctuate in time.

3 Rotor streamwise vortices appear as a round core of swirling flow. An idealized representation of such a streamwise vortex will be considered here as an interesting contrast to the situation of tip leakage vortex.

1.2 Motivation. A compressor blade row perceives the upstream wakes as "jets" directed away from the suction surface (Kerrebrock and Mikolajczak, 1970; Hodson, 1985). This jet imposes a peak velocity on the boundary layer, sometimes exceeding 20 percent of the bulk flow. Such strong disturbances can influence boundary layer behavior by mechanisms unrelated to transition. *The role of such nontransitional, wake-driven disturbances on loss has not been quantitatively addressed.*

Experimentally, Howard et al. (1994) found that the loss in the tip region of the stator increases significantly when the tip clearance of the upstream rotor is increased from 1.2 to 3 percent chord. This increased stator loss leads to 30 percent stage efficiency reduction associated with increased tip clearance. Results from Navier–Stokes simulations by Dawes (1994) appear to suggest this experimental observation. However, *the precise underlying mechanism has yet to be delineated on a sound physical basis.*

The transport of wakes and vortices can have an impact on performance by mechanisms other than boundary layer response. The efficiency benefit from Smith's (1966) mechanism of reversible wake recovery depends on the balance between attenuation by stretching and attenuation from turbulent mixing. Annular cascade data by Poensgen and Gallus (1991) indicate that in the presence of a downstream stator, wakes are attenuated twice as fast as without a stator. *This suggests that reversible recovery effects are significant even when turbulent mixing is present and it would thus be of interest to assess this on a quantitative basis.*

It is reasonable to assume that upstream vortices also undergo some form of reversible processing. Denton (1993) notes that stretching a streamwise vortex filament amplifies its secondary kinetic energy proportionally to the stretching squared. Such amplification is detrimental for performance, because the energy taken from the core flow in this process may be irreversibly

Nomenclature

a_r = reversible velocity attenuation factor
A = passage cross-sectional area
A_b = blocked area set by crossflow sectional area containing flow defect associated with tip leakage vortex at rotor exit
A_e = passage cross-sectional area at rotor exit
A_j = velocity excess of the upstream disturbance "jet" in the stator frame
A_r = velocity defect in the relative rotor frame
c = stator blade chord
C_t = total pressure loss coefficient = $(p_t - p_{t,1})/\frac{1}{2}\rho U_\infty^2$
d = axial gap between rotor and stator
l_{ile} = length of disturbance segment at entrance/exit of blade row
L = time and mass-averaged total pressure loss coefficient
L_i = L from mixing-out flow at the inlet of the stator passage
L_e = L from mixing-out flow at the exit of the stator passage
L_p = L between inlet and exit of the stator passage
Q = dynamic head
$Q_{2\tau}$ = relative dynamic head at distance 2τ away from endwall at rotor inlet
p = static pressure
p_t = total pressure
Re = Reynolds number
(s, n) = (streamwise, normal to streamline)
S = blade-to-blade spacing at pitchline
t = dimensionless time
t_w = wake thickness (at 99 percent velocity in relative frame)
T_p = blade passing time period
T_t = time period of fluctuations within vortices and wakes
u = axial velocity
$\mathbf{u}$ = axial velocity
U = total velocity
V_1, V_2 = relative velocities at the inlet and exit of rotor blade row
x = axial direction
z = spanwise direction
ΔP = pressure rise
ΔV_n = local time-averaged velocity disturbance normal to the boundary layer
β_e = relative flow angle at edge of defect associated with tip leakage flow at midpitch
β_{vm} = vector mean flow angle (rotor)
Γ = circulation
θ_w = wake momentum thickness
$\theta_{1,R/S}/\theta_{2,R/S}$ = relative flow angle at inlet/exit of rotor/stator

dissipated. However, rotor tip leakage vortices are structurally more similar to wakes, for which stretching would recover part of the kinetic energy. *It is not known whether some of the tip vortex secondary kinetic energy can be recovered or not.*

2.0 Problem Statement and Technical Objectives

The two-part paper addresses, on a quantitative basis, the impact of upstream rotor vortical disturbances on the performance of a representative core compressor stator. The specific technical objectives are:

- Quantify the effect of upstream rotor tip leakage vortex and wake on the time-average performance of the stator *relative to the commonly used steady flow approximation in which wakes and vortices are mixed out in the space between blade rows.*
- Identify the unsteady phenomena of significance and explain how they cause loss to increase or decrease.
- Determine the key controlling parameters that influence the performance impact of wakes and tip vortices.
- Utilize the resulting understanding to develop a flow model and to suggest recommendations on design choices that lead to enhanced performance and likely potential benefits.

In addition the following questions in compressor aerodynamics will be addressed:

- Is the kinetic energy within the rotor tip vortex recoverable?
- What is the effect on loss from transporting the tip vortex through the stator?
- What is the effect on loss of the nontransitional response of the stator boundary layer to upstream vortices and wakes?
- What is the effect of wake and tip vortex fluctuations on loss, relative to the assumed ensemble-averaged wakes and vortices?
- What is the effect of unsteady secondary flows on loss?
- How much of the energy in upstream disturbances is actually recovered by Smith's (1966) dispersion mechanism? Do the mechanisms considered here add up to the amount of efficiency benefit measured and quoted by Smith (1970)?

3.0 Scope and Organization of the Two-Part Paper

The central ideas and key results are arranged as follows. Part 1 of the paper presents the technical approach followed by a description on the impact of rotor wake–stator interaction on performance. In Part 2 we will present results that elucidate the impact of upstream rotor tip leakage- and streamwise vortex–stator interaction on performance and the associated controlling parametric trends; this is followed by the application of results to suggest: (1) recommendations on design choices that could potentially lead to enhanced performance; and (2) strategies for mitigating detrimental effects of unsteady vortical disturbances-stator interactions. Finally the key new findings are encapsulated in the section on Overall Summary and Conclusions.

4.0 Technical Approach

The approach consists of first developing a framework for assessing the effects of upstream vortical disturbances on blade row performance and selecting a representative high-performance compressor geometry; this is then followed by the computational implementation of the framework, and the definition of computational experiments specifically directed at accomplishing the stated objectives and at answering the questions posed in Section 2.0.

4.1 Framework for Assessment of Unsteady Flow Effects. It would be difficult to get a clear answer to the questions of interest if all the interactions within the multistage compressor were represented. Thus, the focus will be on the situation of a single stage, where the stator is subjected to the vortical disturbances from the upstream rotor, but no information from the stator reaches the rotor (Fig. 2, top). Such an approximation can be based on the argument that the rotor immediately upstream is the strongest source of vortical disturbances to the stator. However, it cannot represent two aspects of unsteady interaction: (1) fluctuation of the wakes/vortices due to the stator pressure field, and (2) disturbances from blade rows other than the upstream rotor. The first aspect can be modeled by allowing the velocity defect of the wakes to have a temporal variation on a physically relevant time scale.

For assessing the "effects of unsteadiness" on stator performance, the time-averaged figures of merit (efficiency, loss, and pressure rise) from the unsteady situation are compared to those in a steady-state approximation derived through mixing out the flow nonuniformities in between the blade rows (Fig. 2, bottom). Thus, the loss change due to unsteady flow *within the stator passage* is quantified by the difference $\Delta L_p = L_{p,u} - L_{p,s}$ between time-averaged unsteady and steady-state loss coefficients.

Nomenclature (cont.)

μ = working fluid viscosity
ν = dimensionless net viscosity = 1/Re + υ_t
υ_t = dimensionless eddy viscosity
ρ = working fluid density
σ = blading solidity
τ = tip clearance
ϕ = stage flow coefficient at pitchline
χ = disturbance impingement angle relative to stagger direction
ψ = stage pressure coefficient
ω = vorticity
Ω = steady flow spanwise vorticity

Subscripts and Superscripts

$()_m$ = referring to a mixed-out flow quantity
$()_p$ = pertains to the stator passage
$()_s$ = designates a flow quantity in the steady (base) flow
$()_t$ = stagnation quantity
$()_u$ = designates a flow quantity in the unsteady flow
$()_1$ = designates a quantity at the inlet of the blade row
$()_2$ = designates a quantity at the exit of the blade row
$()_\infty$ = referring to mixed-out flow conditions upstream of the stator
$\overline{()}$ = time-averaged
$\overline{()}^a$ = area-averaged over flow defect region associated with tip leakage vortex at rotor exit
$\Delta()$ = difference operator between unsteady and base flows

Abbreviations

BL = boundary layer
BLD = boundary layer disturbance/distortion
LE = leading edge
LSRC = General Electric low-speed research compressor
N-BLD = boundary layer disturbances containing normal vorticity
PS = pressure surface
S-BLD = boundary layer disturbances containing streamwise vorticity
SS = suction surface
TE = trailing edge
TL = rotor tip leakage vortex
SW = rotor streamwise vortex
ID = inviscid design-point steady/base flow
VD = viscous design-point steady/base flow
VH = viscous high-loading steady/base flow
VS = viscous high-shear steady/base flow
2D/3D = two-dimensional/three-dimensional

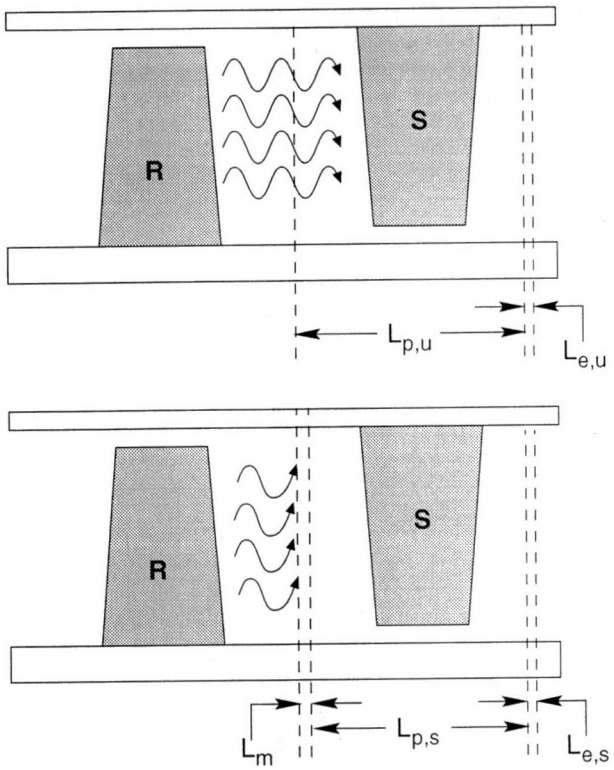

Fig. 2 Effect of rotor on stator as considered here (top); mixing-plane (reference) steady flow approximation (bottom)

The secondary kinetic energy of upstream vortical disturbances may be recovered in the stator without an increase in entropy. Vortices shed in response to upstream disturbances carry kinetic energy that is eventually dissipated. The sum of these effects can be quantified by comparing the time-averaged disturbance mixing losses between the exit and the inlet of the stator, and are represented in the coefficient $\Delta L_m = L_{i,u} - (L_{e,u} - L_{e,s})$. The net effect of upstream wakes and vortices on stator loss is thus $\Delta L = \Delta L_p - \Delta L_m$.

The LSRC geometry, representative of an embedded stage in a modern aircraft gas turbine engine compressor (Wisler, 1985), is used in this investigation. This configuration is an aerodynamically scaled model of stage 7 of the 10 stage, 23:1 pressure ratio NASA/GE E^3 (Energy Efficient Engine) compressor. The stator blading is characterized by tailored loading, high hub-to-tip ratio of 0.85, low aspect ratio of 1.34, high solidity of 1.67, and a stagger angle of 32 deg.

The present framework is based on comparing the performance at design rotor–stator axial gap against a steady-state approximation corresponding to an infinite gap. To investigate the effects of axial spacing and to connect them to Smith's (1970) data, two categories of wakes and vortices baseline and "strong," are used. Baseline wakes and vortices have a velocity profile that corresponds to blade rows separated by a distance of 0.37 chords (the same as in Smith's baseline experiment). "Strong" wakes and vortices have a velocity profile that corresponds to a blade row separation of 0.07 chords.

4.2 Computational Implementation. Numerical experiments form the basis of implementing the framework of investigation delineated above. The unsteady flow in the LSRC stator passage can be adequately described by the time-dependent incompressible Reynolds-averaged Navier–Stokes equations:

$$\frac{\partial u}{\partial t} - u \times \omega = -\nabla p_t + \nabla(\nu \nabla u); \quad \nabla \cdot u = 0 \qquad (1)$$

The unsteadiness of the flow is represented as a disturbance flowfield superimposed upon the premixed steady flow (Fig. 2, bottom):

$$\Delta u = u_u - u_s; \quad \Delta p = p_u - p_s; \quad \text{etc.} \qquad (2)$$

Equation (1) is not solved directly, but rather the disturbance flow is obtained by solving the following form of the Navier–Stokes equations:

$$\frac{\partial \Delta u}{\partial t} = u_s \times \Delta\omega + \Delta u \times \omega_s + \Delta u \times \Delta\omega - \nabla \Delta p_t + \nabla(\nu_s + \nabla\nu)\nabla\Delta u + \Delta\nu \nabla u_s \qquad (3)$$

Both the nonlinear and the viscous effects are fully represented in Eq. (3); the turbulent viscosity is essentially based on the algebraic Baldwin–Lomax turbulence model and its extension (Valkov, 1997). The steady flow employed is a solution of the Navier–Stokes equations. The time average of the disturbance flow $(\overline{\Delta u}, \overline{\Delta p})$ is nonvanishing so that the time-averaged flow differs from the steady flow.

A fractional time-stepping procedure, using fully spectral expansion in the spanwise direction and spectral-element expansion in the blade-to-blade plane, is employed to solve Eq. (3). The computational domain is appropriately divided into a number of regularly sized regions, followed by a high-order expansion of the flowfield within each region to achieve both geometric flexibility and high accuracy. The computational method employed here constitutes an extension of high-order techniques based on time-accurate spectral-element techniques for direct simulation of viscous flows (Patera, 1984; Tan, 1989; Renaud, 1991). The basis function used in the spectral expansion is a Chebyshev polynomial.

The use of the disturbance form of the Navier–Stokes Eq. (3) offers several advantages in terms of isolating and manipulating specific aspects of blade row interaction. In particular, the unsteady flow obtained in each computational experiment is completely defined by the following two inputs:

1 A representative disturbance profile from the upstream rotor (e.g., tip leakage vortex) at the inlet of the stator. The parameters of this disturbance (e.g., displacement thickness) can be held constant or varied independently of other parameters.

2 A steady flow in the stator, obtained beforehand at given operating conditions. Aspects of the steady flow (such as loading, three dimensionality or presence of boundary layers) can be precisely controlled or altogether eliminated to reveal the role of a specific mechanism (e.g., boundary layer interaction) in altering the stator performance.

The steady flow as defined in (2) above can be obtained using any reliable steady-state Navier–Stokes solver. Here the steady-state solver as described by Adamczyk et al. (1990) and Khalid (1995) is used.

Details of the numerical techniques, their assessments and validations against known solutions and measurements can be found in Valkov (1997).

Unless otherwise stated, lengths are nondimensionalized by axial chord, velocities by mean axial velocity, times by blade throughflow time (axial chord/mean axial velocity), and pressure by inlet dynamic head.

4.3 Representation of Inlet Disturbances. *Rotor wakes* are represented by a Gaussian velocity defect profile in the rotor frame. The profile is characterized by a peak relative velocity defect A_r and by a 99 percent velocity thickness t_w. In a first set of computations, A_r and t_w are kept steady in time but varied from experiment to experiment in a manner representative of different degrees of "mixedness" of a baseline LSRC rotor wake at nominal loading (Table 1). This approximates the effect of changing the axial separation between blade rows.

In the second set of computational experiments, the wake defect

Table 1 Set of wake defects and thickness for wake–stator interaction calculations

A_r (%)	12	25	37	50	65
t_w (chord)	0.33	0.20	0.15	0.12	0.10

is varied sinusoidally in time with a time period ranging from $\frac{1}{7}$ to 2 times the rotor blade passing period.[1] This allows one to assess the role of velocity fluctuations within the wakes on stator time-average performance.

Rotor tip leakage (TL) vortices are represented as a core of steady, slowly swirling low-energy fluid. Two TL vortices are used in the computational experiments: "nominal" and "strong." The "nominal" vortex velocity profile is extracted from Khalid's (1995) Navier–Stokes simulation of tip leakage flow in an isolated LSRC rotor at design loading with 3 percent tip clearance. The peak p_t defect in the nominal vortex core at the exit of the rotor is 45 percent of the local dynamic head. The core extends roughly over 60 percent of the blade-to-blade spacing and over 15 percent of the span.

The "nominal" and "strong" vortices differ by the magnitude of the velocity defect in the vortex core. For the strong vortex, this defect is scaled up by using a wake decay relationship proposed by Stauter et al. (1991). This scaling is employed to simulate the effect of reducing axial spacing.

Rotor streamwise (SW) vortices are represented by an exponential viscous core with a diameter of 15 percent of span and circulation of 0.45 cU_∞.

These disturbances assume a different form in the stator frames. This is due to the relative orientation between rotor and stator blade sections. In a compressor stage such as that of the LSRC, rotor and stator blades are approximately perpendicular. As a result, rotor disturbances associated with blockage (wakes, TL vortex core) appear as "jets" directed away from the suction surface and toward the pressure surface of the stator. On the other hand, crossflow disturbances in the rotor frame (SW vortex) appear to the stator as fluctuations in the plane of the blade. This is illustrated in Fig. 3.

4.4 Representation of Steady Flows. Four types of steady flow in the stator passage are considered:

- *Nominal* steady flow (denoted by "VD") at a flow coefficient of 0.45 and a Reynolds number of 247,000 (design). The midspan inlet flow angle is 46 deg, and the diffusion factor is 0.43.
- *High-loading* steady flow (denoted by "VH"), at a flow coefficient of 0.38, corresponds to that near the peak of the characteristic. At midspan, the inlet flow angle is 51 deg, and the diffusion factor is 0.52.
- *Embedded-stage* steady flow (denoted by "VS") has the same loading characteristics as "VD" flow, but is obtained using an inlet shear profile that is representative of the flow at the inlet of an embedded stator.
- *Inviscid* steady flow (denoted by "ID"), at the same flow coefficient as the nominal flow ("VD"), is irrotational, and thus free of loss, secondary flow and boundary layers.

4.5 Definition of Computational Experiments. The computational experiments are defined in terms of the inlet disturbances and steady flows. Three groups of computational experiments have been carried out. In the first, the wakes interact with a midspan section of the stator on a two-dimensional basis and at design point conditions; this serves to answer unresolved issues on the extent of wake recovery and the role of nontransitional boundary layer response. The second group of computational experiments serves to identify key loss-producing mechanisms associated with tip leakage and streamwise vortices. The third group of computational experiments explores the sensitivity of TL vortex interaction to steady-state operating parameters, characteristics of vortex structure, and axial spacing. Key results from the first group are described below, while those from the second and third group in Part 2.

5.0 Two-Dimensional Wake–Stator Interaction

This section examines the unsteady flow arising from the two-dimensional interaction of upstream wakes with a midspan section of the stator. The objective is to identify the mechanisms by which wakes influence time-averaged performance, and to quantify: (1) the role of nontransitional boundary layer response; (2) the importance of wake recovery; and (3) the effect of fluctuations within the wakes.

Two series of computational experiments are carried out at a design flow coefficient of 0.45, Reynolds number of 247,000. The first series consists of five computational experiments, using the same wake at different degrees of "mixedness." In these experiments, the wake relative defect A_r and wake thickness t_w at the inlet of the computational domain are varied as shown in Table 1 (but kept steady in time). This series of experiments shows the effect of changing the blade row axial spacing (but ignores the change in potential effect).

In the second series of experiments, the wake has constant ensemble-averaged properties, but the defect is sinusoidally varied in time at a fraction of the blade passing frequency. This is a *simplified representation* of wake fluctuations seen in the data (Kotidis and Epstein, 1991; Brookfield and Waitz, 1996).

5.1 Unsteady Flow Features for Steady Wakes. The disturbance flow can be described in terms of disturbance vorticity $\Delta\omega$, defined as the difference in vorticity between the unsteady flow and the steady flow. The instantaneous disturbance vorticity field is shown in Fig. 4 for baseline 25 percent wakes. The wakes are essentially transported in the manner put forth by Smith (1966). Individual wake segments are stretched. Their SS and PS end travel at different speed, and leave the stator with a shift relative to the other wakes. The stronger wakes are characterized by a more pronounced migration. Figure 4 also shows vortex shedding from the trailing edge and nontransitional vortical disturbances in the boundary layer; the suction side boundary layer disturbances (referred to as BLDs) are the leading source of passage loss change.

The BLDs seen in wake interaction calculations have a characteristic structure. Each BLD originates on the leading edge at the moment of wake interception. It is composed of two thin regions of high negative and positive shear, respectively. These regions are lifted away from the suction surface by the wake, and are convected along the edge of the boundary layer. Computational experiments reported in Valkov and Tan (1995) show that these

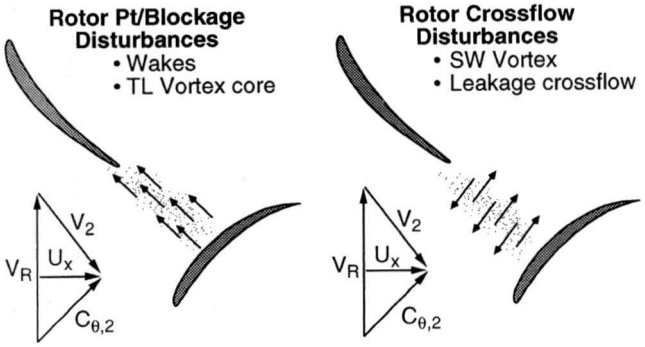

Fig. 3 Two generic types of disturbances perceived by a downstream blade row: normal "jets" (relative total pressure defect/blockage in rotor frame) and planar perturbation (crossflow disturbances in rotor frame)

[1] The authors are grateful to Professor Waitz of MIT Gas Turbine Laboratory for suggesting this calculation.

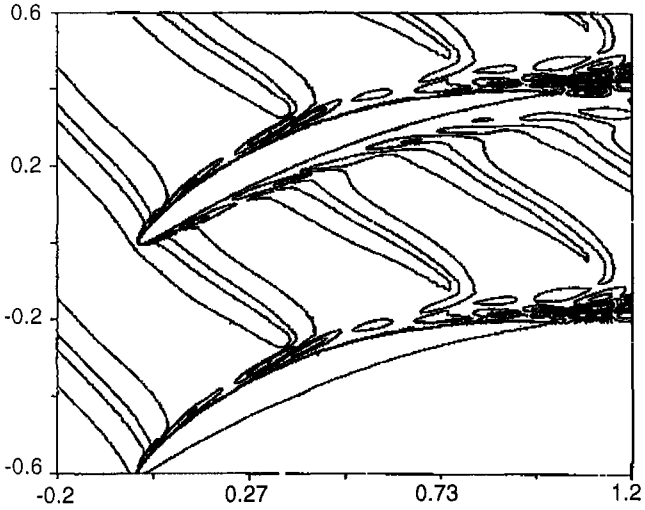

Fig. 4 Isocontours of disturbance vorticity at instant between wake interceptions; Re = 247,000

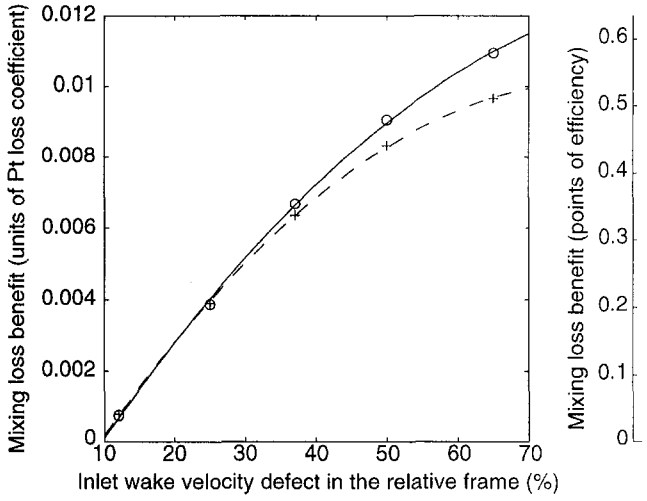

Fig. 6 Mixing loss benefit ΔL_m from processing of rotor wakes by stator (ϕ = 0.45, ψ = 0.65, Re_s = 2.47 × 10^5) associated with wake-blade boundary layer interaction: circles + solid line from Navier–Stokes solutions; crosses + dash line from wake transport model

vortical disturbances originate from displacement of the boundary layer vortex filaments under the suction effect of the wakes, while those on pressure surface is a result of wake jet directed toward it. A simplified model based on distortion of boundary layer vortex could describes the balance between transport of disturbance vorticity $\Delta\omega$, and "production" from convective redistribution of steady flow boundary layer fluid under the effect of a transverse velocity disturbance ΔV_n. The model helps explain why: (*a*) BLDs are primarily produced in the boundary layer/bulk flow interface over the foremost part of the blade, and (*b*) the primary BLDs contain negative disturbance vorticity. A loss model based on similar premise (see appendix) captures the parametric trend (see Fig. 5) in the time-averaged passage loss.

5.2 Time-Averaged Effects on Performance for Steady Wakes. Interaction with constant-strength wakes has two opposite effects on stator loss. First, wakes cause the time-averaged passage loss to increase by an amount denoted as ΔL_p. This increase (Fig. 5) is small for the 25 percent (baseline-spacing) wakes but becomes appreciable for the 50 percent (close-spacing) wakes. However, mixing the unsteady flow leaving the stator entails less loss than mixing the wakes prior to the stator. The resulting loss benefit, ΔL_m, shown in Fig. 6, is relatively small for the 25 percent wakes, but becomes important for the 50 percent wakes. This benefit is due to a reduction of the nonuniform velocity in the wake. The computed magnitude of ΔL_m is in accord with the simplified kinematic model of wake transport and recovery (dashed line in Fig. 6) given below. In the range of wake defects examined, the benefit from wake recovery ΔL_m outweighs the passage loss increase ΔL_p. Consequently, the net effect of wakes on loss, $\Delta L_n = \Delta L_p + \Delta L_m$, is beneficial.

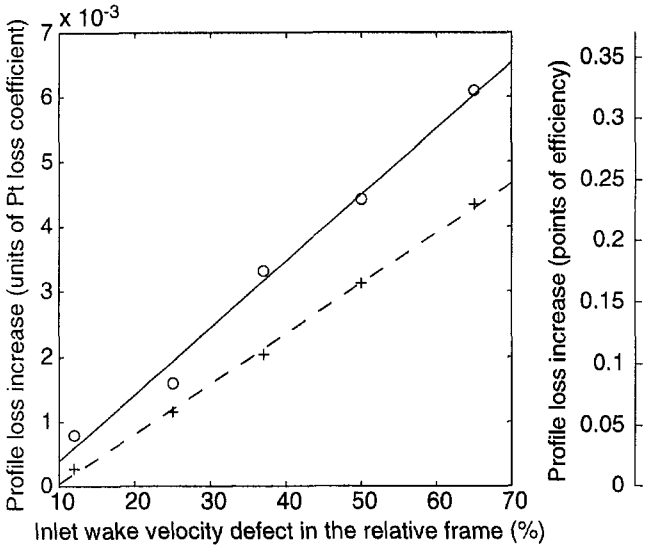

Fig. 5 Increase in time-averaged stator passage loss ΔL_p (ϕ = 0.45, ψ = 0.65, Re_s = 2.47 × 10^5) associated with wake-blade boundary layer interaction: circles + solid line from Navier–Stokes solutions; crosses + dash line from boundary layer distortion model

5.3 Causal Mechanisms for Changes in Performance. Computed results (Valkov, 1997) indicate that the instantaneous velocity profiles in the blade-to-blade direction on the leading and trailing edge planes suggest that the wakes are strongly attenuated during their transport through the stator in terms of velocity and thickness. This is the principal cause for the mixing loss benefit ΔL_m. In principle, wake attenuation is the result of two processes: reversible recovery (Smith, 1966) and irreversible mixing. Only the first process is beneficial. The computed results indicate that most of the wake energy is recovered. This finding can be explained by noting that recovery generally occurs over a shorter length scale than wake turbulent diffusion.

Recovery Length Scale. An approximate expression for mixing loss benefit (Smith, 1966; Adamczyk, 1996; Valkov, 1997) is:

$$\Delta L_m \cong (1 - a_r^2)\Delta L_i \tag{4}$$

where ΔL_i is the mixing loss of the wake at the inlet, and a_r is an attenuation factor given by the stretching of the wake segments l_i/l_e (this expression captures the computed mixing loss benefit, see Fig. 6). Physically, a_r is essentially a function of the flow turning in the passage; for a typical stator, most of the wake energy is recovered over a distance of 0.25 to 0.33 chords. For instance, in the present stator the flow turns by 10 deg over the first 0.2 chords and about one-half of the wake energy is recovered within this distance.

Diffusion Length Scale. The good agreement between the inviscid recovery model and the Navier–Stokes results in Fig. 6 implies that reversible recovery attenuates the wake defect quite rapidly, and thus outcompetes turbulent diffusion for the energy in the wake. For this reason, wake diffusion is not a significant loss mechanism over the range of wake defects considered (12–65

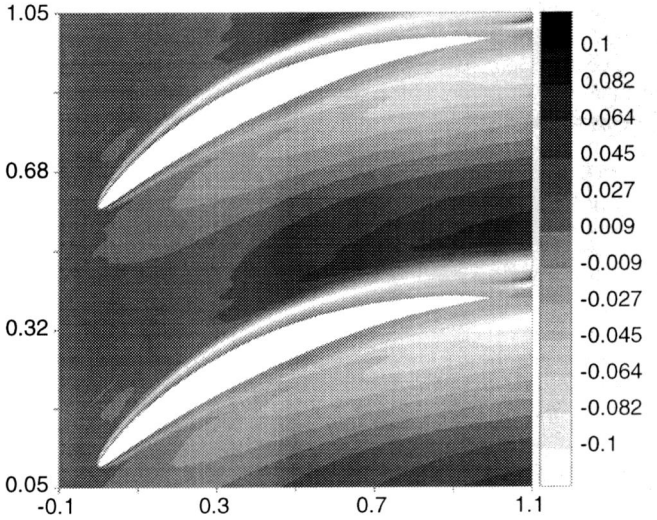

Fig. 7 Isocontours of time-averaged total pressure difference ΔC_t between unsteady and reference steady flows. Note high-loss band over stator suction surface.

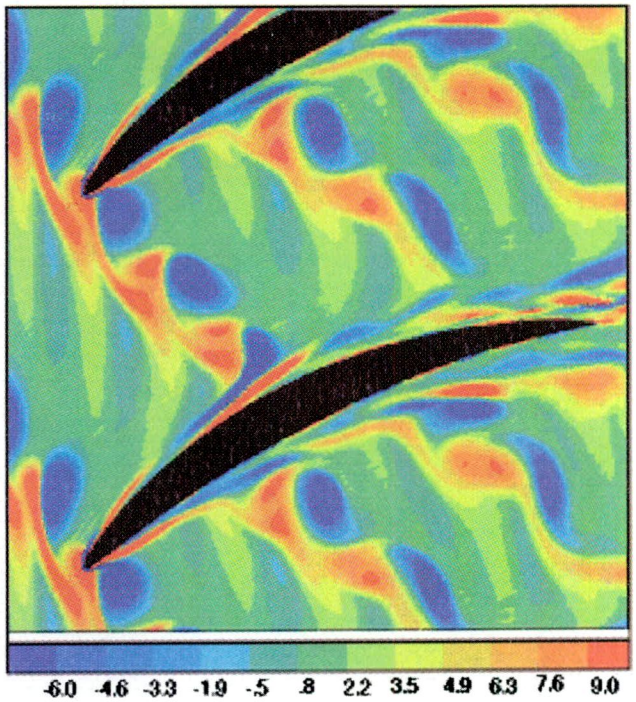

Fig. 8 Instantaneous contours of disturbance vorticity in simulation with time-varying wake defect at $T_i/T_p = 0.4$

percent). Most of the wake energy is recovered reversibly. As shown below, boundary layer response is the leading cause for the observed passage loss increase.

5.3.1 Boundary Layer Response. Regions of increased passage loss can be identified by examining the time-averaged total pressure difference ($\overline{\Delta C_t}$) in Fig. 7. This quantity is equivalent to the time and mass-averaged total pressure flux ($\overline{\Delta u C_t}$) for computing loss. Figure 7 shows two features. First, two regions of high and low $\overline{\Delta C_t}$, respectively, develop in the aft part of the passage. Second, there is a thin band of significant low-$\overline{\Delta C_t}$ over the suction surface. This band coincides with the trajectory of the BLDs shown in Fig. 4. These total pressure changes are due to the redistribution of passage vorticity on a time-averaged basis, denoted by $\overline{\Delta\omega}$. The connection between $\overline{\Delta C_t}$ and vorticity redistribution is embodied in following modified Crocco's equation:

$$\frac{\partial \overline{\Delta C_t}}{\partial n} \approx -2U\overline{\Delta\omega}$$

The largest passage loss changes occur over the suction surface of the stator that encompasses the vorticity fluctuations due to the distortion of the boundary layer vortical filaments by the "jet" velocity associated with the upstream wakes.

In physical terms, the "suction" effect of the wake transports low total pressure boundary layer fluid from near the wall toward regions of higher mass flux. Mass-averaged total pressure flux thus increases, and so do the time-averaged passage loss. This process is essentially convective in nature. Its effect on loss can be approximated by a relatively simple model, based on vorticity kinematics (see appendix):

$$\Delta L_p \approx \frac{6}{U}\int_{LE}^{TE} \times \overline{\Delta V}\frac{dL_{p,s}}{dx}\,dx \approx \frac{2\Delta V_n}{\cos\theta_1} L_{p,s}$$

which states that the time-averaged increase in passage loss under the effect of a "jet" disturbance depends upon the steady flow passage loss $L_{p,s}$, and is proportional to the time-averaged transverse velocity disturbance ΔV_n at the edge of the boundary layer. The latter is roughly proportional to the wake displacement thickness at the inlet of the stator and to the wake reduced frequency. As Fig. 5 shows, the model compares reasonably with the Navier–Stokes simulations and captures the linear trend in the CFD results.

5.3.2 Impact on Time-Averaged Pressure Rise Across Stator. Upstream wakes cause the pressure rise coefficient to increase by 1 to 3 percent of steady value (for wake relative velocity defect of 30 to 60 percent). The increase is modest, and is principally a consequence of a loading augmentation at leading edge. This augmentation is a time-averaged effect of the pressure pulses associated with leading edge intercepting the wakes.

5.4 Effects of Unsteady Fluctuations Within Wakes. Experimental data show temporal fluctuations of velocity within compressor wakes. These fluctuations may be a substantial fraction of the wake velocity defect. Thus, the second series of computational experiments assesses the role of such fluctuations on rotor wake–stator interaction. Two specific questions are addressed: (1) Are the two mechanisms identified still valid in the presence of a time-varying wake velocity defect; and (2) What is the effect on performance relative to the "ensemble-averaged" situation?

The wakes used for this purpose have the same "ensemble-averaged" profile and properties (33 percent wake relative defect, wake thickness of 0.15 at midgap, axial gap of 0.2 chords). For each wake, the defect is sinusoidally varied in time with an amplitude equal to the "ensemble-averaged" value, and with a time period T_i ranging from $\frac{1}{7}$ to 2.0 times the blade passing period T_p. The choice of amplitude is representative of fluctuations seen near the rotor trailing edge (Brookfield and Waitz, 1996). The ratio T_i/T_p takes fractional values ensuring that a fixed point on the blade does not experience the same disturbance at every interaction. Small T_i/T_p ratios (1/7–3/7) constitute a simplified representation of measured wake fluctuations (Kotidis and Epstein, 1991; Brookfield and Waitz, 1996) while large ratios (4/3–2) are used to bound the time scale.

5.4.1 Unsteady Flow Features. Figures 8 and 9 illustrate the typical vortical structure of the unsteady flowfield for T_i/T_p (wake fluctuation time scale/interaction time scale) with values of 0.4 and 2. Thus T_i/T_p influences the dynamics of the wake during its transport through the stator. Computed results indicate the existence of three distinct regimes: low-frequency ($T_i/T_p \geq 1.3$) intermediate-frequency ($0.2 \leq T_i/T_p \leq 1.3$), and high frequency ($T_i/T_p \leq 0.2$) fluctuations. For high-frequency fluctuations, the individual vortices comprising the wake appear to coalesce into a steady wake, transported through the stator in the same manner

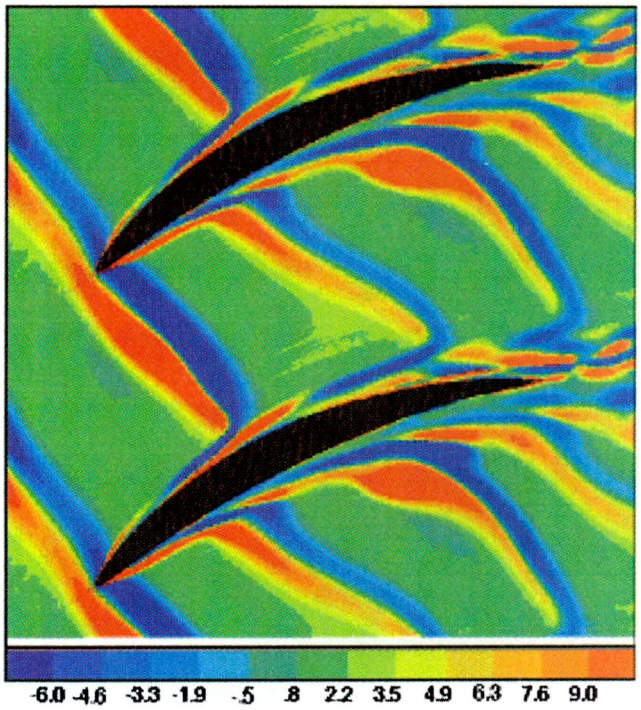

Fig. 9 Instantaneous contours of disturbance vorticity in simulation with time-varying wake defect at $T_i/T_p = 2.0$

described above. For low-frequency fluctuations, the length scale over which wake properties vary is larger than the blade-to-blade spacing, and the individual wake segments are also transported as described above (Fig. 9). For intermediate frequencies, however, the wake fluid forms passage vortices that persist far downstream (Fig. 8). Boundary layer disturbances (BLDs), similar to those seen with ensemble-averaged wakes, are present over the suction surface for all frequencies.

5.4.2 Effect of Unsteady Wake Fluctuations on Loss. Figure 10 shows the net loss change for the stator in the presence of fluctuating wakes, and compares it to that obtained for an ensemble-averaged wake. It is apparent that the timescale ratio T_i/T_p has an important effect on the amount of benefit to be expected from wake interaction. In the low-frequency regime, fluctuating and ensemble-averaged wakes have basically the same impact on loss. This is because the length scale over which wake properties vary is larger than the local scales over which the mechanisms identified in Section 5.3 operate. In the high-frequency regime, fluctuating and ensemble-averaged wakes also have similar effects on loss, although the latter produce somewhat higher benefit. This is due to the coalescence of small vortices, which effectively smooths out variations along the wake. However, there is some loss associated with the coalescence, which reduces the benefit from interaction slightly (Valkov, 1997). In the intermediate-frequency regime, fluctuating wakes have a different effect from that of ensemble-averaged wakes. In this regime, wake interaction is detrimental for stator performance, albeit by a small amount. This is due to the formation of passage vortices (Fig. 8), which prevent recovery of the wake energy.

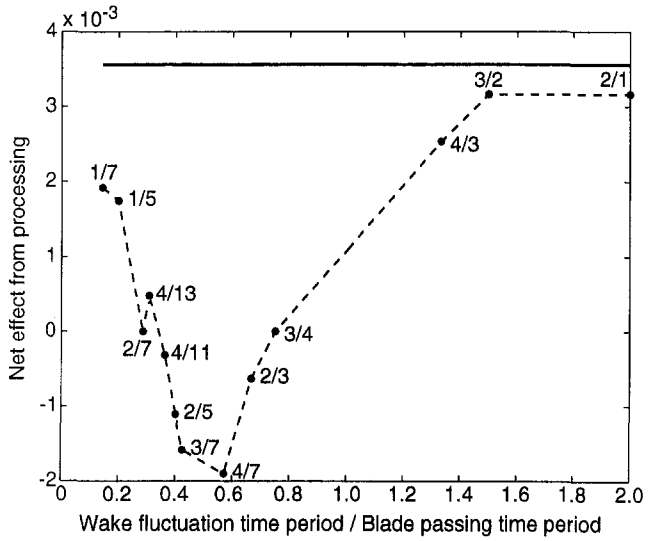

Fig. 10 Net loss effect ΔL_n from wake interaction for various values of the time scale ratio parameter T/T_p shown next to data points; solid line denotes level of ΔL_n for interaction with a steady wake; circles + dashed line for fluctuating wake with same "ensemble-averaged" properties (A_r = 0.33, t = 0.15, ϕ = 0.45, ψ = 0.65, Re = 2.47 × 10^5).

6.0 Summary and Conclusions

Three issues have been addressed: (1) the role of nontransitional boundary layer response for loss, (2) the importance of wake recovery, and (3) the effect of wake fluctuations.

- There are two opposing mechanisms by which ensemble-averaged wakes influence performance: reversible recovery and boundary layer distortion. In a stage geometry such as the GE/LSRC, the benefit from reversible recovery is relatively small at typical axial spacings, but becomes significant with tightly coupled blade rows. The recovery occurs in the manner proposed by Smith (1966). Almost all of the kinetic energy of the ensemble-averaged wakes is recovered.
- Boundary layer distortion leads to an increase in passage loss that partly reduces the benefit from reversible recovery. In the LSRC geometry, this loss increase is relatively small at typical axial spacings, but becomes nonnegligible with tightly coupled blade rows. The loss increase is due to "lifting" of high-loss boundary layer vortical fluid into regions of higher mass flow by the "suction" effect of the wakes. A kinematic model of boundary layer vortical filament displacement can capture reasonably well the amount of increase, and shows that it depends on the steady loss and on the wake displacement thickness.
- For the stator configuration under consideration, the recovery benefit is larger than the passage loss increase. As a result, there is a small net benefit from wake interaction at typical axial spacings, and a moderate benefit with tightly coupled blade rows. Only about 0.25 points of the 1 point efficiency gain observed by Smith (1970) in the LSRC can be attributed to rotor wake–stator interaction alone.
- The level of benefit from wake recovery depends on the frequency of fluctuations in the wake, expressed as a time scale ratio T_i/T_p between fluctuation period T_i and blade passing period T_p. There is an interval of T_i/T_p where the wake forms discrete vortices and no recovery occurs. Outside this interval, wake interaction is beneficial and can be captured using an ensemble-averaged form of the wakes. Experimentally observed values of T_i/T_p appear to be between 1/8 and 1/3. This range partly overlaps with the interval where recovery does not occur.

Acknowledgments

Support for this work was provided by NASA Lewis Research Center under Grants NAG3-660 and NAG3-1679, Dr. John Adamczyk as technical monitor. We would also like to thank John Adamczyk, N. A. Cumpsty, M. Graf, E. M. Greitzer, F. E. Marble, and I. A. Waitz for helpful comments and discussions. Additional computational resources have also been provided by NASA Lewis Research Center LACE Cluster of computers and this support is

gratefully acknowledged. The critical comments of the reviewers for improving the manuscript are also gratefully acknowledged.

References

Adamczyk, J. J., Celestina, M. L., Beach, T. A., and Barnett, M., 1990, "Simulation of Three-Dimensional Viscous Flow Within a Multistage Turbine," ASME JOURNAL OF TURBOMACHINERY, Vol. 112, pp. 370–376.

Adamczyk, J. J., 1996, "Wake Mixing in Axial Flow Compressors," ASME Paper No. 96-GT-029.

Brookfield, J. B., and Waitz, I., 1996, private communication, MIT.

Cumpsty, N. A., 1989, *Compressor Aerodynamics,* Longman Group Ltd.

Dawes, W. N., 1994, "A Numerical Study of the Interaction of a Transonic Compressor Rotor Overtip Leakage Vortex With the Following Stator Blade Row," ASME Paper No. 94-GT-156.

Denton, J. D., 1993, "Loss Mechanisms in Turbomachines," ASME JOURNAL OF TURBOMACHINERY, Vol. 115, pp. 621–656.

Deregel, P., and Tan, C. S., 1996, "Impact of Rotor Wakes on Steady State Performance of Compressor," ASME Paper No. 96-GT-253.

Dorney, D. J., and Sharma, O. P., 1996, "Evaluation of Flow Field Approximations for Transonic Compressor Stages," ASME JOURNAL OF TURBOMACHINERY, Vol. 119, pp. 445–451.

Hodson, H. P., 1985, "An Inviscid Blade-to-Blade Prediction of Wake-Generated Unsteady Flow," ASME JOURNAL OF TURBOMACHINERY, Vol. 107, pp. 337–344.

Howard, M. A., Ivey, P. C., Barton, J. P., and Young, K. F., 1994, "Endwall Effects at Two Tip Clearances in a Multistage Axial Flow Compressor With Controlled Diffusion Blading," ASME JOURNAL OF TURBOMACHINERY, Vol. 116, pp. 635–647.

Kerrebrock, J. L., and Mikolajczak, A. A., 1970, "Intra-Stator Transport of Rotor Wakes and Its Effect on Compressor Performance," ASME *Journal of Engineering for Power,* Vol. 92, pp. 359–368.

Khalid, S. A., 1995, "The Effects of Tip Clearance on Axial Compressor Pressure Rise," Doctoral Thesis, Department of Mechanical Engineering, MIT.

Kotidis, P. A., and Epstein, A. H., 1991, "Unsteady Radial Transport in a Transonic Compressor Stage," ASME JOURNAL OF TURBOMACHINERY, Vol. 113, pp. 207–218.

Mikolajczak, A. A., 1977, "The Practical Importance of Unsteady Flow," in: "Unsteady Phenomena in Turbomachinery," AGARD CP-144, North Atlantic Treaty Organization.

Nikolaou, I. G., Giannakoglou, K. C., and Papailiou, K. D., 1996, "Study of a Radial Tip Clearance Effects in a Low-Speed Axial Compressor Rotor," ASME Paper No. 96-GT-37.

Patera, A. T., 1984, "A Spectral Element Method for Fluid Dynamics: Laminar Flow in a Channel Expansion," *Journal of Computational Physics,* Vol. 54, No. 3.

Poensgen, C., and Gallus, H. E., 1991, "Three-Dimensional Wake Decay Inside of a Compressor Cascade and Its Influence on the Downstream Unsteady Flow Field: Part I—Wake Decay Characteristics in the Flow Passage," ASME JOURNAL OF TURBOMACHINERY, Vol. 113.

Renaud, E. W., 1991, "Secondary Flow, Total Pressure Loss and the Effect of Circumferential Distortions in Axial Turbine Cascades," Doctoral Thesis, Department of Aeronautics and Astronautics, Massachusetts Institute of Technology.

Silkowski, P., 1995, "Measurements of Rotor Stalling in Matched and Mismatched Multistage Compressor," MIT Gas Turbine Laboratory Report No. 221.

Smith, L. H., 1996, Discussion of ASME Paper 96-GT-029, Birmingham, United Kingdom.

Smith, L. H., 1970, "Casing Boundary Layers in Multistage Axial Flow Compressors," *Flow Research on Blading,* L. S. Dzung, ed., Elsevier Publishing Co.

Smith, L. H., 1966, "Wake Dispersion in Turbomachines," ASME *Journal of Basic Engineering,* Vol. 88.

Stauter, R. C., Dring, R. P., and Carta, F. O., 1991, "Temporally and Spatially Resolved Flow in a Two-Stage Axial Flow Compressor: Part 1—Experiment," ASME JOURNAL OF TURBOMACHINERY, Vol. 113, pp. 219–226.

Storer, J. A., and Cumpsty, N. A., 1991, "Tip Leakage Flow in Axial Compressors," ASME JOURNAL OF TURBOMACHINERY, Vol. 113, pp. 252–259.

Tan, C. S., 1989, "A Multi-Domain Spectral Computation of Three-Dimensional Laminar Horseshoe Vortex Flow Using Incompressible Navier–Stokes Equations," *Journal of Computational Physics,* 85, No. 1.

Valkov, T., and Tan, C. S., 1995, "Control of the Unsteady Flow in a Stator Blade Row Interacting With Upstream Moving Wakes," ASME JOURNAL OF TURBOMACHINERY, Vol. 117, pp. 97–105.

Valkov, T., 1997, "The Effect of Upstream Rotor Vortical Disturbance on the Time-Average Performance of Axial Compressor Stators," Gas Turbine Laboratory Report No. 227, MIT.

Valkov, T., and Tan, C. S., 1999, "Effect of Upstream Rotor Vortical Disturbances on the Time-Averaged Performance of Axial Compressor Stators: Part 2—Rotor Tip Vortex/Streamwise-Vortex-Stator Blade Interactions and Implications on Design," ASME JOURNAL OF TURBOMACHINERY, Vol. 121, this issue, pp. 387–397.

Wisler, D. C., 1985, "Loss Reduction in Axial-Flow Compressors Through Low-Speed Model Testing," ASME *Journal of Engineering for Gas Turbines and Power,* Vol. 107, pp. 354–363.

Zierke, W. C., and Okiishi, T. H., 1982, "Measurement and Analysis of Total-Pressure Data From an Axial-Flow Compressor Stage," ASME *Journal of Engineering for Power,* Vol. 104, pp. 479–488.

APPENDIX

A Model for Boundary Layer Response to a Two-Dimensional Upstream Wake

This appendix describes a simplified model for evaluating the time-averaged passage loss associated with boundary layer distortion under the effect of the two-dimensional disturbance jet. In developing a model for calculating the increase in passage loss ΔL_p due to boundary layer distortion by the wake jet, we use the linearized two-dimensional form of the mechanistic relationship between total pressure loss and vorticity:

$$\Delta L_p \approx -6 \int\int v_s \omega_s \overline{\Delta\omega} dx dy \tag{A.1}$$

and the two-dimensional linearized inviscid form of the equation governing the disturbance vorticity in the flow. Such linearization is based on the observation that $|\Delta\omega| < |\omega|$ in the disturbed boundary layer region, contributing to increased loss in the CFD solution. The use of inviscid form of the vorticity equation is based on the observation that the response of the boundary layer to the wake is essentially an inviscid process. In addition, these equations are applied to a simplified representation of the suction side boundary layer, shown in Fig. A.1, that makes the problem of estimating ΔL_p tractable. This representation neglects the curvature of the surface, and assumes a thin boundary layer in which the streamwise variation of steady and disturbance flow quantities occurs on a much longer scale than the one associated with transverse variation. Thus, the equation for the disturbance vorticity is

$$\frac{\partial \Delta\omega}{\partial t} + U\frac{\partial \Delta\omega}{\partial x} + V\frac{\partial \Delta\omega}{\partial y} \approx -\Delta v \frac{\partial \Omega}{\partial y} \tag{A.2}$$

which governs the balance between production (right-hand side) and convective transport (left-hand side) of disturbance vorticity. It is to be noted that capital letters have been used to denote the steady flow velocity components (U, V) and vorticity Ω (see Fig. A.1). Equation (A.2) implies that disturbance vorticity is produced in regions of high steady flow vorticity gradient. For law-of-the wall profiles, $\partial\Omega/\partial y$ is positive and takes its largest value where the boundary layer is thinnest (leading edge), and at the "knee" of the velocity profile (near the edge of the boundary layer). This explains why the boundary layer vortical disturbances appear to be produced at the leading edge upon wake interception. Equation (A.2) also explains why these disturbances contain negative-sign spanwise vorticity.

Four additional simplifications need to be made. First, one may take $V = 0$ while retaining the essence of the mechanism that is being modeled (motion of boundary layer vortex filaments under the effect of ΔV). Second, to determine the change in loss due to the wake, only the time average of $\Delta\omega$ is required. Since Eq. (A.2)

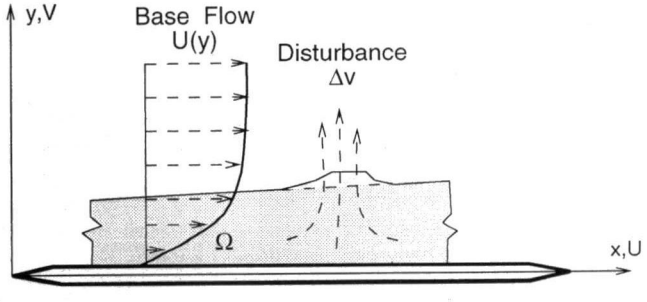

Fig. A.1 Simplified representation of boundary layer distortion under the effect of a wake jet. The boundary layer (BL) is approximated as a uniform sheet of spanwise vorticity with highest vorticity gradients at the knee of BL profile.

is linear, $\overline{\Delta\omega}$ can be obtained by first time-averaging the equation and then solving it. Time-averaging Eq. (A.2) yields:

$$\frac{d\overline{\Delta\omega}}{dx} \approx -\frac{\overline{\Delta v}}{U}\frac{d\Omega}{dy} \tag{A.3}$$

The third simplification consists in prescribing a simplified profile for Δv; at the surface it assumes a value 0 while at the edge of the boundary layer it assumes the value $v_n(t)$, the velocity imposed by the wake. It is thus reasonable to use a linear profile for Δv:

$$\overline{\Delta v} = \frac{y}{\delta}\Delta V_n \tag{A.4}$$

where δ is the thickness of the boundary layer, and ΔV_n the time-averaged transverse velocity imposed by the wake at the edge of the boundary layer.

The fourth simplification involves assuming a given profile for the steady flow boundary layer. The profile assumed here is linear, and one in which the boundary layer thickness varies as $\sqrt{x}$ (i.e., $\Omega \sim \Omega_{ref} x^{-1/2}$).

With these simplifications,

$$\overline{\Delta\omega} = -\frac{2y\Delta V_n}{\delta U} \times \frac{d\Omega}{dy} + \text{const} \tag{A.5}$$

The change in passage loss (Eq. (A.1)) now becomes

$$\Delta L_p = 6\frac{\Delta V_n}{U}\int_0^1 \times \frac{dL_{p,s}}{dx}\,dx \tag{A.6}$$

which states that the increase in profile loss due to the upstream wake-boundary layer interaction depends only on the chordwise distribution of profile loss of the steady flow, and is proportional to the average transverse velocity imposed by the wake on the edge of the boundary layer. This is a useful and insightful relationship that is not qualitatively affected by the foregoing assumptions. It can further be simplified by assuming a linear rate of increase of the steady flow loss. This yields

$$\Delta L_p \approx 2\frac{\Delta V_n}{U} L_{p,s} \tag{A.7}$$

which agrees to a reasonable extent with the CFD result.

Effect of Upstream Rotor Vortical Disturbances on the Time-Averaged Performance of Axial Compressor Stators: Part 2—Rotor Tip Vortex/ Streamwise Vortex–Stator Blade Interactions

T. V. Valkov
Shell International Gas Limited,
Shell Center,
London SE1 7NA United Kingdom

C. S. Tan
MIT Gas Turbine Laboratory,
Cambridge, MA 02139

In a two-part paper, key computed results from a set of first-of-a-kind numerical simulations on the unsteady interaction of axial compressor stator with upstream rotor wakes and tip leakage vortices are employed to elucidate their impact on the time-averaged performance of the stator. Detailed interrogation of the computed flowfield showed that for both wakes and tip leakage vortices, the impact of these mechanisms can be described on the same physical basis. Specifically, there are two generic mechanisms with significant influence on performance: reversible recovery of the energy in the wakes/tip vortices (beneficial) and the associated nontransitional boundary layer response (detrimental). In the presence of flow unsteadiness associated with rotor wakes and tip vortices, the efficiency of the stator under consideration is higher than that obtained using a mixed-out steady flow approximation. The effects of tip vortices and wakes are of comparable importance. The impact of stator interaction with upstream wakes and vortices depends on the following parameters: axial spacing, loading, and the frequency of wake fluctuations in the rotor frame. At reduced spacing, this impact becomes significant. The most important aspect of the tip vortex is the relative velocity defect and the associated relative total pressure defect, which is perceived by the stator in the same manner as a wake. In Part 2, the focus will be on the interaction of stator with the moving upstream rotor tip and streamwise vortices, the controlling parametric trends, and implications on design.

1.0 Introduction

In Part 1 the rotor wake–stator interaction problem was examined. In Part 2 the same framework of technical approach will be used to address the topic of rotor tip/streamwise vortex–stator interaction. The unsteady flow and performance changes in the stator interacting with upstream vortices are first examined for the case where the steady flow at design point is assumed inviscid, and then for steady flow representative of that in practical flow situations with boundary layers on solid surfaces. The results from these two cases can thus be contrasted to assess the role of blade surface boundary layer on tip leakage/streamwise vortex–stator interaction so that the following specific questions can be answered:

1 How does the boundary layer respond to rotor TL and streamwise vortices?
2 What are the resulting quantitative effects on stator performance at design?

This is followed by an assessment on the sensitivity of rotor tip leakage vortex interaction with stator to axial spacing, characteristics of vortex structure and stator steady-state operating parameters. The implications on compressor design and performance will be discussed. Finally, the overall key results and new findings from the two parts paper are summarized.

Please note that the Nomenclature is as listed in Part 1.

2.0 Rotor Tip Leakage/Streamwise Vortex–Stator Interaction on Inviscid Flow Basis

Two calculations, each using a different vortex, are carried out:

- *ID/SW:* Interaction with an upstream streamwise vortex (SW) with a core radius of 15 percent span and a circulation of 0.45 cU_∞; this vortex is introduced at a location 0.12 span away from the casing at the inflow boundary.
- *ID/TL:* Interaction with a tip leakage (TL) vortex, based on Khalid's (1995) computed flowfield at the exit of an isolated LSRC rotor at design loading and 3 percent tip clearance (Fig. 1).

The unsteady flows are obtained by means of a slip-free disturbance flow formulation[1] about an inviscid steady flow. Such an approach provides: (1) the means to determine how much of the tip vortex energy is recovered in the presence of turbulent diffusion; and (2) a basis against which results from the case of viscous flow can be compared to assess the effects of boundary layer response.

Contributed by the International Gas Turbine Institute and presented at the 43rd International Gas Turbine and Aeroengine Congress and Exhibition, Stockholm, Sweden, June 2–5, 1998. Manuscript received by the International Gas Turbine Institute February 1998. Paper No. 98-GT-313. Associate Technical Editor: R. E. Kielb.

[1] The disturbance flow has vanishing velocity component normal to solid surface but non-vanishing tangential component; the turbulent diffusion term has been retained in the disturbance flow.

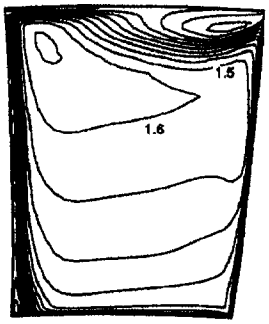

Fig. 1 Velocity contour at exit of LSRC rotor, tip clearance to chord ratio of 0.03, design point (Khalid, 1995)

2.1 ID/SW: Unsteady Flow Features

2.1.1 Transport of Vortex Core. As shown in Fig. 2, the SW vortex core is transported across the stator without significant change in shape. The vortex core is stretched by an amount (l_e/l_i = 1.7) in accord with the kinematic transport model for two-dimensional wakes (Adamczyk, 1996; Valkov, 1997). The vorticity in the core should be intensified in proportion to this stretching. The computed results in Fig. 3 show that at the inlet of the stator, the SW vortex core contains virtually no streamwise vorticity because the rotor and stator blades are approximately perpendicular. Farther downstream, however, a streamwise vorticity component appears and grows at the expense of the normal component. This is due to the change in angle between the bulk flow and the vortex core. Another consequence of the change in angle is the existence of two vortex cores at the exit of the stator. In addition to the SW vortex core, the only other vortical feature of significance is the shedding of spanwise and trailing streamwise vortices from the trailing edge. In the present case, the circulation around these vortices is 0.16 cU_∞, which is significant when compared to the circulation around the upstream vortex core itself (0.45 cU_∞). Therefore, the kinetic energy in the shed streamwise vortices is about one-fourth to one-third that of the incoming SW vortices. Thus, the contribution of three-dimensional trailing vortices to loss is substantially larger than that of two-dimensional shed vortices investigated by Fritsch (1992).

2.1.2 Pressure Fluctuations. SW vortex interaction leads to a distinctive pattern of static pressure fluctuations in the passage and on the blade surface, characterized by (1) a leading edge pressure pulse, and (2) a train of "tornado-like" regions of low static pressure sweeping over the blade surface. These are shown in Fig. 4. The pressure pulse appears near the casing at the moment of vortex interception. It can be attributed to the local disturbance velocity component normal to the blade. The time-averaged effect of this pulse is to unload the leading edge over the outer 15–20 percent span. The train of low-pressure regions sweeping the blade is a reflection of the low static pressure in the SW vortex core.

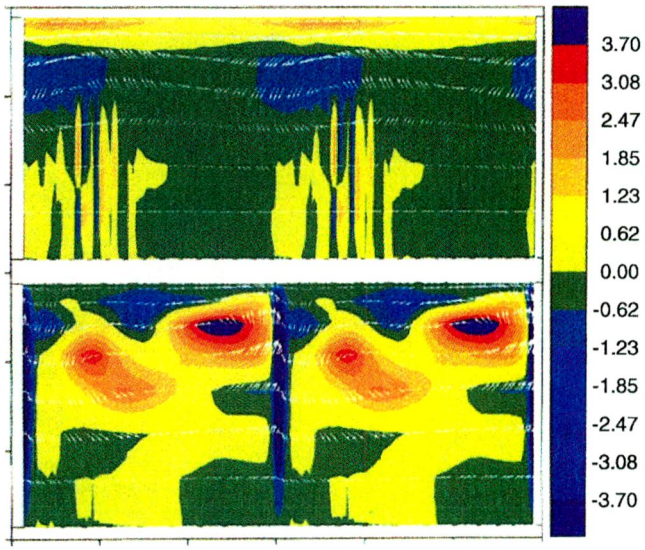

Fig. 3 Isocontours of streamwise vorticity on LE crossflow plane (top) and TE crossflow plane (bottom) extending over the outer quarter span of two stator passages; regions of $+|\Delta\omega|$ are vortex cores while bands of $-|\Delta\omega|$ along TE consist of shed vorticity

2.2 ID/SW: Impact on Time-Averaged Performance Changes. Overall, SW vortex interaction is detrimental for the stator performance, increasing the net loss by about 0.2 efficiency points. Approximately two-thirds of this loss increase is associated with the increase in secondary kinetic energy of the unsteady flow leaving the stator. The other third is due to turbulence mixing of the vortex.

The increase in secondary kinetic energy of the unsteady flow leaving the stator is associated with: (*a*) stretching of the SW vortex core, and (*b*) shedding of trailing vorticity from the TE of the stator blade. Vortex stretching is the dominant mechanism leading to performance deterioration. Figure 5 shows how vortex

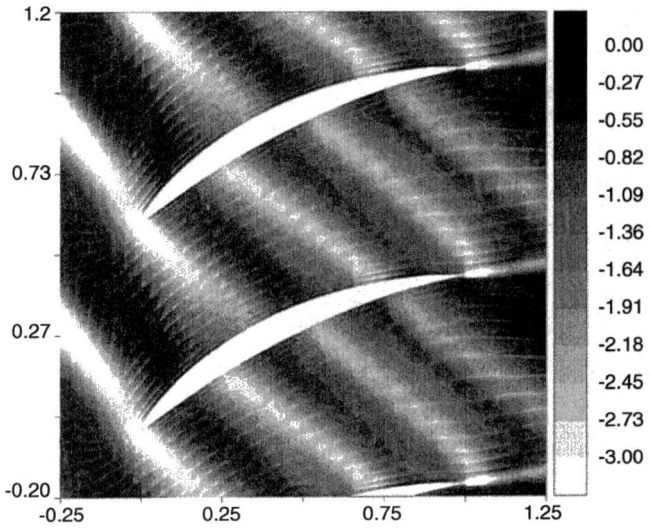

Fig. 2 Location of SW vortical fluid (regions of $-|\Delta\omega|$) in stator passage at moment of vortex interception

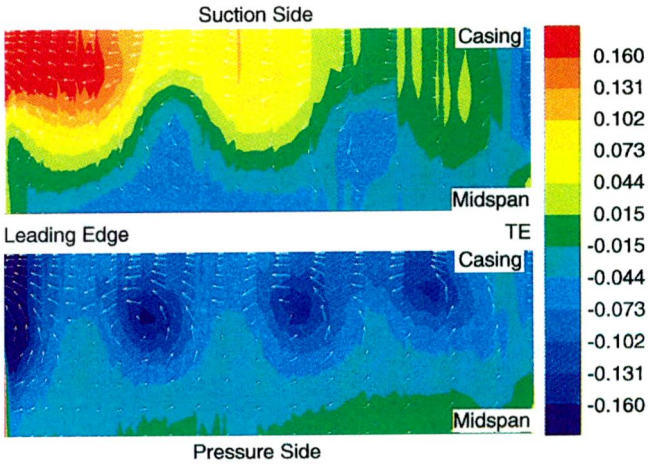

Fig. 4 Disturbance static pressure contours and disturbance velocity vectors on SS (top) and PS (bottom) at instant of wake interception

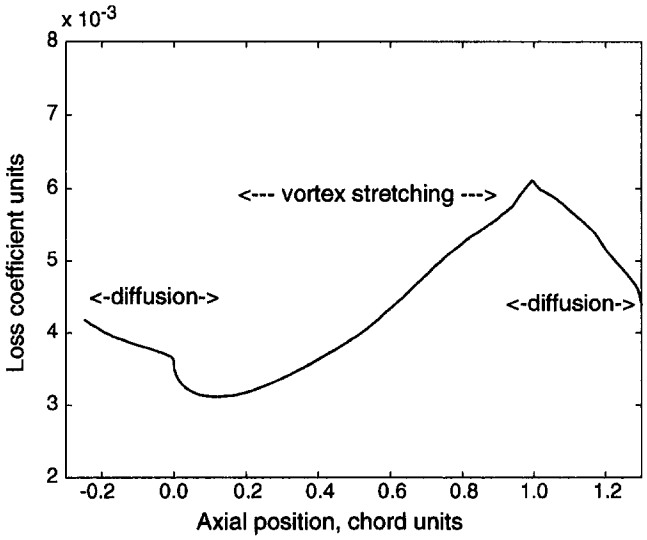

Fig. 5 Axial variation of time-averaged secondary kinetic energy of unsteady disturbance flow (LE at axial position 0, TE at 1)

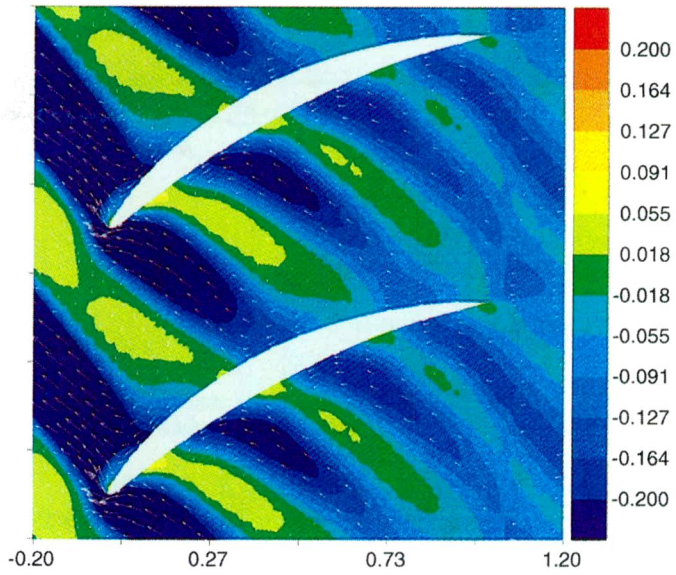

Fig. 7 Disturbance axial velocity isocontours and disturbance velocity vectors on blade-to-blade plane at 91 percent span (coinciding approximately with TL vortex core)

stretching in the stator causes the mixing-out loss of the vortex to increase within the blade passage; mixing out of the vortex causes a decrease ($x \leq 0.1$ or $x \geq 1.0$) while stretching causes an increase ($0.1 \leq x \leq 1.0$) in the secondary kinetic energy.

Processing of SW vortices also decreases the static pressure rise coefficient by about 3 percent. This coefficient is related to the axial force on the stator blade, which decreases because the pressure pulses from vortex interceptions decrease the leading edge loading on a time-averaged basis.

2.3 ID/TL: Unsteady Flow Features

2.3.1 Unsteady Velocity Field. The velocity disturbance associated with the tip leakage vortex is quite different from that of the streamwise vortex. At the inlet of the stator, the TL vortex appears as a core of axial velocity deficit and tangential velocity excess (see Fig. 6). In this sense, the incoming disturbance resembles a thick wake limited to the outer 15 percent of blade span.

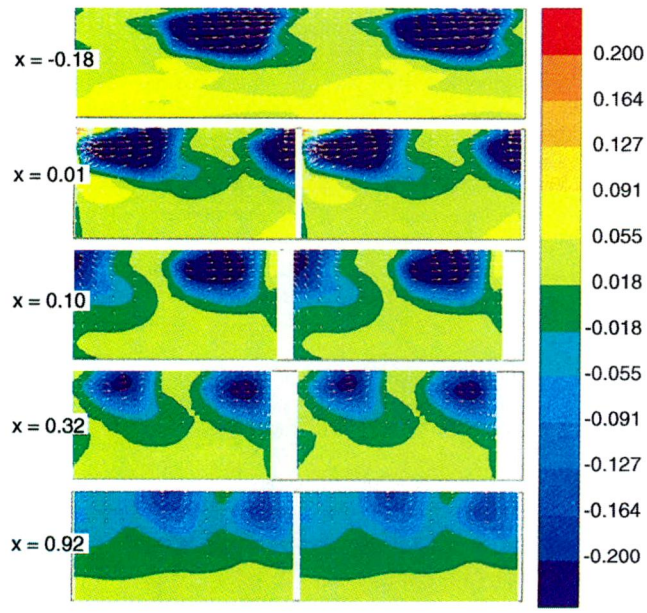

Fig. 6 Disturbance axial velocity isocontours and disturbance crossflow velocity vectors on successive crossflow planes (LE at $x = 0$, TE at $x = 1$) extending over outer third of span

Therefore, the TL vortex appears to the stator as a jet of fluid directed away from the suction surface toward the pressure surface. The overall shape of the jet changes little in time. The most significant aspects of the vortex transport appear to be: (*a*) the attenuation of the core velocity nonuniformity, and (*b*) the migration of vortical fluid toward the pressure surface. Both aspects can be appreciated in Fig. 7, which emphasizes the wakelike nature of the unsteady flow in the passage. The attenuation mechanisms shall be discussed in the next section. Figure 7 shows that the peak velocity disturbance in the vortex is attenuated by a factor of three between the inlet and the exit of the stator. This attenuation is somewhat higher than that for wake (Part 1), and indicates the recovery of the vortex energy. The migration of vortical fluid is due to a tangential velocity excess of the jet in the stator frame.

2.3.2 Structure and Recovery of Vortex. The vortical structure of the tip vortex follows from its appearance as a jet. At the inlet, the normal vorticity component is similar to that of a wake, while the streamwise vorticity component appears as two opposite-sign layers in the tip region (see Fig. 8). To understand how the tip leakage flow is attenuated, it is useful to consider the normal and streamwise vorticity components separately. The disturbance velocity associated with the normal vorticity component is attenuated in essentially the same manner as a wake (i.e., in proportionality to the stretching of vortex). The disturbance velocity associated with the streamwise vorticity component is attenuated in a different manner, illustrated schematically in Fig. 8. The slowing of the flow in the stator leads to "shortening" of the streamwise vortex filaments. This leads to the attenuation of streamwise vorticity component itself. In analogy with a line vortex going through a diffuser, the attenuation of streamwise vorticity is proportional to the vortex stretching l_i/l_e. Thus this analogy implies that the recovery of the tip vortex scales in the same manner as that of wakes (Part 1). This is an important finding, implying that: (1) processing of tip vortices in a stator passage is beneficial; and (2) most of the kinetic energy of the vortex can be recovered in the stator.

The attenuation of streamwise vorticity is the most notable aspect of the unsteady vortical flow in the ID/TL flow situation. In contrast to SW vortices, which appear as "tornadolike" disturbances sweeping the surface of the blade, TL vortices appear as jets of fluid directed toward the pressure side of the stator.

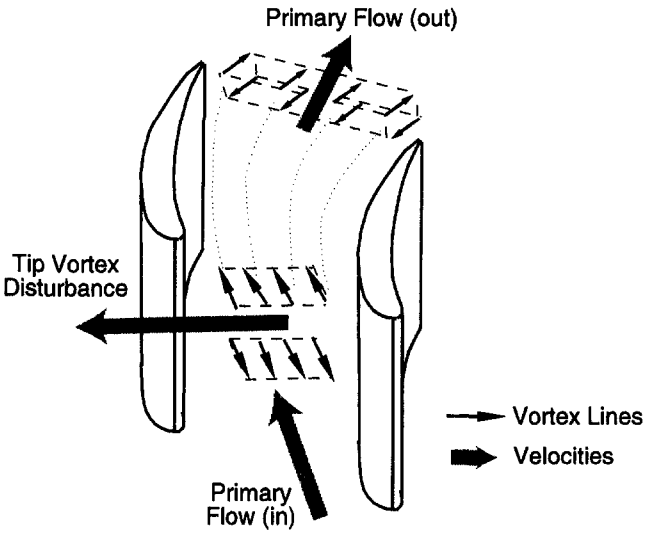

Fig. 8 Schematic model of recovery associated with streamwise vorticity components in incoming tip vortex

2.4 ID/TL: Impact on Time-Averaged Performance Changes. Overall, TL vortex interaction is beneficial for stator performance. The gain in efficiency is about 0.25 points relative to the mixing-plane steady flow approximation. This gain is due to the reversible recovery of energy in the vortex, which scales in the same manner as that of a two-dimensional wake. Most of the kinetic energy in the vortex core is recovered in a reversible manner. This can be explained by the argument developed for two-dimensional wakes: Recovery occurs over shorter length scales than diffusion.

Time-averaging of p_t fluctuations at the inlet of the stator yields a distribution that is nearly uniform circumferentially. However, the computed results (Valkov, 1997) show a core of low-p_t fluid in the pressure side casing corner at the exit of the stator. This "segregation" of total pressure correlates to within a few percent with the time-averaged redistribution of normal vorticity, and is the result of tangential migration of vortical fluid. This redistribution of total pressure in the flow can be viewed as a three-dimensional equivalence to Kerrebrock and Mikolajczak's (1970) total temperature segregation of rotor wakes.

2.5 Summary. It was found that the effects associated with SW and TL vortices interacting with a stator are markedly different:

- Most of the TL vortex energy is recovered in the stator. In the ID/TL case; this yields a 0.25 point efficiency enhancement with respect to the mixed-out steady flow approximation.
- Processing of SW vortices by stator is detrimental for stator performance (by 0.20 efficiency points for the ID/SW flow situation).
- Recovery of the TL vortex energy is due to the stretching of TL vortex. The recovery process is three-dimensional in nature (it involves compression of streamwise vortical filaments) but scales in the same way as two-dimensional wake recovery.
- Stretching of the SW vortex core is the primary reason for efficiency degradation in the ID/SW flow situation. This is in agreement with the result of Denton (1993). While unsteady vortex shedding might not be important in a two-dimensional flow (Fritsch, 1992), this is not the case for the present three-dimensional flow. In the ID/SW flow situation, shedding of streamwise vorticity from the TE of the blades is a noticeable source of loss.

3.0 Rotor Tip Leakage/Streamwise Vortex–Stator Interaction on Viscous Flow Basis

This section examines the unsteady flow and performance changes in stator subjected to the following two types of upstream vortices at design point loading and Reynolds number ($\phi = 0.45$, $\mathrm{Re} = 2.47 \times 10^5$):

- Nominal tip leakage (TL) vortex, based on Khalid's (1995) computed flowfield at the exit of an isolated LSRC rotor at design loading and 3 percent tip clearance (Fig. 1). This computational experiment is referred to as VD/TL.
- Simple streamwise vortex (SW) with a core radius of 15 percent span and a circulation of 0.45 cU_∞ in the rotor frame. This computational experiment is referred to as VD/SW.

3.1 VD/TL: Unsteady Flow Features. The pressure fluctuations induced by the upstream tip leakage vortex are similar in nature and amplitude to those seen in the "inviscid" ID/TL, and appear primarily as an instantaneous increase of the loading on the leading edge in the stator tip region upon vortex interception.

3.1.1 Structure and Attenuation of Vortex Cores. In viscous flow, the vortex core velocity nonuniformity is still strongly attenuated in the stator. However, there are two differences with respect to the inviscid ID/TL flow situation:

1 Vortex core "filaments" closer to the casing are convected at a slower rate than those away from it. This leads to "skewing" of the TL vortex core on the crossflow plane; this "skewing" does not appear to be important as far as vortex energy recovery is concerned.
2 Migration of vortex fluid is relatively more pronounced because of a lower steady flow velocity in the VD/TL flow situation than that in the ID/TL flow situation. Therefore, the vortex fluid in VD/TL migrates closer to the pressure surface for the same distance traveled.

3.1.2 Nontransitional Boundary Layer Response. The interaction between the tip leakage vortex and the boundary layers results in vortical disturbances not seen in the inviscid case. These disturbances originate on the leading edge at the time of vortex interception, and are located in the tip region of the stator blade (~75–95 percent span). Each disturbance has normal as well as streamwise vorticity components. Each of these will be examined separately.

Normal vorticity disturbances are the component of $\Delta\omega$ that is perpendicular to the local flow direction. Figure 9 shows the spanwise component of the normal vorticity disturbances. This is the dominant component of the disturbance normal vorticity, and the most appropriate one to illustrate the wakelike nature of the flow. The disturbances shown in Fig. 9 are morphologically similar to the boundary layer distortions (BLDs) seen in two-dimensional calculations with wakes (Part 1). For this reason, these disturbances shall be referred to as N-BLDs (normal vorticity boundary layer disturbances). N-BLDs are present over both pressure and suction surfaces. Pressure side N-BLDs remain flattened against the blade surface. Suction side N-BLDs, on the other hand, are more prominent. They are lifted away from the surface, and are convected in the downstream direction behind the suction side end of the tip vortex. Each N-BLD has a characteristic vortical structure that consists of two opposite-sign vortical regions. The positive region is closer to the blade surface and somewhat smaller than the negative region.

Streamwise vorticity disturbances originate on the suction side leading edge upon vortex interception. These disturbances are shown in Fig. 10. They appear as an elongated core of positive streamwise component of $\Delta\omega$, transported under the suction side end of the TL vortex. These disturbances shall be referred to as S-BLD in the following.

3.1.3 Mechanisms for Boundary Layer Response. From a theoretical standpoint, any change in the vorticity field can lead to

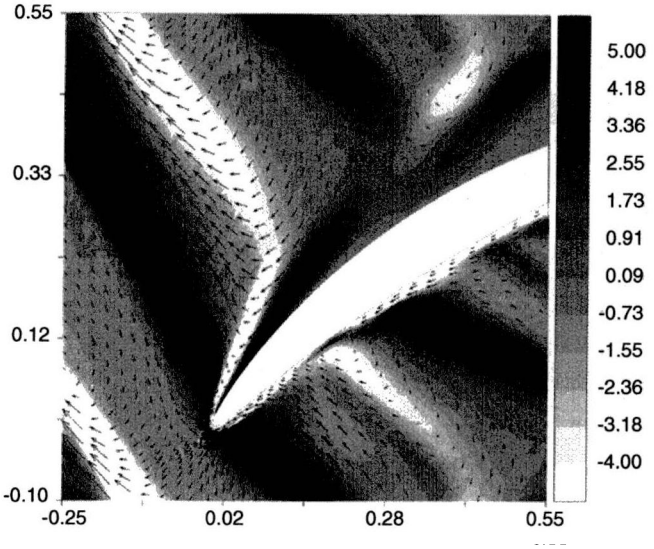

Fig. 9 Spanwise component of disturbance normal vorticity and velocity vectors on 91 percent span blade-to-blade plane, coinciding with center of vortex core

a change in loss. In the present case, the foregoing N-BLDs do lead to a noticeable increase in passage loss. It is therefore useful to elucidate what mechanisms are involved in their production. The similarity between N-BLDs and disturbances from two-dimensional wake calculations (Part 1) implies that the redistribution of boundary layer vortical filaments is one such mechanism. This hypothesis can be verified by comparing the contributions of the four mechanisms through which disturbance vorticity can appear in the flow (Valkov, 1997):

1 Normal distortion of the steady flow boundary layer vortex filaments under the effect of velocity disturbances associated with wakes and vortices. This mechanism is present in both two-dimensional and three-dimensional flows, and is represented by the term $T_1 = (\Delta u \cdot \nabla)\omega_s$.
2 Stretching and tipping of steady flow boundary layer vortex filaments by the same velocity disturbances. Although similar to the above, this mechanism exists only in three-dimensional flows, and is represented by the term $T_2 = (\omega_s \cdot \nabla)\Delta u$.
3 Stretching and tipping of vortex filaments present in the upstream disturbances by the steady flow velocity gradient. This mechanism also exists only in three-dimensional flows, and is represented by the following term: $T_3 = (\Delta\omega \cdot \nabla)(U_s + \Delta u)$.
4 Diffusion of additional vorticity produced on the solid surfaces and changes in vorticity diffusion rates due to velocity disturbances from wakes and vortices. This mechanism is represented by the following term: $T_4 \approx \nu_u \nabla \times \Delta\omega + \Delta\nu\nabla \times \omega_s$.

Quantification of these terms (T_1 to T_4) by Valkov (1997) showed that the normal displacement of the steady boundary layer vortical filaments (mechanism "1" above) is the leading cause of disturbance vorticity production from blade-vortex interaction. Tipping and stretching of *disturbance* vortical "filaments" (mechanism "3" above) is a close second contributor, while tipping and stretching of steady boundary layer vortical lines (mechanism "2" above) is somewhat less important.

This comparison does not allow one to identify which vortical filaments in particular are distorted to give rise to the vortical disturbances. Such information can, however, be obtained by comparing the *components* of T_1 to T_3 in the spanwise and streamwise directions, respectively. The comparison in the spanwise direction indicates that N-BLDs are produced by redistribution of spanwise vortical filaments in the blade boundary layers under the "suction" effect of the TL vortex "negative jet." This mechanism is essentially the same as in two-dimensional wake interaction. It explains (1) the morphological similarity between two-dimensional and three-dimensional disturbances, and (2) the absence of such disturbances in computations where the steady flow is assumed inviscid. The comparison in the streamwise direction shows that S-BLDs are produced primarily by tipping of spanwise vortical filaments in the vortex itself by the velocity gradients in the endwall corner of the steady flow.

3.2 VD/TL: Impact on Time-Averaged Performance Changes. In contrast to the ID/TL situation, the increase in time-averaged passage loss associated with the response of the boundary layer results in a 0.2 point drop in efficiency. As shown in Fig. 11, the increase in passage loss is confined to the tip region of the stator (75–95 percent span). Locally, the increase is rather significant (~30–50 percent), and warrants a more detailed anal-

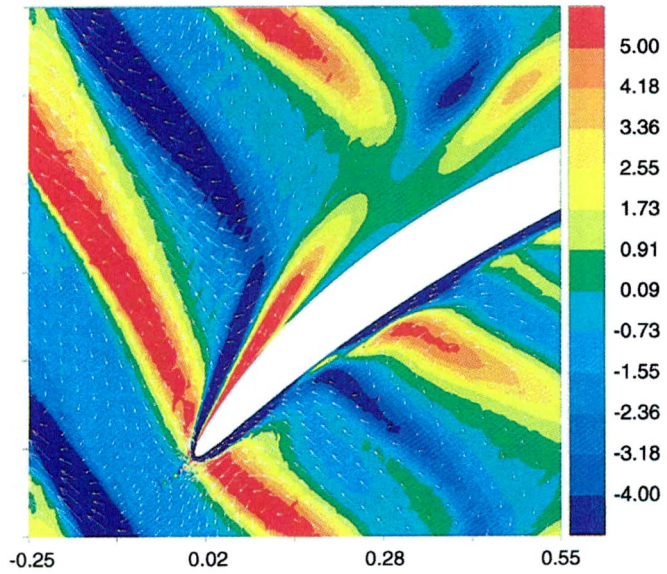

Fig. 10 Disturbance streamwise vorticity isocontours and velocity vectors on 91 percent span blade-to-blade plane

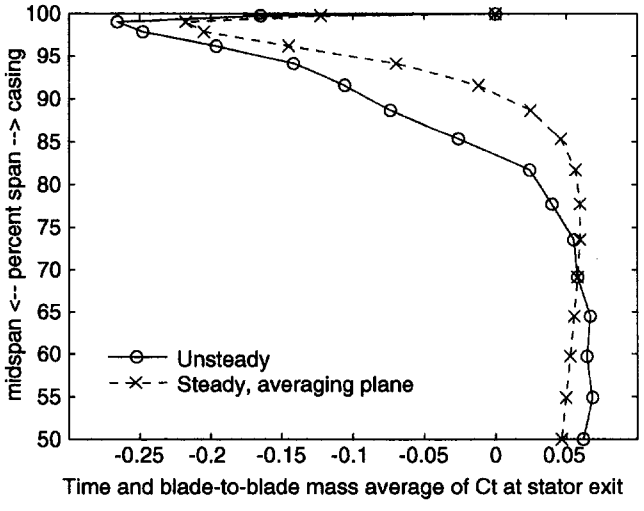

Fig. 11 Distribution of time and blade-to-blade mass-averaged flux of total pressure leaving the stator at various spanwise locations, for both unsteady premixed flows; large negative values are indicative of high loss

ysis of the underlying causes. Howard et al. (1994) have noted a similar increase in stator tip loss when the tip clearance of the upstream rotor is opened up. Qualitatively, their observations supports the results here. The passage loss increase nearly cancels the loss benefit from reversible recovery of the tip leakage vortex.

3.2.1 Role of Boundary Layer Response. There is a strong resemblance between tip leakage vortex and two-dimensional wake interaction, noted above in terms of boundary layer response. The change in time-averaged total pressure, $\Delta\overline{C_t}$, is also very similar to that due to two-dimensional wakes when examined on blade-to-blade planes between 80–95 percent span. This can be appreciated through the computed results in Fig. 12, which show the existence of (*a*) a band of high-loss fluid over the suction side of the stator, and (*b*) two wide regions of high and low-loss fluid that progressively develop in the middle of the passage. These features are localized between 75–95 percent span. No significant vortical or total pressure disturbances occur below 75 percent span. In the ID/TL situation, where no boundary layers are present, only feature (*b*) is observed.

The connection between $\Delta\overline{C_t}$ and vorticity redistribution given by

$$\frac{\partial\Delta\overline{C_t}}{\partial n} \approx -2U_s\Delta(\bar{\omega})_{\text{normal component}} \tag{1}$$

fits the computed results (this is analogous to the wake-stator interaction presented in Part 1). The total pressure changes in Fig. 12 are due to a re-arrangement of vortex filaments normal to the flow direction. On the basis of correlating total pressure and vorticity changes using Eq. (1), two mechanisms involving different vortex filaments can be identified in the unsteady flow:

1 Spanwise vorticity fluctuations in the suction surface boundary layer (N-BLDs) are associated with a high-loss band over the suction surface of the stator.
2 Migration and piling of vortical fluid against the pressure surface of the stator leads to the two regions of low and high p_t that progressively develop in the middle of the passage. It leads to segregation of high-loss vortical fluid in the circumferential direction.

Mechanism (2) is present in both ID/TL and VD/TL computational experiments, while mechanism (1) is present in the VD/TL situation only. This indicates that normal distortion of the suction side boundary layer is the cause for the noticeable passage loss increase in case VD/TL. In physical terms, the "suction" effect of the tip leakage vortex transports high-loss boundary layer fluid from near the wall toward regions of higher mass flux. This leads to increased loss in the tip region of the stator.

The normal distortion mechanism is the same as the one responsible for the passage loss increase in two-dimensional wake interaction. In the VD/TL case, this mechanism appears to be operating on a locally two-dimensional basis. The common origin of passage loss increase suggests that the two-dimensional model of Part 1 can be extended to the three-dimensional tip vortex interaction. This extension (see appendix) relates the increase in passage loss ΔL_p, to the steady flow loss distribution on the blade L_p, and to the time-averaged disturbance velocity transverse to the boundary layer $\overline{\Delta V_n}$:

$$\Delta L_p \approx 2\,\frac{\Delta V_n}{V}\,L_{ps} \tag{2}$$

From a design viewpoint, it can be shown that ΔV_n is proportional to the clearance-related blockage A_b/A_e as defined by Khalid (1995). It also depends on the angle between the vortex core and the stator stagger axis. Thus:

$$\Delta V_n \approx V_2\,\frac{A_b}{A_e}\sin\chi \tag{3}$$

For the situation under consideration, $A_b/A_e = 0.04$, $\sin\chi \approx 1$, $L_{p,s} = 0.03$. With these values, Eq. (2) yields a passage loss increase of 0.0021 units of dynamic head, which is reasonably close to the computed value 0.0023 units. Equation (2) can be used to determine how ΔL_p scales with changes in design.

3.2.2 Role of Unsteady Secondary Flows. The foregoing analysis indicates that the main mechanism for passage loss increase, ΔL_p, in the VD/TL situation is the normal distortion of spanwise vortex filaments. Upon decomposing the vorticity vector into its streamwise and normal component, ΔL_p is given as:

$$A\,\frac{d\Delta L_p}{dx} = \int_x \Delta\overline{v(\omega)^2_{\text{normal}}}dA + \int_x \Delta\overline{v(\omega)^2_{\text{streamwise}}}dA \tag{4}$$

The ratio of normal to streamwise vorticity terms in Eq. (4) can be used to express the relative importance of unsteady streamwise vorticity for loss. Over the critical front third of the stator, the contribution from normal component is 2–10 times larger than that from the streamwise component, despite the presence of significant streamwise vorticity fluctuations (Valkov, 1997). When disturbance vorticity vectors are aligned with the steady flow vorticity, their contribution to loss may be far larger, relative to the situation where disturbance and steady flow vortex filaments are at right angles. Although normal and streamwise vorticity fluctuations observed in the flow are of similar magnitude, the latter are perpendicular to the boundary layer vorticity. Thus the contribution of streamwise vorticity fluctuations to passage loss is relatively small.

3.2.3 Role of Reversible Recovery. Recovery of the tip leakage vortex energy is the main beneficial aspect of rotor–stator interaction. The performance benefit from recovery in the VD/TL situation is virtually identical to that in the ID/TL situation. The loss figures indicate that this recovery is not significantly affected by turbulent diffusion of the vortex core, nor by distortion of core vortical filaments due to the presence of endwall boundary layers.

The recovery of the vortex energy proceeds at the same rate as that of the two-dimensional wakes (Part 1). This explains the recovery of a substantial fraction (~75 percent) of the kinetic energy present at the inlet in the TL vortex. For two-dimensional wakes, results in Part 1 indicate that most of the energy is recovered over a length scale of about 0.25 chord. As distortion takes

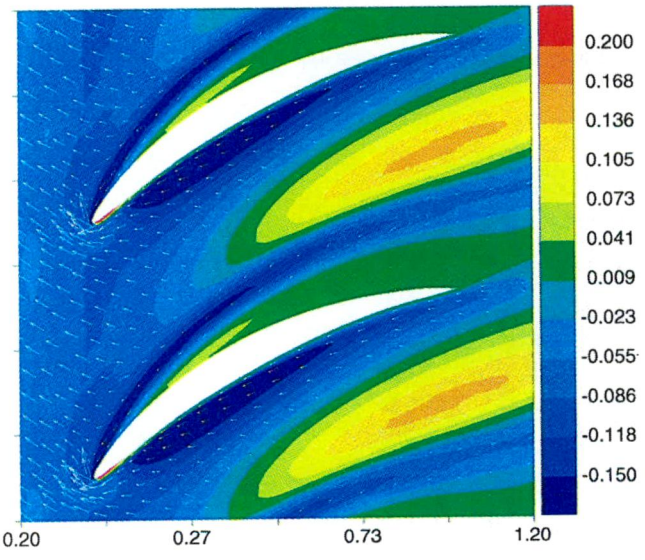

Fig. 12 Isocontours of time-averaged total pressure difference $\Delta\overline{C_t}$ between unsteady and steady flow on 91 percent span blade-to-blade plane elucidating an area with distinct C_t decrease coinciding with trajectory of BLDs

place over length scales comparable to one chord length, vortex energy is thus recovered before distortion can significantly change the dynamics of recovery. Stauter et al. (1991) surveys indicate that the length scale over which turbulent diffusion alone would significantly dissipate wakes entering the stator is of the order of 0.5–1.0 blade chords. Therefore, vortex energy is recovered faster than it is dissipated, on the assumption that TL vortex diffusion proceeds at a rate similar to that of wakes.

3.3 VD/SW: Impact on Time-Average Performance Changes. The effects of upstream streamwise vortices on stator performance are different from those of tip leakage vortices; streamwise vortices lead to a 0.3 point drop in efficiency. In contrast to the "inviscid" ID/SW case, the vortex is attenuated instead of being amplified while the passage loss increase ΔL_p due to unsteadiness is substantially larger. The increase is a result of boundary layer response to SW vortex. The computed results in Valkov (1997) shows that the BL disturbances induced by the SW vortex consist of a strong streamwise vortex accompanied by a normal vortical component over the suction surface of the stator. These features can be explained in terms of the uplifting of boundary layer vortical filaments by the "tornadolike" velocity and static pressure fields associated with the SW vortex core.

3.4 Summary. The interaction between upstream vortices and steady flow boundary layers has an important effect on stator performance and unsteady flow features. Interaction with simple streamwise vortices is detrimental for performance. Rotor tip leakage vortices are processed in a manner different from the simple streamwise vortices. For the geometric configuration and operating conditions under consideration, it was found that:

- Most of the tip leakage vortex energy is recovered during its transport through the stator (~75 percent in the case being considered here). This results in a loss benefit of 0.3 efficiency points. The recovery scales in the same way as that of a two-dimensional inviscid wake (Smith, 1966; Adamczyk, 1996; Valkov, 1997), and is not significantly affected by diffusion or vortex core distortion.
- A noticeable increase in passage loss (~0.2 efficiency points) occurs in the tip region of the stator in the presence of a tip leakage vortex. Such an increase is not observed in calculations when the steady flow is assumed inviscid. The increase is due to normal displacement of high-loss boundary layer vortical fluid by the "negative jet" velocity of the tip leakage vortex. This mechanism is identical to that in two-dimensional wake–stator interaction.
- This passage loss increase can potentially cancel the benefit from vortex energy recovery.

The spanwise extent and the magnitude of passage loss increase computed here are in accord with previous measurements of stator loss behind a rotor for two different tip clearances (Howard et al., 1994).

4.0 A Parametric Study on Rotor Vortex–Stator Interaction

The following set of computational experiments serves to assess the sensitivity of TL vortex–stator interaction to parameters characterizing TL vortex and to those characterizing stator steady-state performance. In each experiment, only a single parameter is changed with respect to those in the VD/TL flow situation.

4.1 Sensitivity to Parameters Characterizing Tip Leakage Vortex

4.1.1 Closely Coupled Blade Rows. Since the position of the inlet boundary of the computational domain is held fixed, reduction of axial spacing between the rotor and stator is represented by scaling the disturbance velocity prescribed at the inlet of the stator in the VD/TL situation by a factor f_x:

$$f_x = \exp\left[-2.295\,\frac{d_{\text{reduced}} - d_{\text{design}}}{2c}\right] \tag{4}$$

This equation is based on the assumption that the tip leakage vortex diffuses at the same rate as rotor wakes, and uses a correlation proposed by Stauter et al. (1991) for wake decay in a research compressor. Wake data are used to determine the amount by which the nominal vortex needs to be scaled. Equation (4) shows that a factor of 1.41 is required to simulate the reduction in axial spacing from 0.37 to 0.07 chords in Smith's (1970) experiment. The scaled-up tip leakage vortex is then used as inlet boundary conditions in the computation. The computed results (Valkov, 1997) showed that the amount of energy that is reversibly recovered is significant (~0.5–0.6 efficiency points). However, the increase in passage loss is also appreciable (~0.3–0.4 efficiency points). Examination of the disturbance vorticity and total pressure fields indicates that the larger performance changes relative to the baseline case VD/TL, are simply due to the larger relative total pressure/velocity nonuniformity in the vortex, and not to new causal mechanisms.

4.1.2 Effect of TL Crossflow. In this computational experiment the leakage crossflow associated with the tip leakage vortex in the rotor relative frame is removed, only the velocity defect is retained so that the vortex behaves essentially like a wake. The increase in passage loss, ΔL_p, is not significantly different from that in the baseline VD/TL situation. This is in accord with the model for ΔL_p. Given that the rotor and stator blades are approximately perpendicular, crossflow disturbances in the rotor frame appear parallel to the stator surface, while velocity defect disturbances are perpendicular to the surface. Removing the crossflow component of the vortex does not significantly affect ΔV_n. Consequently, boundary layer vortical disturbances and the resulting passage loss changes are similar to those in the baseline VD/TL case. Thus, one deduces that the relative total pressure/velocity defect in the tip leakage vortex is the most important factor in inducing unsteady flow and in affecting the performance of the downstream stator. However, the crossflow component accounts for about one-third of the energy in the vortex at the inlet of the stator so that the benefit from reversible recovery is not as large as in the baseline VD/TL situation.

4.2 Sensitivity to Parameters Characterizing Stator Steady State Performance

4.2.1 Increased Stator Loading. The increase in stator loading is achieved by using a steady stator flow at an operating point corresponding to unstalled operation near the peak of the characteristic ($\phi = 0.38$, midspan $\theta_{1s} = 51$ deg, diffusion factor = 0.52). The upstream vortex is kept the same as in the baseline VD/TL case so that stator loading effects are separated from other changes in the flowfield.

Passage loss: The most significant effect of increasing the stator loading is to alter the increase in passage loss, ΔL_p, due to the upstream vortex. The change in passage loss, though not substantial, is in accord with the simplified loss model for ΔL_p. The axial variation of steady flow loss $L_{p,s}$ for high and design point loading is shown in Fig. 13. The change in time-averaged passage loss ΔL_p is a consequence of displacing the high-loss fluid away from the surface into the primary stream by the velocity field of the upstream vortex. This happens mostly in the front part of the blade where ΔV_n is the largest. The computed results of Fig. 13 shows that, for the stator considered here, the steady flow at $\phi = 0.38$ has a lower loss than the VD steady flow ($\phi = 0.45$) over that part of the blade. Therefore, the boundary layer distortion process above has less of a performance impact. The passage loss degradation ΔL_p at high loading is thus smaller than that at design point loading, which agrees with the computed time-averaged results. This finding suggests that *the passage loss increase due to wakes and tip leakage vortices can be reduced by tailoring the loss distribution on the blade.* All other parameters being equal, the

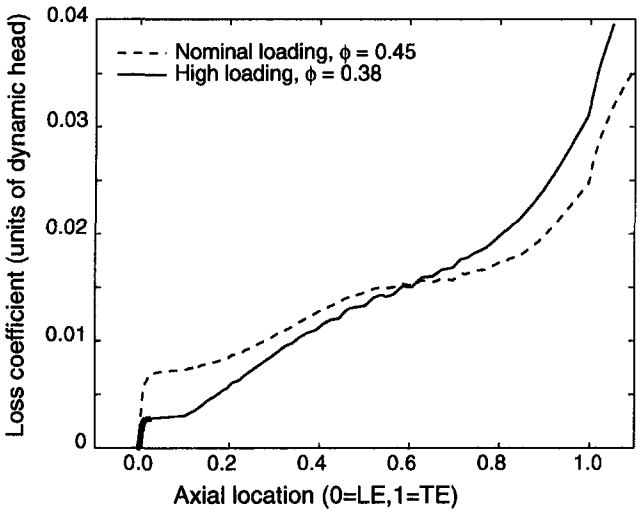

Fig. 13 Axial distribution of steady flow passage loss coefficient at high and at design point loading

passage loss increase would be smaller for designs where most of the steady-state loss is generated in the aft portion of the blade section. This dependency is described by the full equation (from which the simplified model is derived) that takes into account the axial variation of the loss production, dL/dx:

$$\Delta L_p \approx \frac{6}{U} \int_{\text{LE}}^{\text{TE}} x \Delta V_n(x) \frac{dL_{p,s}}{dx} dx \tag{5}$$

Recovery of tip leakage vortices: The benefit from recovery of wakes and tip vortices is linked to loading through the amount of flow turning. A larger portion of the disturbance energy is expected to be recovered for high flow turning angles. For the present configuration, however, most of this energy is recovered at design point flow turning; thus no substantial change in mixing loss benefit, ΔL_m, should be anticipated with respect to the design-point VD/TL situation.

Unsteady flow features. Qualitatively, the disturbance flowfield is similar to that at design-point loading. Thus no new unsteady loss mechanisms arises for highly loaded unstalled blading.

4.2.2 Increased Axisymmetric Flow Nonuniformity. The inlet profile to the stator (based on data from a four-stage low-speed research compressor) in the baseline VD flow situation is relatively uniform. In multistage machines, however, the inlet velocity profiles to embedded blade rows can exhibit substantial spanwise variation (Cumpsty, 1989). Thus the objective here is to determine the effect of such variation on stator interaction with tip leakage vortices. This is done by changing the inlet profile of the steady flow so that it is representative of an embedded stage (Smith, 1970). The resulting steady flow is characterized by stronger secondary flows and by more pronounced spanwise loading variation than the design-point (steady) flow. The performance effects of the upstream TL vortex in stator subjected to strong inlet shear are not significantly different from the baseline case. The computed results show a somewhat larger time-averaged passage loss increase because of a higher steady passage loss in the tip region of the stator. This, again, is in accord with the time-averaged passage loss model developed above. Except for minor changes due to spanwise variation of the velocity at which the vortex is convected, the unsteady flow features are also similar to those observed in the baseline VD/TL computational experiment. Thus computed results show that the effect of the tip leakage vortex on stator performance does not appear to be sensitive to axisymmetric flow nonuniformity. The results also indicate that *the detrimental effects of tip vortex interaction would be larger in stators with high loss in the tip region.*

4.4 Stacked-Plane Two-Dimensional (Strip Theory) Approximations. The purpose of the computational experiment based on strip theory approximation is to confirm the hypothesis that the most important effects of tip leakage vortices on stator performance occur through the similar mechanisms as was found in wake–stator interaction (Part 1). This is accomplished by confining the unsteady flow in the stator to a collection of blade-to-blade planes at discrete spanwise locations. While the inlet boundary conditions vary from plane to plane (as set by that used in the original three-dimensional simulations), the flow on each plane is strictly two dimensional. This representation of the interaction still retains the three-dimensional flow structure of the incoming vortex, but is essentially two dimensional from a mechanistic viewpoint. The unsteady flowfield obtained in this manner is very similar to that of the fully three-dimensional VD/TL simulation. The vortex is attenuated during its transport through the stator. This confirms the hypothesis that tip vortex recovery can be described on a quasi-two-dimensional basis. As shown in Fig. 14, the unsteady flow over the suction surface is characterized by spanwise vortical disturbances similar to those for wakes. These disturbances are responsible for the passage loss increase that partly reduces the benefit from tip vortex recovery. Thus *the tip leakage vortex interacts with the stator in the same manner as an upstream two-dimensional wake.*

4.5 Summary. The following key results can be deduced from a set of computational experiments implemented for assessing the sensitivity of tip leakage vortex interaction to axial spacing, vortex structure, and stator operating parameters:

- The unsteady flow mechanisms through which upstream tip leakage vortices influence stator performance are generic. These mechanisms consist of: (*a*) recovery of disturbance energy by means of vortex stretching, and (*b*) increase in passage loss due to boundary layer distortion by the upstream disturbance velocity field.
- Vortex recovery is beneficial for performance. Its benefit is significant relative to the mixed-out steady flow approximation. Vortex recovery benefits are reduced to a large extent by the passage loss increase.
- Blading design changes may reduce the passage loss increase, and thus retain a larger portion of the recovery

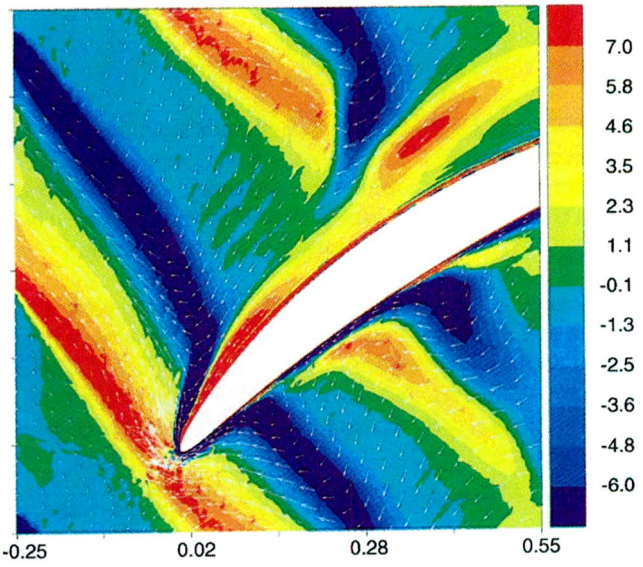

Fig. 14 Disturbance spanwise vorticity on 91 percent span blade-to-blade plane at instant of vortex interception for 2D/TL situation

benefits. All other factors being constant, stators in which the steady losses are "concentrated" in the tip region or in the front part of the blades will experience a higher passage loss increase from tip leakage vortex–stator interaction.

- These unsteady flow mechanisms can be described on a locally two-dimensional basis. In this sense, the most important aspect of the tip leakage vortex is the velocity/relative total pressure defect associated with the vortex core. Secondary flows and spanwise variation of steady inlet profiles do not affect these mechanisms and their performance impact in a significant manner.

5.0 Implications on Compressor Performance and Design

These newly found results can be used to assess the influence of compressor design on the performance impact of upstream wakes and tip leakage vortices, and to bound such effects. This was accomplished in Valkov (1997) by examining how stage design influences the efficiency change, $\Delta\eta$, associated with interaction between rotors and stators that involves rotor and stator wakes, as well as rotor tip leakage vortices. The calculation of $\Delta\eta$ for a given design involves two aspects. First, the wakes and vortices for this design are characterized using simple correlations. Second, the effect of these wakes and vortices on blade row loss are estimated using models of recovery and boundary layer response developed here. The procedure for using these models to estimate/calculate the performance change is given in the appendix.

Within the approximate limits of the de Haller criterion (Cumpsty, 1989) and for a nominal axial spacing of 0.37 chords and DF = 0.45, blade row interaction is moderately beneficial ($\Delta\eta \sim$ 0.5 points), and relatively insensitive to stage design. Outside these limits, blade row interaction benefits rapidly disappear. This is due to: (*a*) an increase in the loss associated with boundary layer response to unsteadiness, and (*b*) a decrease of the benefit associated with wake recovery.

Blade row interaction effects are moderately sensitive to the choice of diffusion factor. The efficiency estimation with a diffusion factor of 0.52 yields results that differ from those with 0.45 by about 0.2 point.

Blade row spacing is an important factor and reducing the spacing from 0.37 chords to 0.07 chords increases the net efficiency benefits from blade row interaction to significant levels (~1 point). Based on these results here, the GE/LSRC compressor at design point (ϕ = 0.45, ψ = 0.65, 63 percent reaction) indicates that a reduction of the blade row axial spacing from 0.37 to 0.07 chords yields a significant improvement in efficiency.

5.1 Assessment of Design Options. The design parameter space can be divided into two regions (Valkov, 1997). The relative extent of these regions depends on the blading diffusion factor; for a typical value of 0.45, the boundary between these regions coincides approximately with the de Haller criterion (Cumpsty, 1989). Within the limits of this criterion, the impact of blade row interaction on efficiency is moderately beneficial with respect to the mixing-plane steady flow approach (~0.4–0.6 points). There is relatively little variation in efficiency benefit from design to design. Outside the limits of this criterion, blade row interaction benefits disappear rapidly. The results also suggest that designs where high pressure ratio is achieved by means of increased solidity might fall outside the design space where interaction is beneficial.

Some efficiency improvement can be achieved by mitigating the detrimental effect of nontransitional boundary layer response. For the LSRC design examined here, the maximum potential improvement is of the order of 0.4 efficiency points. This value assumes that the 0.3 points deterioration from BL response to the rotor tip vortex, and the 0.1 points deterioration from BL response to rotor and stator wakes, can be completely eliminated.

Two methods are available for mitigating the effect of boundary layer response. The first method consists of using sections for which the loss is "moved" from the front toward the back of the blades. The second method consists in the removal of boundary layer fluid from the front portion of the blade suction surface. This eliminates the cause for passage loss increase (normal redistribution of vortical lines in the boundary layer under the effect of upstream velocity disturbances). The suction method entails increased mechanical and structural complexity. Since tip vortex/boundary layer interaction in the tip region of the stator contributes the most to the increase in passage loss, a promising strategy is to apply suction over the outer 75–95 percent of stator span; the mass flow removed may be used as bleed air.

6.0 Overall Summary and Conclusions for the Two-Part Paper

First-of-a-kind computational experiments have been designed and carried out to assess quantitatively the effect of upstream rotor wakes and tip leakage vortices on the performance of a typical stator, relative to a steady flow approximation based on mixing out such disturbances between blade rows. The key objectives are: (1) to identify the unsteady flow mechanisms responsible for performance changes, (2) quantify these changes, and (3) translate this information into design insights. In Part 1, the framework of technical approach and results on the interaction of stator with upstream rotor wakes were presented. In Part 2 the focus was on the interaction of stator with upstream rotor tip leakage vortices and discrete streamwise vortices, the controlling parametric trend and the implications on compressor design. The key findings are summarized below:

Two generic mechanisms with significant impact on performance have been identified. These are the reversible recovery of the energy in the disturbances (beneficial), and the nontransitional boundary layer response (detrimental). These mechanisms appear to be generic.

- Tip vortex recovery involves three-dimensional vorticity kinematics. However, the energy benefit from tip vortex recovery scales in the same manner as that associated with wake recovery, and can be described in the same two-dimensional terms.
- Nontransitional boundary layer response involves the normal displacement of boundary layer vortex lines under the "suction" effect of the upstream disturbances. The resulting redistribution of vorticity leads to an increase in passage loss. For tip vortex interaction, the loss increase occurs in the tip region of the stator (Howard et al., 1994).
- Both mechanisms are associated with the relative total pressure/velocity defect of the disturbances in the relative frame. The effects of these mechanisms can be described in the same two-dimensional terms for both wakes and tip leakage vortices.

Quantitative effect and dependency: The effect of the upstream wakes and vortices on the stator loss is important. It depends on the following parameters: axial spacing, loading, and the frequency of wake fluctuations in the relative frame.

- For the present design, passing the rotor wakes and vortices through the stator results in a stage efficiency that is 0.2 points higher than that obtained using the steady flow approximation (0.5 efficiency points recovery benefit minus 0.3 points from boundary layer response). Individually, the effects of rotor tip vortex and wake are comparable.
- The effect of tip vortices and wakes becomes significantly more important at reduced axial spacing. For a spacing of 0.07 chords, the stage efficiency is 0.6 points higher relative to the steady flow (1.2 points recovery benefit minus 0.6 points from boundary layer response).
- For the geometric configuration under consideration, an increase in loading redistributes boundary layer vortical fluid

in a manner that decreases the additional loss from boundary layer response because of lower steady state loss over the front part of the blade.
- There is a range of fluctuation frequencies (~0.3–0.8 times the blade passing frequency) for which recovery does not occur. Within this range, there is a significant difference between the effects of fluctuating and steady wakes with the same ensemble-averaged properties. Thus, the use of ensemble-averaged wakes in interaction studies is not necessarily correct.
- The most important aspect of the tip vortex is the relative total pressure/velocity defect, which is perceived by the stator in the same manner as a wake. Stator flow three-dimensionality and unsteady secondary vorticity are not important as far as the performance effects of tip vortex–stator interaction are concerned.

Design implications: A model of recovery and boundary layer response has been used to explore how blade row interaction effects change from design to design. The model considers interaction in a repeating embedded stage environment, and indicates that:

- Steady flow approximations based on mixing out the disturbances between the blade rows underestimate stage efficiency by 0.3–0.5 points (for typical designs) and by as much as 0.6–1.0 points (for designs with closely spaced blade rows).
- A region in design space exists where interaction has a beneficial and relatively constant impact on efficiency. Outside this region, interaction benefits rapidly disappear. The extent of the beneficial region is determined by the choice of blading diffusion factor; for typical values of 0.45, the beneficial limits coincide approximately with the de Haller criterion.
- The detrimental aspects of boundary layer response may be mitigated by: (*a*) tailoring the blade loading to reduce steady-state loss in the front part of the blade, or (*b*) selective removal of boundary layer fluid. For typical designs, the maximum efficiency gain from such measures could be as high as about 0.4 points.

Although differences in compressor design prevent a back-to-back comparison, the present results would suggest that $\frac{1}{2}$ to $\frac{2}{3}$ of the efficiency gain obtained by Smith (1970) can be attributed to interaction with upstream wakes and vortices.

Impact of rotor streamwise vortices on stator performance: Processing of discrete streamwise vortices from upstream rotor by the stator has an adverse effect on the time-averaged stator performance. Stretching of the SW vortex core is the primary reason for efficiency degradation when the steady flow through the stator is assumed inviscid. However, when a steady flow with representative boundary layers on stator blade surfaces and casing wall is assumed, the interaction of the endwall and blade surface boundary layers with the upstream discrete streamwise vortex is largely responsible for the performance degradation. Thus, the effects of upstream streamwise vortices on stator performance are different from those of tip leakage vortices.

Acknowledgments

Support for this work was provided by NASA Lewis Research Center under Grants NAG3-660 and NAG3-1679, Dr. John Adamczyk as technical monitor. We would also like to thank John Adamczyk, N. A. Cumpsty, M. Graf, E. M. Greitzer, F. E. Marble, and I. A. Waitz for helpful comments and discussions. Additional computational resources have also been provided by the NASA Lewis Research Center LACE Cluster of computers and this support is gratefully acknowledged. The critical comments of the reviewers for improving the manuscript are also gratefully acknowledged.

References

Adamczyk, J. J., 1996, "Wake Mixing in Axial Flow Compressors," ASME Paper No. 96-GT-029.

Cumpsty, N. A., 1989, *Compressor Aerodynamics,* Longman Group Ltd.

Denton, J. D., 1993, "Loss Mechanisms in Turbomachines," ASME JOURNAL OF TURBOMACHINERY, Vol. 115, pp. 621–656.

Fritsch, G., 1992, "An Analytical and Numerical Study of the Second-Order Effects of Unsteadiness on the Performance of Turbomachines," MIT Gas Turbine Laboratory Report No. 210.

Howard, M. A., Ivey, P. C., Barton, J. P., and Young, K. F., 1994, "Endwall Effects at Two Tip Clearances in a Multistage Axial Flow Compressor With Controlled-Diffusion Blading," ASME JOURNAL OF TURBOMACHINERY, Vol. 116, pp. 635–647.

Kerrebrock, J. L., and Mikolajczak, A. A., 1970, "Intra-Stator Transport of Rotor Wakes and Its Effect on Compressor Performance," ASME *Journal of Engineering for Power,* Vol. 92, pp. 359–368.

Khalid, S. A., 1995, "The Effects of Tip Clearance on Axial Compressor Pressure Rise," Doctoral Thesis, Department of Mechanical Engineering, Massachusetts Institute of Technology.

Smith, L. H., 1966, "Wake Dispersion in Turbomachines," ASME *Journal of Basic Engineering,* Vol. 88.

Smith, L. H., 1970, "Casing Boundary Layers in Multistage Axial Flow Compressors," *Flow Research on Blading,* L. S. Dzung, ed., Elsevier Publishing Company.

Stauter, R. C., Dring, R. P., and Carta, F. O., 1991, "Temporally and Spatially Resolved Flow in a Two-Stage Axial Flow Compressor: Part 1—Experiment," ASME JOURNAL OF TURBOMACHINERY, Vol. 113, pp. 219–226.

Valkov, T., 1997, "The Effect of Upstream Rotor Vortical Disturbance on the Time-Average Performance of Axial Compressor Stators," MIT Gas Turbine Laboratory Report No. 227.

APPENDIX

The appendix consists of three sections: Section A.1 describes the tip vortex characterization used in this paper, Section A.2 presents a simplified model for loss associated with boundary layer response due to tip vortex–stator interaction, and Section A.3 outlines a procedure for estimating the efficiency change associated with blade-rows interactions.

A.1 Tip Vortex Characterization

The velocity field of the tip leakage vortex of the LSRC computational study ($\tau = 0.03$, $\psi = 0.64$), is scaled using the following relationship proposed by Khalid (1995) for the vortex blockage at the exit of the blade row:

$$\frac{A_b \cos \beta_e}{\tau s / \sin \beta_{vm}} = G\left(\frac{\overline{\Delta P^a} - \overline{\Delta P_t^a}}{Q_{2\tau}}\right) \tag{A.1}$$

where G is a quadratic fit of Khalid's (1995) computational experiments. Khalid's (1995) work also suggests a wake representation of the overtip leakage flow can capture the trends in clearance-related blockage. For this reason, it has been assumed that the interblade decay of the TL vortex follows the same relationship as that of a wake presented in Part 1. While crude, this treatment captures to some extent the effect of design point selection on the strength of the tip leakage vortex.

A.2 Boundary Layer Response

It was shown that the increase in loss due to tip vortex/boundary layer interaction occurs through the same mechanisms involved in two-dimensional wake/boundary layer interaction and that the disturbance vortical flow here can be described in the blade-to-blade plane on a locally two-dimensional manner. Therefore, the increase in passage loss due to the upstream tip leakage vortex can be estimated by dividing the blade in individual sections of thickness dz, and by applying the two-dimensional model presented in the appendix of Part 1 to each section. This would result in:

$$\Delta L_p = 6 \int \frac{\Delta V_n(z)}{U} \int_0^1 x \frac{dL_{p,s}(z)}{dx}\, dx dz \tag{A.2}$$

which can be simplified as

$$\Delta L_p \approx 2 \frac{\Delta V_n}{U} c L_{p,s} \tag{A.3}$$

The transverse disturbance velocity, ΔV_n, can be related to the tip leakage blockage A_b/A_e in the rotor frame as defined by Khalid (1995) using continuity. This yields:

$$\Delta V_n = 2 \frac{A_b}{A_e} \frac{\sin \chi}{\cos \theta_{2r}} \tag{A.4}$$

A.3 Estimation of Efficiency Change

This section outlines the steps for applying the flow models for estimating the change in efficiency associated with wake/tip vortex–blade row interaction for different designs.

The first step involves estimating the "strength" of the upstream wakes and vortices, followed by computing the attenuation coefficient a_r for the design under consideration. The loss benefit from recovering upstream wakes in the frame of the downstream blade row is then estimated using expression for ΔL_m given in Part 1. The increase in passage loss from each wake/boundary layer and tip leakage vortex/boundary layer interaction is computed according to Eq. (A.7) given in the appendix of Part 1 and Eq. (A.3).

The loss changes can be converted to efficiency figures by using the relative dynamic head and the stage pressure coefficient:

$$\Delta \eta = \frac{\phi^2}{2\psi} \left[\frac{(\Delta L_p + \Delta L_m)_{\text{rotor}}}{\cos \theta_{1,r}} + \frac{(\Delta L_p + \Delta L_m)_{\text{stator}}}{\cos \theta_{1,s}} \right] \tag{A.5}$$

The equations implicitly assume that there is one rotor wake entering a stator passage per wake passing period.

Periodic Transition on an Axial Compressor Stator: Incidence and Clocking Effects: Part I—Experimental Data

G. J. Walker

J. D. Hughes

School of Engineering,
University of Tasmania,
Hobart, Australia

W. J. Solomon
Ohio Aerospace Institute/General Electric
Aircraft Engines,
Cincinnati, OH 45215

Periodic wake-induced transition on the outlet stator of a 1.5-stage axial compressor is examined using hot-film arrays on both the suction and pressure surfaces. The time-mean surface pressure distribution is varied by changing the blade incidence, while the free-stream disturbance field is altered by clocking of the stator relative to an inlet guide vane row. Ensemble-averaged plots of turbulent intermittency and relaxation factor (extent of calmed flow following the passage of a turbulent spot) are presented. These show the strength of periodic wake-induced transition phenomena to be significantly influenced by both incidence and clocking effects. The nature and extent of transition by other modes (natural, bypass, and separated flow transition) are altered accordingly. Leading edge and midchord separation bubbles are affected in a characteristically different manner by changing free-stream periodicity. There are noticeable differences between suction and pressure surface transition behavior, particularly as regards the strength and extent of calming. In Part II of this paper, the transition onset observations from the compressor stator are used to evaluate the quasi-steady application of conventional transition correlations to predict unsteady transition onset on the blading of an embedded axial compressor stage.

Introduction

The unsteady flow field seen by an embedded blade row in a multistage axial turbomachine is dominated by the effects of the adjacent upstream stage. The major source of periodic disturbance is usually provided by relative motion of blade wakes from the row immediately upstream. The second upstream row provides the greatest contribution to the random disturbance field through dispersion of its chopped wake segments. Farther upstream rows contribute lower level periodicity and a generally increased level of background random turbulence.

The blade boundary layer behavior under these conditions is dominated by periodic wake-induced transition. Transition by other modes is observed in regions between the wake-induced transitional or turbulent strips. Mayle (1991, 1992) refers to this phenomenon as "multimode transition." The problem has been extensively studied since the late 1970's and a good summary of the relevant literature is provided by Mayle's (1991, 1992) reviews. Most workers investigating this problem have used large-scale experiments on flat plates, with moving bar wakes and turbulence grids to simulate the periodic and random disturbance components of the actual disturbance field in a turbomachine. Little attention has been paid to leading edge effects (which were generally suppressed in these experiments) or to the direction of the wake-jet impinging on the plate surface. Walker (1993) suggested that the latter effect might be important, and the experimental data of Orth (1993) and Funazaki et al. (1997a) support this view.

Experiments on profiles typical of turbomachine blades, or in actual machines, have been quite rare. Cumpsty et al. (1995) investigated unsteady flow transition in a large-scale two-dimensional compressor cascade with bar passing. Hodson et al. (1994) reported transition observations in a three-dimensional LP turbine rig under actual engine conditions. Halstead et al. (1997) reported an extensive series of observations on both compressor and turbine blades in low-speed multistage axial machines. The latter results are usefully complemented by studies in a 1.5-stage axial compressor by Solomon and Walker (1995a, b) and Solomon (1996).

Current aeroengine design practice generally ignores unsteady effects and uses steady flow theory to design compressor and turbine blade elements. A notable exception is the application of recent knowledge about the effects of calming after wake-induced turbulent spots (Schulte and Hodson, 1998a, b) to improve the performance of LP turbine blades. Boundary layer analyses usually employ integral calculation methods with a bypass transition criterion such as that of Abu-Ghannam and Shaw (1980) to predict turbulent onset. The transition prediction is based on standard values of free-stream turbulence level known to give reasonable results for the time-mean flow. This simple procedure is fast enough to be used interactively and has produced many successful designs, although shown by recent investigations to give a poor representation of the instantaneous flow behavior.

The present paper reports a detailed study of unsteady transition on the outlet stator of a 1.5-stage axial compressor over a wide range of loading. The relative importance of periodic and random free-stream disturbances for transition on a stator blade element at midspan is examined by clocking of the inlet guide vane (IGV) row to vary the inflow disturbance field. Part I details the experimental observations. Part II attempts a quasi-steady model of the transition behavior using a time-mean boundary layer calculation and conventional transition criteria applied in a quasi-steady manner using instantaneous local values of free-stream turbulence level.

Encouraging results are obtained for the regions between wake-induced turbulent strips. The new procedure can be recommended for design applications and is fast enough to be used interactively. Comparison of the predicted and measured transition behavior also gives some physical insight into the nature of transition on the

Contributed by the International Gas Turbine Institute and presented at the 43rd International Gas Turbine and Aeroengine Congress and Exhibition, Stockholm, Sweden, June 2–5, 1998. Manuscript received by the International Gas Turbine Institute February 1998. Paper No. 98-GT-363. Associate Technical Editor: R. E. Kielb.

compressor blade and questions the dominance of the bypass mechanism in this situation.

Wake-induced transition on the compressor stator does not correlate at all well with instantaneous free-stream turbulence level. Two additional unsteady flow mechanisms may have contributed to this discrepancy: first, the fluctuating pressure field generated by incidence changes as the rotor wakes convect over the stator leading edge (which we will refer to as "potential flow interaction effects"); second, the fluctuations in pressure gradient associated with impingement of rotor wake fluid onto the stator pressure surface, or entrainment of fluid from the stator suction surface into passing rotor wakes (which we will refer to as "rotor wake-jet effect"). Comparison of the present observations with the predictions to be presented in Part II of this paper give some idea of the relative importance of these phenomena.

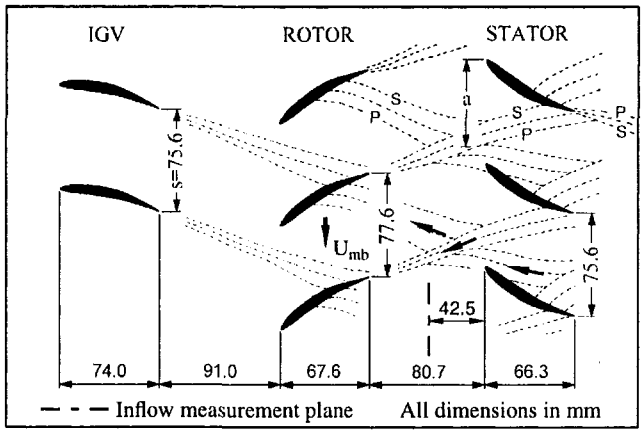

Fig. 1 Cross section of compressor blading at midblade height, showing typical instantaneous wake dispersion. *S* = suction side; *P* = pressure side. Arrows indicate relative flow in wakes. *a* = circumferential offset of stator leading edge from the center of the IGV wake street.

Experimental Detail

Research Compressor. Air enters the compressor radially through a cylindrical screened inlet 2.13 m diameter by 0.61 m wide. A flared bend with a 6.25 to 1 contraction ratio then turns the flow through 90 deg into a concentric cylindrical duct with 1.14 m outside diameter and 0.69 m inside diameter, which contains the compressor blade rows. Downstream of the compressor there is an annular diffuser, and a cylindrical sliding throttle at the outlet is used to control the through flow.

The compressor is a 1.5-stage axial flow machine with three blade rows: inlet guide vanes (IGV), rotor, and stator. Figure 1 shows a cross section of the compressor blading at midpassage. There are 38 blades in each of the stationary rows and 37 blades in the rotor, giving space/chord ratios at midblade height of 0.99 and 1.02, respectively. The blades all have a constant chord of 76.2 mm and an aspect ratio of 3.0. The blade sections were designed for free vortex flow with 50 percent reaction at midblade height at a flow coefficient ($\phi = V_a/U_{mb}$) of 0.76. The design values of inlet and outlet blade angles from axial at midblade height are, respectively: IGV 0.0 deg, 27.8 deg; rotor and stator 45.0 deg, 14.0 deg. However, for these tests the rotor was re-staggered by 2.0 deg to give blade angles of 43.0 deg and 12.0 deg with a resultant increase in stalling flow coefficient.

Instrument slots in the outer casing of the compressor allow radial and axial traversing of measuring probes at a fixed circumferential position. The IGV and stator rows are each mounted on rotatable supporting rings to permit circumferential traversing of these blades relative to a stationary probe or clocking of one row relative to the other.

Further details of the research compressor can be found in Oliver (1961), Walker (1972), and Solomon (1996).

Range of Investigation. All measurements were conducted at midspan, where radial flows are small. Data were obtained for flow coefficients ($\phi = V_a/U_{mb}$) of 0.600, 0.675, and 0.840. These correspond, respectively, to stator midspan incidence values of 4.1, 1.2, and −6.1 deg, and will be referred to as high, medium, and low loading cases. The medium loading case is close to the Howell (1945) nominal incidence value of 0.6 deg.

The corresponding surface velocity distributions obtained from midspan surface pressure tappings are shown in Fig. 2. For the high and medium loading cases, the peak suction surface velocity occurs closer than 5 percent chord from the leading edge, with a roughly linear deceleration over the whole surface. At low loading the suction surface distribution exhibits a plateau, which peaks much farther rearward near 30 percent chord; a discontinuity in velocity gradient around 70 percent chord clearly indicates the development of a laminar separation bubble. This range of behavior encompasses the design conditions for modern high-pressure

Nomenclature

a = circumferential offset of stator blade leading edge from center of IGV wake avenue
c = blade chord
e^n = amplification ratio
i = blade incidence
s = surface distance
$s^* = s/s_{max}$ = dimensionless surface distance from leading edge
t = time
$t^* = t/T$ dimensionless time
u = streamwise velocity
w = circumferential distance
w_1 = relative inlet velocity
x = distance along chord line
E = anemometer output voltage
E_0 = anemometer voltage at zero flow
$H = \delta^*/\theta$ = shape factor
$\mathrm{Re}_1 = w_1 c/\nu$ = chord Reynolds number
$\mathrm{Re}_{ref} = U_{mb}c/\nu$ = reference Reynolds number
$\mathrm{Re}_\theta = \theta U/\nu$ = momentum thickness Reynolds number
S = blade pitch
T = rotor blade passing period
Tu = random disturbance level (turbulence)
Tu_D = total disturbance level
$\tilde{T}u$ = periodic disturbance level (unsteadiness)
U = local free-stream velocity
U_{mb} = rotor midspan velocity
V_a = mean axial velocity
α = flow angle from axial
γ = turbulent intermittency
δ^* = displacement thickness
θ = momentum thickness
κ = relaxing nonturbulent flow probability
$\lambda_\theta = (\theta^2/\nu)(dU/dx)$ = Pohlhausen pressure gradient parameter
ν = kinematic viscosity
τ = quasi-wall shear stress
τ_w = wall shear stress
$\phi = V_a/U_{mb}$ = flow coefficient

Superscripts, Subscripts, etc.

$\langle\ \rangle$ = ensemble (phase-lock) average value
$\bar{\ }$ = time-mean value
$'$ = instantaneous fluctuation from time-mean
$''$ = instantaneous fluctuation from ensemble mean
crit = critical
in = inlet
reat = re-attachment
s = pitchwise average
sep = separation
trans = transition

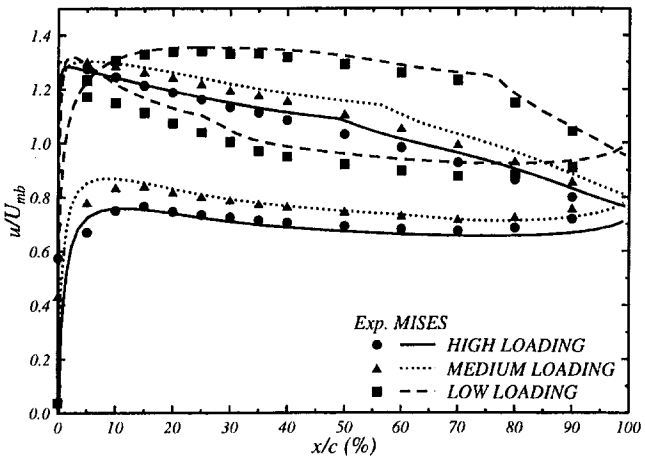

Fig. 2 Variation of stator blade surface velocity distribution with loading at midblade height; Re_{ref} = 120,000

compressor airfoils, which typically exhibit a well-rounded suction peak around 20 percent chord. (See the baseline compressor case 2B reported by Halstead et al., 1997.)

The suction surface velocity distribution for the high loading case of the present investigation is quite similar to that for the near-stall case of Halstead et al. (1997). Hence, the present study should also give a useful indication of the importance of unsteady flow effects for modern compressor blade sections operating at off-design conditions.

The stator pressure surface velocity distributions all show a deceleration over the forward part of the blade, followed by an acceleration toward the trailing edge. The deceleration is very mild for the high loading case, but progressively strengthens as incidence is decreased. For the low loading case, the velocity gradient becomes severe enough to cause a leading edge laminar separation bubble.

A constant reference Reynolds number of Re_{ref} = 120,000 was used for all tests. This gives stator inlet Reynolds numbers of Re_1 = 110,000, 117,000 and 130,000 for the high, medium, and low loading cases. These values are low compared with those typical of aircraft gas turbine engine operation, as reported by Hourmouziadis (1989) and Mayle (1991); they are also generally lower than those in the experimental studies of Halstead et al. (1997). The test compressor was nevertheless operating above the critical Reynolds number range where laminar separation starts to cause a significant increase in blade losses (see Walker, 1975). As discussed by Solomon (1996) the critical Reynolds number for the test machine is lower than that for modern compressors because of the generally milder pressure gradients on the suction surface of C4 blading. Surface hot-film observations on the stator blading reported by Solomon and Walker (1995a, b) show essentially similar behavior to that in the higher Reynolds number multistage compressor experiments of Halstead et al. (1997).

The influence of IGV clocking on the stator boundary layer transition behavior was investigated for a/S = 0.00 and 0.50. The coordinate a is the circumferential distance of the stator leading edge from the center of the avenue of dispersed IGV wake segments, as shown in Fig. 1. These two clocking positions correspond approximately to the cases of minimum and maximum rotor wake periodicity experienced by the stator blade element at midblade height (as indicated by measurements of the temporal variation of ensemble-averaged stator wake momentum thickness reported by Walker et al., 1997a).

Operating conditions for the stator at midblade height are summarized in Table 1.

Measurement Techniques. The compressor and measurement systems were controlled by two IBM-compatible 486 personal computers. One computer was used to control the compressor and acquire data from slow response instrumentation. The other was used for high-speed data acquisition from the hot-wire and hot-film anemometers. Operating speeds at Re_{ref} = 120,000 were typically 500 rpm, and the compressor speed was continuously adjusted with a speed setting accuracy of ±0.1 rpm to maintain constant Reynolds number. The throttle setting was left unchanged for an individual flow traverse, after setting the desired flow coefficient prior to the start of measurement.

Hot-wire measurements with a Dantec 55P03 probe and TSI IFA-100 anemometer were obtained at 55.7%c axial distance upstream of the stator to provide information on the inflow disturbance field. Slow response pressure measurements with a United Sensor CA-120 three-hole cobra probe at the same nominal position provided data for in-situ anemometer calibrations and pitch-averaged flow angles.

Surface velocity distributions were obtained from static pressure measurements on two adjacent stator blades fitted with pressure tappings opening into the same blade passage. Total pressure values were obtained from a Kiel probe 50%c upstream of the stator leading edge. The overall uncertainty of time-averaged pressure data was 0.15 percent.

One of the pressure-tapped stator blades was replaced by a blade instrumented with an array of 61 hot-film sensors at midblade height. The metal sensors, spaced at 2.54 mm intervals, were plated onto a kapton sheet wrapped around the whole blade surface. Data were acquired simultaneously from sets of five film gages using TSI IFA-100 anemometers.

For both hot-wire and hot-film observations, the anemometer output was backed with a DC offset voltage, amplified, and low-pass filtered at 20 kHz before sampling at 50 kHz and data storage. The signal conditioner amplification and DC offset were set automatically for each spatial measurement point to optimize signal-to-noise ratio. The frequency response of the hot-wire and hot-film measurements were better than 70 kHz and 30 kHz, respectively. The rotor blade passing frequency for these tests was typically 300 Hz.

Ensemble-averaged values of measured quantities were obtained from 512 records, with sampling triggered at the same point on each rotor revolution by an optical encoder mounted on the motor end of the drive shaft so that the wakes of the same rotor blades were observed in each record. Each record consisted of 1024 samples covering about six rotor blade passing periods for a set of wakes previously found by Solomon (1996) to exhibit good periodicity. Circumferential traverses upstream of the stator used 32 points per blade spacing, with a greater concentration of points in the IGV wake regions. Time-mean flow data were determined from separate sets of flow observations with continuous sampling at random phase relative to the rotor motion and an averaging time of about 30 seconds.

Hot-film data were processed to give quasi-shear stress, defined by

$$\tau = \left(\frac{E^2 - E_0^2}{E_0^2} \right)^3 \tag{1}$$

which is proportional to the actual wall shear stress τ_w. This technique was originally developed by Hodson et al. (1994) and has also been used by Halstead et al. (1997). Further detail on the hot-film data processing can be found in Solomon and Walker

Table 1 Stator operating conditions at midblade height

Loading	ϕ (V_a/U_{mb})	i (°)	Re_1	Tu_s (%)	Tu_{D_s} (%)
High	0.600	4.1	110000	3.15	5.39
Medium	0.675	1.2	117000	2.27	3.75
Low	0.840	-6.1	130000	2.03	3.07

(1995a, b) and Solomon (1996). The latter references provide typical individual gage records, as well as time-mean and envelope curves of quasi-shear stress for some of the test cases reported here.

Disturbance and Turbulence Level Analysis. The reduction of turbulence and unsteadiness data from the hot-wire measurements follows the procedure of Evans (1975) with some changes in notation. The instantaneous velocity may be expressed as

$$u = \bar{u} + u' = \langle u \rangle + u'' \tag{2}$$

where $\bar{u}$ is the long-term time-mean of a continuous record, and $\langle u \rangle(t_i)$ is the ensemble average of N samples at time t_i relative to the rotor phase reference, defined by

$$\langle u \rangle(t_i) = \frac{1}{N} \sum_{k=1}^{N} \{u(t_i)\}_k \tag{3}$$

The ensemble-averaged velocity only exhibits blade-to-blade periodicity in the test machine, owing to the equal blade counts in the IGV and stator rows.

The periodic disturbance level or "unsteadiness" is defined by

$$\tilde{T}u = (\langle u \rangle - \bar{u})_{\text{rms}}/U \tag{4}$$

Values of $\tilde{T}u$ must be evaluated from averages over an integral number of blade-passing periods.

The random disturbance level or "turbulence" associated with fluctuations about the ensemble-averaged value is given by

$$Tu = u''_{\text{rms}}/U \tag{5}$$

and the total disturbance level associated with fluctuations about the long-term mean is given by

$$Tu_D = u'_{\text{rms}}/U \tag{6}$$

Assuming $(\langle u \rangle(t) - \bar{u})$ and u'' to be statistically independent, the three disturbance levels are related by

$$Tu_D^2 = \tilde{T}u^2 + Tu^2 \tag{7}$$

Observations and Discussion

Stator Inlet Flow Field. Figure 3 shows the stator inflow velocity field, as observed from circumferential hot-wire traverses at 55.7%c axial distance upstream of the stator leading edge. These data were acquired by moving the IGV and stator rows together at a fixed circumferential offset. The upstream influence of the stator pressure field is negligible at this axial station. The data were obtained over one IGV pitch only, but have been plotted over two blade pitches by assuming pitchwise periodicity. Ensemble-averaged velocity (nondimensionalized by pitchwise-averaged time-mean velocity) is indicated by shading. The line contours indicate ensemble-averaged values of random velocity fluctuations about the ensemble mean (or "turbulence"), $\langle Tu \rangle$ (percent).

Each subfigure represents the instantaneous spatial distribution that would be observed on a cylindrical surface if the flow disturbances were convected unaltered downstream of the measuring station with zero whirl. The variable w/S on the axis represents dimensionless circumferential position relative to an arbitrary fixed origin, which is the same for all subfigures. Dimensionless time t^* on the abscissa has been plotted in the reverse direction so that the earliest observed points appear at the right, corresponding to the farthest downstream convection. The data for each subfigure have been time-shifted to make the rotor–IGV relative circumferential position constant for each probe relative position w/S. This is necessary because the IGV row was clocked relative to the trigger point, which was fixed relative to the machine and the probe.

The rotor wakes can be identified as the parallel bands of high turbulence running diagonally from bottom left to top right as in Fig. 1. The avenue of dispersed IGV wake segments runs horizontally from left to right. This differs from the picture of instantaneous wake dispersion in Fig. 1 because whirl velocity has been ignored. The suction and pressure surface sides of both IGV and rotor wakes (indicated by symbols S and P) are at the top and bottom of the wake regions, respectively.

The rotation of the IGV wake segments relative to the local flow direction (constant w/S in this figure due to neglecting the whirl velocity) increases with rotor blade loading and thus broadens the IGV wake street. The peak ensemble-averaged turbulence level $\langle Tu \rangle$ in the IGV wakes is about 3 percent and rather insensitive to loading, while the minimum level in the free stream (corresponding to inflow regions uncontaminated by wakes) is about 0.5 percent. The time-mean turbulence level Tu (plotted at left) is dominated by random disturbances from the IGV wakes. The background level of time-mean turbulence also increases with loading.

Interactions with adjacent IGV wake segments produce periodic variations in the rotor wake thickness. The resulting restriction of relative flow produces local accumulations of low-energy rotor wake fluid on the suction side of the IGV wake street. The development of this phenomenon downstream of the rotor trailing edge is discussed in detail by Lockhart and Walker (1974) and Walker et al. (1997). Fluctuating rotor lift and vortex shedding from the rotor may contribute to this effect, which produces regular circumferential variations in time-mean velocity.

The time-mean velocity distribution exhibits two periodic minima. One is associated with the accumulation of rotor wake fluid against the suction side of the IGV wake street. The other arises from the velocity defect within the IGV wake itself. The magnitude of the former variation increases with loading, and exceeds 10 percent of the pitchwise-averaged velocity for the high loading case.

The time-mean total disturbance level Tu_D is dominated by the periodic disturbance component, except in the IGV wake region at low loading. The maximum periodicity occurs in the regions of accumulated low-energy rotor wake fluid. Walker et al. (1997) provide more detailed information on the variation of the total, random, and periodic disturbance components downstream of the rotor for the medium loading case.

Stator Surface Hot-Film Observations

(a) Ensemble-Averaged rms Quasi-Shear Stress. Time–distance contour plots of ensemble-averaged rms quasi-shear stress observations from the stator surface hot-film array at midblade height are presented in Fig. 4. Following the recommendations of Solomon and Walker (1995a), the values of $\langle \tau_{\text{rms}} \rangle$ have been normalized by the local time-mean quasi-shear stress $\bar{\tau}$. The rms quasi-shear stress tends to identify the center of transition regions, as it reaches a maximum where the most frequent switching between laminar and turbulent flow (with correspondingly low and high wall shear stress) is occurring. The $t^* \sim s^*$ plot of $\langle \tau_{\text{rms}} \rangle$ contours is overlaid with trajectories of particles traveling at $1.0U$, $0.88U$, $0.70U$, $0.50U$, and $0.35U$ to assist in interpretation of the wake-induced transition phenomena. These trajectories originate at the stator leading edge ($s^* = 0$) at the instant t^* corresponding to the rotor wake passage.

Gages adjacent to the stator leading edge show marked fluctuations on each surface, except on the suction surface in the low loading case where the incidence is large and negative. These fluctuations could arise partly from local turbulent breakdown, but are thought to be caused mainly by leading edge potential flow interactions. The leading edge peaks in $\langle \tau_{\text{rms}} \rangle$ are generally lower for the clocking case $a/S = 0.00$, where the stator is immersed in the IGV wake street and therefore subjected to a lower level of periodic disturbance associated with the rotor wake passage.

The high and medium loading cases show strong rotor wake induced periodicity, with wedge-shaped regions of high $\langle \tau_{\text{rms}} \rangle$ extending close to the leading edge on both suction and pressure

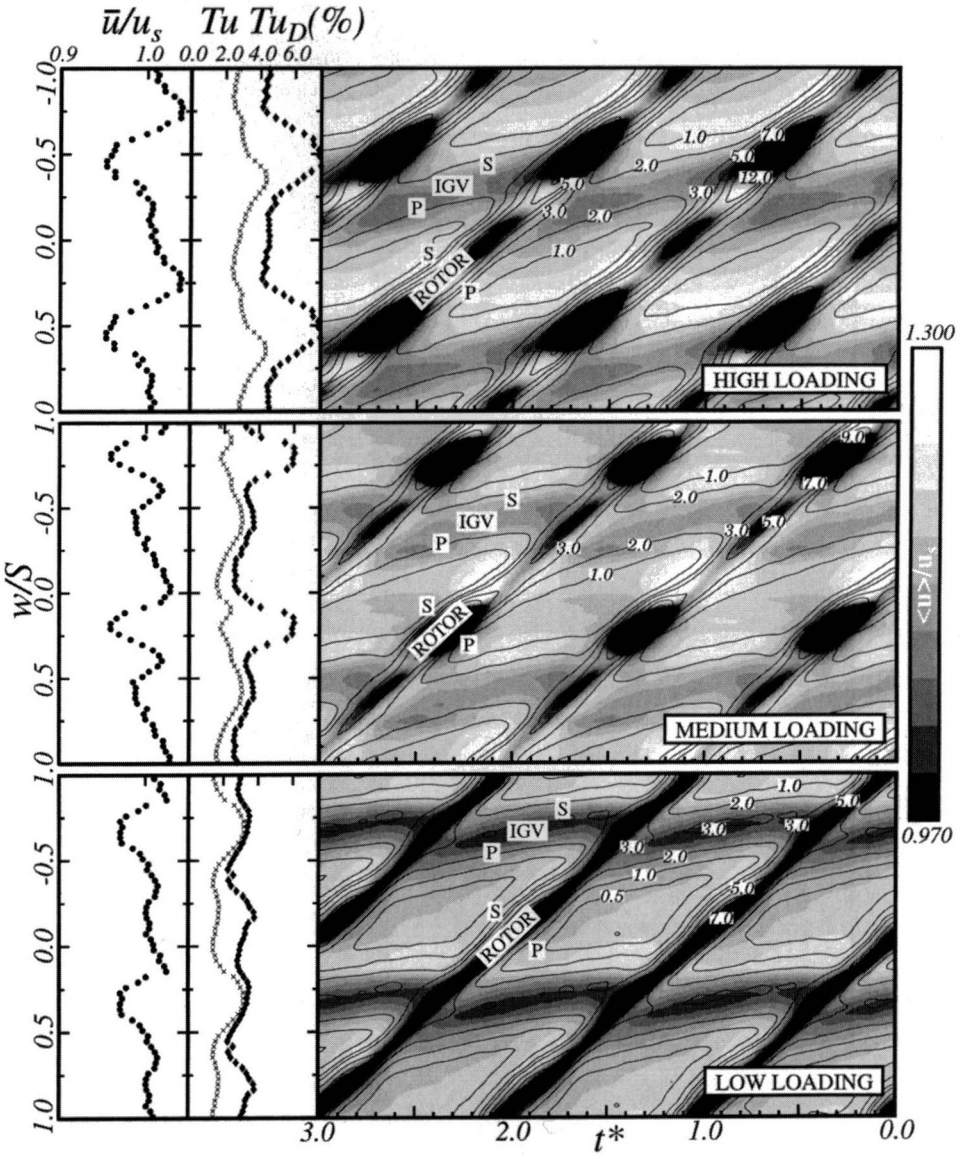

Fig. 3 Inflow velocity field from hot-wire measurements 55.7%c axial distance upstream of stator leading edge at midblade height (showing IGV wake dispersion and interaction with rotor wakes). Line contours indicate ensemble-averaged turbulence level $\langle Tu \rangle$ (percent). Gray shading indicates dimensionless ensemble-averaged velocity $\langle u \rangle / u_s$.

surfaces. These are interspersed with regions of lower $\langle \tau_{rms} \rangle$ where transition is delayed. The latter effect is most marked for $a/S = 0.50$, where the IGV wake street lies in the middle of the stator passage and the stator blades are subjected to a higher level of periodic disturbance from the rotor wakes. The level of dimensionless $\langle \tau_{rms} \rangle$ in the wake-induced transition path initially falls away from the leading edge, but subsequently rises as sustained transition commences.

The behavior at low loading is noticeably different due to transition occurring through laminar separation bubbles on both surfaces. The periodicity and extent of suction surface transition is significantly reduced for both clocking cases. Here transition occurs through a midchord bubble, with re-attachment around $s^* = 0.75$ where the wall shear stress fluctuations peak. It should be noted that the normalizing process accentuates the values of dimensionless shear stress fluctuations in regions of low wall shear prior to turbulent re-attachment. Pressure surface transition occurs through a leading edge bubble with re-attachment around $s^* = -0.10$. There is evidently a much greater susceptibility to changes in the free-stream disturbance field when transition occurs close to the leading edge.

A region of high dimensionless $\langle \tau_{rms} \rangle$ is observed close to the trailing edge on the stator suction surface in all cases. This is due to incipient turbulent separation reducing the value of the normalizing quantity $\bar{\tau}$, rather than a true increase in wall shear stress fluctuations.

(b) Ensemble-Averaged Intermittency and Relaxing Flow Probability. Ensemble-averaged values of turbulent intermittency $\langle \gamma \rangle$ obtained from the surface hot-film measurements are indicated by shading on $t^* \sim s^*$ plots in Fig. 5. The grading is from white for laminar flow ($\langle \gamma \rangle = 0$) to black for fully turbulent flow ($\langle \gamma \rangle = 1$). Values of γ were determined by a hybrid probability distribution function and peak-valley counting method described by Solomon and Walker (1995b) and Solomon (1996).

Figure 5 also shows line contours of constant ensemble-averaged relaxing nonturbulent flow probability $\langle \kappa \rangle$. The latter type of flow was identified by $d\tau/dt$ remaining negative immediately following the passage of a turbulent spot (i.e., switching of intermittency from 1 to 0). It is characterized by a higher wall shear stress, with a resulting increase in stability and resistance to separation compared to a steady laminar boundary layer subjected

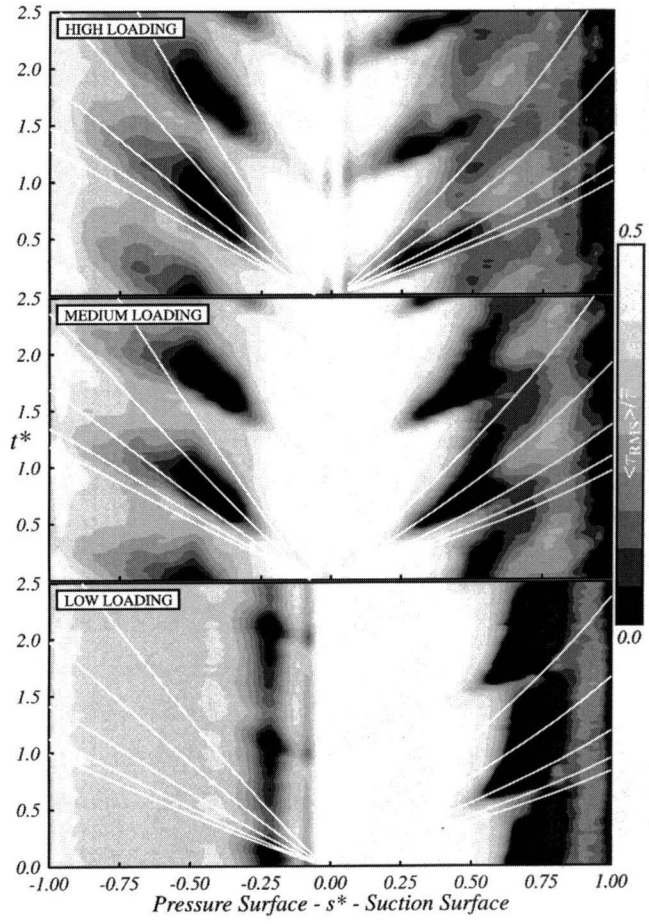

Fig. 4(*a*) IGV wake street on stator (*a*/*S* = 0.00)

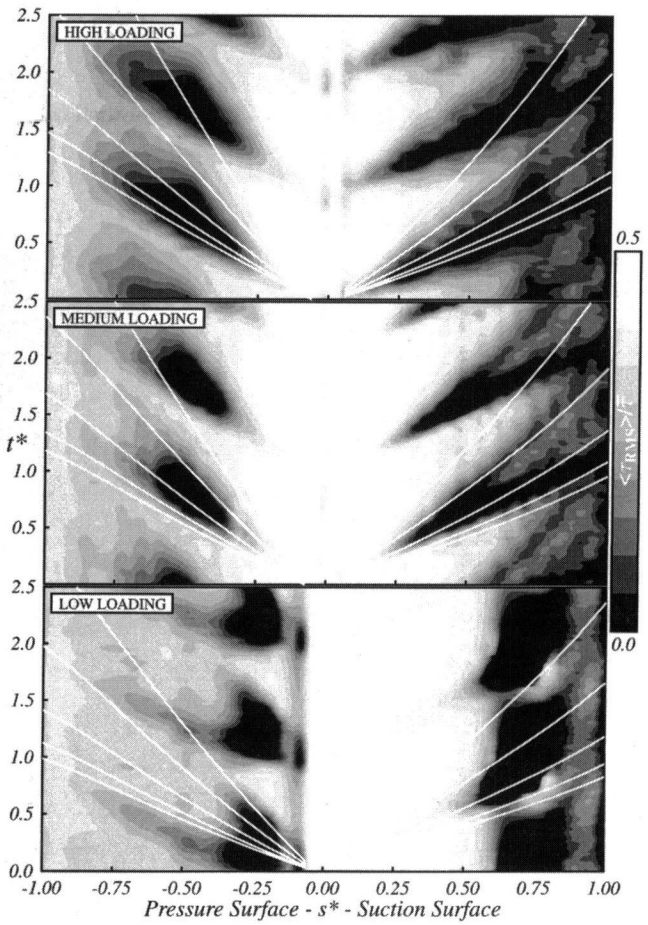

Fig. 4(*b*) IGV wake street in passage (*a*/*S* = 0.50); particle trajectories for 1.0*U*, 0.88*U*, 0.7*U*, 0.5*U*, 0.35*U* overlaid

Fig. 4 Ensemble-averaged rms quasi-shear stress (normalized by $\bar{\tau}$); surface hot-film observations on stator at midblade height

to the same streamwise pressure gradient. Higher values of $\langle\kappa\rangle$ indicate a greater degree of such "calming" effects, and a more regular appearance of the preceding turbulent spots, which are a necessary prerequisite for this type of flow. The results shown in Fig. 5 have been processed without manual intervention, apart from setting of universal window time and threshold parameters.

Superimposed on Fig. 5 are curves showing the periodic variation in random free-stream disturbance level $\langle Tu\rangle$ obtained from the inflow measurements 55.7%c upstream of the stator leading edge. The peak value of $\langle Tu\rangle$ is always observed within passing rotor wake regions. Direct comparisons of free-stream turbulence variations for the two clocking cases are presented in Fig. 4, Part II of this paper.

There is some identification of turbulence close to the leading edge that mirrors the high levels of $\langle\tau_{rms}\rangle$ seen in Fig. 4. This may be partly due to genuine incipient turbulent spots that subsequently decay, or to spurious turbulence identification associated with leading edge potential flow fluctuations produced by passing free-stream disturbances. In any case, this "turbulence" rapidly decays away from the leading edge. There is an associated region of calmed flow ($\langle\kappa\rangle > 0$) near the leading edge on the pressure surface, possibly also spurious, which is antisymmetric with the turbulent flow patch identified on the suction surface. The strength of these leading edge effects increases with loading.

It should be recognized that the values of intermittency obtained from surface hot-film observations will underestimate the peak value of intermittency obtained in a decelerating boundary layer. This explains the anomalous fall in $\langle\gamma\rangle$ close to the trailing edge on the suction surface, where the turbulent or transitional boundary layer is approaching separation. The anomalous increase in $\langle\kappa\rangle$ in this region is probably due to incipient separation events being misidentified as relaxing flow. Apart from these local leading and trailing edge effects, Fig. 5 is considered to give a fairly reliable indication of the transitional flow behavior on the stator blade surface. The contours of $\langle\gamma\rangle$ certainly give a much clearer indication of transitional flow behavior than those of $\langle\tau_{rms}\rangle$. The wake-induced turbulent strips appear as dark tongues followed by regions of strong calming with high values of relaxing flow probability $\langle\kappa\rangle$.

The contours of $\langle\kappa\rangle$ give the best indication of transitional flow periodicity. This is significantly greater for the clocking case $a/S = 0.50$ shown in Fig. 5(*b*), which corresponds to the IGV wakes passing through the stator passage and relatively pure rotor wakes impinging on the stator leading edge. In this case, peak values of $\langle\kappa\rangle$ exceeding 0.8 are observed on the suction surface at high and medium loading, and on the pressure surface at low loading. This indicates that a wake-induced turbulent strip is occurring in over 80 percent of rotor wake passing events. Peak values of $\langle\kappa\rangle$ on the pressure surface only reach about 0.4 on the pressure surface at medium and high loading, and there is little variation in the transition behavior for these two cases. The lowest periodicity occurs on the suction surface for the low loading case, where the blade is operating at large negative incidence and transition occurs through a midchord separation bubble with turbulent re-attachment around $s^* = 0.75$. Here the contours of $\langle\gamma\rangle$ are nearly straight.

The transitional flow periodicity is markedly reduced for the clocking case $a/S = 0.00$ shown in Fig. 5(*a*), which corresponds to the IGV wake street being incident on the stator. On the suction surface at high and medium loading the peak value of $\langle\kappa\rangle$ is now

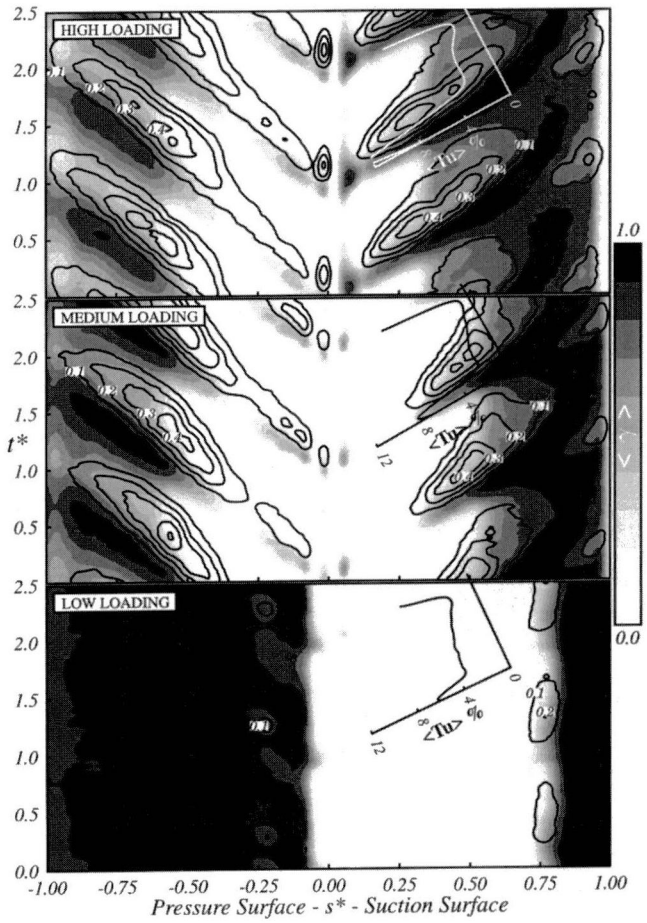

Fig. 5(*a*) IGV wake street on stator (*a*/*S* = 0.00)

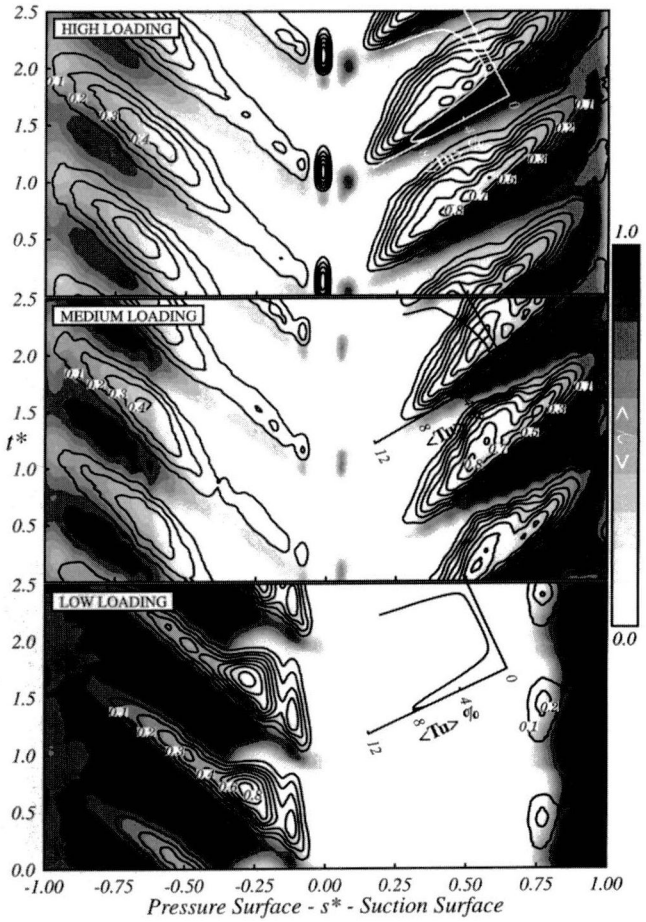

Fig. 5(*b*) IGV wake street in passage (*a*/*S* = 0.50); temporal variation of ensemble-averaged turbulence level ⟨*Tu*⟩ (percent) on stator stagnation streamline at inflow plane also shown

Fig. 5 Ensemble-averaged intermittency (shading) and probability of relaxing flow (line contours)

only 0.4, and the chordwise extent of transitional flow is much smaller. On the pressure surface at low loading, the flow periodicity has almost disappeared. However, for the cases showing weaker periodicity with $a/S = 0.50$ (namely the pressure surface at high and medium loading, and the suction surface at low loading) the transitional flow behavior is quite similar to that for $a/S = 0.00$.

Transition in the wake-induced path apparently commences at the leading edge on both suction and pressure surfaces in the high and medium loading cases. However, the values of intermittency initially decay or remain at a low level until some critical situation is reached and sustained transition can occur. The values of $\langle\gamma\rangle$ then increase monotonically until transition is complete (ignoring the spurious reductions near the trailing edge described above). As expected, there is a general trend for the transition onset to move forward on the suction surface and rearward on the pressure surface as loading is increased.

This behavior is most clearly seen on the pressure surface at high and medium loading, where a streak of low-level intermittency in the rotor wake path extends to the leading edge, but sustained transition does not commence until about $s^* = -0.4$. Another factor here could be the impingement of the rotor wake jet on the stator pressure surface, which will directly impress turbulent rotor wake fluctuations on the boundary layer fluid. This provides further potential for the inception of unsustainable turbulent spots, or the misidentification of these free-stream fluctuations as boundary layer turbulence. This situation should not occur on the suction surface, where the wake jet is convecting rotor wake fluid away from the stator.

(c) Long-Term Mean Intermittency and Relaxing Flow Probability. Plots of time-mean intermittency $\bar{\gamma}$ and relaxing flow probability $\bar{\kappa}$ give a simplified picture of the variation in transitional flow behavior due to IGV clocking and the associated changes in calming effects arising from altered free-stream periodicity.

Curves of $\bar{\gamma}$ shown in Fig. 6 exhibit local peaks in apparent intermittency at the leading edge for both the high and medium loading cases. These decay rapidly until a sustained increase in $\bar{\gamma}$ occurs farther along the blade surface. The level of $\bar{\gamma}$ prior to this increase is significantly higher on the pressure surface, possibly due to boundary layer perturbation by rotor wake jet impingement. Transition is completed more rapidly on the suction surface at high and medium loading and the pressure surface at low loading for the lower periodicity clocking case $a/S = 0.00$. On the opposite surface of the stator in these respective cases, altering the free-stream periodicity by IGV clocking produces little change in the distribution of $\bar{\gamma}$.

Figure 7 indicates that the significant variations in $\bar{\gamma}$ seen in Fig. 6 are accompanied by marked changes of the relaxing flow probability $\bar{\kappa}$. The stronger free-stream periodicity for $a/S = 0.50$ produces corresponding increases in the transitional flow length and the magnitude of calming (as indicated by higher peak values of $\bar{\kappa}$). At high and medium loading, relaxing flow events (or calming) are observed over 70–80 percent of the suction surface, and the distributions of $\bar{\kappa}$ indicate that transition is not quite complete at the trailing edge. For the cases in which IGV clocking produces a negligible change in the intermittency distribution there is a similarly small variation in the relaxing flow probability.

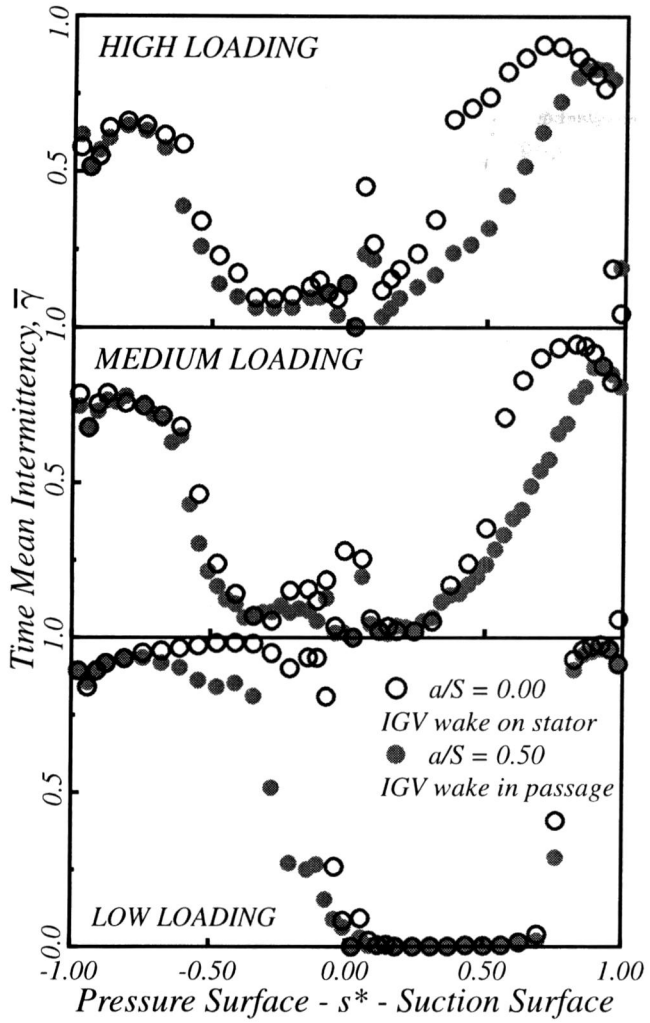

Fig. 6 Long-term mean intermittency; variation with stator loading and IGV clocking

(d) Extent of Transitional Flow. The extent of transitional flow on the stator is presented on an ensemble-averaged basis in Fig. 8. The periodic variations in transitional flow are indicated by shading on the $t^* \sim s^*$ diagram between limits of $\langle\gamma\rangle = 0.10$ for transition onset and $\langle\gamma\rangle = 0.90$ for transition completion. These limiting values were chosen to minimize spurious effects of turbulence misidentification, which occur at very low and very high intermittency. The full extent of transitional flow will be a little greater than that indicated.

A slight difference in arrival times of the wake-induced transitional strips is evident for the two IGV clocking positions. This differential increases with loading, and may be due to circumferential variations in mean velocity altering the rotor wake convection speed. This effect would be smaller for the reduced axial row spacings typical of practical machines.

Periodic fluctuations in the onset of transition are much weaker for the clocking case $a/S = 0.00$, where the IGV wake street impinges on the stator and the free-stream periodicity is lowest. This is seen most clearly on the suction surface at high and medium loading. For $a/S = 0.50$, transition onset occurs much later in the regions between successive rotor wake passages. It will be seen from the theoretical predictions in Part II of this paper that the earlier onset of $a/S = 0.00$ is largely due to the higher level of free-stream turbulence $\langle Tu\rangle$ when the IGV wake impinges on the stator. The calming effects of preceding wake-induced transitional strips appear to have had only a slight influence on the interwake transition onset for $a/S = 0.50$.

There are two main reasons for this behavior. First, the wake-induced transitional strips do not occur on every rotor wake passage; hence there will always be some transition events where calming is nonexistent. Second, the region in which calming is significant spreads only gradually from the vertex of the wake-induced transitional strips, with a limiting convection speed of around $0.3U$ at its trailing edge.

Increased free-stream periodicity generally produces both a later transition onset and a lengthening of the transition region between successive rotor wake passages. The interwake transitional region extends to the rear of the suction surface at high and medium loading, and will apparently be terminated only by turbulent contamination from adjacent wake-induced turbulent strips. The lengthening of the transition region will be influenced by calming from the wake-induced transitional strips and also by the effects of fluctuating blade surface pressure distributions on boundary layer stability. Calculations with the unsteady hybrid Navier–Stokes/Euler code UNSFLO (Giles and Haimes, 1993) suggest that the latter effect may be most marked on the pressure surface at medium and high loading, where unsteadiness may cause the pressure gradient to fluctuate between positive and negative.

The most dramatic effect of increased periodicity is observed on the pressure surface for the low loading case. Here transition occurs through a leading edge separation bubble, which is little affected by free-stream unsteadiness for the case of IGV wake impingement on the stator, $a/S = 0.00$; but the impingement of stronger rotor wake disturbances for $a/S = 0.50$ produces a

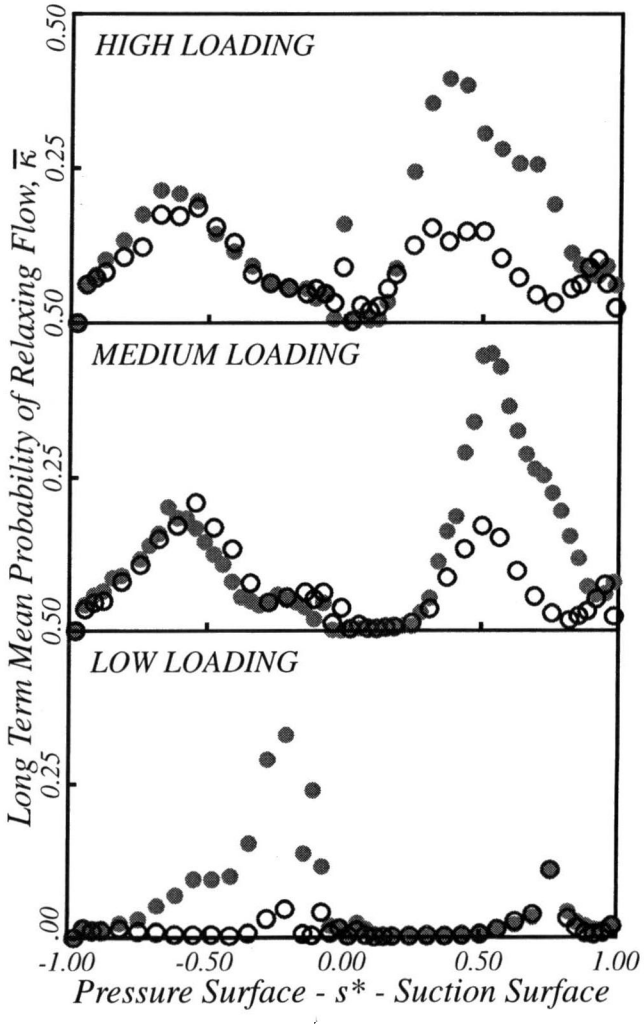

Fig. 7 Long-term mean probability of relaxing flow; variation with stator loading and IGV clocking

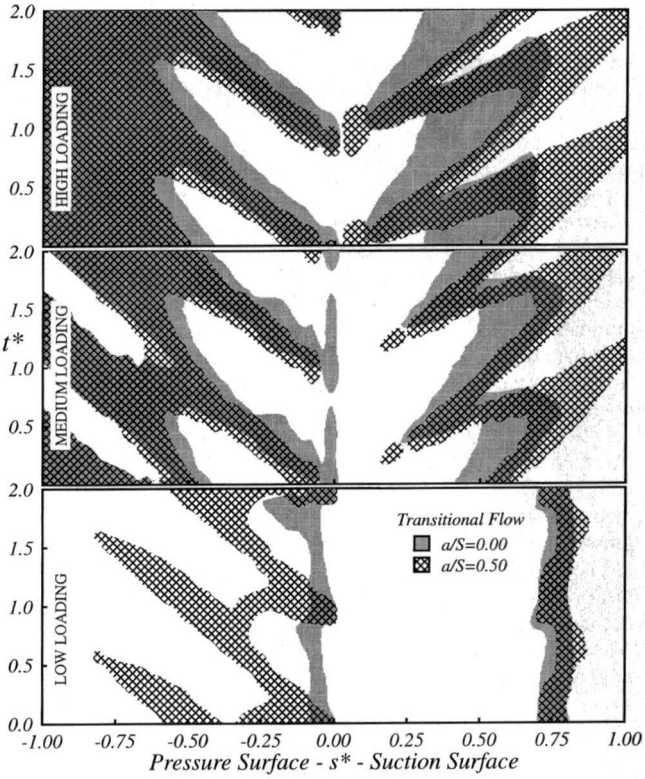

Fig. 8 Extent of transitional flow on stator, showing influence of stator loading and IGV clocking (transition onset: $\langle\gamma\rangle = 0.10$; transition end: $\langle\gamma\rangle = 0.90$)

marked change in the transitional flow distribution. Transition onset occurs at the leading edge in a thin strip along the rotor wake path for $a/S = 0.50$. This is immediately followed (in time) by a region of strong calming ($\langle\kappa\rangle_{max} \simeq 0.8$) along which the transition region is greatly extended. After this calming region there appears to be a marked leading edge separation, with reattachment around 25 percent chord characterized by a very short transition and associated region of very high wall shear stress fluctuations (shown in Fig. 4(*b*)).

The theoretical transition onset predictions in Part II of this paper match the low loading pressure surface observations very well, suggesting that this behavior is due to changes in the periodic variation of free-stream turbulence level $\langle Tu\rangle$. A similar sensitivity to clocking effects is not observed on the suction surface at low loading, where transition occurs through a midchord separation bubble.

Concluding Remarks

The periodicity of transition on the outlet stator of a 1.5-stage axial compressor was strongly influenced by both blade loading and clocking of the upstream IGV row. The magnitude of these effects tended to increase with incidence, and were strongest when transition occurred through a leading edge separation bubble. Little change occurred when transition occurred though a midchord separation bubble. Marked variations in transitional flow periodicity were never observed on both suction and pressure surfaces at once, in all the cases examined. The surface hot-film observations showed significant fluctuations from leading edge potential flow interactions with rotor wake disturbances; they also indicated perturbed laminar boundary layer behavior on the pressure surface in regions of rotor wake jet impingement. The existence of significant potential flow (pressure field) interaction at the stator leading edge is confirmed by hot-wire observations outside the boundary layer and UNSFLO calculations not reported here.

The measurements reported here relate to a single blade element at midspan. Skewing of the IGV wake street relative to the radial direction as it convects downstream will cause stator blade elements at different radial positions to experience unsteady flow behavior ranging between the two limiting cases of maximum and minimum periodicity. The blades of an embedded rotor row in a multistage machine will experience similar flow variations.

It is important for designers to appreciate the resulting range of unsteady conditions under which axial turbomachine blade elements have to operate. It appears from observations of the stator suction surface behavior at low loading that flow acceleration at the leading edge will reduce transitional flow periodicity at design conditions. Thus more modern blade sections with peak suction further rearward could show a reduced transitional flow periodicity. On the other hand, the lower axial spacings in practical turbomachines would tend to increase the magnitude of periodic free-stream disturbances and associated periodic transition phenomena.

In Part II of this paper, the experimental data will be used to validate various schemes of transition prediction using quasi-steady models. The comparisons between prediction and experiment will give further insights into the transition behavior observed here, and the physical nature of transition processes on the compressor blade.

Acknowledgments

Financial support from Rolls-Royce plc is gratefully acknowledged.

References

Abu-Ghannam, B. J., and Shaw, R., 1980, "Natural Transition of Boundary Layers—the Effects of Pressure Gradient and Flow History," *Journal of Mechanical Engineering Science,* Vol. 22, No. 5, pp. 213–228.

Cumpsty, N. A., Dong, Y., and Li, Y. S., 1995, "Compressor Blade Boundary Layers in the Presence of Wakes," ASME Paper No. 95-GT-443.

Evans, R. L., 1975, "Turbulence and Unsteadiness Measurements Downstream of a Moving Blade Row," ASME *Journal of Engineering for Power,* Vol. 97, pp. 131–139.

Funazaki, K., Kitazawa, T., Koizumi, K., and Tanuma, T., 1997a, "Studies on Wake-Disturbed Boundary Layers Under the Influences of Favourable Pressure Gradient and Free-Stream Turbulence, Part I: Experimental Setup and Discussions on Transition Model," ASME Paper No. 97-GT-451.

Funazaki, K., Kitazawa, T., Koizumi, K., and Tanuma, T., 1997b, "Studies on Wake-Disturbed Boundary Layers Under the Influences of Favourable Pressure Gradient and Free-Stream Turbulence, Part II: Effect of Freestream Turbulence," ASME Paper No. 97-GT-452.

Giles, M., and Haimes, R., 1993, "Validation of a Numerical Method for Unsteady Flow Calculations," ASME JOURNAL OF TURBOMACHINERY, Vol. 115, pp. 110–117.

Halstead, D. E., Wisler, D. C., Okiishi, T. H., Walker, G. J., Hodson, H. P., and Shin, H.-W., 1997, "Boundary Layer Development in Axial Compressors and Turbines: Parts 1–4," ASME JOURNAL OF TURBOMACHINERY, Vol. 119; Part 1: pp. 114–127; Part 2: pp. 426–444; Part 3: pp. 225–237; Part 4: pp. 128–139.

Hodson, H. P., Huntsman, I., and Steele, A. B., 1994, "An Investigation of Boundary Layer Development in a Multistage LP Turbine," ASME JOURNAL OF TURBOMACHINERY, Vol. 116, pp. 375–383.

Hourmouziadis, J., 1989, "Aerodynamic Design of Low Pressure Turbines," pp. 8.1–8.40, Fottner, L., ed., *AGARD Lecture Series No. 167, Blading Design for Axial Turbomachines,* AGARD.

Howell, A. R., 1945, "Fluid Dynamics of Axial Compressors," *Proc. Inst. Mech. Eng. E,* Vol. 153, pp. 441–452.

Lockhart, R. C., and Walker, G. J., 1974, "The Influence of Viscous Interactions on the Flow Downstream of an Axial Compressor Stage," presented at the 2nd International Symposium on Air Breathing Engines, Sheffield, UK.

Mayle, R. E., 1991, "The Role of Laminar–Turbulent Transition in Gas Turbine Engines," ASME JOURNAL OF TURBOMACHINERY, Vol. 113, pp. 509–537, The 1991 IGTI Scholar Lecture.

Mayle, R. E., 1992, "Unsteady Multimode Transition in Gas Turbine Engines," AGARD PEP 80.

Oliver, A. R., 1961, "Comparison Between Sand Cast and Machined Blades in the Vortex Wind Tunnel," Report ME 103, Aeronautical Research Laboratories, Melbourne, Australia.

Orth, U., 1993, "Unsteady Boundary-Layer Transition in Flow Periodically Disturbed by Wakes," ASME JOURNAL OF TURBOMACHINERY, Vol. 115, pp. 707–713.

Schulte, V., and Hodson, H. P., 1998a, "Unsteady Wake-Induced Boundary Layer

Transition in High Lift LP Turbines," ASME JOURNAL OF TURBOMACHINERY, Vol. 120, pp. 28–35.

Schulte, V., and Hodson, H. P., 1998b, "Prediction of the Becalmed Region for LP Turbine Profile Design," ASME JOURNAL OF TURBOMACHINERY, Vol. 120, pp. 839–846.

Solomon, W. J., 1996, "Unsteady Boundary Layer Transition on Axial Compressor Blades," Ph.D. Thesis, University of Tasmania, Hobart.

Solomon, W. J., and Walker, G. J., 1995a, "Incidence Effects on Wake-Induced Transition on an Axial Compressor Blade," *Proc. 12th International Symposium on Air Breathing Engines,* Melbourne, Australia.

Solomon, W. J., and Walker, G. J., 1995b, "Observations of Wake-Induced Transition on an Axial Compressor Blade," ASME Paper No. 95-GT-381.

Walker, G. J., 1972, "An Investigation of the Boundary Layer Behaviour on the Blading of a Single-Stage Axial-Flow Compressor," Ph.D. Thesis, University of Tasmania.

Walker, G. J., 1975, "Observations of Separated Laminar Flow on Axial Compressor Blading," ASME Paper 75-GT-63, Houston.

Walker, G. J., 1993, "The Role of Laminar-Turbulent Transition in Gas Turbine Engines—A Discussion," ASME JOURNAL OF TURBOMACHINERY, Vol. 117, pp. 207–217.

Walker, G. J., Hughes, J. D., Köhler, I., and Solomon, W. J., 1998, "The Influence of Wake-Wake Interactions on Loss Fluctuations of a Downstream Axial Compressor Blade Row," ASME JOURNAL OF TURBOMACHINERY, Vol. 120, pp. 695–704.

Walker, G. J., Hughes, J. D., Solomon, W. J., and Köhler, I., 1997, "Wake Mixing and Blade Clocking Effects in an Axial Compressor," *Proc. 13th Int. Symp. on Air Breathing Engines,* Chattanooga.

Periodic Transition on an Axial Compressor Stator: Incidence and Clocking Effects: Part II—Transition Onset Predictions

W. J. Solomon
Ohio Aerospace Institute,
General Electric Aircraft Engines,
Cincinnati, OH 45215

G. J. Walker

J. D. Hughes

School of Engineering,
University of Tasmania,
Hobart, Australia

Transition onset observations from a 1.5-stage axial compressor outlet stator presented in Part I of this paper are compared with the predictions of conventional transition correlations applied in a quasi-steady manner. The viscous/inviscid interaction code MISES is used to predict the blade surface pressure distributions and boundary layer development. The temporal variation in transition onset is then predicted using ensemble-averaged free-stream turbulence data from the compressor measurements. This simple procedure captures most significant features of the complex transition process on the compressor, and is clearly superior to fixed transition models based on long-term average free-stream turbulence levels. Parallel computations for both natural and bypass transition modes indicate that the natural transition mode tends to dominate on the compressor. This is at variance with turbine airfoil experience, where bypass transition is clearly more important. Comparison of prediction and experiment highlights the significance of leading edge potential flow interactions in promoting periodic wake-induced transition. Viscous/inviscid interactions in the neighborhood of transition can also have an important influence on boundary layer stability and separation phenomena.

Introduction

Measurements of the turbulence levels experienced by gas turbine engine blading are difficult to make and are not widely available. It is generally accepted that turbulence levels are high enough that the dominant mode of transition for attached boundary layers is bypass transition (Mayle, 1991). Methods for predicting the onset of bypass transition based on the correlations of Abu-Ghannam and Shaw (1980) or Mayle (1991) are widely used for turbomachinery design. These empirical correlations are based on steady flow data. Mayle and Schulz (1997) and Johnson and Ercan (1996) present alternative methods for predicting bypass transition, which calculate the effect free-stream turbulence has on the pre-transitional laminar boundary layer. Johnson and Ercan (1996) found that low-frequency disturbances were most likely to cause bypass transition while Mayle and Schulz (1997) suggest that the highest frequency free-stream turbulence fluctuations that are not damped will be first to produce fluctuations in the laminar boundary layer. Again, these semi-empirical models were developed for steady flow.

Time-resolved measurements of the transition process in the presence of wake passing, such as those presented in Part I of this paper, or by Halstead et al. (1997), reveal a complex variation of the transition onset location through a blade passing period. This paper explores the possibility of using the existing empirical steady flow transition methods to predict the unsteady transition onset location.

The fluctuations in boundary layer thickness associated with transition onset unsteadiness can be extremely large. Halstead et al. (1997) observed a twofold variation in momentum thickness over a rotor wake passing period at 90 percent suction surface length for their third-stage high-pressure compressor stator baseline case (2B). For the compressor stator of the present investigation, Walker et al. (1998) reported near-wake momentum thickness varying by a factor of about 4 in the peak unsteadiness configuration. Such large perturbations in boundary layer thickness may have important implications for stall inception. Cherret's (1996) study of rotor–stator interaction in a single-stage transonic fan concluded that "at midspan the rotor wakes augmented an incipient stator suction surface separation, causing a transient (larger) separation and reattachment."

Schulte and Hodson (1998) have demonstrated an unsteady model of the transition process that closely matches experimental measurements of unsteady boundary layer parameters through the transition zone. This model gives important insight into the wake-induced transition process and the nature of the becalmed flow following a turbulent spot, but it still requires that the transition onset location be specified. The simple quasi-steady approach presented in the current paper addresses this deficiency and has the advantage that it can be applied using existing steady flow models. It is purely concerned with describing the transition onset behavior and does not attempt to model the subsequent transitional flow.

A quasi-steady approach to predicting the onset of wake-induced transition on a turbine cascade was presented by Addison and Hodson (1990). They found that the periodic unsteadiness due to the wake velocity defect is of secondary importance in triggering wake induced transition compared with the elevated free-stream turbulence in the passing wakes. In the model proposed by Addison and Hodson (1990), allowance was made for the decay of wake turbulence intensity and spreading of wakes as they are convected through the turbine blade passage. The current work achieved reasonable results without considering these effects, possibly due to the differing natures of turbine and compressor blade potential flow-fields and wake-jet directions.

The vehicle used in the current paper to test the steady flow transition models is the MISES code of Youngren and Drela (1991). This is a steady flow code that does not model the full unsteady wake-induced transition process. Instead, the ensemble average inlet flow turbulence measured over a wake passing period has been discretized and the flow at each instant calculated using the instantaneous inlet turbulence level as if the flow was steady.

Contributed by the International Gas Turbine Institute and presented at the 43rd International Gas Turbine and Aeroengine Congress and Exhibition, Stockholm, Sweden, June 2–5, 1998. Manuscript received by the International Gas Turbine Institute February 1998. Paper No. 98-GT-364. Associate Technical Editor: R. E. Kielb.

In this way, a "quasi-steady" simulation of the unsteady boundary layer transition process is constructed. When the results are plotted, allowance is made for the time taken for the turbulence to propagate from the inlet to the transition point.

A quasi-steady approach would fail if the frequency of the variation in inlet conditions (blade passing) was comparable with the propagation time of disturbances into the boundary layer. Addison and Hodson (1990) have demonstrated that, for typical turbomachinery applications, diffusion across the boundary layer is sufficiently faster than the wake passing period for the quasi-steady assumption to be applicable. The quasi-steady approach must also fail to predict unsteady potential flow effects such as blade-row interaction. The compressor used in the current investigation has axial gaps several times larger than would be used in an engine, making blade row potential-flow interactions effectively negligible. However, the localized potential-flow interactions associated with the passage of rotor wakes over the stator leading edge were still significant.

A simple quasi-steady application of existing transition onset models has been found to give surprisingly good agreement with the experimental transition measurements of Part I of this paper. The inherent inability of the current model to predict the unsteady boundary layer behavior and calming effects downstream of transition onset would limit the accuracy of loss estimates that could be obtained by integrating the results over a blade passing period, especially in cases with periodic separation, which is known to be influenced by calming. Nevertheless, this simple model allows a designer to estimate the importance of unsteady transition, given a reasonable estimate of the range of inlet turbulence levels during a wake-passing period. If considered significant, a full unsteady analysis of the transitional flow can be carried out by the method of Schulte and Hodson (1998) using the transition onset behavior specified by the present procedure.

Description of the MISES Code

The MISES code of Youngren and Drela (1991) is a steady-flow blade-to-blade method, which uses a global Newton–Raphson scheme to solve simultaneously the viscous boundary layer equations and the inviscid flow field. The simultaneous viscous/inviscid coupling yields a robust method for strongly interacting flows with boundary layer separation bubbles and is fast enough for a designer to run interactively.

The viscous flow is solved using an integral boundary layer method. A two-equation model is used for the laminar boundary layer. A third equation is solved to calculate the amplification of instabilities in the laminar boundary layer. Downstream of the transition point, this third equation is replaced by a lag equation in a three-equation turbulent boundary layer formulation. At least two equations must be used for the laminar boundary layer method to allow the model to be applied in both attached and separated flow. A single-equation model, where the shape factor H is uniquely related to the local pressure gradient parameter, will fail.

The inviscid flow is solved using a conservative form of the steady Euler equations on an intrinsic finite volume grid. One family of grid lines corresponds to the streamlines.

Transition Models in MISES. MISES evolved from external aerodynamics flow solvers and inherited an e^n-type transition correlation. This method, based on the Orr–Somerfield equation, is used to predict the growth of Tollmien–Schlichting (T–S) waves in the laminar boundary layer. Natural transition is predicted when the amplification ratio has reached some critical level, $e^{n_{crit}}$. At the low turbulence levels commonly found in external aerodynamics, $n_{crit} = 9.0$ is typically used. The transition model in MISES uses a correlation due to Mack (1977) to adjust n_{crit} for different raised turbulence levels. Further adjustment to n_{crit} is made to allow for larger turbulence levels than the original Mack correlation. The relationship between n_{crit} and turbulence Tu used in MISES is given by

$$n_{crit} = -8.43 - 2.4 \ln (0.027 \tanh (Tu/2.7)) \quad (1)$$

A bypass transition criterion based on the Abu-Ghannam and Shaw (1980) correlation is also included in MISES. Drela (1995) found that when this transition correlation is expressed in its original form, using pressure gradient parameter λ_θ, the coupled viscous–inviscid problem becomes ill-posed. Drela re-expressed the correlation in terms of shape factor H to avoid this problem. The MISES version of the Abu-Ghannam and Shaw correlation is given by

$$\mathrm{Re}_{\theta s}(H, n_{crit}) = 155 + 89.0\left[0.25 \tanh\left(\frac{10}{H-1} - 5.5\right) + 1\right] \times (n_{crit})^{1.25} \quad (2)$$

This expression closely matches the original Abu-Ghannam and Shaw correlation for $Tu > 0.5$ percent. At lower turbulence levels, Eq. (2) overpredicts $\mathrm{Re}_{\theta,crit}$ compared with the original formulation.

Nomenclature

a = circumferential offset of stator blade leading edge from center of IGV wake avenue
c = blade chord
e^n = amplification ratio
i = blade incidence
s = surface distance
$s^* = s/s_{max}$ = dimensionless surface distance from leading edge
t = time
$t^* = t/T$ = dimensionless time
u = streamwise velocity
w = circumferential distance
w_1 = relative inlet velocity
x = distance along chord line
E = anemometer output voltage
E_o = anemometer voltage at zero flow
$H = \delta^*/\theta$ = shape factor
$\mathrm{Re}_1 = w_1 c/\nu$ = chord Reynolds number
$\mathrm{Re}_{ref} = U_{mb} c/\nu$ = reference Reynolds number
$\mathrm{Re}_\theta = \theta U/\nu$ = momentum thickness Reynolds number
S = blade pitch
T = rotor blade passing period
Tu = random disturbance level (turbulence)
Tu_D = total disturbance level
$\tilde{T}u$ = periodic disturbance level (unsteadiness)
U = local free-stream velocity
U_{mb} = rotor midspan velocity
V_a = mean axial velocity
α = flow angle from axial
γ = turbulent intermittency
δ^* = displacement thickness
θ = momentum thickness
κ = relaxing nonturbulent flow probability
$\lambda_\theta = (\theta^2/\nu)(dU/dx)$ = Pohlhausen pressure gradient parameter
ν = kinematic viscosity
τ = quasi-wall shear stress
τ_w = wall shear stress
$\phi = V_a/U_{mb}$ = flow coefficient

Superscripts, Subscripts, etc.

$\langle\ \rangle$ = ensemble (phase-lock) average value
$\bar{}$ = time-mean value
$'$ = instantaneous fluctuation from time-mean
$''$ = instantaneous fluctuation from ensemble mean
crit = critical
in = inlet
reat = re-attachment
s = pitchwise average
sep = separation
trans = transition

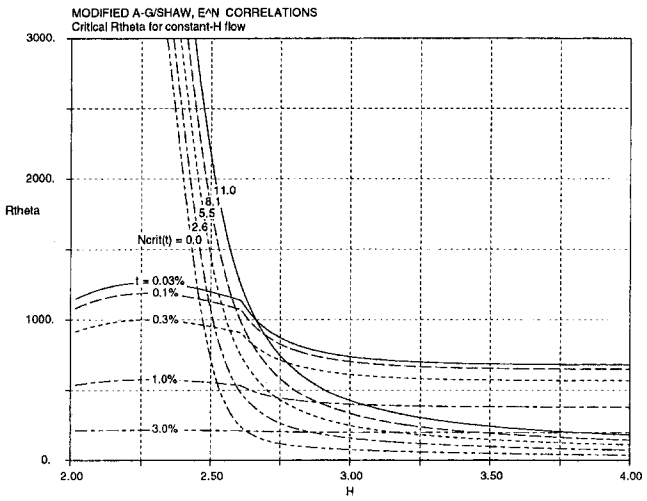

Fig. 1 Critical R_θ versus shape parameter H for similar flows; comparison of e^n method and Abu-Ghannam and Shaw method predictions (from Drela, 1995)

In the standard version of MISES, both the e^n and Abu-Ghannam and Shaw (natural and bypass) transition models are active simultaneously. Transition is initiated by whichever of the two alternative criteria is satisfied first. Figure 1 (from Drela, 1995) compares the behavior of the two transition models for similar flows. In adverse pressure gradients, where shape factor H is high, the e^n method predicts transition significantly earlier at all turbulence levels. The discrepancy in $\mathrm{Re}_{\theta,\mathrm{crit}}$ predictions at similar conditions for the two alternative transition modes brings the accuracy of both correlations into question. Experimental observations of Walker and Gostelow (1990), who found strong T–S wave activity in an adverse pressure gradient boundary layer, lend support to possibility that the e^n transition mode is important in this flow regime.

The length of the transition, where intermittency varies from 0 to 1, is unrealistically short in the MISES calculation and the turbulent spot growth mechanism is not modeled. A more accurate transition length model would require the addition of another equation into MISES and has not yet been attempted (Drela, 1995).

Modifications Made to MISES. A modified version of MISES was compiled with the e^n transition mode disabled in order to study the behavior of the Abu-Ghannam and Shaw model. The original Abu-Ghannam and Shaw correlation was constructed so that transition was impossible upstream of the neutral stability point of a laminar zero-pressure gradient boundary layer (Re_θ = 163). This criterion is physically unrealistic in adverse pressure gradients and in any flows with bypass transition, where turbulent breakdown occurs by a totally different process. As an alternative to the Abu-Ghannam and Shaw model, the following transition correlation recommended by Mayle (1991):

$$\mathrm{Re}_{\theta t} = 400Tu^{-5/8} \tag{3}$$

has also been tested. The Mayle correlation is insensitive to the local pressure gradient. Mayle justifies this on the grounds that the effect of pressure gradient on transition onset location is weak at turbulence levels above 3 percent.

The transition onset predictions using the unmodified MISES version (with both e^n and Abu-Ghannam and Shaw modes active) were used in the final comparison with the unsteady experimental data presented in this paper.

Experimental Test Cases

A 1.5-stage low-speed research compressor at the University of Tasmania was used to obtain the experimental data for this paper. The experiment is fully described in Part I of this paper. An array of surface-mounted hot-film sensors was used to measure the temporal variation of the transitional intermittency on both surfaces of the outlet stator blade at midblade height.

Testing was performed at a constant chord based Reynolds number of Re_c = 120,000 for three different loading levels (set by a cylindrical sliding throttle at the diffuser exit) and two different clocking positions of the Inlet Guide Vanes corresponding approximately to maximum and minimum rotor wake periodicity seen by the stator midheight blade element.

Matching Experimental Velocity Distributions. Stator blade surface velocity distributions were measured at the test conditions using surface pressure tappings. These data are reported in Solomon (1996). Comparisons between the measured velocity distributions and MISES calculations at the three loading levels are plotted in Fig. 2. These results were all obtained using n_{crit} = 4.0 in MISES, which is equivalent to inlet turbulence levels in the range 0.43 to 0.7 percent. (The inlet turbulence, calculated using a frozen turbulence hypothesis, varies with the local velocity at the transition point.) At these conditions, the flow was fully attached for ϕ = 0.60. (The slope discontinuity on the suction surface velocity prediction at s^* = 0.50 is a result of the very short transition length assumed by MISES.) For ϕ = 0.675 separation was at s^* = 0.54 and re-attachment was at s^* = 0.57 on the suction surface. For ϕ = 0.84, separation was at s^* = 0.65 with re-attachment at s^* = 0.78 on the suction surface.

The velocity distributions shown were measured at a clocking location with the IGV trailing edge and stator leading edge at the same circumferential location. Solomon (1996) measured changes in the velocity distribution of ±1.5 percent u/U_{mb} at s^* = 0.6 (the approximate location of the separation bubble) as the clocking was varied over one period at medium loading. Tests of the same blade section by Blight and Howard (1952) in a two-dimensional cascade under steady flow conditions with an inlet turbulence level of 0.2 percent showed a greater development of separation on the suction surface at incidences close to the medium and low loading cases.

To improve the agreement with the experimental velocity distributions, the MISES inlet angle was reduced from the measured value by 1.5 deg at ϕ = 0.60 and 1.0 deg for the ϕ = 0.675 and ϕ = 0.84 cases. The need for this adjustment may have arisen from uncertainties in the experimental data. The experimental surface velocity measurements were thought to be accurate to ±0.9 percent, although this did not include uncertainties associated with locating the stagnation streamline. The measured flow angles were nominally accurate to ±0.2 deg. Alternatively the trailing edge model in MISES may be inaccurate, which would cause an incorrect circulation prediction. At ϕ = 0.60 a linear stream-tube

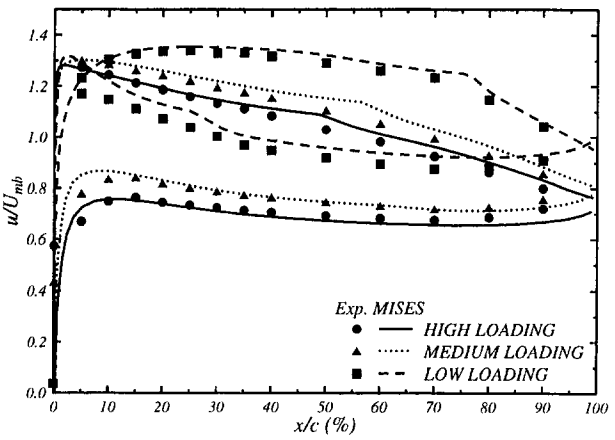

Fig. 2 Comparison of MISES predictions with measured velocity distributions at three loading levels, Re_c = 120,000

Table 1 Incidence angles, as measured and as used for calculation

Loading	ϕ	i°_{test}	i°_{MISES}
High	0.600	4.11	2.61
Medium	0.675	1.24	0.24
Low	0.840	-6.11	-7.11

contraction of 2.2 percent was also included in the calculation. This is consistent with measurements of axial-velocity ratio reported by Walker (1972). Table 1 compares the inlet angles measured in the test with those used for the MISES calculation. With these adjustments made, the agreement between the measured velocity distributions and the MISES calculations are very good and the predicted separation behavior matches the measurements of Walker (1972) very well.

The experimental data was expressed in terms of rotor midblade velocity U_{mb} for convenience. In each case, the calculated velocities were converted from u/U_{in} to u/U_{mb} using the nominal flow coefficient and the incidence angle i used in the MISES calculation by the relation

$$\frac{u_1}{U_{mb}} = \frac{\phi}{\cos(\alpha_1)} \tag{4}$$

where α_1 is the stator blade element air inlet angle from axial (α_1 = 45.0 deg + i).

Prediction of Transition Onset: Steady Flow

The MISES code was used to predict transition onset and separation bubble locations over the full range of ensemble-averaged inlet turbulence levels experienced by the stator blade. Each inlet turbulence level in turn was used as the steady flow turbulence level for a different MISES calculation. Note that the ensemble-averaged turbulence levels do not include the periodic unsteadiness caused by the wake passing ($\tilde{T}u$).

Results of these calculations for the three loading cases are presented in Fig. 3. These results have been plotted versus $Tu_{mb} = u''_{rms}/U_{mb}$ instead of the more usual $Tu_{in} = u''_{rms}/U_{in}$. Tu_{mb} was introduced to simplify the application of a frozen-turbulence assumption. It was considered necessary to account for the decrease in turbulence level that occurs as the flow accelerates from the inlet to the transition location on the blade. (This type of correction would be even more important for a turbine blade.) Given the velocity u/U_{mb} at the transition point (from Fig. 2), the local turbulence level is $Tu_{local} = Tu_{mb}/(u/U_{mb})$. It could be argued that Tu_{local} should be the value at the neutral stability point for the e^n mode, instead of at transition, but the difference in the results would be minor. This method of estimating the local turbulence through the blade passage neglects any turbulence decay.

Both the stator suction and pressure surfaces are represented in Fig. 3, with the leading edge corresponding to the point $s^* = 0.0$. At high turbulence levels, transition occurs in the attached flow and is indicated by a single point in the plot. At low turbulence levels, in cases where transition is downstream of laminar separation, three points are shown on the plot. These correspond to laminar separation, transition, and re-attachment. Re-attachment closely follows separated flow transition.

The solid line shows the results from the standard version of MISES with both the Abu-Ghannam and Shaw and e^n transition modes active. The other two sets of curves were obtained with the e^n model disabled. In both of these cases, calculation of separation bubbles was not very successful and failed completely at low turbulence. This is not surprising since neither of these models simulate the growth of disturbances in the separated shear layer. At low loading the pressure surface boundary layer undergoes laminar separation without re-attachment at the low turbulence level with the Mayle and Abu-Ghannam and Shaw models. This changed the

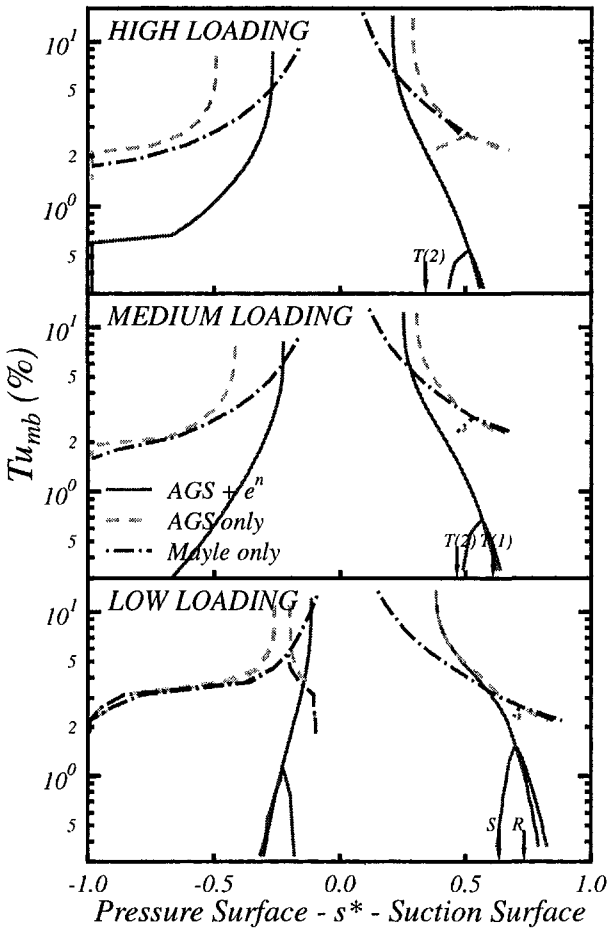

Fig. 3 Location of transition, separation, and reattachment on stator versus inlet free-stream turbulence level Tu_{mb}; variation with blade loading

velocity distribution sufficiently to affect the prediction of the laminar separation location on the suction surface.

In the low loading case, where the pressure surface boundary layer calculation underwent complete laminar separation, a separate study was performed to test the effect that the very thick pressure surface boundary layer had on the suction surface transition location. When the pressure surface boundary layer was tripped so it stayed attached, the suction surface transition location moved back closer to the location predicted by the Abu-Ghannam and Shaw correlation.

At high loading, transition by the e^n mode was predicted upstream of transition by the Abu-Ghannam and Shaw correlation except on the pressure surface for $Tu_{mb} < 0.6$ percent, where the boundary layer was laminar to the trailing edge. For the medium loading case, transition was by the e^n mode at all turbulence levels. At low loading, the e^n mode again dominated, except on the suction surface for $Tu_{mb} > 2.65$ percent where transition was by Abu-Ghannam and Shaw. Figure 1 shows that in adverse pressure gradients, where H is high, e^n transition occurs at a lower Re_θ. Both the Abu-Ghannam and Shaw and e^n (as modified by Mack) transition criteria were derived from correlation with experimental data. Ideally, in the range of turbulence levels where both are valid, both should match experimental data and consequently match each other if they were developed from the same data base. The discrepancy between the two methods observed here indicates either that insufficient data in strong adverse pressure gradients were available for the Abu-Ghannam and Shaw correlation, or that the e^n model is not accurate at these turbulence levels.

The Mayle transition model predicts transition upstream of the

other two at high turbulence levels and tends toward the Abu-Ghannam and Shaw transition location as turbulence level falls.

Arrows on Fig. 3 indicate transition, separation, and reattachment locations measured by Walker (1972) at similar flow conditions. $T(2)$ at high and medium loading indicates the transition location detected using a total head tube connected to a stethoscope. $T(1)$ in the medium loading case is the transition/reattachment point observed using a china-clay technique. The S and R arrows at low loading also indicate location of the separation bubble found using china-clay flow visualization for the reattachment and a steady-flow Thwaites calculation for the separation point.

Prediction of Transition Onset: Temporal Variation

Free-Stream Turbulence Variations. The first step in predicting the temporal variation of transition onset on the stator blade was to estimate the temporal variation of ensemble-averaged turbulence level $\langle Tu \rangle$ seen on the stator blade surface. This was done by the following procedure:

(a) Ensemble-averaged hot-wire measurements at $13.3\%c$ axial distance downstream of the stator trailing edge at midblade height were used to estimate the circumferential position of the stator relative to the center of the IGV wake street for each loading case and the nominal clocking positions $a/S = 0.00$ and $a/S = 0.50$. Examples of such measurements for the medium loading case have been published by Walker et al. (1997, 1998);

(b) The circumferential positions of the IGV wake street center $55.7\%c$ axial distance upstream of the stator leading edge were determined from hot-wire measurements of the inflow velocity field shown in Part I of this paper, Fig. 2. These measurements were obtained for one clocking position only, as the upstream effect of the stator at this position is known to be minimal;

(c) The stator stagnation streamline for each loading and nominal clocking case was assumed to lie at the respective circumferential offset from the position determined in (a) above;

(d) The variation of $\langle Tu \rangle$ with t^* for each case was determined from Fig. 2, Part I, for the corresponding values of w/S at the $55.7\%c$ upstream position;

(e) A frozen turbulence assumption was employed to estimate the values of $\langle Tu \rangle$ seen farther downstream on the stator blade surface.

The resulting temporal variations in $\langle Tu \rangle$ $55.7\%c$ upstream of the stator are plotted in Fig. 4. Two curves are presented for each loading case: $a/S = 0.00$ corresponding to the IGV wake street passing over the stator blade surface; and $a/S = 0.50$ with the IGV wake street passing through the center of the stator passage at midblade height. It is noted that these clocking positions are nominal, and accurate to no better than 0.1 in a/S. It is difficult to determine clocking positions a priori with great precision, and the circumferential blade positions initially selected were not readjusted after obtaining detailed hot-wire measurements to establish the exact clocking positions.

The clocking case with the IGV wake on the stator corresponds to a generally higher level of random turbulence $\langle Tu \rangle$ on the blade surface. For the other clocking case with the IGV wake street passing through the blade passage, the stator surface sees the passage of essentially isolated rotor wake disturbances with little adjacent IGV wake turbulence and a lower background turbulence level. The slight difference in behavior of the curves for the medium loading case is largely due to a small misalignment in stator circumferential position relative to the IGV wake street as noted above. This does not affect the validity of the present study, which is purely concerned with predicting the transition behavior on the stator for a given inflow disturbance field.

The transition calculations for the stator use the temporal variations in $\langle Tu \rangle$ from Fig. 4 together with a frozen turbulence assumption, which means that the local value of $\langle Tu \rangle$ is assumed

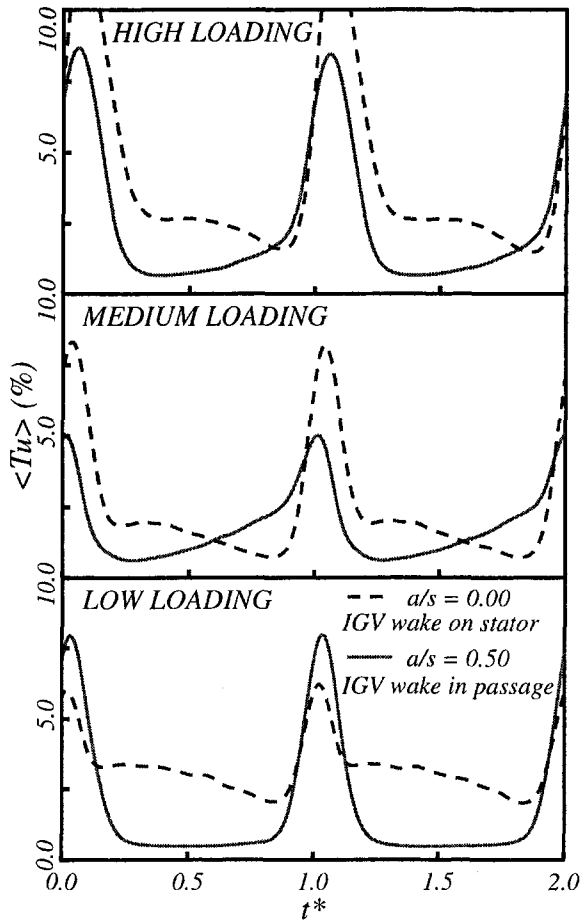

Fig. 4 Temporal variation of ensemble-averaged turbulence level $\langle Tu \rangle$ (percent) on stator stagnation streamline at inflow measurement plane 55.7%c axial distance upstream of stator leading edge; variation with stator loading and IGV clocking

to vary inversely with the local velocity farther downstream. This model neglects turbulence decay during convection downstream, and also possible turbulence production through straining near the stator leading edge. Measurements downstream of the rotor by Walker et al. (1997) showed the random turbulence component to vary only slowly with axial position.

Comparison of Predicted and Measured Transition Onset

Measured Onset. The temporal variations in stator blade transition onset position $\langle s^*_{trans} \rangle$ determined from this calculation procedure will now be compared with experimental observations of $\langle s^*_{trans} \rangle$ from surface hot-film measurements. The experimental onset variations are taken as the 10 percent ensemble-averaged intermittency contours from Fig. 4, Part I of this paper. The criterion $\langle \gamma \rangle = 0.10$ was chosen as giving a position reasonably close to the start of transition, which would not be too sensitive to errors in intermittency measurement. The actual transition onset will be a little farther upstream, but the error in its location from this simple procedure should be at worst a few percent of chord.

The contours of $\langle s^*_{trans} \rangle$ shown on Figs. 6(a) and 6(b) are rather ragged for $-0.1 < s^* < 0.1$ due to leading edge interaction effects with passing free-stream disturbances. However, this does not influence the comparison of measured and predicted transition onset in most cases.

Predicted Onset. Plotting of the predicted onset contours requires some thought. First the quasi-steady computation model

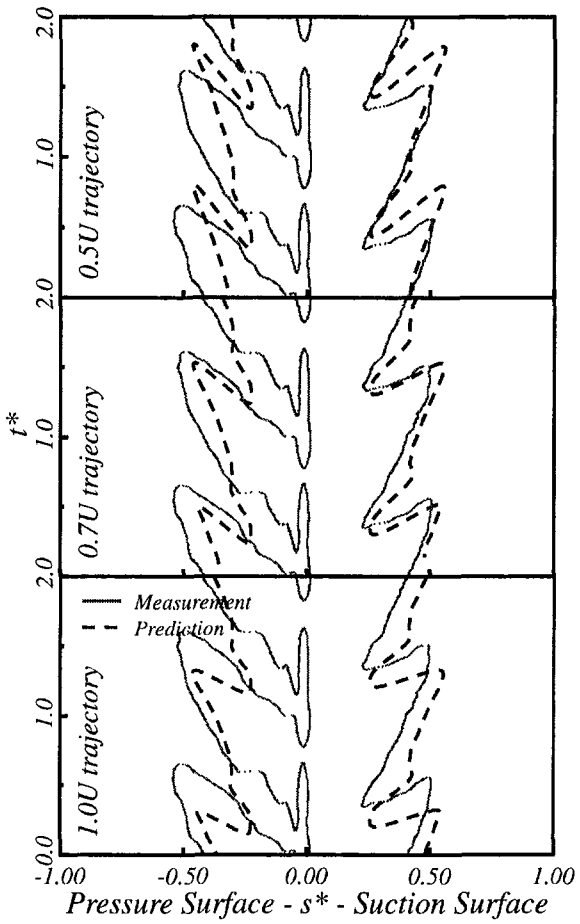

Fig. 5 Comparison of measured and predicted transition onset locations at medium loading, *a/s* = 0.00; effect of propagation velocity of transition-promoting disturbances

described above is applied to predict a transition onset position $\langle s^*_{\text{trans}} \rangle$ for a free-stream turbulence value $\langle Tu \rangle$ from the measured inflow disturbance variation for a particular value of t^*. Before this can be plotted on the predicted $\langle s^*_{\text{trans}} \rangle \sim t^*$ contour it is necessary to apply a time delay to allow for the disturbance convection from the inflow measuring station to the point on the blade surface where turbulent breakdown in the boundary layer is subsequently generated.

Simple bypass transition models such as that of Abu-Ghannam and Shaw (1980) assume the boundary layer to respond instantly to local free-stream disturbances. In this case time-shifting of the computed transition point according to the delay time for a particle to convect at the local free-stream velocity ($1.0U$ trajectory) to the predicted onset position is appropriate. However, because the exact transition mechanism is uncertain a priori, we first choose to compare the measured transition onset contours with predicted onset contours obtained with the transition-promoting disturbances propagating at different velocities of $1.0U$, $0.7U$, and $0.5U$. This comparison is presented in Fig. 5 for the particular case of medium loading and clocking position $a/S = 0.00$.

Figure 5 indicates a significantly better level of agreement between measurement and experiment when the predicted results are time-shifted along the $0.7U$ trajectory. For this reason, the $0.7U$ time-shifting is adopted for all the curves shown as prediction (*a*) in Fig. 6.

The fact that better agreement is obtained with a convection velocity less than the free stream suggests that the growth or convection of disturbances within the stator blade boundary layer is playing a major role in transition. This is consistent with the MISES prediction of transition onset by natural transition in most of the cases examined here. A natural transition model would assume that disturbances propagate in the free stream at $1.0U$ up to the neutral stability point, where they are impressed on the boundary layer and provide an initial Tollmien–Schlichting wave amplitude for the ensuing amplification process. The T–S waves will subsequently convect at about $0.4U$ within the boundary layer until they reach the location where a critical amplitude for turbulent breakdown occurs.

Contours of predicted turbulent onset based on the latter model are shown as prediction (*b*) in Fig. 6. These are based on a $1.0U$ trajectory up to the neutral stability point computed from the time-mean boundary layer properties, with a $0.4U$ trajectory thereafter. The relative lengths of stable and unstable laminar flow on the compressor blade typically give a mean convection speed of about $0.7U$ for time shifting the computed transition positions. This explains the agreement obtained with prediction (*a*), which is purely fortuitous. In general, the mean disturbance convection speed will vary with the surface pressure distribution, and prediction (*b*) is therefore to be preferred.

Discussion

(a) Wake-Induced Path. In comparing the measured and computed transition onset behavior it is convenient to follow other workers and divide the process into a wake-induced path (where earlier onset is promoted by the rotor wake disturbances) and a region where transition occurs between the rotor wakes. The wake-induced paths are clearly defined by tongues in the measured onset contours extending closer to the leading edge. The present quasi-steady model obviously fails in this situation in most cases, as the differences are far too large to be explained by possible uncertainties in intermittency measurement. It seems likely that unsteady effects are playing a major role in wake-induced transition on the compressor blade. Potential flow interactions associated with changing incidence provide the greatest source of unsteadiness as the rotor wake passes the stator leading edge. Farther rearward the wake-jet effect would become relatively more important.

Evidence of leading edge interaction effects can also be seen in transition observations by Chakka and Schobeiri (1999) for periodic unsteady flow over a curved plate. Another possible mechanism influencing wake-induced transition could be the phenomenon of turbulence amplification at a leading edge reported by Hobson et al. (1996) from observations at high incidence in a compressor cascade.

Mayle (1991) also noted the inadequacy of current models for predicting wake-induced transition, and suggested that wake-induced transition onset would occur near the point of minimum pressure in most cases. Inspection of the data from Table 2 shows some significant departures from this model for the lower surface at medium and high loading and the upper surface at low loading. Assuming wake-induced transition onset at the time-mean neutral stability point would be similarly inaccurate. Further work is clearly needed in this area.

(b) Path Between Wakes. Figure 6 indicates that the present quasi-steady procedure is surprisingly effective in predicting the transition onset contours between the rotor wake-induced turbulent strips on the suction surface. Most features of the contour shape are captured, and the transition onset between the rotor wakes is generally predicted within $10\%c$. The agreement is not quite as good on the pressure surface, where the effects of calming from wake-induced transitional strips and/or stability changes associated with fluctuations in pressure gradient appear relatively more important. This becomes particularly noticeable for the pressure surface at high loading with $a/S = 0.00$.

Prediction (*b*) (with the assumption of disturbance propagation within the boundary layer) performs a little better than prediction (*a*) on average. This provides further support for the free-stream turbulence influenced natural transition model for the compressor blade transition behavior. In making these comparisons it should

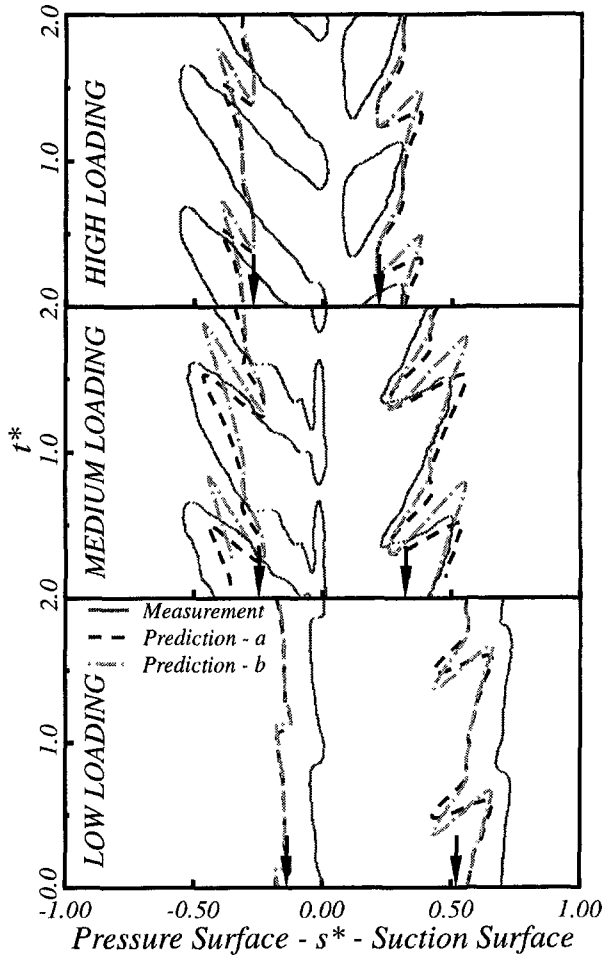

Fig. 6(*a*) IGV wake street on stator (*a*/*s* = 0.00)

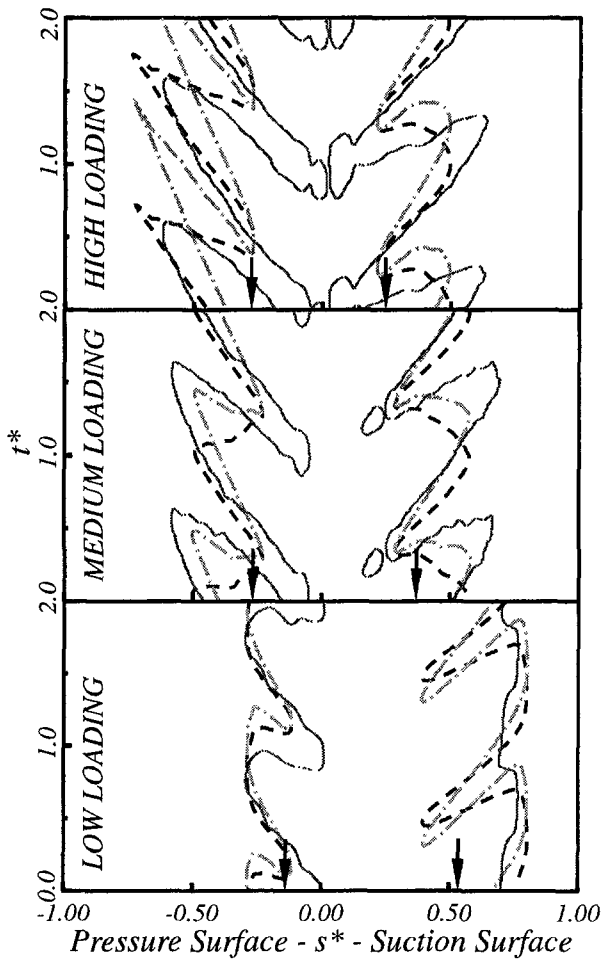

Fig. 6(*b*) IGV wake street in passage (*a*/*s* = 0.50)

Fig. 6 Comparison of predicted and measured transition onset. Measured onset from $\gamma = 0.10$ contour. ↓ indicates transition onset based on Tu_D for stagnation streamline. Prediction (*a*): onset based on 0.7*U* trajectory for disturbance propagation. Prediction (*b*): onset based on 1.0*U* trajectory for disturbance propagation up to neutral stability point and 0.4*U* trajectory thereafter.

be noted that any deviations within the wake-induced paths can be ignored.

The conclusion that a natural transition process was dominant on the compressor stator may be considered surprising. The conventional view is that bypass transition should always dominate in a turbomachine because of the high freestream turbulence level. However, Drela's (1995) comparison of the natural and bypass transition criteria (Fig. 1), the evidence regarding disturbance convection speeds, and the good agreement of the MISES transition onset predictions with experiment provide strong evidence to the contrary. Tollmien–Schlichting wave activity on the compressor stator pressure surface has been directly observed by Solomon and Walker (1996); instability wave activity was also clearly evident in the extensive series of flat plate transition observations with varying adverse pressure gradient and free stream turbulence level reported by Walker and Gostelow (1990).

There is generally little evidence of calming delaying transition onset on the stator blade. This may at first appear anomalous, but it should be recalled that a calming effect is dependent on the presence of a well-developed turbulent spot. As noted by Halstead et al. (1997) the randomness of passing wake disturbances in the free stream means that a turbulent spot and associated calming region need not occur on each wake passage. In cases where the calming region is absent, transition by other modes is free to occur; this may explain why a model that ignores wake periodicity is still able to predict the first appearance of transition fairly well. It appears that the major effect of calming associated with wake-induced transition is rather to prolong the extent of the transition region between the rotor wakes. This prolongation can most clearly be seen from the curves of time-mean intermittency and $t^* \sim s^*$ diagrams of transitional flow shown in Figs. 6 and 8, Part I of this paper.

Figure 6 also shows the stator surface transition locations computed from the values of time-mean disturbance level at the inflow measuring station. These are all too far forward, with the exception of the leading edge separation bubble case. It is concluded that using the random component of free-stream disturbance alone is more appropriate for predicting transition between the wakes.

Table 2 Peak velocity location, $s^*_{U\max}$, and neutral stability location, s^*_i

ϕ	Suction Surface			Pressure Surface		
	$s^*_{U\max}$ EXP	$s^*_{U\max}$ MISES	s^*_i MISES	$s^*_{U\max}$ EXP	$s^*_{U\max}$ MISES	s^*_i MISES
0.600	0.058	0.039	0.161	-0.157	-0.102	-0.205
0.675	0.058	0.077	0.197	-0.157	-0.102	-0.165
0.840	0.255	0.263	0.411	-0.059	-0.029	-0.078

Concluding Remarks

Transition on the compressor stator between the rotor wake-induced transition paths in the $t^* \sim s^*$ plane evidently occurred through free-stream disturbance modified natural transition rather than a bypass transition mode in most cases.

Application of the viscous–inviscid interaction code MISES in a quasi-steady manner using ensemble-averaged random turbulence

data from upstream measurements captured most features of the turbulent onset contours outside the wake-induced turbulent strips and generally predicted transition onset locations to within $10\%c$. This simple procedure gives results of engineering accuracy and is fast enough to be used interactively by turbomachine blade designers. It will predict the importance of unsteady transition effects, given a reasonable estimate of the range of inlet turbulence levels over a wake passing period.

A major advantage of the MISES code is its ability to predict separation bubbles with good accuracy. Computations based solely on bypass transition criteria (such as Abu-Ghannam and Shaw or Mayle) cannot capture separation bubble phenomena at all. Codes with both attached flow bypass transition and separated flow transition criteria are able to predict laminar separation bubbles, but in a much less satisfactory manner: Inconsistencies between the two different criteria mean that continuous movement of the predicted transition onset through the incipient separation point is impossible; this often leads to numerical instabilities in iterative calculations, such as viscous–inviscid interaction procedures.

Prediction of transition onset in the wake-induced paths at off-design conditions was poor. These discrepancies are thought to have arisen from unsteady flow effects—principally potential flow interactions associated with the passage of rotor wakes and other free stream disturbances over the stator leading edge, but wake-jet interactions on the blade surface may have been a contributing factor. Further study of these unsteady phenomena is needed.

The range of stator surface pressure distributions investigated in the present study covers those observed on modern high pressure compressor airfoils from near stall to design operating conditions. Further MISES calculations (not detailed here) have given close agreement for the variation of transition onset over the whole rotor blade passing period for the third-stage compressor stator investigated by Halstead et al. (1997). This indicates that the present method can be applied with more confidence to predict transition onset fluctuations in modern multistage industrial compressors.

The accuracy of the current quasi-steady flow model for loss prediction was examined by Solomon et al. (1996) for the high-pressure compressor stator design flow case (2B) of Halstead et al. (1997). Their two-dimensional boundary layer calculations gave a momentum thickness increase of about 50 percent in the wake-induced path at 90 percent suction surface length compared with the increase of about 100 percent observed experimentally, despite the fact that the location and extent of the transition zone were correctly modeled. The discrepancy was probably due to a combination of flow convergence effects associated with the rotor wake jet and deficiencies in modeling low-Reynolds-number highly nonequilibrium turbulent boundary layer development.

Finally, it is noted that the present work has been confined entirely to incompressible flow situations. The basic MISES code remains valid at transonic conditions, and could in principle be used to predict transition onset at high subsonic conditions and above (excepting complex situations such as shock boundary layer interactions). However, this application would require a revision of transition criteria to account for the influence of compressibility on boundary layer stability.

Acknowledgments

Financial support from Rolls-Royce plc for the experimental program at the University of Tasmania is gratefully acknowledged. The authors also thank Professor Drela at MIT for permission to reproduce Fig. 1 and to GE Aircraft Engines for the use of their copy of the MISES code and computational facilities. The first author acknowledges financial support from the Ohio Aerospace Institute, the NASA Lewis Low Pressure Turbine Research Program (grant numbers NCC3-588, 1998, and NCC3-549, 1997) and GE Aircraft Engines.

References

Abu-Ghannam, B. J., and Shaw, R., 1980, "Natural Transition of Boundary Layers—the Effects of Pressure Gradient and Flow History," *Journal of Mechanical Engineering Science,* Vol. 22, No. 5, pp. 213–228.

Addison, J. S., and Hodson, H. P., 1990, "Unsteady Transition in an Axial Flow Turbine: Part 2—Cascade Measurements and Modeling," ASME JOURNAL OF TURBOMACHINERY, Vol. 112, pp. 215–221.

Blight, F. G., and Howard, W., 1952, "Tests on Four Aerofoil Cascades. Part 1: Deflection, Drag and Velocity Distribution," Report E 74, Aeronautical Research Laboratories, Melbourne, Australia.

Chakka, P., and Schobeiri, M. T., 1999, "Modeling Unsteady Boundary Layer Transition on a Curved Plate Under Periodic Unsteady Flow Conditions: Aerodynamic and Heat Transfer Investigations," ASME JOURNAL OF TURBOMACHINERY, Vol. 121, pp. 88–97.

Cherret, M. A., 1996, "Rotor–Stator Interactions in a High-Speed Axial Compressor," pp. 40.1–40.14, *Loss Mechanisms and Unsteady Flows in Turbomachines,* AGARD CP-571, NATO.

Drela, M., 1995, "MISES Implementation of Modified Abu-Ghannam/Shaw Transition Criterion," *MISES Code Documentation,* MIT.

Halstead, D. E., Wisler, D. C., Okiishi, T. H., Walker, G. J., Hodson, H. P., and Shin, H.-W., 1997, "Boundary Layer Development in Axial Compressors and Turbines: Parts 1–4," ASME JOURNAL OF TURBOMACHINERY, Vol. 119; Part 1: pp. 114–127; Part 2: pp. 426–444; Part 3: pp. 225–237; Part 4: pp. 128–139.

Hobson, G. V., Wakefield, B. E., and Roberts, W. B., 1996, "Turbulence Amplification With Incidence at the Leading Edge of a Compressor Cascade," ASME Paper No. 96-GT-409.

Johnson, M. W., and Ercan, A. H., 1996, "A Boundary Layer Transition Model," ASME Paper No. 96-GT-444.

Mack, L. M., 1977, "Transition and Laminar Instability," Jet Propulsion Laboratory Publication 77-15, Pasadena, CA.

Mayle, R. E., 1991, "The Role of Laminar-Turbulent Transition in Gas Turbine Engines," ASME JOURNAL OF TURBOMACHINERY, Vol. 113, pp. 509–537, The 1991 IGTI Scholar Lecture.

Mayle, R. E., and Schulz, A., 1997, "The Path to Predicting Bypass Transition," ASME JOURNAL OF TURBOMACHINERY, Vol. 119, pp. 405–411.

Schulte, V., and Hodson, H. P., 1998, "Prediction of the Becalmed Region for LP Turbine Profile Design," ASME JOURNAL OF TURBOMACHINERY, Vol. 120, pp. 839–846.

Solomon, W. J., 1996, "Unsteady boundary Layer Transition on Axial Compressor Blades," Ph.D. Thesis, University of Tasmania, Hobart.

Solomon, W. J., Walker, G. J., and Gostelow, J. P., 1996, "Transition Zone Predictions for Rapidly Varying Flows," Henekes, R. A. W. M., and van Ingen, J. L., eds., *Transitional Boundary Layers in Aeronautics,* North-Holland, pp. 321–332.

Walker, G. J., 1972, "An Investigation of the Boundary Layer Behaviour on the Blading of a Single-Stage Axial-Flow Compressor," Ph.D. Thesis, University of Tasmania, Australia.

Walker, G. J., and Gostelow, J. P., 1990, "Effects of Adverse Pressure Gradients on the Nature and Length of Boundary Layer Transition," ASME JOURNAL OF TURBOMACHINERY, Vol. 112, pp. 196–205.

Walker, G. J., Hughes, J. D., Köhler, I., and Solomon, W. J., 1998, "The Influence of Wake–Wake Interactions on Loss Fluctuations of a Downstream Axial Compressor Blade Row," ASME JOURNAL OF TURBOMACHINERY, Vol. 120, pp. 695–704.

Walker, G. J., Hughes, J. D., Solomon, W. J., and Köhler, I., 1997, "Wake Mixing and Blade Clocking Effects in an Axial Compressor," *Proc. 13th Int. Symp. on Air Breathing Engines,* Chattanooga.

Youngren, H., and Drela, M., 1991, "Viscous–Inviscid Method for Preliminary Design of Transonic Cascades," presented at the AIAA Joint Propulsion Conference.

Design and Testing of Swept and Leaned Outlet Guide Vanes to Reduce Stator–Strut–Splitter Aerodynamic Flow Interactions

A. R. Wadia

P. N. Szucs

GE Aircraft Engines,
Cincinnati, OH 45215

K. L. Gundy-Burlet
NASA Ames Research Center,
Moffet Field, CA 94035

Large circumferentially varying pressure levels produced by aerodynamic flow interactions between downstream stators and struts present a potential noise and stability margin liability in a compression component. These interactions are presently controlled by tailoring the camber and/or stagger angles of vanes neighboring the fan frame struts. This paper reports on the design and testing of a unique set of swept and leaned fan outlet guide vanes (OGVs) that do not require this local tailoring even though the OGVs are closely coupled with the fan frame struts and splitter to reduce engine length. The swept and leaned OGVs not only reduce core-duct diffusion, but they also reduce the potential flow interaction between the stator and the strut relative to that produced by conventional radial OGVs. First, the design of the outlet guide vanes using a single blade row three-dimensional viscous flow analysis is outlined. Next, a two-dimensional potential flow analysis was used for the coupled OGV–frame system to obtain a circumferentially nonuniform stator stagger angle distribution to reduce the upstream static pressure disturbance further. Recognizing the limitations of the two-dimensional potential flow analysis for this highly three-dimensional set of leaned OGVs, as a final evaluation of the OGV–strut system design, a full three-dimensional viscous analysis of a periodic circumferential sector of the OGVs, including the fan frame struts and splitter, was performed. The computer model was derived from a NASA-developed code used in simulating the flow field for external aerodynamic applications with complex geometries. The three-dimensional coupled OGV–frame analysis included the uniformly staggered OGV configuration and the variably staggered OGV configuration determined by the two-dimensional potential flow analysis. Contrary to the two-dimensional calculations, the three-dimensional analysis revealed significant flow problems with the variably staggered OGV configuration and showed less upstream flow nonuniformity with the uniformly staggered OGV configuration. The flow redistribution in both the radial and tangential directions, captured fully only in the three-dimensional analysis, was identified as the prime contributor to the lower flow nonuniformity with the uniformly staggered OGV configuration. The coupled three-dimensional analysis was also used to validate the design at off-design conditions. Engine test performance and stability measurements with both uniformly and variably staggered OGV configurations with and without the presence of inlet distortion confirmed the conclusions from the three-dimensional analysis.

Introduction

Transition ducting between the fan and the compressor of a turbofan engine usually contains fan frame struts and a splitter to divide the flow between the core stream and the bypass region, as shown in Fig. 1(*a*). The fan frame struts and the splitter are placed at a sufficient distance from the fan outlet guide vanes (OGVs) such that there is enough length from the OGV trailing edge to the strut leading edge that nonuniform flows in the struts do not locally back-pressure the OGVs and cause high losses, reduced stall margin, or high distortion transfer.

The driving force behind the present work was a need for a reduction in overall engine length when GE Aircraft Engines (Kandebo, 1996) adapted the F118-GE-100, originally designed for the B-2 bomber, to fit in the F-16 fighter's engine bay. This was done to obtain the benefits of the high-efficiency F118 fan to improve durability, performance, and thrust. In cutting the engine length to make it adaptable, the outlet guide vanes were packaged closer, as illustrated in Fig. 1(*b*). Although only 1.4 in. shorter in length to the frame struts, this reduction could not only create an undesired aerodynamic back-pressure, with potential to hurt performance and aerodynamic stability, but it could also adversely impact the fan distortion transfer to the compressor.

The principle of using nonaxisymmetric stator configurations ahead of pylons/struts to achieve a uniform flow field upstream of the stators in aircraft engines has been known for a long time, as described in the works of Hemsworth (1969), who encountered the problem in the development of the General Electric TF-39 turbofan engine. Rubbert et al. (1972) addressed a similar alternative engine installation issue in the Boeing 747 aircraft. Rubbert used two- and three-dimensional potential flow analyses to conceptually develop stators with varying degree of camber angles in the vicinity of the strut to protect the rotor from the pressure disturbance induced forward by the service strut. Later, more systematic experiments of O'Brien et al.

Contributed by the International Gas Turbine Institute and presented at the 43rd International Gas Turbine and Aeroengine Congress and Exhibition, Stockholm, Sweden, June 2–5, 1998. Manuscript received by the International Gas Turbine Institute February 1998. Paper No. 98-GT-70. Associate Technical Editor: R. E. Kielb.

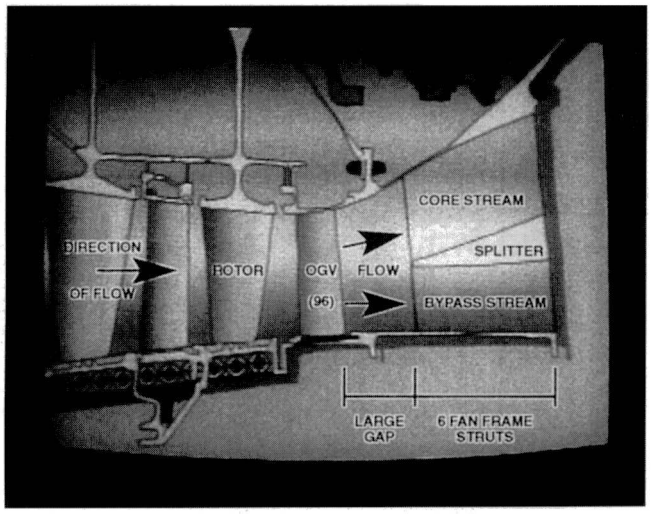

(a) Conventional OGV-Frame System

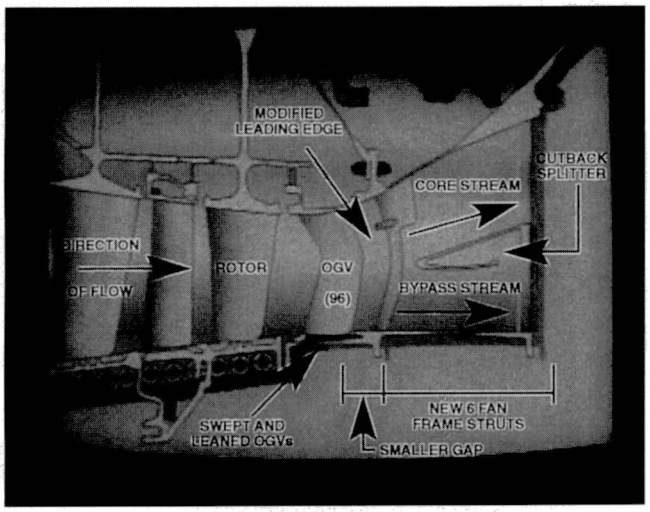

(b) Swept and Leaned OGV-Frame System

Fig. 1 Flowpath schematic showing: (*a*) the conventional radial OGV–frame and splitter system and (*b*) the swept and leaned OGV–frame and splitter system with the reduced axial gap between the OGVs and the fan frame

(1983) and Woodard and Balombin (1984) confirmed the importance of the potential flow interaction between rotor, stator, and struts in the production of rotor blade pressure fluctuations. In 1996, Parry, using a simpler calculation scheme, arrived at results similar to those obtained by Rubbert, showing the relative benefits of increasing the number of vane types to alleviate the OGV–frame flow interaction. Additional results of the OGV–pylon interaction problem were reported later by Parry and Bailey (1997). Also along similar lines, Shrinivas and Giles (1995) performed detailed sensitivity studies to arrive at a cyclically varying OGV trailing edge camber configuration while maintaining the leading edge airfoil shape, thus retaining uniform OGV incidence angle. These types of stator camber modifications described above, while technically very effective, are usually unattractive from a manufacturing cost and maintenance perspective.

As a practical alternative to building stator cascades with different camber angles, a slightly more attractive option that lowers the cost of implementation uses circumferentially restaggered stator vanes in front of the struts to channel the exit flow from the stator trailing edge smoothly around the strut leading edge. Yokoi et al. (1981) tested several such stator restagger options, showing large reductions in upstream pressure disturbance. Their analysis modeled the stator rows as one-dimensional diffusers, thus ignoring the stator loading and leading edge incidence in the optimization process. Cerri and O'Brien (1989) used the classical Douglas–Neumann singularity superposition method to solve the cascade–strut system to arrive at an optimal staggering of the stator configuration that predicted the lowest upstream pressure disturbance. The work was later extended by Cerri et al. (1994) to include the rotating blade row effects. Kodama (1986) and later Kodama and Nagano (1989) reduced the size of the analytical problem encountered with the Douglas–Neumann method by using the small disturbance theory to replace the stator row with an actuator disk and verified the theory with experimental measurements. Jones et al. (1996) used the Douglas–Neumann formulation of Cerri and O'Brien to design and test OGVs with circumferentially nonuniform stator stagger angle distribution and showed reduced static pressure disturbance on the rotor. Other studies directed at reducing the flow interactions to improve fan acoustic levels are described by McArdle et al. (1980); Ho (1981); Nakamura et al. (1986); and Preisser et al. (1981).

All the references cited above either used the concept of several different "vane types" in the cascade, which is expensive to implement in the field, or the option to restagger the vanes. This latter method, though less expensive, still requires "stamping" variably staggered vanes in a segmented vane sector and "Murphy-proofing" (i.e., avoid the possibility of misassembly) of the sectors themselves to avoid a mismatch in the vane passages between sectors.

This article reports on the design and testing of a unique set of swept and leaned fan OGVs for a military application that does not require this local tailoring (i.e., different "vane types" or "vane restagger") to alleviate cost and maintainability issues with past concepts. This design approach is shown to be very effective even though these OGVs are closely coupled with the fan frame struts and splitter to reduce engine length.

Design of Swept and Leaned OGVs

Figure 1(*b*) shows the closely coupled swept and leaned OGV–frame–splitter system. Relative to Fig. 1(*a*), which

Nomenclature

c = airfoil section chord
Cp = pressure coefficient = (Ps − Ps_f)/(Pt_f − Ps_f)
Cv = specific heat at constant volume
Entropy = Cv*ln ((Pt/Pt_f)*(Rho/Rho_f)**k)
IMM = radial immersion (0 = tip, 1 = hub)
k = ratio of specific heats
LE = leading edge
Pt = total pressure, psia
Pt_f = free-stream total pressure, psia
Ps = static pressure, psia
Ps(avg) = circumferentially averaged static pressure, psia
Ps_f = free-stream static pressure, psia
Ps(max) = maximum static pressure, psia
Ps(min) = minimum static pressure
OGV = Outlet Guide Vanes
Rho = density
Rho_f = free-stream density
tmax = airfoil section maximum thickness
TE = trailing edge
Theta = circumferential coordinate, deg
Z = axial distance, in.
ΔPs = Ps(max) − Ps(min)

shows the conventional OGV–frame–splitter configuration, the diffusion length from the OGV trailing edge to the fan frame strut trailing edge was reduced by 1.4 in. and is illustrated as "smaller gap" in Fig. 1(*b*) with the leaned OGVs. The maximum axial widths of the struts in Figs. 1(*a*) and 1(*b*) are identical.

In principle, the primary benefit of the tangential lean in the OGVs is lowering the OGV hub exit Mach number, thus reducing the required duct velocity diffusion ratio.

Sweeping aft of the airfoil is done to move the trailing edge meridional projection at midspan further aft relative to the OGV hub trailing edge, as shown in Fig. 1(*b*). This helps prolong the benefit due to lean (lowering the inner wall Mach number) farther downstream from the OGV hub trailing edge and thereby providing better control of the core–duct hub diffusion. Engine system considerations allowed the OGVs to be designed to leave some swirl in the flow at the exit, lowering the OGV diffusion factor. To accommodate the OGV exit swirl, the original struts, shown in Fig. 1(*a*), were staggered and cambered, and the strut leading edges were modified, to follow the OGV trailing edge sweep. Table 1 summarizes the geometric and flow design parameters for the OGVs and the strut.

The swept and leaned OGVs were designed using a single blade row three-dimensional viscous code. The design was checked for performance at multiple operating points. The details of the code used, which has found wide usage within General Electric Company for compressor and turbine design, has been reported by Jennions and Turner (1993). Figure 2 shows the calculated OGV surface isentropic Mach number distribution at midspan for two points along a fan operating line. The high leading edge incidence condition occurs at design speed and low-bypass ratio, while the high negative leading edge incidence case corresponds to a lower speed point at high-bypass ratio. The OGV design is therefore required to sustain significant variation in leading edge incidence and loading levels in the flight envelope. The need to operate efficiently at multiple points, with the need to tolerate back-pressure effects from the downstream splitter and struts, made the design of the closely coupled system even more challenging.

Nonaxisymmetric OGV Circumferential Stagger Variation

Figure 3 shows a composite three-dimensional view of a 16-vane sector in front of a strut and the splitter. This frontal view shows that, due to the lean imparted to the OGVs, more than one OGV crosses the leading edge face of the strut. These crossings are limited to small localized areas along the OGV and strut heights, resulting in lower upstream propagation of static pressure distortion relative to that with conventional radial OGVs.

Table 1 OGV–strut design parameters

Parameter	
Number of OGVs	96
Number of Struts	6
OGV Leading Edge Tip Diameter (in.)	34.2
OGV Leading Edge Hub Diameter (in.)	25.1
Strut Trailing Edge Tip Diameter (in.)	34.2
Strut Trailing Edge Hub Diameter (in.)	18.8
OGV Tip, Pitch, and Hub Chords (in.)	1.85, 1.7, 1.82
OGV Tip, Pitch, and Hub Stagger (Deg.)	18.2, 17.8, 19.1
OGV Tip, Pitch, and Hub Camber (Deg.)	49.0, 44.0, 36.1
OGV tmax/c	0.063
Strut Axial Length (in.)	6.00
OGV Inlet Mach Number	0.595

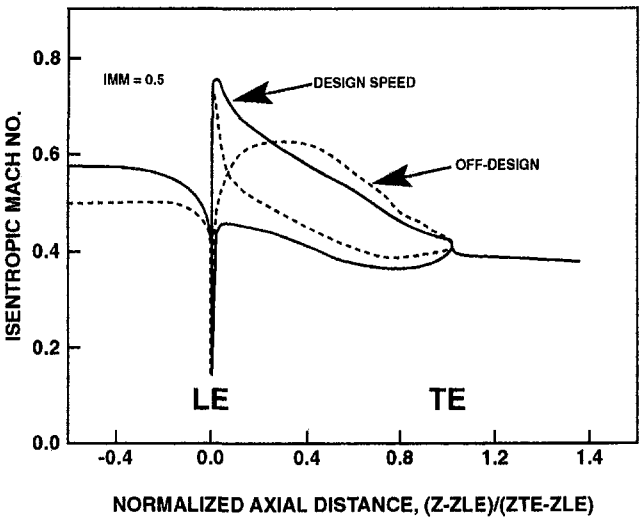

Fig. 2 Comparison of the OGV midspan surface isentropic Mach number distribution at design speed (low-bypass ratio) and at part speed (high-bypass ratio) calculated by the single blade row three-dimensional viscous analysis

A further reduction in the upstream circumferential variation in back-pressure due to the vane–strut interaction was attempted by individually restaggering the vanes, similar to that reported by Chiang and Turner (1996) and Jones et al. (1996). An implicit two-dimensional CFD solver developed by Turner and Keith (1985) was used to solve for the rotor trailing edge static pressure distortion from the OGVs and the struts. The rotor was not included in the analysis. There are 96 OGVs and six struts (five nominal struts and one "king" strut). Simplifying the analysis by assuming all nominal struts, the two-dimensional implicit code was used to model a 60-deg sector, which consists of 16 OGVs and a strut. An option built into the code to determine the flow angle distribution entering the struts, which minimizes the potential disturbance propagating upstream, was used to obtain the flow angle distribution needed to guide the flow smoothly around the struts. As the OGVs are leaned, one could have a situation where a fraction of the height of one of the OGVs was on the pressure side of the struts while the rest of the span of the same OGV was on the suction side of the strut. Therefore, it was essential to run the two-dimensional CFD solver along several spanwise strips in the core and bypass streams. As expected, there was no one unique set of OGV

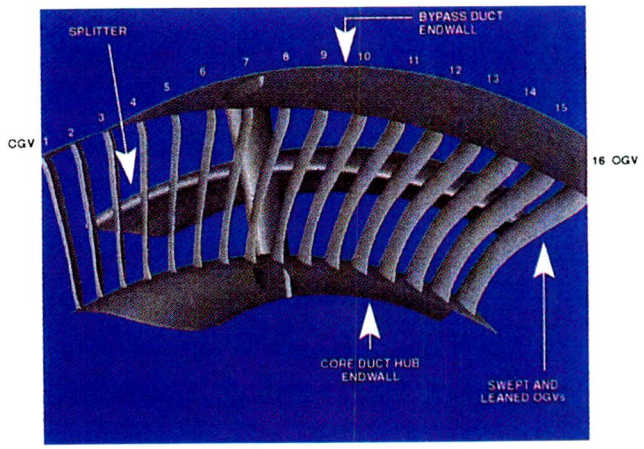

Fig. 3 Composite three-dimensional view of the swept and leaned OGVs in front of the fan frame and splitter system showing more than one OGV crossing the leading edge face of the fan frame strut

stagger angles that significantly reduced the upstream static pressure along the entire span.

Being a military application, maintainability and cost considerations prevented using vanes with different spanwise twist angle distributions for this design. Optimization of the OGV stagger angles to reduce circumferential static pressure variation was biased to favor the core stream. The reduction in circumferential static pressure variation was quantified by calculating the magnitude of the predicted disturbance as:

$$\text{Disturbance} = (\text{Ps(max)} - \text{Ps(min)})/\text{Ps(avg)} \quad (1)$$

at the rotor exit plane. The resulting OGV stagger angle distribution is shown in Fig. 4. The vane rotations about the stacking axis showing some rather large nonsymmetric variations that do not average to zero is a result of the spanwise variation of the airfoil lean. Figure 5 shows the calculated circumferential distribution of static pressure approximately at midheight in the corestream with the variably staggered vanes at two operating conditions. The stator upstream circumferential variation of static pressure was not eliminated, but minimized. The calculated ratio of the difference between the maximum and minimum static pressures and the average static pressure (Eq. (1)) with the staggered configuration was less than 5.5 percent at the design speed condition.

It was obvious that the radial flow migration effects associated with the stator lean, and its impact on the OGV flow field, could not be modeled by the two-dimensional analysis. To obtain a more realistic aerodynamic evaluation of the OGV–strut system, it was decided to pursue a full three-dimensional analysis of this complex flow interaction problem. One of the prerequisites of the three-dimensional analysis selected was its ability to model highly complex geometries. The search led to the OVERFLOW code developed at NASA/Ames for external aerodynamic applications with intricate geometries. The next section describes the computational model and its conversion for application to internal flow problems.

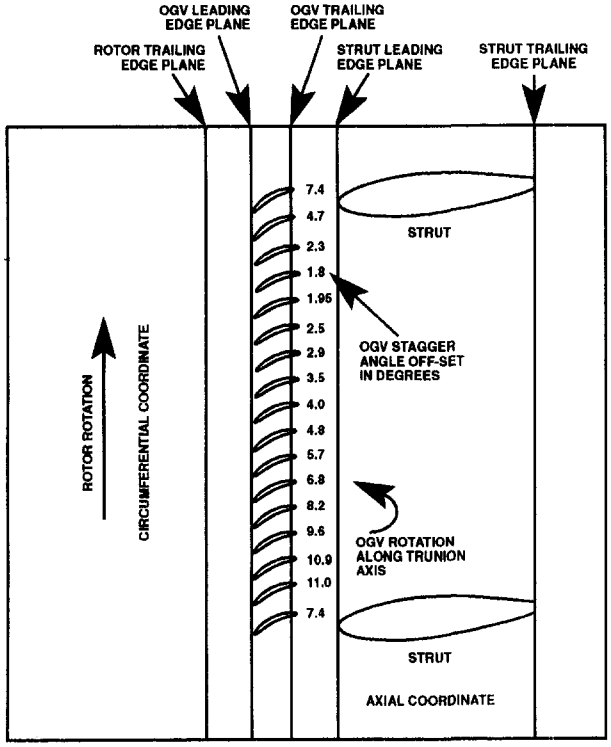

Fig. 4 Variably staggered OGV configuration selected based on the two-dimensional potential flow analysis and biased toward reducing upstream distortion in the core stream

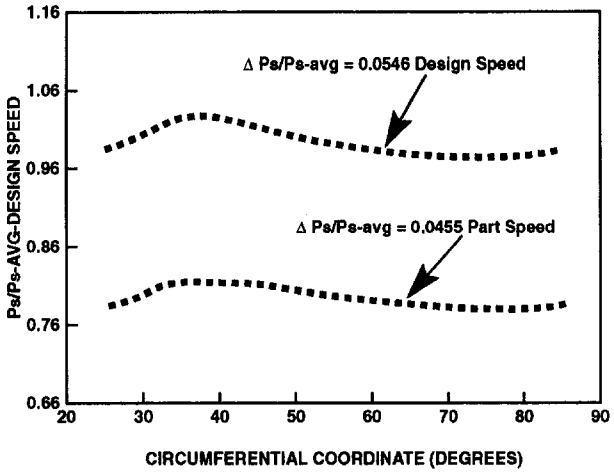

Fig. 5 Rotor exit plane circumferential static pressure distribution predicted by the two-dimensional potential flow analysis for the variably staggered OGV configuration at 70 percent immersion for design and off-design conditions

Three-Dimensional Computational Model

The system of 16 variably staggered OGVs, strut, and splitter shown in Fig. 3 posed a very complex geometric problem for computational analysis. A chimera grid technique (Benek et al., 1985) was chosen to make the discretization of the system a tractable problem, and the OVERFLOW code (Buning et al., 1993) was used to compute the flow field.

The grid generation process was extremely complicated. The process started with untrimmed initial surface grids for each component that were generated from CAD data using the ICEM CFD program. A series of Fortran programs, shell scripts. OVERFLOW grid tools and Collar Grid tools (Parks et al., 1991) were then used to rotate components into their respective positions, find surface-to-surface intersections, and construct the final surface grids. Volume grids for the strut and vanes were generated using the Hypgen program (Chan et al., 1993), while an algebraic grid generator was developed for the other components. The Pegasus program (Suhs and Tramel, 1991) was used to perform the hole generation and determine the grid-to-grid boundary interpolation coefficients. The entire process was controlled by a makefile in which all the grid dependencies were defined. The makefile minimized grid generation time by only updating grids that were affected by a parameter change. It also reduced errors by automatically propagating changes through all affected grids. The final grid configuration consisted of 16-vane grids overlaid on an outer grid, a strut grid, and core and bypass section grids, as summarized in Table 2. With a few additional collar grids that defined the strut/splitter intersection, the entire grid system was comprised of 2.7 million grid points. The volume grids were generated such that stretching ratios did not exceed 1.3, and the initial spacing off the body corresponded to a $y+$ value around 1.0. These requirements were important to maintaining accuracy in the computation. The side view of the grid for the entire OGV–frame–splitter system shown in Fig. 6 illustrates the voluminous magnitude of the problem being solved.

Table 2 OVERFLOW code grid dimensions

Body	Streamwise	Spanwise	Surface-normal
Vane	109	39	18
Strut	109	46	23
Core/Bypass Ducts	180	29	55
Outer Grid	251	39	75

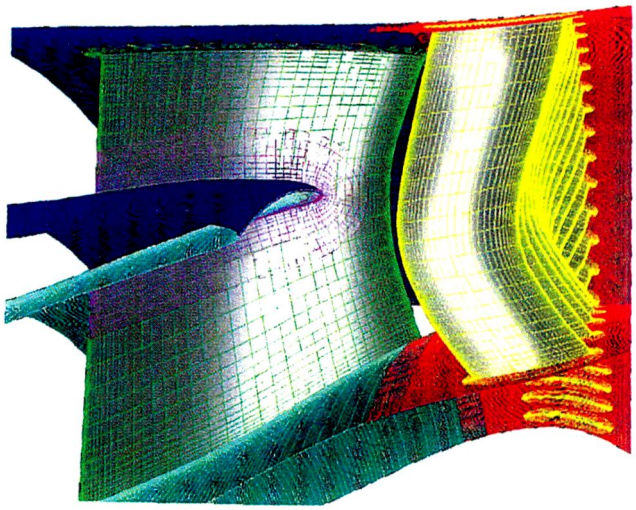

Fig. 6 OGV–frame–splitter system grid used in the three-dimensional calculations

The 1.6ad version of OVERFLOW required some modification in order for these computations to be performed. It was deemed that a full-annulus computation would prove to be too expensive. The 16-vane/1-strut configuration represented $\frac{1}{6}$ of the annulus, so periodic boundary conditions had to be implemented for the circumferential-direction periodicity. A Reimann inlet condition was implemented in which radial distributions of total temperature and total pressure could be prescribed. The exit condition allowed for separate specification of a back-pressure at one radius for each of the core and bypass sections. The radial-momentum equation was then satisfied across each of these faces. For the 1.6ad version of OVERFLOW, it was considered best to use the default central-difference scheme and a spatially varying time step. Each of the grids was computed with viscous terms only in the wall-normal grid direction (thin-layer assumption). The Baldwin–Barth one-equation turbulence model was used for these computations.

Three-Dimensional Viscous Analysis Results

Before proceeding with the detailed vane–strut coupled solution, the changes made to the OVERFLOW code were validated by comparing its results with the single blade row code calculations used in the design of the OGVs. This was important because, in addition to the numerical approach, differences in the turbulent boundary layer models also existed between the two codes: The OVERFLOW code used the Baldwin–Barth one-equation turbulence model while the design code was run with the two-equation k–e turbulence model. The comparison of calculated surface pressure coefficient distribution from the two approaches, illustrated in Fig. 7 for the pitchline section, showed reasonable agreement over the entire span except at the OGV trailing edge near the tip endwall, where the OVERFLOW code showed regions of higher losses and separated flow not present in the solution with General Electric's internal viscous analysis code. Considering the significant differences in griding and solution techniques between the two codes, the agreement was reasonably good; it was recognized that the difference in turbulence models was most likely responsible for the differences near the tip endwall. Once the OVERFLOW code's predictions were deemed satisfactory, the full three-dimensional solution for the entire OGV–frame system was obtained with the OVERFLOW code.

The three-dimensional evaluations were specifically planned to determine which of the OGV configurations (variably staggered versus uniformly staggered) reduced the effects of back-pressure yet ensured the flow into the compressor was not compromised. The first approach selected was based on the results of the two-dimensional calculations (Fig. 4)—one used by other investigators to negate back-pressure by uniquely varying the stagger angle of select OGVs. The design speed computation was performed with radial profiles of inlet total pressure, temperature, and flow angle based on a circumferentially averaged through-flow analysis of the fan. The exit static pressures in the core and bypass streams were adjusted to arrive at the required flow split (bypass ratio) between the two streams.

The results of the three-dimensional analysis of the variably staggered configuration were quite unexpected. The surface static pressure distribution for the staggered OGVs, instead of showing uniformity, showed significant variation. Individual OGVs that had been staggered closed indicated choked conditions. Due to the choked OGVs, the calculation sequence showed a significant drop in flow relative to the design intent, and the numerical calculations started to go unstable. Figure 8 shows the surface static pressure contours represented nondimensionally by the pressure coefficient, Cp, as:

$$Cp = (Ps - Ps\_f)/(Pt\_f - Ps\_f) \qquad (2)$$

for all the OGVs and the frame in the variably staggered OGV configuration. In this case, unlike the two-dimensional analysis predictions, the quality of the airflow was highly nonuniform as shown by the wide range of contours (colors) on the OGVs.

After the three-dimensional analysis results with the variably staggered OGVs were seen, a second configuration having uniform OGV stagger angles was evaluated using the three-dimensional code, even though the two-dimensional potential flow analysis suggested this to be worse than the variably staggered OGVs configuration. Figure 9 shows the pressure coefficient contours on all the OGVs and frame with the uniformly staggered OGVs configuration. The three-dimensional analysis revealed the flow and pressure distributions to be nearly uniform and well behaved over the entire computational domain, as indicated by the uniform pressure coefficient contours (colors) amongst all the OGVs. While these results using the three-dimensional analysis make the uniformly staggered OGVs the configuration of choice, a detailed comparison of one of the OGVs from both the variably staggered and uniformly staggered OGVs configurations was made to further explore and understand the three-dimensional relief phenomenon with the swept and leaned OGVs.

For the OGV most directly in front of the strut (like OGV 7 in Figure 3). Figure 10 compares the surface pressure coefficient distribution at 10, 50, and 90 percent span for both the configurations. Recall (see Fig. 4) that in response to the strut back-

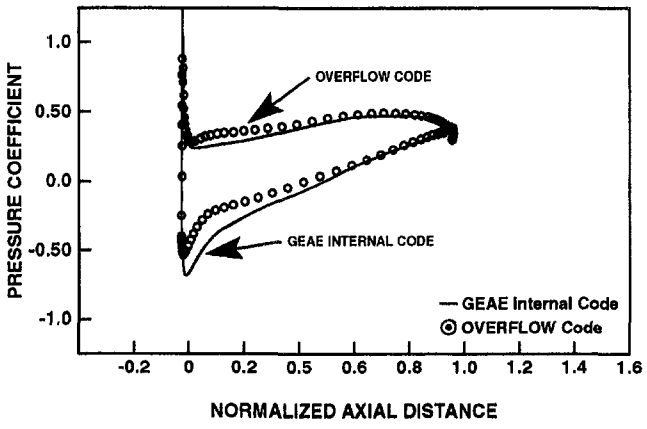

Fig. 7 Comparison of the single blade row OGV midspan surface pressure coefficient distribution calculated by the three-dimensional viscous code solvers (GE Aircraft Engines internal code and NASA's OVERFLOW code)

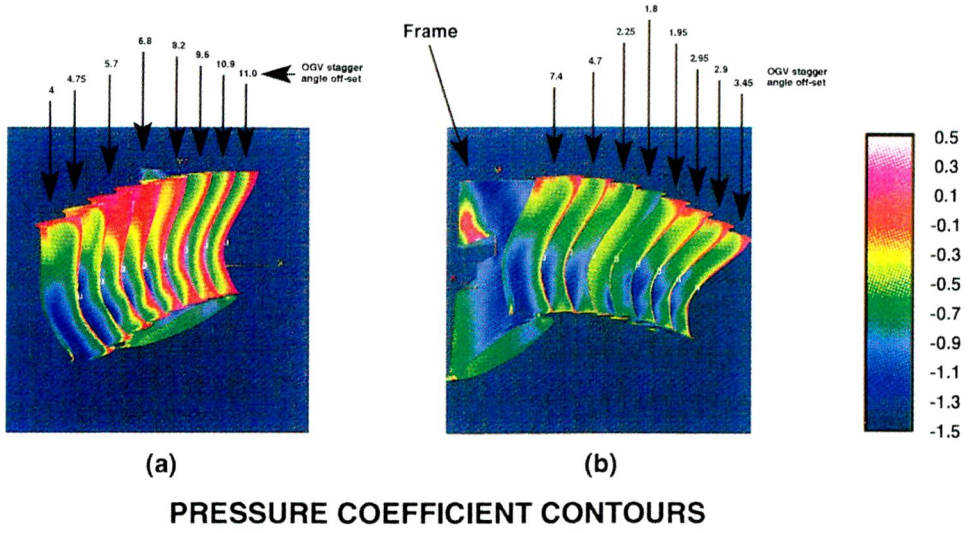

Fig. 8 OGV and frame surface pressure coefficient contours at design speed for the variably staggered OGV configuration calculated by the OVERFLOW code

pressure field predicted by the two-dimensional potential flow analysis in the variably staggered configuration, the OGVs were restaggered closed (i.e., in the direction of lowering the leading edge incidence). The three-dimensional relief with the swept and leaned OGVs, however, reduced the back-pressure effect from the struts. This is illustrated in Fig. 10 with the uniform stagger angles, since the vane pitch region being in line with the strut's stagnation region (as illustrated in Fig. 3) has a higher loading at the leading edge relative to that at the tip and hub immersions. Implementation of the vane stagger closure in this highly three-dimensional relieved flow field for the variably staggered OGV configuration resulted in the severe unloading of the OGV leading edges in the tip and hub regions of the vanes as shown in Fig. 10. Recall from Fig. 2 that the leading edge unloading is expected to be even worse at the off-design conditions.

Although not shown here, this undesirable vane surface pressure coefficient distribution shown in Fig. 10 was typical of all the other stators in the variably staggered OGV configuration and was worse for OGV with higher stagger angles. The results suggest that the back-pressure on the OGV from the splitter and fan frame strut appeared to be simultaneously relieved in the spanwise and tangential directions in the three-dimensional analysis.

Figure 11 shows the vane surface pressure coefficient distribution for selected OGVs in the uniformly staggered OGV configuration at three immersions. Figure 3 shows the locations of these selected OGV relative to the strut. The outer panel of OGV 7 and the inner panel of OGV 8 are in direct line of sight with the strut. The adjacent OGV 5, 9, and 11 are located on either side of the struts. Considering that all the OGVs in this configuration have identical stagger angles, the vane surface static pressure distributions at each immersion are quite similar from vane to vane, and much reduced in magnitude from what was expected based on the two-dimensional potential flow analysis. Again, it appears that the flow within the stator passages had been redistributed both radially and circumferentially in the three-dimensional solution with the OVERFLOW code. This is similar to the leading edge incidence relief due to radial flow migration at stator endwalls experimentally measured in a low speed research compressor and analytically verified using three-dimensional analysis by Wadia and Beacher (1990).

Considering all the surface pressure coefficient distribution data shown in Fig. 11, the strut appears to have the most detri-

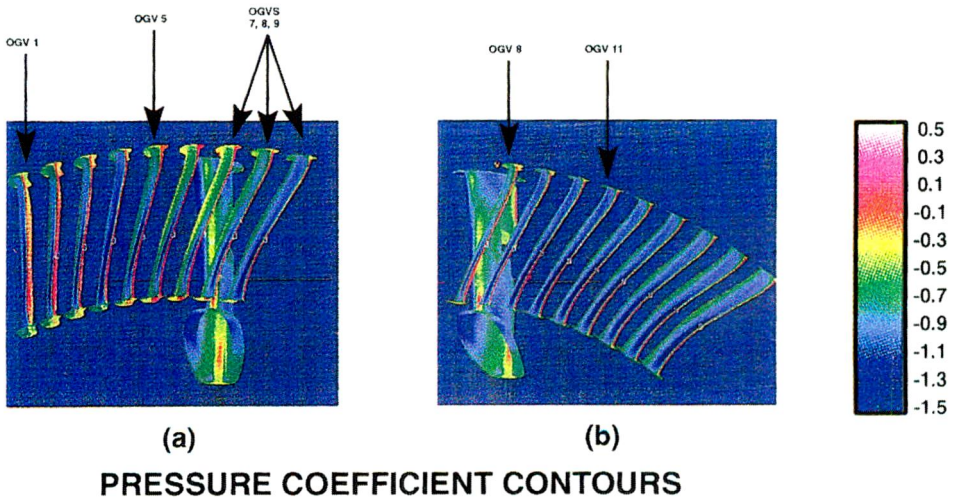

Fig. 9 OGV and frame surface pressure coefficient contours at design speed for the uniformly staggered OGV configuration calculated by the OVERFLOW code

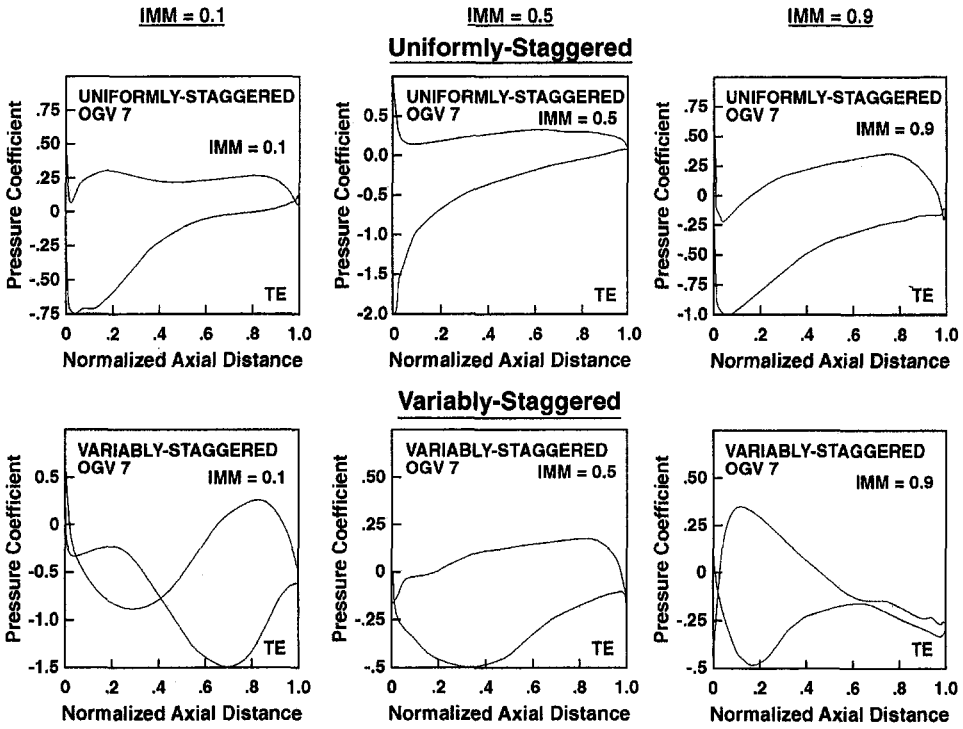

Fig. 10 Comparison of the calculated surface pressure coefficient distribution for OGV 7 from the uniformly staggered OGVs configuration and the variably staggered OGV configuration at 10, 50, and 90 percent immersions

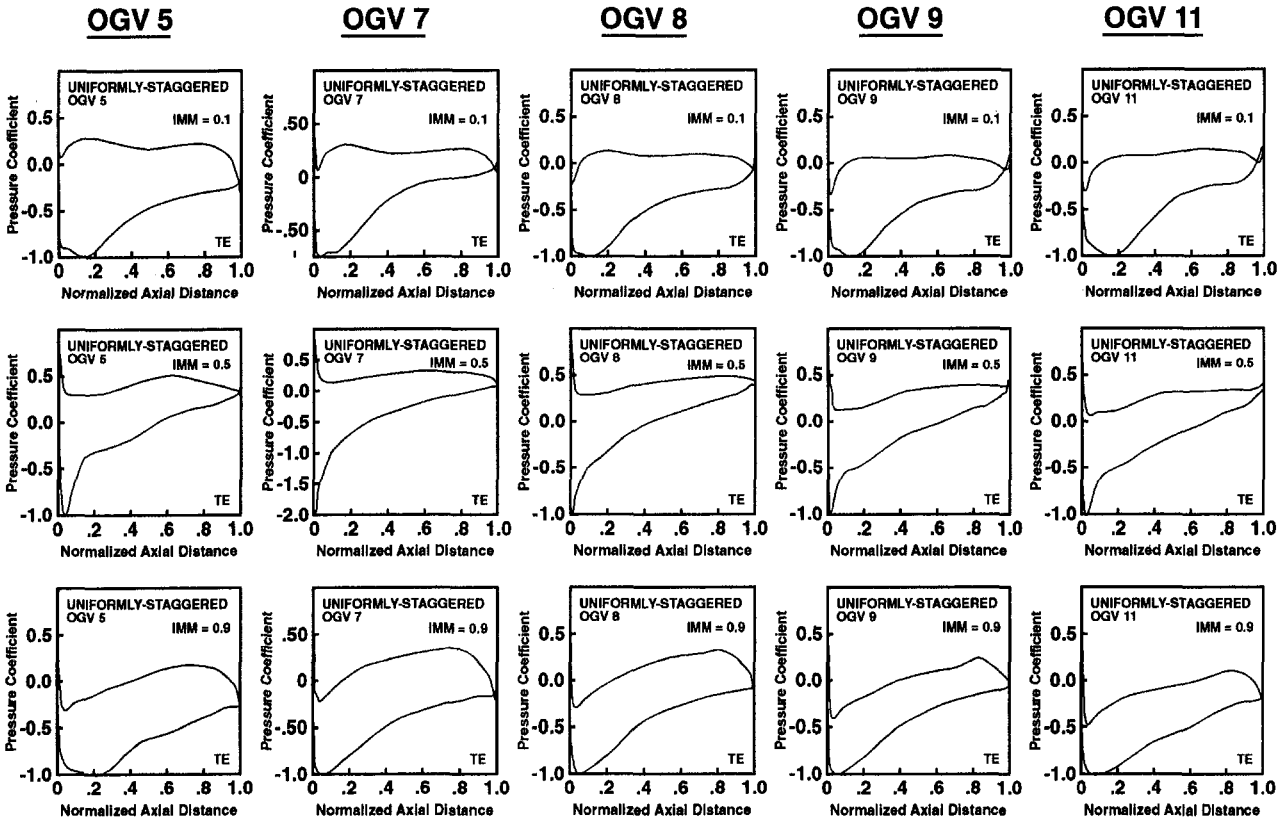

Fig. 11 Selected OGV surface pressure coefficient distribution from the uniformly staggered OGV configuration at 10, 50, and 90 percent immersions calculated by the OVERFLOW code

mental influence (resulting in higher leading edge incidence) on OGV 7. Although the effect is rather small, its top and bottom halves in the spanwise direction are affected in an opposing manner by the two sides of the strut, as seen in Fig. 3. The additional blockage due to the filet on the splitter as it intersects the strut further aggravates the situation on OGV 7 at 50 percent immersion relative to the other OGVs.

The three-dimensional analysis was further exercised to evaluate the uniformly staggered OGV configuration at the part-speed high-bypass-ratio off-design condition. Figure 12 shows the comparison of surface pressure coefficient distributions for OGV 7 for the two conditions. The OGVs performed as expected (see Fig. 2) with the switch in leading edge incidence from positive incidence at the design condition to negative incidence at the off-design condition. As mentioned earlier, balancing the blade surface loading levels between the design and off-design modes of operation, both of which represent critical engine cycle mission points, is one of the main aerodynamic design challenges here. The results in Fig. 12 indicate the achievement of a good balance between the two operating conditions and puts in perspective the relatively high incidence selection at 50 percent immersion at the design speed condition.

For the uniformly staggered OGVs configuration, Fig. 13 shows the circumferential variation of the upstream static pressure predicted by the OVERFLOW code at both conditions for one immersion in the bypass stream, one in the core stream, and one near the splitter. No comparisons with the variably staggered OGV configuration are shown in Fig. 13 as the three-dimensional solution was numerically unstable. The values of the disturbance were calculated using Eq. (1) for both conditions at all three immersions and are also presented in Fig. 13. While the calculated levels of the disturbance were not zero, the resulting amplitudes of the static pressure circumferential nonuniformity are slightly higher at design speed and lower at the off-design condition at part speed relative to the best two-dimensional potential flow analysis results with the variably staggered OGVs shown in Fig. 5. These levels of amplitude were estimated and confirmed by test data to have no significant adverse impact on the performance and aerodynamic stability of the upstream turbomachinery. The tabulated data in Fig. 13 suggest that the magnitude of the pressure pulse felt upstream is lower at part speed for all immersions. At the low-bypass condition at design speed, the core stream sees a slightly higher magnitude of the disturbance relative to the bypass stream and vice versa at the high-bypass condition at part speed.

Figure 14 shows the entropy (loss) contours on the pressure and suction surfaces of OGV 7 in the uniformly staggered OGV configuration at design speed. The high-loss region shown in red occurs near the tip endwall on the suction surface near the OGV trailing edge. As discussed earlier, this could be a result of the Baldwin–Barth one-equation turbulence model used with the OVERFLOW code. The next lower loss-prone region shown in yellow occurs near the hub endwall corner on the suction side of the OGV. The particle traces on the suction side of OGV 7 calculated by the three-dimensional analysis are shown in Fig. 15. Consistent with the high-loss region at the tip endwall, the flow rolled up into a vortex at the trailing edge on this OGV. This vortex roll-up occurred only on OGV 7 whose outer panel cuts across the leading edge of the strut. The classical secondary flow pattern where the fluid migrates inward from the tip to the hub at the OGV trailing edge was also captured by the analysis. No regions of hub corner stall were observed on any of the OGVs at either design condition.

Figure 16 shows the entropy contours along some of the body surfaces of the OGV–strut system. Every fourth OGV is shown in the figure. The splitter, which also has to accommodate a significant swing in its leading edge incidence with changes in bypass ratio, is well behaved, as represented by the very low

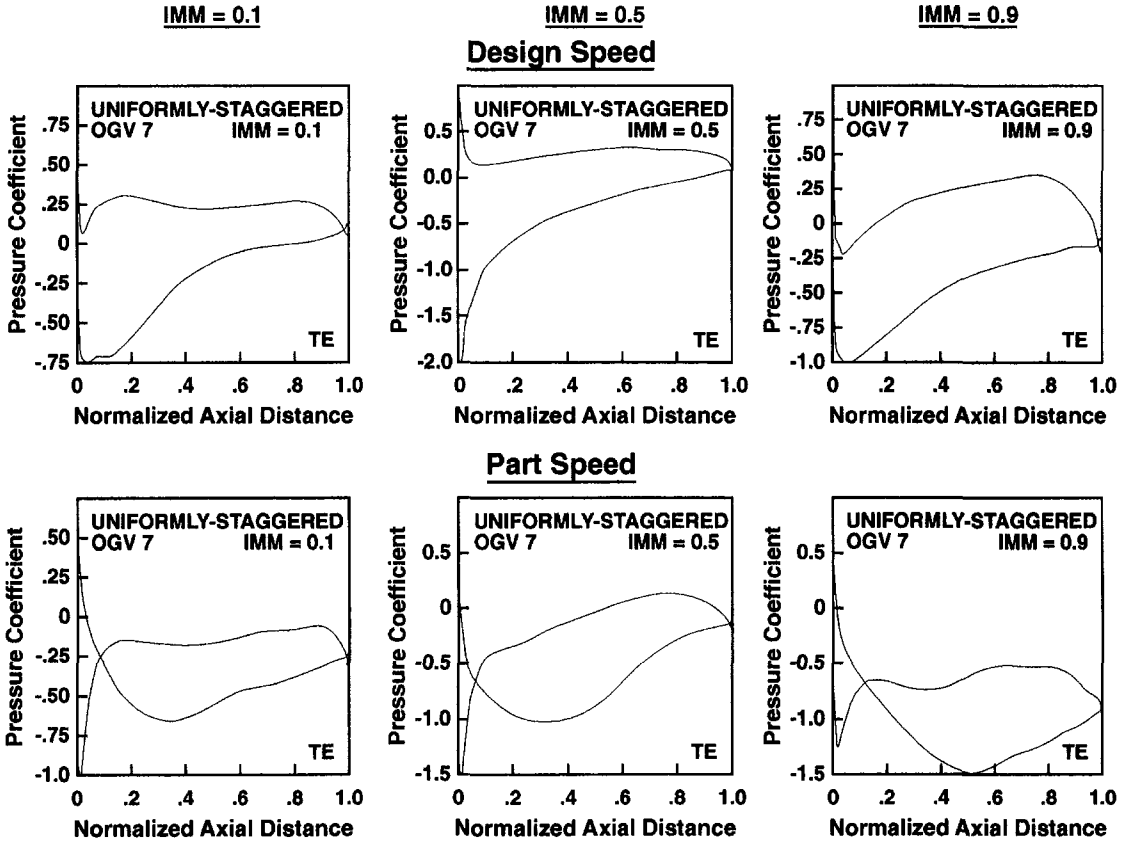

Fig. 12 Comparison of the calculated surface pressure coefficient distribution for OGV 7 from uniformly staggered OGV configuration at 10, 50, and 90 percent immersions at design speed and part-speed conditions

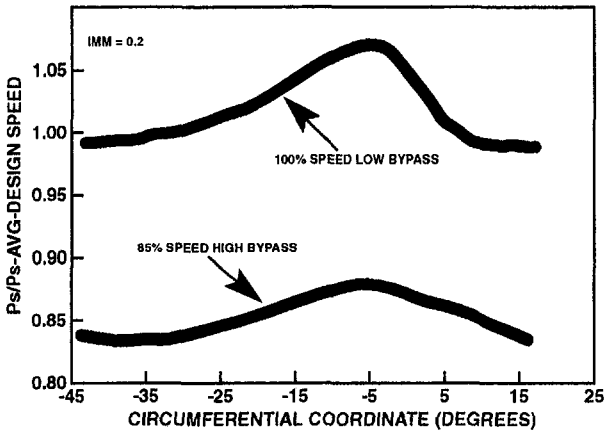

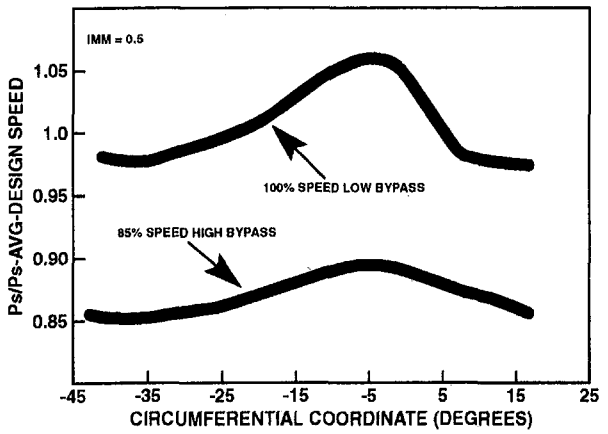

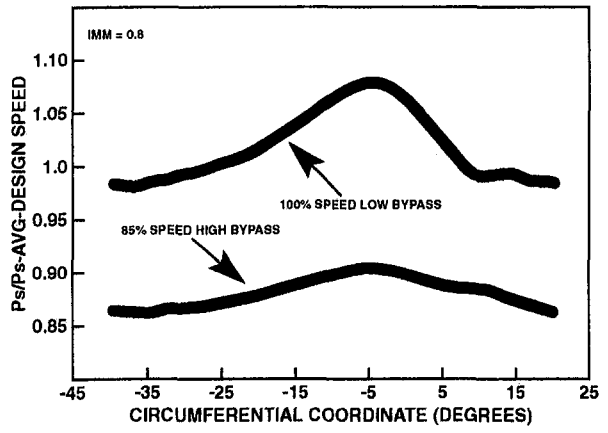

IMM	Δ Ps/Ps-avg (Design)	Δ Ps/Ps-avg (Off-Design)
20%	0.076	0.051
50%	0.085	0.048
80%	0.082	0.040

Fig. 13 Circumferential variation of OGV upstream static pressure at design and part-speed conditions at 20 percent (bypass stream), 50 percent (splitter), and 80 percent (core stream) immersions calculated by the three-dimensional OVERFLOW code for the uniformly staggered OGV configuration

loss level shown in blue. The highest loss levels once again are near the outer endwall of the bypass stream and are attributed to the turbulence model. The OGV wakes show up as distinct dark blue and red entropy contours along the splitter and endwall surfaces. The OGV wakes mix out sooner along the endwalls than along the splitter surfaces. In fact, the OGV wakes can be clearly seen all the way back to the trailing edge of the splitter. This has considerable influence on the physical placement of the verniered pressure and temperature rakes to measure the performance of the fan module. The core duct diffusion was also found to be well behaved, as seen by the mixed-out lower entropy level in green at the downstream end of the core duct.

Although the three-dimensional analysis results provided an emphatic vote against the configuration with variably staggered OGVs derived from the two-dimensional potential flow analysis, a diluted version of the variably staggered OGV configuration was retained as an option to be evaluated in the engine test. The stagger angle offsets calculated by the two-dimensional analysis and shown in Fig. 4 were halved in the diluted version of the variably staggered OGV configuration for test evaluation.

Engine Test Setup and Instrumentation

The goals from the OGV–strut system test were to demonstrate that no reduction in the fan's performance and stability came as a result of this reduced-length design. The assessment of this unique closely coupled OGV–strut system was carried out as an integral part of the new fan development test. The testing was done in the complete engine environment. Doing component evaluation in the full engine environment has several advantages. In terms of the measured component performance levels, engine fuel flow and turbine temperature indications are independent checks to confirm or refute the measurements. In terms of aerodynamic stability, derived limits for the compression components in the two-spool environment represent a true engine system stability level, including interaction effects between the fan and the core compressor (Greitzer et al., 1978) that can be especially significant when inlet distortion is present.

The basic engine control logic was modified to allow constant-speed fan throttles to stall using the engine's variable exhaust nozzle. The fan module was heavily instrumented, including special instrumentation to evaluate and quantify the OGV–strut aerodynamic interaction. Using Fig. 1(*b*) as a reference, this special instrumentation consisted of a circumferential row of 11 static pressure taps on both the hub and casing endwalls located upstream and downstream of the OGVs. The upstream static pressure taps were placed 0.35 OGV gaps in front of the OGV leading edge, while the downstream static pressure taps were located midway between the OGV trailing edge and the strut leading edge. The row of 11 static pressure taps extended circumferentially to sample 36 deg (more than half) of the 60 deg between struts. Unlike the schematic shown in Fig. 1(*b*), each of the 96 OGVs had adjustable stagger angle, providing the option for uniform or individual stagger resets of the vane row.

From the three-dimensional analysis results, the uniformly staggered OGV configuration was selected as the baseline OGV configuration to begin the engine test. Fan performance was based on measurements made by seven verniered radial rakes that were located approximately 2.5 OGV chord lengths downstream of the OGV trailing edges. The radial rakes were equipped with combination total pressure and total temperature sensors, and sampled four immersions in the bypass stream and five immersions in the core stream.

A 180-deg one-per-rev inlet distortion screen was selected to evaluate the aerodynamic stability aspects of the OGV–strut system. The inlet was configured with an inlet distortion screen rotating mechanism to be able to assess the fan's stability limit accurately with various degrees of alignment between the inlet screen's low-pressure sector and the peak back-pressure location produced by the OGV–strut interaction. Note that in the distorted half of the fan after accounting for phasing as the

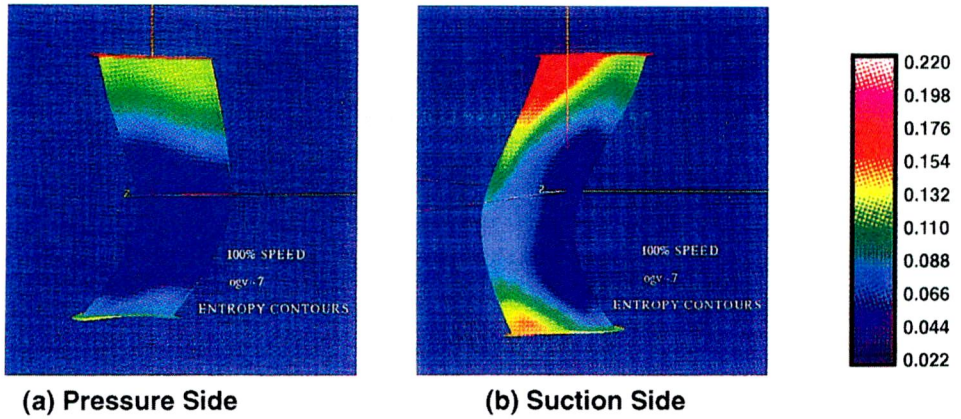

Fig. 14 Calculated entropy contours on the pressure and suction surfaces of OGV 7 from the uniformly staggered OGV configuration at the design speed condition

distortion propagates through the fan, the alignment of the screen's low-pressure sector and the peak back-pressure location from the OGV–strut interaction represents the most destabilizing condition. Comparison of the resulting fan stall limit with the various degrees of alignment between the distortion screen's low-pressure sector and the peak back-pressure location were used to quantify the destabilization from the OGV–strut aerodynamic interaction. For consistency between the distortion level and the fan's operating point, this comparison was made at 95 percent fan corrected speed. With clean inlet, using interstage Kulite data, the fan's last stage was determined to be the stalling stage at this speed.

Engine Test Results

A series of power calibrations were performed to establish the baseline fan performance. Having the OGVs in the uniformly staggered OGV configuration, the fan met (or exceeded by as much as 0.75 point) its predicted performance level along its operating line. This initial test result provided significant credibility to the OVERFLOW code analysis, which had predicted the uniformly staggered OGVs to be the preferred configuration.

Being a military application, investigation of the stability of the fan with the closely coupled OGV–strut configuration was of prime importance. Three OGV stagger configurations were evaluated: (*a*) the base configuration with the uniform stagger, (*b*) a circumferentially varying stagger configuration with half the offsets shown in Fig. 4, and (*c*) another uniform-stagger configuration with all 96 OGVs staggered 5 deg closed (representing approximately the maximum offset in the variably staggered OGV configuration) relative to the base stagger level in (*a*).

At 95 percent speed the fan's stability limit was defined with the one-per-rev inlet distortion screen positioned in three different circumferential locations. The three screen positions represent alignment between the screen's low sector and the peak back-pressure location, and a 20-deg offset on either side of this alignment. Among the three OGV configurations tested, the largest variation with screen position in the resulting stability limits was found to be 1.5 percent in terms of the stall flow divided by the stall pressure ratio, and this occurred with the variably staggered OGV configuration. There was also some randomness in the stability results with the three OGV configurations in that the worst and the most favorable stability limit results did not always correspond with a particular inlet distortion screen position setting. Statistically, the expected tolerance band (repeatability) on the measured stability limit is ±1 percent. Accordingly, the test results indicate that the OGV–strut aerodynamic interaction causes at worst a 0.5 percent compromise in the fan's aerodynamic stability limit, which is excellent.

The measured circumferential variation in the static pressure generated upstream of the OGV at the casing endwall by the OGV–strut interaction is shown in Fig. 17. The results with all

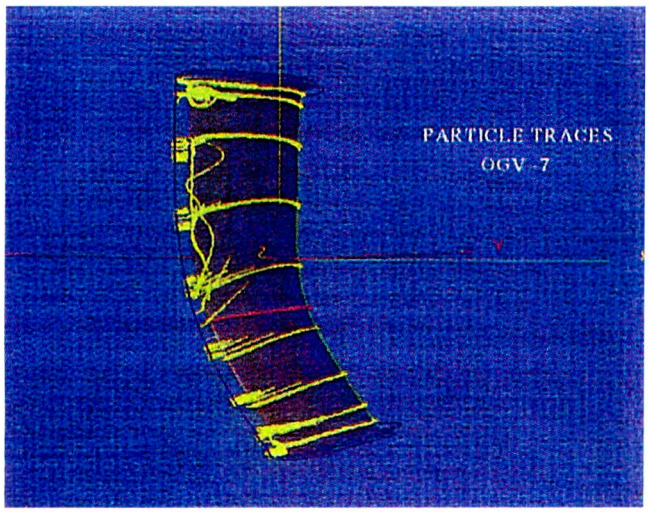

Fig. 15 Particle traces on the suction side of OGV 7 from the uniformly staggered OGV configuration showing vortex roll-up at the trailing edge near the tip endwall and the classical secondary flow migration down the trailing edge from tip to hub

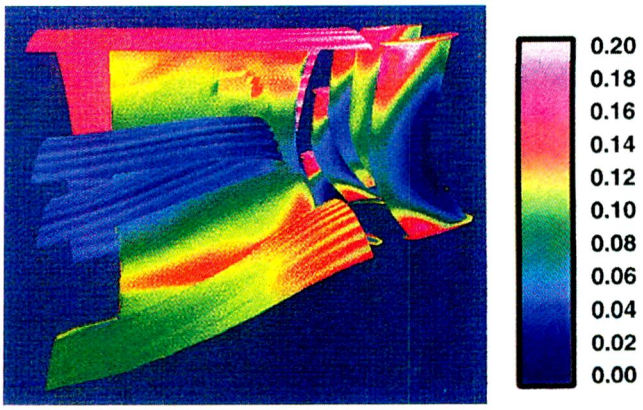

Fig. 16 Entropy contours along the strut and OGV suction surfaces and along the splitter, hub and tip endwalls showing the OGV wake streaks along both the upper and lower splitter surfaces and also along the inner and outer flowpath surfaces

three stagger configurations are shown. The measurements at the hub were similar in both amplitude and phasing. Comparison of Fig. 17 with Fig. 13 illustrates that the phasing and the amplitude (considering that the test data are at 95 percent speed) are in good agreement with the OVERFLOW code results, in spite of the fact that the OVERFLOW code analysis was done without the rotor characteristic. Figure 17 indicates that the back-pressure characteristics were not altered to any appreciable extent by the three OGV stagger configurations tested. Recall that the stagger variation in the variably staggered OGVs configuration tested represents half the magnitude that was analyzed by the OVERFLOW code yielding the disappointing results. The minor variation in the back-pressure characteristic noted in Fig. 17 in a way is a negative result for the variably staggered OGV configuration, since it represents no improvement at added cost and with added supportability/maintainability problems. From a fan stability and practical point of view, the OGV configuration with the uniform 5-deg stagger closure remained a candidate at the conclusion of the stability testing. However, severe performance penalties encountered with this configuration, under clean inlet conditions (shown in Fig. 18) eliminated it from being a viable contender. The large magnitude of the performance penalties along low operating line settings, represented in Fig. 18 by flow levels at and below cruise, which was produced by roughly half the maximum stagger angle offset levels of the variably staggered OGV configuration (Fig. 4) analyzed with the OVERFLOW code, lends further credibility to the three-dimensional code's negative performance results.

Concluding Remarks

An advanced concept of using swept and leaned stators relying on three-dimensional relief to alleviate nonuniform back-pressure disturbances is presented. Numerical models involving various degrees of sophistication were used to develop and analyze the closely coupled OGV–splitter–strut system. Three-dimensional analysis results using the NASA-developed OVERFLOW code revealed the inner workings and feasibility of the concept. The pretest three-dimensional OVERFLOW code calculations provided an accurate assessment of the performance of both the uniformly staggered and variably staggered OGV configurations and the final test results confirmed the shortcomings of the two-dimensional analysis as applied to the design of the swept and leaned OGV–strut–splitter system.

A frequently ignored issue, the off-design problem, was also explored in detail. The design intent was verified by the three-dimensional analysis, thus providing the means for developing blade designs optimized for a range of operating conditions instead of just at one point.

The results of these sophisticated analyses yielded significant insights and resulted in large savings in development test time and overall cost for a key engine program.

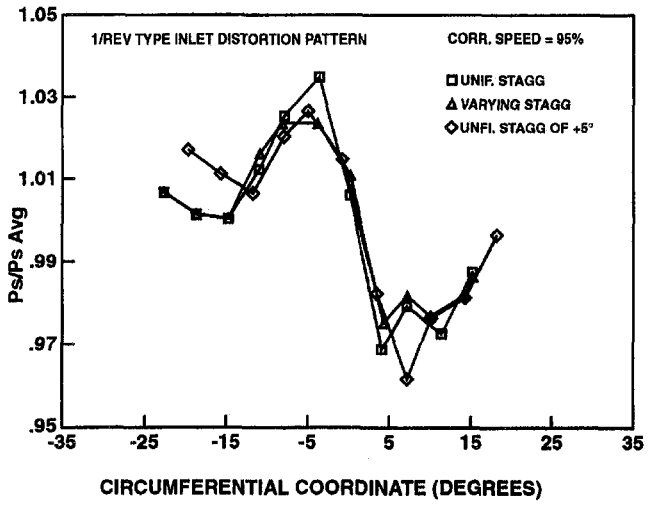

Fig. 17 Comparison of the measured casing endwall rotor exit circumferential static pressure distributions for the different OGV configurations tested

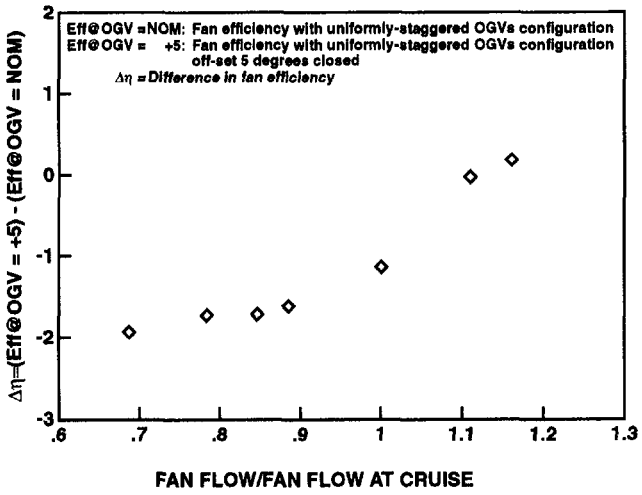

Fig. 18 Comparison of the performance between the uniformly staggered OGV configuration and the configuration with all OGVs closed an additional 5 deg relative to the uniformly staggered OGVs configuration

Acknowledgments

The authors are very grateful to Freeman James, Manager, Large Military Product Engineering for his constant encouragement and significant support during the course of this investigation. The authors would also like to acknowledge the help of Dr. Petty of the USAF and NASA, Ames management for providing us with excellent support and free computer resources.

References

Benek, J. A., Buning, P. G., and Steger, J. L., 1985, "A 3-D Chimera Grid Embedding Technique," AIAA Paper No. 85-1523.

Buning, P. G., Chan, W. M., Renze, K. J., Sondak, D. L., Chiu, I., and Slotnick, J. P., 1993, "OVERFLOW User's Manual, Version 1.6ad," NASA Ames Research Center, Moffett Field, CA.

Cerri, G., and O'Brien, W. F., 1989, "Sensitivity Analysis and Optimum Design Method for Reduced Rotor–Stator–Strut Flow Interaction," ASME JOURNAL OF TURBOMACHINERY, Vol. 111, pp. 401–408.

Cerri, G., Boatto, P., Sorrenti, A., and O'Brien, W. F., 1994, "Optimization of Rotor–Stator–Strut Potential Flow Interaction Including Rotor Feedback Effects," ASME Paper No. 94-GT-274.

Chan, W. M., Chiu, I. T., and Buning, P. G., 1993, "User's Manual for the HYPGEN Hyperbolic Grid Generator and the HGUI Graphical User Interface," NASA TM 108791, Oct.

Chiang, H. D., and Turner, M. G., 1996, "Compressor Blade Forced Response Due to Downstream Vane–Strut Potential Interaction," ASME JOURNAL OF TURBOMACHINERY, Vol. 118, pp. 134–142.

Greitzer, E. M., Mazzawy, R. S., and Fulkerson, D. A., 1978, "Flow Field Coupling Between Compression System Components in Asymmetric Flow," ASME *Journal of Engineering for Power*, Vol. 100, pp. 66–72.

Hemsworth, M. C., 1969, "Development and Experiences of the First High-Bypass Ratio Engine, TF39," Paper No. 21, presented at the 11th Anglo-American Aeronautical Conference, London.

Ho, P. Y., 1981, "The Effect of Vane-Frame Design on Rotor–Stator Interaction Noise," AIAA Paper No. 81-2043.

Jennions, I. K., and Turner, M. G., 1993, "Three-Dimensional Navier–Stokes Computations of Transonic Fan Flow Using an Explicit Flow Solver and an Implicit K-E Solver," ASME JOURNAL OF TURBOMACHINERY, Vol. 115, pp. 261–272.

Jones, M. G., Barton, M. T., and O'Brien, W. F., 1996, "The Use of Circumferentially Nonuniform Stators to Attenuate LP Compressor Rotor–Stator–Strut Aerodynamic and Mechanical Interactions," ASME Paper No. 96-GT-154.

Kandebo, S., 1996, "GE Developing Longer-Life F110," *Aviation Week and Space Technology*, Feb. 26, pp. 42–43.

Kodama, H., 1986, "Performance of Axial Compressor With Nonuniform Exit Static Pressure," ASME JOURNAL OF TURBOMACHINERY, Vol. 108, pp. 76–81.

Kodama, H., and Nagano, S., 1989, "Potential Pressure Field by Stator/Downstream Strut Interaction," ASME JOURNAL OF TURBOMACHINERY, Vol. 111, pp. 197–203.

McArdle, J. B., Jones, W. L., Heidelberg, L. J., and Homyak, L., 1980, "Comparison of Several Inflow Control Devices for Flight Simulation of Fan Tone Noise Using a JT15D-1 Engine," AIAA Paper No. 80-1025.

Nakumara, Y., Isomura, K., and Kodama, H., 1986, "Rotor–Strut Interaction Noise of a Model Fan," AIAA Paper No. 86-1971.

O'Brien, W. F., Reimers, S. L., and Richardson, S. W., 1983, "Interaction of Fan Rotor With Downstream Struts," AIAA Paper No. 83-0682.

Parks, S. J., Buning, P. G., Steger, J. L., and Chan, W. M., 1991, "Collar Grids for Intersecting Geometric Components Within the Chimera Overlapped Grid Scheme," Paper No. AIAA-91-1587.

Parry, A. B., 1996, "Optimization of Bypass Fan Outlet Guide Vanes," ASME Paper No. 96-GT-433.

Parry, A. B., and Bailey, R. H., 1997, "The Use of Cyclic Variations in Strut Stagger to Reduce Coupled Blade–Vane–Strut–Pylon Interaction and System Losses," ASME Paper No. 97-GT-470.

Preisser, J. S., Schoenster, J. A., Golub, R. A., and Horne, C., 1981, "Unsteady Fan Blade Pressure and Acoustic Radiation From a JT15D-1 Turbofan Engine at Simulated Forward Speed," AIAA Paper No. 81-0096.

Rubbert, P. E., Boctor, M. L., Cowan, S. J., and Laprete, R. D., 1972, "Concept and Design of Stators Tailored to Shield a Fan From Pressure Disturbances Arising in the Downstream Fan Ducts," AIAA Paper No. 72-84.

Shrinivas, G. N., and Giles, M. B., 1995, "OGV Tailoring to Alleviate Pylon–OGV–Fan Interaction," ASME Paper No. 95-GT-198.

Suhs, N. E., and Tramel, R. W., 1991, "PEGSUS 4.0 User's Manual," AEDC-TR-91-8, AEDC/PA, Arnold Air Force Base, TN.

Turner, M. G., and Keith, J. S., 1985, "An Implicit Algorithm for Solving 2D Rotational Flow in an Aircraft Engine Fan Frame," AIAA Paper No. 85-1534.

Wadia, A. R., and Beacher, B. F., 1990, "Three-Dimensional Relief in Turbomachinery Blading," ASME JOURNAL OF TURBOMACHINERY, Vol. 112, pp. 587–598.

Woodard, R. P., and Balombian, J. R., 1984, "Tone Generation by Rotor-Downstream Strut Interaction," *AIAA Journal of Aircraft,* Vol. 21, pp. 135–142.

Yokoi, S., Nagano, S., and Kakehi, T., 1981, "Reduction of Strut Induced Rotor Blade Vibration With the Modified Stator Setting Angles," *Proc. International Symposium on Airbreathing Engines,* Bangalore, India, Feb. 16–21, pp. 61-1 to 61-7.

Simulation of Vortex Shedding in a Turbine Stage

D. L. Sondak
Boston University,
Boston, MA 02215

D. J. Dorney
GMI Engineering and Management Institute,
Flint, MI 48439

Vortex shedding in a turbomachine blade row is affected by the passing of blades in the adjacent downstream blade row, but these effects have not been examined in the literature. A series of flow simulations has been performed to study vortex shedding in a turbine stage, and to quantify the blade interaction effects on the unsteady pressure response. The numerical issues of spatial order of accuracy and the use of Newton subiterations were investigated first. Second-order spatial accuracy was shown to be inadequate to model the shedding frequency response and time-averaged base pressure accurately. For the small time step employed for temporal accuracy, Newton iterations were shown to be unnecessary. The effects of the adjacent blade row were examined by comparing the shedding frequency response for the stage simulations to the response for isolated cascades. The vane shedding was shown to occur exactly on a series of harmonics of the blade passing frequency for the stage case, compared to a single predominant frequency for the isolated cascade. Losses were also examined in the wake region. It was shown that close to the trailing edge, losses were mainly due to wake mixing. Farther downstream of the trailing edge, losses were predominantly due to the trailing edge shock wave.

Introduction

The prediction of vortex shedding from the trailing edges of turbomachinery blades can aid in the mechanical, acoustic, and aerodynamic aspects of blade design. Unsteady pressure loads due to vortex shedding can affect the structural integrity of the blades. Vortex shedding is a source of noise, and it also affects aerodynamic performance as the vortices interact with downstream blade rows. Ability to capture the correct shedding frequency in flow simulations is affected by numerical issues such as order of accuracy and solution technique, and by the ability to model physical phenomena, such as the potential interaction between the blade rows, accurately.

A body of research is available in which the physics of vortex shedding from isolated airfoils and airfoils in cascades, with particular emphasis on the shedding frequency, has been examined experimentally and computationally (e.g., Paterson et al., 1973, Sieverding and Heinemann, 1990, Arnone and Paciani, 1997). In turbomachinery, the interaction between vanes (or stators) and rotor blades can modify the shedding frequencies, but little research is available that addresses this issue.

In the present study, a series of unsteady flow simulations has been performed for a transonic turbine stage, and the resulting trailing edge pressure frequency responses have been examined. Simulations have also been performed for isolated vane and rotor blade cascades, operating at the same conditions as the airfoils in the stage, in order to assess the interaction effects between the vanes and the rotor blades.

Numerical Method

The quasi-three-dimensional, Reynolds-averaged, unsteady Navier–Stokes equations are solved using an implicit, time-marching, finite-difference scheme (Rai, 1989). The inviscid fluxes are discretized using the TVD (total variation diminishing) scheme of Chakravarthy and Osher (1985), and viscous fluxes are discretized using standard central differences. The procedure is second-order accurate in time, and second or third-order spatial accuracy may be specified. The equations are solved using approximate factorization and a block tridiagonal solver. The Baldwin–Lomax (1978) turbulence model is employed for turbulence closure.

Characteristic boundary conditions are used at the inflow and outflow boundaries. At the inflow boundary, total pressure, total temperature, and flow angle are specified, and the streamwise derivative of the upstream running Riemann invariant, $R_2 = u - 2a/(\gamma - 1)$, is set to zero. At the outflow boundary, the streamwise derivative of the v velocity component, entropy, and the downstream running Riemann invariant are set to zero, and the average pressure ratio, P_3/P_{t1}, is specified. Periodicity is enforced in the circumferential direction. On airfoil surfaces, the no-slip boundary condition is employed, the normal derivative of pressure is set to zero, and surfaces are assumed to be adiabatic. The flow variables at zonal boundaries are explicitly updated after each time step by interpolating values from the adjacent grid.

Configuration

The present simulations are based upon a proprietary high-pressure, high-speed turbine stage geometry with a ratio of two vanes to three rotor blades. The spacing between the blade rows is 20 percent of the vane axial chord. The Mach number at the vane inlet is $M_1 = 0.16$, and the flow angle is $\alpha_1 = 0.0$ deg. The rotor speed is $\Omega = 11{,}400$ rpm. The ratio of exit static pressure to inlet total pressure of $P_3/P_{t1} = 0.25$ results in transonic flow, with shock waves attached to the trailing edges of the vanes and rotor blades. The Reynolds number based on upstream velocity and vane chord is 410,000. The ratio of the specific heats, γ, is set to 1.39.

Each vane and rotor blade passage is modeled with an overset **O-H** grid system. The vane passages are discretized with 221×51 grid points in each **O**-grid and 120×45 grid points in each **H**-grid, for a total of 33,342 grid points for the two vane passages. The rotor passages are discretized with 221×51 grid points in each **O**-grid and 115×45 grid points in each **H**-grid, for a total of 49,338 grid points for the three rotor passages. The total number of grid points for both blade rows is 82,680. The grid is shown in Figs. 1 and 2.

Since the quasi-three-dimensional Navier–Stokes equations were solved, streamtube contraction ratios were employed. These ratios were obtained from the original streamline curvature calculations used to design the turbine.

For the isolated vane cascade cases, the grid was similar to the vane grid shown in Fig. 1, except that the **H**-grid was extended on

Contributed by the International Gas Turbine Institute and presented at the 43rd International Gas Turbine and Aeroengine Congress and Exhibition, Stockholm, Sweden, June 2–5, 1998. Manuscript received by the International Gas Turbine Institute February 1998. Paper No. 98-GT-242. Associate Technical Editor: R. E. Kielb.

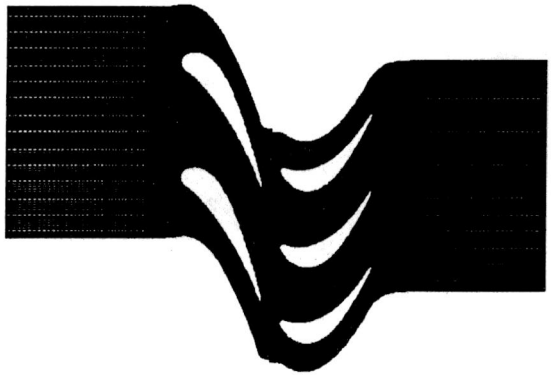

Fig. 1 Grid: entire domain

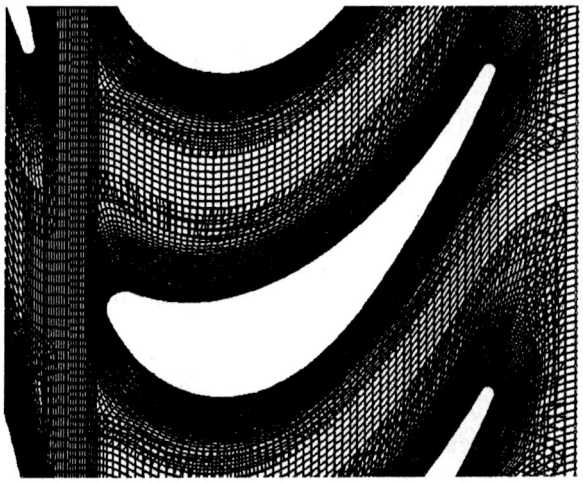

Fig. 2 Close-up of blade region

the downstream side. The extended **H**-grid contained 187 × 45 grid points. The isolated rotor blade cascade **H**-grid was similarly extended upstream, and contained 182 × 45 grid points.

The simulations were run on a single processor of an SGI Origin2000 containing R10000 processors running at 195 MHz. The unsteady stage simulations were run for approximately 15 global cycles at 15,000 iterations/cycle. A global cycle corresponds to the three rotor blades traversing the two vanes. Typical calculations required approximately 62 μs/point/iter CPU time.

Results

Due to the proprietary nature of the present geometry, comparisons between the computational results and experimental data are not shown. In a companion study of vortex shedding in a different turbine geometry (Sondak and Dorney, 1998), results of simulations using the present code have been shown to match well with experimental frequency spectra of the unsteady pressure response. The present code has also been validated in the past by comparing results with experimental data for the unsteady response in a wide variety of turbine configurations similar to those in the present study (Dorney et al., 1992, Dorney and Schwab, 1996, and Dorney and Sondak, 1996).

The primary goal of the current study was to examine the effects of vane/blade interaction on vortex shedding. Simulations were performed for an isolated vane cascade, an isolated rotor blade cascade, and for the full stage. Before performing the full set of simulations, several cases were run to examine numerical issues which can affect the results.

Pressure histories were saved at the trailing edges of both the vanes and the rotor blades. The pressure histories were initially examined directly at the trailing edge points and also at points on the trailing edge radii, but off-center. The off-center points showed more pressure variation, as was also observed in the computations of Mensink (1996) and in the experiments of Cicatelli and Sieverding (1997), so all trailing edge pressure traces are shown for the off-center locations. The locations of the points at which the pressure histories were saved are shown in Figs. 3 and 4 for the vane and rotor blade, respectively.

Assessment of Numerical Effects. Unsteady turbomachinery flow simulations are often performed using difference schemes with either second or third-order spatial accuracy. Lower order schemes tend to be more stable due to increased numerical dissipation, at the expense of reduced accuracy. The current simulations were performed with both second and third-order schemes to assess the effects of spatial accuracy on the pressure response at the trailing edges. The pressure traces near the trailing edge of the vane cascade and their Fourier decompositions are shown in Figs. 5 and 6, respectively. The Strouhal number is defined as

$$\mathrm{St} = \frac{fd}{U} \tag{1}$$

where f is the frequency and d is the trailing edge diameter. The velocity scale U was obtained by time-averaging the midpassage velocity at the axial location of the trailing edge. Based on the value of 15,000 steps per cycle, frequencies up to St $\approx$ 20 are resolved. The amplitude of the pressure variations is approximately the same for both cases, with the third-order case showing a slightly lower average pressure. The Strouhal number for the second-order case is 0.177, while it is 0.188 for the third-order case. (Strouhal numbers for cascades are often referenced to the outflow velocity rather than the trailing edge midpassage velocity. Using the outflow velocity, the Strouhal numbers are 0.183 for the second-order case and 0.194 for the third-order case.) These values fall within the expected range of 0.1–0.4 (Gostelow, 1984). The lower frequency of the second-order solution is apparently caused by its higher numerical dissipation.

Plots of the pressure trace and shedding frequency for the rotor

Nomenclature

a = speed of sound
e_t = total energy
M = Mach number
P = static pressure
P_t = total pressure
Re = inlet reference Reynolds number
St = Strouhal number
T = static temperature
U = time-averaged midpassage velocity
u, v = x, y components of velocity
α = absolute flow angle
β = relative flow angle
ρ = density
Ω = rotor rotational speed
ω = loss coefficient = $(P_{t,in} - P_t)/P_{t,in}$

Subscripts

A, B = upstream and downstream of shock
in = inlet condition
rel = relative reference frame quantity
s = shock
t = stagnation quantity
x, y = first derivative with respect to x, y
1 = vane inlet
2 = rotor inlet
3 = rotor exit
∞ = free stream

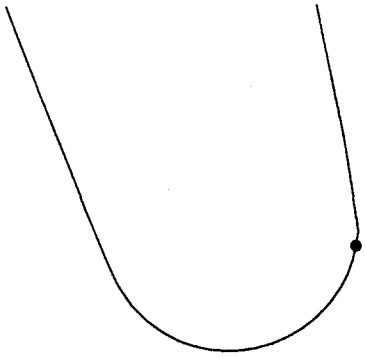

Fig. 3 Vane trailing edge pressure trace location

blade cascade are shown in Figs. 7 and 8. The rotor blade exhibits the same behavior as the vane; the third-order solution has a slightly lower average pressure and a higher frequency. The Strouhal numbers corresponding to the primary peaks in Fig. 8 are 0.243 for the second order solution and 0.266 for the third-order solution (0.265 and 0.290, respectively, when referenced to the outflow velocities).

Simulations of the full-stage flowfield were also performed with both second and third-order spatial accuracy. The pressure traces and shedding frequencies near the trailing edge of the vane are shown in Figs. 9–11. Figure 9 shows the pressure trace for one "cycle," which constitutes the passing of the two vanes by the three rotor blades. The effect of the three rotor blades passing the vane is seen as the low-frequency oscillation with three predominant peaks, and the higher frequency oscillations are due to the vortex shedding. The second-order accurate solution has a damping effect on the amplitude of the pressure variation due to vortex shedding.

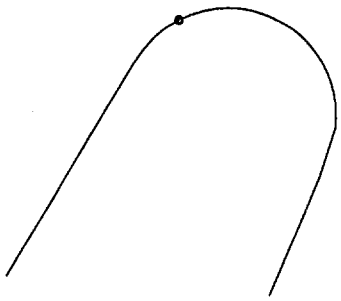

Fig. 4 Rotor blade trailing edge pressure trace location

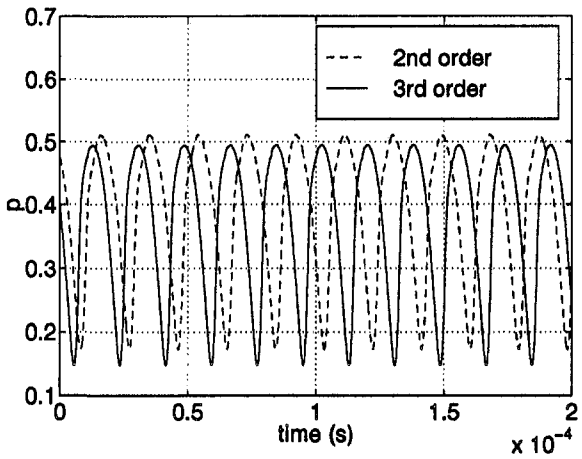

Fig. 5 Pressure trace: vane cascade trailing edge

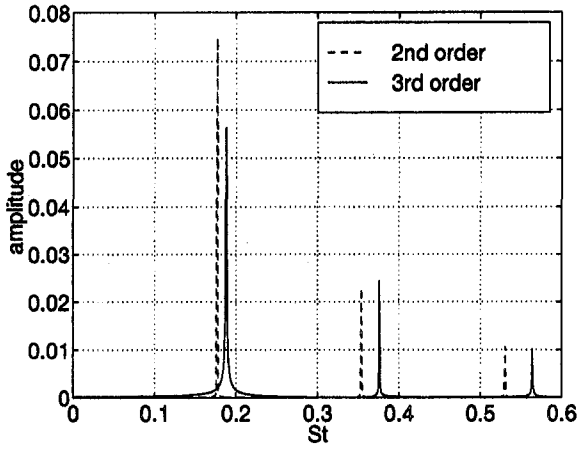

Fig. 6 FFT of pressure trace: vane cascade trailing edge

Figures 10 and 11 show that the predominant peaks occur at harmonics of the blade passing frequency for both cases, although the amplitudes differ.

Time-averaged surface pressures for the vane and rotor blade are shown in Figs. 12 and 13, respectively. The vane shows some differences between the second and third-order schemes at the throat and in the base pressure region. The rotor blade also shows some differences, although they are smaller. Close-ups of the base

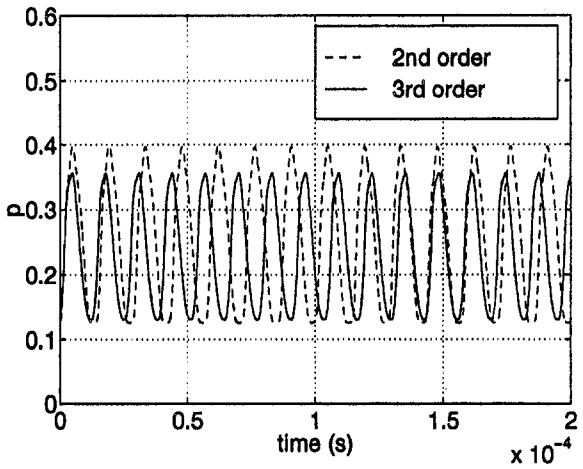

Fig. 7 Pressure trace: rotor blade cascade trailing edge

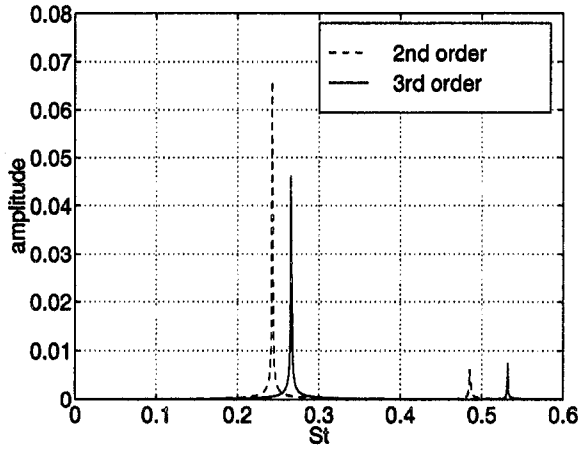

Fig. 8 FFT of pressure trace: rotor blade cascade trailing edge

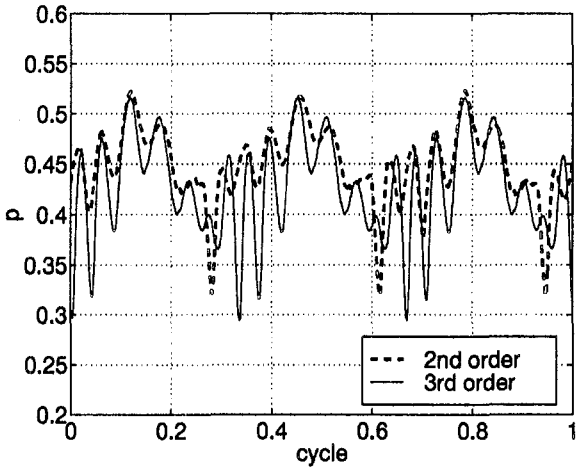

Fig. 9 Pressure trace: vane trailing edge, stage computation

Fig. 12 Time-averaged surface pressure, vane, stage computation

pressure regions are shown in Figs. 14 and 15. For both the vane and the rotor blade, the base pressure is higher for the lower order scheme. The maximum difference is approximately 4.8 percent for the vane and 3.9 percent for the rotor blade.

Newton subiterations can be employed in the flow solver to improve temporal accuracy and to minimize factorization errors. The disadvantage of subiterations is a much higher computational cost. It was thought that subiterations might not be required for the present problem due to the small time step used to capture evolution of the vortices. In order to verify this supposition, initial stage interaction cases were run with no subiterations and with one

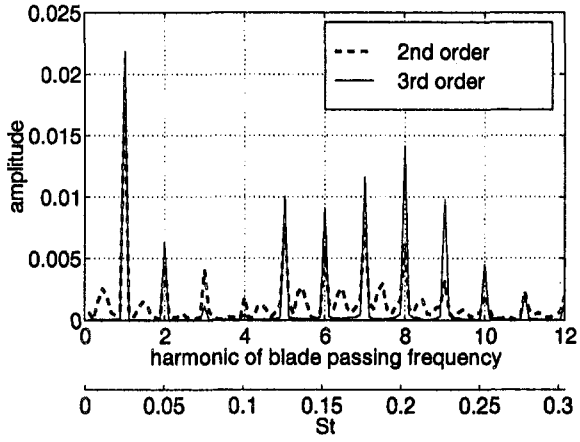

Fig. 10 FFT of pressure trace: vane trailing edge, stage computation

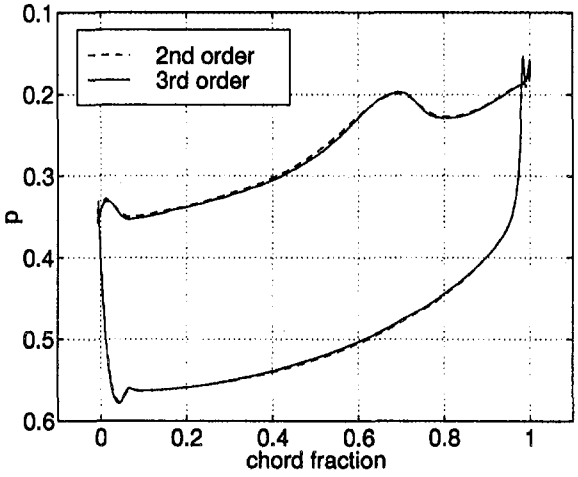

Fig. 13 Time-averaged surface pressure, rotor blade, stage computation

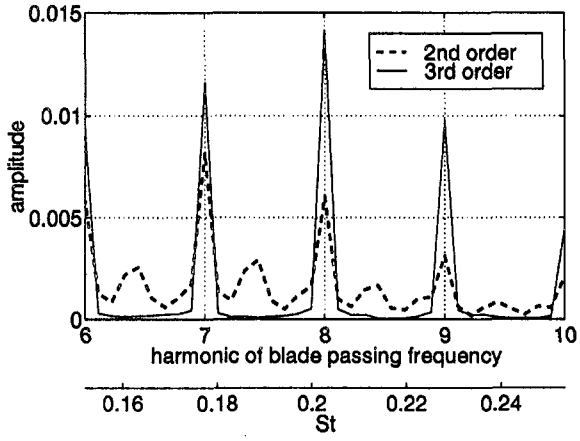

Fig. 11 Close-up of FFT of pressure trace: vane trailing edge, stage computation

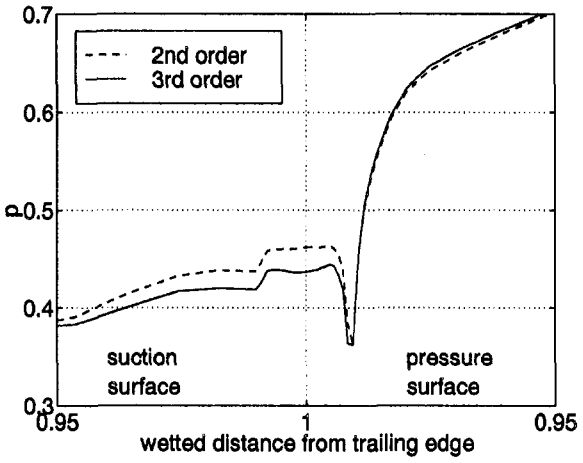

Fig. 14 Time-averaged base region surface pressure, vane, stage computation

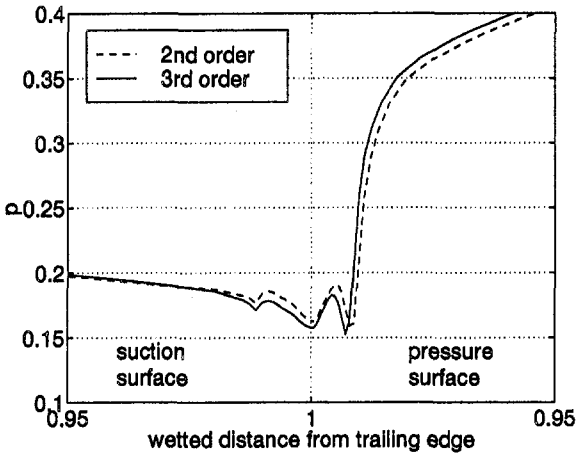

Fig. 15 Time-averaged base region surface pressure, rotor blade, stage computation

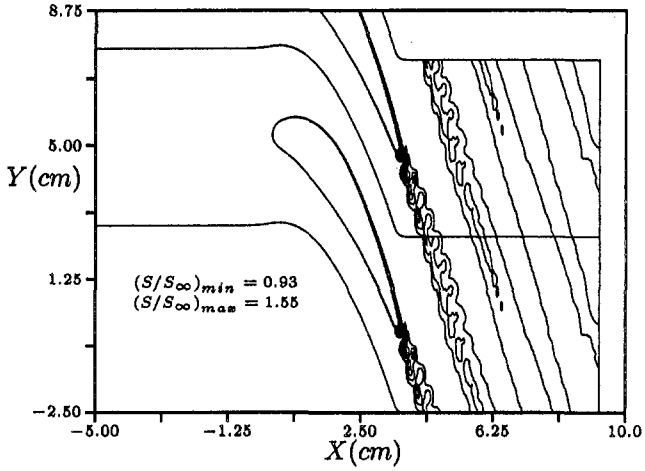

Fig. 18 Instantaneous entropy, vane cascade

subiteration, both with third-order spatial accuracy. The results for the pressure traces near the vane trailing edge are compared in Fig. 16. The differences are extremely slight, so remaining cases were run without employing subiterations.

Interaction Effects. The effects of the interaction between the vane and the rotor blades on vortex shedding will now be examined in more detail. Instantaneous "snapshots" of the entropy fields, which highlight vortex shedding, are shown for the stage and vane cascade cases in Figs. 17 and 18, respectively.

Unsteady pressure envelopes for the vane and rotor blade are shown in Figs. 19 and 20, respectively. For the vane, unsteadiness occurs on the suction surface from the throat to the trailing edge. The pressure surface also exhibits unsteadiness at the trailing edge. It is interesting to note that the vane cascade also shows some unsteadiness at the throat, although it is much smaller in amplitude that for the stage case.

The rotor blade pressure distribution for the stage case is unsteady over both the suction and pressure surfaces due to the passing of the wakes from the upstream vanes, the potential interaction between the blade rows, and the interaction between the vane trailing edge shock wave and the rotor blade. The isolated rotor blade cascade case shows a small amount of unsteadiness at the throat as well as higher amplitude unsteadiness at the trailing edge. (Note that the minimum pressure line for the rotor blade cascade case is very close to that for the stage case just downstream of the throat.)

Close-ups of pressure envelopes in the trailing edge regions are shown in Figs. 21 and 22. The interaction between the blade rows is seen to cause a significant shift in the pressure envelope at the trailing edge of the vane. The rotor blade trailing edge shows a much smaller difference, since the trailing edge is far from the potential effects of blade passing.

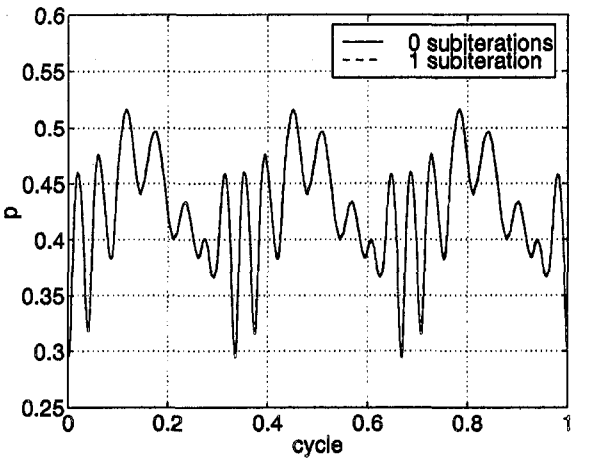

Fig. 16 Vane trailing edge pressure history: effect of Newton subiterations

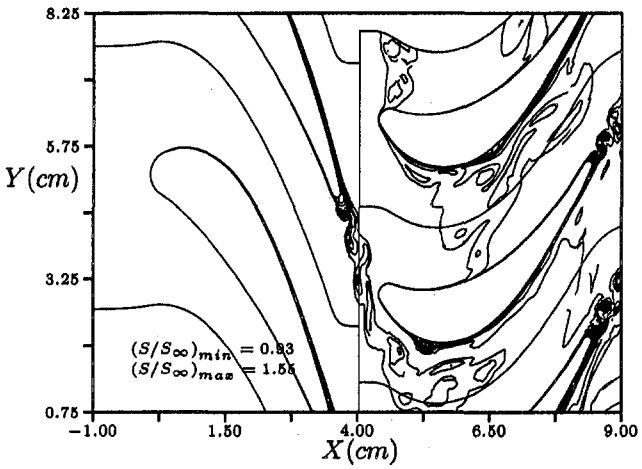

Fig. 17 Instantaneous entropy, stage

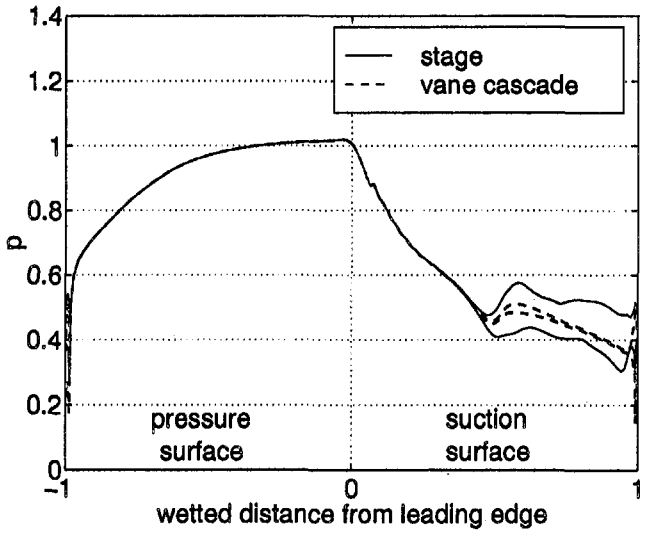

Fig. 19 Unsteady pressure envelope, vane

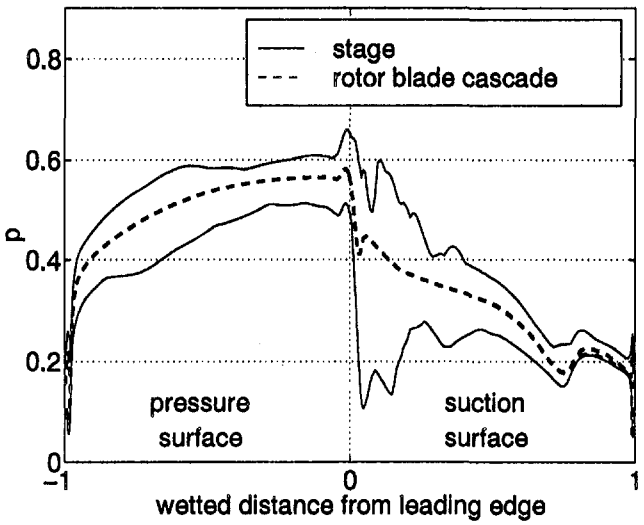

Fig. 20 Unsteady pressure envelope, rotor blade

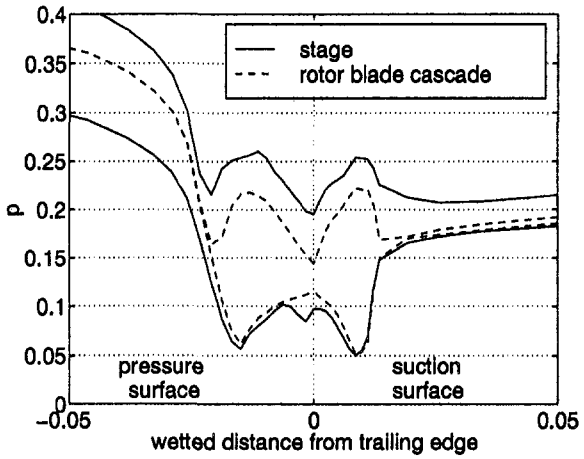

Fig. 22 Unsteady pressure envelope, rotor blade trailing edge

Figure 23 shows the pressure traces at the trailing edge of the vane. Since each vane is passed by three rotor blades per cycle, the stage pressure trace shows three distinct occurrences of a periodic waveform. The average pressure is clearly greater for the stage case, although the maximum pressures are very close between the two cases.

Fourier decompositions of the two signals from Fig. 23 are shown in Fig. 24. Two abcissas are shown, harmonics of blade passing frequency and Strouhal number. The isolated vane cascade shows a predominant frequency of St = 0.188. The stage case shows a strong peak at the blade-passing frequency. In addition, strong peaks occur exactly on harmonics of the blade-passing frequency in the vicinity of the vortex shedding frequency of the vane cascade. The vortex shedding is being influenced by the harmonics of the blade-passing frequency, and the shedding energy is redistributed among a contiguous subset of these frequencies.

Losses. Since the base pressures have been shown in Fig. 21 to differ between the stage and vane cascade cases, and base pressure affects losses, losses through the vane passage warranted further examination. The axial distribution of total pressure loss through the vane is shown in Fig. 25. Here, the loss is defined as:

$$\omega = \Delta P_t / P_{t,in} \tag{2}$$

where $\Delta P_t = P_{t,in} - P_t$. There is no significant difference between the losses for the two cases. It is interesting to note the increase in slope of the curve from the leading edge to trailing edge as the boundary layer thickens, with approximately half of the loss on the blade surface occurring over the last 10 percent chord. The mixing loss and shock loss downstream of the blade row are quite significant, particularly close to the trailing edge.

In order to examine the interaction between the vortex street and the trailing edge shock waves in the vane cascade, a Mach number contour plot is shown in Fig. 26. The shock wave emanates from the trailing edge in a nearly axial direction. Within the domain, three wakes interact with the shock wave downstream of the blade. The locations of the wake–shock interactions are indicated by arrows in Fig. 25. Figure 26 shows significant dissipation of the wake each time it passes through the shock wave.

The total pressure loss across the shock wave can be estimated using oblique shock relationships. By estimating the shock loss, the mixing loss can also be estimated, since the overall loss is known from Fig. 25. There is no significant total pressure loss due to numerical dissipation, which may be verified by the negligible loss at the leading edge in Fig. 25.

Flow properties were examined at an arbitrary axial location approximately halfway between the trailing edge and the first wake–shock intersection, just upstream of the shock wave. At this point, the flow angle is 74 deg, the shock angle is 4 deg, and the Mach number is 1.261, yielding a Mach number normal to the shock wave of 1.185. Using the subscript A to indicate locations

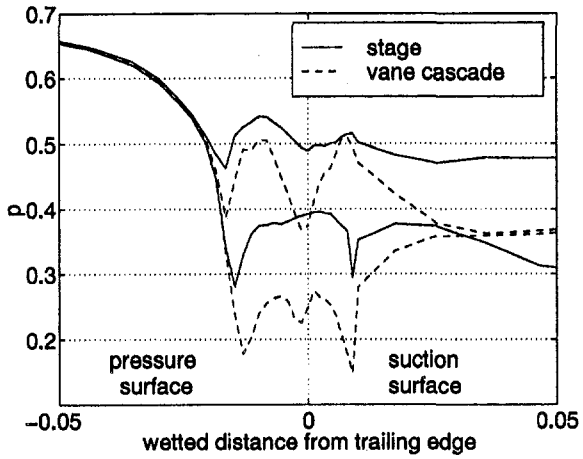

Fig. 21 Unsteady pressure envelope, vane trailing edge

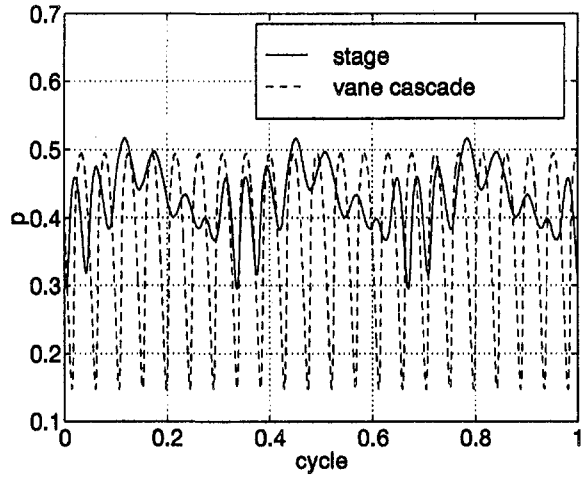

Fig. 23 Vane trailing edge pressure traces

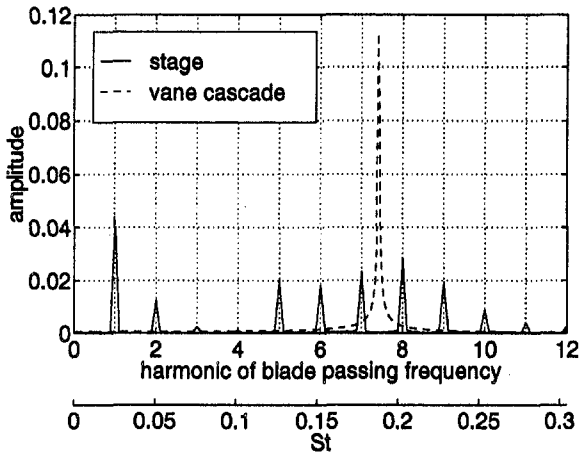

Fig. 24 Frequency spectra of vane trailing edge pressure traces

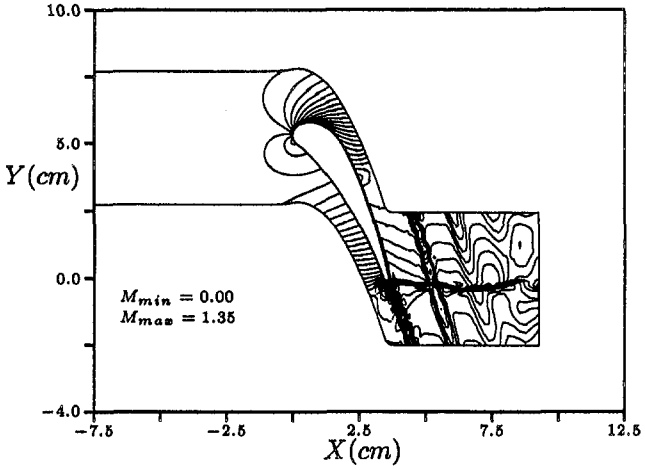

Fig. 26 Instantaneous Mach number, vane cascade

upstream of the shock and B to indicate locations downstream of the shock, the total pressure ratio across the shock is $P_{t,B}/P_{t,A} = 0.99421$ from standard shock tables. From Eq. (2),

$$d\omega = -\frac{dP_t}{P_{t,in}} \tag{3}$$

Approximating dP_t by ΔP_t, the loss across the shock is given by

$$\Delta\omega_s = \frac{P_{t,A} - P_{t,B}}{P_{t,in}} \tag{4}$$

Using the expression for ω_A from Eq. (2),

$$\Delta\omega_s = \left(1 - \frac{P_{t,B}}{P_{t,A}}\right)(1 - \omega_A) \tag{5}$$

Obtaining $\omega_A = 0.0423$ from Fig. 25, Eq. (5) yields $\Delta\omega_s = 0.00555$. The pitch of the blades, normalized by the axial chord, is 1.398. At a flow angle of 74 deg, the flow moves axially $\Delta x = 1.398 \times \cot(74\text{ deg}) = 0.401$ each time the pitch is traversed. The slope of the shock loss curve on Fig. 25 will therefore be $\Delta\omega_s/\Delta x = 0.0138$. Figure 27 shows the total pressure loss in the wake region compared with the slope of the shock loss curve. Close to the trailing edge of the blade, the losses increase at a much higher rate than the shock loss, so the loss in this region can be attributed primarily to wake mixing. The slope of the loss curve gradually decreases until it asymptotes to the slope of the shock

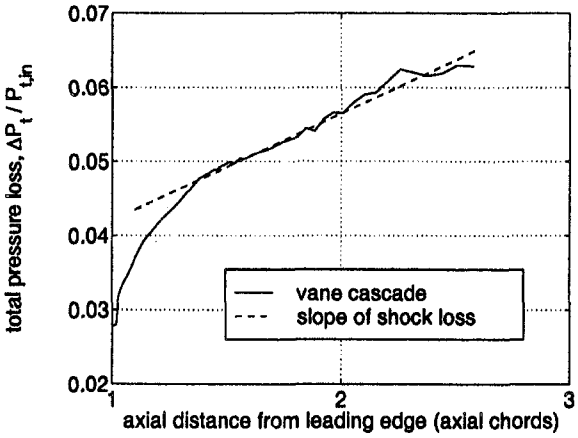

Fig. 27 Wake region total pressure loss

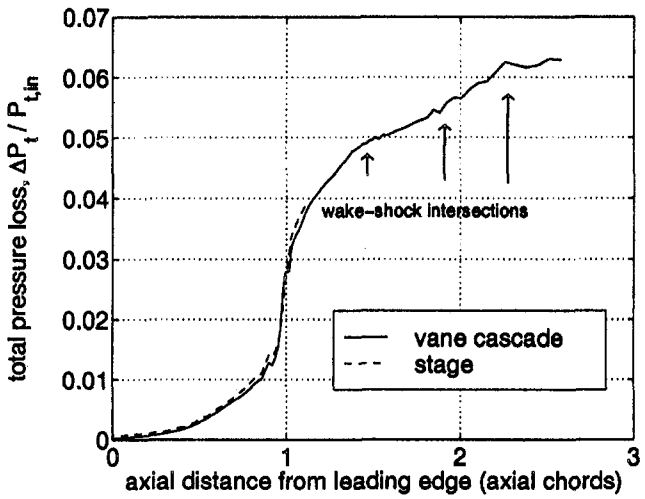

Fig. 25 Total pressure loss through vane

loss at approximately 0.36 axial chord beyond the trailing edge. At this point, the wake has dissipated sufficiently such that shock loss is the primary loss mechanism.

Conclusions and Recommendations

- Vane trailing edge vortex shedding occurs at harmonics of the blade-passing frequency.
- Second-order spatial accuracy is insufficient to capture the trailing edge vortex shedding frequency or time-averaged base pressure accurately.
- Vane losses are not affected significantly by the rotor blade interaction.
- Close to the trailing edge, wake losses are caused predominantly by wake mixing. Further downstream, the losses are predominantly due to the shock wave.
- A difference scheme with fourth-order spatial accuracy should be examined to determine whether or not the same frequency spectra are obtained as with third-order spatial accuracy.

References

Arnone, A., and Pacciani, R., 1997, "Numerical Prediction of Trailing Edge Wake Shedding," ASME Paper No. 97-GT-89.

Baldwin, B. S., and Lomax, H., 1978, "Thin-Layer Approximation and Algebraic Model for Separated Turbulent Flows," AIAA Paper No. 78-257.

Chakravarthy, S. R., and Osher, S., 1985, "A New Class of High Accuracy TVD Schemes for Hyperbolic Conservation Laws," AIAA Paper No. 85-0363.

Cicatelli, G., and Sieverding, C. H., 1997, "The Effect of Vortex Shedding on the

Unsteady Pressure Distribution Around the Trailing Edge of a Turbine Blade," ASME JOURNAL OF TURBOMACHINERY, Vol. 119, pp. 810–819.

Dorney, D. J., Davis, R. L., and Edwards, D. E., 1992, "Investigation of Hot Streak Migration and Film Cooling Effects on Heat Transfer in Rotor/Stator Interacting Flows," NAVAIR report N00140-88-C-0677.

Dorney, D. J., and Schwab, J. R., 1996, "Unsteady Numerical Simulations of Radial Temperature Profile Redistribution in a Single-Stage Turbine," ASME JOURNAL OF TURBOMACHINERY, Vol. 118, pp. 783–791.

Dorney, D. J., and Sondak, D. L., 1996, "Study of Hot Streak Phenomena in Subsonic and Transonic Flow," *International Journal of Turbo and Jet Engines,* Vol. 13, No. 2.

Gostelow, J. P., 1984, *Cascade Aerodynamics,* Pergamon Press, Oxford.

Mensink, C., 1996, "Numerical Prediction of Periodic Vortex Shedding in Subsonic and Transonic Turbine Cascade Flows," *International Journal for Numerical Methods in Fluids,* Vol. 22, pp. 881–897.

Paterson, R. W., Vogt, P. G., Fink, M. R., and Munch, C. L., 1973, "Vortex Noise of Isolated Airfoils," *AIAA Journal of Aircraft,* Vol. 10, No. 5, pp. 296–302.

Rai, M. M., 1989, "Three-Dimensional Navier–Stokes Simulations of Turbine Rotor-Stator Interaction: Part I—Methodology," *AIAA Journal of Propulsion,* Vol. 5, No. 3, pp. 305–311.

Sieverding, C. H., and Heinemann, H., 1990, "The Influence of Boundary Layer State on Vortex Shedding From Flat Plates and Turbine Cascades," ASME JOURNAL OF TURBOMACHINERY, Vol. 112, pp. 181–187.

Sondak, D. L., and Dorney, D. J., 1998, "Vortex Shedding in a Turbine Cascade," AIAA Paper No. 98-3573.

V. Michelassi

F. Martelli

Energetics Department "Sergio Stecco,"
University of Florence,
Florence, Italy

R. Dénos

T. Arts

C. H. Sieverding

Von Karman Institute for Fluid Dynamics,
Rhode Saint Genèse, Belgium

Unsteady Heat Transfer in Stator–Rotor Interaction by Two-Equation Turbulence Model

A transonic turbine stage is computed by means of an unsteady Navier–Stokes solver. A two-equation turbulence model is coupled to a transition model based on integral parameters and an extra transport equation. The transonic stage is modeled in two dimensions with a variable span height for the rotor row. The analysis of the transonic turbine stage with stator trailing edge coolant ejection is carried out to compute the unsteady pressure and heat transfer distribution on the rotor blade under variable operating conditions. The stator coolant ejection allows the total pressure losses to be reduced, although no significant effects on the rotor heat transfer are found both in the computer simulation and the measurements. The results compare favorably with experiments in terms of both pressure distribution and heat transfer around the rotor blade.

Introduction

Despite the inherently unsteady nature of turbomachinery flows, the numerical and experimental analysis of modern turbine stages is quite often done under steady conditions. With the constant improvement in the experimental and computational techniques, it is now possible to investigate unsteady turbomachinery flows in more detail, although investigation is limited to two-dimensional cases (Moss et al., 1997). The possibility to study unsteady three-dimensional stages is still limited by memory and computer time requirements and can be performed only by using quite coarse grids, which do not allow the boundary layers to be accurately modeled. If the three-dimensional nature of the flow is of primary importance, it is possible to use the pitch-averaging technique (Ho and Lakshminarayana, 1996). Still, the availability of unsteady simulations and measurements will contribute to a better comprehension of the unsteady phenomena together with the effect of changes in the operating conditions such as the Reynolds and Mach numbers, the rotational speed, etc.

Jameson (1991) proposed a time-marching algorithm with a double physical-numerical time step, which could be easily employed for the calculation of unsteady flows. From his work other authors computed unsteady flows in turbomachines (Rao and Delaney, 1990; Rao et al., 1992). Unfortunately, the unequal number of blades in the stator and rotor rows can require the computation of the whole cascade, which is often unfeasible because of the large memory and computer time requirements. Accordingly, the stage geometry is often slightly modified to allow a simulation with a reasonable computing effort.

The problem of heat transfer deserves special attention, especially for the first stage downstream of the combustor, because of the high fluid temperatures. In fact, a large portion of the turbine blade boundary layer can be transitional. This implies that an accurate prediction of the effects of turbulence is of primary importance if losses and/or heat transfer are to be computed in presence or absence of cooled blades (Tanuma et al., 1997).

The present work is devoted to the study of a transonic turbine stage with trailing edge coolant ejection and heat transfer on the rotor blade under variable operating conditions. The investigation was carried out in cooperation with other international institutions, which provided the design of the blade and the experimental results that are compared with the computations. To the knowledge of the authors, most of the unsteady calculations in the literature so far are devoted to the prediction of the pressure and velocity field. Still, the unsteady heat transfer phenomenon is of primary importance and there is no evidence that a steady heat transfer calculation will perform like an unsteady calculation. Accordingly, the study of the interaction between the stator and rotor rows was carried out, accounting for the unsteady transitional nature of the boundary layers and heat transfer.

Description of the Solver

Algorithm. The implicit time-marching code MDFLOS3D solves the unsteady Favre-averaged three-dimensional Navier–Stokes (N–S) equations in terms of conservative variables. The code is here used in a two-dimensional manner, so the two-dimensional version of the algorithm will be briefly described. The solver is based on the scalar approximate factorization proposed by Pulliam and Chaussée (1981) and applied to the computation of transonic turbine flows by Michelassi et al. (1994, 1997). The transport equations, the stencil of which is given in Eq. (1), are discretized by using centered finite volumes in curvilinear non-orthogonal structured grids:

$$\underbrace{\left.\frac{\Delta Q}{\Delta t}\right|_p}_{\text{physical}} + \underbrace{\left.\frac{\partial Q}{\partial t}\right|_n}_{\text{numerical}} + \frac{\partial F}{\partial \xi} + \frac{\partial G}{\partial \eta} - \frac{1}{\mathrm{Re}} \cdot \left(\frac{\partial F_d}{\partial \xi} + \frac{\partial G_d}{\partial \eta} \right) + H = 0 \tag{1}$$

The implicit scalar approximate factorization is originally developed for the computation of steady flows. To take full advantage of the implicit formulation, the solver advances in time by using a local time step strategy. The unsteady time-accurate solver introduces a double time step, as originally suggested by Jameson (1991) for explicit time marching algorithms, as shown in Eq. (1). The numerical time derivative (n) is used to advance in the numerical time with a local time step strategy. The physical time accurate derivative (p) acts like a source term, so that when the numerical time transient is eliminated, and the numerical time derivative is zero, Eq. (1) becomes an unsteady time accurate equation. Equation (1) is solved by the usual scalar approximate factorization in which the unsteady terms are treated implicitly as source terms. For further details about the algorithm see Michelassi et al. (1996).

Contributed by the International Gas Turbine Institute and presented at the 43rd International Gas Turbine and Aeroengine Congress and Exhibition, Stockholm, Sweden, June 2–5, 1998. Manuscript received by the International Gas Turbine Institute February 1998. Paper No. 98-GT-243. Associate Technical Editor: R. E. Kielb.

Turbulence Model. The two-equation model by Wilcox (1988) is based on the characterization of the local state of turbulence by two parameters: the turbulent kinetic energy k and the frequency $\omega = \epsilon/k$, where ϵ is the rate of dissipation of k. The eddy viscosity μ_t is related to k and ω by

$$\mu_t = C_\mu \frac{\rho k}{\omega} \tag{2}$$

and the distribution of k and ω is calculated from two model transport equations with the original set of constants (Wilcox, 1988).

The k–ω model, as all the other two-equation turbulence models, was found to overestimate the turbulent kinetic energy in stagnation points (i.e., near the leading edge of turbine blades) followed by a developing boundary layer. As shown by Kato and Launder (1993), the overprediction of k is caused by the presence of normal stresses in the expression of the production. To avoid this, they reformulated the production rate as the product of rotational and irrotational contributions. This approach, while sorting a positive effect in terms of losses and transition prediction (Michelassi et al., 1997), lacks any physical justification and was therefore abandoned in favor of a constraint on the turbulence time scale τ recently proposed by Durbin (1996). This realizability constraint, which ensures that the turbulent kinetic energy is always positive, is formulated assuming that the velocity fluctuation component normal to the wall is known (i.e., a third transport equation is required). When retaining the two-equation model stencil under the assumption of isotropic turbulence, the constraint on τ can be reformulated as a constraint for the frequency ω as follows:

$$\omega = \frac{1}{\tau} = \frac{\epsilon}{k} = \max\left(\omega,\ 1\Big/\left(\frac{1}{\beta^*}\cdot\sqrt{\frac{3}{8\cdot|S^2|}}\right)\right) \tag{3}$$

Equation (3) clips the specific dissipation rate, which cannot reach values below a certain limit, which varies depending on the local mean strain S and applies only in boundary layers where the local M is below 0.2–0.3. The implementation of Eq. (3) in the k–ω model helped solve a large portion of the numerical problems, together with the desired limitation of the production rate.

Transition Model. Transition to turbulence in flows over turbine blades has been extensively measured and computed (Mayle, 1991; Hazarika and Hirsch, 1995). The mechanism of bypass transition is influenced by a number of parameters, such as turbulence level, pressure gradient, flow curvature, which are difficult to include into a model. Transition has a dramatic impact on the heat transfer over turbine blades, the proper prediction of which has a crucial importance in the design phase. Most of the studies on transition for the flow in gas turbines have been carried out in steady situations (Johnson and Ercan, 1997) and in the presence of turbulence levels that are often smaller than what are found in real turbomachines (Hoogendoorn et al., 1997). Addison and Hodson (1992) analyze an unsteady transitional boundary layer in a low-Re, low-M turbine stage, but the model they present still requires validation and tuning for high speed flows. Cho et al. (1993) measured an unsteady boundary layer over a turbine blade under the influence of a series of wakes generated by a squirrel cage. A transition model was tested positively against the measurements for the low Mach number under consideration. Following this work, Michelassi et al. (1997) adapted the formulation to the k–ω turbulence model for the computation of steady transonic turbine blades. The model evaluates a critical Reynolds number, Re_{tr}, which, if exceeded, indicates that transition has started. Re_{tr} is computed by using the empirical formulation proposed by Abu-Ghannam and Shaw (1980). The intermittency function is cast into the expression for the turbulent viscosity Eq. (2) as:

$$\mu_t = f_t \cdot C_\mu \cdot \frac{\rho k}{\omega} \tag{3}$$

in which f_t is computed by using the following expression (Michelassi et al., 1997):

$$f_t = \left(\frac{A_t^+}{A_t^+ + (300 - A_t^+)\cdot\left(1 - \sin\frac{\pi}{2}\left(\frac{\mathrm{Re}_\theta - \mathrm{Re}_{tr}}{\mathrm{Re}_{tr}}\right)\right)}\right)^\alpha \tag{4}$$

Equation (4), which refers to model version A, reaches unity when $\mathrm{Re}_\theta = 2\cdot\mathrm{Re}_{tr}$, which indicates that the boundary layer is turbulent. The parameter α in Eq. (4) controls the rise of f_t in the transition region (the larger the value of α, the longer the transition length).

Observe that both the Abu-Ghannam and Shaw correlation and the intermittency function, Eq. (4), require the computation of the momentum thickness θ and an estimate of the boundary layer thickness. Following the work of Cho et al. (1993), who used a similar approach, and after intense numerical testing and validation in typical turbine geometries (Michelassi et al., 1977; Migliorini and Michelassi, 1997), this was accomplished by defining the boundary layer edge as:

$$\bar{\omega} \approx \bar{\omega}_{\min} + (\bar{\omega}_{\max} - \bar{\omega}_{\min})\cdot 0.01$$

in which $\bar{\omega}_{\min}$ and $\bar{\omega}_{\max}$ are respectively the minimum and maximum values of the vorticity in the cross section. The intermittency function was computed at each time step on the basis of the instantaneous velocity, pressure, and turbulence fields.

Using the previous model the predicted intermittency function might have large variations from one time step to the next. In order to introduce a sort of *history effect* on the intermittency and stabilize the boundary layer state, it was decided to add a transport equation for f_t in the model version B as follows:

$$\frac{\partial f_t}{\partial t} + \frac{\partial u_\xi f_t}{\partial \xi} + \frac{\partial u_\eta f_t}{\partial \eta} = 0 \tag{5}$$

Nomenclature

A^+ = transition model constant
C = chord
C_μ = turbulence model constant
f_t = intermittency function
F, G = convective flux vectors
F_d, G_d = diffusive flux vectors
H = source vector
k = turbulent kinetic energy
M = Mach number
Nu = Nusselt number
P = pitch
q = mass flow rate
Q = vector of unknowns
Re = Reynolds number
S = mean strain
t = time
T = temperature
Tu = turbulence level
α = transition model constant
β^* = turbulence model constant
ϵ = turbulence dissipation rate
θ = momentum thickness
ξ, η = curvilinear coordinates
μ = viscosity
ρ = density
τ = turbulence time scale
$\bar{\omega}$ = vorticity
ω = turbulence frequency

Subscripts

ex = exit
is = isentropic
r = rotor
s = stator
t = turbulent
tr = transitional
0 = total quantity

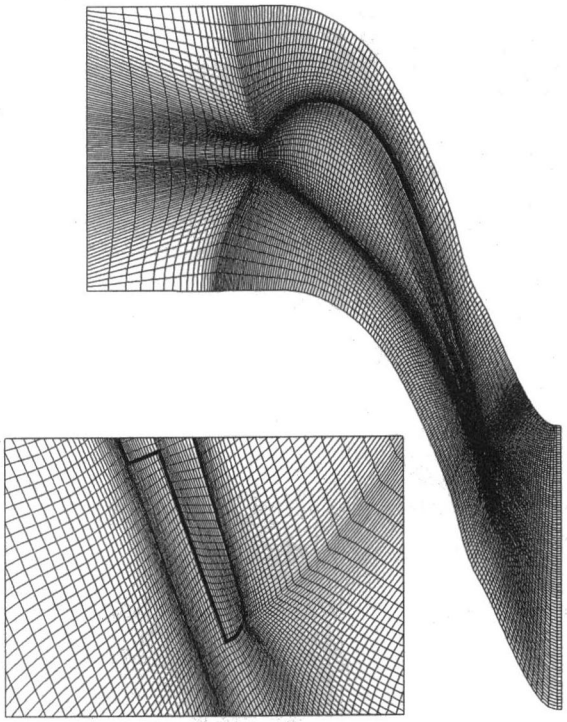

Fig. 1 Stator grid

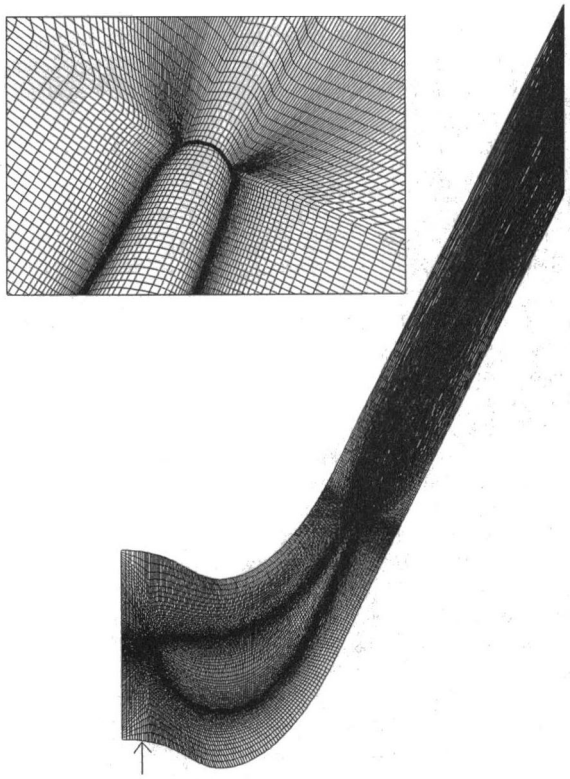

Fig. 2 Rotor grid

The value of the intermittency function placed in Eq. (3) is the maximum of the values computed by Eqs. (4) and (5) at each time step. The model is not used in a narrow region on the rotor leading edge since the assumption of a laminar or turbulent leading edge did not affect the further development of the boundary layer.

Grids. Although the experiments are carried out on a annular test rig, the computer simulations are run in a two dimensional midspan geometry to reduce the computational effort. The computer program, coded in three dimensions, is used here in a two-dimensional manner by solving one control volume only in the radial direction. The stator and rotor blade rows are then assumed to be linear. The I-type 200 × 104 grid, shown in Fig. 1, is one of the most general possibilities when staying with simply connected or single block grids. The equivalent grid for the rotor blade with 258 × 153 points is shown in Fig. 2. The grids are nearly orthogonal in the crucial stagnation point region. A close up view of the trailing edges is shown in Figs. 1 and 2, with the cut on the pressure side of the stator blade for the coolant ejection.

The exact rotor pitch at midspan is $P_s = 54.0427$ mm, while for the rotor row the pitch is $P_r = 36.3099$ mm. To have a nearly periodic problem, one can solve two stator blades and three rotor blades since the pitchwise extension of the stator is $2 \times P_s = 108.0854$ and the pitchwise extension of the rotor is $3 \times P_r = 108.9297$. To have a fully periodic calculation, the previous two lengths should be equal. Since the mass flow rate is controlled by the size of the stator row, it was decided to keep the dimensions of the stator row unaltered and change the dimensions of the rotor row to have $2 \times P_s = 3 \times P_r$. The dimensions of the rotor row can be changed in three ways:

- Reshape the pitch and the blade size by a scaling factor $SC = 2 \times P_s/3 \times P_r = 0.992249$. In this way the overall rotor row is reduced in size by a factor 0.775 percent.
- Change the pitch of the rotor row so as $2 \times P_s = 3 \times P_r$. In this way the overall shape and size of the rotor blade is kept unaltered, while the throat area is reduced approximately of 0.7 percent.
- Operate the scaling of the previous point, but rotate the rotor blade to maintain the original throat area.

Of the three, it was decided to use the first. The third option, while theoretically able to give a realistic reproduction of the original geometry, alters the rotor exit flow angle, which can cause the boundary layer separation on the suction side.

While the stator has a constant height, the rotor passage has the variable height in the test rig qualitatively sketched in Fig. 3. The small reduction in the rotor throat area was then compensated by the grid expansion in the radial direction. This shape of the channel requires a quasi-three-dimensional calculation, which is simulated by using a variable cross section thickness in the radial direction. The spanwise expansion of the rotor channel was further adjusted so as to match the measured mass flow rate.

Boundary Conditions. The stator inlet total pressure, temperature, and inlet flow angle, and the rotor exit static pressure are

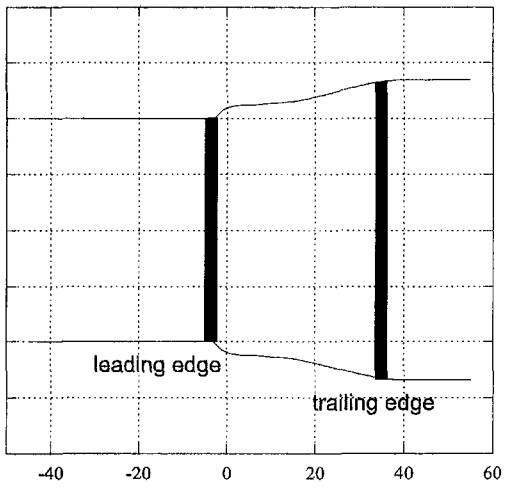

Fig. 3 Qualitative shape of the rotor channel

given to match with the experimental conditions. The inlet turbulence level (1.6 percent) and turbulence length scale (1 percent P_s) are fixed at the stator inlet. The value of the turbulence length scale, which governs the decay rate of turbulence, was selected on the basis of a previous validation of the model (Migliorini and Michelassi, 1997) against similar wind tunnel data. At the stator inlet, the static pressure is extrapolated, while the transported quantities are extrapolated at the rotor exit. A viscous adiabatic condition is set on the stator blade surface, whereas the surface temperature is fixed on the rotor blade, where the velocities are set to zero and the static pressure is computed by using a zero derivative normal to the wall. The turbulent kinetic energy is set to zero and ω has a constant value on the solid boundaries (Wilcox, 1988). On the interface of the five subdomains the grid point distribution is not periodic. The continuity of the solution is enforced by extending the grid of each subdomain which overlaps on the neighboring subdomain. Details of the grid overlapping can be found in Michelassi et al. (1997).

Experimental Data Set

The wide set of measurements (Sieverding et al., 1998) have been carried out on a annular cascade. The test rig is a compression tube annular cascade of the blow-down type. Air is supplied by a large cylinder, which stores compressed air at 250 bars, through a free-moving lightweight piston. The testing time varies from 0.5 to 1 s. The operating conditions are as close as possible to modern aeroengines, with the only exception of the inlet total temperature, which was set to 450 K in the experiments against values of the order of 1800 K for real operating conditions. The stator and rotor Re based on exit conditions and axial chord length are 9×10^5 and 7×10^5.

The midspan pressure distribution on the rotor blade is measured in 24 points by using flush-mounted fast response pressure transducers, the accuracy of which is approximately 1 percent (Sieverding et al., 1998). The midspan heat transfer rate is measured in the same 24 positions by using thin film gages. The gages allow Nu to be measured with an accuracy of 7 percent (Sieverding et al., 1998). The transducers are connected to the in-shaft electronics.

The measurements are performed for several rotor revolutions to extract average and instantaneous values of M_{is} and Nu with a sampling frequency of 4300, 4658, and 4873 Hz for 6000, 6500, and 6800 rpm, respectively. The design rotational speed is 6500 rpm, which implies a tangential velocity of 250 m/s at midspan. The angular speed of the rotor blade changes approximately 5 percent during a typical 0.5 s test with an initial 6500 rpm and an acceleration of 700 rpm/s. The effect of the change on the heat transfer and pressure measurements on the rotor blade surface is negligible (Sieverding et al., 1997).

The stator exit M_{is} is approximately 1.05 with an inlet flow angle of 0-deg. The relative rotor inlet M is 0.45, and the relative exit Mach number of the rotor row is 0.934. Under these conditions the stator row is chocked and controls the mass flow rate. The inlet turbulence level is approximately 1.6 percent. Measurements have been carried out with and without cool air ejected through a slot from the pressure side of the stator blade (see Fig. 1). The coolant mass flow rate was 3 percent of the inlet mass flow rate, and the coolant total temperature was $0.72T_0$.

Computational Results and Comparison With Experiments

Computational Details. The computer simulations of the stator–rotor interaction are initialized with a still rotor. Once a steady converged solution is reached, the rotor grids are shifted in the tangential direction. Each rotor blade requires 50 or 100 physical time steps to pass in front of a full stator blade pitch. The CFL number is 15 for the N–S equations and 10 for the k–ω step. The artificial damping weights are $\frac{1}{2}$ for the second order and $\frac{1}{64}$ for the fourth order. All the numerical simulations were performed on a Digital-Alpha Workstation 600/333. The code size is 120 Mb and it requires approximately 24 to 36 hours to compute a solution, which is periodic in time.

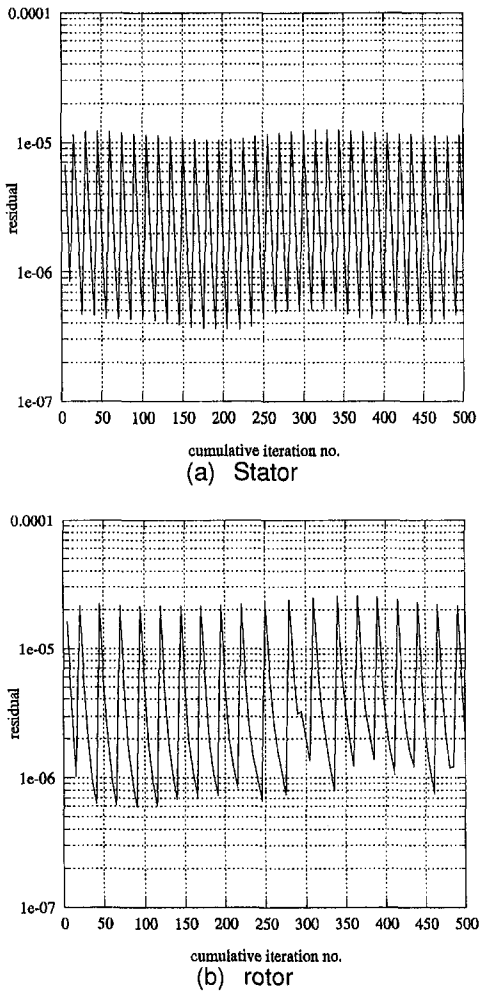

Fig. 4 Convergence histories

Figure 4 shows the typical convergence history of an unsteady run. The abscissa gives the cumulative iteration number, while the ordinate reports the equation residual. Each time step is considered converged when the residual drops below 10^{-6}. Figure 4(a) shows that the stator rows converge in approximately 5 to 15 iterations, while the rotor requires typically twice as much iterations to reach the same convergence level. This is due to the transonic nature of the stator according to which the stator row feels only very weak disturbances from the rotor. Conversely, the rotor row feels the passing stator wakes, which can induce large modifications in the flow field from one time step to the other.

A good indicator of the time-periodicity of the solution is the load, computed as the integral of the pressure distribution around the stator and rotor blades. Figure 5 shows the behavior of the stator and rotor blade loads against the time step. 100 steps correspond to a rotor translation equal to the stator pitch. Figure 5(a) shows that the stator reaches steady state quite soon. The small load fluctuations are caused by changes in the backpressure induced by the passing rotor. Still, the fluctuations are very small, if compared to those of the rotor shown in Fig. 5(b). The rotor blade reaches a periodic state after approximately 200–250 time steps, thereby after a 2–2.5 $\times$ P_s shift of the rotor. This amount of iterations for the startup constitutes a sort of computational overhead since the results obtained in this preliminary phase are substantially useless. To reduce the computational time of the

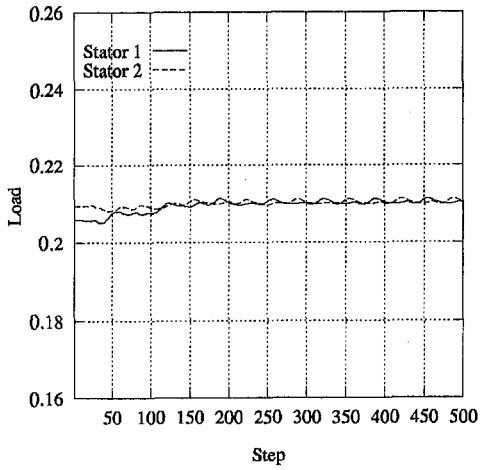

(a) Stator

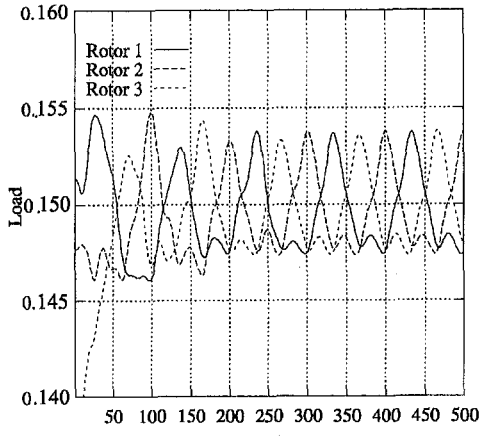

(b) Rotor

Fig. 5 Unsteady blade load

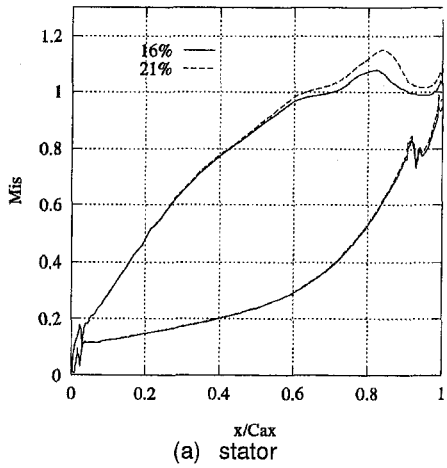

(a) stator

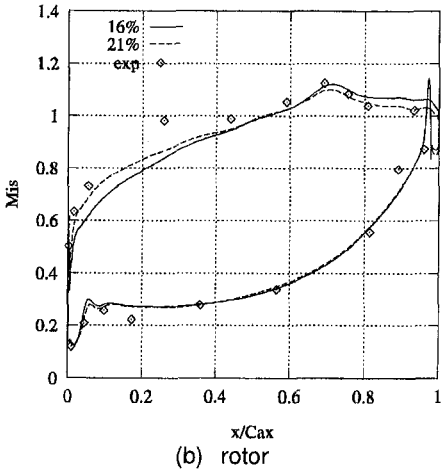

(b) rotor

Fig. 6 M_{is} profiles on the stator and rotor rows

start-up time, it was decided to perform the first 200 iterations doubling the physical time step, thereby reducing by half the number of steps required to reach a periodic solution.

The numerical simulations are performed in two basic configurations, which differ in the gap between the stator trailing edge and the rotor leading edge. In the first computed configuration the gap is $0.5 \times C_{s-ax}$, whereas in the second the gap is reduced to $0.35 \times C_{s-ax}$. The same two geometries were measured at VKI (Sieverding et al., 1997) with and without coolant ejection from the stator pressure side. Of the two, only the large gap case was modeled here with and without coolant ejection, while the small gap case was computed with the coolant jet only. A set of preliminary runs were performed to set up the quasi-three-dimensional grid able to reproduce the experimental geometry with the best accuracy possible. As mentioned in the section about the computational grid, the spanwise expansion of the rotor channel, which is present in the experiments (see Fig. 3), was adjusted to compensate the reduction in the rotor size. The quasi-three-dimensional nature of the grid was compulsory since a set of preliminary calculations indicated that the mass flow rate of the stage was limited by the throat area of the rotor when assuming a constant thickness of the stream tube in both the stator and the rotor rows. This caused the choking of the rotor and not of the stator. The constant thickness stream tube approximation was then abandoned in favor of the quasi-three-dimensional approach. Figure 6 shows the effect of the spanwise expansion of the rotor channel on the distribution of the isentropic Mach number on both the stator and rotor blades. The plots show the M_{is} profile averaged over 100 time steps for both the stator and the rotor blades. When expanding the rotor blade height from 16 to 21 percent there is a large change in the stator blade M_{is} (see Fig. 6(*a*)) especially in the throat and supersonic sections. This change is due to the increase in the rotor throat area with a consequent increase on the mass flow rate. The design isentropic exit Mach number of the stator is 1.05, and this value is matched only when using the 21 percent spanwise expansion ratio. The kink visible at $x/C_{ax} = 0.9$ on the pressure side is caused by the sharp edge in proximity to the coolant ejection hole. Figure 6(*b*) shows the effect of the expansion variation on the rotor relative M_{is} profile, including the average unsteady measurements (Sieverding et al., 1998). Here the prediction on the suction side tends to the experiments when moving from 16 to 21 percent.

Isolated Stator and Rotor Rows. Prior to the final runs, the flow around the stator and the rotor blades have been computed separately to assess the grid requirements. On the basis of previous experience with this solver it was decided to use a relatively coarse grid for the stator (200×104) because of the adiabatic nature of the boundaries. Figure 7 compares the computations and the measurements of the stator-only exit flow angle. The flow turning is overestimated of less than one degree, which corresponds to a positive incidence on the rotor blade. Figure 8 shows the effect of the positive incidence on the M_{is} profile around the rotor blade. The leading edge section is highly affected and, as will be seen in the following sections, this can have an impact on the heat transfer predictions.

The rotor grid is more refined (258×153) because of the need to compute the Nusselt number profile around the blade. The turbulence and transition models implemented for the calculations

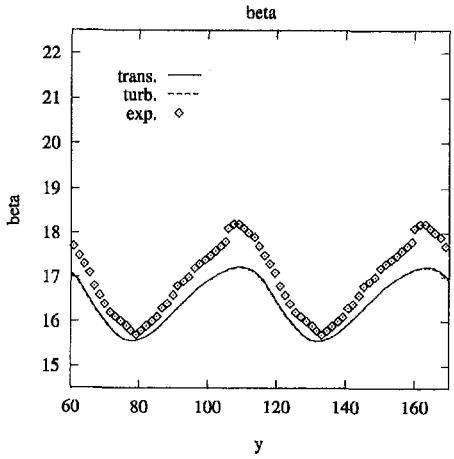

Fig. 7 Isolated stator row exit flow angle

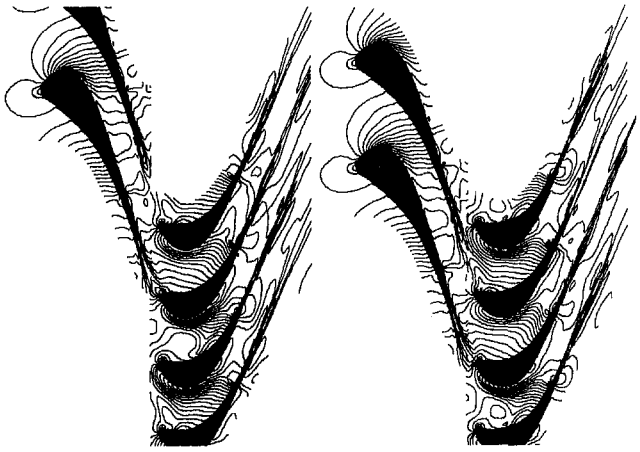

Fig. 10 Local Mach number at two consecutive time steps

has been validated in several steady flows (Michelassi et al., 1997; Migliorini and Michelassi, 1997).

The isolated rotor row was studied with an inlet turbulence level of 1.6 percent (equal to the stator inlet level) and an inlet turbulence length scale equal to $0.01 \times P_s$.

Figure 9 compares the average experimental Nusselt number for the $0.5 \times C_{ax,s}$ case with the predictions obtained by computing the rotor row alone. The various curves refer to different values of the coefficient α in Eq. (4). The plot shows that the predicted level of Nu on the pressure side are always in good agreement with experiments. On the suction side the average experimental profile shows that the onset of transition is probably spread in the range $0.4 < s/S < 0.8$. This comparison shows that, regardless of the choice of the transition model constant α, which allows the length of transition to be controlled, the computation of the isolated rotor gives an unrealistic description of the Nusselt number on the suction side. Although the differences can be partly imputed to deficiencies in the turbulence and transition models, most of them are caused by the unsteadiness and the turbulence characteristic changes across the stator row, which can be accounted for only by computing the unsteady stator–rotor interaction, which is the subject of the next sections.

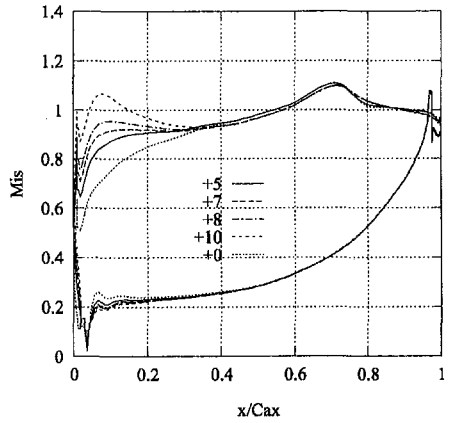

Fig. 8 Isolated rotor M_{is} at variable incidence

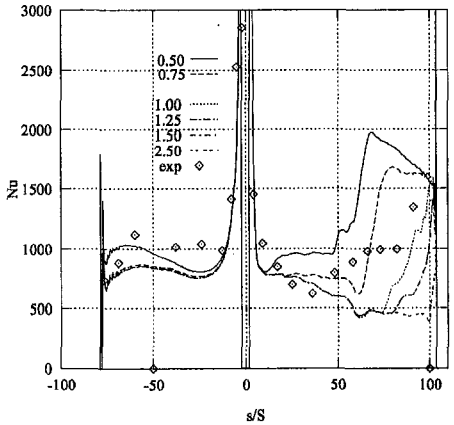

Fig. 9 Isolated rotor row Nu with different values of α

The Unsteady Flow Pattern. Prior to the quantitative analysis, the overall rotor flow pattern is described. Figures 10 and 11 refer to the large gap case with coolant ejection from the stator blade trailing edge.

Figure 10 shows the local Mach number isolines at two consecutive time steps. The three rotor domains show the relative Mach number so that the isolines are not continuous across the stator–rotor interface. A weak shock impinges on the suction side of the stator. Its reflection is weak and can be hardly detected in the plots. When the stator wake hits the rotor leading edge, a large low-speed–low-total-pressure spot is convected downstream on the pressure side. On the suction side the disturbance is convected at a higher speed with respect to the pressure side. This causes a complex interaction between the wake effect on the suction and pressure sides of the wake, which gives the complex blade load pattern shown in Fig. 5(*b*). The development of the low-momentum area can be clearly followed until the trailing edge,

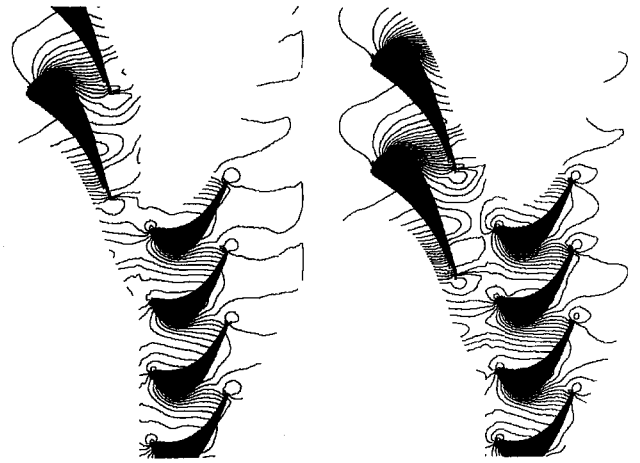

Fig. 11 Static pressure at two consecutive time steps

although the effect of the large turbulence level, which will be discussed next, highly promotes the wake smearing.

On the pressure side, the low-Mach-number spot can be easily detected and survives till the trailing edge. The static pressure isolines (Fig. 11) show the expansion and recompression waves interaction between stator and rotor. Apparently, the supersonic flow region departing from the stator suction side does not reach the rotor blade, since the pressure isolines on suction side exhibit a pattern that is very weakly affected by the passing wakes. The static pressure pattern on the suction side of the rotor blade varies in time also after the expansion where the flow reaches its maximum velocity of the order of M = 1.1. The small variations of the stator pressure distribution are limited in the supersonic region in between the weak shock and the trailing edge. Figure 11 indicates that the pressure fluctuations fade away in the stator vane due to the filtering effect of the supersonic flow region. Figures 12 and 13 show the turbulence level based on local velocities and streamlines on the rotor for three consecutive time steps. In the first (Figs. 12(*a*) and 13(*a*)) the stator wake travels close to the rotor suction side, then hits the rotor leading edge (Figs. 12(*b*) and 13(*b*)), and finally reaches the rotor pressure side (Figs. 12(*c*) and 13(*c*)). Figure 12(*a*) shows that *Tu* reaches a peak of 18–20 percent in the core close to the left-most side of the computational domain. Anywhere else *Tu* is below 2 to 4 percent. When the wake hits the leading edge (arrow in Fig. 12(*b*)) the large velocity gradients together with the large values of the kinetic energy convected from the stator trailing edge increase *Tu* by 30 percent and more. This peak is located in proximity to the rotor leading edge, and is then convected downstream, as pointed out by the arrow in Fig. 12(*c*) where the peak of *Tu* moves with the mainstream on the pressure side. Apparently the maximum *Tu* spot moves downstream with a small rate of decay. Still, the flow acceleration on the pressure side decreases and eventually moves and stretches this spot toward the wall, as shown by the arrow in Fig. 12(*a*). When looking at the suction side, only the first plot indicates large values of *Tu*, which are then dissipated while the effect of the wake fades away. Unlike on the pressure side, on the suction side there is no evidence of high turbulence spots. In general the cooling jet produced small changes in the turbulence flow field in the wake.

The streamlines at the first of the three time steps (Fig. 13(*a*)) show a thickening of the boundary layer on the pressure side in proximity to the *Tu* spot evidenced in Fig. 12(*a*). This spot is then convected away in Fig. 13(*b*). Figure 13(*c*) shows the formation of the next thickening of the boundary layer (in the same position of the high-*Tu* spot) as visible on the pressure side in proximity to the leading edge.

Large Gap ($0.5 \times C_{ax,s}$) With and Without Coolant Ejection. In this configuration the axial distance between the stator t.e. and the rotor l.e. is $0.5 \times C_{ax,s}$. The large gap case is computed without and with the stator pressure side coolant ejection and at 6000, 6500, and 6800 rpm. The coolant mass flow rate is 3 percent of the overall mass flow rate at the nominal 6500 rpm rotational speed.

Figure 14 compares the computed and measured average M_{is}. The profiles are averaged over a full rotor revolution for the experiments and over one passage of a rotor vane in front of two stators after a periodic-in-time solution is achieved for the computations. The stator row shows how large the aerodynamic effect of the coolant is in case of the pressure side ejection. When the coolant mass flow rate is zero, the first shock is caused by the expansion wave followed by a compression departing from the flow recirculation on the pressure side (see Fig. 15(*a*)). The second shock is the usual fish-tail shock departing from trailing edge vortices. When switching on the coolant jet, the first expansion-shock wave is washed away since the flow recirculation on the pressure side disappears (see Fig. 15(*b*)). The effect of the coolant jet is evident in Fig. 14(*a*), which shows that only the fish-tail shock survives. This effect was already observed in the steady calculations.

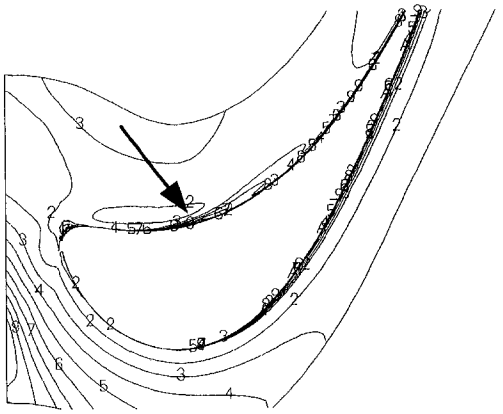

(a) Tu=0-20% 10 levels

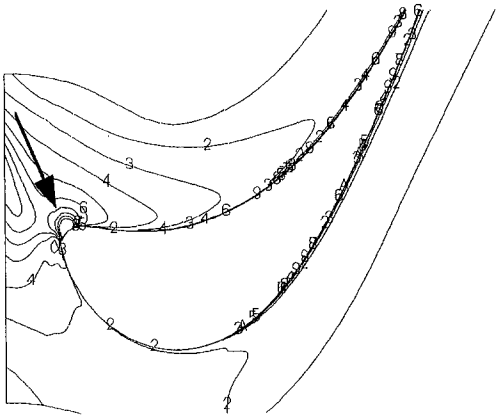

(b) Tu=0-40% 10 levels

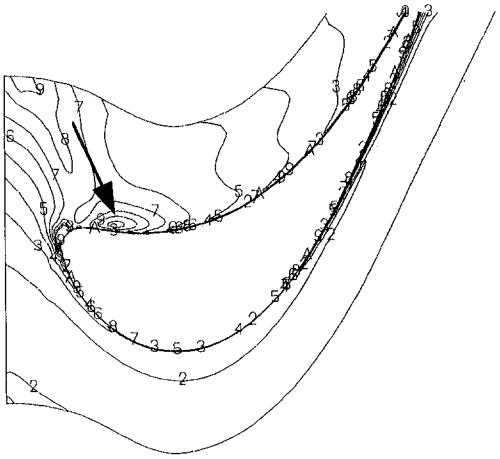

(c) Tu=0-20% 10 levels

Fig. 12 Turbulence level isolines at three time steps

The effect of the coolant jet on the rotor fades away, as proved by the M_{is} profiles in Fig. 14(*b*). There are only marginal differences in the averaged isentropic Mach number profiles, and these are due to the small changes in the wake depth caused by the coolant jet. The M_{is} profile on the rotor is very similar to a set of

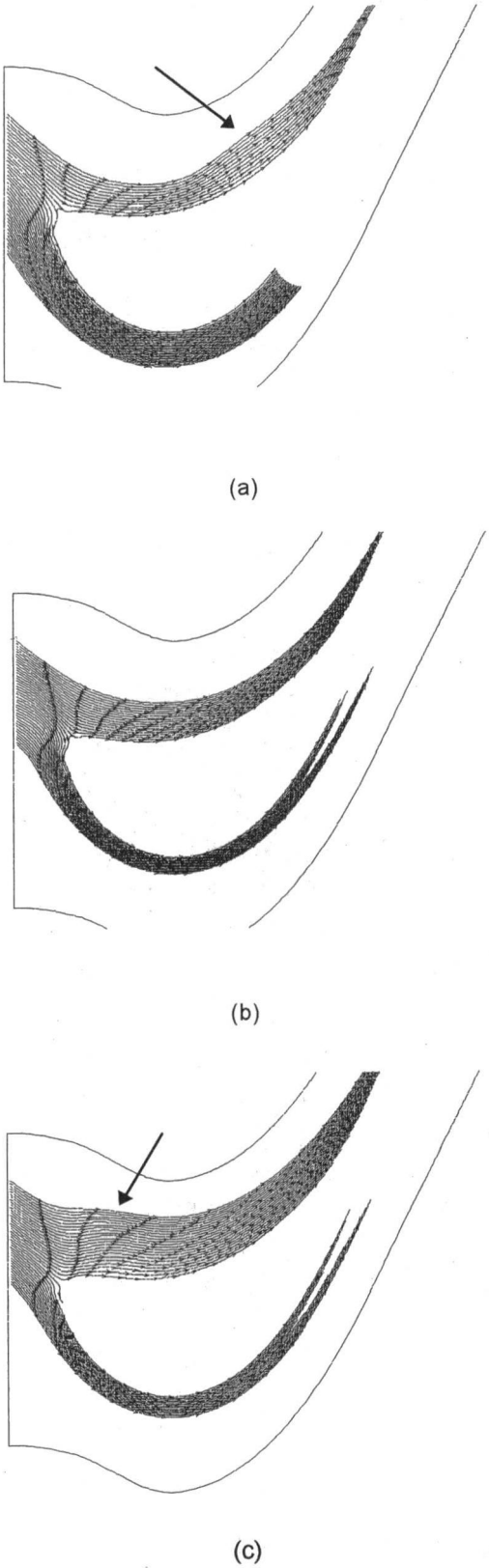

Fig. 13 Streamlines at three time steps

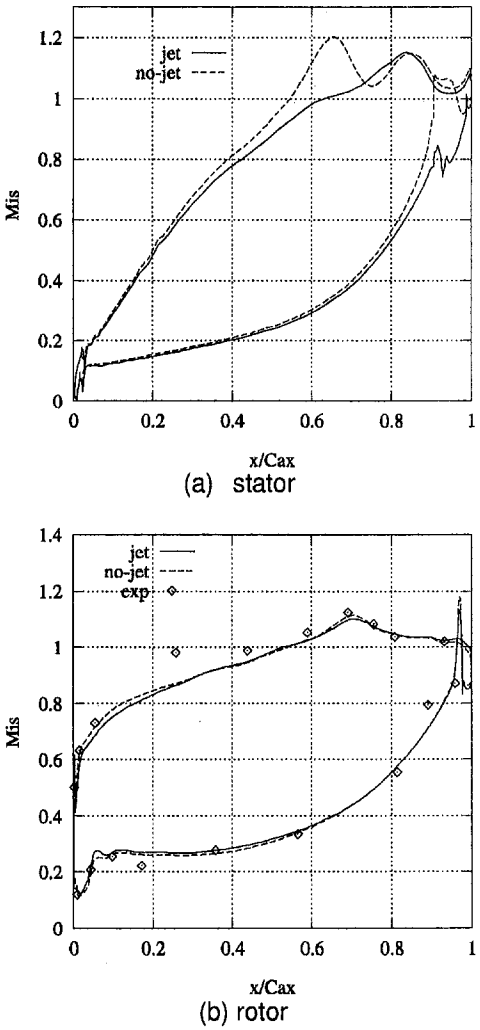

Fig. 14 Isentropic Mach number profiles

steady three-dimensional calculations performed on the annular rotor cascade (Sieverding et al., 1998) and to those of Fig. 6(*b*). Some very small differences arise in the leading edge region on the suction side where the flow acceleration predicted by the unsteady computations is slightly stronger than that given by the steady calculations. This seems to indicate an interaction between the rotor and the wake, which affects the rotor inlet flow angle.

The effect of changes in the rotational speed are shown in Fig. 16 where the large gap configuration is studied at 6000 and 6800 rpm. It is interesting to observe that the reduction in rpm induces a positive incidence on the rotor, as proved by the acceleration on the suction side in proximity to the leading edge, and also a modification of the M_{is} profile on the stator in which the shock moves slightly downstream. The rotor profile is largely affected by the rpm variation, but the computations showed no flow separation despite the large angle of attack. Figures 14 and 16 show that the simulations, while predicting the correct trend with rpm, always tend to underestimate the flow acceleration on the suction side in proximity to the leading edge. This disagreement with the experiments fades away while moving downstream, and cannot be imputed only to some inaccuracy in the prediction of the flow angle, but are probably also due to some shock smearing. In fact, a positive angle of attack always gives a subsonic flow in the region $0.2 < x/C_{ax} < 0.4$ (see Fig. 8), whereas the unsteady measurements indicate that the average flow is transonic (see Fig. 14(*b*)). In other words the measurements seems to indicate that the flow acceleration for $0.2 < x/C_{ax} < 0.4$ is caused by the interaction with the trailing edge shock departing from the rotor.

The computed rotor inlet/outlet flow angles, mass-averaged over one pitch, are shown in Figs. 17 and 18. The lack of flow measurements prevents from any comparison, but the analysis of the computed angles helps in understanding the flow pattern. Figure 17(*a*) shows that the stator exit flow angle ranges from 72.5 to 73.7

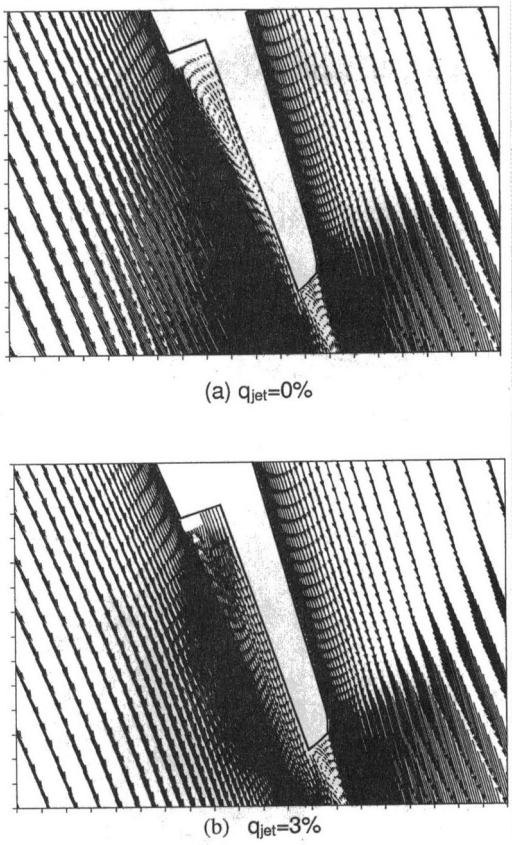

Fig. 15 Flow pattern detail in proximity to the stator t.e.

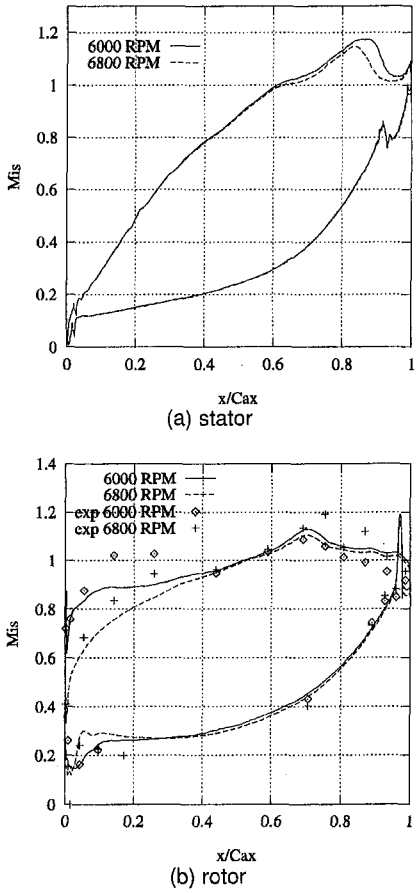

Fig. 16 Effect of rotational speed variation

deg, which is close to what is found for the isolated stator row in which the average exit flow angle (with respect to the axial direction) is 73.6 deg.

Still, changes in rotor rpm and coolant mass flow rate do not affect the average and scatter of the flow angle. When considering the relative flow angle, computed in the tangential plane immediately upstream of the rotor leading edge shown by the arrow in Fig. 2, the differences are amplified. The computations with and without coolant jet show a difference of the order of 3 deg, which explains the small changes observed in the M_{is} profiles in Fig. 14(*b*). The large variations of the 6000 and 6800 rpm calculations are due to the change of the rotational speed. Still, the shape of the angle variation versus the time step is similar for the four calculations. This indicates that the overall flow pattern remains substantially unaltered. The computed relative exit flow angles, shown in Fig. 18, refer to the large gap case with and without coolant ejection at the nominal rpm (6500) and with coolant ejection at variable rpm (6000–6800). The plot shows that the rotor relative exit flow angle does not feel the presence or absence of the cooling jet and it is also insensible to the angular speed variations.

The analysis of the heat transfer is made by comparing the measured and computed Nusselt number over the rotor surface. The leading edge is positioned at $s = 0$ and the curvilinear wall distance is normalized by the distance of the last measured point on the suction side. Figure 19 compares the averaged Nusselt number in which the experiments have been conducted only with the cooling jet. There is a dramatic change with respect to the steady calculations of Fig. 9. The computations with the coolant jet are closer to the experiments on both the suction and the pressure sides, although in the leading edge region the code predicts values of Nu, which are smaller than the experiments. The agreement rapidly improves when moving downstream. The small level of the predicted Nusselt number in the range -20 percent $< s <$ 20 percent is not likely to be caused by an insufficient turbulence level predicted in the leading edge region since the turbulence levels shown in Fig. 12 are well above 5 to 10 percent, which is more than enough to induce transition. The situation is not substantially altered when introducing an extra transport equation for the intermittency function (model *B* in Fig. 20) which causes a steeper rise of Nu on the suction side and a small improvement on the pressure side. The exponent α in Eq. (4) allows the length of transition to be controlled. Values of α below unity and smaller than two induce a steep rise of the intermittency function thereby reducing the transition length. Moreover, Fig. 20 indicates that when reducing α from 2.00 to 1.25, the situation marginally improves in the range $-20 < s < 20$.

Apparently, the underestimation of Nu close to the leading edge is partly governed by some inaccuracy in the aerodynamics prediction. This is proved by Fig. 21, in which the predicted averaged, minimum, and maximum values of M_{is} are compared with the respective measurements. On the pressure side, and on the suction

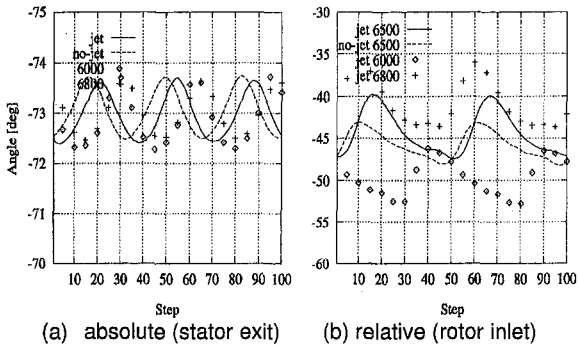

Fig. 17 Flow angles in the stator–rotor gap

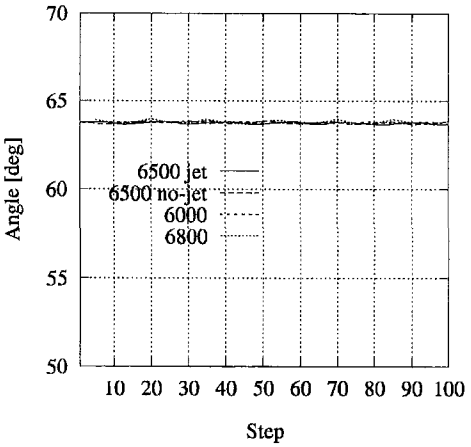

Fig. 18 Relative rotor exit flow angle

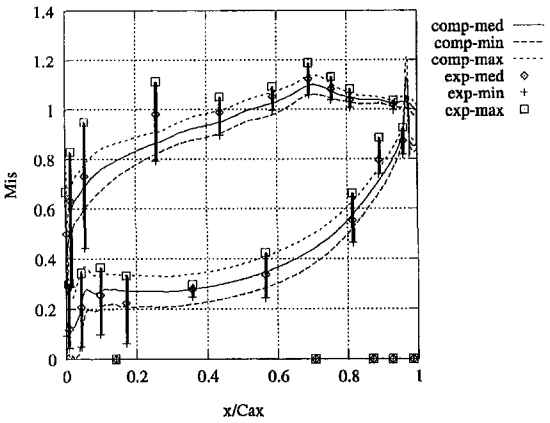

Fig. 21 Isentropic Mach number fluctuation range

side for $x/Cax > 0.45$, computations and experiments agree on both the average and the minimum and maximum values. The agreement deteriorates on the leading edge suction side where the code predicts velocity levels up to 20 percent smaller than what is indicated by the experiments. This disagreement is stemming from an underestimation of the angle of attack in some wake interference configurations, as indicated by Fig. 8, which shows how a large positive angle of attack can modify the leading edge pressure distribution. Moreover, as proposed by Giles (1988), the shock departing from the suction side of the stator trailing edge impinges on the nose of the passing rotor blade thereby inducing large pressure fluctuations. The predicted pressure, and M_{is}, fluctuations are somewhat smeared because of the grid skewness, which introduces some numerical diffusion.

A more significant comparison is done in Fig. 22, which shows the instantaneous measured and computed Nu in 24 instants with a $0.04 \times P_s$ step. The leading edge Nusselt number is generally underpredicted at each step, but it is interesting to see that the

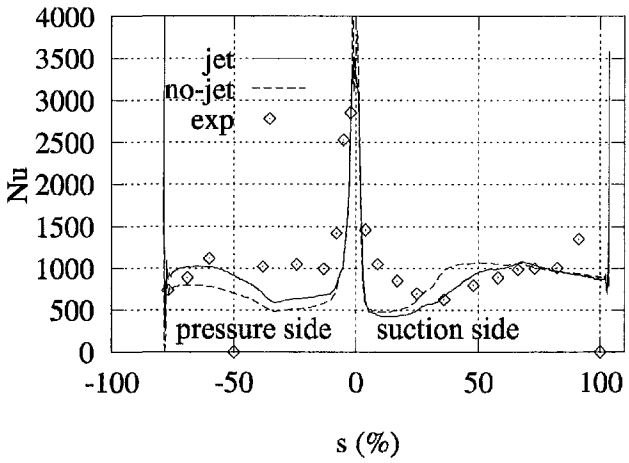

Fig. 19 Nu profile with and without jet, large gap: model A

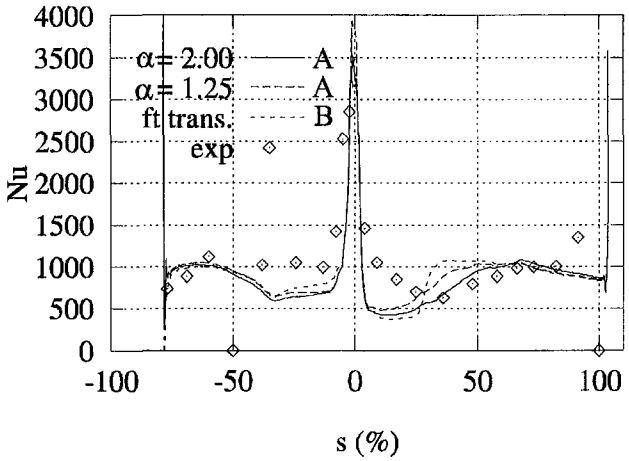

Fig. 20 Effect of model modifications on Nu

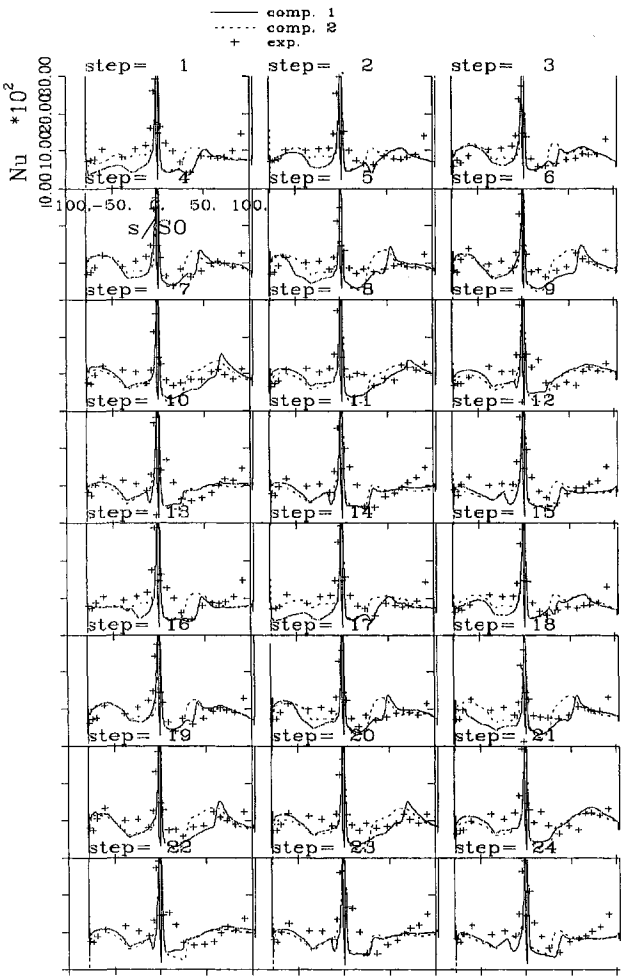

Fig. 22 Unsteady Nu (comp1 = standard transition model, comp2 = added transport equation for intermittency)

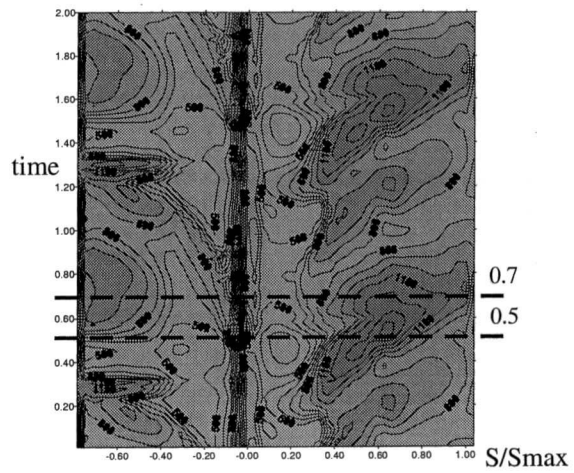

(a) q_{jet}=3%.

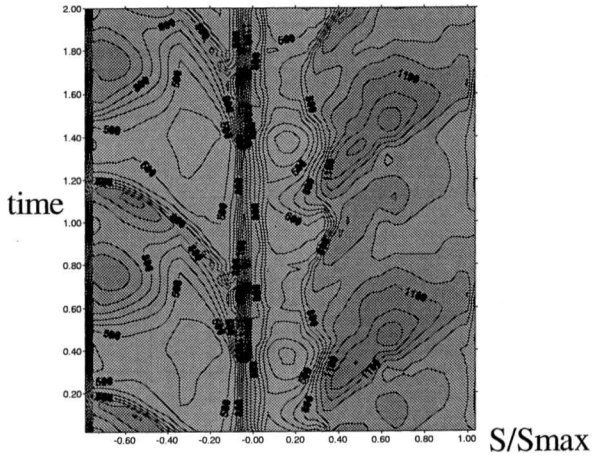

(b) q_{jet}=0%

(c)

Fig. 23 Unsteady Nusselt number

transition point on the suction side is often detected correctly such as at steps 4-5-9-10 and others. The use of the extra transport equation for the intermittency function generally improves the predictions mostly on the pressure side where the experiments show a weak effect of the passing wake. Conversely, on the suction side, it is possible to follow the passing wake by observing the peak of the measured and computed heat transfer, which is shifted downstream and slowly smeared. This phenomenon is captured by the computations with a good degree of accuracy.

The effect of the passing wakes on the rotor heat transfer can be traced in Fig. 23, which shows how the peak of Nu is moving downstream. It is now easy to follow the development of the transition point in time. The triggering effect of the wake is not very large since the transition point on the suction side ranges between $0.2 < S/S_{max} < 0.38$, regardless of the presence of the cooling jet. This is understandable on account of the large turbulence level, which is mainly responsible for the onset of transition, at least in the computer simulation code. The peak on Nu tends to smear in time and apparently the heat transfer increases in time while approaching the trailing edge because of the mentioned effect of the wake. This phenomenon is caused by the developing transition of the boundary layer. When comparing steps 0.5 and 0.7, the isolines spread in space and the Nusselt number increases also in the upstream direction for both the $q_{jet} = 0$ and 3 percent mass flow rate cases. In such a situation the computations indicate that the boundary layer thickness has increased and the elliptic flow region close to the rotor blade suction side has grown. This

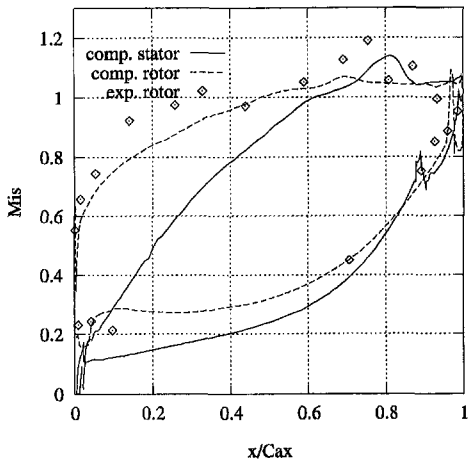

Fig. 24 Isentropic Mach number profiles

elliptic effect can have a large impact on the determination of the hot spots on the rotor blade.

Small Gap ($0.35 \times C_{ax,s}$) With Coolant Ejection. When reducing the gap between the blade rows, the overall flow pattern remains unchanged. Figure 24 shows the isentropic Mach number profiles on both the stator and rotor blades. The stator behaves very similarly to the larger gap case, while the rotor shows some differences with respect to the larger gap case especially in the throat. Apparently the average pressure distribution on the rotor feels the stronger disturbances coming from the stator row because of the shorter distance the wake and the shocks have to travel. Surprisingly, this has a weak impact on the averaged heat transfer rate that shows very little changes with respect to the $0.5 \times C_{ax}$ case (see Fig. 25). The computations like the experiments do not show a clear average onset of transition on the suction side, unlike the $0.5 \times C_{ax}$ case, in which the onset of transition was clearly detectable at $s/s_{max} \approx 30$. Experiments and computations agree in indicating a nearly flat Nusselt number distribution on the blade suction side. The pressure side profile is almost identical to the larger gap case with the same underestimation of the heat transfer rate, which extends up to 50 percent of the blade. Overall, the $0.35 \times C_{ax,s}$ gap case does not give any extra information with respect to the $0.50 \times C_{ax,s}$ case in terms of unsteady behavior and flow angles.

Conclusions

The availability of a set of unsteady experimental data on the interference between the stator and rotor rows of a transonic

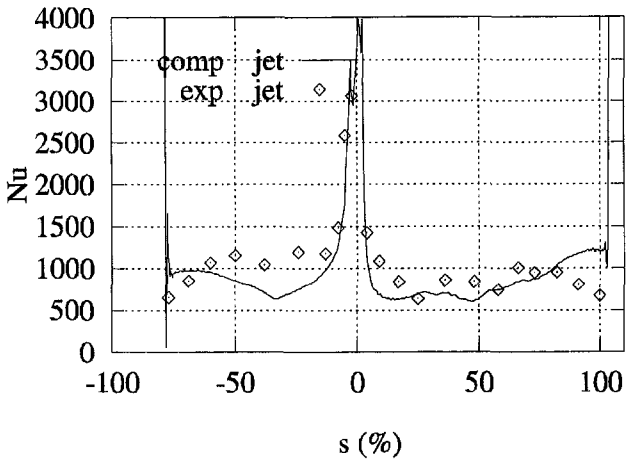

Fig. 25 Nu profile with jet, small gap

turbine stage allowed a careful testing of an unsteady flow solver. The various configurations differ in the gap in between the stator and rotor rows and in the mass flow rate of the pressure side coolant ejection in the stator blade. The computed steady and unsteady average isentropic Mach number distribution show very little differences for all the configurations reported here. The experiments show some interaction between the stator wake, the shock pattern, and the rotor leading edge pressure distribution which is slightly underestimated by the predictions. The measurements do not include any flow angle traversing immediately upstream of the rotor leading edge, but the numerical simulation proved that the isentropic Mach number distribution moves toward the right direction when applying a positive incidence angle. This corresponds to the flow status immediately upstream of the stator trailing edge shock, where the absolute velocity is maximum. Conversely, the rotor experiences a negative incidence angle deep in the wake so that the pressure distribution range, especially in proximity to the leading edge, is governed by the mutual effect of the wake and of the shock. Part of the inaccuracy of the predictions in the rotor leading edge area could be induced by the interaction between the stator trailing edge shock impinging on the rotor leading edge and the stator wake. Apparently the impact of the artificial dissipation, which is undeniably responsible of some of the numerical diffusion, could not be controlled by decreasing the artificial dissipation weights.

The heat transfer rate, here computed in terms of Nusselt number, changes dramatically from a steady to an average unsteady case. The large number of unsteady computations performed indicates that the Nusselt number profile on the rotor blade is not highly sensitive to the length of the gap between the stator and the rotor and to the mass flow rate of the coolant jet. The transitional nature of the rotor boundary layer seems to be governed mainly by the stator trailing edge shocks and static pressure unsteadiness for the leading edge region of the rotor. When the stator blade shock does not impinge on the rotor blade, the boundary layer is mostly governed by the large turbulence level convected downstream of the stator row. This analysis is confirmed by the underprediction of the computed Nusselt number with respect to the measurements in the first 20 percent of the rotor blade where the effect of the stator shocks is large. The agreement progressively improves while moving downstream along the rotor blade surface. In this flow region, the effect of turbulence (the turbulence level reaches values of the order of 30 percent) on the boundary layer status and heat transfer rate is very large and the effect of the stator shocks fades away. The heat transfer rate predictions, and experiments, indicate that the transition point travels downstream and this presumably follows the high turbulence level spot induced by the stator wake.

In conclusion, the comparison between predictions and measurements definitely proves that the heat transfer rate on a rotor blade cannot be realistically computed by assuming a steady flow condition, and a full unsteady computation is compulsory. The adopted turbulence and transition models, although not specifically developed and/or tuned for this test case, proved adequate for the determination of the unsteady heat transfer level with a reasonable degree of accuracy. It is necessary to observe that the computational model was validated so far only for steady flow situations. The computations also showed that the aerodynamic field and the heat transfer are strictly linked and that some of the inaccuracy in the predictions of the former have an impact on the latter.

Acknowledgments

This research was sponsored by the EEC in the frame of the BRITE-EURAM Program, IMT Area 3 Turbine Project, Contract No. AER2-CT92-0044. The support of EEC is gratefully acknowledged.

References

Abu-Ghannam, B. J., and Shaw, R., 1980, "Natural Transition of Boundary Layers—The Effects of Turbulence, Pressure Gradient, and Flow History," *Journal of Mechanical Engineering Science,* Vol. 22, No. 5, pp. 213–228.

Addison, J. S., and Hodson, H. P., 1992, "Modeling of Unsteady Transitional Boundary Layers," ASME JOURNAL OF TURBOMACHINERY, Vol. 114, pp. 580–589.

Cho, N.-H., Liu, X., Rodi, W., and Shönung, B., 1993, "Calculation of Wake-Induced Unsteady Flow in a Turbine Cascade," ASME JOURNAL OF TURBOMACHINERY, Vol. 115, pp. 675–686.

Durbin, P. A., 1996, "On the k–ϵ Stagnation Point Anomaly," *Int. J. Heat and Fluid Flow,* Vol. 17, pp. 89–90.

Giles, M. B., 1988, "Stator–Rotor Interaction in a Transonic Turbine," Paper No. AIAA-88-3093.

Hazarika, B. K., and Hirsch, C., 1995, "Transition Over C4 Leading Edge and Measurements of Intermittency Factor Using pdf of Hot-Wire Signal," ASME JOURNAL OF TURBOMACHINERY, Vol. 119, pp. 412–425.

Ho, Y.-H., and Lakshminarayana, B., 1996, "Computation of Three-Dimensional Steady and Unsteady Flow Through a Compressor Stage," ASME Paper No. 96-GT-70.

Hoogendoorn, C. J., de Lange, H. C., van Steenhoven, A. A., and van Dongen, M. E. H., 1997, "Influence of Turbulence Intensity on Intermittency Model in By-Pass Transition," ASME Paper No. 97-GT-473.

Jameson, A., 1991, "Time Dependent Calculations Using a Multigrid With Applications to Unsteady Flows Past Airfoils and Wings," AIAA Paper No. 91-1596.

Johnson, M. W., and Ercan, A. H., 1997, "Predicting Bypass Transition: A Physical Model Versus Empirical Correlations," ASME Paper No. 97-GT-475.

Kato, M., and Launder, B. E., 1993, "The Modelling of Turbulent Flow Around Stationary and Vibrating Square Cylinders," *Proc. Ninth Symposium of "Turbulent Shear Flows,"* Kyoto, Japan, Aug. 16–18.

Mayle, R. E., 1991, "The Role of Laminar–Turbulent Transition in Gas Turbine Engines," ASME JOURNAL OF TURBOMACHINERY, Vol. 113, pp. 509–537.

Michelassi, V., 1997, "Shock-Boundary Layer Interaction and Transition Modelling in Turbomachinery Flows," *Proc. 2nd European Conference on Turbomachinery-Fluid Dynamics and Thermodynamics,* Antwerpen, Belgium, Mar. 5–7.

Michelassi, V., Rodi, W., and Giess, P.-A., 1997, "Experimental and Numerical Investigation of Boundary-Layer and Wake Development in a Transonic Turbine Cascade," ASME Paper No. 97-GT-483.

Michelassi, V., Martelli, F., and Amecke, J., 1994, "Performance of a Transonic Turbine Guide Vane With Trailing Edge Coolant Ejection—Part II: Numerical Approach," ASME Paper No. 94-GT-248.

Michelassi, V., Adami, P., and Martelli, F., 1996a, "An Implicit Algorithm for Stator-Rotor Interaction Analysis," ASME Paper No. 96-GT-68.

Migliorini, F., and Michelassi, V., 1997, "Transition and Heat Transfer Modelling in Transonic Linear Cascades," *Proc. 2nd European Conference on Turbomachinery-Fluid Dynamics and Thermodynamics,* Antwerpen, Belgium, Mar. 5–7, 1997.

Moss, R. W., Ainsworth, R. W., Sheldrake, C. D., and Miller, R., 1997, "The Unsteady Pressure Field Over a Turbine Blade Surface: Visualization and Interpretation of Experimental Data," ASME Paper No. 97-GT-474.

Pulliam, T. H., and Chaussee, D. S., 1981, "A Diagonal Form of an Implicit Approximate-Factorization Algorithm," *Journal of Computational Physics,* No. 39.

Rao, K., and Delaney, R. A., 1990, "Investigation of Unsteady Flow Through a Transonic Turbine Stage, Part I, Analysis," AIAA Paper No. 90-2408.

Rao, K., Delaney, R. A., and Dunn, M., 1992, "Vane-Blade Interaction in a Transonic Turbine, Part II—Heat Transfer," AIAA Paper No. 92-3324.

Sieverding, C. H., Dénos, R., Arts, T., Brouckaert, J. F., and Paniagua, G., 1998, "Experimental Investigation of the Unsteady Rotor Aerodynamics and Heat Transfer of a Transonic Turbine Stage," VKI Lecture Series on "Blade Row Interference Effects in Axial Turbomachinery Stages," Feb.

Tanuma, T., Shibukawa, N., and Yamamoto, S., 1997, "Navier–Stokes Analysis of Unsteady Transonic Flows Through Gas Turbine Cascades With and Without Coolant Ejection," ASME Paper No. 97-GT-479.

Wilcox, D. C., 1988, "Reassessment of the Scale-Determining Equation for Advanced Turbulence Models," *AIAA Journal,* Vol. 26, No. 11, pp. 1299–1310.

Effect of Unsteady Wake With Trailing Edge Coolant Ejection on Film Cooling Performance for a Gas Turbine Blade

H. Du
Schlumberger SPT Center,
14910 Airline Road,
Rosharon, TX 77583-1590

S. V. Ekkad
Allison Engine Company,
Indianapolis, IN 46206

J.-C. Han
Turbine Heat Transfer Laboratory,
Department of Mechanical Engineering,
Texas A&M University,
College Station, TX 77843-3123

The effect of unsteady wakes with trailing edge coolant ejection on surface heat transfer coefficients and film cooling effectiveness is presented for a downstream film-cooled turbine blade. The detailed heat transfer coefficient and film effectiveness distributions on the blade surface are obtained using a transient liquid crystal technique. Unsteady wakes are produced by a spoked wheel-type wake generator upstream of the five-blade linear cascade. The coolant jet ejection is simulated by ejecting coolant through holes on the hollow spokes of the wake generator. For a blade without film holes, unsteady wake increases both pressure side and suction side heat transfer levels due to early boundary layer transition. Adding trailing edge ejection to the unsteady wake further enhances the blade surface heat transfer coefficients particularly near the leading edge region. For a film-cooled blade, unsteady wake effects slightly enhance surface heat transfer coefficients but significantly reduces film effectiveness. Addition of trailing edge ejection to the unsteady wake has a small effect on surface heat transfer coefficients compared to other significant parameters such as film injection, unsteady wakes, and grid generated turbulence, in that order. Trailing edge ejection effect on film effectiveness distribution is stronger than on the heat transfer coefficients.

Introduction

Turbine blade surface heat transfer is affected by the unsteady wakes generated by upstream vane trailing edges and blade rotation. Typical first stage vanes are cooled and some of the spent coolant is ejected from slots in the trailing edges. The ejected jets combine with the unsteady wakes and produce complex effects on the downstream blade heat transfer. The knowledge of effects of trailing edge ejection on downstream blades is important to estimate the actual heat load on the blades. Typically, studies have focused on the effects of unsteady wakes on uncooled and film cooled blades. However, there is no comprehensive study on the combined effects of upstream unsteady wakes and trailing edge ejection jets on a downstream film-cooled blade.

Nirmalan and Hylton (1990) and Camci and Arts (1990) studied heat transfer coefficients on film cooled turbine blades. Takeishi et al. (1992) compared the film effectiveness values for a stationary cascade influenced by 4 percent mainstream turbulence intensity and for a rotor blade using the heat-mass transfer analogy. Ito et al. (1978) and Haas et al. (1992) studied the effect of coolant density on film cooling effectiveness on turbine blades under low mainstream turbulence levels. Abhari and Epstein (1994) conducted heat transfer experiments on a film-cooled transonic turbine stage in a short duration turbine facility. They measured steady and time resolved, chord-wise heat flux distributions at three spanwise locations. They concluded that film cooling reduces the time-averaged heat transfer by about 60 percent on the suction surface compared to the uncooled rotor blade. However, the effect is relatively low on the pressure surface.

Ou et al. (1994), Mehendale et al. (1994), and Du et al. (1998) simulated unsteady wake conditions over a linear turbine blade cascade with film cooling. They studied the effects of unsteady wakes on a model turbine blade with multiple-row film cooling using air and CO_2 as coolant. They concluded that local heat transfer coefficients increase and film effectiveness values decrease with an increase in unsteady wake strength. They also concluded that higher density coolant (CO_2) provides better film effectiveness at higher blowing ratios than lower density coolant (air). Du et al. (1998) presented detailed heat transfer coefficient and film effectiveness distributions using a transient liquid crystal technique. The detailed distributions indicate strong film jet effect in the near-hole regions on the blade. The detailed results also clearly show the local film cooling behavior and its effect on the start of boundary layer transition on the suction surface.

Dunn (1986) measured heat flux ratios for the rotor blade of a Garrett TFE 731-2 HP full-stage rotating turbine under the effects of NGV trailing edge ejection. They found that the trailing edge ejection significantly increases local blade heat transfer up to 20 percent streamwise distance from the leading edge on the suction surface and up to 10 percent streamwise distance on the pressure surface. Du et al. (1997) studied the effect of trailing edge ejection from a spoked wheel type wake generator on an uncooled blade in a five-blade linear cascade. They indicated that the trailing edge jets compensate the velocity defect caused by unsteady wakes and cause an increase in free-stream velocity and produce a more uniform turbulence intensity profile impinging on the downstream blades. The net effect of trailing edge ejection was to increase heat transfer near the leading edge region on both the pressure and suction surfaces.

The present study is a continuation to Du et al. (1997, 1998). Du et al. (1998) presented the singular effect of unsteady wakes on blade surface heat transfer coefficients and film effectiveness for a Reynolds number of 5.3×10^5. Du et al. (1997) presented the combined effects of grid-generated turbulence, unsteady wake, and trailing edge jet ejection on surface heat transfer coefficients for an uncooled blade at cascade exit Reynolds

Contributed by the International Gas Turbine Institute and presented at the International Gas Turbine and Aeroengine Congress and Exhibition, Stockholm, Sweden, June 2–5, 1998. Manuscript received by the ASME Headquarters April 1, 1998. Paper No. 98-GT-259. Associate Technical Editor: R. Kielb.

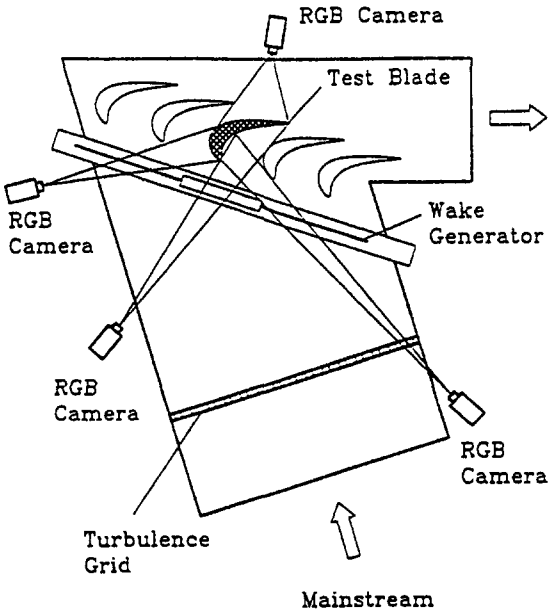

Fig. 1 Schematic of test section and camera arrangement

numbers of 5.3×10^5 and 7.6×10^5. The present study presents the combined effects of unsteady wakes, grid-generated turbulence, and trailing edge jet ejection for both uncooled and film cooled turbine blades for a Reynolds number of 7.6×10^5. The real turbine rotor blade is affected by combustor-generated turbulence (about 5–10 percent), unsteady wakes shed by upstream vane trailing edges, and coolant ejection from the vane trailing edge. The aim of this study is to simulate flow conditions most similar to actual turbine rotor blades. Also, the present study uses a transient liquid crystal technique for detailed heat transfer coefficient and film effectiveness measurements on the blade surface. The transient liquid crystal technique provides very detailed data on the film-cooled surface especially in the near film-hole region which may not be obtained using conventional heat transfer measurement techniques.

Experimental Apparatus

Figure 1 shows the schematic of the test section and camera locations. The test apparatus consists of a low speed wind tunnel with a suction type blower. The five-blade linear cascade is shown in the figure. Mainstream flow turns 107.49 deg and is accelerated 2.5 times from inlet to exit of the cascade. The test apparatus is described in detail by Du et al. (1997, 1998). A heater box is used to preheat the middle test blade prior to the transient test. The middle blade is coated with a thin layer of thermochromic liquid crystals. Blade surface color changes during the transient test are analyzed using a high speed, high resolution image processing system. Image processing system consists of four cameras individually connected to a color frame grabber board inside the PC. RGB (Red, Green, Blue) outputs from the four cameras are displayed using a color monitor. Commercial software is used to digitize the liquid crystal color changes. During a transient test, only one camera is operational. Since the color changes are processed real time and no frames are stored in the PC, the frame speed will be reduced if all the four cameras are operated at the same time. Hence, four separate tests are required to map the entire blade surface using four different camera locations as shown in the figure. Frequency controllers and flow meters effectively ensure similar flow conditions for all four tests. Details on the image processing system are presented by Du et al. (1997, 1998).

The spoked wheel-type wake generator is 8.82 cm upstream of the cascade leading edge. Thirty-two (32) hollow rods are used to simulate the trailing edge of upstream vanes. Figure 2 presents a detailed sketch of each rod. Each rod has an outside diameter of 0.63 cm and an inside diameter of 0.32 cm. There are 32 ejection holes opening toward the downstream blade to simulate trailing edge ejection from each rod. The ejection holes are 0.16 cm in diameter and are evenly spaced at three hole-diameters apart from one another. A compressed air source feeds the wake rod with coolant for trailing edge ejection. The wake generator is adjusted by controlling the motor speed.

Figure 3 shows a section of the film cooled turbine blade model. Each blade in the linear cascade has an axial chord length of 17 cm and radial span of 25.2 cm. Blade-to-blade spacing is 17.01 cm at the cascade inlet and the blade throat-to-span ratio is 0.2. The blade configuration, scaled up five times, produces a scaled velocity distribution typical of an advanced high pressure turbine blade row. Coolant is supplied to various locations on the blade surface through five cavities. The first cavity supplies coolant to the three leading edge film hole rows and each of the other four cavities supply coolant to each row on the pressure and suction surfaces. Coolant is fed into each cavity from the bottom of the blade and flow rate into

Nomenclature

C_x = blade axial chord length (17 cm)
D = film hole diameter
d = wake generator rod diameter
DR = coolant-to-mainstream density ratio, ρ_c/ρ_m
h = local heat transfer coefficient
k = thermal conductivity of blade material (0.159 W/m-°C)
k_{air} = thermal conductivity of mainstream air
L = length of film injection hole
M_t = trailing edge jet-to-mainstream mass flux ratio, $\rho_t V_t/\rho_m V_1$
M = coolant-to-mainstream mass flux ratio or blowing ratio, $\rho_c V_c/\rho_m V$
Nu = local Nusselt number based on axial chord, hC_x/k_{air}
$\overline{\text{Nu}}$ = span-averaged Nusselt number
P = film hole pitch
PL = streamwise length on the pressure surface (25.6 cm)
Re = Reynolds number based on exit velocity and axial chord, $V_2 C_x/\nu$
S = wake Strouhal number, $2\pi Ndn/(60 V_1)$
SL = streamwise length on the suction surface (33.1 cm)
t = liquid crystal color changes time
T_c = coolant temperature
T_i = initial temperature of blade surface
T_m = mainstream temperature
T_w = local wall temperature when liquid crystal color changes from green to red
Tu = free-stream turbulence intensity
$\tilde{T}u$ = ensemble-averaged turbulence intensity
$\bar{T}u$ = time-mean averaged free-stream turbulence intensity
V = local mainstream velocity along the blade pressure or suction surface
$V(t)$ = instantaneous velocity at cascade inlet
V_1 = cascade inlet velocity
V_2 = cascade exit velocity
V_c = coolant hole exit velocity
$\tilde{V}$ = ensemble-averaged cascade inlet velocity
X = streamwise distance from blade leading edge
α = thermal diffusivity of blade material (0.135×10^{-6} m^2/s)
η = local film cooling effectiveness
$\bar{\eta}$ = spanwise-averaged film cooling effectiveness
ν = kinematic viscosity of mainstream air
ρ_c = coolant density
ρ_m = mainstream flow density

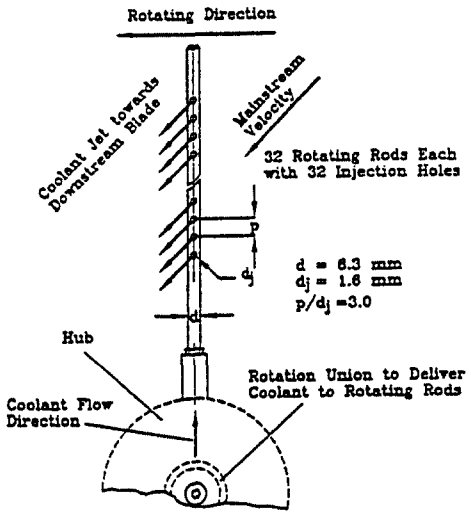

Fig. 2 Sketch of the rotating rod with ejection holes

each cavity is controlled using a flowmeter. Coolant flow from each flowmeter is passed through a solenoid-controlled three-way diverter valve before the flow enters the coolant cavity inside the blade. Each solenoid-controlled valve is connected to a switch which triggers the coolant flow into the cavities at the instant the transient test is initiated. Blade film hole row geometry and configuration are shown in the figure. The liquid crystal coated surface region is 15.2 cm wide and the data acquisition region is 7.6 cm wide along the midspan section of the test blade. A table shown below the figure indicates the hole geometries of each individual row.

The transient test requires that the blade be heated to a temperature higher than the liquid crystal color range (37.2°C). During the transient test, the hot blade surface is suddenly cooled by exposing it to a cooler mainstream flow. The middle blade is heated by a heater box that covers the blade while heating. The heater box has the blade profile and is slightly larger than the test blade. A gap of 3 mm exists between the blade outside surface and the heater box inner surface. The insides of the heater box are instrumented with thin foil heaters and controlled using several variacs to provide a near uniform blade surface temperature. The blade surface temperature is monitored using embedded thermocouples during heating. Uniformity of surface temperature with heating is within ±1.2°C. An interpolation scheme was used to further reduce the temperature variations in the initial surface temperature distribution to within ±0.2°C. When the surface is heated to the required uniform temperature, the suction type blower is switched on. The mainstream reaches full flow within 20–30 s. Once the mainstream has reached required flow, the heater box is raised completely exposing the test blade to the cooler mainstream within 0.1 s. The coolant flow and image processing system are automatically triggered at the same instant the test surface is exposed to the mainstream. Liquid crystal color changes during the transient test are monitored by the system. The times of color change on the blade surface to red at every pixel location is measured.

Before the blade surface is heated, the camera is focused on the particular region of the blade. The blade is uniformly illuminated such that the entire region the camera is focused on indicates a uniform background intensity. This intensity and light settings help in correcting camera angles and blade curvature problems indicated by other studies using liquid crystal techniques. Once the heater box is lifted, the color intensity profiles at each pixel on the region are analyzed during the transient test. Once the required color intensity is matched, the actual time of color change for a particular color band appearance is noted. This color change time is used in the data analysis explained below.

Data Analysis

A vertically oriented single hot wire is used to measure the instantaneous velocity profile for the mainstream just upstream of the cascade leading edge. Due to the periodic nature of the wake passing and shedding, the unsteady random signal behavior cannot be characterized by time-averaging only. The phase-averaged (or ensemble-averaged) method was used to obtain the time-dependent periodic velocity and turbulence intensity. The ensemble-averaged turbulence intensity, $\tilde{T}u$, for the flow is obtained from the root mean square (rms) value of the fluctuation of the velocity with respect to the ensemble-averaged velocity ($\tilde{V}$) and divided by the ensemble-averaged velocity. A time-mean averaged turbulence intensity ($\bar{T}u$) is also used to describe the total turbulence level of the mainstream at the blade cascade inlet under combined effects of grid generated turbulence, unsteady wakes, and trailing edge ejection. The time-mean averaged turbulence intensity definition is based on the integration of the ensemble-averaged turbulence intensity over a rod passing period. This methodology is described in detail by Zhang and Han (1995).

A transient liquid crystal technique was used to measure the detailed heat transfer coefficients and film effectiveness on the blade surface. The technique is similar to the one described by Du et al. (1998). A one-dimensional transient conduction model into a semi-infinite solid with convective boundary condition is assumed. The solution for surface temperature is obtained as

$$\frac{T_w - T_i}{T_m - T_i} = \left[1 - \exp\left(\frac{h^2\alpha t}{k^2}\right) \operatorname{erfc}\left(\frac{h\sqrt{\alpha t}}{k}\right)\right], \qquad (1)$$

where T_w is the wall temperature when liquid crystals change to red from green (32.7°C) at time t, T_i is the initial surface temperature, T_m is the oncoming mainstream flow temperature, and α and k are the thermal diffusivity and conductivity of the blade material, respectively. The heat transfer coefficient is obtained from Equation (1). For film cooling tests, the mainstream temperature (T_m) in Eq. (1) is replaced by the local film temperature (T_f) which is a mixture of the coolant (T_c) and mainstream temperatures. The film temperature is defined in terms of η, which is the film effectiveness.

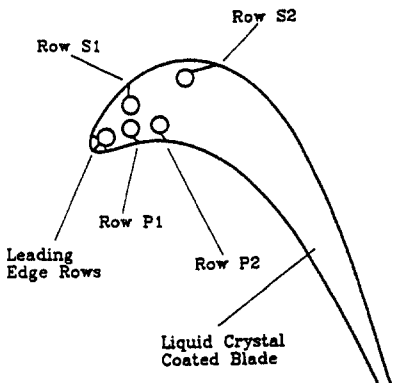

Film Hole Location	P/D	L/D	Axial Angle	Radial Angle	Tangential Angle
LE	7.31	2.7	90°	27°	-
S1	4.13	7.6	-	90°	45°
S2	5.71	12.8	-	90°	30°
P1	6.79	4.2	-	32°	55°
P2	5.00	6.7	-	35°	50°

Fig. 3 Test blade geometry with film injection holes

Table 1 Test conditions

Case No.	Tu	S	M_t	M	Tu
1	0.7%	No Wake	0.0	No holes	0.7%
2	0.7%	No Wake	0.0	0.8	0.7%
3	0.7%	0.1	0.0	0.8	10.4%
4	0.7%	0.1	0.5	0.8	10.0%
5	5.0%	0.1	0.0	No holes	13.7%
6	5.0%	0.1	0.5	No holes	13.0%
7	5.0%	0.1	0.0	0.8	13.7%
8	5.0%	0.1	0.5	0.8	13.0%

$$\eta = \frac{T_f - T_m}{T_c - T_m}; \quad \text{or} \quad T_f = \eta T_c + (1 - \eta) T_m \qquad (2)$$

For the film cooling test, we obtain an equation similar to Eq. (1)

$$\frac{T_w - T_i}{T_f - T_i} = \frac{T_w - T_i}{\eta T_c + (1 - \eta) T_m - T_i} = \left[1 - \exp\left(\frac{h^2 \alpha t}{k^2}\right) \operatorname{erfc}\left(\frac{h\sqrt{\alpha t}}{k}\right) \right]. \qquad (3)$$

Two similar transient tests are run to obtain the heat transfer coefficient (h) and film effectiveness (η). In the first test, the blade surface is heated and the coolant and mainstream temperatures are nearly the same. In this case, there is only one unknown, h, in the equation. For the second test, the coolant is heated to a temperature close to blade initial temperature. The calculated local heat transfer coefficient from the first test is substituted in the equation to obtain the local film effectiveness. The above equation is solved at each point (57,760 points) on the blade surface to obtain the detailed heat transfer coefficient and film effectiveness distributions. Lateral and axial conduction into the blade are assumed to be negligible.

The experimental uncertainty in the measurement of the local heat transfer coefficient (h), based on Kline and McClintocks' (1953) methodology, is about ±4.5 percent. The individual uncertainties of all the parameters in Eq. (1) have been included. The uncertainty in the film effectiveness measurement includes the additional uncertainty in heat transfer coefficient measurement and was estimated to be about ±6.8 percent. The above uncertainty values are the average uncertainty values depending upon the location on the blade. Some locations can have lower uncertainty in the measured values. It should be noted that the uncertainty in the immediate vicinity of the hole (less than 1 diameter around the hole) and close to blade trailing edge could be as high as ±17 percent due to invalidation of the semi-infinite model assumption. However, the semi-infinite solid assumption can be applied where thickness of material is higher than 0.51 cm. The uncertainty in the velocity measurement using the single hot wire was estimated to be ±4 percent.

Results and Discussion

Tests were performed at the chord Reynolds number of 7.6×10^5 at the cascade exit. The corresponding velocity at the cascade exit is 75 m/s. Unsteady wake strength is defined by wake Strouhal number (S) = $2\pi Ndn/(60\ V_1)$. It can be achieved by the combination of the number of rods (n), diameter of rod (d), and wake rod rotation speed (N). Table 1 presents the test cases for which heat transfer measurements were obtained for this study. Case 1 is for a no wake case and no-film holes blade. Case 2 is for a film cooled blade with cooling blowing ratio (M) of 0.8 with no wake effect. Case 3 is for a cooled blade under the effect of wake Strouhal number S = 0.1. Case 4 is for the cooled blade under the effect of unsteady wakes and trailing edge ejection with jet blowing ratio (M_t) of 0.5. Case 5 is for an uncooled blade with grid generated turbulence and unsteady wake. Case 6 is for an uncooled blade with grid generated turbulence and unsteady wake with trailing edge ejection (M_t = 0.5). Case 7 is for a cooled blade under the effects of grid generated turbulence and unsteady wake. Case 8 is for the cooled blade under the effects of grid generated turbulence and unsteady wake with trailing edge ejection. The grid generated turbulence (Tu) and the time-mean averaged turbulence intensities ($\bar{T}u$) for each case are shown in the table. The parameters are chosen in this study to simulate typical of engine conditions. The cascade exit mainstream Reynolds number of 7.6×10^5 represented the nondimensional engine flow conditions. An unsteady wake Strouhal number of S = 0.1 simulates the blade rotation frequency and velocity defect effects. As indicated earlier, the combustor generated free-stream turbulence levels downstream of the nozzle guide vanes are of the order of 5–6 percent which is generated using an upstream grid. The trailing edge ejection jet blowing ratio (M_t) of 0.5 and film cooling blowing ratio (M) on the blade of 0.8 are in the range of typical coolant flow conditions.

Free-stream Flow Measurements. Figure 4(a) presents the local-to-exit velocity ratio (V/V_2) distribution around the blade. A pressure tap instrumented blade was used to measure the surface static pressure distributions which was then converted to local mainstream isentropic velocity distribution around the blade (Ou et al., 1994). Figure 4(b) and 4(c) present the instantaneous velocity profiles for cases 7 and 8. Case 7 is for a free stream with grid generated turbulence (Tu = 5.0 percent) and unsteady wake (S = 0.1) and case 8 is for a free stream with grid generated turbulence (Tu = 5.0 percent) and unsteady wake (S = 0.1) with trailing edge ejection (M_t = 0.5). Comparing both figures, it is evident, that in Fig. 4(b), the velocity deficit is clearly seen with the passing of the unsteady wake and this deficit appears slightly reduced in Fig. 4(c). This indicates that the trailing edge jets enhance the mean value of mainstream velocity. Figure 4(d) presents the ensemble averaged velocity ($\tilde{V}$) and turbulence intensity ($\tilde{T}u$) profiles at the cascade inlet for the same cases as in Figs. 4(b) and 4(c). The turbulence intensity profile for the trailing edge ejection case is more uniformly disturbed in the time period. Based on these measurements, it is evident that the addition of trailing

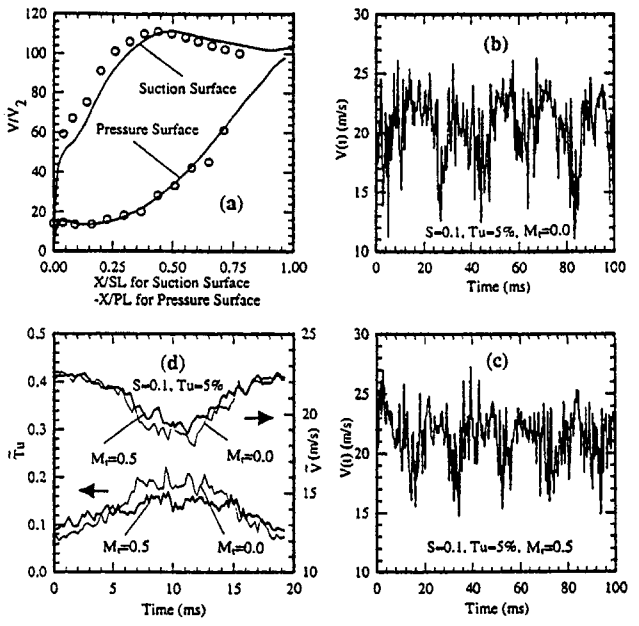

Fig. 4 Local-to-exit velocity ratio (V/V_2) distributions on the test blade surface, profiles of instantaneous velocity, ensemble-averaged velocity and turbulence intensity

edge ejection to unsteady wake profile produces increased mainstream velocity and slightly reduced but more uniformly disturbed turbulence intensity profile.

Film Cooling. For all film cooled cases, air was used as coolant to simulate coolant-to-mainstream density ratio of $DR = 1.0$ at a blowing ratio of 0.8. Air was used for trailing edge ejection ($M_t = 0.5$).

Nusselt Number Distributions. Figures 5 and 6 present the detailed and spanwise averaged Nusselt number distributions on the blade suction and pressure surfaces for cases 1–4, respectively. All cases are with no grid-generated turbulence intensity of $Tu = 0.7$ percent. The figure compares the no-wake, no-film holes blade (case 1) to no-wake film cooled blade with $M = 0.8$ (case 2); film cooled blade with $M = 0.8$ and wake $S = 0.1$ (case 3); and film cooled blade with $M = 0.8$, wake $S = 0.1$, and trailing edge ejection $M_t = 0.5$ (case 4).

Effect on Suction Surface. The no-film holes surface Nusselt number (case 1) levels drop significantly from the leading edge with increasing streamwise distance on the suction surface. Nusselt numbers are lowest around $X/SL = 0.5$ after which the Nusselt numbers increase again. This is due to boundary layer transition to turbulence. Nusselt numbers are higher towards the trailing edge as the transition is not completed. For a film cooled blade (case 2) with no wake, Nusselt numbers are high due to film cooling jets immediately downstream of leading edge holes. Further downstream of LE row injection, Nusselt numbers decrease rapidly and the injection effect is dissipated upstream of the first film hole row on the suction surface (S1). Downstream of the hole row S1, jet streaks of higher Nusselt numbers are obtained along the holes. The streaks extend all the way up to the next film hole row S2. However, the jets do not cause Nusselt number enhancement between the holes for row S1 due to lack of spanwise mixing between the jets. Downstream of film hole row S2, the Nusselt numbers are significantly higher than for case 1. Film injection from row S2 causes boundary layer instabilities which promote earlier laminar to turbulent boundary layer transition. This also produces higher heat transfer coefficient downstream of injection. Nusselt numbers decrease after transition with growth of the turbulent boundary layer and dissipation of coolant jet effect. Further addition of unsteady wake to the film cooled blade (case 3) shows small effect on the blade surface Nusselt numbers compared to case 2. Nusselt number distributions appear to be similar to case 2 except in the region downstream of hole row S2. It appears that the additional effect of unsteady wakes is small due to the reason that surface Nusselt numbers are already significantly enhanced by film injection. Addition of trailing edge ejection to the unsteady wake (case 4) on the film cooled blade does not affect the Nusselt number distributions.

Effect on Pressure Surface. For case 1, the Nusselt numbers drop rapidly till $X/PL = 0.15$ and then increase a little bit over the entire surface. For case 2, film injection has a very small effect immediately downstream of leading edge row injection. However, Nusselt numbers are enhanced between the leading edge row and first row P1 over case 1. Downstream of rows P1 and P2, film injection enhances Nusselt numbers slightly over case 1. The effect of film injection on the pressure surface is not as significant as on the suction surface. Since the boundary layer on the pressure surface is thicker than on the suction surface, the effect on Nusselt numbers due to film injection is less. Jet streaks are also not evident on the pressure surface. Addition of unsteady wake (case 3) causes slight increases over case 2 in the region between LE holes and hole row P1. Further addition of trailing edge ejection to case 3 (case 4) causes only slight increases in Nusselt numbers on the pressure surface in the region downstream of hole row P1.

Nusselt numbers with film injection are significantly enhanced due to the boundary layer disturbance cause by film injection. Earlier studies on film cooling have shown that film injection can create local turbulence intensities as high as 15–20 percent depending on blowing ratio. With such high local turbulence, heat transfer coefficients downstream of injection are significantly enhanced as seen in the figure. This may cause significantly reduced effects of other factors such as unsteady wakes and trailing edge ejection on film cooled blades. The spanwise-averaged results in Fig. 6 present the same trends as discussed above.

Figure 7 presents the span-averaged Nusselt number distribution for cases 5–8. All the cases are for a grid generated turbu-

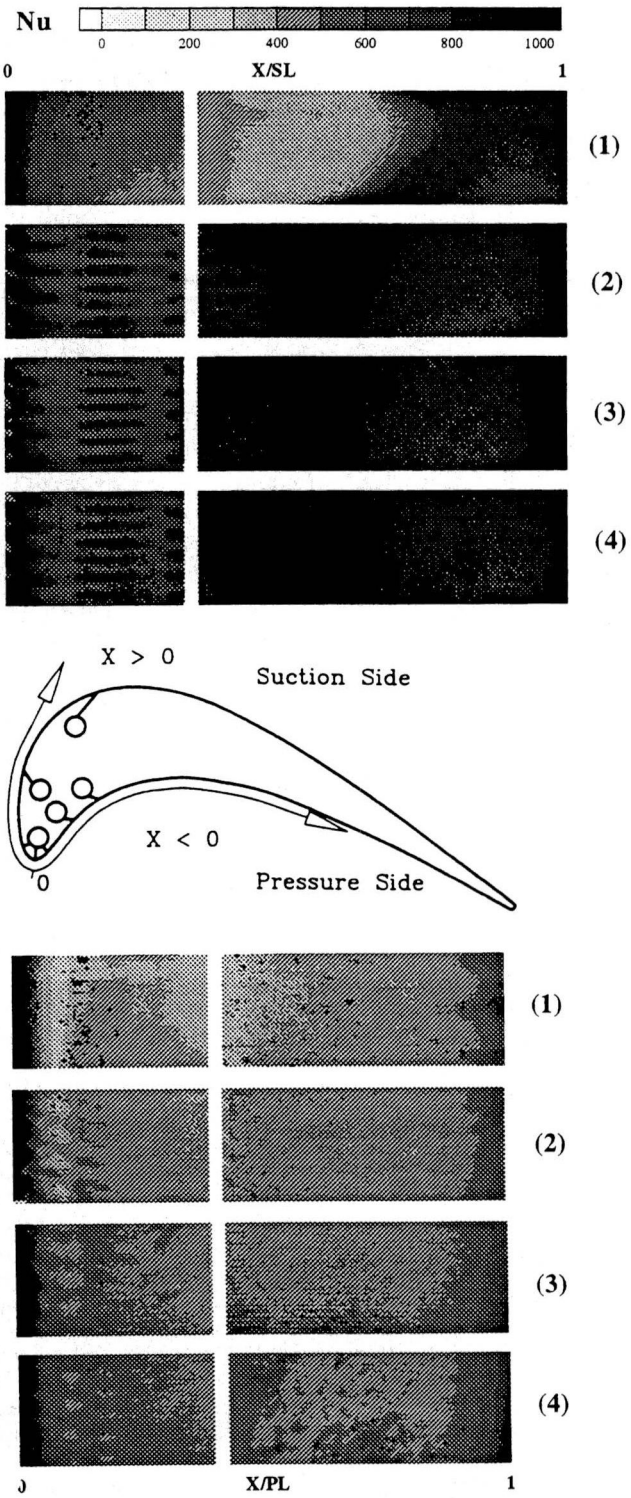

Fig. 5 Detailed Nusselt number distributions for cases 1–4

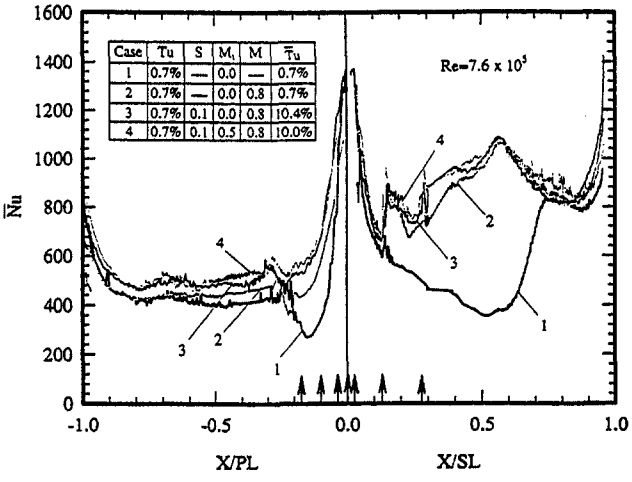

Fig. 6 Span-averaged Nusselt number distributions for cases 1–4

lence of $Tu = 5.0$ percent. The figure compares an uncooled blade with wake $S = 0.1$ (case 5) with an uncooled blade with wake $S = 0.1$ and trailing edge ejection, $M_t = 0.5$ (case 6); a film cooled blade with wake $S = 0.1$, $M = 0.8$ (case 7); and a film cooled blade with wake $S = 0.1$, $M = 0.8$, and trailing edge ejection, $M_t = 0.5$ (case 8).

Effect on Suction Surface. The no-film holes surface Nusselt number (case 5) levels drop significantly from the leading edge to $X/SL = 0.25$ and then increases due to transition to turbulent boundary layer toward the trailing edge. Comparing to case 1, case 5 has both grid generated turbulence and unsteady wake effects included. The added influence of both the unsteady wake and grid generated turbulence can cause transition location to move upstream towards the leading edge. The differences in cases 5 and 6 are in the region downstream of leading edge on the suction surface. Nusselt numbers are enhanced up to 20 percent in the region from leading edge to $X/SL < 0.3$ on the suction surface. The effect of trailing edge ejection on the uncooled blade is also strongly evident over the entire pressure surface and in the transition region on the suction surface. For a film cooled blade (case 7) with wake and grid generated turbulence, Nusselt numbers are significantly enhanced in the region between LE holes and the suction side second row holes S2. Additional effect of film injection is to cause local instabilities in the boundary layer and causing higher heat transfer region immediately downstream of hole rows. Further downstream of hole row S2, the Nusselt numbers are only slight enhanced compared to case 6. Further addition of trailing edge ejection to case 7 (case 8) causes very small changes in the detailed heat transfer coefficient distributions. The trailing edge ejection effect is not as significant as the other effects of film injection, unsteady wakes, and grid generated turbulence, in that order.

Effect on Pressure Surface. For case 5, the Nusselt numbers drop rapidly till $X/PL = 0.15$ and then increase a little bit over the entire surface. For case 6, Nusselt numbers are enhanced from leading edge to $X/PL < 0.1$ on the pressure surface compared to case 5. For case 7, the effect of film injection on the pressure surface is more in the region immediately downstream of injection holes. Further addition of trailing edge ejection to case 7 (case 8) causes slight decreases in Nusselt numbers on the pressure surface just downstream of LE hole rows.

The trailing edge ejection jets for a low $Tu = 0.7$ percent may be attached to the unsteady wake generated by the rods. However, with grid generated turbulence, the trailing jets may not be uniformly impinging on the LE region. This may cause slight changes in the heat transfer distributions as compared to the no-grid case. The grid turbulence effect seems to be stronger on the pressure surface. Overall effect of trailing edge ejection imposed on a free-stream disturbed by unsteady wakes and grid generated turbulence on the film-cooled blade heat transfer is slightly incremental.

Film Effectiveness Distributions. Figures 8 and 9 present the detailed and spanwise-averaged film effectiveness distributions for cases 2, 3, and 4, respectively. The figure compares the no-wake film cooled blade with $M = 0.8$ (case 2) to film cooled blade with $M = 0.8$ and wake $S = 0.1$ (case 3); and film cooled blade with $M = 0.8$, wake $S = 0.1$, and trailing edge ejection $M_t = 0.5$ (case 4).

Effect on Suction Surface. For case 2, film effectiveness immediately downstream of leading edge holes is as high as 0.5 but drops rapidly. The coolant protection dissipates rapidly in this high curvature region. Effectiveness is high along the holes for row S1. The film streaks are clearly evident along the injection holes. The film streaks extend up to the next hole row S2. However, the film effectiveness between the holes is lower due to lack of spanwise mixing of jets. Effectiveness downstream of injection from row S2 shows shorter streaks with the jets coalescing downstream. The high curvature of the blade and the boundary layer transition to turbulence in this region (Fig. 5) may be the reason for spanwise mixing of jets. With addition of unsteady wake to the mainstream flow (case 3), effectiveness is significantly reduced. The effectiveness downstream of the LE rows is lower as coolant jets dissipate rapidly. The oncoming free-stream disturbed by passing wakes breaks down the jets. Also the advancement of the boundary layer transition location can cause more spanwise mixing of jets specially for the coolant downstream of hole row S1. Also, effectiveness reduces far downstream of the last injection row S2. For case 4 with trailing edge ejection, effectiveness distributions are similar to that for case 3. Film effectiveness distribution on the suction surface appears to be slightly affected by the further addition of trailing edge ejection to a free-stream already affected by unsteady wakes.

Effect on Pressure Surface. For case 2, effectiveness distributions on the pressure surface do not show strong jet like streaks as on the suction surface. Effectiveness levels are also not very high downstream of injection holes but decrease rapidly downstream of hole row P2 and any coolant protection is not evident for distance $X/PL > 0.5$. Addition of unsteady wake (case 3) reduces effectiveness downstream of hole row P2. However, upstream of P1, the effectiveness values are similar to case 2. Addition of trailing edge ejection seems to produce some variations in the effectiveness distributions (case 4). The effectiveness in the LE region decreases significantly. However,

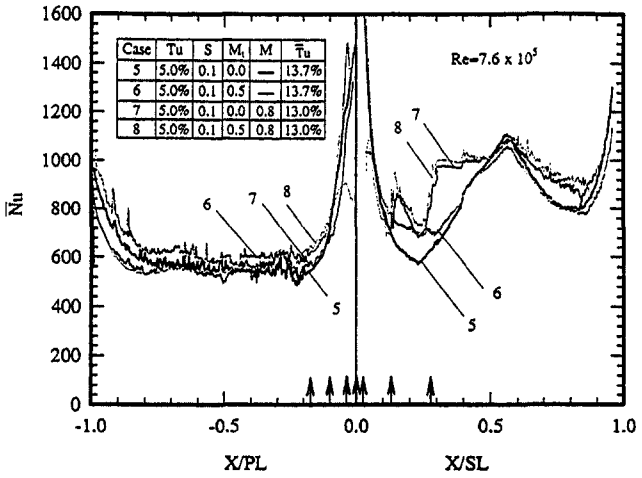

Fig. 7 Span-averaged Nusselt number distributions for cases 5–8

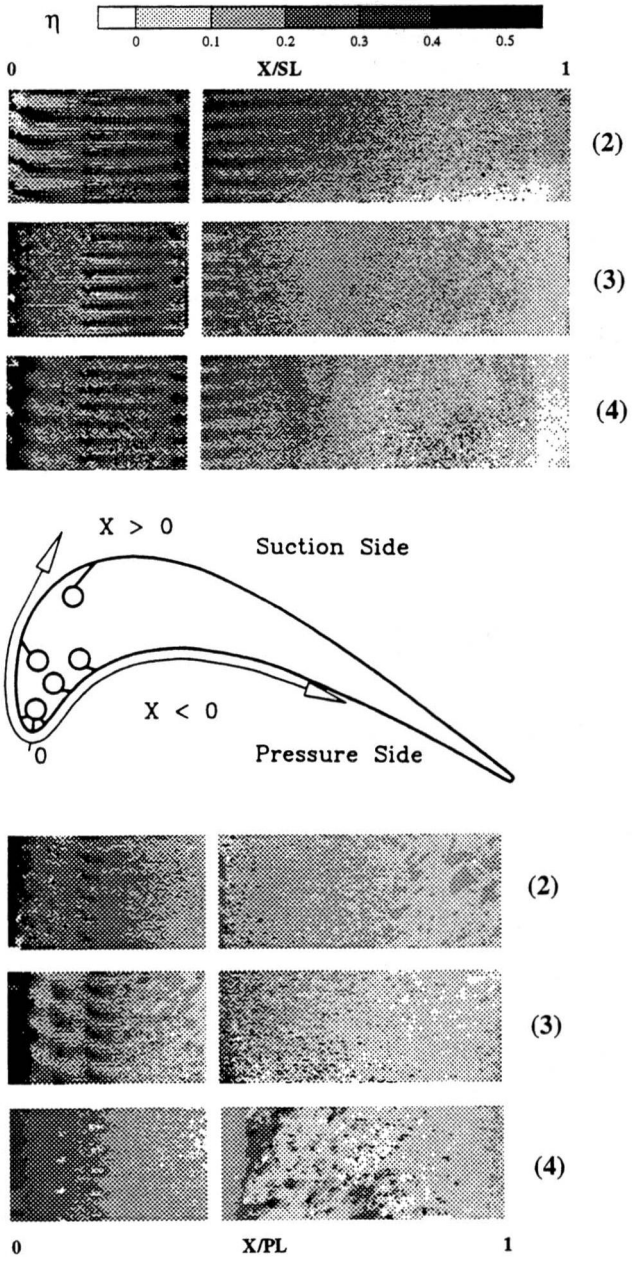

Fig. 8 Detailed film effectiveness distributions for cases 2–4

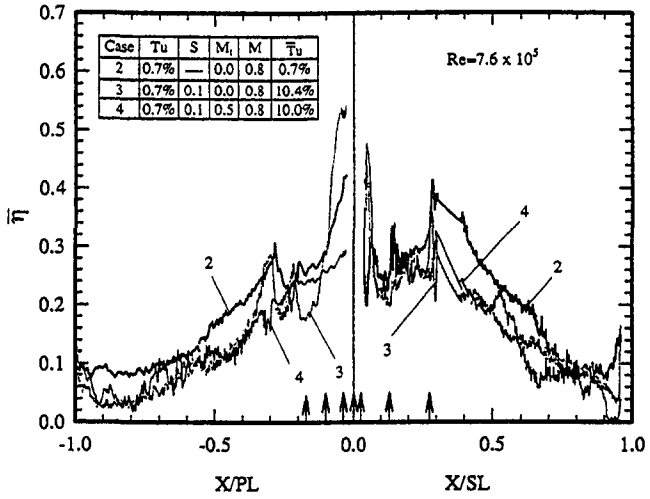

Fig. 9 Span-averaged film effectiveness distributions for case 2–4

downstream of the LE hole row, the effectiveness values are higher for case 4. This may be due to the reason that some of the trailing edge coolant may be convected downstream into the low velocity region thus providing more protection.

Figure 10 presents the span-averaged film effectiveness distributions for cases 7–8. The figure compares a film cooled blade with wake $S = 0.1$, $M = 0.8$ (case 7) and a film cooled blade with wake $S = 0.1$, $M = 0.8$, and trailing edge ejection, $M_t = 0.5$ (case 8).

Effect on Suction Surface. Case 7 is for a turbine blade with film cooling under the effect of grid turbulence and unsteady wakes. Effectiveness is high immediately downstream of LE row holes. Effectiveness decreases rapidly to hole row S1. Weak jets streaks are observed downstream of hole row S1 due to the unsteady wake affected free stream. Downstream of hole row S2, effectiveness is greatly reduced due to spanwise mixing of jets in the transition and fully turbulent boundary layer region. With an addition of trailing edge ejection (case 8), effectiveness reduces downstream of LE and S1 holes. However, effectiveness levels are not significantly affected over the rest of the suction surface. Some of the trailing ejection coolant might penetrate the coolant jets from the LE row holes and disturb the already weak protection thus reducing the film effectiveness. Further downstream, the effect of the trailing edge jets might be weaker and hence the lack of reduction in film effectiveness.

Effect on Pressure Surface. For case 7, effectiveness downstream of LE rows is as high as 0.4 but rapidly decreases downstream. Some high effectiveness is observed upstream of hole row P2 due to accumulation of coolant in the low velocity region. For case 8, effectiveness levels are similar but lower than that for case 7. The effect of trailing edge jets is noticeable on the pressure surface.

On the suction surface, case 8 provides lower effectiveness values downstream of LE film hole rows. Downstream of hole row S1, both cases provide similar effectiveness values. Case 8 provides lower effectiveness over the entire pressure surface.

Conclusions

The effect of upstream trailing edge ejection combined with unsteady wake on downstream blade heat transfer coefficients and film effectiveness is presented for a film cooled blade. All experiments were conducted for a cascade exit Reynolds num-

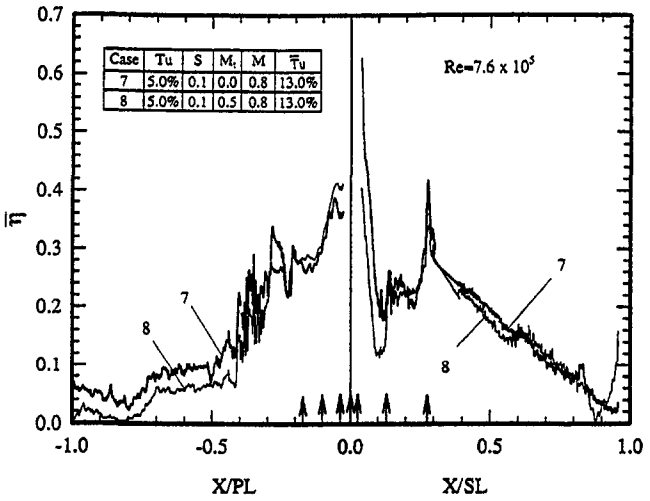

Fig. 10 Span-averaged film effectiveness distributions for cases 7–8

ber of 7.6×10^5 with air as coolant and blowing ratio of $M = 0.8$. The paper presents a comprehensive listing of the individual effects of film injection, unsteady wakes, grid generated turbulence, and trailing edge ejection on blade surface heat transfer coefficient and film effectiveness distributions.

1 Blade surface Nusselt numbers are significantly enhanced by film injection. Film injection also promoted earlier boundary layer transition on the suction surface. Higher film effectiveness is obtained on the suction surface compared to the pressure surface.
2 Addition of unsteady wake to the free-stream produces slightly enhanced Nusselt numbers on a film cooled blade. However, unsteady wake significantly reduces film effectiveness.
3 Addition of grid generated turbulence to unsteady wakes (case 3 versus case 7) does not produce any further significant increases in Nusselt numbers for a film-cooled blade. However, adding grid generated turbulence to unsteady wakes reduces film effectiveness further.
4 Trailing edge ejection jets compensate the velocity defect cause by wake rod passing and hence produces a slightly more uniform velocity and turbulence intensity profile. Trailing edge ejection increases (up to 20 percent) both pressure surface heat transfer in the leading edge region and suction surface heat transfer before boundary layer transition for the uncooled blade. The trailing edge ejection effects diminish further downstream on both pressure and suction surfaces.
5 For a film cooled blade, trailing edge ejection has only a small effect on blade surface heat transfer coefficients compared to other significant parameters such as film injection, unsteady wakes, and grid generated turbulence, respectively in that order of decreasing effect. Film effectiveness decreases with the addition of trailing edge ejection in the leading edge region on both pressure and suction surfaces. However, the effect decreases further downstream.

Acknowledgment

This paper was prepared with the support of the NASA-Lewis Research Center under grant number NAG3-1656. The NASA technical team is Dr. Philip E. Poinsatte and Dr. Raymond Gaugler. Their support is greatly appreciated. Technical discussions with Dr. C. P. Lee of GE Aircraft Engines were helpful and are acknowledged.

References

Abhari, R. S., and Epstein, A. H., 1994, "An Experimental Study of Film Cooling in a Rotating Transonic Turbine," ASME JOURNAL OF TURBOMACHINERY, Vol. 116, pp. 63–70.

Camci, C., and Arts, T., 1990, "An Experimental Convective Heat Transfer Investigation Around a Film-Cooled Gas Turbine Blade," ASME JOURNAL OF TURBOMACHINERY, Vol. 112, pp. 497–503.

Du, H., Han, J. C., and Ekkad, S. V., 1998, "Effect of Unsteady Wake on Detailed Heat Transfer Coefficient and Film Effectiveness Distributions for a Gas Turbine Blade," ASME JOURNAL OF TURBOMACHINERY, Vol. 120, pp. 808–817.

Du, H., Ekkad, S. V., and Han, J. C., 1997, "Effect of Unsteady Wake With Trailing Edge Coolant Ejection on Detailed Heat Transfer Coefficient Distributions for a Gas Turbine Blade," ASME *Journal of Heat Transfer,* Vol. 119, pp. 242–248.

Dunn, M. G., 1986, "Heat Flux Measurements for the Rotor of a Full-Stage Turbine: Part I—Time-Averaged Results," ASME JOURNAL OF TURBOMACHINERY, Vol. 108, pp. 90–97.

Haas, W., Rodi, W., and Schönung, B., 1992, "The Influence of Density Difference Between Hot and Coolant Gas on Film Cooling by a Row of Holes: Predictions and Experiments," ASME JOURNAL OF TURBOMACHINERY, Vol. 114, pp. 747–755.

Ito, S., Goldstein, R. J., and Eckert, E. R. G., 1978, "Film Cooling of a Gas Turbine Blade," ASME *Journal of Engineering for Power,* (renamed the ASME *Journal of Engineering for Gas Turbines and Power* in 1984), Vol. 100, pp. 476–481.

Kline, S. J., and McClintock, F. A., 1953, "Describing Uncertainties in Single Sample Experiments," *Mechanical Engineering,* Vol. 75, pp. 3–8.

Mehendale, A. B., Han, J. C., Ou, S., and Lee, C. P., 1994, "Unsteady Wake Over a Linear Turbine Blade Cascade With Air and CO_2 Film Injection: Part II—Effect on Film Effectiveness and Heat Transfer Distributions," ASME JOURNAL OF TURBOMACHINERY, Vol. 116, pp. 730–737.

Nirmalan, V., and Hylton, L., 1990, "An Experimental Study of Turbine Vane Heat Transfer With Leading Edge and Downstream Film Cooling," ASME JOURNAL OF TURBOMACHINERY, Vol. 112, pp. 477–487.

Ou, S., Han, J. C., Mehendale, A. B., and Lee, C. P., 1994, "Unsteady Wake Over a Linear Turbine Blade Cascade With Air and CO_2 Film Injection: Part I—Effect on Heat Transfer Coefficients," ASME JOURNAL OF TURBOMACHINERY, Vol. 116, pp. 721–729.

Takeishi, K., Aoki, S., Sato, T., and Tsukagoshi, K., 1992, "Film Cooling on a Gas Turbine Rotor Blade," ASME JOURNAL OF TURBOMACHINERY, Vol. 114, pp. 828–834.

Zhang, L., and Han, J. C., 1995, "Combined Effect of Free-Stream Turbulence and Unsteady Wake on Heat Transfer Coefficients From a Gas Turbine Blade," ASME *Journal of Heat Transfer,* Vol. 117, pp. 296–302.

Numerical Simulation of the Shock-Tip Leakage Vortex Interaction in a HPC Front Stage

M. Hoeger

G. Fritsch

D. Bauer

Daimler-Benz Aerospace,
MTU Motoren- und Turbinen-Union
München GmbH,
Dachauer Straße 665,
München, Germany 80995

For a single-stage transonic compressor rig at the TU Darmstadt, three-dimensional viscous simulations are compared to L2F measurements and data from the EGV leading edge instrumentation to demonstrate the predictive capability of the Navier–Stokes code TRACE_S. In a second step the separated regions at the blade tip are investigated in detail to gain insight into the mechanisms of tip leakage vortex-shock interaction at operating points close to stall, peak efficiency, and choke. At the casing the simulations reveal a region with axially reversed flow, leading to a rotationally asymmetric displacement of the outermost stream surface and a localized additional pitch-averaged blockage of approximately 2 percent. Loss mechanisms and streamline patterns deduced from the simulation are also discussed. Although the flow is essentially three-dimensional, a simple model for local blockage from tip leakage is demonstrated to significantly improve two-dimensional simulations on S1-surfaces.

Introduction

The continuing trend toward increased thrust-to-weight ratio engines has led to highly loaded compressors with greatly reduced blade and stage count. Cybyk et al. (1997) pointed out that the steady increase in stage pressure ratio and performance resulted in a gradual evolution from high-aspect-ratio rotors in the 1960s toward wide-chord blading with leading-edge sweep, first to the rear but eventually also to the front. Low-aspect-ratio rotors, however, also lead to an increased importance of secondary flow at hub and tip. Secondary flow phenomena are particularly pronounced in LPC and modern HPC front stages, where high Mach numbers lead to complex three-dimensional shock structures and boundary layer separation. It is the tip region, where tip leakage and shock system interact, that holds the key to highly efficient transonic compressors and, most important, sufficient surge margin to insure stable and dependable off-design operation.

Multistage three-dimensional Navier–Stokes solvers can aid in the design of efficient compressors with advanced transonic blading and can help to meet time and cost targets. Three-dimensional multistage simulations started in the mid-1980s with Euler solvers incorporating loss models for stage matching; see, e.g., Denton (1986). By the early 1990s multistage Euler simulations with turnaround times of a couple of hours were routinely performed to check and optimize component matching; see, e.g., Huber and Ni (1989). With computer hardware powerful enough to allow viscous three-dimensional simulations, Navier–Stokes solvers were added to the tool kit of researchers and designers; see, e.g., Denton (1986), Dawes (1993), Jennions and Turner (1993), or Rhie et al. (1998). Today, three-dimensional steady multistage Navier–Stokes solvers are standard design tools and are being extended to incorporate the time-mean effect of unsteady blade row interaction; see, e.g., Adamzcyk et al. (1990), Rhie et al. (1998), LeJambre et al. (1998), and Turner (1996). The three-dimensional steady approach is complemented by unsteady viscous simulations; see, e.g., Hah et al. (1997), Puterbaugh and Brendel (1997), and Dorney and Sharma (1997).

Although the accurate prediction of compressor performance is imperative, three-dimensional (multistage) simulations alone do not necessarily increase the insight into flow physics. Only through a thorough analysis of the three-dimensional data is insight generated, which, in turn, paves the way to simple but instructive models incorporating the dominant flow physics. These models the engineer can ultimately translate into improved designs.

The mixing of the clearance jet and the main flow, presumably the most important contributor to leakage loss, is the basis for the inviscid tip leakage flow model of Storer and Cumpsty (1991, 1993). Wall movement was found to exert only a minor influence in compressors; see Nikolos et al. (1995). A semi-empirical formula for the tip vortex trajectory inside the blade passage, developed by Chen et al. (1991), shows the vortex path to be independent of the gap width and to be governed primarily by inviscid convective phenomena. Simulations by Perrin and LeBoeuf (1992) indicate a rapid decay of vorticity in the vortex core over 30 percent of the rotor chord in a transonic compressor. A large influence of the clearance width on shock structure and efficiency of a transonic compressor rotor is reported by several authors; see, e.g., Copenhaver et al. (1996). Especially at stall, a strong leakage flow vortex interaction causes a high blockage/low Mach number region, see Suder and Celestina (1996), which is thought to play an important role in the onset of stall. Theoretical investigations by Adamczyk et al. (1993) showed an improved surge margin for a rotor blade with the clearance removed over the front 50 percent chord. A simple inviscid model for the shape of the vortex core was developed by Puterbaugh and Brendel (1997), with mixing and shock-induced static pressure rise as the dominant variables.

All authors quoted above addressed the blockage near the casing only in qualitative manner. In this paper, however, the *displacement* of the casing streamlines *by axially reversed flow* is introduced as a new variable, to investigate quantitatively the blockage generated by leakage vortex-shock interaction.

Background

The design of modern transonic compressor blading is an iterative process, which often requires ten or more iterations until an individual rotor blade meets aerodynamic as well as

Contributed by the International Gas Turbine Institute and presented at the 43rd International Gas Turbine and Aeroengine Congress and Exhibition, Stockholm, Sweden, June 2–5, 1998. Manuscript received by the International Gas Turbine Institute February 1998. Paper No. 98-GT-261. Associate Technical Editor: R. E. Kielb.

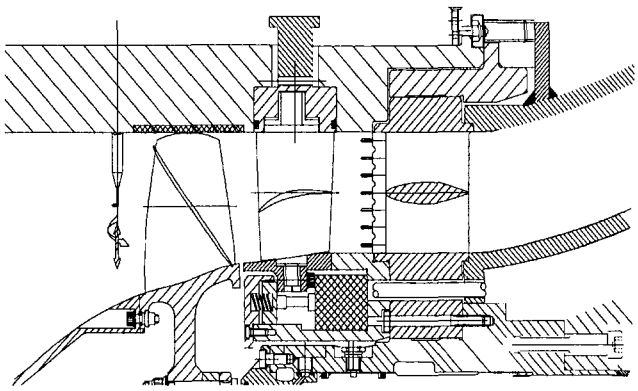

Design parameter	stage
design pressure ratio	1.50
ISA-corrected mass flux [kg/s]	16.0
work coefficient	0.81
flow coefficient	0.60
inlet hub/tip ratio	0.745
annulus diameter [m]	0.38
tip Mach number	1.2
axial Mach number inlet	0.48
axial Mach number outlet	0.49

Fig. 1 Single-stage compressor rig at TU Darmstadt

structural constraints; see Fritsch et al. (1997) for a more detailed description of the design process. Neither the complete blading, i.e., rotor and stator geometry for all stages, nor the exact blade and vane counts may be available at this point in the design sequence such that the designer has to rely on S1/S2-methods. The flow field is split into circumferentially (S1) and meridionally (S2) oriented stream surfaces with the three-dimensional flow physics partly accounted for by semi-empirical formulas and simple models. Only if the dominant three-dimensional effects are incorporated at this early design stage, may the results of a fully three-dimensional Navier–Stokes simulation toward the end of blading design be used for (aerodynamic) fine-tuning rather than for major redesigns.

Single-Stage Transonic Compressor Rig at TU Darmstadt

The single-stage transonic compressor rig at Technical University of Darmstadt, although without inlet guide vane, is representative of first stages in modern high compressors; see Fig. 1 and design parameters in Table 1.

The rig serves three main purposes: the advancement of the insight into compressor aerodynamics, as a test-bed for new concepts in three-dimensional aero-design, and for calibration of aero-design tools. For a detailed description of rig and experiments the interested reader is referred to Blaha et al. (1997).

Instrumentation

For the operating points near peak efficiency and stall, which are considered in detail, traverse data are available ahead of the rotor and between stator and strut. L2F data of the rotor flow field have been taken on five radial planes, with a maximum of sixteen points pitchwise, and twelve points axially.

Total pressure and temperatures from the *EGV leading edge instrumentation,* see Fig. 1, are available at all operating points. Only at peak efficiency, however, was the pitchwise variation due to stator wakes captured by varying the clocking between stator and EGV. The stator loss deduced in this manner was assumed constant along the operating line and used to correct the total pressures from the EGV leading edge instrumentation. Traverse measurements with a *five-hole probe* ahead of the EGV were carried out near peak efficiency and at stall only.

Three-Dimensional Navier–Stokes Simulations

Details of the three-dimensional Navier–Stokes solver TRACE_S are found in Fritsch et al. (1997). Its multistage extension and its extension to parallel architectures are found in Fritsch and Möhres (1997).

Geometry. A gridded nominal rotor tip gap of 1 percent was used unless noted otherwise. To ensure that the relevant flow physics near the casing does not depend on the details of the gap model, additional simulations with a modified gap height and resolution were performed. Quantitative differences between experiments and simulation in the tip region, however, cannot clearly be attributed to either a shortcoming in the gap model or a shortcoming the turbulence model only. With an additional uncertainty in the EGV leading edge data, the use of a modified gap was deemed inappropriate. The hub gap between rotor and stator and the stator clearance were neglected.

Grid Topology and CPU-Time. Figure 2 shows the rotor grid topology. Block-structured grids are employed to obtain high-quality grids and accurate convergent simulations for the complex geometry found in turbomachinery. All simulations utilized a composite **H/O**-grid with 155 × 33 nodes for the **H**-grid and 177 × 11 nodes for the **O**-grid in the S1-plane of the rotor; 65 nodes were used in the radial direction. A simple **H**-grid with 81 ×

Table 1 Selected compressor stage design parameters

Design parameter	rotor	stator
aspect ratio	0.88	1.50
blade count	16	29
solidity	1.5	1.6
gap [% span]	1.0	0.275
max. Inlet Mach number	1.34 (tip)	0.66 (hub)
Reynolds number	$2.1*10^6$	$0.7*10^6$
diffusion factor	0.39	0.38

Nomenclature

AVDR = Axial Velocity Density Ratio
b.l. = boundary layer
c_{ax} = axial chord
l.e., t.e. = leading edge, trailing edge
Ma = Mach number in the relative frame
p = static pressure
pt, Tt = relative frame total pressure and temperature
PS, SS = pressure, suction surface
x, r, θ = cylindrical coordinates
w = velocity (relative frame)
ξ = immersion = $r_{cas} - r$
δ_{ar} = displacement from axial flow reversal
$\omega_{S,10}$ = secondary loss coefficient over outer 10 percent mass flux

Subscripts

1, 2 = rotor in- and outlet plane
cas = location at the outer casing
p = pitch-averaged quantity

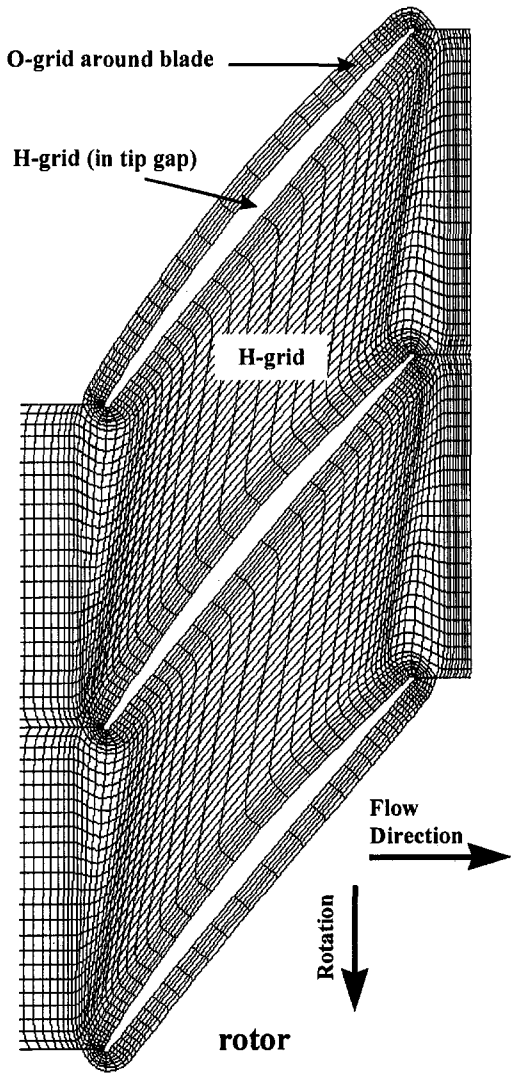

Fig. 2 Grid topology on S1-plane near casing (coarsened)

9×11 nodes was used to grid the tip gap. A comparable resolution in the stator yielded a combined total of 896,231 nodes. Extensive grid studies, partly documented in Fritsch et al. (1997), were performed to ensure that a comparison between experiment and simulation is not compromised by a lack of resolution. Execution time to convergence is approximately 6 CPU-hours on three processors with multigrid active.

Turbulence Model. For economy, a high Reynolds' k–ϵ model, resulting in a mean wall distance of $y^+ = 25$ for rotor blade and casing and $y^+ = 75$ for the hub, was used; stator resolution was comparable with the exception of the casing region, where the wall distance was increased to $y^+ = 75$. Wall distance for operating points away from peak efficiency varies with the flow state. All simulations were run fully turbulent with wall functions applied to represent the wall shear accurately.

Boundary Conditions. ISA standard conditions with purely axial flow were assumed at the nonreflecting inflow boundary. The turbulence intensity measured in the experiment, $Tu_1 = 1$ percent, was prescribed. A rather pronounced incoming casing boundary layer was prescribed via the total pressure profile; see Fig. 4. A thickness of 17 mm, translating into a displacement thickness of 2.1 mm, was extrapolated from measurements several chords upstream of the rotor at peak efficiency; this profile was kept constant for all operating points. Due to a strong acceleration over the spinner, a negligible boundary layer was assumed for the hub.

Table 2 Performance parameters

	mass flux	η_s %	π
experiment near stall (EGV)	0.9381	83.8	1.562
experiment near stall (traverse)	0.9245	81.1	1.511
simulation near stall	0.9254	81.9	1.529
simulation with halved gap	0.9375	83.9	1.566
experiment near peak efficiency	1.005	85.4	1.483
simulation near peak efficiency	1.004	86.7	1.484
simulation with halved gap	1.016	87.7	1.488
experiment near choke	1.023	78.7	1.348
simulation near choke	1.027	79.5	1.351

The relative motion of casing and rotor tip was accounted for via the wall functions. Adiabatic wall boundary conditions were prescribed.

TU-Darmstadt Transonic Compressor Rig Simulation and Experiment

Overall Performance. Table 2 and Fig. 3 compare measured and computed stage isentropic efficiency and stage total

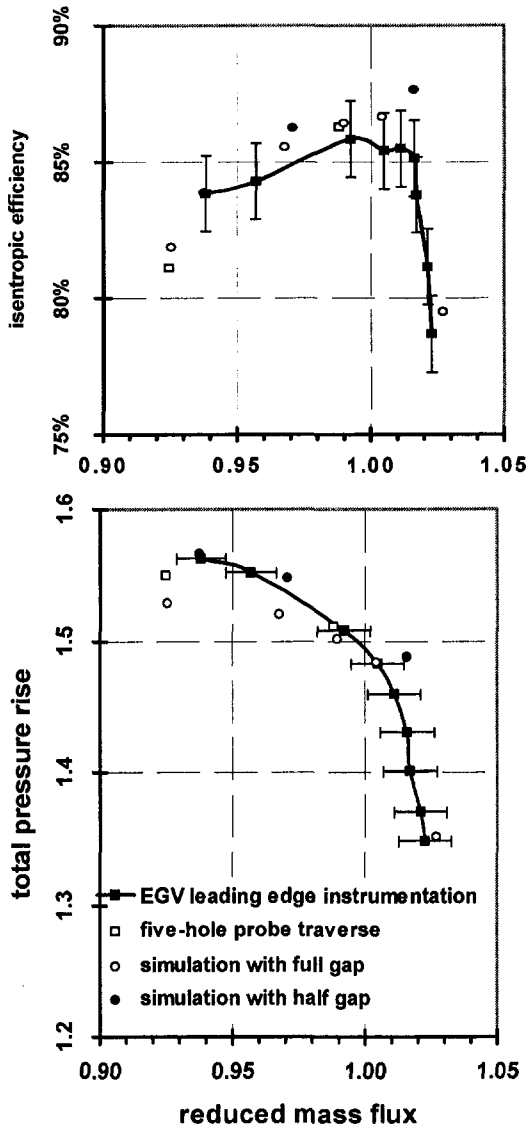

Fig. 3 Efficiency and pressure rise on the 100 percent speed line

pressure rise on the 100 percent speed line as a function of mass flux. The mass flux in Table 2 has been reduced by the design mass flux; isentropic efficiencies have been deduced from total pressures and total temperatures from the leading edge instrumentation of the exit guide vane. For the operating point near peak efficiency, the match between experiment and simulation is excellent. With the experimental back-pressure prescribed, the simulation almost exactly reproduces measured mass flux and pressure rise. The efficiency is slightly overpredicted but within the range of the experimental uncertainty. The rig efficiency deduced from the mechanical work input into the rig rather than the total temperatures is identical with the computed efficiency. The stall mass flux, obtained by traversing with a five-hole probe ahead of the EGV leading edge, is captured very well in the simulation. The efficiency is also predicted with surprising accuracy. For back-pressures higher than 1.53, driving the compressor to even lower mass fluxes, the simulation with full rotor tip gap exhibits slow divergence. Note that differences between traverse measurements and EGV leading edge measurements in Fig. 3 are due to the shortcomings in the EGV leading edge data, as explained earlier in the section on instrumentation. Near choke overall mass flux and pressure rise are predicted accurately.

Comparing simulations with full half gap one finds that the efficiency increase is in line with the experience base collected in rig tests, stipulating an efficiency loss of approximately 2 percent per 1 percent increase in clearance; see, e.g., Schmücker and Schäffler (1994).

Figure 4(*a*) compares measured and computed radial profiles of flux-averaged total temperature and pressure near peak efficiency. The match between measured and computed stator outflow profiles is excellent, even in the tip region. Work input into the flow as well as loss mechanisms and level are predicted correctly. Deviations

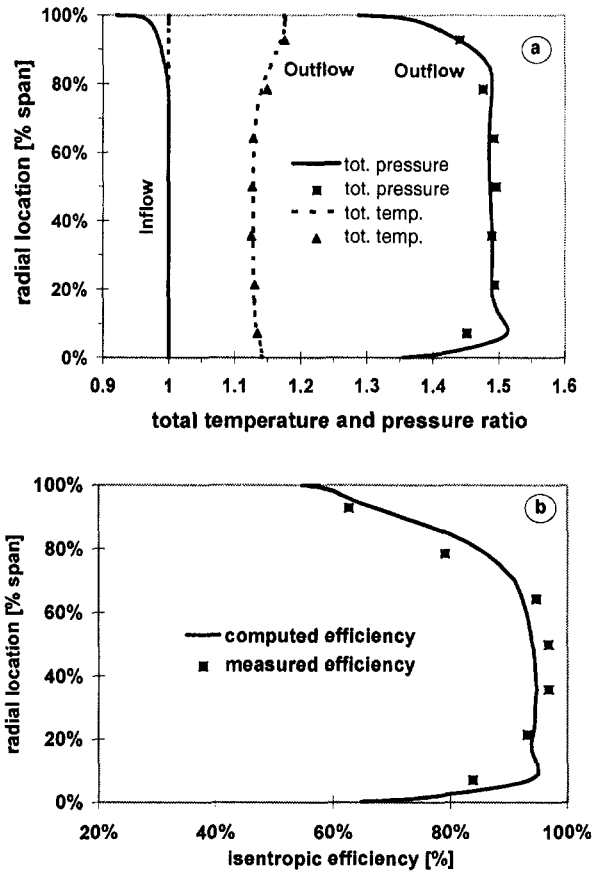

Fig. 4 Radial profiles of total pressure and temperature and efficiency at the design point

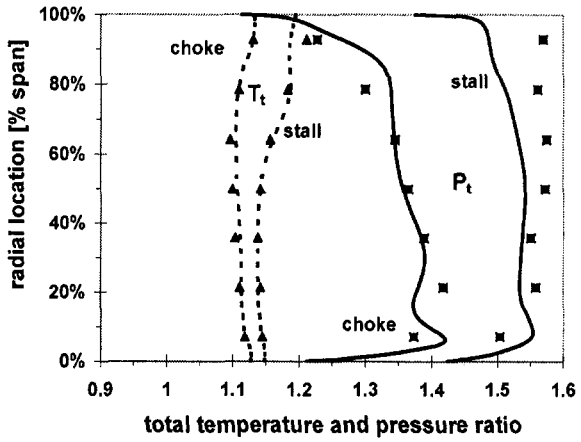

Fig. 5 Radial profiles of total pressure and temperature near stall and choke

show in the total pressure near the hub, possibly due to a larger radial grid spacing or to the flow disturbance created by holes for fasteners connecting spinner and rotor disk. Measured and computed radial profiles of the isentropic efficiency in Fig. 4(*b*) are in good agreement.

Figure 5 shows radial profiles of flux-averaged total pressure and temperature and isentropic efficiency near stall and choke. The temperature profiles at off-design conditions suggest that, particularly toward choke, the work input is still captured well. The deviation in the pressure profiles implies that loss levels, particularly toward stall, are not predicted with sufficient quantitative accuracy. Near stall the simulation underpredicts the total pressure from 40 percent span outward. It must, however, be pointed out that there is a difference in mass flux near stall between simulation and experiment due to the fact that the experiment was conducted at a mass flux 1.3 percent higher, i.e., at the operating point where the EGV leading edge data were taken.

Mach Number Distributions From Simulation Versus L2F Data

S1-Plane. Figure 6 compares computed and measured Mach number distributions near stall, peak efficiency, and choke at 95 percent span. Mach numbers for varying spanwise locations at peak efficiency are found in Fritsch et al. (1997).

Near peak efficiency, the trace of the tip vortex can clearly be identified in both experiment and simulation. Due to its low total pressure and streamwise momentum, the vortex core forms an extensive low-Mach region after being forced to comply with the pressure rise imposed by the passage shock. High-loss fluid subsequently collects on the adjacent pressure side. Experiment and simulation show good agreement in the interaction region, although the extent of the post-shock low Mach number region is slightly overpredicted. The typical bulged shock front, resulting from an interaction of shock and tip vortex, can clearly be identified in experiment and simulation.

Near stall, clearance vortex-shock interaction is overpredicted in the simulation, leading to a pronounced region of high blockage filled with low-momentum fluid. The higher blockage in the simulation may again be evidence of an operation closer to stall. Near choke, details of the shock structure and position are captured well. Since high tip gap pressure gradients do not arise ahead of the shock position on the pressure side, vortex formation is delayed until midchord; tip clearance vortex-shock interaction is captured well.

Meridional Plane. Figure 7 shows a projection of the Mach number in the midpitch plane onto the meridional plane. Measured and computed Mach numbers and shock position are in good agreement over the entire span. In the experiment the low Mach region

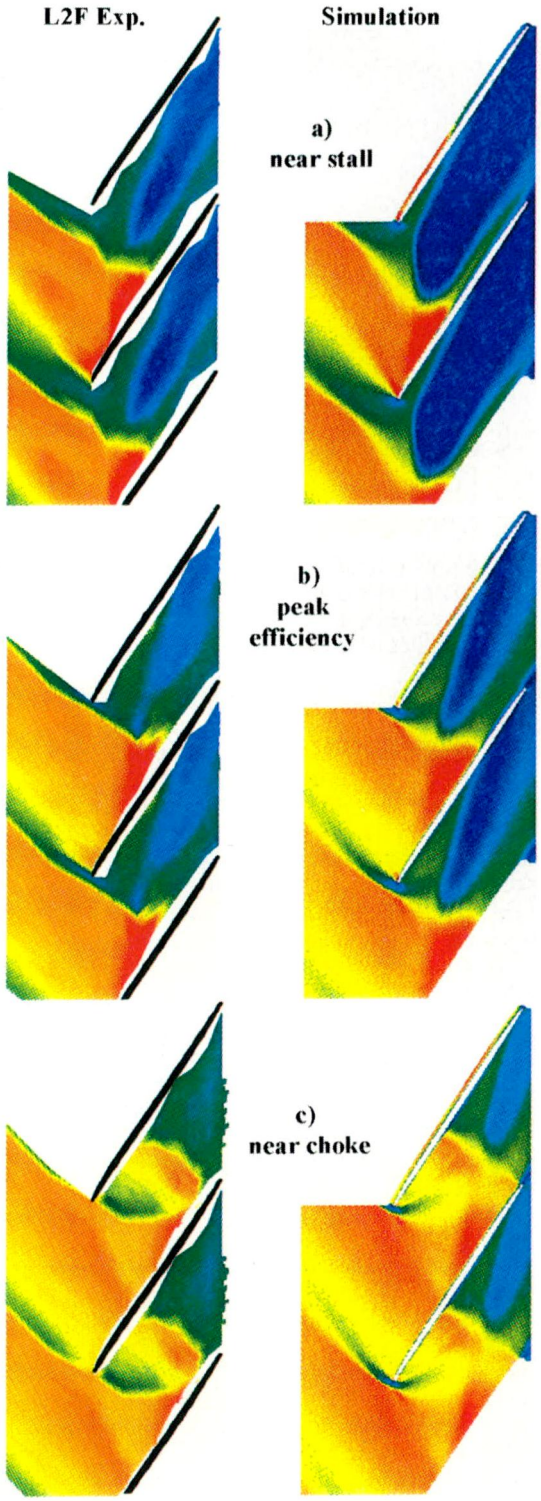

Fig. 6 Mach number distribution in a S1-plane at 95 percent span

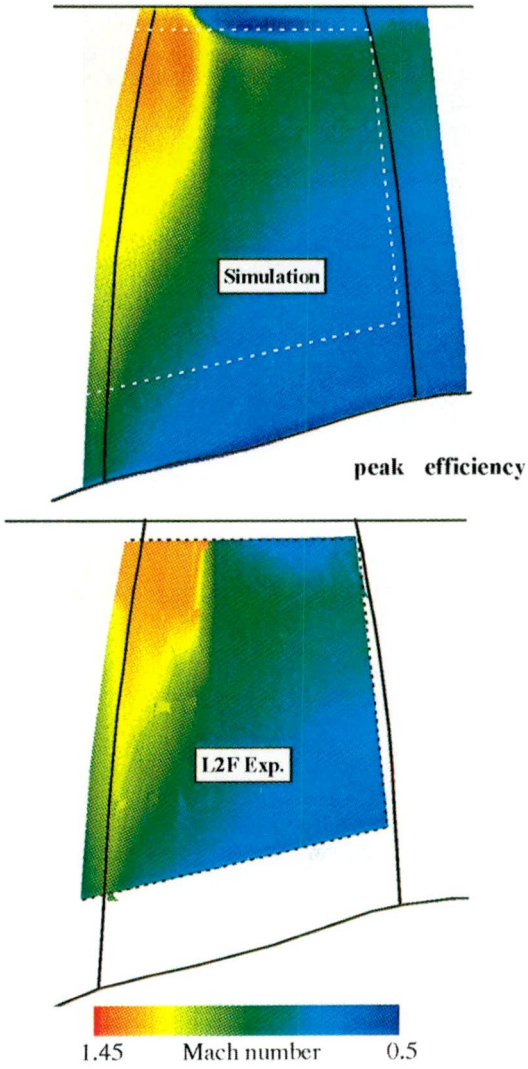

Fig. 7 Mach number distributions in a S2-plane at midpitch

Numerical Simulation of the Shock-Tip Leakage Vortex Interaction

With good agreement between experiment and simulation, also see Fritsch et al. (1997), it is reasonable to assume that the code captures the relevant flow features with sufficient qualitative and quantitative accuracy to allow a detailed analysis based on results of the simulation only. Although the size of the interaction region is slightly overpredicted, a tip clearance model, as suggested by Adamczyk et al. (1993), was not applied.

extends further inward (to about 85 percent span). It is caused by a strong shock-vortex interaction identified in Fig. 6 and also manifests itself in a pronounced drop in efficiency over the outer 30 percent span, compare Fig. 4(*b*). Low-energy material convects with the tip leakage vortex, forming a low Mach number region near the pressure side trailing edge, see Fig. 6(*b*).[1]

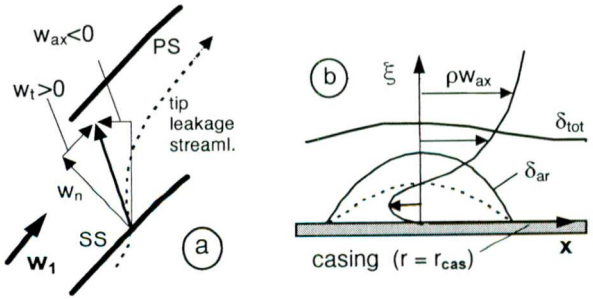

Fig. 8 Displacement from axially reversed tip leakage flow

[1] The dashed white line in Fig. 7 indicates the region where L2F measurements were taken.

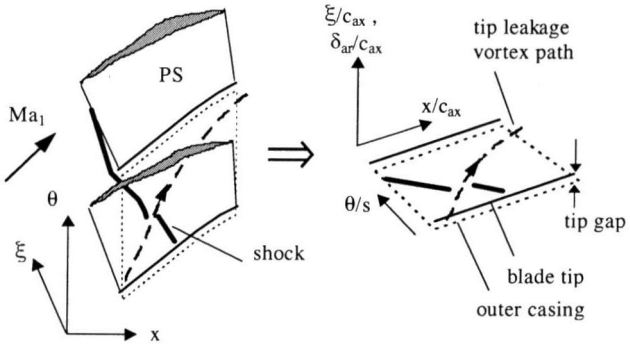

Fig. 9 Normalized blade passage; view from hub down on casing

Displacement by Axial Flow Reversal. Due to a high stagger at the tip, the strong part of the vortex induces a velocity component directed axially upstream. Although the dominating velocity component of the leakage fluid emanating from the gap is in the cross-passage direction (w_n) it retains a component in the through-flow direction (w_t); see Fig. 8(*a*).

While the three-dimensional nature of the flow close to the outer casing prevents the application of the classical boundary-layer approach, a local displacement thickness δ_{ar} from axially reversed flow, see Fig. 8(*b*), may be defined as:

$$-2\pi \int_0^{\delta_{ar}} (\rho w_{ax}(r_{cas} - \xi))d\xi = 0 \qquad (1)$$

Equation (1) captures the influence of both the tip clearance vortex and the separated boundary layer on the displacement in the reversed flow region. It does, however, not include the influence of the free shear layer. The displacement from axial flow reversal is presented in a normalized rectangular blade passage; see Fig. 9 for an illustration. The shock location on the displacement surface is obtained from the pressure gradient in the mean main flow direction. All lengths are normalized[2] by the rotor tip axial chord. A perspective radially inward from the casing is along increasing values of immersion ξ.

3D Displacement Surfaces. Figure 10(*a*) shows the displacement surface from tip leakage at *peak efficiency*. Near the blade suction surface, the leakage jet does not contribute to axial mass transport. With an axial velocity component pointing upstream, it leads to a flat displacement body. At midpitch, where the bow shock crosses the line defining onset of axial flow reversal, a strong interaction is observed and the displacement δ_{ar} reaches approximately 10 percent axial chord. The build-up of a normal shock is enforced, causing a weak shock-induced separation ahead of the displacement body in the casing boundary layer. Flow reversal extends all the way to the neighboring pressure side, feeding the gap flow with low energy/low velocity fluid. Following the work of Storer and Cumpsty (1993), this increases the deviation angle between the fluid emanating from the gap and the mean flow, leading to higher loss and increased blockage.

Tip Gap Height. A simulation near peak efficiency with halved tip gap, see Fig. 10(*b*), nearly halves the radial extent of the reversed flow region; it now no longer extents across the whole passage. Shock-vortex interaction is less pronounced with a more oblique shock. At other operation points a similar behavior was found for simulations with halved gap.

Off-Design Operation. Near choke, see Fig. 11(*a*), the tip clearance vortex starts to develop further downstream, i.e., after the in-passage shock generates a significant driving pressure gradient across the gap. With the throat area hardly affected, no mass flow reduction occurs near the casing, allowing a weak bow shock to establish itself. The gradient of the subsequent passage shock is locally reduced by strong shock-vortex interaction, leading to a diffuse compression system, see Fig. 6(*c*).

Near stall the strength of the clearance vortex has increased with the static pressure gradient across the gap and the fact that the vortex path and the bow shock are nearly parallel. In combination with an increased shock strength, shock-vortex interaction is substantially stronger than at operating points near peak efficiency, see Fig. 11(*b*). The shock-induced casing boundary layer separation extends over a third of the passage from the pressure side toward midpitch. The displacement body generated by casing boundary layer separation merges with the one due to tip clearance vortex-shock interaction.

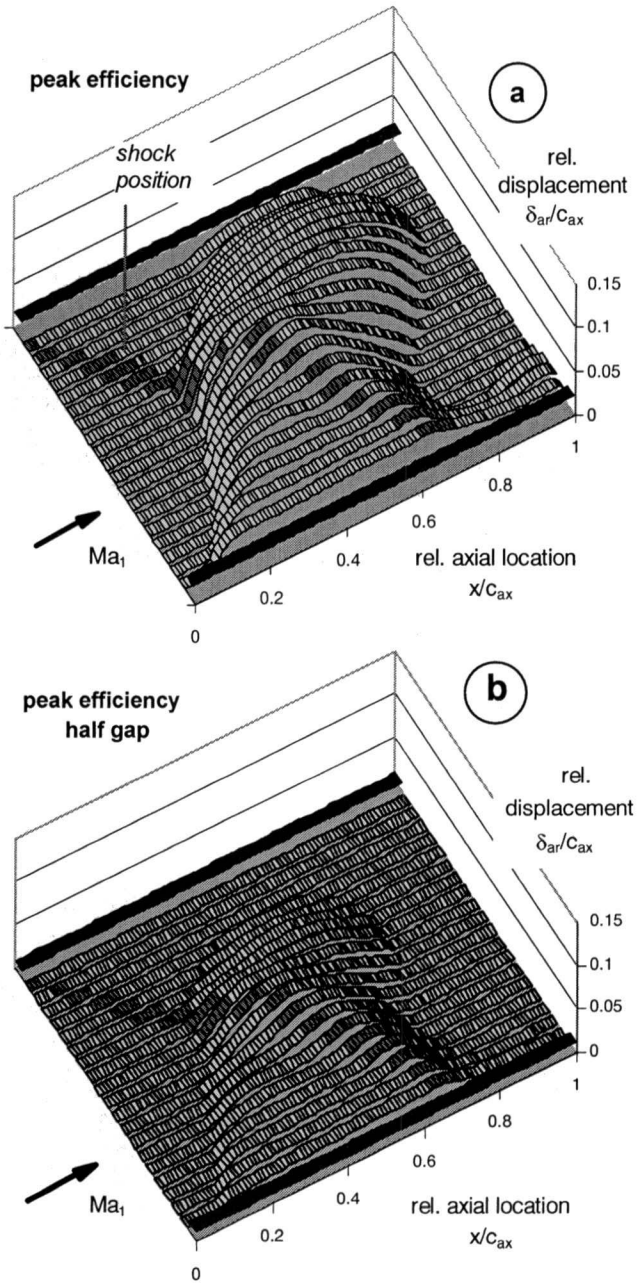

Fig. 10 Displacement δ_{ar} from axial reversed flow at peak efficiency; (*a*) nominal, (*b*) half tip gap

[2] With an aspect ratio based on the axial chord of roughly two, all lengths are translated into percent span.

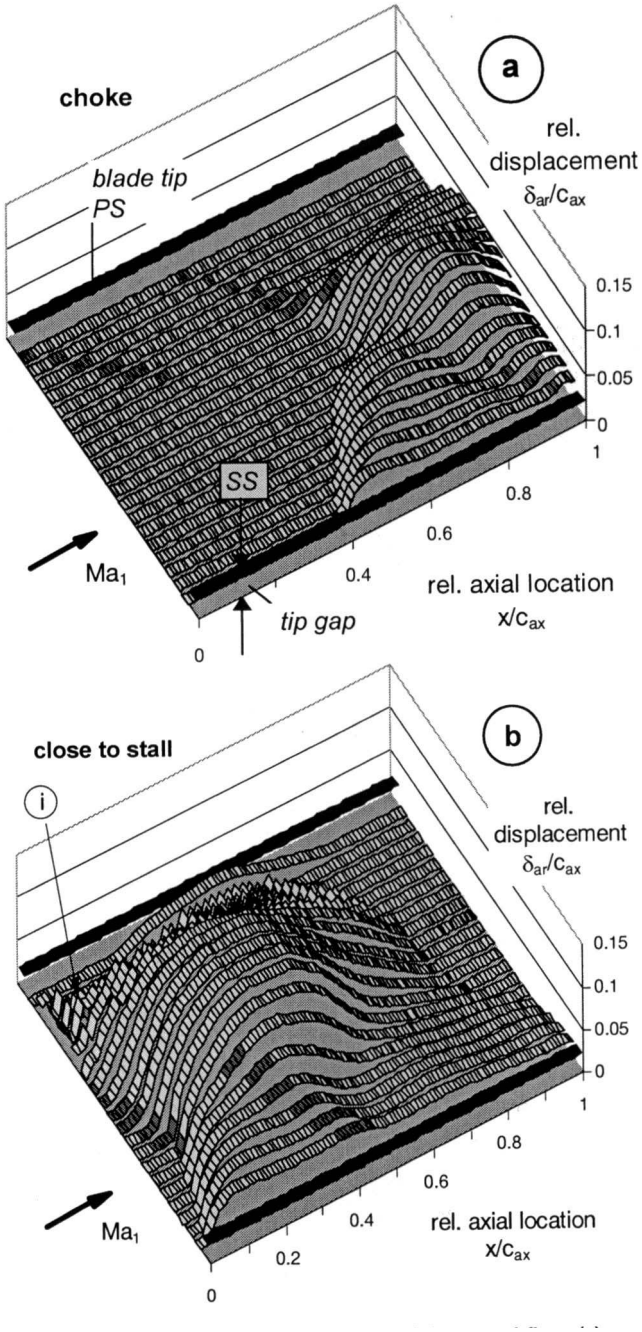

Fig. 11 Displacement thickness δ_{ar} from axial reversed flow: (*a*) near choke and (*b*) near stall

Stall Inception. The displacement in Fig. 11(*b*) indicates that (numerical) stall, defined as divergence of the simulation, indirectly results from a reduced mass flux near the tip. It is a consequence of a locally increased blockage and not of a boundary layer separation caused by excessive incidence or diffusion. In contrast to experimental observations for stall in a subsonic cascade by Stark and Bross (1996), massive recirculation induced by boundary layer separation is not apparent in the rear of the passage.

Just before stall onset, i.e., at the last stable operating point (rms density change down to 2×10^{-7}), instabilities, interpreted as stall precursors, are found. At point *i* in Fig. 11(*b*) periodic bow shock-induced separation of the casing boundary layer is observed. Farther downstream from *i* the separated boundary layer reduces the remaining corridor between pressure surface and strong interaction region; for an illustration see Fig. 12. Further reductions in mass flux likely lead to a fully separated boundary layer in turn causing a sudden upstream dislocation of the displacement body,

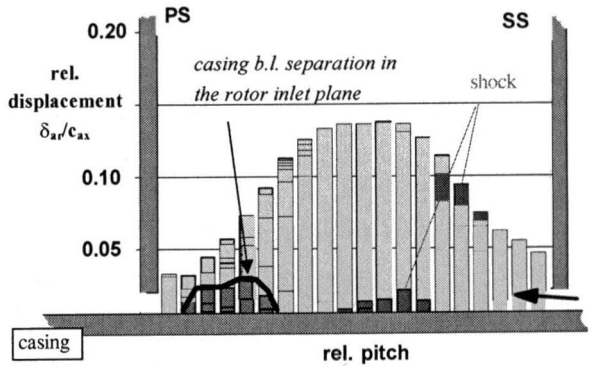

Fig. 12 Downstream view of displacement by axial flow reversal with casing boundary layer separation in the rotor inlet plane near stall

as was observed by Adamczyk et al. (1991). The instabilities in the *displacement* δ_{ar} are resolved due to the unsteady formulation of the time-marching scheme used to obtain the steady-state solution, but are not regarded as regular since the scheme is not time accurate. An adequate simulation of unsteady phenomena in an isolated compressor rotor by Copenhaver et al. (1997) showed

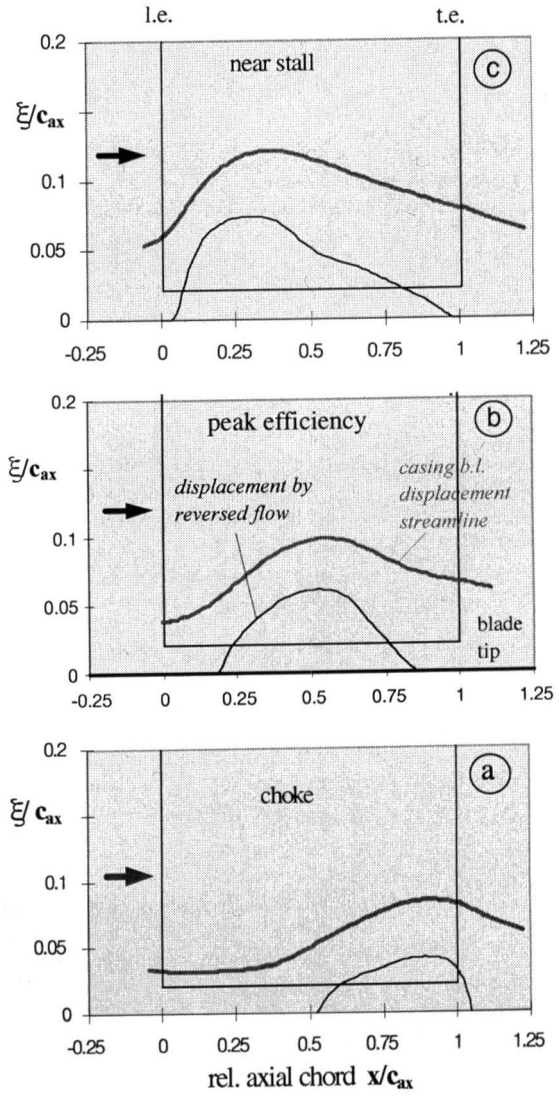

Fig. 13 S2-averaged displacement of incoming casing boundary layer streamline by axial flow reversal

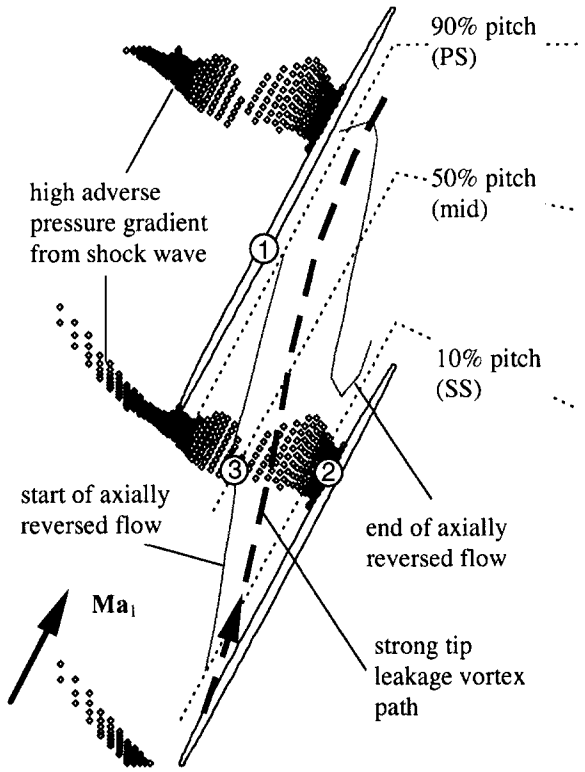

Fig. 14 Shock structure and displacement by tip leakage flow, outer casing, peak efficiency

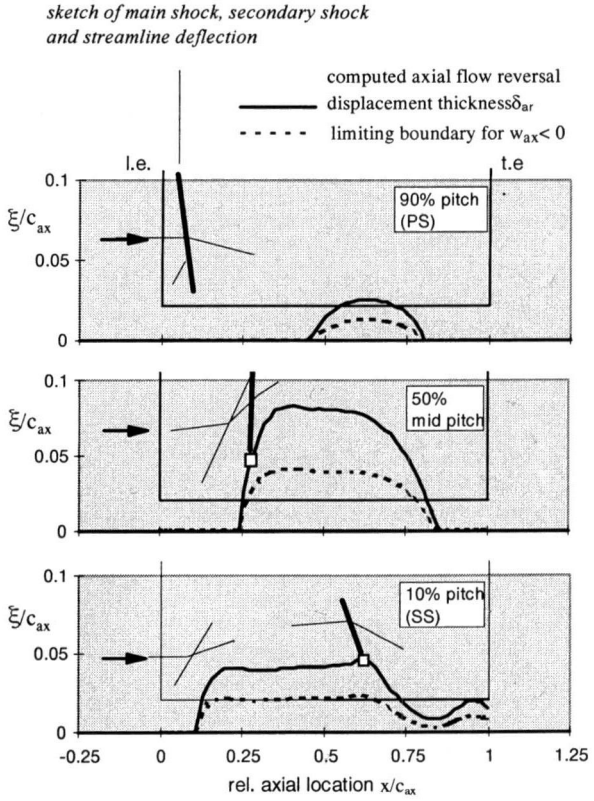

Fig. 15 Displacement and shock structure from tip leakage on quasi-stream surfaces at constant pitch (peak efficiency)

unsteadiness from shock oscillation only, while measurements revealed an additional post-shock unsteadiness in *static pressure* downstream of the strong vortex-shock interaction.

Pitch-Averaged Analysis. By integration of the pitchwise averaged flow, the displacement δ_{ar} from axial flow reversal and the total displacement δ_{tot} of the inlet boundary layer displacement streamline may be obtained in the meridional plane.

Near peak efficiency, Fig. 13(*b*) reveals an additional mean blockage due to flow reversal of approximately 3 percent axial chord. This substantially differs from a continuous increase in blockage between the in- and outlet plane as was obtained in subsonic plane cascades without clearance; see Stark and Hoheisel (1981). A characteristic maximum in the local displacement or blockage occurs at 30 percent chord near stall, at midchord near peak efficiency, and close to the trailing edge at choke; see Fig. 13.

Toward stall, the strength of the bow shock increases and its location moves upstream. Here the casing boundary layer has already thickened upstream of the inlet plane and only a little blockage increase occurs between rotor inlet and exit plane.

At choke, acceleration of the main flow decreases the displacement of the wall streamline over the front part of the passage; see Fig. 13(*c*). Only in this case, a linear transition function for the blockage near the casing yields a reasonable approximation within the blade passage.

Loss Mechanisms. The main sources of loss are difficult to separate in the rotor tip region because generation and convection of loss are superimposed. The streamline patterns given in Fig. 19–21 help distinguish loss convection from production.

Characteristic Flow Areas. At peak efficiency, the region of axially reversed flow close to the outer casing is outlined in Fig. 14. Three main features need to be pointed out: point 1 marking the onset of axial flow reversal flow on the pressure side, point 2 marking the shock location on the suction side, and point 3 marking the onset of strong shock-tip leakage interaction near midpitch. The shock structure, obtained from the pressure gradient in the mean flow direction at the outer casing, is plotted in Fig. 14; it reveals the typical bulge or shift of the passage shock near the strong interaction region.

Shock Structure. Figure 15 illustrates the dependence of the shock structure on the displacement from tip leakage; the locations of the three cut planes at constant pitch correspond to the dashed lines in Fig. 14. Near the suction side, at 10 percent pitch, the displacement from tip leakage decays with reducing driving pressure gradient across the shock and allows an oblique shock to establish itself. At midpitch the low-energy material concentrated in the vortex is forced to comply with the static pressure rise imposed by the shock. Here a large region of axially reversed flow leads to a λ-shaped normal shock configuration, as is typically observed at the casing; see, e.g., Hah and Wennerstrom (1991). Close to the pressure side and at 90 percent pitch a region of axially reversed flow is observed that supplies the leakage flow with low-energy material.

Secondary Loss Coefficient. For a quantitative discussion of the influence of the tip gap on secondary loss production, a weighted secondary loss coefficient is introduced by

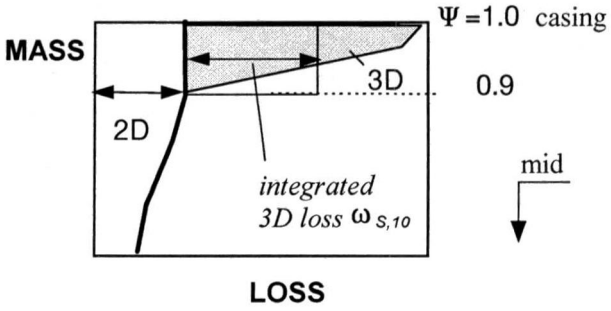

Fig. 16 Definition of secondary loss coefficient ω_{S10}

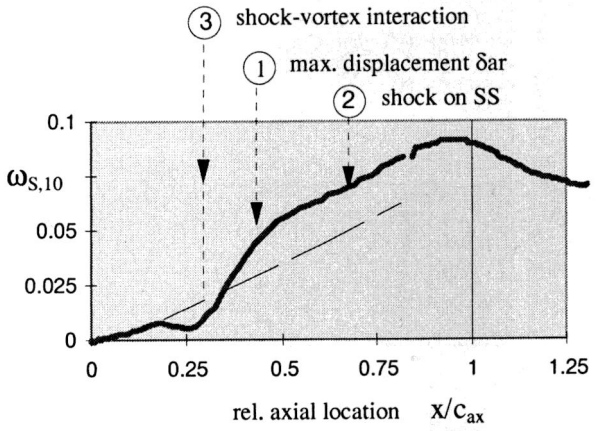

Fig. 17 Pitch-averaged secondary loss coefficient from leading to trailing edge at the rotor tip, peak efficiency

$$\omega_{S,10}(x) = 10 \int_{0.9}^{1.0} \omega_p(\psi, x)d\psi - \omega_p(\psi = 0.9, x) \qquad (2)$$

with

$$\omega_p(\psi, x) = (pt_{p1} - pt_p)/(pt_{p1} - p_{p1}), \qquad (3)$$

where ψ denotes the normalized stream function, assuming a value of $\psi = 0$ at the hub and $\psi = 1$ at the casing. Equation (2) represents an additional loss due to tip leakage and secondary flow, which is to be added to an approximately constant two-dimensional loss over the outer 10 percent of mass flux; see Fig. 16.

Peak Efficiency Operation. A continuous increase in the secondary loss coefficient is observed in Fig. 17 over the first 15 percent chord; it is the consequence of vortex dissipation and mixing. Farther downstream, at approximately 20 percent chord, where the shock strength is reduced (relative to its strength below $\psi = 0.9$) by shock-vortex interaction, a decay of the loss coefficient is calculated. The sudden increase in loss at point 3 in Fig. 17 signals the onset of strong shock-vortex interaction. At the local maximum in displacement from flow reversal near point 1, the rate of increase in loss matches the one over the first 20 percent chord, suggesting a change in loss mechanism back to vortex dissipation and mixing.[3] Figures 17 and 18, showing only a minor increase in loss and entropy over the front part of the passage, underscore that dissipation of vorticity in the strong part of the tip leakage vortex is less important compared to other loss sources.

Between point 1 and the suction side shock at point 2, low-energy material is driven into the neighboring passage by the large gap pressure gradient and wraps around the vortex core. The corresponding streamline pattern in the so-called weak part of the leakage vortex is found in Fig. 20. It is instructive to point out that the strong part of the leakage vortex, i.e., the core, does not increase its cross section upon going through the shock-imposed pressure rise, suggesting an exchange of kinetic energy for static pressure with a shock as the mechanism. The increase in blockage through the shock must therefore stem from material fed into the weak part of the leakage vortex and wrapped around the core.

Off-Design Operation. The loss development at off-design is illustrated in Fig. 18 in terms of the entropy.[4] High-loss fluid, i.e., high-entropy fluid, of the clearance vortex reaches the pressure surface around 60 percent chord at choke, around 30 percent chord at peak efficiency, and just aft of the leading edge at stall. A sudden increase in entropy, particularly pronounced at stall in Fig. 18(*a*), marks the strong interaction of shock and leakage vortex; it is a consequence of the increased shock strength and a large amount of low energy material collected in the vortex core.

In contrast to peak efficiency, the streamline pattern at stall, Fig. 19 left, reveals an increase in the cross section of the vortex core, as was already observed by Puterbaugh and Brendel (1997). The cross section increase across the shock-imposed pressure rise indicates an exchange of kinetic energy for static pressure as in subsonic flow and not a pressure rise complying with shock jump relations. With the assumption of a (locally) inviscid flow, the subsequent decrease in vorticity, qualitatively deduced from the streamline pattern in Fig. 19 left, may be explained with Kelvin's theorem.

[3] The dashed line helps visualize the matching slopes.

[4] With a color range tailored to resolve the loss best at choke, casing boundary layer loss cannot be discerned.

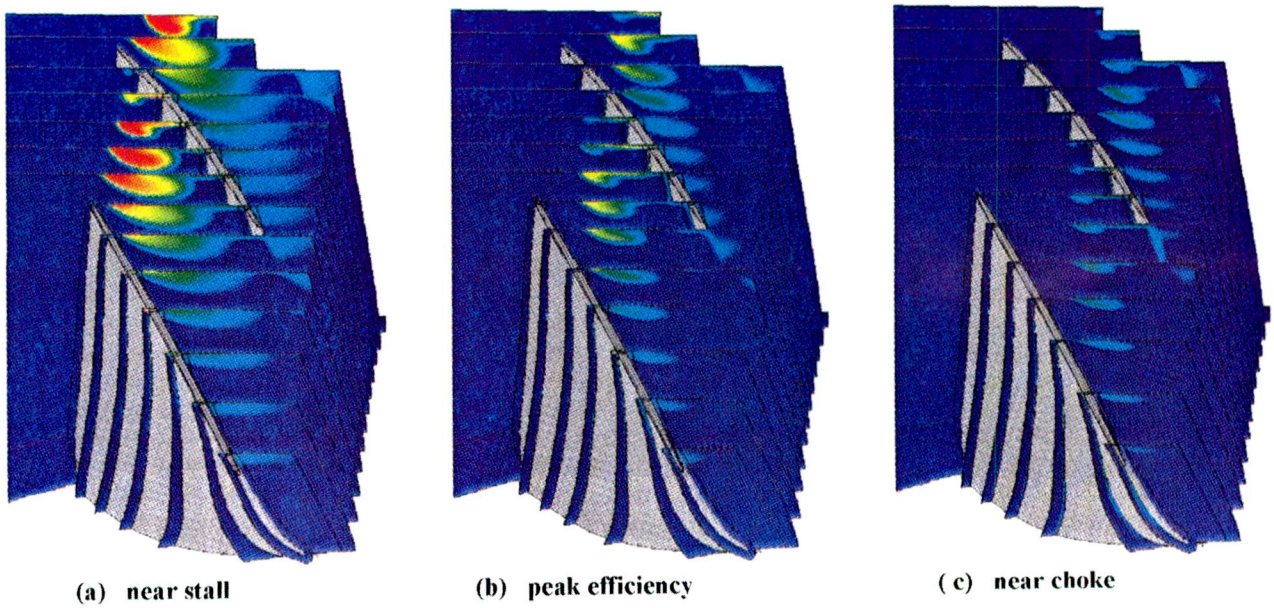

Fig. 18 Production and convection of entropy (loss)

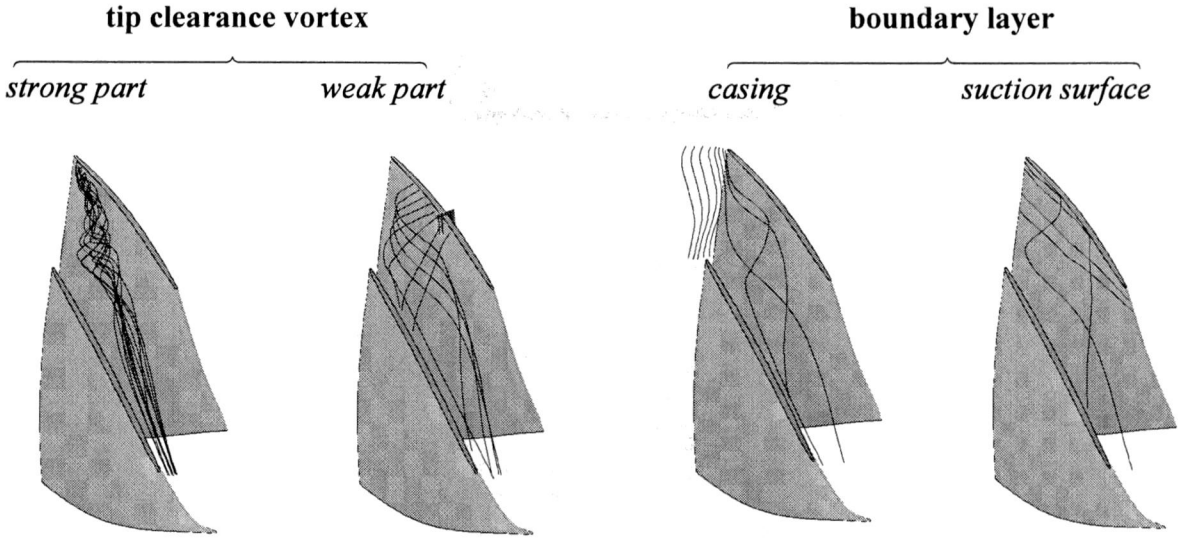

Fig. 19 Tip leakage vortex, streamlines near stall

Convective Loss Transport. At peak efficiency, Fig. 20, about two thirds of the incoming rotor casing boundary layer is driven into the tip gap. Although streamlines inside the suction side boundary layer do not show a pronounced radial crossflow from profile boundary layer separation or corner stall, the incoming casing boundary layer streamlines near stall in Fig. 19 turn toward higher flow angles, ending almost parallel to the pitchwise direction in the inlet plane. Only a small part of the flow near the casing enters the blade passage, traveling through a corridor near the pressure surface. At stall, Stark and Bross (1996) observed casing boundary layer fluid separating ahead of the rotor inlet plane and entering neighboring passage after moving radially inward.

Near choke and peak efficiency the strong part of the clearance vortex core is mostly fed low-loss fluid. Near stall, however, it is fed high-loss fluid from the (weak part of the) clearance vortex in the neighboring passage; compare Figs. 19 and 20. As a conse-

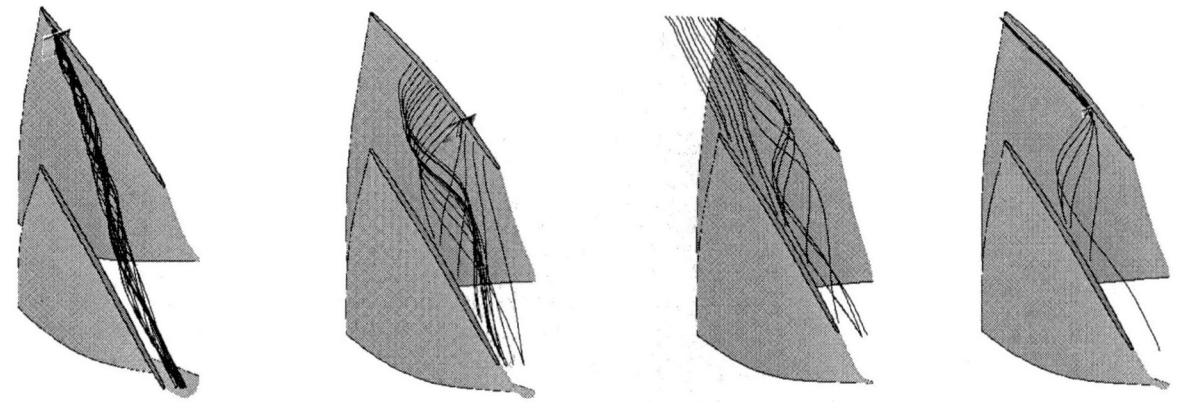

Fig. 20 Tip leakage vortex, streamlines at peak efficiency

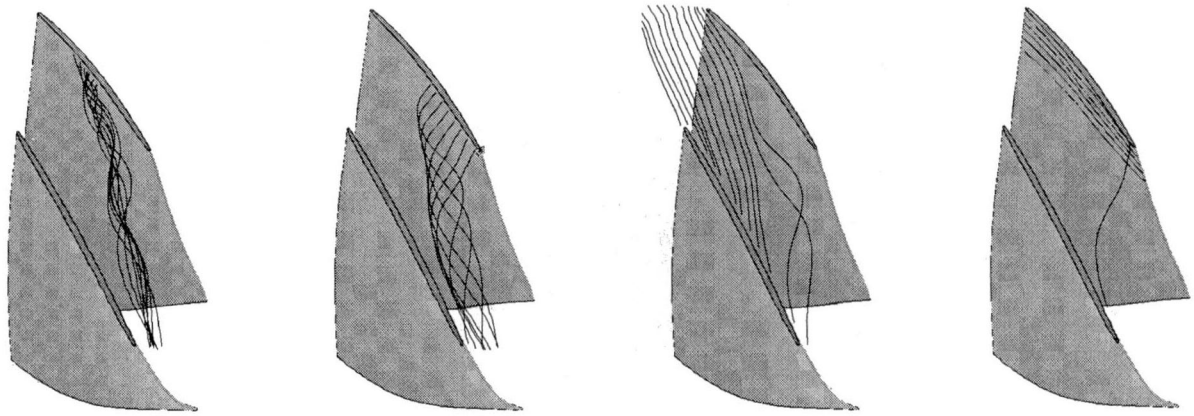

Fig. 21 Tip leakage vortex, streamlines at choke

quence thereof, a confined structure of the weak part of the leakage vortex is observed at choke. The comparatively small angle deviation, see Fig. 21, between leakage flow and main flow indicates that high-energy fluid with comparative large tangential velocities enters the tip gap.

Influence on Design Mach Number Distribution

Modeling for S1/S2-Design. Because viscous endwall blockage is included in most S2-design codes, see De Ruyck and Hirsch (1981), it is important to investigate the deviation from a standard blockage distribution caused by the predominantly nonviscous three-dimensional tip leakage effect. The deviations of the pitch-averaged blockage δ_{tot} in the three-dimensional simulations from a continuous increase between rotor in- and outlet plane was approximated and fed into a S2 throughflow streamline curvature method. With the effective casing contour set by a displaced outermost streamline, this results in a change in the stream tube geometry. Departures of the actual displacement from rotational symmetry, see Fig. 10, were not accounted for.

Mach Number Distributions. In Fig. 22, rotor Mach number distributions from a three-dimensional simulation are compared to those obtained in a two-dimensional simulation on S1-surfaces via a coupled Euler/Integral boundary layer scheme; see, e.g., Hoeger and Broichhausen (1992). Dashed lines correspond to S1-solutions with standard stream tube geometry, while thin solid lines correspond to solutions obtained with a tube geometry modified for tip

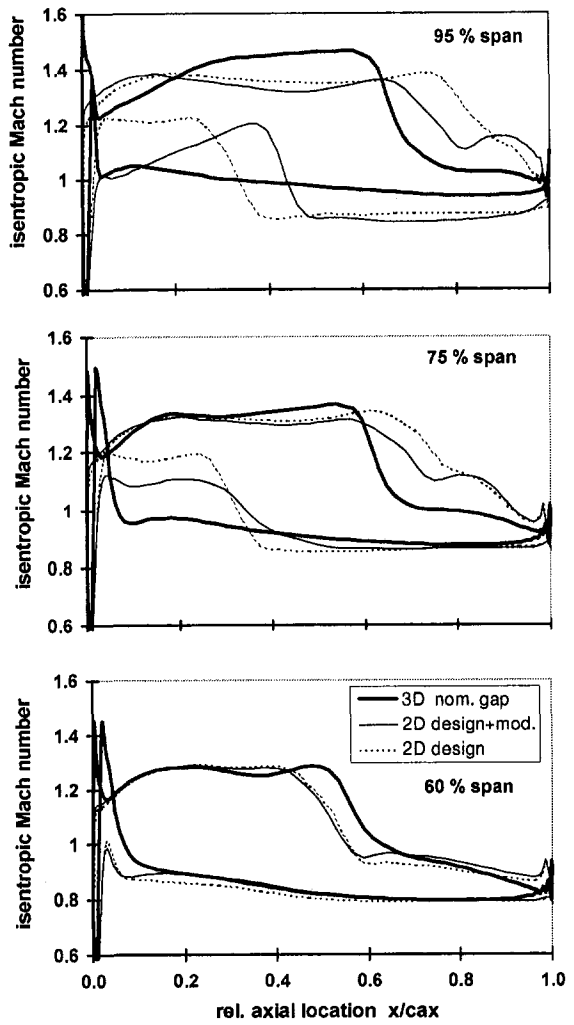

Fig. 22 Dependence of the design Mach number distribution on blockage from tip leakage

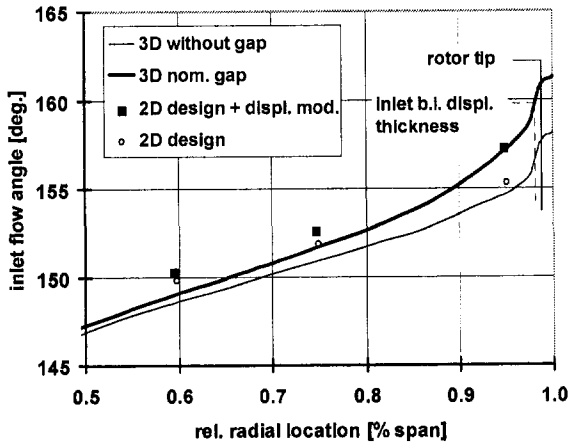

Fig. 23 Dependence of the inlet flow angle on the blockage from tip leakage at peak efficiency

leakage blockage. In the S1-simulations back-pressures obtained in the three-dimensional simulation were prescribed except at 95 percent span, where an increased value was set to approximately reproduce the shock position of the three-dimensional simulation.

At 60 percent span the throat area reduction due to tip leakage blockage only slightly affects the Mach number distribution. At 75 percent span, on the contrary, the result of the S1-simulation with additional blockage is in improved agreement with that of the three-dimensional simulation. Near the casing, at 95 percent span, the flow is essentially of a three-dimensional nature. With little displacement at the pressure side found in the three-dimensional simulation, see Fig. 10(*b*), the use of a pitch-averaged (additional) blockage in the S1-simulation results in a second shock on the pressure surface. On the suction side the flow is supersonic and the Mach number distribution for a rotationally symmetric stream tube shape is closely linked to blade geometry by the so-called unique incidence condition, see Lichtfuß and Starken (1974). Differences in the suction surface Mach number distribution between the three-dimensional simulation and the S1-simulation with rotationally symmetric stream tube geometry cannot be attributed to blockage, see Tweed et al. (1988), or stream tube shape alone.[5] Further three-dimensional simulations without casing boundary layer did not significantly improve the agreement. Tip gap height variation could eliminate only half of the difference in the suction side Mach number. These observations strongly suggest a three-dimensional shock structure and rotationally asymmetric stream surface geometry as the major cause for the difference between two-dimensional and three-dimensional simulation.

Inlet Flow Angle. For supersonic inflow, the inlet flow angle at choked operation is dictated by the unique incidence condition. While the suction surface Mach number is found to be nearly unaffected by the stream tube geometry, inlet flow angle and mass flow strongly depend on it. With the additional blockage from the tip leakage modeled in the S2-solution, the S1-simulation does reproduce the 2 deg increase in the inlet flow angle due to tip leakage as given by the three-dimensional simulations, see Fig. 23. As already pointed out by Suder and Celestina (1996), additional blockage from tip leakage vortex/shock interaction at reduced mass flow increases the inlet flow angle and seems to be closely linked to stall onset.

Conclusions

With a moderate loading and a relative inlet Mach number of 1.35 the single stage transonic rig at TU Darmstadt is representative of current high compressor front stages. The three-

[5] The investigations for several AVDR transition functions were performed as part of the diploma work by A. Peters at the TU Aachen, 1992.

dimensional flow was investigated in detail using the Navier–Stokes solver TRACE_S. Comparison of simulations near peak efficiency, choke and stall to extensive L2F data and EGV leading edge data demonstrated the solver's predictive capabilities. Detailed analyses of simulations were performed to gain insight into the complex mechanisms governing tip leakage vortex-shock-interaction.

1 The phenomenon is addressed in terms of an entirely new variable: the *displacement* of the casing streamline *by axial flow reversal.* The displacement surface at the casing is of a three-dimensional shape. Near peak efficiency, its maximum radial extent amounts to approximately 10 percent axial chord at midpitch, in the immediate vicinity of the strong shock-vortex-interaction.
2 In the present study radial and pitch-wise extent of the displacement are almost proportional to the gap height.
3 While the vortex core goes through the shock-induced pressure rise without change in cross section at peak efficiency it substantially increases in cross section near stall. This indicates that, contrary to stall, only the weak part of the vortex contributes to the increased blockage at peak efficiency.
4 The vortex core is fed with high-loss/low-momentum fluid from the neighboring passage, particularly at stall.
5 Reducing the mass flux increases the blockage from axial flow reversal induced by tip clearance effects until only a small corridor near the blade pressure surface remains open to the flow. At stall a bow shock-induced separation of the casing boundary layer further reduces the corridor and localized instability waves occur on the displacement surface in the post shock region.
6 Near peak efficiency a pitch-averaged secondary loss coefficient, defined over the outer 10 percent mass flux near the casing, shows an almost continuous increase of loss from leading to trailing edge. In the strong shock-vortex-interaction region, however, a steep increase in loss is found.

A simple model was established, which approximately accounts for the additional local blockage from tip leakage flow in a S2 throughflow method. The resulting modified stream tube geometry subsequently was input into a two-dimensional Euler simulation coupled to an integral boundary layer scheme.

1 The two-dimensional blade surface Mach number distributions with the modified stream tube geometry show improved agreement with those of the three-dimensional simulation. Even near the casing, where the flow is predominantly three-dimensional, the modified two-dimensional solution is better in line with the three-dimensional simulation. It fails, however, to correctly predict the shock position.
2 The mean inlet flow angle predicted in the two-dimensional simulation, however, quite accurately approximates the increase due to tip leakage blockage predicted by the three-dimensional simulation.

Particularly at reduced mass flux, an understanding of phenomena relating tip clearance flow to the onset of stall is crucial and can lead to substantial extension in operating range. The simple model for the additional local blockage induced by the tip clearance vortex allows to approximately introduce three-dimensional effects into S1/S2 compressor simulations already at an early stage of the design process.

Acknowledgments

The support for code development and validation as well as experimental and numerical investigation of the compressor rig through the German Ministry of Education and Research under contract numbers 20T9402 of the E3E program and 0327040J of the AG Turbo program is gratefully acknowledged. The authors would also like to thank Mr. C. Blaha of the Department of Gas Turbines and Flight Propulsion at Technical University of Darmstadt for providing the experimental data and Dr. G. Ramm at MTU München GmbH for his assistance in post-processing the numerical data.

The code was jointly developed by MTU München GmbH and the Institute for Propulsion Technology of the German Aerospace Research Establishment (DLR).

References

Adamczyk, J. J., Celestina, M. L., Beach, T. A., and Barnett, M., 1990, "Simulation of Three-Dimensional Viscous Flow Within a Multistage Turbine," ASME JOURNAL OF TURBOMACHINERY, Vol. 112, pp. 370–376.

Adamczyk, J. J., Celestina, M. L., and Greitzer, E. M., 1993, "The Role of Tip Clearance in High-Speed Fan Stall," ASME JOURNAL OF TURBOMACHINERY, Vol. 115, pp. 28–39.

Blaha, C., Hennecke, D. K., Fritsch, G., Hoeger, M., and Beversdorff, M., 1997, "Laser-2-Focus Measurements in a Transonic Compressor Blisk-Rotor and Comparison With 3D Numerical Simulations," presented at the ISABE Conference.

Chen, G. T., Greitzer, E. M., Tan, C. S., and Marble, F. E., 1991, "Similarity Analysis of Compressor Tip Clearance Flow Structure," ASME JOURNAL OF TURBOMACHINERY, Vol. 113, pp. 260–271.

Chima, R. V., 1998, "Calculation of Tip Clearance Effects in a Transonic Compressor Rotor," ASME JOURNAL OF TURBOMACHINERY, Vol. 120, pp. 131–140.

Copenhaver, W. W., Puterbaugh, S. L., and Hah, C., 1997, "Unsteady Flow and Shock Motion in a Transonic Compressor Rotor," *Journal of Propulsion and Power,* Vol. 13, No. 1.

Copenhaver, W. W., Mayhew, E. R., Hah, C., and Wadia, A. R., 1996, "The Effect of Tip Clearance on a Swept Transonic Compressor Rotor," ASME JOURNAL OF TURBOMACHINERY, Vol. 118, pp. 230–239.

Cybyk, B. Z., Car, D., and Hah, C., 1997, "Impact of CFD on Test and Evaluation at the Compressor Research Facility," AIAA Paper No. 97-2881.

Dawes, W. N., 1993, "The Extension of a Solution-Adaptive Three-Dimensional Navier–Stokes Solver Towards Geometries of Arbitrary Complexity," ASME JOURNAL OF TURBOMACHINERY, Vol. 115, pp. 283–295.

Denton, J. D., 1986, "The Use of a Distributed Body Force to Simulate Viscous Effects in 3D Flow Calculations," ASME Paper No. 86-GT-144.

De Ruyck, J., and Hirsch, C., 1981, "Investigations of an Axial Compressor End-Wall Boundary Layer Prediction Method," ASME *Journal of Engineering for Power,* Vol. 103, No. 1.

Dorney, D. J., and Sharma, O. P., 1997, "Evaluation of Flow Field Approximations for Transonic Compressor Stages," ASME JOURNAL OF TURBOMACHINERY, Vol. 119, pp. 445–451.

Fritsch, G., and Giles, M. B., 1995, "An Asymptotic Analysis of Mixing Loss," ASME JOURNAL OF TURBOMACHINERY, Vol. 117, pp. 367–374.

Fritsch, G., and Möhres, W., 1997, "Multistage Simulations for Turbomachinery Design on Parallel Architectures," presented at the Parallel Computational Fluid Dynamics Conf.

Fritsch, G., Hoeger, M., Blaha, C., and Bauer, D., 1997, "Viscous 3D Compressor Simulation on Parallel Architectures," AIAA Paper No. 97-2876.

Hah, C., and Wennerstrom, A. J., 1991, "Three-Dimensional Flowfields Inside a Transonic Compressor With Swept Blades," ASME JOURNAL OF TURBOMACHINERY, Vol. 113, pp. 241–251.

Hah, C., Puterbaugh, S. L., and Copenhaver, W. W., 1997, "Unsteady Aerodynamic Flow Phenomena in a Transonic Compressor Stage," *Journal of Propulsion and Power,* Vol. 12, No. 3, May–June.

Hoeger, M., and Broichhausen, K. D., 1992, "Prediction of 2D Viscous Transonic Flow in Compressor Cascades Using a Semi-Empirical Shock/Boundary-Layer Interaction Methods," ASME Paper No. 92-GT-277.

Huber, F. W., and Ni, R. R., 1989, "Application of a Multi-Stage 3D Euler Solver to the Design of Turbines for Advanced Propulsion Systems," AIAA Paper No. 89-2578.

Jennions, I. K., and Turner, M. G., 1993, "Three-Dimensional Navier–Stokes Computations of Transonic Fan Flow Using an Explicit Flow Solver and an Implicit k–ϵ Solver," ASME JOURNAL OF TURBOMACHINERY, Vol. 115, pp. 261–272.

LeJambre, C. R., Zacharias, R. M., Biederman, B. P., Gleixner, A. J., and Yetka, C. J., 1998, "Development and Application of a Multistage Navier–Stokes Solver: Part II—Application to a High-Pressure Compressor Design," ASME JOURNAL OF TURBOMACHINERY, Vol. 120, pp. 215–223.

Lichtfuß, H. J., and Starken, H., 1974, "Supersonic Cascade Flow," in: *Progress in Aerospace Science,* Küchemann, ed., Vol. 15, Pergamon Press Ltd., Oxford, New York.

Nikolos, I. K., Douvikas, D. I., and Papailliou, K. D., 1995, "Theoretical Modelling of Relative Wall Motion Effects in Tip Leakage Flows," ASME Paper No. 95-GT-88.

Perrin, G., and Leboeuf, F., 1992, "Analysis of Three-Dimensional Viscous Flow in a Supersonic Axial Flow Compressor Rotor with Emphasis on Tip Leakage Flow," ASME Paper No. 92-GT-388.

Puterbaugh, S. L., and Brendel, M., 1997, "Tip Clearance Flow-Shock Interaction in a Transonic Compressor Rotor," *Journal of Propulsion and Power,* Vol. 13, No. 1.

Rhie, C. M., Gleixner, A. J., Spear, D. A., Fishberg, C. J., and Zacharias, R. M., 1998, "Development and Application of a Multistage Navier–Stokes Solver: Part I—Multistage Modeling Using Body Forces and Deterministic Stresses," ASME JOURNAL OF TURBOMACHINERY, Vol. 120, pp. 205–214.

Rhie, C. M., Zacharias, R. M., Hobbs, D. E., Sarathy, K. P., Biederman, B. P., LeJambre, C. L., and Spear, D. A., 1994, "Advanced Transonic Fan Design Procedure Based on a Navier–Stokes Method," ASME JOURNAL OF TURBOMACHINERY, Vol. 116, pp. 291–297.

Schmücker, J., and Schäffler, A., 1994, "Performance Deterioration of Axial Compressors Due to Blade Defects," AGARD-CP-558.

Stark, U., and Hoheisel, H., 1981, "The Combined Effect of Axial Velocity Density Ratio and Aspect Ratio on Compressor Cascade Performance," ASME *Journal of Engineering for Power*, Vol. 103, No. 1.

Stark, U., and Bross, S., 1996, "Endwall Boundary Layer Separations and Loss Mechanisms in Two Compressor Cascades of Different Stagger Angle," AGARD CP-571.

Storer, J. A., and Cumpsty, N. A., 1991, "Tip Leakage Flow in Axial Compressors," ASME JOURNAL OF TURBOMACHINERY, Vol. 113, pp. 252–259.

Storer, J. A., and Cumpsty, N. A., 1993, "An Approximate Analysis and Prediction Method of Tip Clearance Loss in Axial Compressors," ASME Paper No. 93-GT-40.

Suder, K. L., and Celestina, M. L., 1996, "Experimental and Computational Investigation of the Tip Clearance Flow in a Axial Compressor Rotor," ASME JOURNAL OF TURBOMACHINERY, Vol. 118, pp. 218–229.

Turner, M. G., 1996, "Multistage Turbine Simulations With Vortex-Blade Interaction," ASME JOURNAL OF TURBOMACHINERY, Vol. 118, pp. 643–653.

Tweedt, D. L., Schreiber, H. A., and Starken, H., 1988, "Experimental Investigation of the Performance of a Supersonic Compressor Cascade," ASME JOURNAL OF TURBOMACHINERY, Vol. 110, pp. 456–466.

The Role of Tip Leakage Vortex Breakdown in Compressor Rotor Aerodynamics

M. Furukawa

M. Inoue

K. Saiki

K. Yamada

Department of Mechanical Science and Engineering, Kyushu University, Fukuoka, 812-8581, Japan

The breakdown of tip leakage vortex has been investigated on a low-speed axial compressor rotor with moderate blade loading. Effects of the breakdown on the rotor aerodynamics are elucidated by Navier–Stokes flow simulations and visualization techniques for identifying the breakdown. The simulations show that the leakage vortex breakdown occurs inside the rotor at a lower flow rate than the peak pressure rise operating condition. The breakdown is characterized by the existence of the stagnation point followed by a bubblelike recirculation region. The onset of breakdown causes significant changes in the nature of the tip leakage vortex: large expansion of the vortex and disappearance of the streamwise vorticity concentrated in the vortex. The expansion has an extremely large blockage effect extending upstream of the leading edge. The disappearance of the concentrated vorticity results in no rolling-up of the vortex downstream of the rotor and the disappearance of the pressure trough on the casing. The leakage flow field downstream of the rotor is dominated by the outward radial flow, resulting from the contraction of the bubblelike structure of the breakdown region. It is found that the leakage vortex breakdown plays a major role in characteristic of rotor performance at near-stall conditions. As the flow rate is decreased from the peak pressure rise operating condition, the breakdown region grows rapidly in the streamwise, spanwise, and pitchwise directions. The growth of the breakdown causes the blockage and the loss to increase drastically. Then, the interaction of the breakdown region with the blade suction surface gives rise to the three-dimensional separation of the suction surface boundary layer, thus leading to a sudden drop in the total pressure rise across the rotor.

Introduction

"Vortex breakdown" or "vortex bursting" is a well-known phenomenon widely observed in streamwise slender vortices in external vortical flows and internal swirling flows, for example leading edge vortices over delta wings, swirling jets in combustion chambers, and swirling flows in draft tubes of hydraulic turbines and cyclone separators. For the last four decades, practical importance of the vortex breakdown has yielded a large number of experimental and theoretical studies, which have been reviewed by Hall (1972), Leibovich (1978, 1984), Escudier (1988), and Delery (1994). These studies show that two types of vortex breakdown (bubble and spiral types) can be distinguished, that the occurrence of breakdown brings about rapid expansion of the vortex, substantial changes in its velocity field and large-scale flow fluctuations, and that major flow parameters influencing the breakdown are the adverse pressure gradient in the streamwise direction and the swirl intensity of the vortex. In spite of the extensive research, the mechanism of vortex breakdown still remains one of the unresolved and intriguing problems in fluid mechanics. However, the existence of a stagnation point on the centerline of vortex structure is universally accepted as a distinctive feature of the vortex breakdown.

It is well known that compressor rotor performance is affected significantly by tip leakage flow. Behavior and structure of the tip leakage flow have been investigated by experimental and computational research work. Its nature is characterized by rolling-up of a shear layer between leakage jet and main stream. The rolling-up forms a streamwise slender vortex, a so-called tip leakage vortex, in the same manner as the leading edge vortices over delta wings. It is no wonder that the vortex breakdown would occur in the tip leakage flow field under some circumstances. However, no one turned his attention to the occurrence of the leakage vortex breakdown until it happened to be noticed the same time by Furukawa et al. (1998) and Schlechtriem and Lotzerich (1997). Although much progress has been achieved in research on the tip leakage flow, all facets of the leakage vortex breakdown have gone unnoticed.

Schlechtriem and Lotzerich (1997) detected the leakage vortex breakdown caused by a sudden deceleration across a passage shock in a transonic axial compressor rotor at near-stall conditions. They pointed out that a blockage resulting from the breakdown had a major impact on stall. Meanwhile Furukawa et al. (1998) found out that the leakage vortex breakdown occurred even at a design point for a low-speed diagonal compressor rotor with high blade loading. They showed that the breakdown gave rise to substantial changes in the behavior of the tip leakage flow: no rolling-up of the leakage vortex downstream of the rotor, disappearance of the casing pressure trough at the aft part of the rotor passage, large spread of low-energy fluid in the leakage flow. The leakage vortex breakdown has just begun to be studied.

The present study deals with the breakdown of the tip leakage vortex in a low-speed axial compressor rotor with moderate blade loading. The onset of breakdown, its growth at near-stall conditions, and its role in characteristic of the rotor performance are investigated by Navier–Stokes flow simulations with a high-resolution upwind scheme based on a TVD formulation.

Background

Formation of the tip leakage vortex can be clearly observed in a phase-locked velocity field just downstream of a low-speed axial compressor rotor (Inoue et al., 1986) and in a phase-locked pres-

Contributed by the International Gas Turbine Institute and presented at the 43rd International Gas Turbine and Aeroengine Congress and Exhibition, Stockholm, Sweden, June 2–5, 1998. Manuscript received by the International Gas Turbine Institute February 1998. Paper No. 98-GT-239. Associate Technical Editor: R. E. Kielb.

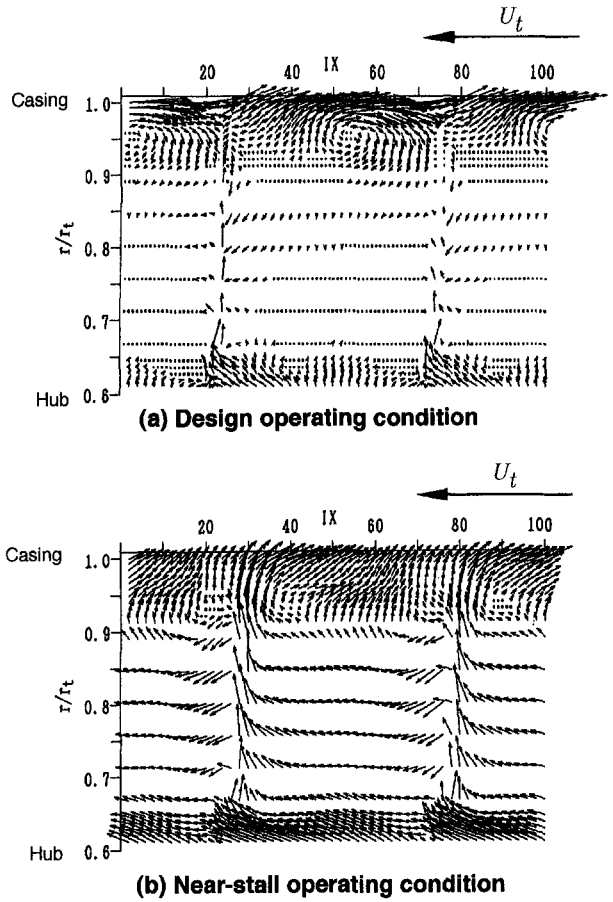

Fig. 1 Secondary flow vectors measured downstream of rotor with tip clearance of 1.7 percent of tip chord, from Inoue et al. (1991)

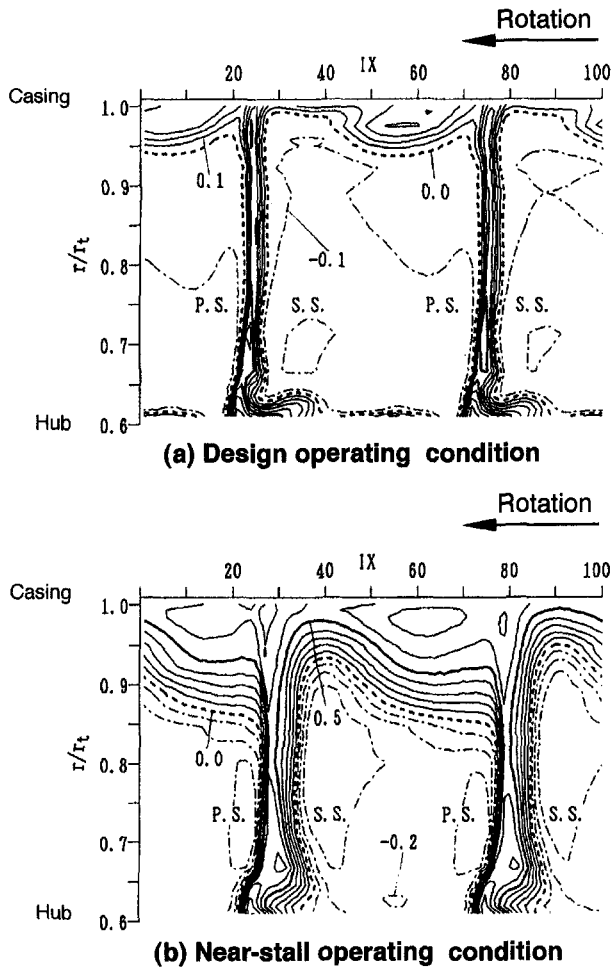

Fig. 2 Relative kinetic energy defect distributions measured downstream of rotor with tip clearance of 1.7 percent of tip chord, from Inoue et al. (1990)

sure field on a casing wall (Inoue and Kuroumaru, 1989). Distinctive features of the tip leakage vortex find their expression in coiling of secondary flow vectors, accumulation of low-energy fluid and casing wall pressure trough. At near-stall operating conditions, however, considerable change in the distinctive features has been observed (Inoue et al., 1990, 1991).

Figures 1 and 2 show secondary flow vectors (Inoue et al., 1991) and relative kinetic energy defect distributions (Inoue et al., 1990) measured just downstream of the low-speed compressor rotor by a hotwire for design and near-stall operating conditions. The rotor has a moderate blade loading and is the same as one investigated in the present study. For the design operating condition, the rolling-up of the leakage vortex and the accumulation of the low-energy fluid around the vortex are readily seen near the casing. On the other hand, for the near-stall condition, there is not a rolling-up of the vortex, but an outward radial flow in the secondary flow field near the casing (Fig. 1(*b*)). Figure 2(*b*) indicates that for the near-stall condition, spread of the low-energy fluid accumulating on the casing is so large that it extends to about 40 percent of span from the casing. This large spread of the low-energy fluid implies a significant growth of the casing wall boundary layer. However, it seems that flow separation on the suction surface near the blade tip does not occur in spite of the near-stall condition, considering that the low-energy fluid near the casing accumulates on the pressure side and that width of the blade wake near the tip is not so thick as to indicate the occurrence of local flow separation on the blade.

Figures 3 and 4 show phase-locked distributions of the casing pressure field measured in the same rotor as Figs. 1 and 2 (Inoue et al., 1991). For the design operating condition, a pressure trough extends from the minimum pressure region close to the blade suction surface to the rotor exit, as shown in Fig. 3(*a*). It is evident that the pressure trough corresponds to a trajectory of the tip leakage vortex (Inoue and Kuroumaru, 1989). Figure 4(*a*) indicates that there is a high-pressure fluctuation region along the pressure trough, which is the effect of the peripheral swaying of the leakage vortex (Inoue and Kuroumaru, 1984). Meanwhile, for

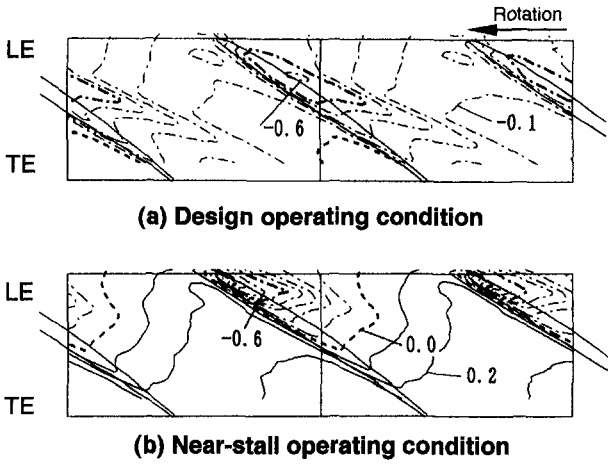

Fig. 3 Phase-locked distributions of mean pressure measured on casing wall in rotor with tip clearance of 1.7 percent of tip chord, from Inoue et al. (1991)

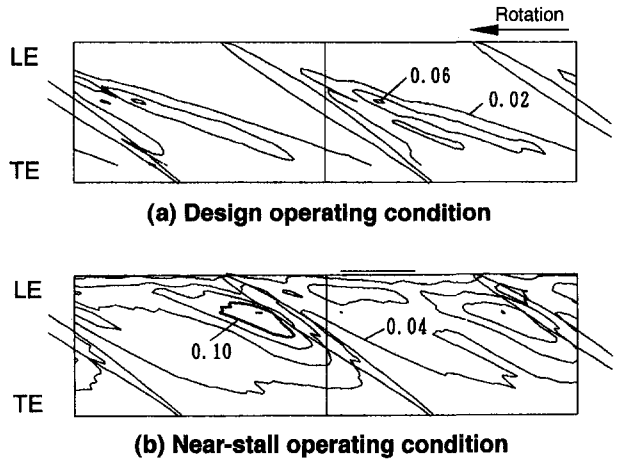

Fig. 4 Phase-locked distributions of pressure fluctuation measured on casing wall in rotor with tip clearance of 1.7 percent of tip chord, from Inoue et al. (1991)

the near-stall operating condition shown in Fig. 3(*b*), the pressure trough formed near the leading edge decays in the streamwise direction, disappearing at the aft part of the passage. Moreover, it is observed in Fig. 4(*b*) that a highly fluctuating pressure field appears across the fore part of the passage and has the highest fluctuation near the pressure side.

It is found that the behavior of the tip leakage vortex near stall is substantially different from that at the design point: no rolling-up of the vortex downstream of the rotor, the outward radial flow in the leakage flow field downstream of the rotor, the large spread of the low-energy fluid in the leakage flow, and disappearance of the casing pressure trough at the aft part of the rotor passage. The behavior is very similar to that observed in a diagonal flow compressor rotor with high blade loading where the breakdown of the leakage vortex occurs at the aft part of the passage (Furukawa et al., 1998). Recently, Lakshminarayana et al. (1995) have also observed no rolling-up of the leakage vortex and the outward radial flow in a leakage flow field downstream of an axial compressor rotor for the peak pressure rise operating condition. To investigate what causes the behavior of the leakage vortex at near-stall conditions, we have carried out the present numerical study.

Test Compressor Rotor

The present investigation was performed on the low-speed isolated axial compressor rotor. In previous studies tip leakage flow fields behind and inside the rotor were measured at the design operating condition by Inoue et al. (1986), and Inoue and Kuroumaru (1989). At near-stall conditions the behavior of the tip leakage flow (Figs. 1, 2, and 3) and statistical characteristics of the casing wall pressure fluctuation (Fig. 4) were investigated experimentally by Inoue et al. (1990, 1991).

The test compressor stage has a design flow coefficient ϕ (mean axial velocity divided by rotor tip speed) of 0.5 and a design total pressure rise coefficient ψ (total pressure rise divided by dynamic pressure corresponding to rotor tip speed) of 0.4. The hub/tip ratio of the rotor is 0.6, with the blade tip diameter of 449 mm. The rotor blade has NACA 65 series profile sections designed by free vortex operation with an axial inlet flow condition, and the number of blades is 12. The blade tip section has a solidity of 1.0 and a chord length of 117.5 mm. In the present study the blade tip clearance τ is 2.0 mm (1.7 percent of tip chord). Details of aerodynamic design parameters of the rotor are given in a previous paper of Inoue et al. (1986).

Numerical Simulation Method

Numerical Scheme. In numerical flow simulations performed for the present study, the compressible Navier–Stokes equations were solved by an unfactored implicit upwind relaxation scheme (Furukawa et al., 1992, 1995). The numerical method used is outlined in the following.

The three-dimensional, Reynolds-averaged Navier–Stokes equations were discretized in space using a cell-centered finite volume formulation and in time using the Euler implicit method. To capture the tip leakage vortex sharply near the casing wall, the inviscid fluxes were evaluated by a high-resolution upwind scheme based on a TVD formulation (Furukawa et al., 1991; Inoue and Furukawa, 1994) where the Roe's approximate Riemann solver of Chakravarthy (1986) and the third-order accurate MUSCL approach of Anderson et al. (1986) with the Van Albada limiter were implemented. Most of numerical flow solvers for turbomachinery problems, however, are based on artificial dissipative schemes in which the inviscid terms are discretized in central differencing manners with artificial dissipation terms. According to studies on the application of high-resolution upwind schemes to the Navier–Stokes equations by van Leer et al. (1987), and Swanson and Turkel (1993), it is found that built-in numerical dissipation terms for the high-resolution upwind schemes using Riemann solvers automatically become much smaller in boundary layers than those for the artificial dissipative schemes. This means that the high-resolution upwind schemes do not contaminate the boundary-layer velocity profile. It should be realized that the high-resolution upwind schemes based on the Riemann solvers have excellent shear-layer capturing capability, as well as shock-wave capturing capability. In the present scheme, the viscous fluxes were determined in a central differencing manner with Gauss's theorem, and the algebraic turbulence model of Baldwin and Lomax (1978) was employed to estimate the eddy viscosity. The boundary layer transition was determined in accordance with an original criterion of transition in the Baldwin and Lomax model. Unfactored implicit equations derived with no approximate factorization were solved by a point Gauss-Seidel relaxation method. The present scheme was stable up to a Courant number of about 100.

Computational Grids. A composite grid system with structured **H**-type grids was used to simulate the tip leakage flow field accurately. A computational domain was divided into two zones. One zone was a main flow region outside the blade tip clearance, and the other was the tip clearance region. In each zone a structured **H**-type grid was generated as shown in Fig. 5. The main grid consisted of 80 cells in the streamwise direction (52 cells on the blade), 96 cells in the spanwise direction, and 64 cells in the

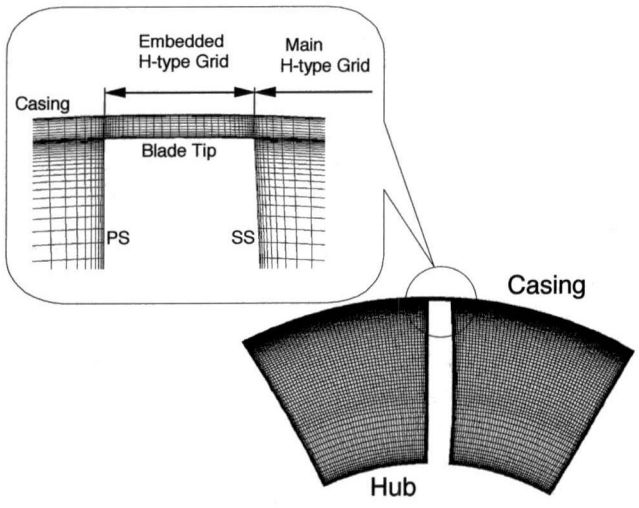

Fig. 5 Typical cross-sectional view of computational grid

pitchwise direction. In order to capture the tip leakage vortex sharply, the grid resolution near the casing was kept high even in the midpitch region, as seen in Fig. 5. Meanwhile the spanwise grid resolution near the hub was lower than that near the casing. The grid embedded in the blade tip clearance consisted of 52 × 32 × 16 cells in the chordwise, pitchwise, and spanwise directions, respectively. The whole grid system had 518,144 cells. The ratio of the minimum grid spacing on solid walls to the blade tip chord length was under 5×10^{-5} to evaluate the viscous fluxes at the walls by applying the no-slip and adiabatic conditions with no wall function method. This minimum grid spacing gave $y^+ \leq 1$ at the walls.

Boundary and Computational Conditions. Boundaries of the computational domain are formed by cell interfaces in the cell-centered finite volume approach. Hence, the boundary conditions must be imposed by the fluxes through the boundaries. In the present scheme, fictitious cells were introduced just outside all the boundaries, and values of conserved variables satisfying boundary conditions were given at the fictitious cells. Using the fictitious cells, numerical fluxes through the boundaries were evaluated in the same way as interior cell interfaces. This treatment of the boundary conditions prevented nonphysical reflections at the inflow and outflow boundaries, because the inviscid fluxes through the boundaries were evaluated according to the approximate Riemann solver, in which the signal propagation properties of the Euler equations were simulated. Details of the boundary conditions can be found from the previous study of Furukawa et al. (1995).

The inflow boundary conditions were given by experimental results measured upstream of the rotor using a five-hole cobra probe (Inoue et al., 1986). The inlet boundary layer on the casing wall had a thickness of 6 mm and a displacement thickness of 0.7 mm. The thickness of the casing wall boundary layer is larger than the blade tip clearance of 2 mm.

The outflow boundary conditions were prescribed in a manner similar to that of Ayder and Van den Braembussche (1994) using a static pressure given at one reference point of the outflow boundary and the flow solution at interior cells adjacent to the outflow boundary. It should be noted that the outflow boundary conditions implemented in the present scheme allowed the pressure to vary on the boundary according to effects of streamline curvature and swirl. The pressure at the reference point was adjusted in the iterative procedure of the computation so that the total flow rate imposed would be satisfied. The numerical simulations were carried out at flow conditions ranging from the design flow rate of $\phi = 0.5$ to a low flow rate of $\phi = 0.35$.

Validity of Numerical Simulation. The present scheme has been already applied to calculations of steady transonic cascade flows (Furukawa et al., 1991), an unsteady flow induced by the trailing edge vortex shedding in a transonic turbine cascade (Furukawa et al., 1992) and a three-dimensional flow in a diagonal flow compressor rotor (Furukawa et al., 1995). In these previous studies the validity of the scheme has been presented by comparing numerical results with experimental ones.

To show the validity of numerical simulations performed in the present study, computational and experimental results at the design flow rate ($\phi = 0.5$) are presented in Fig. 6. In the figure, tangentially averaged flow properties downstream of the rotor are shown, and the abscissa denotes the nondimensional distance from the hub wall. Agreement between computational and experimental results is good except in the vicinity of the hub wall. The discrepancy in the hub region may be due to the relatively low grid resolution in the spanwise direction near the hub; on the other hand the discrepancy in the tip region is not so large that it must be considered an effect caused by a difference in the tip leakage vortex structure between the computational and experimental results. A computational result of the casing wall pressure distribution, which will be presented later for the design operating condition in Fig. 7, agrees well with the experimental result shown in Fig. 3(*a*). It is clearly seen that the pressure trough corresponding to the leakage vortex

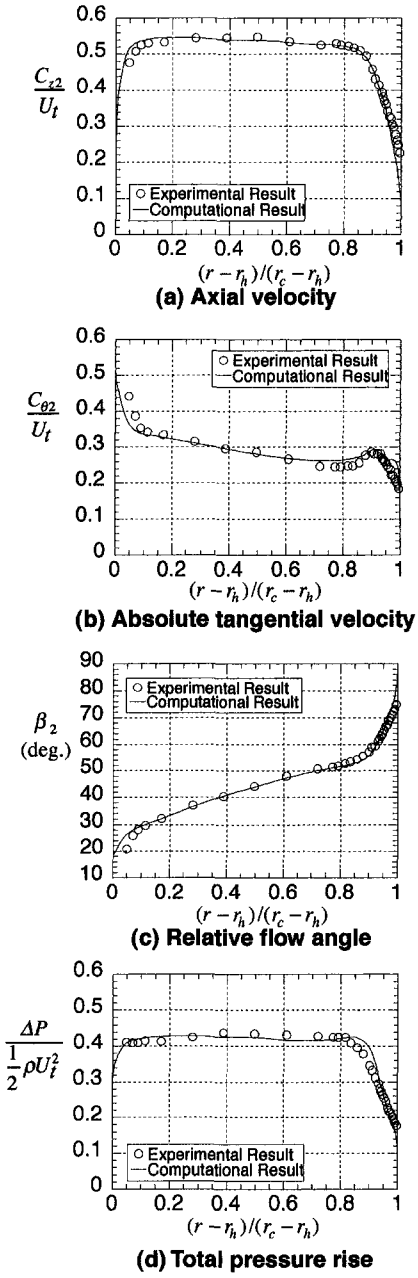

Fig. 6 Spanwise distributions of tangentially averaged flow downstream of rotor for design operating condition

trajectory is well captured in the computation. This implies that flow phenomena near the casing are correctly simulated. Consequently, the tip leakage flow field inside the rotor can be investigated by analyzing the numerical results in detail.

Visualization Techniques for Identifying Vortex Breakdown

The tip leakage flow field in the rotor is highly complicated, in which the leakage vortex interacts with the nonuniform main flow and the boundary layer on the casing wall having a motion relative to the rotor. To understand the complicated flow field, numerical solutions are visualized by three-dimensional computer graphics. It is not easy to detect the vortex breakdown in the tip leakage flow field using only conventional visualization techniques such as three-dimensional particle traces in a computational space or contour plots on computational surfaces. It should be noted that

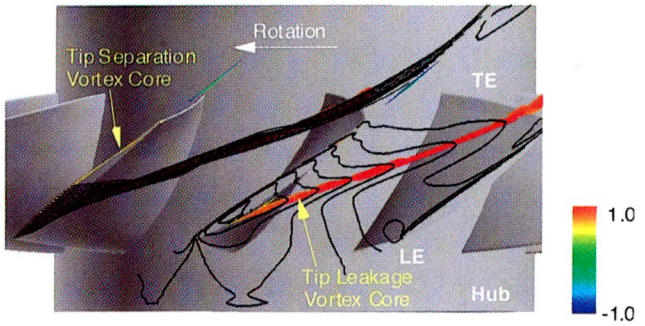

Fig. 7 Vortex cores colored with normalized helicity distribution, casing wall pressure distribution (black lines in right passage) and leakage streamlines surrounding tip leakage vortex (black lines in left passage) for design operating condition (ϕ = 0.50)

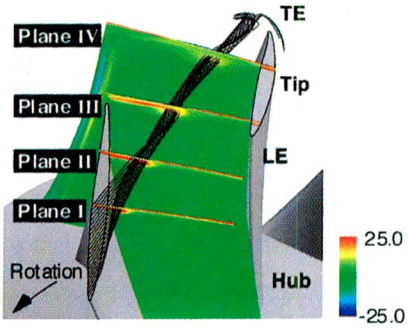

Fig. 8 Streamwise absolute vorticity distributions on crossflow planes perpendicular to tip leakage vortex and leakage streamlines (black lines) for design operating condition (ϕ = 0.50)

particle traces from a region of "vortex core" are crucial to identification of the vortex breakdown. If one does not determine the location of the tip leakage vortex core, which forms a part of numerical solution and is not known in advance, a sufficient number of particle traces must emanate from appropriate locations corresponding to the vortex core by trial and error. Such post-processing for the vortex breakdown identification is quite time consuming. Poor processing cannot extract valuable information about the vortex breakdown from the numerical solutions. Therefore, the following two techniques are introduced here to detect the onset of the tip leakage vortex breakdown readily:

- Semi-analytic method for determining the vortex core
- Normalized helicity

The semi-analytic method of Sawada (1995) very similar to the critical-point theory (Perry and Chong, 1987) is introduced as an intelligent method for determining the vortex core. In Sawada's method, assuming that a local velocity field can be linearly parametrized in a tetrahedral cell, streamline equations become integrable analytically for the cell and as a result the obtained streamline expression provides a possible vortex centerline in the cell. In the present study the computational cell crossed by the vortex centerline is defined as a fraction of the "vortex core." The three-dimensional location of the whole vortex core region can be readily determined by a collection of the computational cells defined as the fractions of the vortex core. The determination of the vortex core makes the identification of the vortex breakdown much easier and more reliable, as will be shown in the numerical results.

In order to investigate the nature of the tip leakage vortex quantitatively, a normalized helicity similar to that used by Levy et al. (1990) is introduced. The normalized helicity used in the present study is the same as that found in the previous paper (Furukawa et al., 1998) which is defined as

$$H_n = \frac{\vec{\xi} \cdot \vec{w}}{|\vec{\xi}||\vec{w}|} \tag{1}$$

where $\vec{\xi}$ and $\vec{w}$ denote vectors of the "absolute" vorticity and the "relative" flow velocity, respectively. Note that the normalized helicity is not defined by the "relative vorticity," but by the "absolute vorticity," considering that secondary flow fields in the rotor are dominated by the component of "absolute vorticity" along the "relative flow" direction. The normalized helicity is the cosine of the angle between the absolute vorticity and relative velocity vectors. This means that the magnitude of the normalized helicity tends to unity in the vortex core, and that its sign indicates the direction of swirl of the vortex relative to the streamwise velocity component. In contrast to the streamwise vorticity, the normalized helicity allows us to examine the nature of the vortex quantitatively, regardless of the decay of vorticity in the streamwise direction. Distributions of the normalized helicity along the vortex core are very useful in finding out changes in the nature of the tip leakage vortex caused by the breakdown.

Results and Discussion

Tip Leakage Vortex Without Breakdown. For the test compressor rotor, the breakdown of the tip leakage vortex is not observed in the range of flow rate from the design operating point (ϕ = 0.5) to the peak pressure rise operating point (ϕ = 0.38). The distinctive behavior of the tip leakage vortex without breakdown is presented here.

A tip leakage flow field at the design flow rate (ϕ = 0.5) is shown in Fig. 7, which is a perspective view from the casing side. In this figure vortex cores identified by the above-mentioned semi-analytic method are colored with the normalized helicity defined by Eq. (1). Red on the vortex cores corresponds to the normalized helicity of 1.0, green to zero, and blue to −1.0. Black lines in the right passage denote a distribution of the casing wall pressure, while black lines in the left passage denote tip leakage streamlines. A distinct pressure trough on the casing wall is clearly seen from the blade suction side near the minimum pressure region to the rotor exit. Its behavior agrees well with the experimental result shown in Fig. 3(*a*). The tip leakage vortex core identified is located along the pressure trough and has the normalized helicity of about unity. The positive high value of the normalized helicity means that the tip leakage vortex is tightly rolled up. The rolling-up of the leakage vortex is also observed as a spiraling of the leakage streamlines around the vortex core shown in the left passage. This behavior of the leakage vortex corresponds well to the experimental result of the secondary flow field downstream of the rotor (Fig. 1(*a*)). Physical explanation of this flow field has been presented by Inoue et al. (1998), who have analyzed the numerical solution in further detail.

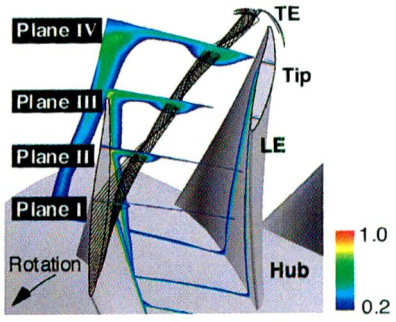

Fig. 9 Total pressure loss distributions on crossflow planes perpendicular to tip leakage vortex and leakage streamlines (black lines) for design operating condition (ϕ = 0.50)

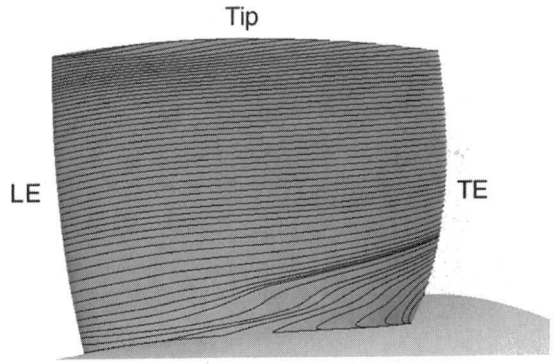

Fig. 10 Limiting streamlines on blade suction surface for design operating condition (ϕ = 0.50)

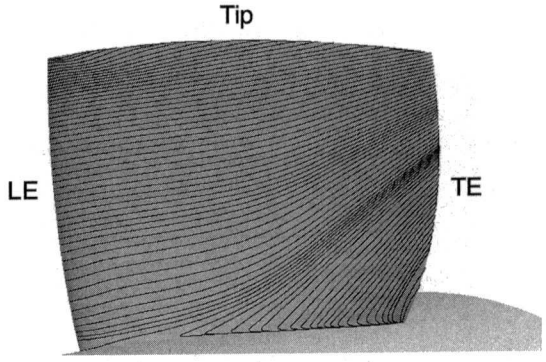

Fig. 12 Limiting streamlines on blade suction surface for peak pressure rise operating condition (ϕ = 0.38)

Distributions of a streamwise absolute vorticity and a total pressure loss for the design flow rate are shown in Figs. 8 and 9 where color contours of the distributions are represented on four crossflow planes nearly perpendicular to the tip leakage vortex core, as shown by planes I, II, III, and IV. In the figures black lines are the same leakage streamlines as those shown in Fig. 7. The streamwise absolute vorticity is defined by the component of absolute vorticity along the relative flow direction and is normalized by twice the angular velocity magnitude of the rotor. The total pressure loss is defined and normalized as

$$\zeta_p = \frac{\omega(rc_\theta - r_1 c_{\theta 1}) - (P - P_1)/\rho}{U_t^2/2} \tag{2}$$

where r is the radius from the axis of rotation, c_θ is the absolute tangential velocity component, P is the total pressure, ρ is the density, U_t is the blade tip speed, and subscript 1 denotes the rotor inlet. Only the region with the total pressure loss above 0.2 is shown in Fig. 9. Although the streamwise absolute vorticity in the tip leakage vortex decays gradually in the streamwise direction, the region with concentrated vorticity corresponding to the vortex core can be clearly observed even at plane IV. In Fig. 9 it is seen that high loss fluid accumulates around the leakage vortex core. The high loss region corresponds to the low-energy fluid accumulation observed near the casing in the experimental result of Fig. 2(*a*). Its size grows larger gradually in the streamwise direction. It is found from Figs. 7, 8, and 9 that the nature of the tip leakage vortex has no abrupt change in the streamwise direction.

Figure 10 shows limiting streamlines on the blade suction surface for the design flow rate. A secondary flow toward the casing is observed near the hub. This flow near the hub is caused by a secondary flow toward the suction surface in the hub wall boundary layer. Near the blade tip an outward radial flow is slightly noticeable. However, there is no considerable effect of the leakage flow on the suction surface boundary layer.

A perspective view of the tip leakage flow field at the peak pressure rise operating condition (ϕ = 0.38) is shown in Fig. 11. The formation of the tip leakage vortex starts from a nearer location to the leading edge than the design operating condition shown in Fig. 7. The casing wall pressure trough is deeper near the leading edge than the design operating condition, while it becomes shallower at the aft part of the blade passage. The tip leakage vortex core with the normalized helicity of nearly unity is observed along the pressure trough even at the aft part of the passage. This implies that the leakage vortex continues rolling up there. According to the behavior of the leakage streamlines shown in the left passage, it appears that the leakage vortex expands gradually in the streamwise direction. In the same manner as the design operating condition shown in Fig. 7, however, any abrupt change in the nature of the vortex is not observed.

Figure 12 shows limiting streamlines on the suction surface for the peak pressure rise operating condition (ϕ = 0.38). Although the secondary flow toward the casing becomes stronger on the hub side, there is no abrupt change in the behavior of the suction surface boundary layer near the tip. The onset of flow separation is not observed on the suction surface.

Onset of Leakage Vortex Breakdown. As mentioned in the previous section, the tip leakage vortex has no significant change in its nature at any flow rate not lower than the peak pressure rise operating condition; on the other hand substantial change in the nature appears at a lower flow rate.

Figure 13 shows a leakage flow field at a flow rate of ϕ = 0.37 slightly lower than the peak pressure rise operating condition (ϕ = 0.38). At the fore part of the rotor passage, the distinctive behavior of the tip leakage vortex can be readily seen, that is, a leakage

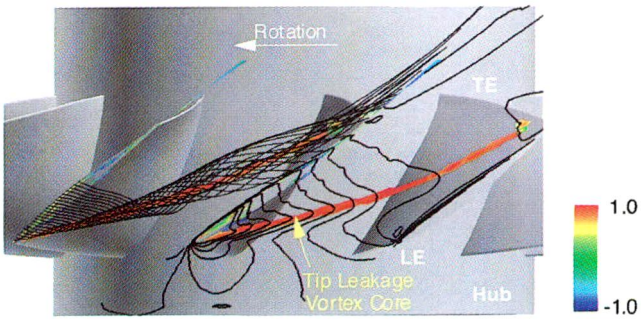

Fig. 11 Vortex cores colored with normalized helicity distribution, casing wall pressure distribution (black lines in right passage), and leakage streamlines surrounding tip leakage vortex (black lines in left passage) for peak pressure rise operating condition (ϕ = 0.38)

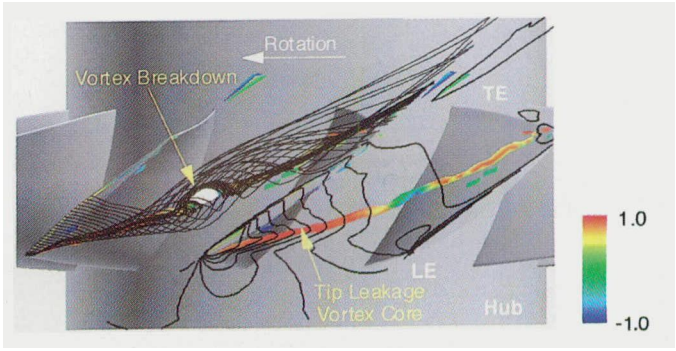

Fig. 13 Vortex cores colored with normalized helicity distribution, casing wall pressure distribution (black lines in right passage), recirculation region in leakage vortex breakdown (colored white in left passage), and leakage streamlines outside recirculation region (black lines in left passage) for ϕ = 0.37

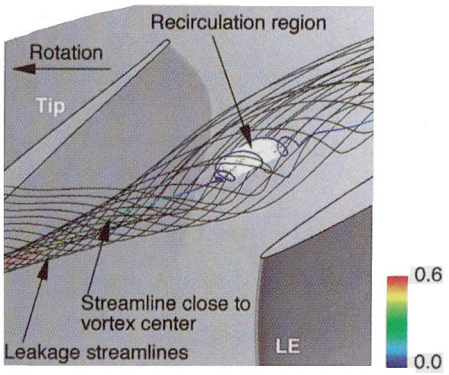

Fig. 14 Streamline close to tip leakage vortex center (colored with relative velocity magnitude), streamline in recirculation region (white line), and leakage streamlines outside recirculation region (black lines) for $\phi = 0.37$

vortex core with the normalized helicity of about unity traces a casing pressure trough in the same manner as the design and peak pressure rise operating conditions (Figs. 7 and 11). Near the middle of the passage, however, the pressure trough decays abruptly in the streamwise direction, disappearing at the aft part of the passage. The pressure distribution on the casing wall is closely related to the behavior of the leakage vortex. The normalized helicity on the leakage vortex core changes drastically near the middle of the passage: As the casing pressure trough decays, the normalized helicity changes rapidly from about unity to about minus unity. This means a drastic change in the nature of the vortex, considering that the normalized helicity corresponds to the angle between the absolute vorticity and relative velocity vectors, and that its sign indicates the swirl direction of the vortex relative to the streamwise velocity component. Downstream of the middle of the passage the normalized helicity on the vortex core becomes positive again. At the left passage in Fig. 13 it is observed that the leakage streamlines spiral tightly around the vortex core at the fore part of the passage, expand near the middle, and spiral weakly at the aft part of the passage. Moreover, it should be realized that a small recirculation region appears around a portion of the vortex core with the negative normalized helicity, as shown by a white region at the left passage in Fig. 13. The behavior of the leakage vortex for this flow rate ($\phi = 0.37$) is found to be substantially different from that for the design and peak pressure rise operating conditions.

A detailed view of the recirculation region for $\phi = 0.37$ is shown in Fig. 14. A streamline close to the leakage vortex center is colored with the relative velocity magnitude normalized by the blade tip speed. A recirculating flow in the leakage vortex core is shown by a white streamline, whereas a leakage flow outside the recirculation region is shown by black streamlines. It is clearly seen that the recirculation region has a bubblelike structure. The relative velocity along the streamline close to the vortex center decreases rapidly in the streamwise direction. It is evident that the

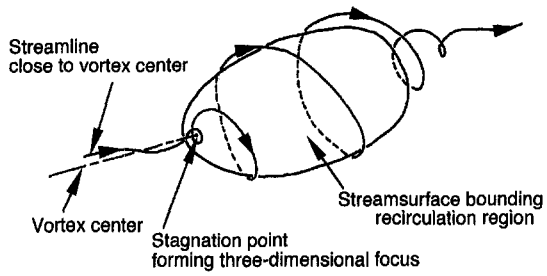

Fig. 15 Flow topology of vortex breakdown

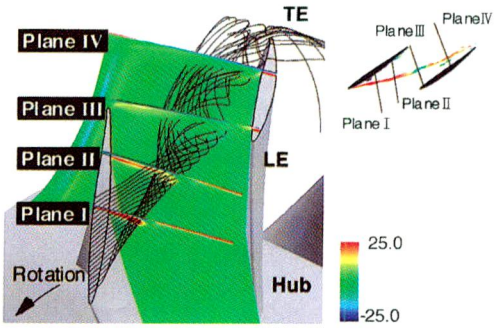

Fig. 16 Streamwise absolute vorticity distributions on crossflow planes perpendicular to tip leakage vortex and leakage streamlines (black lines) for $\phi = 0.37$

deceleration of the vortex core flow followed by the recirculation region causes an expansion of the vortex. Just in front of the recirculation region, the flow near the vortex center is decelerated almost to stagnation, and the streamline close to the vortex center kinks abruptly. This flow behavior implies the existence of a stagnation point forming a three-dimensional focus in front of the recirculation region, as shown in Fig. 15. The existence of the stagnation point in the vortex core is the distinctive feature of vortex breakdown (Leibovich, 1978; Delery, 1994). Therefore, it can safely be said that there is the onset of "vortex breakdown" in the tip leakage flow field for $\phi = 0.37$. In the present case a "bubble-type" breakdown seems to occur at the middle of the passage.

Figures 16 and 17 show distributions of the streamwise absolute vorticity and the total pressure loss, respectively, on the crossflow planes nearly perpendicular to the tip leakage vortex core. In the figures leakage streamlines are shown by black lines. The tip leakage vortex core with concentrated vorticity is observed on plane I in Fig. 16. This corresponds to the strong rolling-up of the vortex shown by a spiraling of the leakage streamlines (black lines). However, as the leakage vortex expands owing to the deceleration of the vortex core flow upstream of the recirculation region, the streamwise absolute vorticity in the vortex core decreases rapidly as shown at plane II. Then, the leakage vortex structure changes drastically at plane III located in the breakdown region: The vortex core with concentrated vorticity disappears, and a region with slightly negative value of the streamwise vorticity appears in the leakage flow field. The concentrated high vorticity is not observed even at plane IV downstream of the recirculation region. The disappearance of the vortex core with the concentrated high vorticity corresponds to the disappearance of the casing pressure trough shown in Fig. 13. This structure of the leakage vortex with breakdown is substantially different from that for the design operating condition shown in Fig. 8. Compared with the

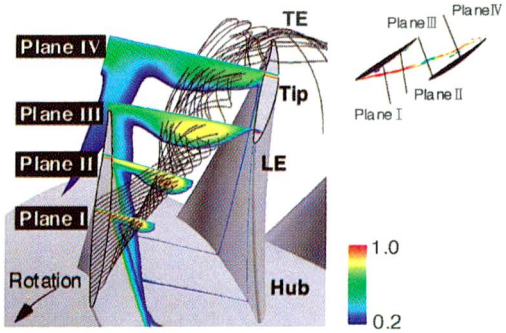

Fig. 17 Total pressure loss distributions on crossflow planes perpendicular to tip leakage vortex and leakage streamlines (black lines) for $\phi = 0.37$

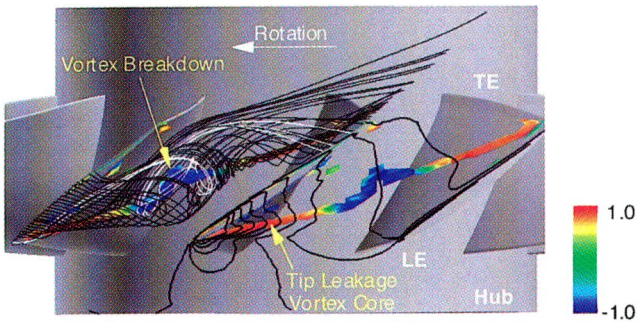

Fig. 18 Vortex cores colored with normalized helicity distribution, casing wall pressure distribution (black lines in right passage), streamlines passing through recirculation region in leakage vortex breakdown (white lines in left passage), and leakage streamlines outside recirculation region (black lines in left passage) for $\phi = 0.36$

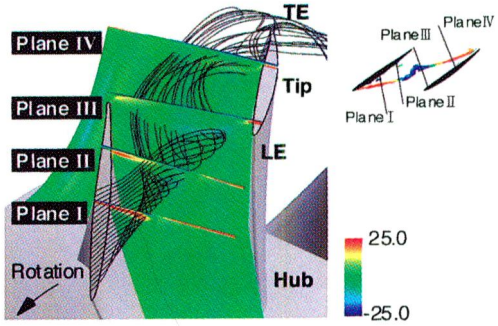

Fig. 19 Streamwise absolute vorticity distributions on crossflow planes perpendicular to tip leakage vortex and leakage streamlines (black lines) for $\phi = 0.36$

total pressure loss distribution for the design operating condition shown in Fig. 9, Fig. 17 indicates that the loss level is higher in the leakage vortex with breakdown, and that an extremely large spread of the high loss region takes place. Obviously, this behavior is closely related to the occurrence of vortex breakdown. Needless to say, the large spread of the high loss region due to the vortex breakdown means a sudden growth of the casing wall boundary layer having a large blockage effect.

Numerous investigations of the vortex breakdown during the last four decades show that two types of breakdown exist: the bubble and spiral types. In this study, however, the bubble-type breakdown is observed in the tip leakage vortex. The bubblelike structure captured by the present simulation, as shown in Fig. 14, should be interpreted as a time-meanlike structure, because the simulation does not have enough grid resolution to capture flow unsteadiness. Although it is well known that instantaneous flow structure in vortex breakdown is highly fluctuating, time-mean measurements of the breakdown always reveal the bubblelike structure (Delery, 1994). Therefore, the results in the present simulation are correct in the sense of time-mean.

Growth of Leakage Vortex Breakdown Near Stall. The breakdown of the tip leakage vortex is likely to have a significant effect on the onset of stall, considering that the breakdown with the recirculation region has a large blockage effect. It is important to investigate how the leakage vortex breakdown grows as the flow rate is decreased.

A tip leakage flow field for a lower flow rate of $\phi = 0.36$ than the breakdown onset condition is shown in Fig. 18. In the left passage in the figure, white lines denote streamlines passing through a recirculation region caused by the breakdown, while black ones denote leakage streamlines outside the recirculation region. The distribution of the casing wall pressure shown by black lines at the right passage corresponds well to the experimental result in Fig. 3(*b*). From the streamlines it is observed that a bubble-type breakdown occurs in the leakage vortex and has a large recirculation region. The recirculation region is open on the downstream side, through which the white streamlines enter and exit. Compared with Fig. 13, it is found that the bubblelike recirculation region grows rapidly in the streamwise and pitchwise directions as the flow rate is decreased. This growth of the vortex breakdown region not only causes a large blockage effect but seems to bring about the highly fluctuating pressure field, which is observed across the passage near the leading edge for the near-stall operating condition shown in Fig. 4(*b*). In the recirculation region, the leakage vortex core has a large kink. The normalized helicity distribution on the vortex core corresponds well to the significant change in the nature of the vortex: the normalized helicity is about unity upstream of the breakdown region, changes rapidly to about minus one in the recirculation region, and becomes about unity again in the downstream. It should be noted that portions of the vortex core with the normalized helicity of zero (green) correspond to the front and rear ends of the recirculation region. A portion of the vortex core with the negative normalized helicity can be regarded as a vortex core region with reverse flow. Near this reverse flow region the casing pressure trough disappears. The disappearance of the casing pressure trough is observed in the experimental result for the same rotor at a near-stall operating condition, as shown in Fig. 3(*b*). Downstream of the reverse flow region, the normalized helicity is about unity, and a very shallow trough of the casing pressure is observed again along the vortex core. These facts mean that there is a weak rolling-up of the vortex, which can be also observed as a spiraling of the streamlines around the vortex core in the downstream of the breakdown region. The blockage effect caused by the leakage vortex breakdown seems to be decreasing downstream of the breakdown region.

Figures 19 and 20 show distributions of the streamwise absolute vorticity and the total pressure loss for $\phi = 0.36$. In Fig. 19 the distinctive structure of the tip leakage vortex with concentrated high vorticity is not observed at planes II and III located in the vortex breakdown region. At plane IV located downstream of the breakdown region, however, a vortex core region with positive low vorticity exists near the casing. This concentrated low vorticity corresponds to the weak rolling-up of the vortex downstream of the breakdown region. Figure 20 indicates that the high loss region related to the leakage vortex becomes larger in the spanwise and pitchwise directions as compared with that for the operating condition of $\phi = 0.37$ shown in Fig. 17. This large growth of the high loss region corresponds to the large spread of the low-energy fluid, which is observed near the casing in the experimental result of Fig. 2(*b*) measured just downstream of the rotor.

Figure 21 shows secondary flow vectors viewed from the upstream on the crossflow planes for $\phi = 0.36$. Only a half span region from the casing is presented in the figure. The crossflow planes are nearly perpendicular to the leakage vortex core and are

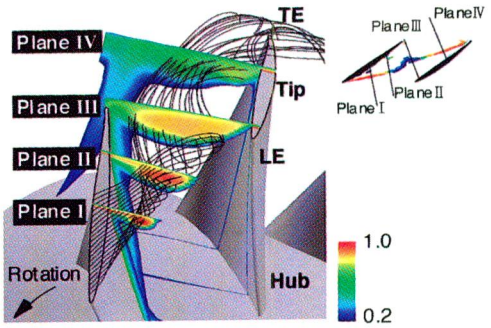

Fig. 20 Total pressure loss distributions on crossflow planes perpendicular to tip leakage vortex and leakage streamlines (black lines) for $\phi = 0.36$

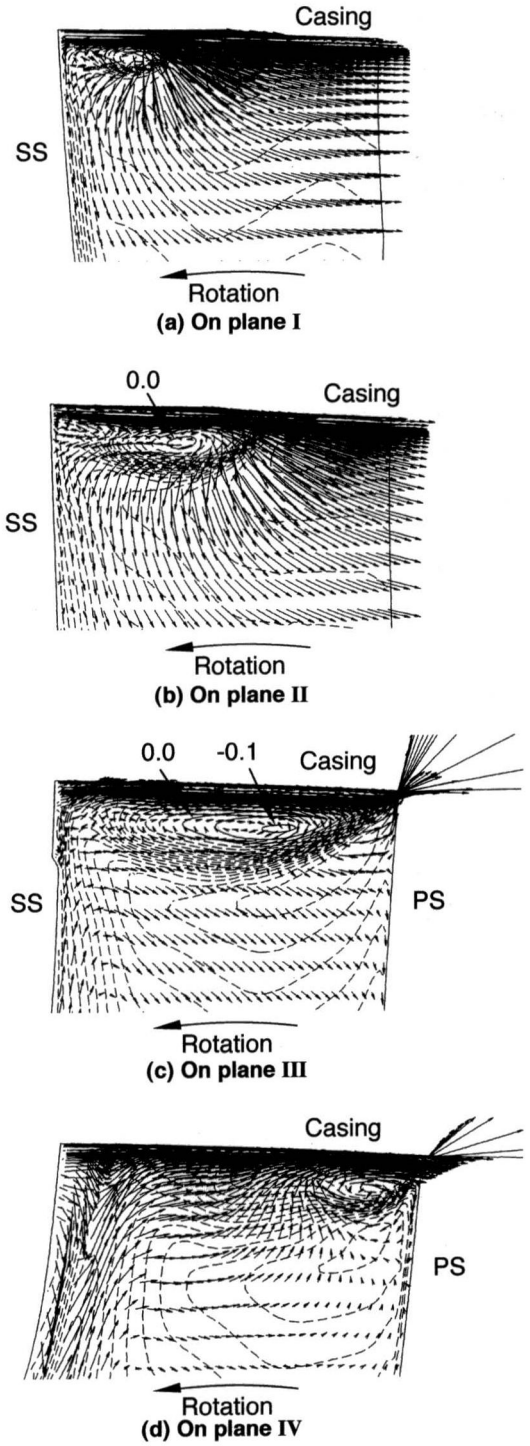

Fig. 21 Secondary flow vectors and distributions of relative velocity component along tip leakage vortex core on crossflow planes inside rotor for $\phi = 0.36$

the same as those in Figs. 19 and 20. The secondary flow is defined by a velocity component perpendicular to a local flow direction determined from a Navier–Stokes flow simulation with no tip clearance at the design operating condition. Distributions of a relative velocity component along the local direction of the leakage vortex core are also shown by contour lines in Fig. 21. This velocity component is normalized by the blade tip speed and is referred to as "vortexwise velocity" in the following. Broken line contours denote positive values of the vortexwise velocity, while solid ones denote negative values corresponding to a reverse flow along the vortex core. A flow radiating out from the leakage vortex core dominates the secondary flow field at planes I and II. This secondary flow results from the blockage effect due to the expansion of the leakage vortex, which is caused by the deceleration of the vortex core flow upstream of the breakdown. It is found that the large blockage effect appears even at plane I located near the rotor inlet. This means that the expansion of the leakage vortex takes place even in the far upstream of the breakdown region. At plane II, an inward radial flow induced by the blockage becomes larger, and a small reverse flow region with negative vortexwise velocity appears in the leakage vortex core. Evidently, just upstream of this region there is an onset point of the breakdown, namely a stagnation point. The reverse flow region grows in the streamwise direction, having the maximum size near plane III. It should be realized, however, that the reverse flow region is located around the vortex center away from the casing wall. At plane III the secondary flow by the blockage decays rapidly. This implies that the reverse flow region stops growing near plane III and becomes smaller downstream. This contraction of the reverse flow region decreases the blockage effect, thus causing an outward radial flow in the secondary flow field. At plane IV located downstream of the breakdown region, the reverse flow in the vortex core disappears, and the outward radial flow can be clearly observed around the vortex core. As seen at plane III, in the reverse flow region the swirl direction of the secondary flow viewed from the upstream is as clockwise as the leakage vortex with no breakdown. This vortical flow structure with the reverse flow corresponds to the vortex core portion with the normalized helicity of about minus one in the breakdown region as shown in Fig. 18. At plane IV the rolling-up of the leakage vortex is visible near the casing/pressure surface corner. It should be noted that the leakage vortex core downstream of the breakdown region has the low streamwise vorticity as shown in Fig. 19.

In Fig. 22, the secondary flow vectors just downstream of the rotor are shown for $\phi = 0.36$. The leakage vortex is not rolled up. The disappearance of the vortex rolling-up may be due to a diffusion of the leakage vortex having low streamwise vorticity downstream of the breakdown region. The outward radial flow caused by the contraction of the reverse flow region is readily seen in the whole leakage flow field. It should be emphasized that effects of the leakage vortex breakdown find their expression in no rolling-up of the vortex and the outward radial flow in the secondary flow field downstream of the rotor. These features are observed in the experimental result of the secondary flow field downstream of the same rotor for a near-stall operating condition, as shown in Fig. 1(*b*). The outward radial flow in the tip leakage flow field has been also observed in the experimental results by Lakshminarayana et al. (1995) for the peak pressure rise operating condition.

Figure 23 shows limiting streamlines on the blade suction surface for $\phi = 0.36$. Divergence of the limiting streamlines near the blade tip results from the large blockage effect of the leakage vortex breakdown. Compared with the limiting streamlines shown

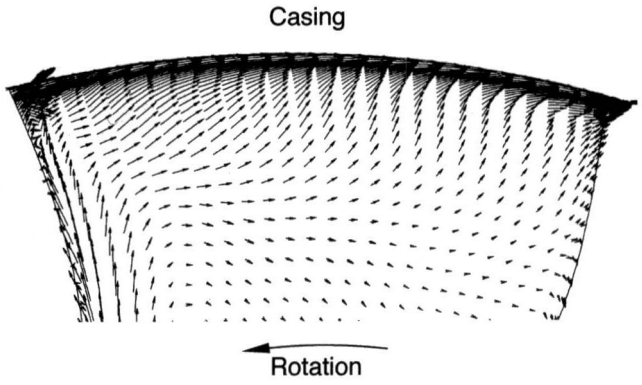

Fig. 22 Secondary flow vectors downstream of rotor for $\phi = 0.36$

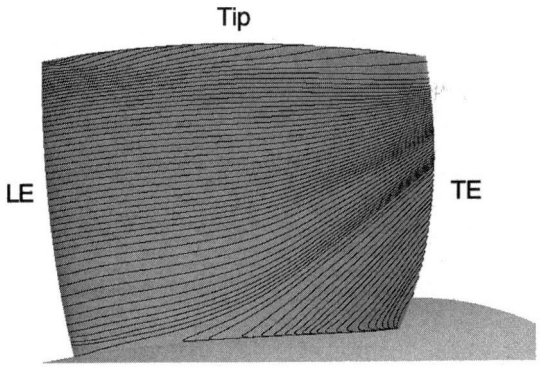

Fig. 23 Limiting streamlines on blade suction surface for $\phi = 0.36$

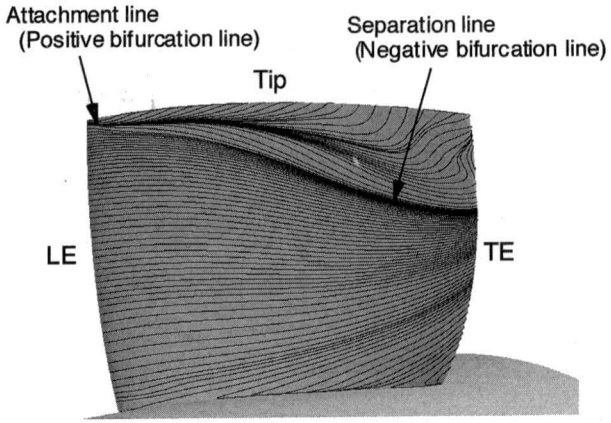

Fig. 25 Limiting streamlines on blade suction surface for $\phi = 0.35$

in Fig. 12 for the peak pressure rise operating condition of $\phi = 0.38$, the blockage effect suppresses the secondary flow toward the casing at the midspan region. Although the substantial change in the tip leakage flow behavior is caused by the large vortex breakdown as shown in Fig. 18, any remarkable change including flow separation is not observed in the suction surface boundary layer.

At a lower flow rate than $\phi = 0.36$, the tip leakage flow field is dominated by the leakage vortex breakdown, and the behavior of the suction surface boundary layer changes drastically. Figure 24 shows a leakage flow field for $\phi = 0.35$. The flow field is occupied by a massive breakdown that can be observed as the vortex core with the normalized helicity of about minus one and the recirculation region shown by white streamlines. An onset of breakdown is located near the leading edge where the normalized helicity on the vortex core changes rapidly from about unity to negative value. The huge bubblelike recirculation region blocks almost the passage. The breakdown region heavily interacts with the suction surface boundary layer. The casing pressure distribution shown by black lines in the right passage indicates that the blade loading near the tip decreases significantly, and that a rolling-up of the leakage vortex takes place only in the vicinity of the leading edge.

Figure 25 shows limiting streamlines on the suction surface for $\phi = 0.35$. A strong secondary flow toward the hub is the effect of the blockage caused by the massive vortex breakdown. A drastic change appears in the suction surface boundary layer interacting with the breakdown region near the tip. Envelopes with divergence and convergence of the limiting streamlines are clearly seen at the fore and aft parts of the suction surface, respectively. The envelope with divergence means three-dimensional flow attachment resulting from the leakage vortex core close to the suction surface as seen near the leading edge in Fig. 24. On the other hand, the envelope with convergence near the trailing edge represents three-dimensional separation. It is open separation (Zhiyong, 1991) in the present case where there is no critical points on the suction surface. For the open separation that can be described by a three-dimensional separation model of Maskell (1955), the separation line starts at a normal point (not critical point), which lies on the limiting streamline originating from the upstream attachment. At the start point of the separation line, a streamline is tangent to the blade surface and is drawn into the flow field. It should be realized that the interaction of the leakage vortex breakdown with the suction surface boundary layer causes the three-dimensional separation substantially different from the two-dimensional blade stall.

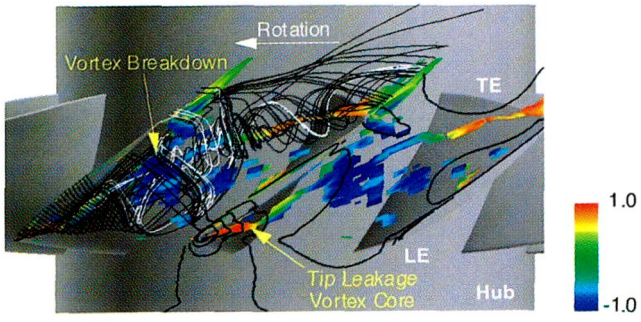

Fig. 24 Vortex cores colored with normalized helicity distribution, casing wall pressure distribution (black lines in right passage), streamlines passing through recirculation region in leakage vortex breakdown (white lines in left passage), and leakage streamlines outside recirculation region (black lines in left passage) for $\phi = 0.35$

Effects of Leakage Vortex Breakdown on Characteristic of Rotor Performance. In the previous sections the onset of tip leakage vortex breakdown and its growth with a decrease in the flow rate have been investigated in terms of the three-dimensional, internal flow field. We will show a major role of the vortex breakdown in characteristic of rotor performance at near-stall conditions.

Total pressure rise characteristics of the test compressor rotor are shown in Fig. 26. The total pressure rise is normalized by the dynamic pressure corresponding to the rotor tip speed, and the flow coefficient is the mean axial velocity divided by the rotor tip speed. Square symbols denote results of the Navier–Stokes flow simulations for the rotor with the blade tip clearance, whereas circular

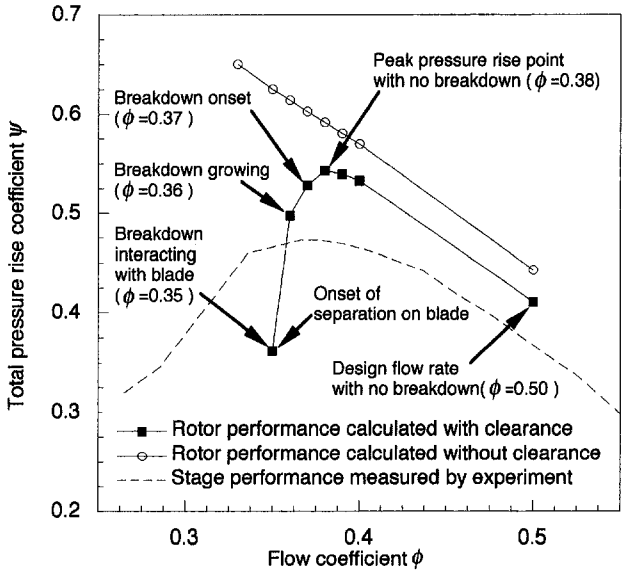

Fig. 26 Total pressure rise characteristics of rotor

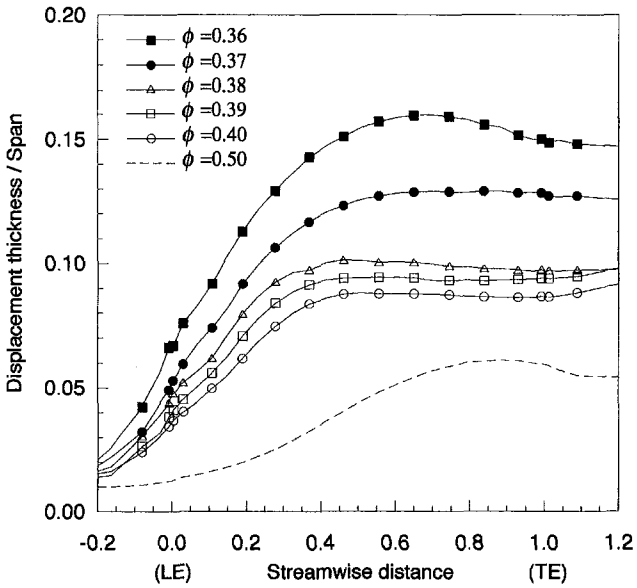

Fig. 27 Streamwise distributions of axial displacement thickness of casing wall boundary layer

symbols for no tip clearance. A performance characteristic of the compressor "stage" including a stator is also shown by a broken line in the figure. The stage performance has been obtained by the experiment of Inoue et al. (1986). It should be noted that the rotor with no tip clearance has a linear characteristic and no stall onset within the range of flow rate considered in the present study. For the rotor with the tip clearance, the breakdown of the tip leakage vortex is not observed at any flow rate not lower than the peak pressure rise operating condition ($\phi = 0.38$); on the other hand it occurs in the rotor at a lower flow rate than $\phi = 0.38$. The onset of bubble-type breakdown is observed at $\phi = 0.37$ where the total pressure rise starts to decrease. As the flow rate is decreased, the breakdown grows rapidly in the streamwise, spanwise, and pitchwise directions, the pressure rise falling further. Even at $\phi = 0.36$, however, any flow separation is not observed on the blade suction surface. If the flow rate is decreased further to $\phi = 0.35$, the massive breakdown occupying the rotor passage interacts with the suction surface boundary layer, thus leading to the three-dimensional separation on the suction surface. As a result, the total pressure rise decreases drastically at $\phi = 0.35$. It is found that the characteristic of the rotor performance near stall and the onset of separation on the blade suction surface are dominated by the leakage vortex breakdown.

Figure 27 shows streamwise distributions of the axial displacement thickness of the casing wall boundary layer, which is evaluated by the tangentially averaged flow. The displacement thickness increases with a decrease in the flow rate. This corresponds well to the behavior of the blockage effect due to the tip leakage vortex. Until the flow rate is decreased to the peak pressure rise operating condition ($\phi = 0.38$), the displacement thickness increases gradually. For $\phi = 0.37$, however, it increases drastically at the aft part of the rotor because of the onset of leakage vortex breakdown at the middle of the passage. At $\phi = 0.36$ where the bubblelike recirculation region grows significantly in the breakdown, the displacement thickness becomes so larger that it has a maximum value of 16 percent of span in the aft part of the rotor. A decrease in the thickness downstream of the maximum corresponds to the outward radial flow observed in the secondary flow field downstream of the breakdown region (Figs. 21(*d*) and 22). It should be realized that the leakage vortex breakdown brings about the extremely large blockage even if it does not give rise to flow separation on the blade. An increase in the displacement thickness upstream of the leading edge indicates that the blockage due to the leakage vortex brings a considerable effect to the upstream boundary layer.

Figure 28 shows streamwise distributions of a total pressure loss which is evaluated by mass-averaging the total pressure loss defined by Eq. (2) on each crossflow computational surface. As the leakage vortex breakdown grows at lower flow rate than the peak pressure rise condition ($\phi = 0.38$), the rate of increase in the loss becomes higher. It is obvious that this higher loss production rate results from the loss production due to the vortex breakdown as shown in Figs. 17 and 20.

Conclusions

The breakdown of the tip leakage vortex has been investigated on the low-speed axial compressor rotor with moderate blade loading. The tip leakage flow fields in the rotor have been simulated by the compressible Navier–Stokes flow solver based on the high-resolution upwind scheme using the TVD formulation. The onset of breakdown has been identified by examining the distribution of the normalized helicity along the leakage vortex core determined semi-analytically. As a result of this investigation, the following conclusions can be drawn:

1 The tip leakage vortex has no significant change in its nature at any flow rate not lower than the peak pressure rise operating condition. On the other hand drastic changes appear in the vortex at the lower flow rate. The rapid deceleration of the vortex core flow followed by a bubblelike recirculation region is observed. The distinctive features indicating the existence of the stagnation point appear just in front of the recirculation region: the flow is decelerated almost to stagnation, and a streamline close to the vortex center abruptly kinks. These features are evidence of the fact that there is the onset of breakdown in the tip leakage vortex.

2 At a lower flow rate than the peak pressure rise operating condition, the bubble-type breakdown is observed in the tip leakage vortex inside the rotor. The occurrence of the breakdown causes significant changes in the nature of the vortex. The deceleration of the vortex core flow followed by the recirculation region give rise to the large expansion of the vortex, leading to the large spread of the high-loss region related to the vortex. The concentration of the high streamwise vorticity around the vortex core disappears in the breakdown region. As a result, the pressure trough disappears on the casing wall close to the breakdown region.

3 The expansion of the tip leakage vortex due to the break-

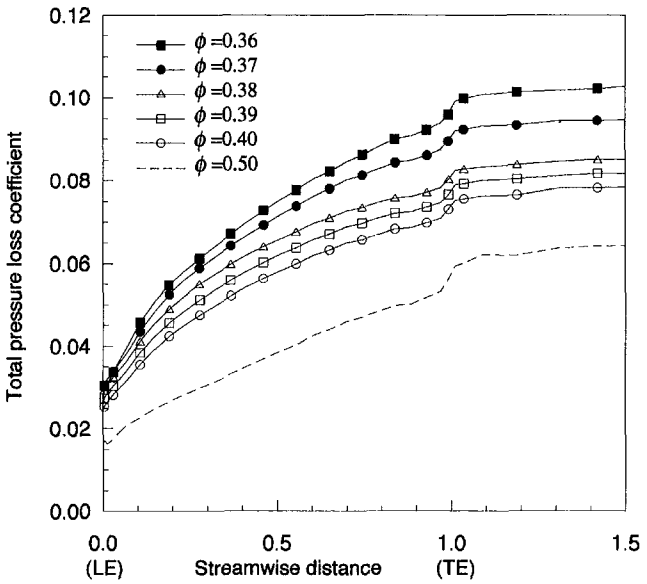

Fig. 28 Streamwise distributions of total pressure loss

down has an extremely large blockage effect. The blockage effect extends to the casing wall boundary layer upstream of the blade leading edge. The blockage causes inward radial flow, which dominates the secondary flow field upstream of the breakdown region. Meanwhile, downstream of the breakdown region where the bubblelike recirculation disappears, the blockage decreases gradually in the streamwise direction. This decrease in the blockage brings about the outward radial flow dominating the whole leakage flow field downstream of the rotor.

4 Downstream of the breakdown region, there is the weak rolling-up of the tip leakage vortex having low streamwise vorticity. Since it decays in the streamwise direction by the diffusion process, the rolling-up of the vortex is not observed in the secondary flow field downstream of the rotor.

5 It is realized that the effects of the leakage vortex breakdown find their expression in the features of experimental results that have never been explicable for a near-stall operating condition: no rolling-up of the leakage vortex downstream of the rotor, the outward radial flow in the leakage flow field downstream of the rotor, the exceedingly large spread of the low-energy fluid in the leakage flow downstream of the rotor, and disappearance of the casing wall pressure trough at the aft part of the rotor passage.

6 The vortex breakdown plays a major role in the characteristic of the rotor performance at near-stall conditions. As the flow rate is decreased from the peak pressure rise operating condition, the breakdown region grows rapidly in the streamwise, spanwise, and pitchwise directions. The growth of the breakdown region causes the drastic rises in the blockage and the loss even if it does not cause the blade boundary layer to separate. If the flow rate is decreased further, the massive breakdown occupying the passage interacts with the suction surface boundary layer. This interaction gives rise to the three-dimensional separation of the open type on the suction surface, which is substantially different from the two-dimensional blade stall. As a result, the total pressure rise across the rotor drops suddenly.

Acknowledgments

The present research was partially supported by the Ministry of Education, Science, Sports and Culture, Grant-in-Aid for Scientific Research (B), 09555066, 1997. The authors gratefully acknowledge the research fund from Harada Memorial Foundation, No. 9-18.

References

Anderson, W. K., Thomas, J. L., and van Leer, B., 1986, "Comparison of Finite Volume Flux Vector Splittings for the Euler Equations," *AIAA Journal,* Vol. 24, No. 9, pp. 1453–1460.

Ayder, E., and Van den Braembussche, R., 1994, "Numerical Analysis of the Three-Dimensional Swirling Flow in Centrifugal Compressor Volutes," ASME JOURNAL OF TURBOMACHINERY, Vol. 116, pp. 462–468.

Baldwin, B. S., and Lomax, H., 1978, "Thin Layer Approximation and Algebraic Model for Separated Turbulent Flow," AIAA Paper No. 78-257.

Chakravarthy, S. R., 1986, "The Versatility and Reliability of Euler Solvers Based on High-Accuracy TVD Formulations," AIAA Paper No. 86-0243.

Delery, J. M., 1994, "Aspects of Vortex Breakdown," *Progress in Aerospace Sciences,* Vol. 30, No. 1, pp. 1–59.

Escudier, M., 1988, "Vortex Breakdown: Observations and Explanations," *Progress in Aerospace Sciences,* Vol. 25, No. 2, pp. 189–229.

Furukawa, M., Yamasaki, M., and Inoue, M., 1991, "A Zonal Approach for Navier-Stokes Computations of Compressible Cascade Flow Fields Using a TVD Finite Volume Method," ASME JOURNAL OF TURBOMACHINERY, Vol. 113, pp. 573–582.

Furukawa, M., Nakano, T., and Inoue, M., 1992, "Unsteady Navier–Stokes Simulation of Transonic Cascade Flow Using an Unfactored Implicit Upwind Relaxation Scheme With Inner Iterations," ASME JOURNAL OF TURBOMACHINERY, Vol. 114, pp. 599–606.

Furukawa, M., Saiki, K., and Inoue, M., 1995, "Numerical Simulation of Three-Dimensional Viscous Flow in Diagonal Flow Impeller," in: *Numerical Simulations in Turbomachinery,* ASME FED-Vol. 227, pp. 29–36.

Furukawa, M., Saiki, K., Nagayoshi, K., Kuroumaru, M., and Inoue, M., 1998, "Effects of Stream Surface Inclination on Tip Leakage Flow Fields in Compressor Rotors," ASME JOURNAL OF TURBOMACHINERY, Vol. 120, pp. 683–692.

Hall, M. G., 1972, "Vortex Breakdown," *Annual Review of Fluid Mechanics,* Vol. 4, pp. 195–218.

Inoue, M., and Furukawa, M., 1994, "Artificial Dissipative and Upwind Schemes for Turbomachinery Blade Flow Calculations," VKI Lecture Series No. 1994-06.

Inoue, M., and Kuroumaru, M., 1984, "Three-Dimensional Structure and Decay of Vortices Behind an Axial Flow Rotating Blade Row," ASME *Journal of Engineering for Gas Turbines and Power,* Vol. 106, pp. 561–569.

Inoue, M., Kuroumaru, M., and Fukuhara, M., 1986, "Behavior of Tip Leakage Flow Behind an Axial Compressor Rotor," ASME *Journal of Engineering for Gas Turbines and Power,* Vol. 108, pp. 7–14.

Inoue, M., and Kuroumaru, M., 1989, "Structure of Tip Clearance Flow in an Isolated Axial Compressor Rotor," ASME JOURNAL OF TURBOMACHINERY, Vol. 111, No. 3, pp. 250–256.

Inoue, M., Kuroumaru, M., and Ando, Y., 1990, "Behavior of Tip Clearance Flow in Axial Flow Impellers at Low Flow Rate," *Proc. 3rd Japan–China Joint Conference on Fluid Machinery,* Vol. II, pp. 179–186.

Inoue, M., Kuroumaru, M., Iwamoto, T., and Ando, Y., 1991, "Detection of a Rotating Stall Precursor in Isolated Axial Flow Compressor Rotors," ASME JOURNAL OF TURBOMACHINERY, Vol. 113, No. 2, pp. 281–289.

Inoue, M., Furukawa, M., Saiki, K., and Yamada, K., 1998, "Physical Explanations of Tip Leakage Flow Field in an Axial Compressor Rotor," Paper No. 98-GT-91.

Lakshminarayana, B., Zaccaria, M., and Marathe, B., 1995, "The Structure of Tip Clearance Flow in Axial Flow Compressors," ASME JOURNAL OF TURBOMACHINERY, Vol. 117, pp. 336–347.

Leibovich, S., 1978, "The Structure of Vortex Breakdown," *Annual Review of Fluid Mechanics,* Vol. 10, pp. 211–246.

Leibovich, S., 1984, "Vortex Stability and Breakdown: Survey and Extension," *AIAA Journal,* Vol. 22, No. 9, pp. 1192–1206.

Levy, Y., Degani, D., and Seginer, A., 1990, "Graphical Visualization of Vortical Flows by Means of Helicity," *AIAA Journal,* Vol. 28, pp. 1347–1352.

Maskell, E. C., 1955, "Flow Separation in Three Dimensions," RAE Aero. Rept. 2655.

Perry, A. E., and Chong, M. S., 1987, "A Description of Eddying Motions and Flow Patterns Using Critical-Point Concepts," *Annual Review of Fluid Mechanics,* Vol. 19, pp. 125–155.

Sawada, K., 1995, "A Convenient Visualization Method for Identifying Vortex Centers," *Trans. Japan Soc. of Aero. Space Sci.,* Vol. 38, No. 120, pp. 102–116.

Swanson, R. C., and Turkel, E., 1993, "Aspects of a High-Resolution Scheme for the Navier-Stokes Equations," AIAA Paper No. 93-3372-CP.

Schlechtriem, S., and Lotzerich, M., 1997, "Breakdown of Tip Leakage Vortices in Compressors at Flow Conditions Close to Stall," ASME Paper No. 97-GT-41.

Van Leer, B., Thomas, J. L., Roe, P. L., and Newsome, R. W., 1987, "A Comparison of Numerical Flux Formulas for the Euler and Navier–Stokes Equations," AIAA Paper No. 87-1104.

Zhiyong, L., 1991, "A Study on Mode of 3-Dimensional Separation and Open Separation," in: *Separated Flows and Jets,* Springer-Verlag, pp. 219–223.

Dual-Laser Probe Measurement of Blade-Tip Clearance

H. S. Dhadwal
Integrated Fiber Optic Systems, Inc.,
25 East Loop Road,
Stony Brook, New York 11790
e-mail: dhadwal@sbee.sunysb.edu

A. P. Kurkov
NASA Lewis Research Center,
Cleveland, OH 44135

This paper describes two dual-laser probe integrated fiber optic systems for measuring blade tip clearance in rotating turbomachinery. The probes are nearly flush with the casing inner lining, resulting in minimal flow disturbance. The two probes are closely spaced in a circumferential plane and are slanted at an angle relative to each other so that the blade tip traverse time of the space between the two laser beams varies with the tip radius, allowing determination of the tip clearance at the rotor operating conditions. The tip clearance can be obtained for all the blades in a rotor with a single system, provided there are no synchronous vibrations present at a particular operating condition. These probes were installed in two holders; one provided an included angle between the probes of 20 deg, and the other provided an included angle of 40 deg. The two configurations were calibrated in a vacuum spin rig facility that is capable of reproducing realistic blade tip speeds.

Introduction

The efficiency of a gas turbine engine, typically used in aircraft, is directly dependent on the clearance between the blade tip and the engine housing, particularly in the compressor stages. Real time sensors capable of providing a measurement of the tip clearance are essential for the development of closed-loop systems, which will maintain the correct gap between the blade tip and the engine casing at all operating conditions. Due to the proprietary nature of tip clearance probes, it has not been possible to find relevant references in the open literature. Most of the background material described below was obtained from a number of issued patents; citations of these was not deemed appropriate for this journal. State-of-the-art engines require a means of sensing and varying the clearance between the blade tips and the engine casing at all times. A variable position engine liner offers one solution to maintaining an optimum tip clearance at all operating conditions. Another scheme uses selective cooling or heating of the engine casing to maintain optimum tip clearance at all speeds. The most common tip clearance probe is based on either a DC or AC measurement of the changes in the electrical capacitance of a parallel plate capacitor formed by the blade tip and an electrode inserted into the engine casing. Such probes have been extensively used because of their low cost and simplicity. However, due to the poor frequency response and the need for ferrous blade tips, capacitance sensors are unlikely to be effective in modern engines. Magnetic tip clearance sensors, which require calibration at various axial positions of the rotor, also have very poor frequency response. For effective utilization, both capacitance and magnetic sensors require an additional sensor for locating the precise axial position of the blade tips at all operating speeds. Recently, this problem has been solved by extending the electrode to cover the entire blade tip. Pneumatic tip clearance sensors require considerable hardware and modification of the engine casing; however, are being considered because of their insensitivity to contamination of blade tips; these sensors correlate differential changes in the pressure of fluid passing through a reference orifice and a sensor orifice as the blade tips pass by the sensor orifice. Laser-based optical techniques for tip clearance have also been developed. Of these, sensors exploiting changes in the signal amplitude due to the varying gap between the engine casing and the blade tip suffer from contamination and are not suitable. Another class of laser-based sensors form an image of a laser spot by reflecting a laser beam from the blade tip surface. The position of the image formed on the surface of a position sensor varies with tip clearance. This type of sensor, though not directly affected by amplitude variation, is still sensitive to surface roughness.

In this paper we describe the design of a blade tip clearance sensor based on the integrated fiber optic laser probe (IFOLP) system for blade tip deflection and clearance measurements (Dhadwal et al., 1996). The active part of the probe is about 3 mm (0.120 in.) in diameter and is easily mounted into the engine casing with negligible flow disturbance. Several IFOLPS can be located along the blade chord to measure blade tip deflection at various operating conditions. The IFOLP illuminates the blade tip surface with a laser spot, having a nominal diameter of 25 μm (0.001 in.) and the entire system has a rise time capability of 50 ns. The IFOLP system has been extensively used for obtaining static deflection data from experimental engines placed in wind tunnel tests. The signals between the control room and the wind tunnel (50 to 200 m) were transmitted through low-loss high-bandwidth optical fibers.

Theoretical Background

Integrated fiber optic transmitters (IFOTs) and IFOLPs have been described elsewhere (Khan et al., 1994a, b) and will not be elaborated upon here. It suffices to say that integrated fiber optics allows wavefront processing of optical fields within optical fibers through fusion splicing of short lengths of one or more dissimilar optical fibers. This technology permits the design of miniature packages that may contain one or more IFOTs for remote delivery of laser beams and one or more high numerical aperture optical fiber for collecting the diffusely scattered light.

Amplitude Based Tip Clearance Sensor. A typical IFOLP system used for measurement of static deflections comprises several IFOLPs, each having a cylindrical stainless steel body of diameter 3 mm and a length of 9 cm; the IFOLPs are mounted into the engine housing at appropriate locations. The other end of the IFOLP is terminated with a FC/PC and a SMA type connector for easy interconnection with fiber optic cable assemblies connecting the control room to the wind tunnel. The active end of the IFOLP has provision for use of purge air for either cooling purposes or for keeping the probe free of contaminants. As depicted in Fig. 1, a single IFOLP contains one IFOT, which is surrounded by one or more (typically five) high numerical aperture multimode fibers. The IFOT illuminates the blade tip with a laser beam of waist

Contributed by the International Gas Turbine Institute and presented at the 43rd International Gas Turbine and Aeroengine Congress and Exhibition, Stockholm, Sweden, June 2–5, 1998. Manuscript received by the International Gas Turbine Institute February 1998. Paper No. 98-GT-183. Associate Technical Editor: R. E. Kielb.

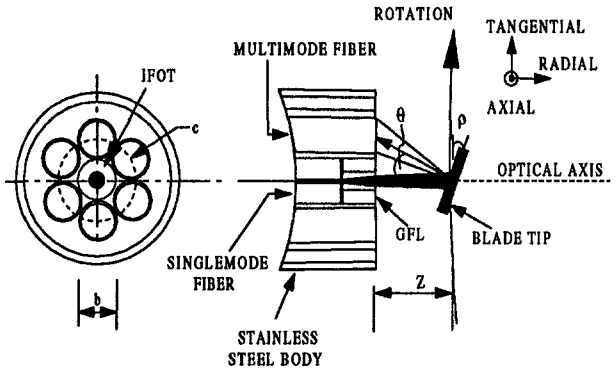

Fig. 1 Schematic of an IFOLP

radius smaller than 25 μm (0.001 in.). Collection efficiency of a single receiving fiber is dependent upon the radial displacement of the blade tip z, the reflectance R_T of the blade tip surface, and the numerical aperture of the fiber. The optical power, P_f, collected by a single receiving fiber is

$$P_f = R_T P_0 \frac{(m+1)}{2} \frac{b^2}{Z^2} \cos^{(m+3)}(\theta + \rho) \tag{1}$$

where P_0 is the incident optical power emanating from the IFOLP, b is the cladding diameter of a receiving optical fiber, m is an indication of the angular distribution of the reflected (scattered) laser light from the blade tip surface, ρ is the angular deviation of the blade surface normal relative to IFOLP axis and $\tan(\theta) = (c - b)/Z$ is a function of the radial displacement. Angle ρ represents undesirable sensitivity to misalignment of the blade tip surface normal; however, this is easily mitigated by using two or more receiving fibers in a symmetric configuration. As shown in Fig. 2, the optical receiver response has two distinct regions I and II; the former domain shows a linear dependence on the radial displacement (tip clearance) with a high spatial resolution at the expense of limited range. The second domain represents a nonlinear dependence with a relatively longer spatial range, but with a moderate resolution. Utilization of Eq. (1) for real time measurements of tip clearance requires precise knowledge of the calibration curve under the desired operating conditions and precise positioning of the IFOLP. This approach is used by many commercial optical distance probes; however, none of these has the bandwidth and size requirements that come close to satisfying the needs of tip clearance in gas turbine engines.

Beam Width-Based Tip Clearance Sensor. The IFOLP optical system can be conveniently described by a linear system whose spatial impulse response is the Gaussian function:

$$h(x) = \frac{\pi\omega_0}{Z\lambda} \sqrt{\frac{\pi}{2}} \exp\left[-2\left(\frac{\pi x \omega_0}{\lambda Z}\right)^2\right] \tag{2}$$

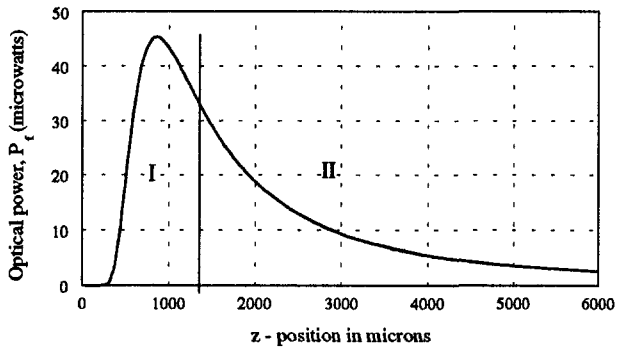

Fig. 2 Output response of a single fiber receiver

where Z is the radial distance (i.e., tip clearance). ω_0 is the waist of the Gaussian laser beam at the tip of the IFOLP ($Z = 0$), x is measured along a line orthogonal to the optical axis, and λ is the incident wavelength. The output response $g(x)$ to a blade function $f(x)$ is given by a convolution

$$g(x) = \int_{-\infty}^{\infty} h(\gamma) f(x - \gamma) d\gamma \tag{3}$$

A blade tip of width W can be described by a rectangular function,

$$f(x) = \text{rect}(x/W) = \begin{cases} 1, & |x| \le \dfrac{W}{2} \\ 0, & \text{otherwise} \end{cases} \tag{4}$$

The output response is then

$$g(x) = \frac{\pi}{4}\left\{\text{erf}\left(\frac{\sqrt{2}\pi\omega_0 x}{\lambda Z}\right) - \text{erf}\left(\frac{\sqrt{2}\pi\omega_0(x - W)}{\lambda Z}\right)\right\} \tag{5}$$

where erf $(\cdot)$ is the *error function.* For a blade tip moving past the probe at u m/s, the rise time is given by

$$t_r = \frac{1}{\sqrt{2\pi}} \frac{\lambda Z}{u\omega_0} \tag{6}$$

Real time monitoring of blade tip transitions requires a collimated scanning beam with a spot diameter, at the blade tip, which is much smaller than the blade width. Figure 3(*a*) shows a typical response of the system at $Z = 1000$ μm for $\omega_0 = 10$ μm, $W = 100$ μm. Equation (6) shows that the spatial resolution of static deflection measurements is proportional to the waist size of the laser spot at the blade tip surface. For example, if $\lambda = 0.67$ μm, $\omega_0 = 25$ μm, $Z = 1000$ μm, and $u = 350$ m/s, then the expected rise time resolution (proportional to spatial resolution) is 30 ns. In order to attain this resolution, the electronic system must also have a rise time capability better than 30 ns.

Figure 3(*b*) shows the response at $Z = 250$ μm (solid line) and $Z = 2000$ μm (dashed line), respectively. The width of the output

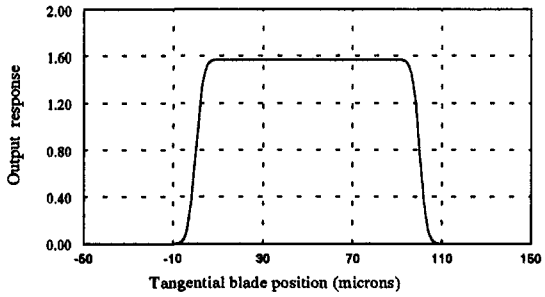

Fig. 3(*a*) Typical output voltage waveform when the laser beam diameter is smaller than blade width

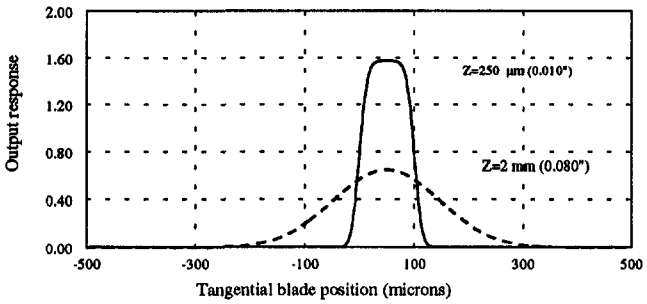

Fig. 3(*b*) Output voltage waveforms when the laser beam diameter is either smaller (solid) or larger (dashed) than the blade width

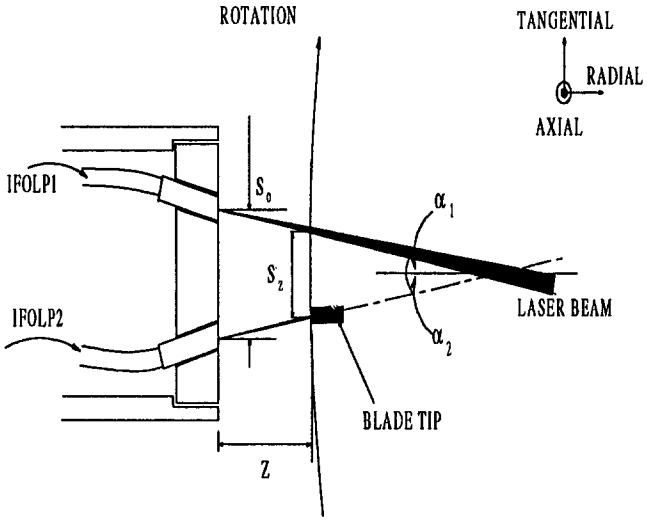

Fig. 4 Schematic of time-of-flight tip clearance sensor

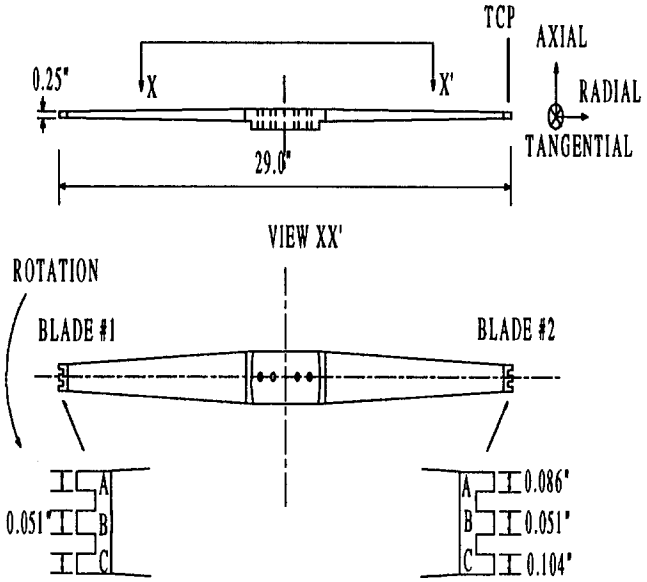

Fig. 5 Schematic of test blade

response is a linear function of the tip clearance, provided that the width of the blade tip is smaller than the width of the laser spot (dashed line). Width measurements are insensitive to amplitude fluctuations, which may be caused by any number of experimental conditions. The drawback with this scheme is that it requires high power laser beams for illumination, as the signal-to-noise ratio is considerably reduced compared with amplitude sensors. Additionally, due to phase noise arising from the surface roughness, the error in width estimation may be considerably increased.

Time of Flight Tip Clearance Sensor. A tip clearance sensor that utilizes the virtues of these two approaches is depicted in Fig. 4. Two IFOLPs, inclined with respect to each other, illuminate the blade tip, but not simultaneously. As the blade tip passes the field of view of each IFOLP, a pulse is detected by each of the IFOLPs, as described above. The time difference between the leading (or trailing) edges of the pulses is inversely proportional to the tip clearance. The actual dependence is a function of the included angles α_1, α_2 and the separation S_0 between the two IFOLPs. Referring to Fig. 4, the tip clearance Z is given by

$$Z = \frac{S_0 - S_Z}{\tan(\alpha_1) + \tan(\alpha_2)} \tag{7}$$

Tip clearance is determined from measurements of S_Z, which are derived from the time stamp of the blade tips as they pass by the probe tip field of view. Equation (7) represents an absolute calibration, which depends on the physical construction of the probe. However, computations of S_Z require knowledge of the precise blade tip speed at the point of measurement. Since all transitions are measured relative to the once-per-revolution signal, S_Z can be expressed in terms of the ratio of the time of flight T_Z between the two IFOLPs, to the time T_0 for one revolution, giving

$$Z = \frac{1}{T_0} \frac{[S_0 T_0 - 2\pi R T_Z]}{[\tan(\alpha_1) + \tan(\alpha_2)]} \tag{8}$$

where R is the nominal radius of the blades. If knowledge of S_0, α_1, α_2, and R is not available, low-speed data can be used to derive a calibration curve. The sensitivity of tip clearance (μs/μm), defined by the inverse gradient of Eq. (8), is proportional to the included angle α ($\approx\alpha_1 + \alpha_2$). However, increases in α result in an elliptical laser spot, which degrades the rise time of the edge, thereby increasing the uncertainty of the time of flight measurement. Another embodiment of this tip clearance sensor can use two IFOTs and a single receiver bundle mounted into the same housing.

Experimental Results

The tip clearance probes (TCPs) described above were tested in NASA's spin rig and the 9′ × 15′ wind tunnel facilities at the Lewis Research Center in Cleveland. The spin rig facility allows calibration of TCPs at typical operating speeds and timing specifications, without the added complication of unknown blade deflections. The spin rig test facility comprises a large cylindrical chamber and a removable instrument platform, which houses the rotor assembly and the test blade. The entire apparatus can be evacuated down to a modest vacuum. The TCP under test is mounted onto an automated translational stage, which can be used to adjust the tip clearance during operation, thereby providing a dynamic calibration of the system. Figure 5 shows a schematic of the blade that was used for testing the IFOLPs. The titanium test blade had a diameter of 73.7 cm (29.0 in.) and two tips. Each blade tip was designed with three teeth, such that the middle tooth (B) would provide a deflection-free measurement and could be used to test the limits of the capabilities of the IFOLP system. All the data presented in this paper were reduced from the time stamp measured from the middle tooth, which had a blade width of 1.295 mm (0.051 in. ± 0.001 in.). The width of the other two teeth for both blades is indicated in Fig. 5. The once-per-revolution synchronizing pulse was obtained by reflecting a laser beam from a mirror mounted on the rotating shaft. The surface of the two blade tips had an axial offset of 229 μm (0.009 in.), that is, blade B#2 was closer to the tip clearance probe compared with blade B#1. Note that for the spin rig test, the TCPs were mounted in the axial

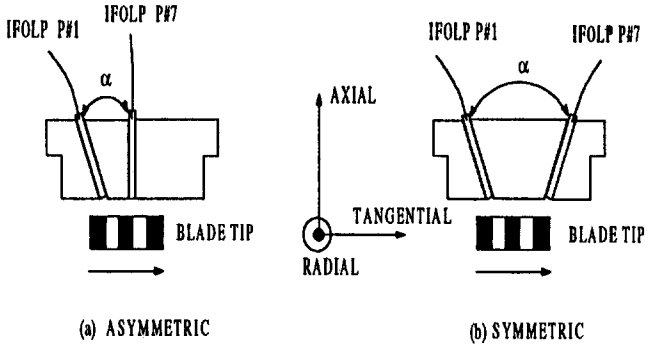

Fig. 6 Time-of-flight tip clearance configurations

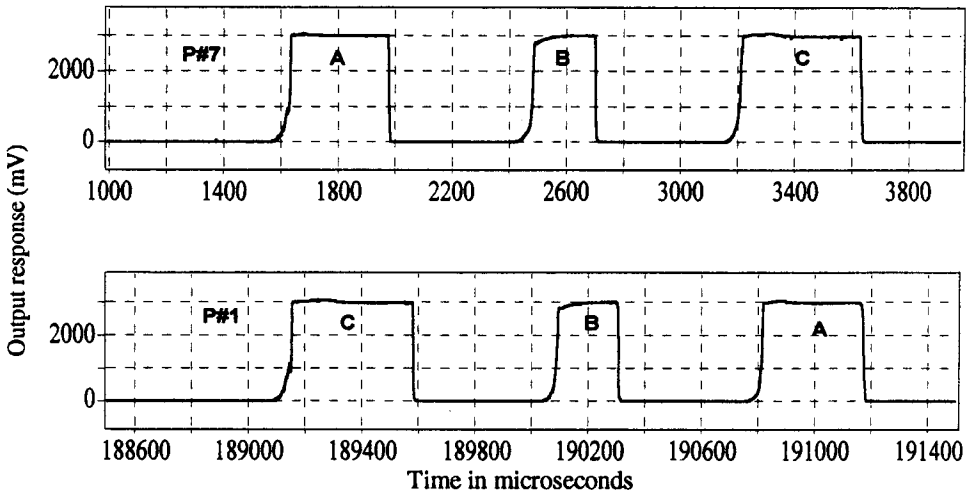

Fig. 7 Measured response using asymmetric probe

direction for convenience; however, in wind tunnel tests the TCPs were mounted in the radial direction.

The integrated fiber optic laser probe system was used for all the measurements. It comprised a laser diode transmitter module, a receiver module, a pair of IFOLPs, and some connecting optical cables. The transmitter module includes all circuitry necessary for operating a low-coherence visible laser diode at a constant output power of 10 mW, with a power stability better than 0.05 percent. The laser diode was pigtailed directly to a single mode optical fiber, the distal end of which was terminated with a FC/PC connector. This arrangement allowed alignment-free and robust coupling to optical cables linking the wind tunnel to the control room. The receiver unit used a reverse biased avalanche photodiode to detect the diffusely scattered optical signal from the blade tip as a current pulse. A transimpedance amplifier converted the current pulse to a voltage pulse, which was further amplified and pulse shaping. The output pulse, when not saturated, corresponded to the blade tip shape, making it possible to measure the blade width. However, the temporal position of the leading or trailing edges, relative to the one-per-revolution synchronization pulse, provided measurement of the static blade tip deflection. The IFOLP system was used to test two configurations of the time-of-flight tip clearance probe described above: an asymmetric positioning of the two IFOLPs with an included angle $\alpha = 20$ deg (Fig. 6(a)) and a symmetric arrangement with an included angle of 40 deg (Fig. 6(b)).

Figure 7 shows a typical pulse response from blade B#2 and blade B#1 at 2000 rpm using the asymmetric tip clearance probe. Figure 7 clearly shows the three teeth, and that the order and width of the pulses is consistent with the geometric configuration illustrated in Fig. 5. The output waveform shown in Fig. 7 was obtained using IFOLP P#7, which was positioned perpendicular to the blade tip surface. The slight differences in the shapes of the leading and trailing edges of the pulses suggest that P#7 was receiving some diffuse light prior to the detection of the leading blade edge.

Figure 8 shows pulse shapes obtained from the middle tooth of blade B#2, using probes P#1 and P#7, respectively. IFOLP P#1,

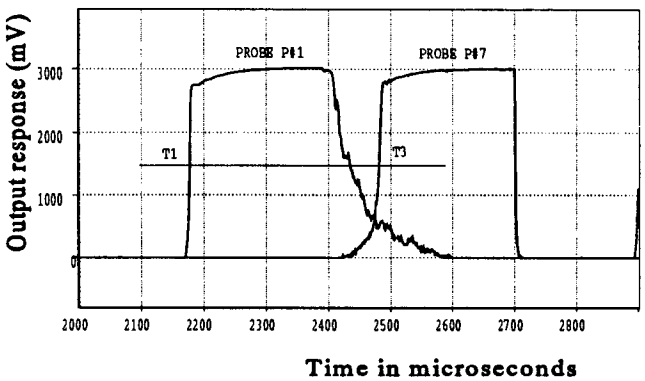

Fig. 8 Two pulses from the two IFOLPS P#1 and P#7

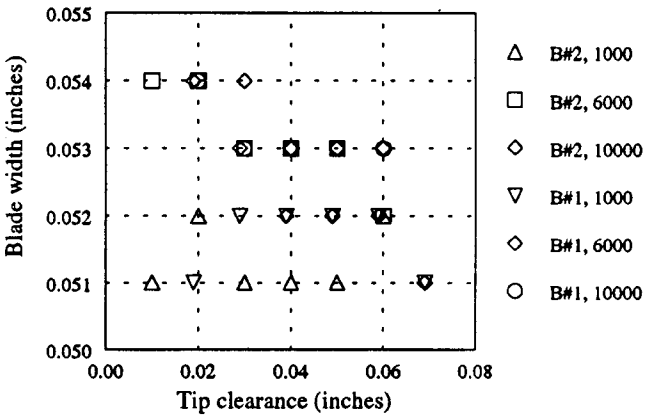

Fig. 9 Measured width of both blades at different set clearances and at various operating speeds (rpm)

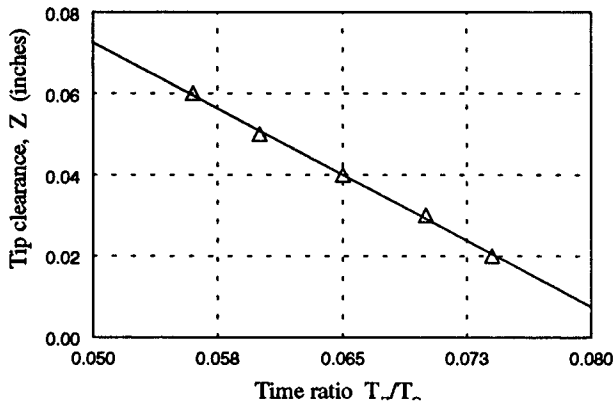

Fig. 10 Calibration data at 1000 rpm for blade B#2 using P#1; $z = 0.181 - 2.170*(T_2/T_0)$

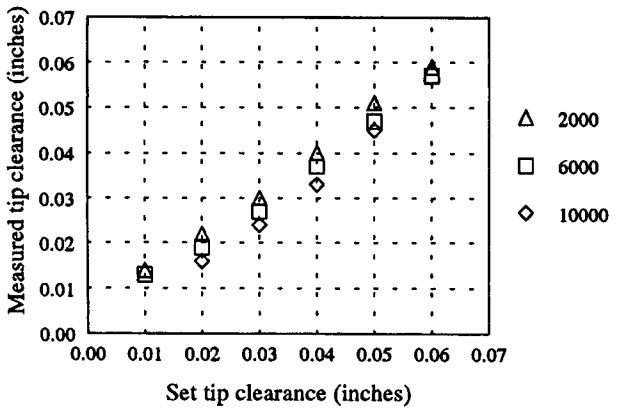

Fig. 11 Blade B#2 tip clearance data for the asymmetric probe at various operating speeds (rpm)

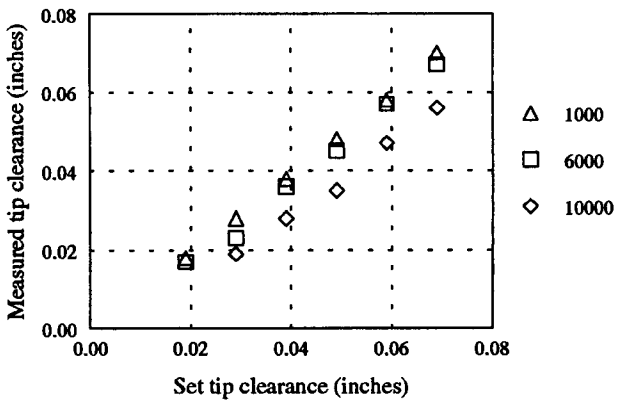

Fig. 12 Blade B#1 tip clearance data for the asymmetric probe at various operating speeds (rpm)

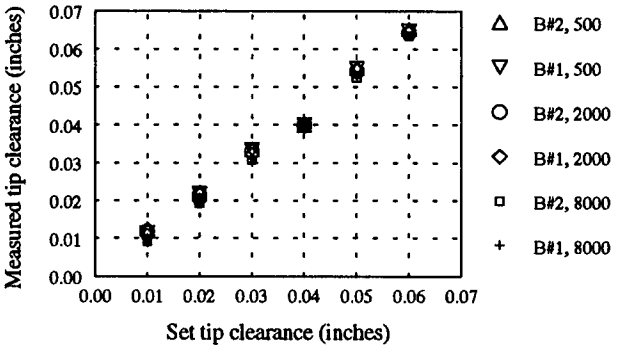

Fig. 13 Tip clearance data for the symmetric probe. Data for both blades and at several operating speeds (rpm).

which was tilted away from the blade surface normal, in the direction of rotation, produced a much sharper leading edge, compared with the trailing edge. The straight IFOLP P#7 produced a slightly sharper trailing edge compared with the leading edge. The accuracy of time of flight T_Z (T3–T1) was strongly dependent on the slope of the leading transitions. Additional improvements in accuracy were obtained by operating the receiver in the nonlinear region, that is, the output signal was saturated.

Figure 9 shows a plot of the computed blade width W at some of the operating points. Blade width was computed over a range of tip clearance settings from 0.01 to 0.07 in. and speeds from 1000 rpm to 10,000 rpm. The measured variation in width ($\approx$0.003 in.) was traced to axial movements of the rotor. Low rpm data give a value of blade width (0.051 in.) that is in agreement with that measured using a micrometer. From these data we can estimate that the deflection sensitivity of the IFOLP system is better than 0.0005 in. for blades with a radius of 14.405 in., corresponding to an angular deflection resolution of 0.002 deg. As indicated in Eq. (7) the tip clearance Z is a linear function of T_Z/T_0, which is computed from data, such as those shown in Figs. 7 and 8. We used the data at 1000 rpm for blade B#2 to compute a calibration curve as indicated in Fig. 10. This linear dependence was used to compute the tip clearance at all other operating points. The results of tip clearance are summarized in Figs. 11 and 12 for blade B#2 and blade B#1, respectively. We estimate that the accuracy of the tip clearance data reported here is better than 0.5 percent at all operating points. Figure 13 shows a plot of the tip clearance data obtained with a symmetric configuration of tip clearance probe.

Conclusions

In this paper we have demonstrated the utility of a dual-laser probe for tip clearance measurements in rotating turbomachinery. The measured accuracy, over a wide range of operating conditions, is better than 0.0005 in. spanning a dynamic range of 0 to 0.08 in. Time-of-flight measurements are robust and reliable; they are not compromised by the degradation of signal caused by any number of experimental conditions. The symmetric configuration offers better resolution.

Acknowledgments

HSD wishes to acknowledge NASA Contract No. NAS3-27538, and both authors sincerely appreciate the help of the technical staff at the 9′ × 15′ wind tunnel and the spin rig facilities.

References

Dhadwal, H. S., Mehmud, A., Khan, R., and Kurkov, A., 1996, "Integrated fiber optic light probe: Measurements of static deflections in rotating turbomachinery," *Review of Scientific Instruments,* Vol. 67, No. 2, pp. 546–552.

Khan, R., Dhadwal, H. S., and Suh, K., 1994a, "Design and characterization of integrated fiber optic imaging probe," *Applied Optics,* Vol. 33, pp. 5875–5881.

Khan, R., and Dhadwal, H. S., 1994b, "Wavefront processing through integrated fiber optics," *Optics Letters,* Vol. 19, No. 22, pp. 1834–1836.

The Influence of Shrouded Stator Cavity Flows on Multistage Compressor Performance

S. R. Wellborn
Rolls-Royce Allison,
Indianapolis, IN 46206

T. H. Okiishi
Iowa State University,
Ames, IA 50011

Experiments were performed on a low-speed multistage axial-flow compressor to assess the effects of shrouded stator cavity flows on aerodynamic performance. Five configurations, which involved systematic changes in seal-tooth leakage rates and/or elimination of the shrouded stator cavities, were tested. Rig data indicate increasing seal-tooth leakage substantially degraded compressor performance. For every 1 percent increase in seal-tooth clearance-to-span ratio, the decrease in pressure rise was 3 percent and the reduction in efficiency was 1 point. These observed performance penalties are comparable to those commonly reported for rotor and cantilevered stator tip clearance variations. The performance degradation observed with increased leakage was brought about in two distinct ways. First, increasing seal-tooth leakage directly spoiled the near-hub performance of the stator row in which leakage occurred. Second, the altered stator exit flow conditions, caused by increased leakage, impaired the performance of the next downstream stage by decreasing the work input of the rotor and increasing total pressure loss of the stator. These trends caused the performance of downstream stages to deteriorate progressively. Numerical simulations of the test rig stator flow field were also conducted to help resolve important fluid mechanic details associated with the interaction between the primary and cavity flows. Simulation results show that fluid originating in the upstream cavity collected on the stator suction surface when the cavity tangential momentum was low and on the pressure side when it was high. The convection of cavity fluid to the suction surface was a mechanism that reduced stator performance when leakage increased.

Introduction

Leakage flows exist in turbomachines. In general, when not accounted for in the design process, leakage flows alter the blockage and loss distributions in the primary flow path, and these in turn may lower the effectiveness and efficiency of a turbomachine from anticipated levels. Axial-flow compressors have leakage in a number of places. Rotor blade tip clearance leakage has been actively studied and publications concerning the negative impact of this leakage on compressor performance are numerous. A general rule is to expect a 1.5 point reduction in efficiency for every 1 percent increase in the tip clearance-to-blade height ratio (Ludwig, 1978; Freeman, 1985) while stall margin can be reduced as much as 6 percent for every 1 percent increase in clearance-to-chord ratio (Wisler, 1988). Studies that detail the impact of other kinds of leakage flows on compressor performance have been reported to a much lesser extent. These other flows include shrouded blade seal-tooth leakage, rotor dovetail leakage, variable stator pivot/clearance leakage, and customer bleed.

In axial-flow compressors, designers commonly consider two options for the construction of stator blades: cantilevered or hub shrouded. The decision to cantilever or shroud stators is generally a mechanical choice. Structural integrity objectives such as keeping the first flex, first torsion, and two-stripe frequencies out of the operating range usually outweigh any aerodynamic considerations (Wisler, 1988). Shrouding usually provides the mechanical stability desired and therefore many modern gas turbine engines typically employ shrouded stator blades. The choice to shroud eliminates the troubles associated with hub clearance leakage flows found with cantilevered stators, but replaces them with the difficulties of shrouded stator leakage in which flow normally recirculates backward through the cavity because of the pressure difference across the stator.

Researchers have briefly commented on the influence of shrouded stator seal-tooth leakage on compressor performance. Jefferson and Turner (1958), Mahler (1972), and Freeman (1985) all showed that efficiency decreased as seal-tooth leakage increased. Freeman's work also suggested that the depth of the cavity did not greatly impact efficiency. Wisler (1988) hinted at the importance of seal-leakage flows when he reported a 2.3 point reduction in efficiency and a 10.3 percent decrease in the average pressure rise of a four-stage compressor when both rotor tip and seal-tooth clearances were increased simultaneously.

Although past experience has revealed that seal-tooth leakage affects compressor efficiency, open literature concerning the importance of including the effects of shrouded stator leakage flows in the design of a multistage compressor is scarce. Adkins and Smith (1982), Wisler et al. (1987), and LeJambre et al. (1998) have documented that cavity flows can alter the spanwise distributions of flow parameters including stator discharge flow angle and blockage. Shabbir et al. (1997) illustrated that a small amount of hub leakage flow upstream of a high-speed axial-flow rotor can result in a corner hub separation and alter blockage distribution across the rotor span. A computational study performed by Heidegger et al. (1996) investigated the influence of many shrouded stator geometric parameters on isolated stator blade performance. While all of these studies com-

Contributed by the International Gas Turbine Institute and presented at the 43rd International Gas Turbine and Aeroengine Congress and Exhibition, Stockholm, Sweden, June 2–5, 1998. Manuscript received by the International Gas Turbine Institute February 1998. Paper No. 98-GT-12. Associate Technical Editor: R. E. Kielb.

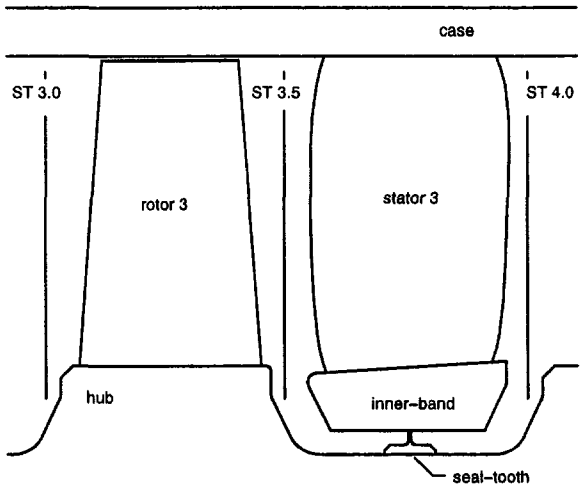

Fig. 1 Meridional view of the LSAC third stage

plement one another, none specifically describe the influence of shrouded stator cavity flows on multistage compressor aerodynamics. The present study of experimental and numerical data details the effects of shrouded stator cavity flows on multistage axial-flow compressor. Designers needing to understand these flows and their effects in multistage compressors better will benefit from this paper.

Objectives and Approach

The overall objectives of this study were to: (1) quantify the importance of shrouded stator cavity flows on the performance of a multistage compressor, (2) document the changes to the flow in an embedded stage when cavity flows are altered; and (3) describe some of the fluid mechanics associated with the interaction between cavity flows and the power stream.

Achievement of these objectives was completed by performing tests on a four-stage low-speed axial-flow compressor and by conducting numerical simulations of the isolated stator 3 coupled cavity–power stream flow. Two separate experiments were completed. In the first, labeled Part A, modifications to the cavity flows of all four stages of the compressor were incorporated. In the second, Part B, alterations were made only to the third-stage cavity flows while the remaining stages were set to the baseline configuration. In both experiments, measurements were taken that allowed overall, individual stage, and blade element performance parameters to be calculated. Four numerical simulations were conducted. These simulations addressed the impact of seal-tooth leakage and upstream cavity tangential momentum on the stator flow field.

Experimental Procedures

The experimental facility and measurement techniques are briefly reviewed here. Additional information concerning the experimental portion of this paper may be found from Wellborn and Okiishi (1996).

Facility. The NASA Lewis Research Center low-speed axial-flow compressor (LSAC) was the test vehicle used for the experimental portion of this study. The four-stage LSAC incorporated a long entrance length to develop thick endwall boundary layers. An inlet-guide vane row was used to generate exit flow angles similar to what embedded stators would produce. The identical stages had a constant case diameter of 1.219 m (48 in.) with a hub-to-tip ratio of 0.80. The third stage was considered the test stage (Fig. 1). All stators were shrouded with one labyrinth seal-tooth in the shrouded stator cavity and were sealed at both the hub and case blade tip interfaces. Detailed information concerning the LSAC was recorded by Wasserbauer et al. (1995).

The blading used for all tests were based on the Rotor B/Stator B geometry designed by General Electric, under Contract No. NAS3-20070. The original blades were designed to reduce loss in the endwalls of a representative core compressor. The rotors consisted of airfoil sections having modified circular-arc meanlines and thicknesses. The stators had 65-series thickness distributions on modified circular-arc meanlines. Complete details of the original designs were given by Wisler (1977). Some simple modifications to the original geometry were incorporated into the NASA blades because of the differences in the hub-to-tip ratios of the two facilities. Important blading parameters are listed in Table 1.

Measurement Techniques. Overall performance data include the compressor pressure rise coefficient (ψ'), work coefficient (ψ), and efficiency (η) deduced from static pressure and shaft torque measurements. These are all given with respect to flow coefficient (ϕ), defined as the measured mean inlet velocity normalized by the measured rotor tip speed (U_{tip}).

Stage performance, blade element performance, and velocity triangle data were calculated from total pressures, static pressures, and flow angles. These were measured in a matrix of circumferential and radial positions by traversing stationary probes across a stator pitch. Data were taken at the rotor inlet, stator inlet, and stator discharge for the third stage. These locations corresponded to Stations (ST) 3.0, 3.5, and 4.0 as shown in Fig. 1. Clustering of measurements near stator wakes and both endwalls allowed better resolution of the flow in those regions. Total pressures were acquired with a miniature kiel-head probe. Static pressures and flow angles were gathered directly with wedge probes. Flow quantities were appropriately area or mass-averaged across one stator pitch to give the radial distributions of the circumferentially averaged flow. For rotor performance, total pressures were first converted to the relative frame at each measurement location before averaging. Velocity components were calculated from the measured corrected pressures and measure flow angles using compressible flow relations. In addition, total temperature was assumed to be constant across the span.

Uncertainty Analysis. An analysis was conducted to estimate the uncertainty of the overall, stage, velocity triangle, and blade element parameters. The analysis used the propagation of error techniques as described in Colemann and Steele (1989). Either analytical or jitter (Moffat, 1985) methods were used to derive these uncertainties. First-order and Nth-order uncertainties for design point and/or pitchline parameters are presented in Table 2. First-order uncertainties refer to precision errors. Nth-order uncertainties include the precision errors together with all bias errors. Independent variable uncertainty values were obtained by taking twice the standard deviation of 30 measured samples while at the design point operating condition. Bias limits were obtained from Blumenthal (1995) or better judgment. If bias limits were dependent, they were assumed to be perfectly correlated. It must be noted that the uncertainty

Table 1 NASA Lewis LSAC pitchline blading parameters

	Rotor	Stator
No. of Airfoils	39	52
Solidity	1.12	1.38
Aspect Ratio	1.20	1.32
Chord, cm	10.2	9.4
Stagger, degree	43.0	42.0
Camber, degree	31.0	40.5
Clearances, % span	1.4 (tip)	0.7 (seal)

Table 2 Uncertainties in performance parameters

Parameter	First-Order	Nth-Order
Flow Coefficient	0.06 %	0.39 %
Pressure Coefficient		
Overall	0.11 %	0.69 %
Stage 1	0.24 %	0.45 %
Stage 2	0.45 %	0.66 %
Stage 3	0.58 %	0.75 %
Stage 4	0.62 %	0.94 %
Work Coefficient	0.22 %	1.09 %
Efficiency	0.25 %	1.20 %
Leakage Massflow	1.23 %	17.0 %
Axial Velocity	1.20 %	1.30 %
Tangential Velocity	1.50 %	3.00 %
Incidence	0.35 deg	1.34 deg
Deviation	0.35 deg	1.34 deg
Diffusion Factor	2.00 %	5.00 %
Loss Coefficient	0.50 %	2.10 %
Blockage Factor	0.32 %	7.50 %

estimates in velocity triangle and blade element performance parameters were truly difficult to assess and are not complete since the analysis did not account for the errors in the slow response pneumatic measurements due to unsteadiness. These types of errors should show up as bias errors and therefore effect Nth-order estimates.

Test Configurations

The experimental portion of this study involved the testing of the LSAC with five different cavity configurations:

- No shrouded stator cavities and no labyrinth seal-tooth leakage (no cavity)
- Minimized labyrinth seal-tooth leakage with shrouded stator cavities (minimized leakage)
- Baseline labyrinth seal-tooth leakage with shrouded stator cavities (baseline leakage)
- Increased labyrinth seal-tooth leakage with shrouded stator cavities (increased leakage)
- Maximum labyrinth seal-tooth leakage with shrouded stator cavities (maximum leakage)

For the no-cavity configuration, wooden extensions were attached to the stator inner-band to cover the cavities. A balsa strip was also adhered to the inner-band inner diameter and the labyrinth seal-tooth was shimmed into the strip. In theory this produced zero (or negative) clearance. In practice this created the minimum clearance attainable with this facility, since the seal-tooth wore into the balsa strip. For this configuration, the seal-tooth clearance was always the smallest of all throttling areas. For the minimized leakage configuration, the wooden extensions were removed and the compressor was reassembled with the balsa strip and shimmed seal-tooth still in place. Although this was intended to be a no-leakage configuration, wear created some clearance and, therefore, some leakage was present. The other three configurations were attained by adjusting the seal-tooth height until the proper clearance was obtained. For these three configurations, the balsa strip was removed from the inner-band, thereby eliminating any rub wear that had previously occurred.

For both Parts A and B, clearances were measured statically before and after each configuration change. These measured clearances, nondimensionalized by the blade span (h = 12.19 cm), are listed in Table 3 for both series of tests. The variations in clearance between stages for a given configuration were caused by machining tolerances on the rotor/inner-band concentricities and run-out of the horizontally mounted cantilevered rotor drum.

Table 3 Clearance values for the different configurations

Configuration	Seal-Tooth Clearance, ε / h x 100					
	Part A Stage 1	Part A Stage 2	Part A Stage 3	Part A Stage 4	Part A Avg.	Part B Stage 3
No Cavity	0.54	0.19	0.21	0.06	0.25	0.46
Minimized Leakage	0.54	0.19	0.21	0.06	0.25	0.46
Baseline Leakage	0.67	0.42	0.69	0.46	0.56	0.71
Increased Leakage	1.35	1.13	1.29	1.17	1.23	1.23
Maximum Leakage	2.02	1.79	1.96	1.83	1.90	1.96

Changes in clearance were correlated to changes in leakage massflow by applying the conservation equations to a control volume enclosing the seal-tooth. A discharge coefficient was included according to Mahler (1972) and the pressure difference across the tooth was measured directly. Figure 2 displays the results of the analysis for two operating conditions. Here, the leakage massflow (w_l) normalized by the power stream massflow (w) is plotted against the clearance-to-span ratio. Each point represents the four-stage average of the calculated massflow values and measured clearance values from Part A. The inconsistency in slope resulted from the change in the pressure difference across the stator for the different operating conditions.

Existing literature indicates the ranges of seal-tooth leakage massflow tested were well within the bounds set by current engine design practice (Mahler, 1972). The baseline configuration produced a leakage rate that could be found in aircraft core compressors utilizing current sealing technology. The no-cavity and minimized leakage configurations could represent leakage rates obtained in advanced sealing technologies such as brush seals (Steinetz and Hendricks, 1994). The increased and maximum leakage configurations represent leakage rates that may occur when labyrinth seal-teeth wear or abradable material erodes.

Four-Stage Changes: Part A

Overall, individual stage and blade element performance data, acquired when configuration changes were made to all four stages of the compressor simultaneously, are reviewed first. Measurements associated with modifications made to only the third-stage cavity geometry are discussed in Part B.

Overall Performance. Increasing seal-tooth leakage degraded the test compressor performance. The systematic influence that increasing leakage had on performance is illustrated in Fig. 3. Near peak efficiency a 4 percent decrease in actual pressure rise and a 2 point drop in efficiency occurred between the no-cavity and maximum leakage configurations. At in-

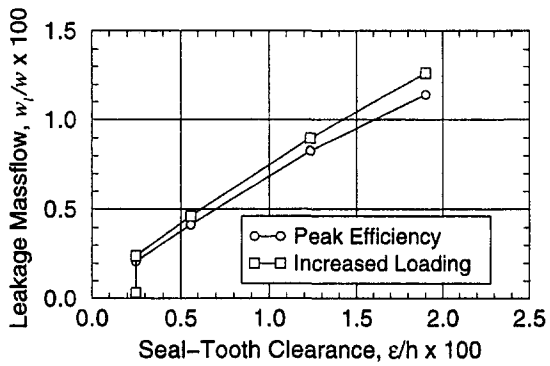

Fig. 2 Correlation between average seal-tooth massflow and average seal-tooth clearance for the first experiment

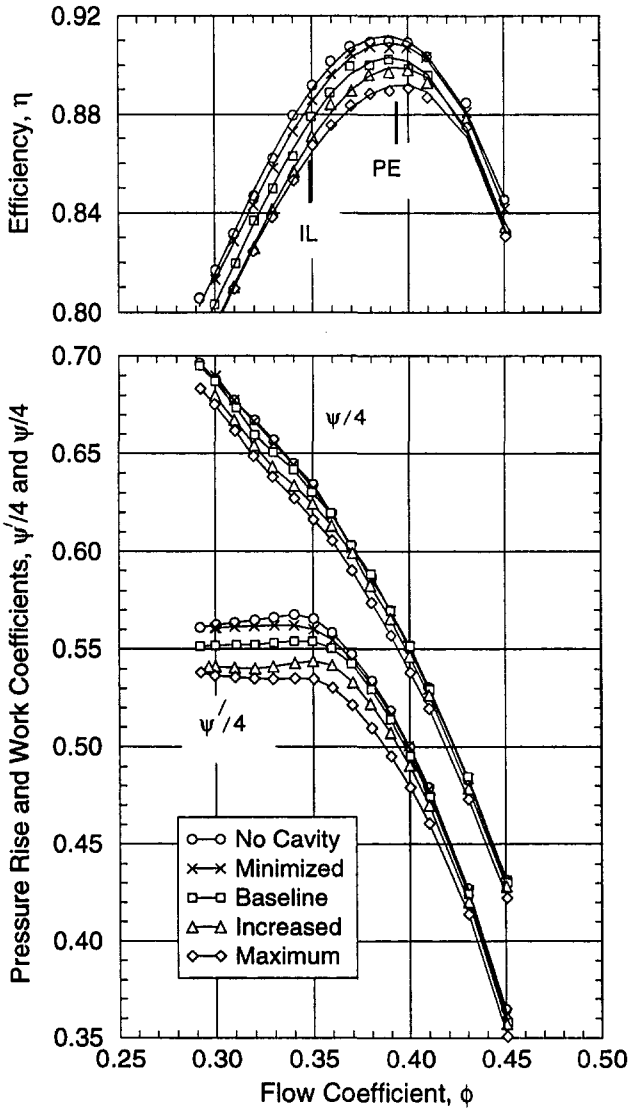

Fig. 3 Overall performance data for Part A

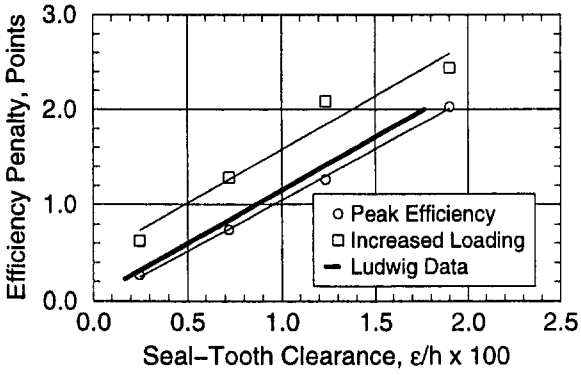

Fig. 4 Efficiency penalties for varying seal-tooth clearance

creased loading, these reductions were nearly 6 percent and 2.5 points. The two largest leakage configurations produced a sizable drop in work input across the entire operating range; however, for the other leakage configurations, an appreciable reduction in work input occurred only at lower flow rates.

Loss in compressor efficiency with increased rotor or stator endwall clearances is expected. Many studies have confirmed and quantified this characteristic. A common rule for rotor blades is to expect a 1.5 point drop in efficiency for each 1 percent increase in the tip clearance-to-span ratio (an efficiency penalty slope of 1.5), although some multistage machines have been reported to have efficiency penalty slopes as high as 2.0. For cantilevered stators these slopes range from 1.0 for large clearances ($\epsilon/h > 1$ percent) to 2.0 for tight clearances ($\epsilon/h < 1$ percent). For many applications larger clearances are the norm. Data from this compressor suggest seal-tooth clearance efficiency penalty slopes near 1.0, as depicted in Fig. 4. These penalty slopes are slightly lower than most values documented for rotors and equal to the values reported for cantilevered stators used in practice. The test data are also consistent with results presented by Ludwig (1978). Therefore, it appears that when predicting overall performance, it is equally important to account for the effects of seal-tooth leakage as it is to include the consequences of rotor tip or stator hub clearance flows.

The influence that shrouded stator cavities (without leakage) had on compressor performance could be inferred from the test data. The vertical intercepts of the regression lines in Fig. 4 indicate open cavities had no influence on performance near-peak efficiency, but contributed a 0.5 point penalty at the increased loading condition. Unfortunately, the scatter and uncertainty in the efficiency data could account for the perceived penalty. Further investigations concerning how open cavities impact performance should be performed before firm conclusions are drawn.

It should be noted that Fig. 3 suggests insignificant change in the flow coefficient where stall first occurred for the different configurations. For the no-cavity, baseline and maximum leakage configurations, the data include the last acquired operating point before dropping into stall ($\phi \approx 0.292$). The slight differences in the stall inception flow coefficient for the minimized and increased leakage configurations were caused by mechanical problems in the throttle sleeve valve, which controlled the massflow through the compressor. This mechanical problem was not present for the other three configurations, and therefore it was concluded that neither the leakage rate nor the presence of the cavity had much influence on the stall inception point of this compressor. The insensitivity of the stall point to hub leakage flow in addition with other data not presented here suggest the first rotor initiated stall in this compressor.

Stage Performance. Individual stage pressure rise data indicated that increasing seal-tooth leakage lowered the pressure rise of each stage and that the performance degradation became progressively worse in downstream stages. This is illustrated in Figs. 5 and 6, where the percent decrease in pressure rise is shown for each stage for the near-peak efficiency and increased loading operating conditions. Both figures show downstream stages suffered more degradation than upstream stages. Near peak efficiency, the trend was most noticeable at larger clearances ($\epsilon/h > 1$ percent), while at increased loading the trend was present for all clearance values.

Third-stage circumferentially averaged radial distributions of pressure rise (ψ'), work input (ψ), and efficiency (η) are displayed in Fig. 7 for increased loading operation. As seen, increasing leakage reduced the actual pressure rise across the entire span, while the actual work input was mainly reduced outboard of 50 percent span. This related to a greater reduction in efficiency near the hub compared to the tip when leakage was increased.

Blade Element Performance and Velocity Triangle Data. Both rotor and stator blade flow fields were influenced by the amount of seal-tooth leakage. In general, increased leakage produced increased stator flow blockage and total pressure loss inboard of 40 percent span. The blockage forced fluid outward, which in turn unloaded a substantial portion of the stator and the downstream rotor. These trends caused the degradation ob-

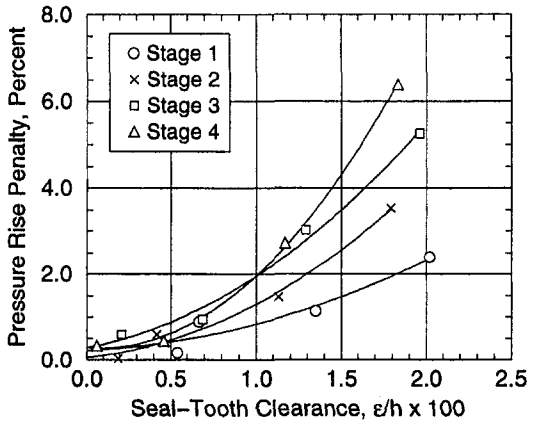

Fig. 5 Stage pressure rise penalties for varying seal-tooth clearance near peak efficiency operating condition

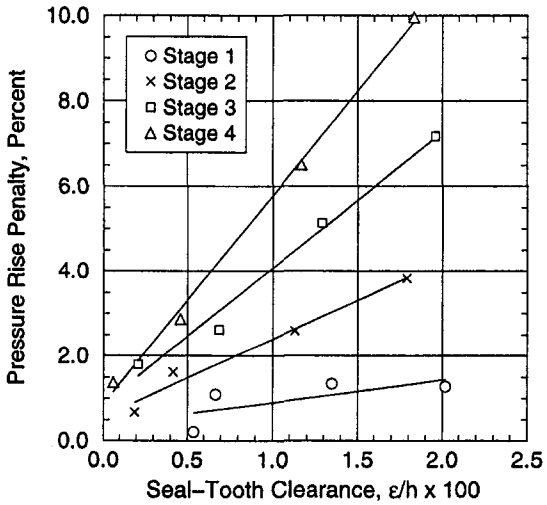

Fig. 6 Stage pressure rise penalties for varying seal-tooth clearance at increased loading operating condition

served in overall and stage performance. Blade element performance and axial velocity data that support these conclusions are shown in Figs. 8 and 9, respectively, for the increased loading operating condition. Similar tendencies in the data were also apparent near peak efficiency. Continuing discussions are therefore a combined view of what happened in common at both operating conditions. Since definite trends can be seen when sequentially viewing data from the no-cavity to maximum leakage configuration, the observed trends are always correlated to increasing seal-tooth leakage.

At the inlet to the third rotor (ST 3.0) a large deficit in axial velocity developed near the hub (5–25 percent span) when seal-tooth leakage increased. Axial velocity data also confirm that the increased blockage near the hub forced fluid outward. Consequently, the rotor near hub incidence increased, while across the rest of the span (30–100 percent) rotor incidence decreased. Even though moderate variations in rotor incidence were present across the entire span, rotor deviation values were only slightly altered with varying leakage. This is consistent with two-dimensional blade element theory for airfoils operating near minimum loss incidence. Decreased rotor loadings for the upper 50 percent span and increased loading for the lower 50 percent illustrated by the diffusion factor data, were consistent with the notion that increased blockage at the stator hub forced more fluid outward, which unloaded the tip and loaded the hub of the rotor. Changes in rotor loss occurred across most the span. Near midspan loss values were raised, while near the hub and very near the tip they were reduced. The negative loss near the hub for many configurations may represent the radial shifting and mixing of the large inlet total pressure deficit as it passed through the rotor. This is supported by the reduced region of flow blockage at ST 3.5 and the increased levels of loss near midspan where rotor incidence values were actually reduced. Here, unlike deviation trends, two-dimensional thinking does not work in three-dimensional flows. The negative loss could also represent the inaccuracy of calculating relative total pressures from stationary slow response instrumentation. Additional data to clarify this trend would be useful.

The incoming third stator flow (ST 3.5) had decreased levels of axial velocity over the lower 25 percent of span and raised levels for the rest of the span when leakage increased. The decreased axial velocity and slightly increased tangential velocity (not shown), led to increased stator incidence near the hub. Near the tip, stator incidence angles were slightly reduced due to the movement of flow outward.

The third stator exit flow also had a large region of flow blockage develop when seal-tooth leakage increased. Note the formation of low axial velocity from 5–25 percent span at ST 4.0 in Fig. 9. Blockage near the hub again forced fluid toward the tip, which increased the axial velocity there. Because of the hub blockage, stator diffusion factor data show decreased loading over much of the span (25–100 percent), while near the hub loading increased. Considerable variations in stator deviation angles existed with varying leakage; from 0–10 percent and 60–95 percent span deviation decreased, but from 10–50 percent span deviation increased. At 15 percent span a 7 deg difference in deviation existed between the no-cavity and maximum leakage configurations at both operating conditions. At the hub (0–10 percent span), reduced deviation values corresponded to decreased tangential velocity levels and indicate a tendency for hub fluid to become overturned. Marginal changes in stator total pressure loss occurred outboard of 50 percent span; however, across the lower 40 percent of span large loss increases transpired. At 20 percent span, the loss more than doubled when going from no cavity to maximum leakage.

These variations in stator hub blockage, deviation, and loss with span and leakage amount appeared to correspond well to the variations in stator incidence angle with span and leakage amount. However, analysis of this experiment data alone cannot determine whether these changes were caused only by stator incidence changes. More discussions on this subject are presented in Part B.

Circumferential Variation Details. At the inlet of the third stator, measurements suggest that the radial variations in circumferentially averaged data with leakage increase were

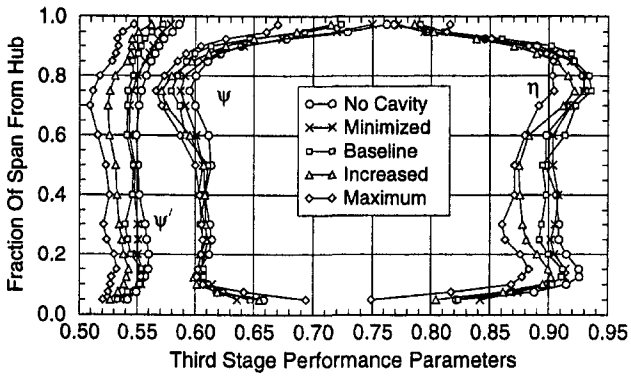

Fig. 7 Radial distribution of third-stage performance parameters at increased loading

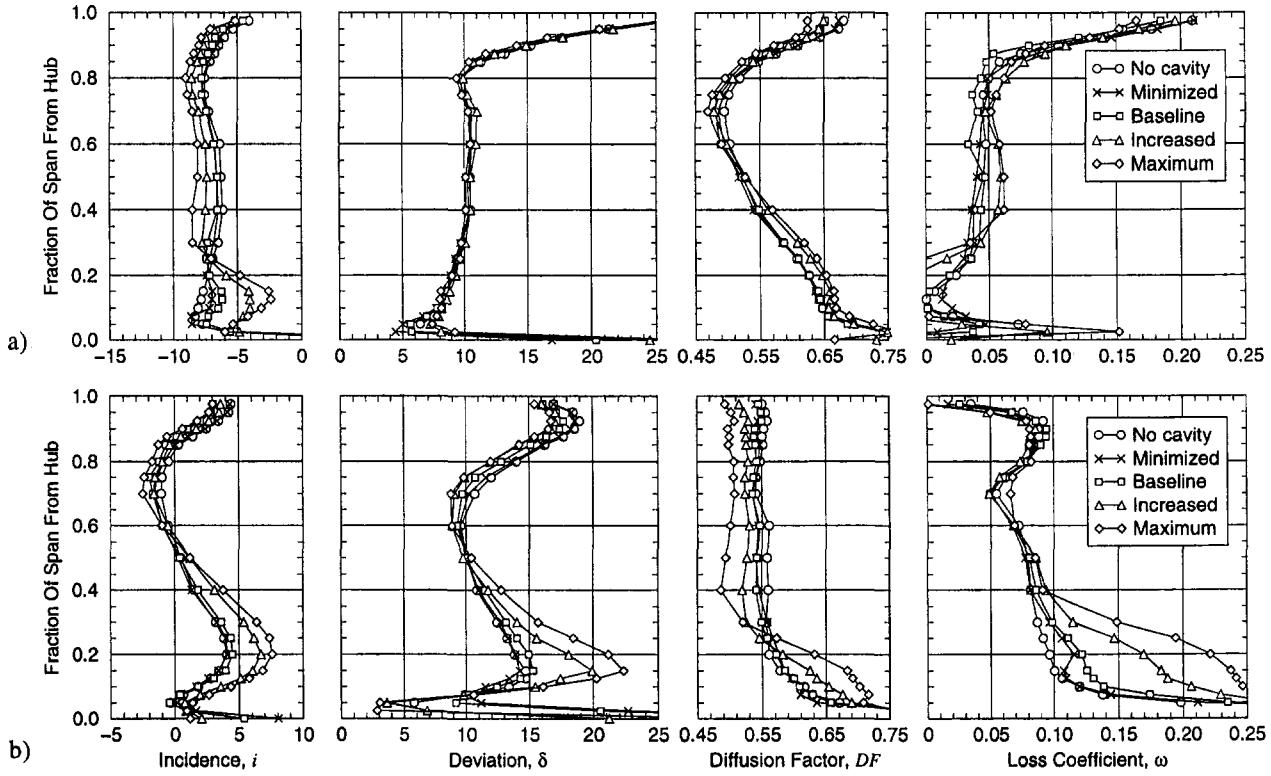

Fig. 8 Variation of blade element performance data for (*a*) rotor 3 and (*b*) stator 3 with varying seal-tooth clearance: increased loading operating condition

caused by incremental shifts in flow parameter levels across the entire pitch and not by changes to the circumferential distributions. This is shown in Fig. 10 for stator 3 incidence at 20 percent span operating at increased loading.

Unlike stator inlet flow, stator discharge flow near the hub demonstrated sizable changes in the pitchwise distributions with leakage increase. Stator exit axial velocity data show (Fig. 10) that at 20 percent span the large region of blockage depicted in Fig. 9 developed on the suction side of the blade. The stator wake width increased from 40 to 80 percent pitch when going from no cavity to maximum leakage, while the wake depth grew from 50 to 90 percent of the midpitch value. Outboard of 50 percent span only small changes to the wake width and depth occurred.

Large variations in deviation and total pressure loss with leakage change were also present across most of the pitch at 20 percent span. A definite trend existed in which the suction side deviation and loss values increased with increased seal-tooth leakage. The deviation value became greater than 40 deg at 20 percent pitch for the maximum leakage case. The local loss in total pressure at the same location and for the same configuration reached nearly 0.7. It is interesting to note that even though the suction side deviation severely worsened, flow deviation between blade wakes (40 to 90 percent pitch) was not significantly altered. The increased loss and deviation values near 20 percent span, along with the decrease in axial velocity there, indicate that the suction surface boundary layer was severely disrupted when seal-tooth leakage increased.

Single-Stage Changes: Part B

The results of Part A revealed that increasing seal-tooth leakage systematically altered overall, individual stage, and blade element performance. With these changes in performance also

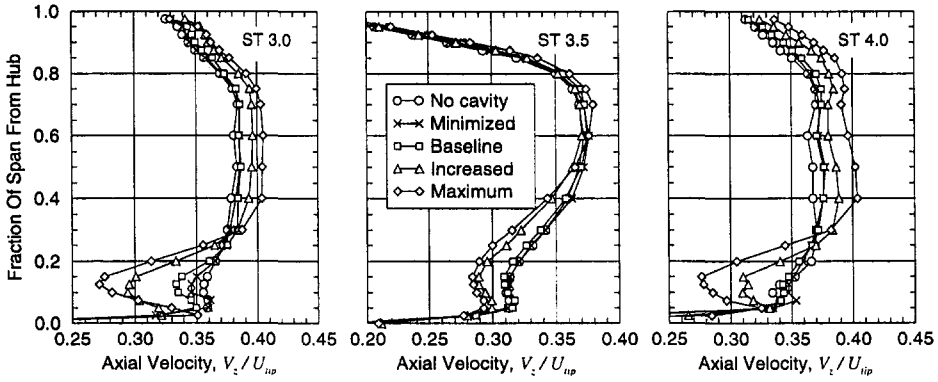

Fig. 9 Variation of circumferential averaged axial velocity with varying seal-tooth clearance at stator 2 discharge (ST 3.0), rotor 3 discharge (ST 3.5), and stator 3 discharge (ST 4.0): increased loading operating condition

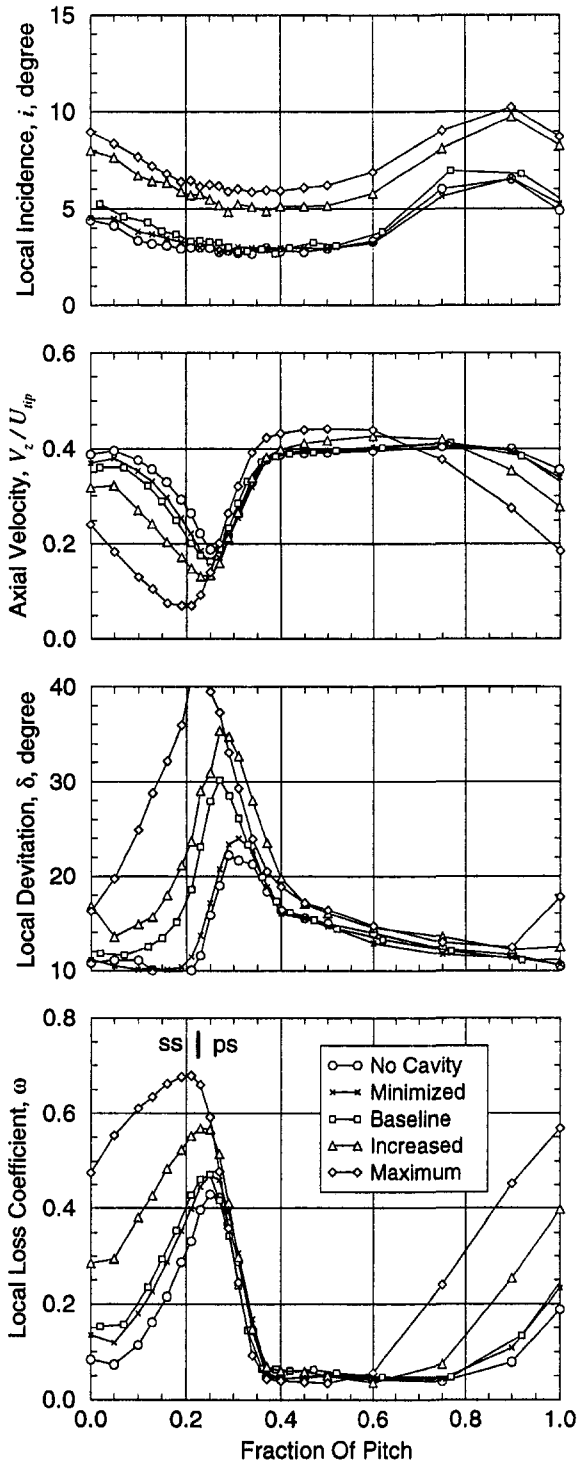

Fig. 10 Circumferential distributions of stator 3 incidence, exit axial velocity, deviation, and loss coefficient at 20 percent span from hub: increased loading operating condition

came variations in the inlet flow profiles of each of the last three stages. These changing conditions made it difficult to identify the fluid mechanics associated with the interaction between seal cavity flows and the primary flow. A second experiment was performed in order to help understand these mechanics better, and specifically to determine the influence of seal-tooth leakage on the performance of an embedded stage. For this second experiment only the third-stage cavity geometry was modified, while the cavities of stages one, two, and four were kept at the baseline configuration geometry. This section summarizes the results of the second experiment (Part B) with frequent reference to data already presented in Part A.

Stage Performance. Changes to the third-stage cavity geometry in Part B did not alter the first and second-stage pressure rise characteristics, but did change the those of the third and fourth stages. Third-stage pressure rise penalty values at two operating conditions are shown in Fig. 11. Part B data show a 2.0 to 2.5 percent stage pressure rise penalty when going from no cavity to maximum leakage. Therefore, nearly 40 percent of the third stage penalty observed in Part A could be directly attributed to the alteration of the third stator seal-tooth leakage alone. Variations in the fourth-stage pressure rise values indicated that nearly half of the fourth-stage pressure rise degradation in Part A was attributed to the variations in the rotor 4 incoming flow. For example, at increased loading operation the forth-stage pressure rise penalty between the configuration extremes was approximately 5 percent for Part B compared to 10 percent for Part A.

These facts indicate that the presence of seal-tooth leakage affects stage performance in two distinct ways. First, a performance penalty will be suffered because of the amount of leakage associated with that stage. Second, performance of downstream stages can be degraded by any upstream flow field disruptions caused by increased seal-tooth leakage within upstream stages.

Blade Element Performance and Velocity Triangle Data. Data collected for Part B indicated no measurable differences in the third rotor exit flow for the increasing leakage of stator 3 except for slightly increased relative tangential velocity near the hub (0–3 percent span). This suggested the downstream stator leakage did not hinder the upstream rotor performance. Therefore, the Part B pressure rise penalty, seen in Fig. 11, was caused only by the poorer performance of stator 3, even though inlet flow conditions into stator 3 were nearly identical for all configurations.

Radial distributions of stator 3 blade element performance and axial velocity data are given in Figs. 12 and 13, respectively, for the increased loading operating condition. The trends established for the stator flow field in Part A when the seal-tooth leakage was increased were repeated in Part B, but to a lesser extent. Increasing the third-stage seal-tooth leakage lowered the axial velocity near the hub (5–25 percent span), while outboard of 25 percent span the axial velocity was raised. Deviation increased from 10–50 percent span and decreased inboard of 10 percent span. Diffusion factor data show increased loading near the hub (0–15 percent span) and reduced loading outboard of 20 percent span. Finally, the region in which the loss increased extended out to 35 percent span. At 12.5 percent span,

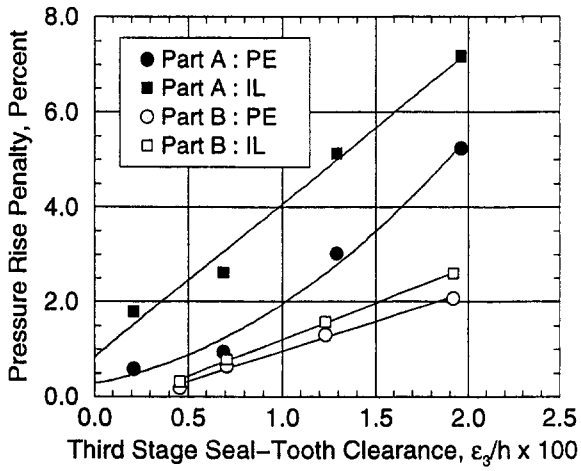

Fig. 11 Third-stage pressure rise penalties for near-peak efficiency (PE) and increased loading (IL) operating conditions

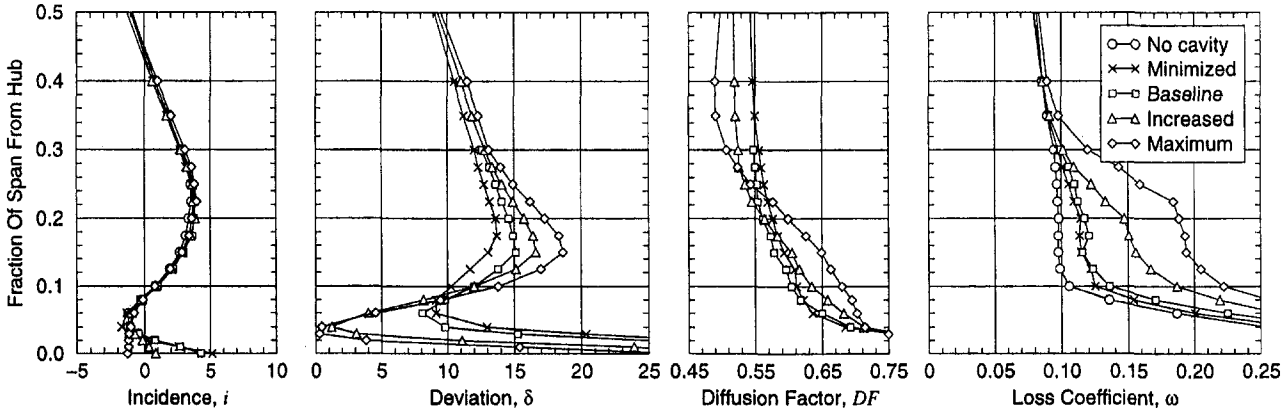

Fig. 12 Variation of blade element performance data for stator 3 with varying seal-tooth clearance: increased loading operating condition

the loss for the maximum leakage configuration was nearly double the value associated with the no-cavity configuration.

To make more quantitative comparisons between Parts A and B data, two additional parameters were calculated. The first was an axial velocity displacement thickness or blockage factor (δ^*) similar to what might be used in a throughflow calculation. The second was mass-averaged total pressure loss (ω) across a spanwise portion of the passage. These parameters were calculated from Part A and Part B data at ST 4.0. Displacement thickness values are illustrated in Fig. 14, while total pressure loss quantities are given in Fig. 15. Note that both displacement thickness and loss for Parts A and B at a specific operating condition were nearly equal for the baseline clearance ($e_3/h \approx 0.7$). This was because nearly identical stator 3 inlet flow conditions and leakage flow rates were present for these cases. For clearances less than the baseline ($e_3/h < 0.7$), Part A near peak efficiency displacement thickness and loss values were less than those of Part B. This indicated the added benefit of having a better flow profile coming into the stator, which occurred in Part A. For clearances greater than baseline ($e_3/h > 0.7$), Part A displacement thickness and loss values were greater than those of Part B. This indicated the extra detriment caused by having a worsened flow profile coming into the stator. For clearances larger than the baseline value, nearly 65 percent of the extra blockage that developed in Part A was attributed solely to the increase in seal-tooth leakage under the third stator. The other 35 percent was caused by different flow conditions into the stator. Likewise, increasing the seal-tooth leakage under stator three accounted for approximately 60 percent of the increase in loss found in Part A while 40 percent may be attributed to the different incoming flow distributions.

Comparison of the data from both experiments (Parts A and B) leads to two major conclusions. First, seal-tooth leakage affects rotor performance in a rather indirect manner, since varying the amount of seal-tooth leakage in a stage negligibly alters the upstream rotor performance. Instead, seal-tooth leakage disrupts the stator flow field, which, in turn, produces different stator exit flow conditions. These different conditions then modify the performance of any downstream stage. Second, seal-tooth leakage influences the performance of a stator both directly and indirectly. Changing the amount of seal-tooth leakage can alter the stator performance in that stage. Furthermore, provided the downstream rotor cannot heal the degraded incoming flow, the flow into the next stator may also be altered, which can change the performance of that downstream stator. From these conclusions it becomes apparent that a designer must not only account for the influence of seal-tooth leakage in the design of the stator row in which leakage occurs but also consider the influence in downstream blade rows.

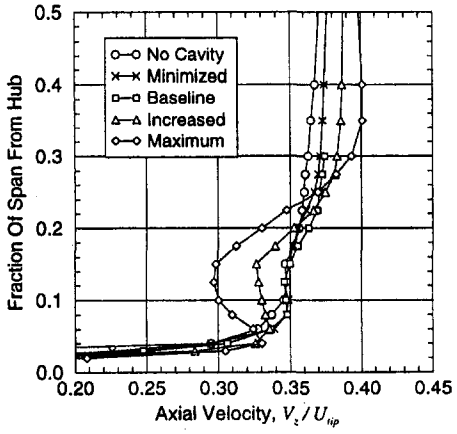

Fig. 13 Variation of circumferential averaged axial velocity with varying seal-tooth clearance at stator 3 discharge (ST 4.0): increased loading operating condition

Isolated Stator 3 Simulations

The impact of the upstream cavity tangential velocity on the near hub flow field is first hypothesized. When cavity fluid having low tangential velocity (momentum) is entrained into the power stream, the cross-passage pressure gradient drives it to the suction side where it collects and worsens the near hub suction side blade boundary layer. More leakage or lower tangential velocity fluid in the upstream cavity will increase this cross-passage flow. When the upstream cavity tangential velocity is high enough to overcome the cross-passage pressure gradient, the cavity fluid collects on the pressure side of the stator blade as it travels downstream. In this case, the suction surface sensitivity to increased leakage is reduced since less cavity fluid collects on the suction side of the blade. Although described here in terms of pressure gradients and fluid momentum, the process is identical to the tilting and stretching of a vorticity vector as it convects through the channel with the production of secondary flows, as envisioned by Adkins and Smith (1982).

Numerical simulations of the LSAC isolated stator 3 flow field were obtained with the ADPAC analysis tool to help support these premises. The code solved the three-dimensional Reynolds-averaged Navier–Stokes equations using a finite volume formulation with an explicit time-marching Runge–Kutta solution scheme. Steady-state flows were obtained as the time-independent limit of the time-marching procedure. Local time stepping, implicit residual smoothing, and multigrid acceleration techniques were utilized along with multiple-block mesh discretization. A standard Baldwin–Lomax turbulence model was used to estimate turbulent shear stresses. Additional infor-

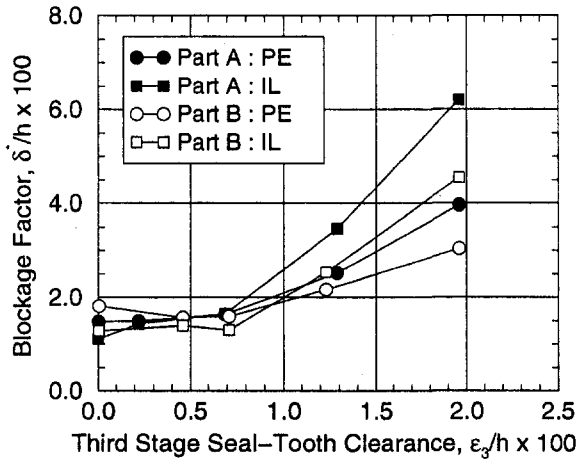

Fig. 14 Blockage factor variations for near-peak efficiency (PE) and increased loading (IL) operating conditions

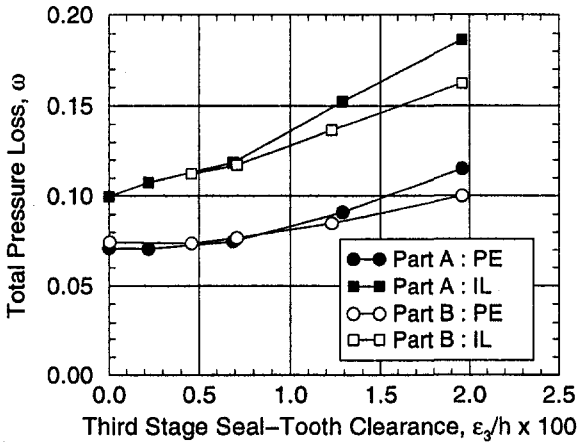

Fig. 15 Variations in mass-averaged total pressure loss for near-peak efficiency (PE) and increased loading (IL) operating conditions

mation concerning numerical algorithm development may be found from Hall and Delaney (1993).

Physical Discretization and Boundary Conditions. The stator power stream and cavity flows were solved simultaneously. A typical meridional mesh distribution used for the calculations is shown in Fig. 16. A sheared **H**-type grid extended the meridional distribution into the circumferential direction. The power stream had a total of 468,195 (193 × 49 × 49) points while the cavity contained 327,320. All simulations were performed with essentially the same grid. Near-wall spacings were kept to within 0.05 percent span for all surfaces. Inlet and exit boundary conditions were prescribed in order to match the measured circumferential averaged flow parameters at Station 3.5 and 4.0 for the Part B baseline configuration at peak efficiency. Design rotational speed was 958 rpm.

Numerical Configurations. This portion of this study involved the simulation of four configurations:

- Baseline clearance with nominal wheel speed (1Ω)
- Maximum clearance with nominal wheel speed (1Ω)
- Baseline clearance with double wheel speed (2Ω)
- Maximum clearance with double wheel speed (2Ω)

The baseline and maximum clearance cavity geometries matched those of the second experiment. For two configurations the hub was rotating at the nominal design speed, while for the other two the wheel speed was doubled in order to produce a higher upstream cavity tangential velocity. Although the wheel speed was doubled, the inlet and exit flow conditions were unaltered. This was permissible since the stator was simulated in isolation.

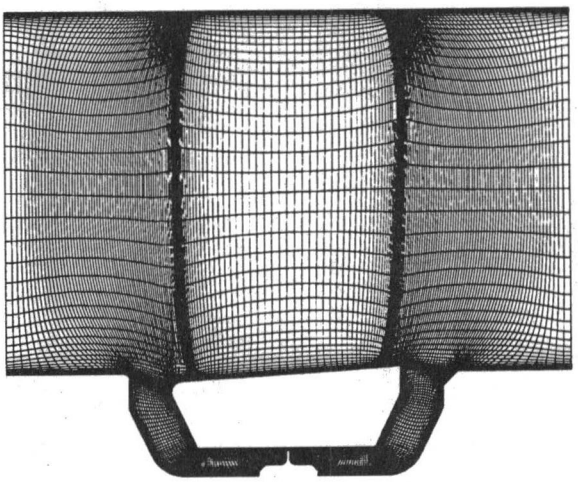

Fig. 16 Meridional mesh distribution used for LSAC isolated stator 3 calculations

Tangential Velocities Within the Upstream Cavity. Before reviewing data that confirm the premises, it is beneficial to look at the circumferentially averaged tangential velocity variations within the upstream cavity. These are illustrated in Fig. 17. Included also are the measured LSAC data for the baseline and maximum leakage configurations. The tangential velocity levels and distributions changed for each simulation. For nominal wheel speed, the maximum clearance geometry reduced the upstream cavity tangential velocity to about 30 percent of the hub speed from the baseline 40 percent value. This reduction closely agreed with measured data. Increasing the hub wheel speed obviously increased the upstream cavity tangential velocity. For the baseline clearance, doubling the wheel speed increased the tangential velocity to about 90 percent of the hub speed, while the maximum clearance produced a value of approximately 70 percent. The bulges in tangential velocity near 0 percent span for the double wheel speed solutions were caused by the convection of high tangential velocity fluid, very near the upstream cavity rotor wall, into the power stream.

Discussion of Numerical Simulations. The predicted and measured spanwise distributions of stator 3 exit axial velocity and deviation are depicted in Figs. 18 and 19, respectively. For nominal wheel speed, the measured increase in hub blockage

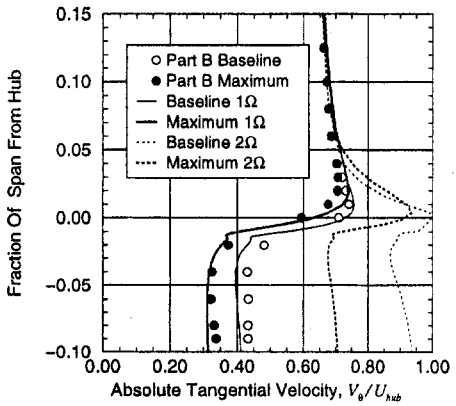

Fig. 17 Variations in circumferentially averaged tangential velocity within the stator 3 upstream cavity (ST 3.5). Symbols represent measured data while lines denote simulation data.

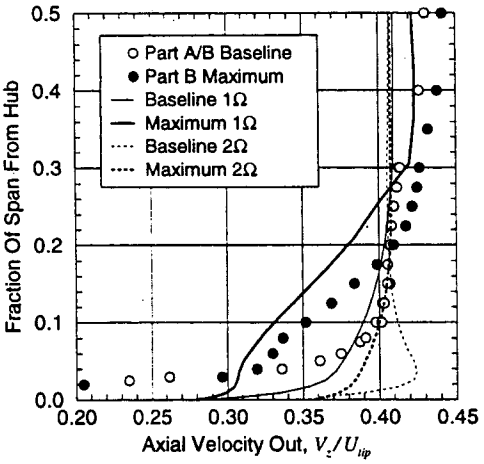

Fig. 18 Variations in circumferentially averaged stator 3 discharge axial velocity (ST4.0). Symbols represent measured data while lines denote simulation data.

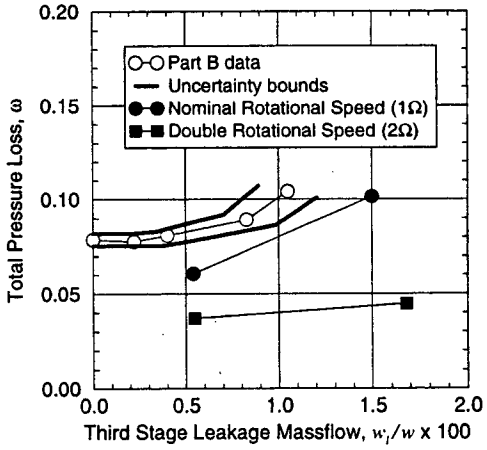

Fig. 20 Variations in stator 3 measured and predicted total pressure loss

with increased seal-tooth clearance was captured in the maximum clearance simulation. The predicted deviation quantities also show adequate representation of the measured data for both nominal wheel speed configurations.

Increasing the upstream cavity tangential velocity influenced the stator flow field. Hub blockage was reduced compared to the nominal wheel speed simulations. Deviation angles show more turning from 10–40 percent span and less overturning at the hub (0–10 percent span). Diffusion factor data (not shown) indicated that the hub loading was reduced when the wheel speed doubled. This corresponded well with the reduced blockage present there.

The increase in loss with increased leakage for the double wheel speed simulations was less than that observed in the nominal speed simulations. The predicted mass-averaged total pressure loss variations are illustrated in Fig. 20. Part B measured data and uncertainty estimates are also included. Both nominal wheel speed simulations under predicted loss compared to measured data, while the leakage rate (for the same clearance) was greater than the estimated test leakage. Although the predicted and measured absolute levels were not the same for these nominal wheel speed data, the trend of increased loss with increased leakage was present. When the wheel speed was doubled, a reduction in total pressure loss occurred. The sensitivity of loss to leakage was also reduced as surmised in the stated premises.

The impact these different cavity flows had on the hub flow field is illustrated in Fig. 21. Here, hub surface flow is represented by near-surface streaklines. These streaklines clearly indicate increased crossflow for maximum clearance compared to baseline clearance. Also doubled wheel speed hub streaklines show less turning than the nominal wheel speed streaklines.

The radial extent of leakage flow at the stator discharge is shown in Fig. 22, which indicates where fluid particles, originating in the upstream cavity, passed through a cross-channel plane at the stator trailing edge. These particles were tagged at the cavity-power stream interface surface just upstream of the stator leading edge and therefore Fig. 22 represents all seal-tooth leakage flow that entered the power stream. The progression of these interface fluid particles from the pressure side to suction side for the different simulations is apparent. For the baseline double wheel speed simulation, most fluid particles originating at the interface ended up near the pressure side of the blade and did not migrate above 2.5 percent span. For the maximum double wheel speed simulation, a large amount of these particles remained in the pressure half of the passage, although some were convected to the suction side of the blade. In the baseline nominal speed simulation, no particles collected on the pressure surface. Instead, they were carried to either the middle of the passage or up the suction surface. Some particles near the suction surface had a spanwise migration of nearly 10 percent span. Finally, for the maximum nominal wheel speed simulation, a substantial amount of interface fluid collected within a suction surface separation region, moved radially outward on the blade surface, and exited the blade at 10–15 percent span.

The simulation results clearly show that the stated hypothesis was qualitatively correct. When the tangential momentum of the upstream cavity fluid was low, that fluid collected on the suction surface and further worsened the near-hub suction side blade boundary layer. More leakage, which produced lower tangential velocity cavity fluid, also increased the cross-passage flow. Furthermore, with high tangential momentum fluid in the upstream cavity, the suction surface sensitivity to increased leakage was reduced since less cavity fluid collected on the suction side of the blade.

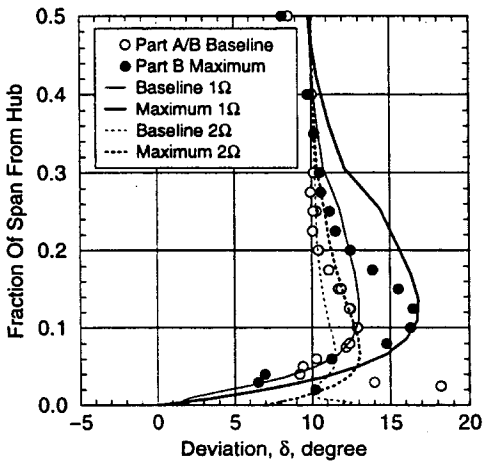

Fig. 19 Variations in circumferentially averaged stator 3 deviation angle (ST4.0). Symbols represent measured data while lines denote simulation data.

Conclusions

Experiments were performed on a low-speed multistage axial-flow compressor to assess the effects of shrouded stator cavity flows on aerodynamic performance. Numerical simulations of the test rig stator flow field were also conducted to help

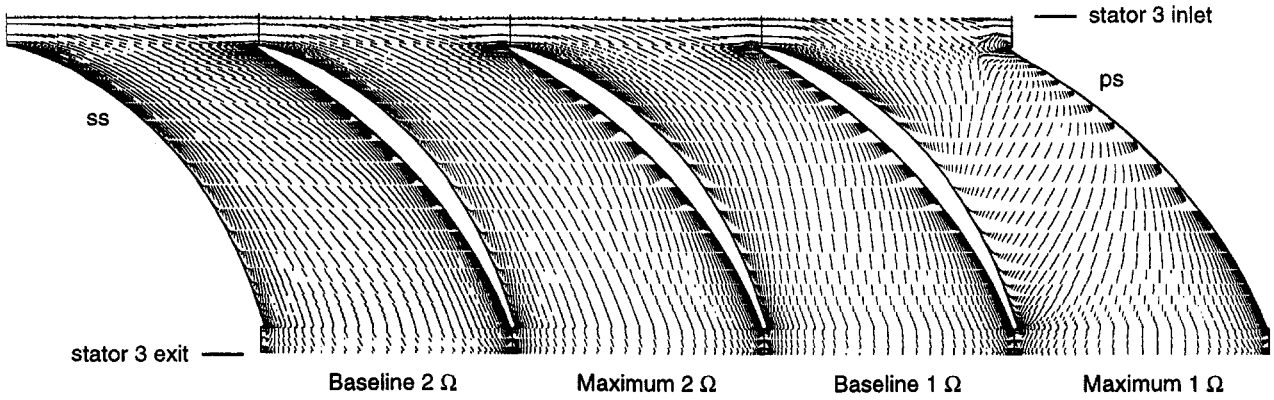

Fig. 21 Streaklines near the hub surface for the four different simulations

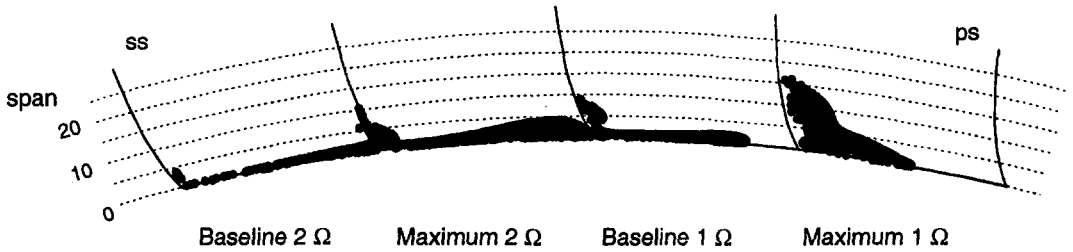

Fig. 22 Location where particle traces, which originated at the upstream cavity-power stream interface, intersected the stator trailing edge surface

resolve some important fluid mechanics details associated with the interaction between the primary and cavity flows.

The rig tests confirmed increasing seal-tooth leakage degraded compressor performance. Data revealed that for every 1 percent increase in seal-tooth clearance-to-span ratio, the pressure rise penalty was nearly 3 percent, while efficiency dropped 1.0 point. The observed efficiency penalty slopes were comparable to those commonly reported for rotor and cantilevered stator tip clearance variations. Therefore, the data suggest it is as important to account for the effects of seal-tooth leakage as it is to include the influence of tip clearance flows when trying to predict overall performance of multistage compressors correctly.

The influence of open cavities alone on performance remains unresolved. More data on this subject would be useful.

It should be noted that neither concealing the cavities nor changing seal-tooth leakage altered the stalling flow coefficient of this test compressor. Again, additional data detailing the influence of seal-tooth leakage on the stalling flow coefficient of different compressors would be useful.

The performance degradation observed when leakage increased was brought about in two distinct ways. First, increasing seal-tooth leakage directly spoiled the near hub performance of the stator row in which leakage occurred. Additional leakage fluid produced additional flow blockage, deviation, and total pressure loss near the stator hub endwall. This extra blockage forced more fluid radially outward toward the shroud, thereby unloading a significant spanwise portion of the stator. Second, the altered stator exit flow conditions caused by increased leakage impaired the performance of the next downstream stage by decreasing the work input of the downstream rotor and increasing total pressure loss of the downstream stator. These effects caused a progressive deterioration of performance for each downstream stage.

Simulation results showed that when the tangential momentum of the fluid in the upstream cavity was low, that fluid collected on the suction surface of the stator blade and further worsened the near hub suction side blade boundary layer. More leakage produced lower tangential velocity cavity fluid and, therefore, cross-passage flow was increased. When the tangential momentum of the upstream cavity was high, the suction surface sensitivity to increased leakage was reduced, since less cavity fluid collected on the suction side of the stator blade.

Acknowledgments

The research reported within owes its existence to the efforts of many. The NASA Lewis Research Center, Cleveland, Ohio, sponsored much of this work under Grant No. NAG 3-1427 (M. Hathaway grant monitor) and Contract No. NAS3-27725 (A. Strazisar contract monitor). NAS computer time, used for some of the simulations, was appreciated. Test cell personnel without whose support this research endeavor would not have been possible include B. Darby, B. Ehrbar, R. Senyitko, C. Wasserbauer, and H. Weaver. Sincere gratitude is also offered to the many peers at NASA Lewis, Rolls-Royce Allison, and other universities who have contributed to the work. Although the existence of the work reported within owes its existence to many, this paper exists because of the constant urging of J. Adamczyk.

References

Adkins, G. G., and Smith, L. H., 1982, "Spanwise Mixing in Axial-Flow Turbomachines," ASME *Journal of Engineering for Power,* Vol. 104, pp. 97–110.

Blumenthal, P. Z., 1995, "A PC Program for Estimating Measurement Uncertainty for Aeronautics Test Instrumentation," AIAA Paper No. 95-3072; also NASA CR 198361.

Colemann, H. W., and Steele, W. G., 1989, *Experimentation and Uncertainty Analysis for Engineers,* Wiley, New York.

Freeman, C., 1985, "Effect of Tip Clearance Flow on Compressor Stability and Performance," von Karman Institute for Fluid Dynamics Lecture Series 1985-05, Apr.

Hall, E. J., and Delaney, R. A., 1993, "Investigation of Advanced Counterrotation Blade Configuration Concepts for High Speed Turboprop Systems," NASA CR 187126, Jan.

Heidegger, N. J., Hall, E. J., and Delaney, R. A., 1996, "Parameterized Study of High-Speed Compressor Seal Cavity Flow," AIAA Paper No. 96-2807.

Jefferson, J. L., and Turner, R. C., 1958, "Some Shrouding and Tip Clearance Effects in Axial Flow Compressors," *International Ship Building Progress,* Vol. 5, pp. 78–101.

LeJambre, C. R., Zacharias, R. M., Biederman, B. P., Gleixner, A. J., and Yetka, C. J., 1998, "Development and Application of a Multistage Navier–Stokes Flow

Solver, Part II: Application to a High-Pressure Compressor Design," ASME JOURNAL OF TURBOMACHINERY, Vol. 120, pp. 215–223.

Ludwig, L., 1978, "Gas Path Sealing in Turbine Engines," *Seal Technology in Gas Turbine Engines,* AGARD Publications, Neuilly Sur Seine France, Apr.; also NASA TM 73890.

Mahler, F. H., 1972, "Advanced Seal Technology," Pratt and Whitney Aircraft Division Tech. Rep. PWA-4372, Feb.; also AFAPL TR-72-8.

Moffat, R. J., 1985, "Using Uncertainty Analysis in the Planning of an Experiment," ASME *Journal of Fluids Engineering,* Vol. 107, pp. 173–178.

Shabbir, A., Celestina, M. L., Adamczyk, J. J., and Strazisar, A. J., 1997, "The Effect of Hub Leakage Flow on Two High Speed Axial Flow Compressor Rotors," ASME Paper No. 97-GT-346.

Steinetz, B. M., and Hendricks, R. C., 1994, "Engine Seal Technology Requirements to Meet NASA's Advanced Subsonic Technology Program Goals," AIAA Paper No. 94-2698, June; also NASA TM 106582.

Wasserbauer, C. A., Weaver, H. F., and Senyitko, R. G., 1995, "NASA Low-Speed Axial Compressor for Fundamental Research," NASA TM 4635, Feb.

Wellborn, S. R., and Okiishi, T. H., 1996, "Effects of Shrouded Stator Cavity Flows on Multistage Axial Compressor Aerodynamic Performance," NASA CR 198536, Oct.

Wisler, D. C., 1977, "Core Compressor Exit Stage Study: Vol. 1—Blade Design," NASA CR 135391, Dec.

Wisler, D. C., Bauer, R. C., and Okiishi, T. H., 1987, "Secondary Flow, Turbulent Diffusion and Mixing in Axial-Flow Compressors," ASME JOURNAL OF TURBOMACHINERY, Vol. 109, pp. 455–482.

Wisler, D. C., 1988, *Advanced Compressor and Fan Systems,* GE Aircraft Engines, Cincinnati, Ohio; also 1986 Lecture to ASME Turbomachinery Institute, Ames, Iowa.

DISCUSSION

Ruixian Cai[1]

The paper studied the influence of shrouded stator seal-tooth leakage on axial compressor performance in detail and gave sound conclusions. However, there is an unsolved problem: Does the existence of stator shroud influence performance markedly? The paper did not answer this problem directly since it had not tested the compressor with unshrouded stator and compared the experimental results. Nevertheless, according to the explanation of Figs. 3 and 4, it seems the answer of the authors was no evident influence. Indeed, there were some axial compressors with shrouded stators whose performances were acceptable. But Jefferson and Turner (1958) did report the negative influence of stator shroud on the aerodynamic performances including efficiency and stall margin.

The discusser had an opportunity to take part in developing a 4500 hp class gas turbine locomotive in China in the 1970s. The design of the compressor was based on a widespread prototype 11-stage unshrouded subsonic compressor, which had been successfully applied in many cases in China. The design philosophy of the prototype was very common in early years; for example, the profile of blades is similar to C-4, the reaction is a little larger than 0.5. The only modifications to the prototype were: shrouding all stators for mechanical considerations, adjusting the size exactly to scale to suit the demand of flow rate (power output), adding an extrapolating stage in front of the original prototype to raise the pressure ratio. Except for the shrouding stator, other modifications had a successful record, so the gas turbine was manufactured without testing the compressor beforehand.

Contrary to everyone's expectation, the aerodynamic performance of the compressor, especially the stability performance, deteriorated seriously. The slope of characteristics in the pressure ratio–reduced mass flow rate diagram became much gentler and the surge line went down a lot compared with the design characteristics, which can be seen in Fig. D.1. At first, we did not believe it was caused by shrouding stators, and adjusted it with many regular approaches, for example, adjusting the rotating inlet guide vane, optimizing the air inlet system to lower inlet distortion, minimizing the shrouded stator cavities and labyrinth seal-tooth leakage, and so on. But no apparent improvement occurred. At last, after we changed the mechanical design and only resumed the cantilevered stators, then the compressor characteristics became very close to the original design condition (see Fig. D1), and the gas turbine locomotive could be developed successfully and run in the Chinese railway.

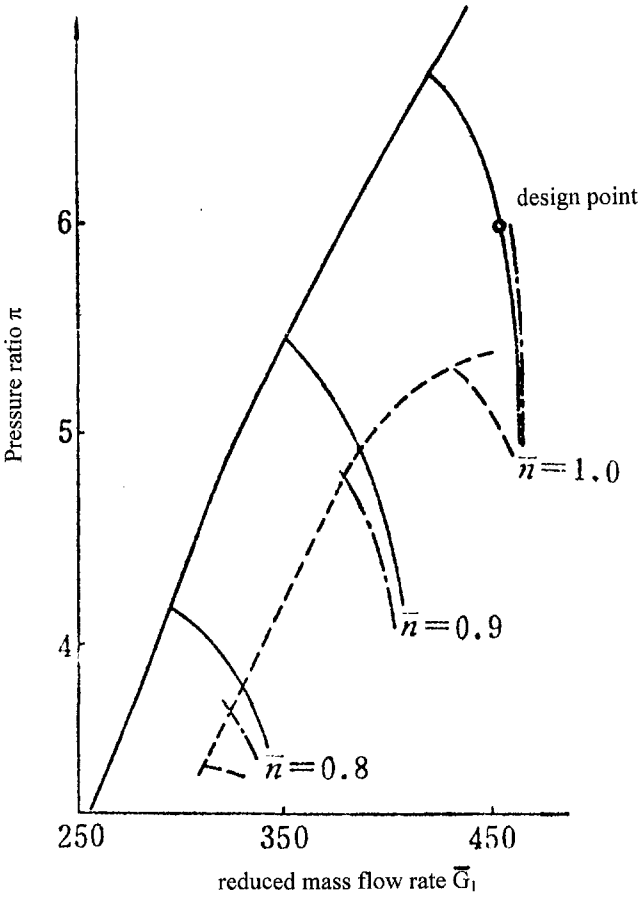

Fig. D1 Compressor characteristics with cantilevered stators and shrouded rotors: —— design - - - with shrouded stators – · – · – · – with cantilevered stators

Owing to conditions in China at that time, we could not study these phenomena in detail. However, it was assumed that the improvement after discarding the shroud was due to the alleviation of stator hub secondary flow caused by the rotating rotor surface, since the rotating direction of rotor is opposite to the hub secondary flow. Then, some stator shroud treatments were proposed to eliminate the negative influence of shroud on aerodynamic performance but maintain the positive influence on the mechanical design.

The detail had been reported in a journal published in Chinese and was not well-known in the world. In the late 1970s and early 1980s, several Chinese gas turbines and jet engines with shrouded stators and poorer stalling performance were changed to cantilevered stators according to above-described discovery. Improvement to varying degrees on stalling performance was obtained; however, it was not as evident as shown in Fig. D1.

Therefore, the influence of stator shroud on the compressor performance, especially the influence mechanism, has not yet been studied thoroughly. Why is the influence strong for some cases but negligible for other cases? The turbomachinery theory and experimental ability have advanced greatly. It is the right time to research it in detail.

[1] Institute of Engineering Thermophysics, Chinese Academy of Sciences, Beijing, China.

Solver, Part II: Application to a High-Pressure Compressor Design," ASME JOURNAL OF TURBOMACHINERY, Vol. 120, pp. 215–223.

Ludwig, L., 1978, "Gas Path Sealing in Turbine Engines," *Seal Technology in Gas Turbine Engines,* AGARD Publications, Neuilly Sur Seine France, Apr.; also NASA TM 73890.

Mahler, F. H., 1972, "Advanced Seal Technology," Pratt and Whitney Aircraft Division Tech. Rep. PWA-4372, Feb.; also AFAPL TR-72-8.

Moffat, R. J., 1985, "Using Uncertainty Analysis in the Planning of an Experiment," ASME *Journal of Fluids Engineering,* Vol. 107, pp. 173–178.

Shabbir, A., Celestina, M. L., Adamczyk, J. J., and Strazisar, A. J., 1997, "The Effect of Hub Leakage Flow on Two High Speed Axial Flow Compressor Rotors," ASME Paper No. 97-GT-346.

Steinetz, B. M., and Hendricks, R. C., 1994, "Engine Seal Technology Requirements to Meet NASA's Advanced Subsonic Technology Program Goals," AIAA Paper No. 94-2698, June; also NASA TM 106582.

Wasserbauer, C. A., Weaver, H. F., and Senyitko, R. G., 1995, "NASA Low-Speed Axial Compressor for Fundamental Research," NASA TM 4635, Feb.

Wellborn, S. R., and Okiishi, T. H., 1996, "Effects of Shrouded Stator Cavity Flows on Multistage Axial Compressor Aerodynamic Performance," NASA CR 198536, Oct.

Wisler, D. C., 1977, "Core Compressor Exit Stage Study: Vol. 1—Blade Design," NASA CR 135391, Dec.

Wisler, D. C., Bauer, R. C., and Okiishi, T. H., 1987, "Secondary Flow, Turbulent Diffusion and Mixing in Axial-Flow Compressors," ASME JOURNAL OF TURBOMACHINERY, Vol. 109, pp. 455–482.

Wisler, D. C., 1988, *Advanced Compressor and Fan Systems,* GE Aircraft Engines, Cincinnati, Ohio; also 1986 Lecture to ASME Turbomachinery Institute, Ames, Iowa.

DISCUSSION

Ruixian Cai[1]

The paper studied the influence of shrouded stator seal-tooth leakage on axial compressor performance in detail and gave sound conclusions. However, there is an unsolved problem: Does the existence of stator shroud influence performance markedly? The paper did not answer this problem directly since it had not tested the compressor with unshrouded stator and compared the experimental results. Nevertheless, according to the explanation of Figs. 3 and 4, it seems the answer of the authors was no evident influence. Indeed, there were some axial compressors with shrouded stators whose performances were acceptable. But Jefferson and Turner (1958) did report the negative influence of stator shroud on the aerodynamic performances including efficiency and stall margin.

The discusser had an opportunity to take part in developing a 4500 hp class gas turbine locomotive in China in the 1970s. The design of the compressor was based on a widespread prototype 11-stage unshrouded subsonic compressor, which had been successfully applied in many cases in China. The design philosophy of the prototype was very common in early years; for example, the profile of blades is similar to C-4, the reaction is a little larger than 0.5. The only modifications to the prototype were: shrouding all stators for mechanical considerations, adjusting the size exactly to scale to suit the demand of flow rate (power output), adding an extrapolating stage in front of the original prototype to raise the pressure ratio. Except for the shrouding stator, other modifications had a successful record, so the gas turbine was manufactured without testing the compressor beforehand.

Contrary to everyone's expectation, the aerodynamic performance of the compressor, especially the stability performance, deteriorated seriously. The slope of characteristics in the pressure ratio–reduced mass flow rate diagram became much gentler and the surge line went down a lot compared with the design characteristics, which can be seen in Fig. D.1. At first, we did not believe it was caused by shrouding stators, and adjusted it with many regular approaches, for example, adjusting the rotating inlet guide vane, optimizing the air inlet system to lower inlet distortion, minimizing the shrouded stator cavities and labyrinth seal-tooth leakage, and so on. But no apparent improvement occurred. At last, after we changed the mechanical design and only resumed the cantilevered stators, then the compressor characteristics became very close to the original design condition (see Fig. D1), and the gas turbine locomotive could be developed successfully and run in the Chinese railway.

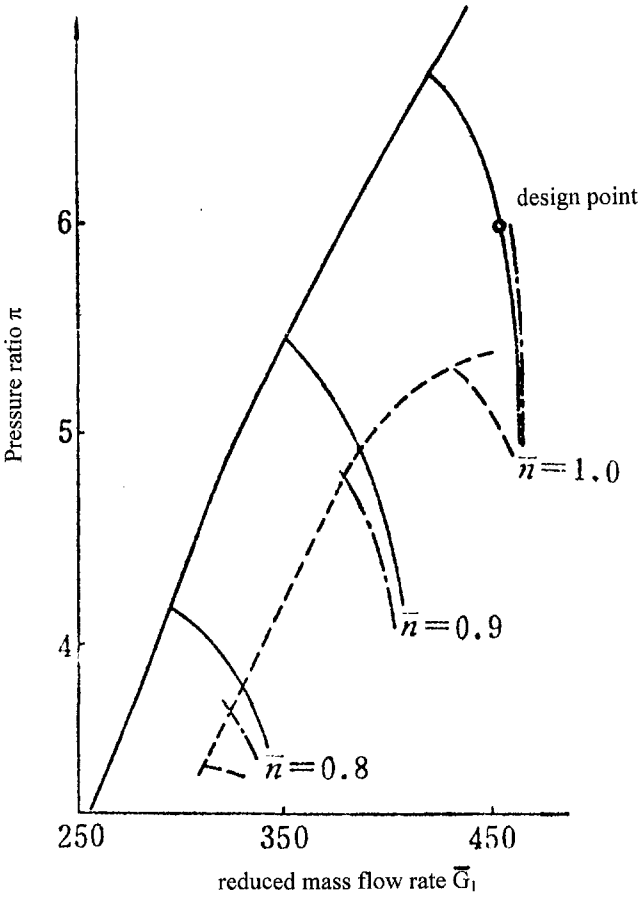

Fig. D1 Compressor characteristics with cantilevered stators and shrouded rotors: —— design - - - with shrouded stators – · – · – · – with cantilevered stators

Owing to conditions in China at that time, we could not study these phenomena in detail. However, it was assumed that the improvement after discarding the shroud was due to the alleviation of stator hub secondary flow caused by the rotating rotor surface, since the rotating direction of rotor is opposite to the hub secondary flow. Then, some stator shroud treatments were proposed to eliminate the negative influence of shroud on aerodynamic performance but maintain the positive influence on the mechanical design.

The detail had been reported in a journal published in Chinese and was not well-known in the world. In the late 1970s and early 1980s, several Chinese gas turbines and jet engines with shrouded stators and poorer stalling performance were changed to cantilevered stators according to above-described discovery. Improvement to varying degrees on stalling performance was obtained; however, it was not as evident as shown in Fig. D1.

Therefore, the influence of stator shroud on the compressor performance, especially the influence mechanism, has not yet been studied thoroughly. Why is the influence strong for some cases but negligible for other cases? The turbomachinery theory and experimental ability have advanced greatly. It is the right time to research it in detail.

[1] Institute of Engineering Thermophysics, Chinese Academy of Sciences, Beijing, China.

Authors' Closure

We thank Ruixian Cai for his thoughtful discussion of our paper. We also appreciate the data he presented from an 11-stage compressor, which show a significant change in performance due to the incorporation of shrouded vanes in place of cantilevered vanes. We are sure that others would not be so eager to present such data, although it is certain that more experiences such as his exist. In our viewpoint, his data emphasize the fact that shrouded stators can alter performance. In our paper, we went one step further and proved that increased seal-tooth leakage or decreased upstream cavity tangential momentum are two reasons that shrouded stators may hinder performance.

Two questions were asked. Both are difficult to answer in general. The reason is that it is impossible, in practice, to uncouple the hub shroud from the shroud cavity and its corresponding flow, since some cavity volume and seal-tooth leakage flow will exist in any real configuration. It is, therefore, hard in experimental practice to sort out the influence of a nonrotating vane hub, by itself, on performance. Our data showed that having the hub shroud with no cavities and no leakage (or as close as we could get to only a hub shroud) produced the best tested aerodynamic performance for this compressor. We also believe that simply replacing a cantilevered vane with a shrouded vane (identical airfoil geometries) without taking into account the different aerodynamics associated with the two vane types could be difficult to accomplish without influencing performance. The stator discharge near hub vorticity fields for the two vane types are substantially different, which can dramatically alter the downstream rotor performance. In a high-speed compressor, it does not take many stages for these differences to greatly change the axial stage matching. This might account for the trends presented in Fig. D1.

Concerning the degree of impact for different designs, a simple mixing loss calculation of the injected leakage flow can illustrate that one reason that shrouded stators might behave differently in various designs is stage reaction. Again we claim that the presence of the hub shroud cannot be uncoupled from the cavity leakage flow. The mixing loss for cavity leakage flow entering the powerstream can be found by applying the conservation equations, neglecting skin friction, to a control volume enclosing the region between blade rows and the flow path. Leakage flow enters the control volume through the hub with axial and tangential velocities not equal to the powerstream values. This loss, for incompressible flow, is defined in the following equation. Here variables subscripted with l pertain to the seal cavity leakage values, the others to powerstream values at the stator inlet.

$$\omega_{mix} = \frac{\Delta P^0_{mix}}{0.5\rho V^2} = \cos^2\beta\left(\frac{\omega_l}{\omega}\right)\left[2 + \frac{\omega_l}{\omega} - 2\frac{Vx_l}{Vx}\right] + \frac{\sin^2\beta}{\left(1 + \frac{\omega_l}{\omega}\right)^2}\left(\frac{\omega_l}{\omega}\right)\left[2 + \frac{\omega_l}{\omega} - 2\frac{Vy_l}{Vy} - \frac{\omega_l}{\omega}\left(\frac{Vy_l}{Vy}\right)^2\right]$$

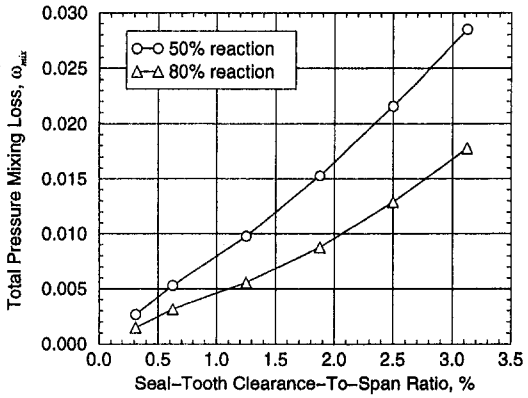

Fig. D2 Total pressure mixing loss associated with cavity leakage flow injection into the powerstream

We focus on two designs of a rear subsonic stage, one having 50 percentreaction, and the other 80 percent. We assume both have the same flow path, cavity volume and geometry, seal-tooth clearance, rotational speed, inlet total pressure, and inlet total temperature. Therefore, only the reaction and corresponding change in aerodynamics and stage static pressure rise split between the rotor and stator are different. The design with 50 percent reaction will produce more seal-tooth leakage flow than the 80 percent reaction design for the same clearance due to the greater pressure differential across the stator. The increased leakage will also lead to lower upstream cavity tangential momentum for the 50 percent reaction design. Exact values of leakage flow, upstream cavity axial and tangential velocities for this example came from a model of the cavity flow developed by Wellborn et al. (1999). Powerstream values came from a throughflow design code. The results of this analysis are shown in Fig. D2. Here the change in total pressure mixing loss with seal-tooth clearance is shown. The 50 percent reaction design has nearly doubled the mixing loss of the 80 percent reaction design for the same seal-tooth clearance. For a nominal clearance value near 1.2 percent of span, the minimum value that could be practically attained in this example, the 50 percent reaction stator loss increase due to mixing of the leakage flow would be 0.01, which is not a trivial amount considering this loss increase would occur across the entire span (leakage flow mixed with the entire powerstream flow). Therefore, even a simple mixing loss calculation indicates that it is easy to have different performance for different designs.

In closing, we welcome other studies that would shed light on the fluid mechanics associated with shrouded stator /seal cavity flows and their impact on compressor performance. We also agree that it is the right time to add to the body of knowledge concerning this subject.

Reference

Wellborn, S. R., Tolchinsky, I., and Okiishi, T. H., 1999, "Modeling Shrouded Stator Cavity Flows in Axial-Flow Compressors," ASME Paper 99-GT-75.

S. A. Khalid
Allison Advanced Development Co.,
Indianapolis, IN 46206-7162
Mem. ASME

A. S. Khalsa
Khalsa International Industries and Trades,
Española, NM 87532

I. A. Waitz

C. S. Tan

E. M. Greitzer

Gas Turbine Laboratory,
Massachusetts Institute of Technology,
Cambridge, MA 02139

N. A. Cumpsty
Whittle Laboratory,
Cambridge University,
Cambridge, United Kingdom

J. J. Adamczyk
NASA Lewis Research Center,
Cleveland, OH 44135

F. E. Marble
California Institute of Technology,
Pasadena, CA 91125

Endwall Blockage in Axial Compressors

This paper presents a new methodology for quantifying compressor endwall blockage and an approach, using this quantification, for defining the links between design parameters, flow conditions, and the growth of blockage due to tip clearance flow. Numerical simulations, measurements in a low-speed compressor, and measurements in a wind tunnel designed to simulate a compressor clearance flow are used to assess the approach. The analysis thus developed allows predictions of endwall blockage associated with variations in tip clearance, blade stagger angle, inlet boundary layer thickness, loading level, loading profile, solidity, and clearance jet total pressure. The estimates provided by this simplified method capture the trends in blockage with changes in design parameters to within 10 percent. More importantly, however, the method provides physical insight into, and thus guidance for control of, the flow features and phenomena responsible for compressor endwall blockage generation.

1.0 Introduction

It has long been known that the flow in the endwall region of an axial compressor has a strong influence on overall performance and stability. For example, Wisler (1985) suggests that more than half the loss in an axial compressor is associated with the flow in the endwall region. The large amount of data presented by Koch (1981) also emphasize the detrimental effect of increasing tip clearance on the maximum pressure rise obtainable within a blade passage.

Figure 1, adapted from Smith and Cumpsty (1984), illustrates the effects of tip clearance on pressure rise capability for a low-speed rotor. As the mass flow is decreased, the pressure rise coefficient increases to a peak and then declines. The peaking of the characteristic is due to the reduction in blade passage exit effective flow area, which can be associated with either the formation of regions of substantial velocity defect or with deviation. Of these, it is the former, commonly referred to as "blockage," that appears to be more important. Similar effects are observed in transonic fans as illustrated by Suder (1998), who attributed endwall blockage primarily to shock/tip leakage vortex interaction.

Further, the present understanding of rotating stall in axial compressors traces a clear line between one route to stall inception and peaking over of the pressure rise characteristic. In compressors in which flow in the tip region is primarily responsible for blockage growth, rotating stall onset is thus linked to phenomena associated with clearance flow. There is therefore strong motivation to understand the key features of the endwall flow field and to develop techniques to modify it. However, in spite of the importance of the endwall flow field in determining the pressure rise capabilities of axial compressors (as well as the existence of many experimental, analytical and, most recently, computational investigations of this topic), complete explanations of the mechanisms through which the endwall flow degrades compressor performance still do not exist. Empirical correlations are typically employed in the design process, with different organizations developing these from quite different physical viewpoints (Koch, 1981; Schweitzer and Garberoglio, 1984).

1.1 Problem Statement. The primary issues addressed in this paper are:

1 The development of a procedure to quantify compressor endwall blockage.
2 The definition of a simplified, physically based model for endwall blockage.
3 The determination of the relative sensitivity of blockage to various compressor design parameters.
4 The development of quantitative criteria for blockage management.

Contributed by the International Gas Turbine Institute and presented at the 43rd International Gas Turbine and Aeroengine Congress and Exhibition, Stockholm, Sweden, June 2–5, 1998. Manuscript received by the International Gas Turbine Institute February 1998. Paper No. 98-GT-188. Associate Technical Editor: R. E. Kielb.

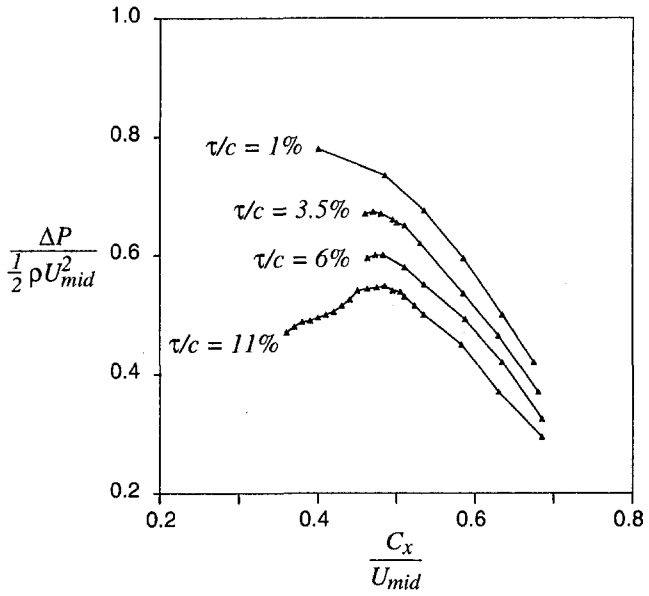

Fig. 1 Compressor characteristic for various tip clearance sizes from Smith and Cumpsty (1984)

1.2 Approach. The approach taken in this paper can be stated as follows. A basic premise (which is shown in the paper) is that many of the features of compressor tip clearance flows can be captured by three-dimensional computations that are in widespread usage. In spite of the computational capability, however, links between design parameters, flow conditions, and compressor endwall blockage are typically still dealt with on a configuration-specific basis. More precisely, there appears to be no unified framework that not only captures the underlying fluid dynamics that define these links, but also allows one to view them on a more global basis. Describing such a framework is the central objective of this paper. The framework is intended to *complement* computations, enabling the development of physically based guidelines for the control of tip leakage flows.

In this context, both computational and experimental results were examined to address the issues listed above. The computations, which allowed detailed flow field investigation, were carried out using the three-dimensional Reynolds-averaged Navier–Stokes solver described by Adamczyk et al. (1989). Wind tunnel experiments designed to simulate a compressor endwall flow were used to isolate key design parameters. Data from a low-speed compressor were used to support and confirm the computations and extend the parameter space studied.

Computations were performed on three blade geometries: the cantilevered stator described by Johnson and Greitzer (1987), the low-speed General Electric E^3 Rotor B described by Wisler (1977, 1981), and the transonic fan, NASA Lewis Rotor 67, whose performance has been reported by Strazisar et al. (1989). The cases cover a range of flow and geometric parameters relevant for the design of modern, efficient compressors. Data from the experiments were used to corroborate the computational results and ensure that the computations captured the physical phenomena examined. The low-speed compressor experiments were carried out at the Whittle Laboratory. Two clearance levels and five loading levels were tested, covering a range of flow conditions similar to the computations. The experiments conducted using this rig were described in detail by Khalsa (1996).

The scope of the paper is as follows. Section 2 describes the method for quantification of blockage in compressors. Section 3 then presents simplified mechanistic arguments about the behavior of a velocity defect in a pressure gradient, which will be later shown to apply directly to the description of compressor blockage formation. Section 4 then shows a number of parametric trends of endwall blockage, using experiments as well as computations. Following from this, Section 5 integrates the ideas of Section 3 with the computations and data of Section 4 to develop a basic analysis for estimating blockage. Applications and parametric trends are given in Section 6.

2.0 Quantification of Endwall Blockage

The term "blockage," which is widely used in discussions regarding axial compressor flows, generally refers to the reduction in effective free-stream or core flow area due to local velocity defects, analagous to the displacement thickness associated with boundary layers. Past assessments of blockage have, for the most part, been limited to qualitative descriptions regarding the size and severity of the apparent nonuniformity or velocity defect present in the flow, e.g., Smith and Cumpsty (1984) and Crook et al. (1993). Some techniques to quantify blockage or displacement thickness have been suggested, notably that of Smith (1970) (see also Dring, 1984), but none have linked the nonuniformity in the local defect region to the free-stream or "core" region velocity and thus, to the pressure rise, in a rigorous manner.

To identify trends in blockage, as well as to help in understanding the underlying mechanisms that affect the generation of blockage, a quantitative means of assessment is required. In this section, we present a method for defining blockage in axial compressors and apply the method to a low-speed rotor and a transonic fan. The resulting blockage values are used to illustrate the role of clearance in blockage growth. The description given here represents an overview of the method; a more detailed description is presented by Khalid (1995).

The concept of a blocked area is similar to a boundary layer displacement thickness, as illustrated in Fig. 2. The challenges associated with defining the blockage in a compressor blade row flow field are that the flow is multidirectional, and the free stream is nonuniform. These aspects raise two questions: (1) What velocity component is relevant for defining blockage? (2) How can the

Nomenclature

A = area
c = chord length
CP_S = static pressure coefficient = $(\overline{P_{S,\text{exit}}}^a - \overline{P_{S,in}}^a)/Q_{in}$
CP_T = defect total pressure coefficient = $(\overline{P_{T,\text{exit}}}^a - \overline{P_{T,in}}^a)/Q_{in}$
C_x = axial velocity
h = blade height
P = pressure
Q = dynamic head
s = blade spacing
u = velocity component
U = velocity magnitude
w = relative velocity magnitude
α = local leakage angle with respect to blade surface
α_0 = ratio of defect velocity to free-stream velocity
β = relative flow angle
δ^* = displacement thickness
ρ = density
σ = solidity = c/s
τ = tip clearance height

Subscripts and Superscripts

a = area-weighted average
b = blocked
e = edge of blockage area
ex = exit
in = inlet
m = mainflow direction
mid = blade midspan
S = static
T = total
tip = blade tip
1 = upstream, inlet
2 = downstream, exit

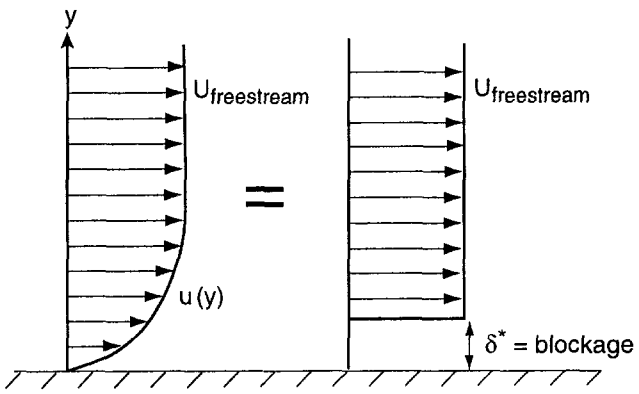

Fig. 2 Blockage schematic

edge of the defect region be identified given the presence of strong gradients in free-stream flow properties?

In addressing these questions, we note some features that are common for many situations of technological interest. First, the compressor freestream or core flow has an identifiable direction, which may be called the throughflow or *mainflow* direction. This mainflow direction can be used to select the velocity component to use in the blockage definition. Second, although the core flow may be nonuniform, we can distinguish between this region and that existing near endwalls or blades because the *gradients* in flow properties in wall regions are significantly greater than those in the core region. This aspect can thus be used to identify the edge of the defect region.

An expression for blocked area applicable for the flow within a compressor blade row is

$$A_b \equiv \int\int \left(1 - \frac{\rho u_m}{\rho_e U_e}\right) \cdot dA \qquad (1)$$

where the integral is taken over the defect region. This is formally the same as the definition of displacement thickness but two clarifying statements need to be made. First, the edge criterion is based on $\vec{\nabla}(\rho u_m)$, where u_m is the component of velocity resolved in the mainflow direction. Specifically, the edge of the defect region is defined by the magnitude of the vector formed by the two gradient components lying in the plane of the integration. Thus, to calculate blockage in an axial plane, the magnitude of the vector formed by the radial and tangential components of $\vec{\nabla}(\rho u_m)$ is used to define the edge. The value selected as the edge criterion is the minimum value not found in the core region. As is shown below, this cutoff value is quite distinct even for the highly nonuniform core regions representative of low hub–tip ratio fans. The edge velocity and density (U_e *and* ρ_e, respectively) in Eq. (1) are the values along the edge of the blockage region nearest to the local area over which the integration is taken.

Figure 3 shows contours of ρu_m and the magnitude of $\vec{\nabla}\rho u_m$ for a transonic fan with a hub-to-tip ratio of 0.67, normalized using the inlet average density, axial velocity, and tip chord. Although the free-stream velocity varies by more than a factor of two, the gradient magnitude provides an unambiguous indication of the defect region. Further, the defect area over which the blockage integration is performed is relatively insensitive to the precise value selected (e.g., 2, 3, or 4) as the edge criterion.

To illustrate the trends with operating condition and clearance, trailing edge blockage values calculated in this manner for the low-speed rotor are plotted as a function of compressor flow coefficient in Fig. 4. In the simulations, the flow coefficient was reduced until a converged solution could no longer be obtained. The open and filled symbols correspond to 1.4 and 3.0 percent clearance, respectively. The solid curves represent blockage calculated over the full span, while the dotted curves represent the

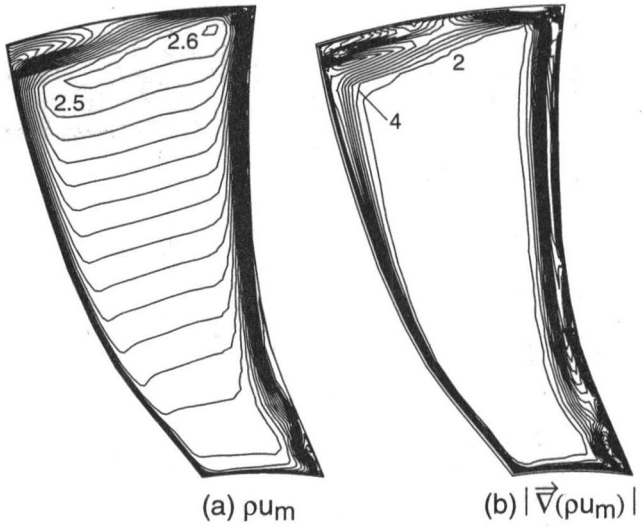

Fig. 3 Example of blockage region definition using velocity gradient

blockage contribution associated with the tip clearance, and the dashed curves represent the contribution of the blade and hub.

For the smaller clearance, comparison of total blockage and tip clearance-related blockage indicates that little of the growth in blockage with increased loading is due to clearance flow. The blockage increase with loading is primarily due to growth of the suction surface boundary layer and the development of endwall-suction surface corner separation as the flow coefficient is reduced.

For the larger clearance, the tip clearance-related blockage, and the total blockage are larger than for the smaller clearance. Furthermore, with 3.0 percent clearance the growth in clearance-related blockage with loading is almost entirely responsible for the growth in total blockage. For this rotor, increasing the clearance changes the region most responsible for limiting the pressure rise from the blade suction surface and the endwall corner at small clearance to the tip region at large clearance.

Regardless of which plane A_b is calculated, it accounts for the free-stream velocity increase in that plane due to the defect region. This link between the local defect region to the free-stream velocity is demonstrated by Khalid (1995).

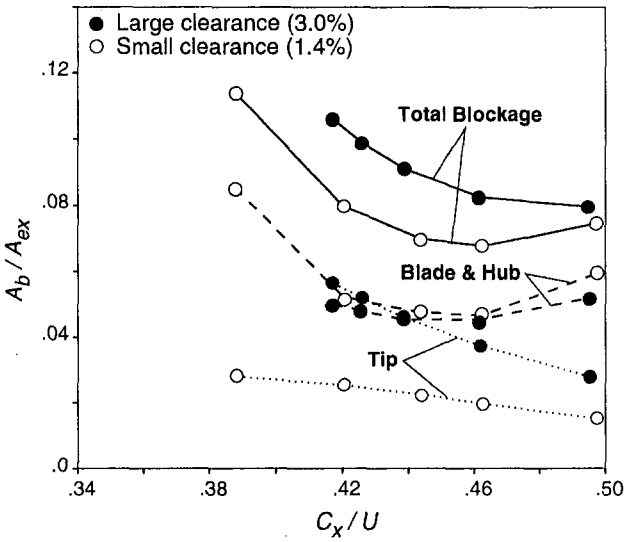

Fig. 4 Blockage versus mass flux

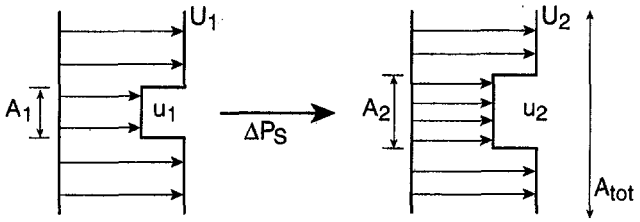

Fig. 5 Schematic of one-dimensional blockage description

3.0 Normalization and Parameterization of Blockage

As background for discussing the endwall blockage trends and to motivate the parameters we use to collapse blockage data onto a single trend line, we first present a simplified description of the behavior of velocity defects passing through a pressure difference. We consider a velocity defect passing through a pressure rise in a quasi-one-dimensional, inviscid, incompressible flow, as indicated in Fig. 5. The initial normalized velocity in the defect has a magnitude $\alpha_0 = u_1/U_1$ and an extent A_1. Of interest is the effective blocked area, A_{b2}, at station 2, after the pressure rise, where A_{b2} is defined as

$$A_{b_2} \equiv \left(1 - \frac{u_2}{U_2}\right) \cdot A_2 \tag{2}$$

Using continuity and Bernoulli's equation gives an expression for A_{b2}/A_1,

$$\frac{A_{b_2}}{A_1} = \alpha_0[(\alpha_0^2 - CP_S)^{-1/2} - (1 - CP_S)^{-1/2}] \tag{3}$$

where $CP_S \equiv \Delta P_S/(\frac{1}{2}\rho U_1^2)$ is a static pressure rise coefficient.

Equation (3) shows that exit blockage is a function of both the initial velocity defect, α_0, and the nondimensional static pressure rise, CP_S. This is illustrated in Fig. 6(*a*), which shows A_{b2}/A_1 versus CP_S for four different values of α_0 spanning the values observed in the flow fields examined in this study. Figure 6(*a*) also shows that each curve possesses an asymptotic behavior in that there is a critical value of CP_S, dependent on the initial defect, where the blockage increases rapidly; Eq. (3) indicates this occurs at a pressure rise coefficient equal to α_0^2.

These statements may be put in a form that is more useful for the present problem if we work in terms of total pressure in the defect rather than α_0. We thus define an exit plane total pressure coefficient:

$$CP_T \equiv \frac{P_{T,\text{defect}} - P_{T,\text{free-stream}}}{Q_{in,\text{free-stream}}} = \alpha_0^2 - 1 < 0 \tag{4}$$

With this definition, Eq. (3) can be rewritten as

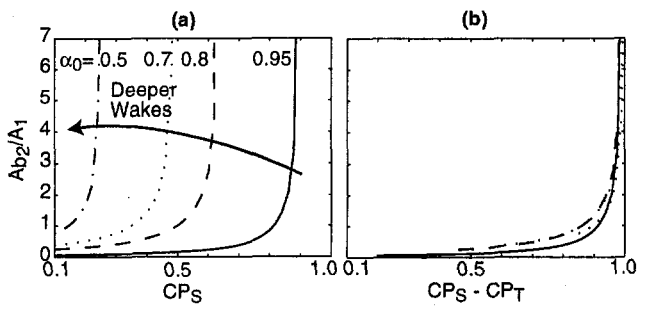

Fig. 6 One-dimensional blockage results: (*a*) blockage as a function of CP_S, (*b*) blockage as a function of $CP_S - CP_T$

Table 1 Low-speed compressor rig blading parameters

Tip chord	119 mm
Tip solidity	1.26
Hub/tip ratio	0.80
Tip camber	25.4°
Inlet δ^*/τ	2.0
Design C_x/U_{tip}	0.63

$$\frac{A_{b_2}}{A_1} = \sqrt{1 + CP_T}\{[1 - (CP_S - CP_T)]^{-1/2} - (1 - CP_S)^{-1/2}\} \tag{5}$$

An advantage of writing the equation this way is that the asymptote in the blockage occurs when $CP_S - CP_T = 1$ for all initial defects. One view of this is that what we will term the loading parameter, $CP_S - CP_T$, is related to the defect dynamic head as follows:

$$CP_S - CP_T = 1 - \frac{Q_{\text{defect}}}{Q_{in}} = 1 - \frac{u_2^2}{U_{in}^2} \tag{6}$$

Blockage will asymptote when the defect velocity decelerates to zero, which will occur when the loading parameter equals one.

Figure 6(*b*) shows how different initial conditions are nearly collapsed to a single trend when blockage is plotted against this loading parameter $CP_S - CP_T$. Thus, although in general exit blockage depends on both CP_S and CP_T independently, Fig. 6 demonstrates that, within the range of initial defects and static pressure rises examined in this study, the primary trend is well-captured by the dependence on $CP_S - CP_T$ only.

We can now link the CP_S and CP_T parameters in the simplified one-dimensional description to a compressor tip leakage flow by defining the initial conditions as leakage jet, mass flux-weighted averages along the blade chord, and the final conditions as averages over the blockage region (as defined in Section 2) in the blade passage exit plane. In Section 4, we show that blockage estimates obtained from experiments and numerical simulations of a range of compressor geometries collapse onto a single trend line when the data are characterized in this manner. A single limiting value of the loading parameter, $CP_S - CP_T$, is thus found to describe the experimental limiting pressure rise condition. This concept, plus the quantification of blockage, will be seen to enable estimation of clearance blockage growth in a wide range of situations.

4.0 Experimental Data and Numerical Simulations

In this section we present blockage estimates obtained from low-speed compressor tests, Navier–Stokes computations, and tests in a wind tunnel model designed to capture the essential elements of tip leakage flows. Descriptions of each of these tools are provided and the blockage estimates are presented using the framework discussed in Section 3.

4.1 Low-Speed Compressor Tests. Tests were performed in the Deverson low-speed compressor at the Whittle Laboratory of Cambridge University. The facility consisted of a calibrated bellmouth inlet with honeycomb flow straighteners, casing boundary layer thickening tabs, inlet guide vanes, a rotor (51 blades) and stator (49 blades) with a hub-to-tip ratio of 0.8, and an auxiliary exhaust fan. The inlet guide vanes were 3.2 rotor chords upstream

of the rotor leading edge, imparting swirl to the flow, but allowing the circumferential nonuniformities due to inlet guide vane (IGV) wakes to mix out. The rotor and stator blading is representative of a modern high-pressure compressor stage, with controlled diffusion airfoils. The primary features of the blading are summarized in Table 1.

Data were collected primarily with a slant hotwire traversed radially 15 percent chord downstream of the rotor trailing edge. At each radial location phase-locked measurements were taken and ensemble-averaged for eight different wire orientations. The data were used to calculate each of the three rotor exit velocity components with 27 data points in the radial direction and 39 across the blade pitch. The error of the rotor exit plane velocities was less than ±5 percent with 95 percent confidence (Khalsa, 1996).

Trailing edge velocity data were taken at a number of points along a speedline. Speedlines were run for two stagger angles (40.5 and 44.7 deg) and two clearance levels (τ/c = 1.24 and 3 percent). For the increased clearance tests, three blades were cropped to increase their clearance. The circumferential nonuniformity in clearance was accounted for in the data reduction using the theory of Horlock and Greitzer (1983) to find the circumferential redistribution of flow coefficient for a given circumferential tip clearance variation. Using this analysis, the local flow coefficient for the large clearance blades was estimated to be approximately 8 percent less than the mean flow coefficient.

Representative contour plots of the relative velocity magnitude normalized by midspan blade speed are shown in Fig. 7 for the datum stagger and clearance geometry at two flow conditions. The triangles along the right-hand edge indicate the radial measurement locations. For both plots the contour intervals are 0.04 w/U_{mid}, and the direction of blade rotation is right to left.

Blockage was calculated at each flow condition using the technique described above, and was normalized by clearance area (τc)

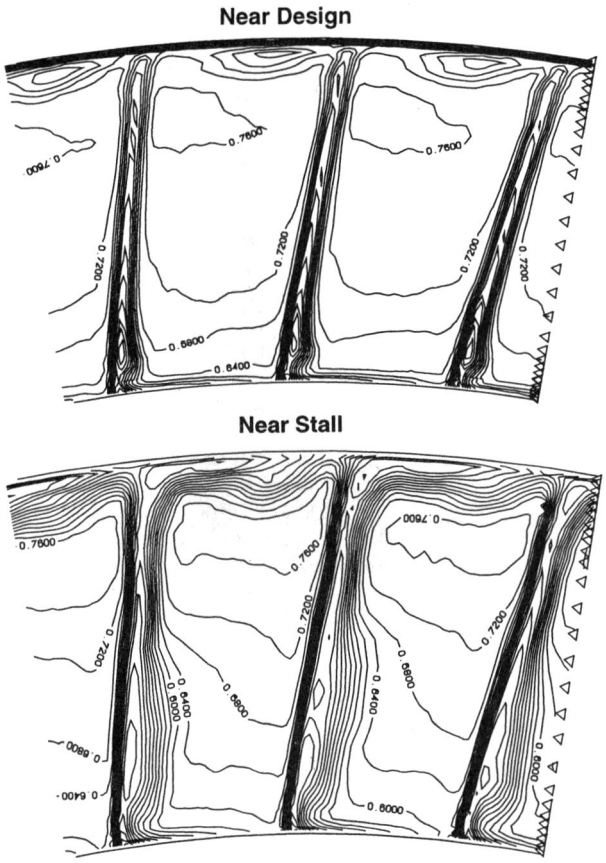

Fig. 7 Relative velocity, w/U_{mid}, contours from rotating rig at trailing edge + 15 percent chord

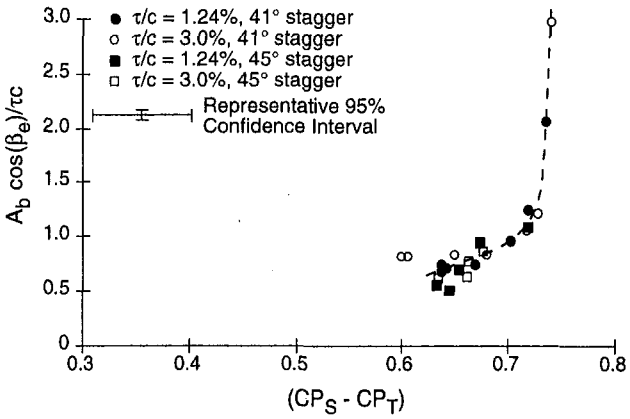

Fig. 8 Blockage versus loading parameter from rotating rig experiments, two clearance heights, two stagger angles

and multiplied by the cosine of the flow angle at the edge of the defect. The cosine factor was included to remove the dependence of blocked area on plane orientation since blocked area calculated in an axial plane will depend not only on the flow defect, but will depend on the angle that the plane makes with the mainflow direction as well.

The loading parameter ($CP_S - CP_T$) was calculated using a mass-average of the local loading parameter $(CP_S - CP_T)_{\text{local}}$ corresponding to each chordwise station along the blade:

$$(CP_S - CP_T)_{\text{local}} = \left[\frac{\overline{P_{S,\text{exit}}}^{a} - P_{S,\text{local,suction side}}}{Q_{\text{local,suction side}}}\right] - \left[\frac{\overline{P_{T,\text{exit}}}^{a} - P_{T,\text{inlet free-stream}}}{Q_{\text{local,suction side}}}\right]$$

where $\overline{(\ )}^{a}$ denotes an area-average over the blockage region (as defined in Section 2.0). The inlet free-stream conditions (used also for Q_{local}) were calculated from the experimental data using an area-average upstream of the blade row over a region extending approximately 10τ outside of the endwall boundary layer.

A plot of blockage versus loading parameter for all the data points taken is shown in Fig. 8. The highest loading points were at "near-stall" conditions (flow coefficients approximately 0.03 C_x/U_{tip} above the onset of rotating stall). The most evident aspect of Fig. 8 is the asymptotic trend similar to that seen in the one-dimensional description given in Section 3. The primary difference between the data and the one-dimensional results is the location of the asymptote that occurs at a limiting loading parameter of approximately 0.72 in the data rather than at a value of 1.0. The difference is due to the averaging used to calculate the local loading parameter. Each chordwise section of the clearance jet undergoes a different static pressure rise[1] and a different amount of loss, and the blockage will reach its asymptote when the loading parameter of a local streamtube approaches unity.

4.2 Wind Tunnel Simulation. Marble suggested that the key feature of the flows of interest was the growth of blockage due to the tip leakage as the clearance vortex negotiated the blade row pressure rise. Based on this idea, an experiment was set up to enable the flow field to be examined in a way that allowed more control over flow conditions than can be achieved in the rotating rig.

In this experiment, the compressor tip clearance flow was represented by an axial slot jet entering a free stream within an adverse pressure gradient, as shown schematically in Fig. 9. The slot produces a symmetric vortex pair, similar to the wall-bounded

[1] The exit pressure is essentially the same for each streamtube, but the initial pressure, the pressure along the blade suction surface, has significant variations along the chord.

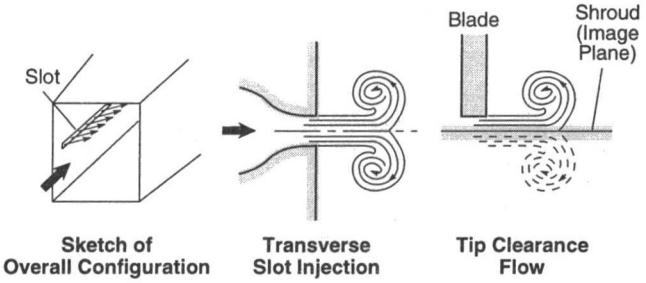

Fig. 9 Wind tunnel concept

single vortex with an image vortex set by the boundary conditions on the casing wall. The advantage of capturing the vortex/image-vortex interaction with a vortex pair is that this implementation, where the symmetry plane between the two vortices represents the casing boundary (Fig. 9), simulates the high total pressure at the casing boundary that exists in a compressor rotor due to the relative motion of the wall without the experimental complications of a moving wall.

The wind tunnel test section was constructed to produce an adverse pressure gradient representative of that found in an axial compressor, with simultaneous turning and diffusion, a local minimum in pressure as the flow accelerates around a bend, and then an increase in pressure. A schematic of the tunnel is shown in Fig. 10. The curved wall in the test section is representative of the suction surface of a rotor blade, and it is through this wall that the leakage jet was injected.

Because of the strong adverse pressure gradients along the curved wall, which correspond to the blade suction surface, several bleeds were located to prevent boundary layer separation. The simulation of the tip leakage flow was produced by blowing from a $\frac{1}{4}$ inch slot located in the center of the tunnel as shown in the three-dimensional view of the tunnel in Fig. 10. A chamber that could be pressurized independently of the main tunnel was used to create the clearance jet. Immediately behind the slot inside the pressurized chamber was a set of vanes (not shown) that turned the flow in a prescribed direction. A series of screens was placed upstream of the vanes to condition the flow. Based on data on clearance flow angles (Storer and Cumpsty, 1991), two sets of turning vanes were used, creating jets which were 41 and 54 deg from the local free-stream direction, uniform along the chord.

The primary diagnostic tool for the wind tunnel tests was a seven hole pneumatic probe with 0.10 in. diameter tip. Having seven measurements allows for the five steady flow quantities of interest, three velocity components, static pressure, and total pressure, to be measured even when the flow is separated over part of the probe tip. The probe could operate with flow angles up to 80

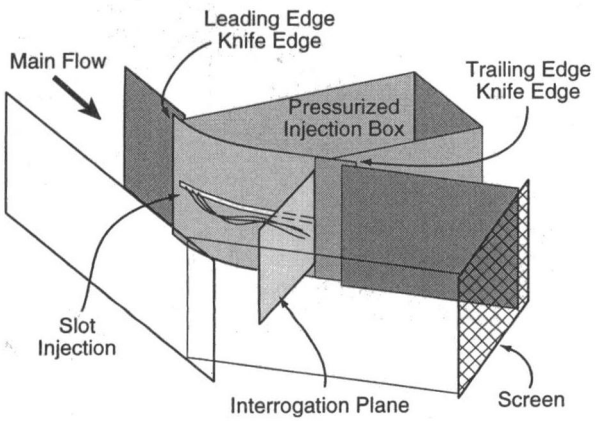

Fig. 10 Three-dimensional schematic of wind tunnel test section

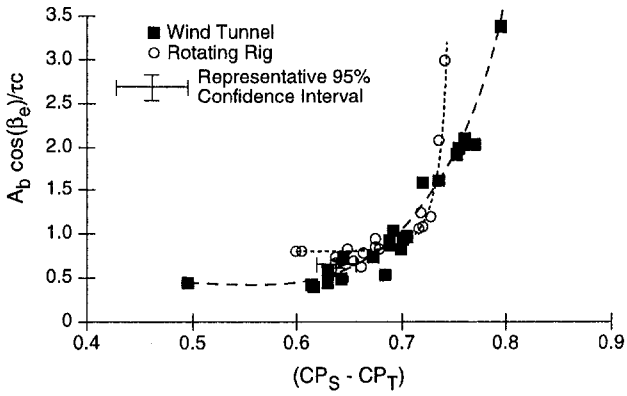

Fig. 11 Comparison between wind tunnel and rotating rig

deg from the probe axis. A description of the probe is given in Rediniotis et al. (1993). The probe measured dynamic head to within 1 percent, and both pitch and yaw angles to within 0.7 deg. These uncertainties result in uncertainty in the normalized blockage of ± 0.14 and uncertainty in the loading parameter of ± 0.035, both with 95 percent confidence. A full description of the experiments can be found in Khalsa (1996).

The wind tunnel experiment neglects effects such as the variation in leakage angle along the chord, and the presence of an inlet casing boundary layer. Estimates of the effects on blockage of these flow features, however, indicate that the wind tunnel should adequately capture the parametric trends of endwall blockage (Khalsa, 1996).

The experimental results from the wind tunnel and from the rotating rig are shown in Fig. 11. The blockage trends from the wind tunnel simulation match the trends observed in the rotating rig to within 7 percent of the inlet dynamic head when viewed in terms of the limiting loading parameter. This not only argues for the use of the wind tunnel to explore the parameter space of interest, but lends additional support to the use of the parameter $CP_S - CP_T$ as a relevant descriptor of blockage formation. Further results from this facility will be presented in Section 6.

4.3 Navier–Stokes Computations. The three-dimensional Navier–Stokes flow solver used was developed by Adamczyk et al. (1989). The equations of motion are Reynolds-averaged, and discretized in cylindrical coordinates. The turbulent viscosity was modeled using the Baldwin and Lomax (1978) mixing length model, and both second and fourth-order artificial viscosity were used in the inviscid regions of the flow field to maintain stability (i.e., artificial viscosity was not used in the boundary layer). The flow solver is not well-suited for very low Mach numbers, so solutions were obtained with an inlet Mach number of 0.3, approximately double the experimental Mach number. Numerical results for two different grid densities and for levels of turbulent viscosity that differed by a factor of 10 were compared to experimental data by Khalid (1995). The grid density and turbulent viscosity that produced the best agreement with the experimental data were used for the studies presented in this paper.

The clearance gap was not gridded in these solutions. The model suggested by Kirtley et al. (1990) was used, in which the region from blade tip to casing is specified as periodic from pressure side to suction side of the passage. Khalid (1995) explicitly examined this modeling assumption and concluded that the clearance-related blockage was adequately captured. He also compared the discharge coefficient from the numerical solutions to experiment and determined that the physical clearance is approximately equal to the specified computational clearance.

Three blade rows were examined, a cantilevered stator, a low-speed rotor, and a transonic fan. The stator blades were cantilevered from the casing and had a rotating hub, as described in the experimental study of Johnson and Greitzer (1987). Simulations

Table 2 Geometric parameters for low-speed computations

Blade	τ/c	c/s	h/c	Stagger	Camber	Inlet δ^*/τ
LSS	1.75	1.2	1.9	45°	30°	2.8
"	3.5	1.2	1.9	45°	30°	1.4
LSR	1.4	1.1	1.2	56°	31°	2.6
"	3.0	1.1	1.2	56°	31°	1.3
"	3.0	1.6	1.2	56°	31°	1.3
"	3.0	1.1	1.2	56°	31°	3.5
"	3.0	1.1	1.2	56°	31°	0.0

were carried out for two tip clearances, 1.75 and 3.5 percent of chord. Loading was specified by an inlet flow angle distribution, with the baseline case using experimental near-stall data. This flow angle was increased uniformly over the span to obtain solutions at a number of mass flows, three for the small clearance case, and five for the large clearance geometry.

The geometry of the low-speed rotor was the General Electric E^3 Rotor B, described in detail by Wisler (1977). Solutions were computed for two clearance heights, 1.4 and 3.0 percent of chord. Loading was varied by specifying the hub static pressure at the exit of the computational domain. Inlet data from experiments were used for the datum solutions. In addition, solutions were also obtained for 50 percent increased solidity. Solutions were computed for a thickened inlet boundary layer (axial displacement thickness three times the datum) and no inlet boundary layer (axial velocity profile uniform to the endwall).

The geometry for the transonic fan was NASA Lewis Rotor 67 whose performance is reported by Strazisar et al. (1989). Solutions were computed for two clearance heights, 1.25 and 2.0 percent of chord. Loading and inlet conditions were obtained in a manner similar to that of the low-speed rotor computations. Only low-speed results are used in the remainder of this paper. Khalid (1995) showed that the trends of endwall blockage with loading and geometry for the transonic fan computations were similar to those of the low-speed computations.

A summary of the low-speed compressor geometries for which speedlines were generated is given in Table 2 where the stator is referred to as LSS and the rotor as LSR.

In Fig. 12, the rotor computations are compared to the rotating rig tests. At low loadings, the experimental blockage trends and computed results agree within the experimental error. More importantly, the limiting values of loading parameter between the two

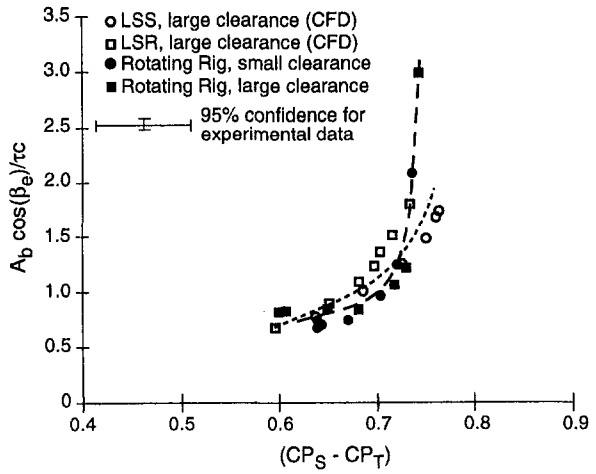

Fig. 12 Comparison between CFD and experiment

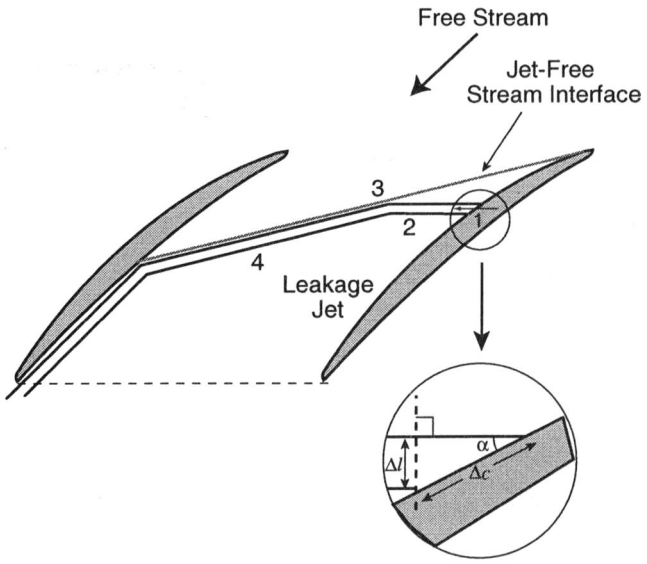

Fig. 13 Radial view illustrating two-dimensional wake segments along the chord

data sets are very close, differing by only 3 percent of the inlet dynamic head. The agreement of limiting loading parameter with experimental data suggests that the CFD solutions can be a useful tool to explore the parameter space of the endwall blockage problem and to examine the conditions at which the rapid rise in blockage occurs.

4.4 Summary of Experimental Data and Numerical Simulations. The experimental data and numerical simulations examined above cover a range of geometric parameters and flow conditions of practical interest. Over this range, there is a clear and consistent parametric trend of blockage variation with the loading parameter $CP_S - CP_T$, seen in the compressor and wind tunnel experiments as well as the computations. This implies not only that the computations can be used to assess these trends, but that the overall ideas are not dependent on specific geometries and the basic physical idea is sound. From this basis, we can construct a simplified model to show the key design parameters that affect blockage, to give insight into the factors that determine its magnitude in a given flow condition, and to provide guidance for developing approaches to reduce or control blockage.

5.0 Simplified Endwall Blockage Calculation Procedure

If, as is argued here, the endwall blockage at the exit of a compressor row can be viewed as similar to the growth of a velocity defect in an adverse pressure gradient, computation of this growth requires estimates of: (1) the initial velocity defect depth and extent, (2) the pressure gradient, and (3) the rate of mixing between defect and freestream (a feature not included in the one-dimensional analysis of Section 3). The complexity of the compressor endwall flow field offers many possible approximations for these flow processes, and the approach developed here is only one possible implementation. As will be shown, however, the procedure captures the experimentally observed parametric trends.

We make two assumptions to relate the actual process to the basic velocity defect description. First, the blockage at the passage exit is taken to be the summation of the blockage due to elemental regions of velocity defect that are created along the blade chord; in other words, each chordwise section of the leakage jet is assumed independent of the other sections. Second, the mixing and pressure rise are treated as if they occur sequentially. The framework for describing the endwall flow field is detailed below and shown schematically in Fig. 13:

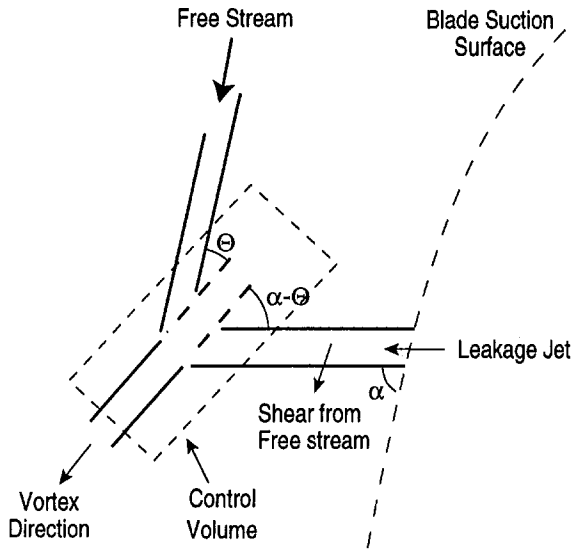

Fig. 14 Jet-free-stream interaction control volume

1 Fluid passes over the blade tip at a known leakage angle and total pressure for each section of the leakage jet. The leakage angle and total pressure can be taken directly from the computations or from a model such as that of Storer and Cumpsty (1991). At each chordwise location a single value, based on the mass average, is used.

2 Each chordwise segment of the leakage jet is taken to travel in a straight line, set by the leakage angle, until reaching either the jet/free-stream interaction region or the passage exit. Shear layer mixing occurs at the interface between the jet and the free stream.

3 A control volume analysis is used to describe the interaction of the jet and the free stream, as shown in Fig. 14. The free-stream velocity vector is assumed to follow the stagger angle of the blade. Conservation of mass and conservation of momentum in a direction parallel to and normal to the resultant vortex direction yield three equations for the angle of the vortex direction, the width, and the depth of the velocity defect (Martinez-Sanchez and Gauthier, 1990). The diminution in total pressure thus calculated provides the initial conditions for the velocity defect to pass through the adverse pressure gradient.

4 The defect growth downstream from the interaction is computed using a two-dimensional integral wake analysis (Hill et al., 1963). In the present application, the defect is assumed to grow in the radial direction only.

Estimates of the errors introduced by the various assumptions associated with this description are outlined in the appendix.

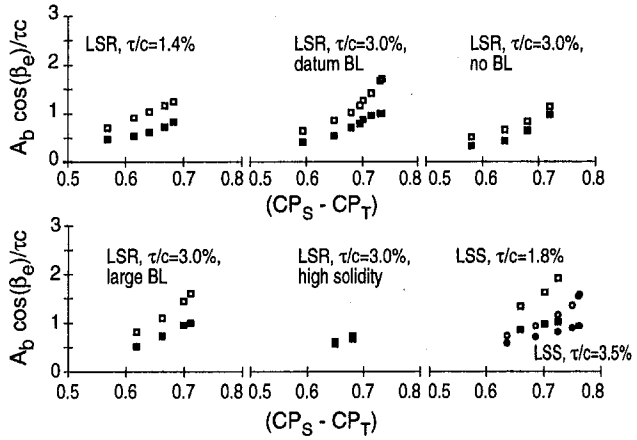

Fig. 15 Normalized blockage versus loading parameter from CFD solutions and from blockage model: □ CFD results, ■ model

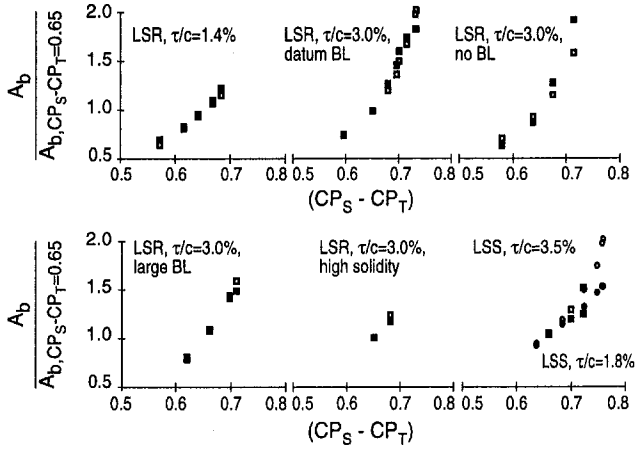

Fig. 16 Blockage normalized by blockage at $CP_S - CP_T = 0.65$ versus loading parameter: □ CFD results, ■ model

Computed values of blockage using the procedure described above are compared in Fig. 15 to the CFD solutions described in Table 2. The average difference between the blockages computed using the model and those obtained directly from the Navier–Stokes solutions is 33 percent, with a maximum difference of 46 percent for the high-loading, low-speed stator case. However, the predictions of absolute values of blockage differ in a systematic manner from the computations so that the parametric trends of endwall blockage for the range of clearances, boundary layer conditions and loadings investigated are, in fact, accurately predicted. This is shown in Fig. 16, which shows the blockage normalized by the blockage at $(CP_S - CP_T)$ of 0.65. The calculation procedure captures the blockage versus loading trend for the low-speed rotor cases with an average error of 5.5 percent, and those for the low-speed stator with an average error of 12 percent.

6.0 Parametric Trends of Endwall Blockage

Results from the numerical and experimental studies previously described were used together with the blockage model to provide quantitative information about the impact of design parameters and flow conditions on endwall blockage. The cases examined include inlet boundary layer thicknesses between zero and 3.5 clearance heights, blade stagger angles between 35 and 65 deg, clearances between 1.4 and 3.5 percent of chord, solidities of 1.1 and 1.6, and jet total pressure coefficients equal to the free stream and to 60 percent greater than the free stream. As stated, while the model provides a rapid estimation of blockage, and thus could be used, for example, in design trade studies, its primary role is seen as providing insight into the relevant physical effects that set compressor endwall blockage.

6.1 Inlet Boundary Layer. To examine the effect of inlet boundary layers on endwall blockage, computations were carried out for three different inlet boundary layer thicknesses. Cumpsty (1989) indicated that typical values of inlet boundary layer displacement thicknesses in axial compressors range from approximately one to three clearance heights, and the cases studied, $\delta^* = 0$ (no inlet boundary layer), $\delta^* = 1.3$ clearance heights (considered the datum case), and $\delta^* = 3.5$ clearance heights, bound this range.

The trends provided by the blockage model are shown in Fig. 17, which gives the ratio of blockages between the thick and thin inlet boundary layer cases for the CFD and the model calculations. Agreement is within 7 percent. For the same value of the loading parameter, the normalized blockage increased from approximately 0.8 of the datum value to 1.2 of the datum value as the inlet displacement thickness changed from 0 to 3.5 clearance heights. The physical reason for the increase is that the inlet boundary layer affects the clearance jet total pressure, and hence the depth of the

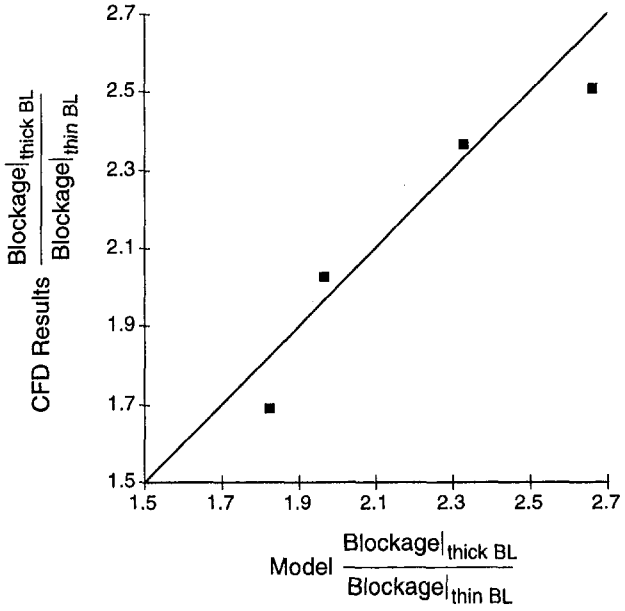

Fig. 17 Effects of inlet boundary layer: ratio of blockages from thick (δ^*/t = 3.5) and thin (δ^*/t = 0.0) inlet boundary layer cases, computational solutions and model

initial velocity defect, resulting in a lower limiting static pressure rise for a thicker inlet boundary layer. The stalling static pressure rise coefficient was 4 percent higher for no inlet boundary layer compared to the thick inlet boundary layer.

6.2 Clearance Height. The effects of clearance size on endwall blockage were given in Fig. 12, where results from the rotating rig and the rotor computations were presented. The blockage values in this figure are shown normalized by the clearance area (τc). Comparing the experimental data for the large clearance to that for the small clearance, and the computations for the large and small clearance, shows less than 20 percent difference in normalized blockage across the entire speedline. The data indicate, therefore, that endwall blockage is approximately proportional to clearance height; thus doubling the clearance size will approximately double the exit plane blockage. The results from the blockage model shown in Fig. 15 are in accord with this conclusion, a 5 percent increase in normalized blockage for a twofold increase in clearance height. Note, however, that for tight clearances, say below 1 percent of chord, Khalid (1995) and Storer and Cumpsty (1991) show that endwall performance is increasingly affected by three-dimensional separation in the endwall-suction side corner and the mechanism for increased blockage with loading will be quite different.

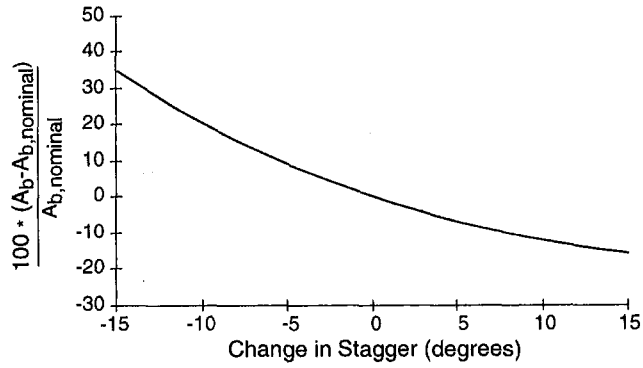

Fig. 18 Predicted changes in blockage with changes in stagger angle for an initial stagger angle of 45 deg, $\Delta P/Q$ = 0.5, σ = 1.1, τc = const

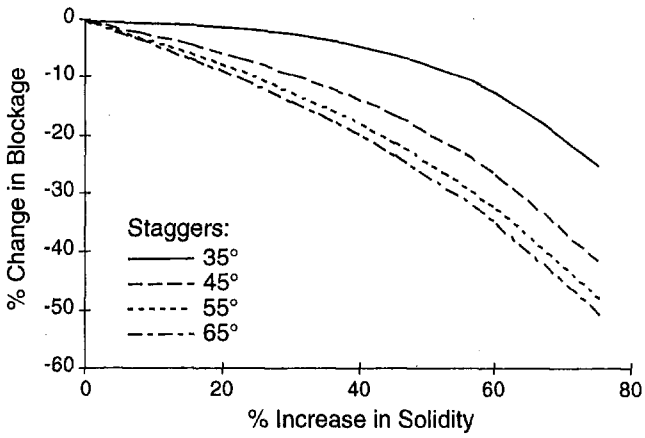

Fig. 19 Predicted changes in blockage with changes in solidity for $\Delta P/Q$ = 0.5, initial solidity = 1.1, and various initial stagger angles

6.3 Stagger Angle. The effect of stagger angle variation on blockage is presented in Fig. 18. The figure shows the percent change in blockage ($A_{b,\text{nominal}}$ is the blockage at the initial stagger angle) versus changes in stagger angle for an initial stagger angle of 45 deg. For the cases shown, the nondimensional solidity is 1.1 and the clearance area, τc, is held constant as stagger changes. The model shows that, as stagger is increased, both the clearance mass flux and the clearance leakage angle decrease. The result of these two effects is a reduction in the exit plane blockage as stagger angle is increased.

6.4 Solidity. Modeled changes in blockage with increasing solidity are shown in Fig. 19 for stagger angles ranging from 35 to 65 deg. The cases shown are for a nondimensional pressure $\Delta P/Q$ of 0.5 and an initial solidity of 1.1. For a 50 percent increase in solidity, blockage is reduced by 5 to 30 percent for stagger angles ranging from 35 to 65 deg, respectively.

This is because increasing the solidity decreases the blade loading for the same overall passage pressure rise, reducing the leakage jet angle and the clearance mass flux. The result is a leakage jet with an effectively higher initial total pressure and hence a reduced normalized blockage. For cases in which the tip leakage vortex trajectory intersects the next blade pressure surface, an increase in solidity results in an increase in double leakage (described in the appendix), increasing clearance jet loss, and partially offseting the blockage reduction caused by the decreased blade loading.

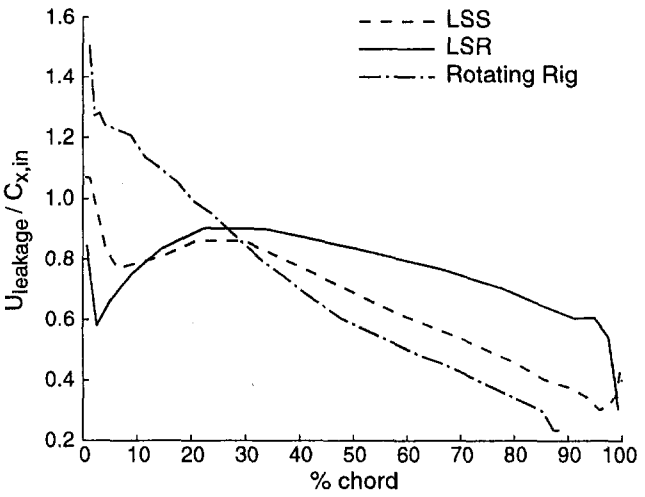

Fig. 20 Leakage velocity versus chord for low-speed stator, low-speed rotor, and Deverson rig tests

6.5 Blade Loading Profile. The effect of blade loading profiles can be seen by comparing the blockage trends of the low-speed rotor, the low-speed stator, and the Deverson rotor. The different pressure distributions for these three cases caused different distributions of leakage velocity (computed using the procedure developed by Storer and Cumpsty, 1991) along the chord as shown in Fig. 20, but the blockage trends for all three are similar. The implication is that the details of the loading profile are not a major factor in determining endwall blockage trends. Storer and Cumpsty have also argued this point, based on analysis of circular and parabolic arc camber line cascades. Unless one considers blade designs that reduce the chord-averaged blade loading near the tip for the same passage pressure rise, it is expected that blade loading profile will not be a large factor in determining endwall blockage. To produce a 50 percent reduction in exit plane endwall blockage, the required reductions in the loading parameter near the tip were estimated to be 74 percent. This suggests that using three-dimensional blade designs to reduce blade tip loading and hence endwall blockage may be difficult.

6.6 Increased Clearance Jet Total Pressure. A technique often used for controlling endwall flow is casing treatment. It has been shown that one of the features of casing treatment is an increased total pressure in the leakage jet. The effect of this high total pressure fluid on endwall blockage was quantified using the wind tunnel and the blockage prediction method. In the wind tunnel two levels of increased jet total pressure ($CP_{T,jet}$ = 0.6 and 0.3) were tested over two different chordwise extents (25 and 50 percent of chord). The total pressure coefficient profiles, which were based on Navier–Stokes modeling of a blade row with casing treatment (see Khalsa, 1996), were created in the wind tunnel described in Section 4.2 using different solidity screens placed behind the jet injector.

Figure 21 shows the measured changes in blockage for various loading conditions and levels of clearance jet total pressure. For a given location, the higher the total pressure, the larger the reduction in blockage. At a given jet total pressure level, a heightened clearance jet total pressure over the first 50 percent of the chord yielded only a 10 to 15 percent improvement compared to high total pressure over the upstream 25 percent of the chord. Near stall, increased jet total pressure reduced blockage approximately 20 percent less than for the low loading cases.

The blockage reduction due to increasing the jet total pressure was also estimated using the simplifed blockage model. Cases were calculated with increased clearance jet total pressure coefficient over the front 50 percent of the clearance jet. The blockage reduction calculated is shown in Fig. 22, which shows that a 60 percent increase in jet total pressure would result in a 45 percent reduction in blockage. This result is in good agreement to the experiments, which indicate a 49 percent reduction in blockage for the same level of blowing at near-stall conditions.

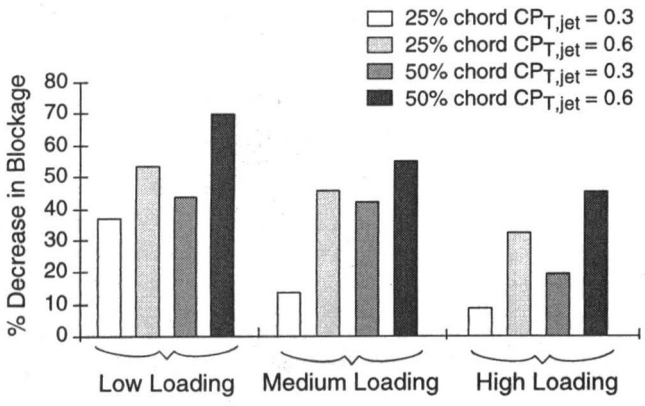

Fig. 21 Measured reduction in blockage due to high total pressure jet. Data obtained from wind tunnel measurements.

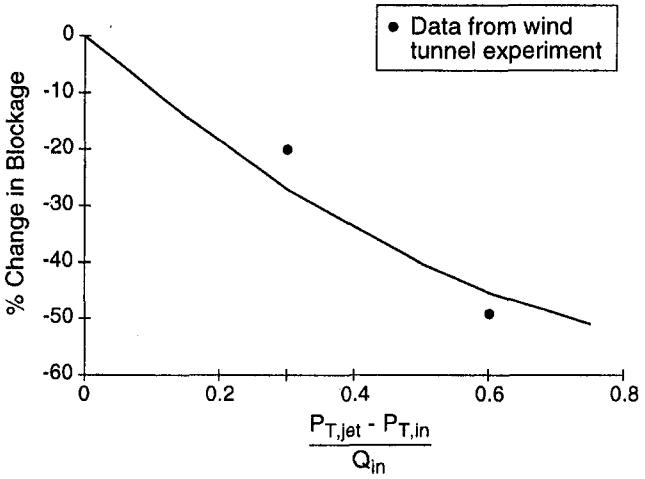

Fig. 22 Modeled reduction in blockage when jet total pressure is increased over the front 50 percent of the chord

7.0 Summary and Conclusions

1 A new methodology for quantifying compressor endwall blockage has been developed. The approach, which can be regarded as adapting the concept of displacement thickness to the three-dimensional flows found in compressors, provides a clear metric for evaluating the effect of endwall flow on pressure rise capability.

2 Computations and experiments have been examined in light of this blockage definition. The results suggest a parameter set, which collapses the experimental and numerical data for endwall blockage onto a single trend line for all situations assessed.

3 A simplified analysis has been developed that enables estimation of endwall blockage with good accuracy (trends captured to better than 10 percent). An additional, and potentially more important application of this tool is that it can provide physical insight into the interacting fluid dynamic processes involved in clearance related blockage generation.

4 The simplified analysis is based on a view of the blockage as due to the growth of the region of low total pressure fluid associated with the tip leakage, with the behavior roughly similar to that of a wake in a pressure rise. The initial conditions for the wake are set by the total pressure loss incurred by the mixing of the leakage flow (which exits the suction side of the blade clearance at an angle to the free stream) with the free stream.

5 A wind tunnel simulation for the tip leakage flow has been developed. The results from the tunnel experiments, which agree with rotating rig measurements of blockage to better than 10 percent, provide information on the variation in blockage with leakage flow angles and clearance total pressure, the latter being a key feature of casing treatment operation.

References

Adamczyk, J. J., Celestina, M. L., Beach, T. A., and Barnett, M., 1989, "Simulation of Three-Dimensional Viscous Flow Within a Multistage Turbine," ASME JOURNAL OF TURBOMACHINERY, Vol. 112, pp. 370–376.

Baldwin, B., and Lomax, H., 1978, "Thin Layer Approximation and Algebraic Model for Separated Turbulent Flows," AIAA Paper No. 78-257.

Crook, A. J., Greitzer, E. M., Tan, C. S., and Adamczyk, J. J., 1993, "Numerical Simulation of Compressor Endwall and Casing Treatment Flow Phenomena," ASME JOURNAL OF TURBOMACHINERY, Vol. 115, pp. 501–512.

Cumpsty, N. A., 1989, *Compressor Aerodynamics,* Longman Scientific and Technical Publications.

Dring, R. P., 1984, "Blockage in Axial Compressors," ASME *Journal of Engineering for Gas Turbines and Power,* Vol. 106, pp. 712–714.

Hill, P. G., Schaub, U. W., and Senoo, Y., 1963, "Turbulent Wakes in Pressure Gradients," ASME *Journal of Applied Mechanics,* pp. 518–524.

Horlock, J. H., and Greitzer, E. M., 1983, "Non-uniform Flows in Axial Compressors Due to Tip Clearance Variation," *Proc. IMechE,* Vol. 197C, pp. 173–178.

Johnson, M. C., and Greitzer, E. M., 1987, "Effects of Slotted Hub and Casing

Treatments on Compressor Endwall Flowfields," ASME JOURNAL OF TURBOMACHINERY, Vol. 109, pp. 380–387.

Khalid, S. A., 1995, "The Effects of Tip Clearance on Axial Compressor Pressure Rise," Internal Gas Turbine Laboratory Report.

Khalsa, A. S., 1996, "Endwall Blockage in Axail Compressors," Ph.D. thesis, Department of Aeronautics and Astronautics, Massachusetts Institute of Technology.

Kirtley, K. R., Beach, T. A., and Adamczyk, J. J., 1990, "Numerical Analysis of Secondary Flow in a Two-Stage Turbine," AIAA Paper No. 90-2356.

Koch, C. C., 1981, "Stalling Pressure Rise Capability of Axial Flow Compressor Stages," ASME *Journal of Engineering for Power,* Vol. 103, pp. 645–656.

Martinez-Sanchez, M., and Gauthier, R. P., 1990, "Blade Scale Effects of Tip Leakage," Gas Turbine Laboratory Report #202.

Rediniotis, O. K., Hoang, N. T., and Telionis, D. P., 1993, "The Seven-Hole Probe: Its Calibration and Use," *Instructional Fluid Dynamic Experiments,* ASME FED-Vol 152, pp. 21–26.

Schweitzer, J. K., and Garberoglio, J. E., 1984, "Maximum Loading Capability of Axial Flow Compressors," *J. Aircraft,* Vol. 21, No. 8, pp. 593–600.

Smith, G. D. J., and Cumpsty, N. A., 1984, "Flow Phenomena in Compressor Casing Treatment," ASME *Journal of Engineering for Gas Turbines and Power,* Vol. 106, pp. 532–541.

Smith, L. H., Jr., 1970, "Casing Boundary Layers in Multistage Axial-Flow Compressors," *Flow Research in Blading,* L. S. Dzung, ed., Elsevier, Amsterdam.

Storer, J. A., and Cumpsty, N. A., 1991, "Tip Leakage Flow in Axial Compresors," ASME JOURNAL OF TURBOMACHINERY, Vol. 113, pp. 252–259.

Strazisar, A. J., Wood, J. R., Hathaway, M. D., and Suder, K. L., 1989, "Laser Anemometer Measurements in a Transonic Axial-Flow Fan Rotor," NASA TP-2879.

Suder, K., 1998, "Blockage Development in a Transonic, Axial Compressor Rotor," ASME JOURNAL OF TURBOMACHINERY, Vol. 120, pp. 465–476.

Wisler, D. C., 1977, "Core Compressor Exit Stage Study, Vol. I—Blading Design," NASA CR-135391.

Wisler, D. C., 1981, "Core Compressor Exit Stage Study, Vol. IV—Data and Performance Report for the Best Stage Configuration," NASA CR-165357.

Wisler, D. C., 1985, "Aerodynamic Effects of Tip Clearance, Shrouds, Leakage Flow, Casing Treatment and Trenching in Compressor Design," Von Karman Institute Lecture Series 1985-05 on Tip Clearance Effects in Axial Turbomachinery.

APPENDIX

Assessment of Primary Assumptions Used in Blockage Estimation Procedure

The assumption that causes the largest error in the simplified blockage calculation method is that the static pressure change from the jet–free-stream interface to the passage exit can be approximated by the static pressure change from the blade surface to the passage exit. This assumption was determined to cause up to a 38 percent underprediction of blockage.

A second assumption is that the leakage jet experiences no pressure change between the blade suction surface and the jet–free-stream interaction region. This assumption was tested by examining representative streamlines in the CFD solutions. The results suggest that this assumption is responsible for less than 10 percent undercalculation of exit-plane blockage.

An assumption not examined is whether the mixing of the defect between the jet–free-stream interface and the passage exit occurs in a manner similar to a two-dimensional wake. The validity of this assumption perhaps can be inferred by the agreement between the model and data.

To predict the clearance jet leakage angle accurately, the total pressure of the fluid exiting the clearance gap must be known. Storer and Cumpsty (1991) assumed that the total pressure of the leakage jet is equal to the free-stream total pressure, which was not valid for some of the cases examined for this paper. Figure A.1 shows a tangential view of the total pressure field in the clearance of the low-speed rotor. The total pressure coefficient over the rear 60 percent of chord was below −0.4. The cause of this reduction in clearance jet total pressure can be seen in plots of total pressure coefficient in an axial–tangential plane at the blade tip radius, shown in Fig. A.2. The leakage flow is transported across the passage to the pressure side of the adjacent blade. This results in a reduction in the total pressure of the fluid at the entrance to the adjacent clearance gap between 40 percent chord and the blade trailing edge.

When fluid from the leakage jet passes under a second blade in this manner, the total pressure of the clearance jet is reduced,

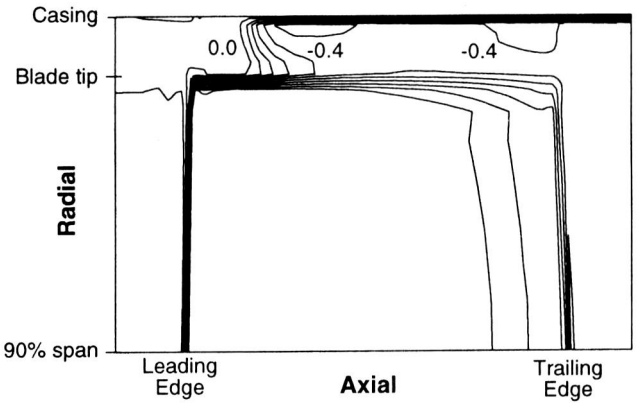

Fig. A.1 Total pressure coefficient at clearance gap exit, τ/c = 3 percent, near stall

lowering the leakage angle. If this reduction in leakage angle is not taken account of in the blockage calculation procedure, the calculated blockage can be as much as 30 percent too high. The calculations presented here used the CFD results to supply the leakage jet total pressure, primarily to avoid this source of error.

A second error that double leakage introduces into these calculations is associated with the assumption that all fluid leaking over the blade tip contributes to that passage's exit plane blockage. However, fluid that passes into any adjacent passage cannot contribute to exit plane blockage of the passage in which it originated. The CFD calculations indicate an upper bound for this error is approximately 20 percent overprediction of blockage using the simplified calculation procedure.

A balance between the errors due to neglecting double leakage (causing the calculated blockage to be too high) and due to the pressure gradient assumptions (causing the calculated blockage to be too low) provides a likely explanation for the more accurate calculation of blockage at increased solidity than at nominal solidity. For similar passage loading, the increased solidity geometries have more double leakage than the one with nominal solidity and hence a larger overprediction error due to neglecting the double leakage.

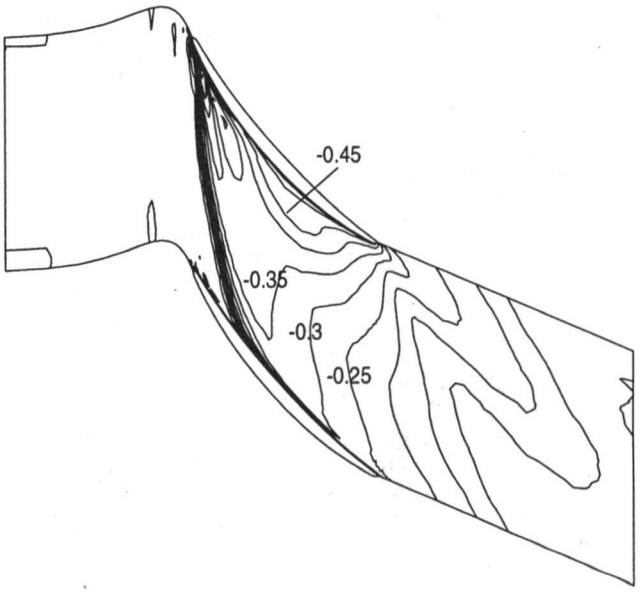

Fig. A.2 Total pressure coefficient at blade tip radius, near stall

Z. S. Spakovszky

H. J. Weigl

J. D. Paduano

Gas Turbine Laboratory,
Department of Aeronautics and Astronautics,
Massachusetts Institute of Technology,
Cambridge, MA 02139

C. M. van Schalkwyk
Scientific Systems Co., Inc.,
Woburn, MA 01801

K. L. Suder

M. M. Bright

NASA Lewis Research Center,
Cleveland, OH 44135

Rotating Stall Control in a High-Speed Stage With Inlet Distortion: Part I—Radial Distortion

This paper presents the first attempt to stabilize rotating stall in a single-stage transonic axial flow compressor with inlet distortion using active feedback control. The experiments were conducted at the NASA Lewis Research Center on a single-stage transonic core compressor inlet stage. An annular array of 12 jet-injectors located upstream of the rotor tip was used for forced response testing and to extend the compressor stable operating range. Results for radial distortion are reported in this paper. First, the effects of radial distortion on the compressor performance and the dynamic behavior were investigated. Control laws were designed using empirical transfer function estimates determined from forced response results. The transfer functions indicated that the compressor dynamics are decoupled with radial inlet distortion, as they are for the case of undistorted inlet flow. Single-input-single-output (SISO) control strategies were therefore used for the radial distortion controller designs. Steady axisymmetric injection of 4 percent of the compressor mass flow resulted in a reduction in stalling mass flow of 9.7 percent relative to the case with inlet distortion and no injection. Use of a robust H_∞ controller with unsteady nonaxisymmetric injection achieved a further reduction in stalling mass flow of 7.5 percent, resulting in a total reduction of 17.2 percent.

1 Introduction

The classic model of Moore and Greitzer (1986) describes the rotating stall dynamics for an incompressible, undistorted flow field. This model predicts that waves of sinusoidal shape (harmonics) travel around the annulus at rotation rate ω_n and grow or decay in time with growth rate σ_n. For example, the two-dimensional pressure perturbation field solution can be written as

$$\delta p(x, \theta, t) = \sum_{n=-\infty}^{\infty} \tilde{p}_n(x, t) e^{jn\theta}, \tag{1}$$

with

$$\tilde{p}_n(x, t) = a_n(x) e^{(\sigma_n - jn\omega_n)t}, \tag{2}$$

where x is the axial and θ the circumferential direction respectively, and t is the time. $\tilde{p}_n(x, t)$ measured at some axial station x is defined as the nth spatial Fourier coefficient of the measured pressure perturbation (Paduano et al., 1993). Hence, the overall compressor stability is defined by the growth rate of the least stable mode. Furthermore, it is assumed that the axial velocity perturbation at a given θ is uniform through the whole compressor. For this incompressible flow field the nth mode contains only the nth harmonic so that the harmonics are all decoupled.

Generally, for distorted inlet flow, the major change in the compressor prestall behavior is that the distortion introduces nonlinearities that couple the compressor dynamics. The mode shapes are no longer purely sinusoidal but have contributions of all the harmonics. In other words, there is *coupling* between the harmonics due to inlet distortion. Spakovszky et al. (1999) discuss this in more detail. However, when the distortion is circumferentially uniform (e.g., radial distortion) the harmonics can still be decoupled.

If the compressor flow field is compressible, as is the case for the NASA Stage 35 compressor, acoustic modes with an axial structure are introduced. Modeling these compressible effects for an undistorted flow field was first done by Bonnaure (1991), extended by Hendricks et al. (1993), and Feulner et al. (1994) who included actuation and converted the model to input–output form compatible with control theory. Since there is no control theoretical, compressible model with inlet distortion in existence, an understanding of the effect of inlet distortion on the compressor dynamics and constraints on control laws is one of the major issues of this paper.

The very first effort using steady blowing and bleeding devices to determine whether tip boundary layer control was an effective means of increasing the unstalled weight flow range of a transonic single-stage compressor with and without inlet flow distortion was conducted by Koch (1970). Prior to the study described in this paper, active stabilization of rotating stall in axial flow compressors has been demonstrated primarily under undistorted inlet flow conditions. The use of an annular array of injectors to extend the stable operating range of the same transonic compressor stage under undistorted inlet flow conditions was reported by Weigl et al. (1998) (also see Weigl, 1997). Each injector was coupled to a high-speed valve. The development and testing of the valve-injector system was described by Berndt et al. (1995). The present work extends the use of steady and controlled injection for transonic compressor stability enhancement to cases which feature distorted inlet flows.

Stall inception and control studies done by Camp and Day (1998) and Day and Freeman (1993) indicate that instability of a long length scale eigenmode is not the cause of rotating stall in some low- and high-speed compressors; in some cases short length scale rotating disturbances called spikes can be the source of instability. Depending on the stall inception pattern exhibited by the compressor, different control strategies were applied. The introduction of radial distortion to the compressor described in this

Contributed by the International Gas Turbine Institute and presented at the 43rd International Gas Turbine and Aeroengine Congress and Exhibition, Stockholm, Sweden, June 2–5, 1998. Manuscript received by the International Gas Turbine Institute February 1998. Paper No. 98-GT-264. Associate Technical Editor: R. E. Kielb.

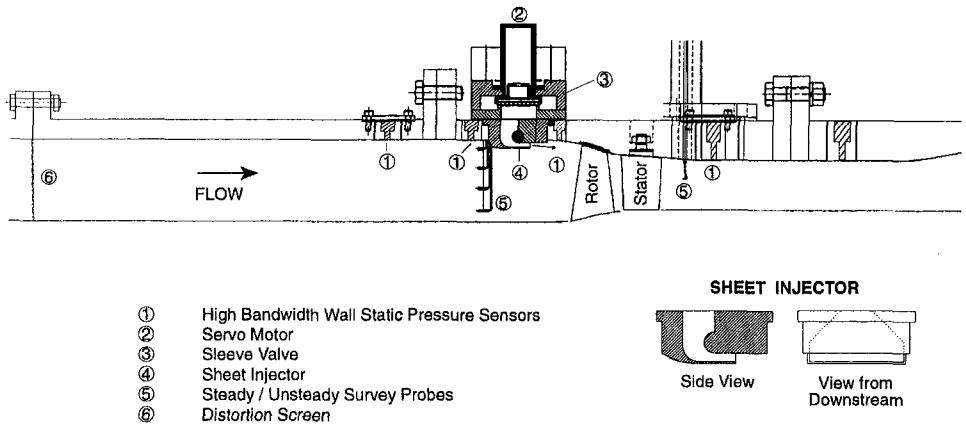

Fig. 1 NASA Stage 35 actuation and instrumentation schematic with inlet distortion

paper shows the interplay of spikes and long length scale stall precursors. The effects of steady and controlled air injection on the compressor prestall behavior will also be discussed.

2 Experimental Setup

All experiments described in this paper were conducted at the NASA Lewis Research Center in the Single-Stage Axial Compressor Test Facility. The NASA Stage 35 test compressor, originally designed as an inlet stage of an eight-stage 20:1 pressure ratio core compressor (Reid and Moore, 1978a), has a total pressure ratio of 1.82, a mass flow of 20.2 kg/s, a rotor tip speed of 455 m/s, and a rotation frequency of 286 Hz at design conditions. Rotor 35 consists of 36 blades with an aspect ratio of 1.19, a hub-to-tip radius ratio of 0.7, and a blade tip diameter of approximately 50 cm. The mean-line rotor chord length is 56 mm. The stator has 46 blades with an aspect ratio of 1.26 and a chord length of 40 mm. Detailed performance descriptions are given by Reid and Moore (1978b).

Atmospheric air is drawn into the test facility through an orifice plate and a plenum chamber upstream of the test section. Downstream of the compressor, the flow is regulated with a sleeve-type throttle valve. The compressor mass flow is controlled by adjusting the exit area of the throttle valve.

The 12 circumferentially equally spaced jet actuators are placed 63 mm (1.1 rotor chord lengths) upstream of the rotor face mounted on the outer casing. They were designed by Berndt et al. (1995) and developed by Moog Inc. and MIT. The actuators are capable of delivering 5.8 percent of the design compressor mass flow when supplied with 100 psi air and have a bandwidth of 400 Hz. Since rotor 35 is tip critical and an extensive study of two different types of injectors (a three-hole injector and a "sheet" injector shown in Fig. 1) conducted by Weigl et al. (1998) showed that the maximal reduction in stalling mass flow was obtained by the sheet injector, all experiments were done with this kind of injector. The sheet injectors affect the outer 7 percent of the rotor inlet span. A detailed description and the actuator design requirements are given in Berndt (1995).

The control computer used for the experiments is a 90 MHz Pentium PC with 64 input and 16 analogue output channels. The sample rate used for all experiments is 3 kHz, while data are acquired in a circular buffer of up to 45 seconds in length (limited only by available RAM). The inputs to the control computer are high-response pressure transducer measurements (Kulite sensors), position sense signals from the actuator motors, and steady-state compressor performance measurements (static pressures at various hub and casing locations, mass flow, pressure rise, and throttle position). The unsteady high-response sensors are circumferentially distributed (8–12 wall static pressure probes) at several axial locations. Unsteady pressure measurements immediately upstream of the rotor had the highest signal-to-noise ratio and were therefore used for system identification and control law testing. The outputs of the control computer are 12 independently commanded mass flow injection rates.

3 Radial Inlet Distortion

The first set of experiments was conducted using a radial distortion screen, which consisted of a fine mesh covering about 38 percent of the blade span in the tip region and which was mounted on a carrier at approximately 2.2 mean radii upstream of the rotor. The inlet flow with radial distortion is still circumferentially uniform but has a total pressure loss in the tip region as shown in Fig. 2. Plotted are the radial distributions (measured about 1.1 mean radii downstream of the distortion screen) of the flow coefficient $\phi = v_x/(\text{mean wheel speed})$, and the total pressure drop $\Delta p_t = p_t - \bar{p}_t$ normalized by the mean dynamic head for the case with undistorted inlet flow and the case with radial distortion. The undistorted inlet flow case refers to measurements with the coarse-mesh carrier screen in the flow path, which interacts with the casing boundary layer and explains the considerable drop in flow coefficient and total pressure in the casing region. Due to the total pressure loss introduced by the screen, the axial velocity is reduced in the tip region resulting in a higher incidence, and therefore a higher loading, of the blades at the tip. The effect of this on the stall inception pattern will be discussed in Section 5.

3.1 Steady-State Experiments. Twelve sheet injectors were mounted at a yaw angle of −15 deg (yawed 15 deg from the axial

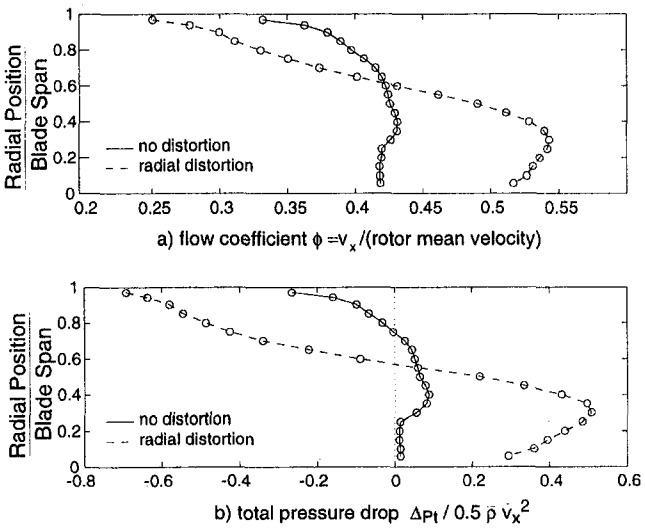

Fig. 2 Measured radial distortion profile

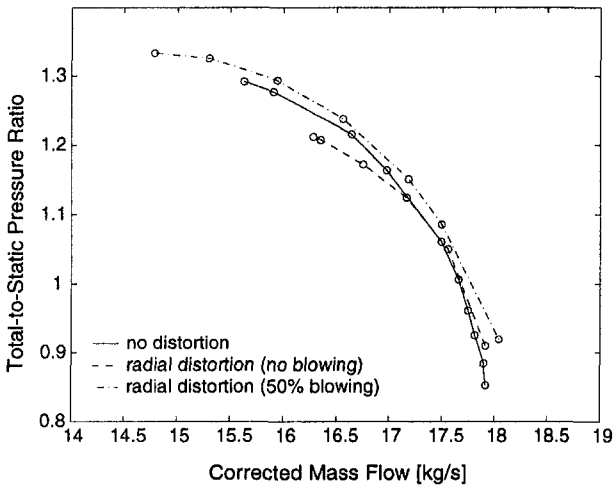

Fig. 3 Speed lines for no distortion and radial distortion

direction so as to inject flow against the direction of rotor rotation), which was found by Weigl et al. (1998) to give the best reduction in stalling mass flow and the highest pressure rise with 50 percent steady-state blowing and no inlet distortion. Throughout this paper, "50 percent blowing" refers to a 100 psi supply pressure with a 50 percent valve opening. This corresponds to an injector exit total pressure of 16.7 psi and an exit total temperature of 30.9°C yielding a corrected injector mass flow of 0.652 kg/s. This represents about 4 percent of the radial distortion, no blowing stalling mass flow of 16.3 kg/s. All experiments were conducted at 85 percent corrected design speed because shaft whirl occurred at speeds above 85 percent, introducing a source of forcing not related to the aerodynamics of the compressor. All speed lines are constructed from the measured total inlet pressure upstream of the actuators, the exit static pressure (average of hub and casing wall static pressures downstream of the stage), and the total corrected mass flow through the compressor. The total corrected mass flow is the sum of the inlet flow rate (measured by an orifice far upstream of the compressor and corrected by the total pressure and temperature at the same location) and the injector flow rate (determined by a separate venturi meter and corrected by the total pressure and temperature in the injector).

First, the nominal speed line at 85 percent corrected design speed (no distortion and no blowing) was measured. The radial distortion screen was then mounted on the carrier and the speed lines were measured without injection and with 50 percent steady-state blowing. Steady blowing at a valve opening of 50 percent is of interest because actively controlled blowing is commanded about a mean valve position of 50 percent open. Steady blowing at 50 percent open therefore forms the baseline condition from which the impact of active blowing is assessed. Figure 3 shows the total-to-static speed lines for the mentioned cases. The slopes of the total-to-static pressure ratios are crucial for the determination of compressor stability.[1] The peak pressure ratio drops and the compressor stalls at higher mass flows when radial distortion is introduced to the compressor. However, steady-state injection can recover this lost performance and even produces a significant reduction in stalling mass flow of 9.7 percent relative to the case with inlet distortion and no injection.

3.2 General Input–Output Compressor Dynamics With Inlet Distortion. All compressor input and output quantities will be defined in terms of spatial Fourier coefficients or SFCs (Paduano et al., 1993) denoted by overhead tilde (e.g., $\tilde{y}_n$ is the nth spatial Fourier coefficient of signal y). If the output vector $\tilde{\mathbf{y}}$ is defined as the SFCs of the pressure perturbations and the input vector $\tilde{\mathbf{u}}$ contains the corresponding SFCs of the injection signal, the transfer function matrix of the compressor can be written, for example for the first three harmonics as follows:

$$\begin{bmatrix} \tilde{y}_0(s) \\ \tilde{y}_1(s) \\ \tilde{y}_2(s) \end{bmatrix} = \begin{bmatrix} G_{00}(s) & G_{01}(s) & G_{02}(s) \\ G_{10}(s) & G_{11}(s) & G_{12}(s) \\ G_{20}(s) & G_{21}(s) & G_{22}(s) \end{bmatrix} \begin{bmatrix} \tilde{u}_0(s) \\ \tilde{u}_1(s) \\ \tilde{u}_2(s) \end{bmatrix}, \quad (3)$$

or, in short form

$$\tilde{\mathbf{y}}(s) = \mathbf{G}(s)\tilde{\mathbf{u}}(s). \quad (4)$$

Note that $\tilde{y}_i(s)$ and $\tilde{u}_j(s)$ are *complex* spatial Fourier coefficients (phasors).

For undistorted and circumferentially uniform inlet flow the off-diagonal elements of $\mathbf{G}(s)$ are zero ($G_{ij}(s) = 0$ for all $i \neq j$) because the harmonics are decoupled as discussed in Section 1. Therefore, the compressor dynamics for uniform inlet flow can be treated on a harmonic by harmonic basis, and single-input–single-output (SISO) control laws can be designed independently for each harmonic. This was done by Weigl et al. (1998) for the compressor being studied. In this paper we show that, with radial inlet distortion, the shape of the transfer functions and the trend of decoupled prestall behavior are similar to the results reported by Weigl et al. (1998).

If circumferentially nonuniform inlet distortion is present, the harmonics are no longer decoupled and the off-diagonal elements of $\mathbf{G}(s)$ are nonzero ($G_{ij}(s) \neq 0$ for all $i \neq j$). The strength of the coupling between the harmonics can be determined by the magnitudes of these transfer functions. The consequence of this coupling is that the harmonics can not be treated independently as SISO systems. The control problem becomes multi-input–multi-output (MIMO) and increases the complexity of system identification and control law design. Part II (Spakovszky et al., 1999) discusses these issues in more detail.

3.3 Open-Loop Compressor Dynamics. An important issue and the basis for empirical control law design is a full understanding of the compression system dynamics. Forced response experiments have been conducted to measure compression system transfer functions.

Measurements of the zeroth, first, and second harmonic transfer functions revealed that the off-diagonal elements $G_{ij}(j\omega)$ for $i \neq j$ have low magnitudes and that the diagonal elements $G_{ij}(j\omega)$ for $i = j$ exhibit roughly the same shape and trends as obtained by Weigl et al. (1998) for undistorted inlet flow. This indicates that, with circumferentially uniform radial inlet distortion, the harmonics are *decoupled.* Figures 4 and 5 show the measured transfer function of the first harmonic $G_{11}(j\omega)$ for two different mass flows. Multiple compressible modes are visible in the zeroth, first, and second harmonic transfer functions. The compressible modes are denoted by $[n, m]$, where n is inferred from the circumferential harmonic that is largest in mode, and m indicates the postulated axial mode number. Mode [1, 0] is traveling around the annulus at approximately 40 percent of rotor speed and can be associated with the classical incompressible Moore–Greitzer mode. Mode [1, 1], the first compressible mode, is also visible and travels approximately at the rotor frequency. In Figs. 4 and 5 we see that the magnitude of mode [1, 0] increased significantly when the mass flow was reduced. This indicates that the damping of the mode decreased with the decrease in mass flow.

Open-loop stall ramps have also been measured. The jet-injectors were operated at a 50 percent steady blowing level while the throttle was closed slowly until the compressor stalled. Pre- and post-stall pressure measurements were taken with eight Kulites located between the jet-injectors and the rotor face. The Kulite pressure signals were decomposed into the first three Fourier harmonics. For each harmonic, the evolution of the power spectrum was then computed. Analysis showed that the first harmonic

[1] For high-speed machines the slope of the total-to-static pressure ratio is analogous to the total-to-static pressure rise coefficient, which is a relevant parameter for rotating stall in low-speed compressors.

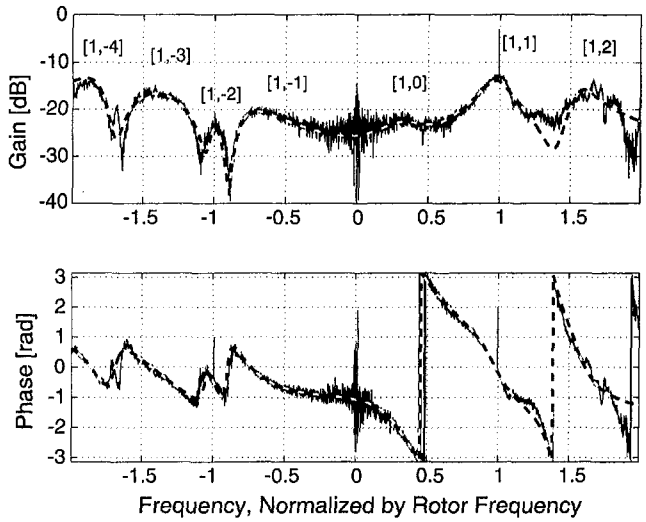

Fig. 4 Measured (solid) and identified (dashed) first harmonic transfer function $G_{11}(j\omega)$ at a corrected mass flow of 15.9 kg/s

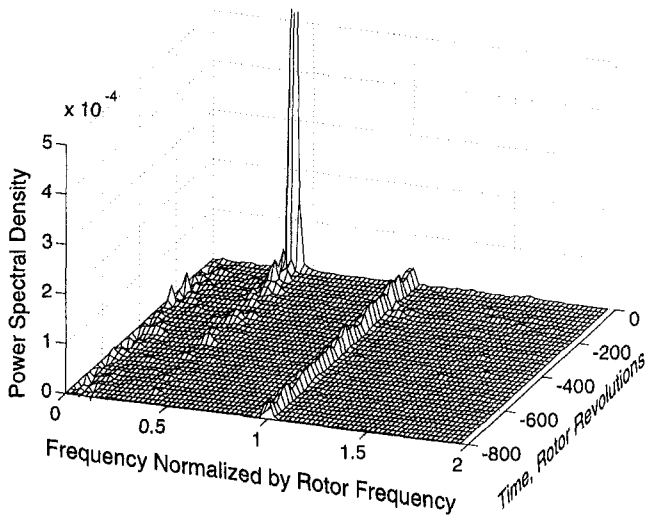

Fig. 6 Spectrogram of the first harmonic pressure perturbations during a stall ramp with 50 percent steady injection

is dominant in the prestall dynamics so we will concentrate on it. Figure 6 shows the evolution of the power density spectrum for the first spatial Fourier harmonic during a stall experiment. The time axis is in rotor revolutions and the frequency axis is normalized by rotor frequency. There are two modes visible in the power density spectrum which correspond to mode [1, 0] and mode [1, 1] in Figs. 4 and 5. It is mode [1, 0] that loses stability as is clear from Fig. 6. Because mode [1, 0] consists only of the first spatial harmonic, we consider the design of first harmonic controllers to stabilize the compressor.

The empirical design of control laws requires an identified model of the compression system dynamics. FORSE (Frequency Observable Range Subspace Estimation), a state-space system identification program developed at the Space Engineering Research Center at MIT (Jacques, 1994), was used to identify a model from the measured transfer functions. The system order was fixed at 14 to reduce the complexity of the compressor model (for details see Spakovszky, 1998). The identified transfer functions are plotted as dashed lines in Figs. 4 and 5.

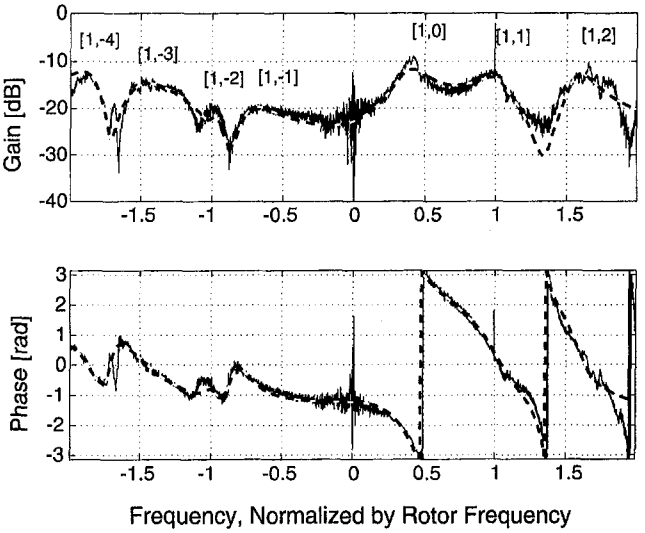

Fig. 5 Measured (solid) and identified (dashed) first harmonic transfer function $G_{11}(j\omega)$ at a corrected mass flow of 15.6 kg/s. Note the change in gain of mode [1, 0] relative to Fig. 4.

4 Control Law Design and Closed-Loop Experiments

This section discusses active control law design and testing. The inputs to the feedback controller are the computed SFCs $\tilde{y}_i(s)$ (output of the compressor transfer function in Eq. (3)) of the measured pressure perturbations. The controller outputs are the actuator commands, which are translated over additional actuator dynamics of the jet-injectors to the injection signals $\tilde{u}_j(s)$. These are the inputs to the compressor transfer functions (see Eq. (3)).

Two strategies have been employed to design control laws for active stall control. The first control experiments were conducted with a constant gain controller. This control law measures the first spatial harmonic of the pressure perturbations upstream of the rotor, multiplies it by a constant complex gain, and feeds it back to the actuator. The gain and phase of the complex gain was found through on-line tuning experiments.

However, as expected from previous results of constant gain experiments conducted by Weigl et al. (1998), none of the constant gain controllers reduced the stalling mass flow. The lack of improvement can be explained as follows. At the operating point (85 percent corrected rotor speed) the compressor dynamics are compressible. As shown in Figs. 4 and 5 there are several lightly damped compressible modes. Suppose we apply a first harmonic constant gain controller and tune it so that it stabilizes the [1, 0] mode. Then the other lightly damped modes (like modes [1, 1] and [1, 2]) may be destabilized because the constant gain controller has a frequency independent phase shift. In situations like these constant gain is not effective and a frequency-dependent control law must be used.

A sophisticated model-based dynamic controller, the H_∞ robust control law, was designed using systematic procedures, which have yielded more effective controllers. This approach is described next.

4.1 Robust Controller With Eigenvalue Perturbations. Using the identified model shown in Fig. 5 a robust, linear, dynamic H_∞ controller was designed to stabilize the $[1, m]$ modes. The basic concept of the control design strategy is a mixed sensitivity H_∞ problem modified with eigenvalue perturbations, since our task here is not to solve a tracking problem but to stabilize the compressor (for details see Kwakernaak, 1993, Smith, 1995, and Weigl, 1997). Such a control law can only be designed using a model of the unstable compressor dynamics. Since, on one hand, a theoretical model is not yet accurate enough (Weigl et al., 1998) and, on the other hand, it is difficult to measure the unstable dynamics of the compressor, an estimated unstable identified model was used. The estimated unstable model was obtained by

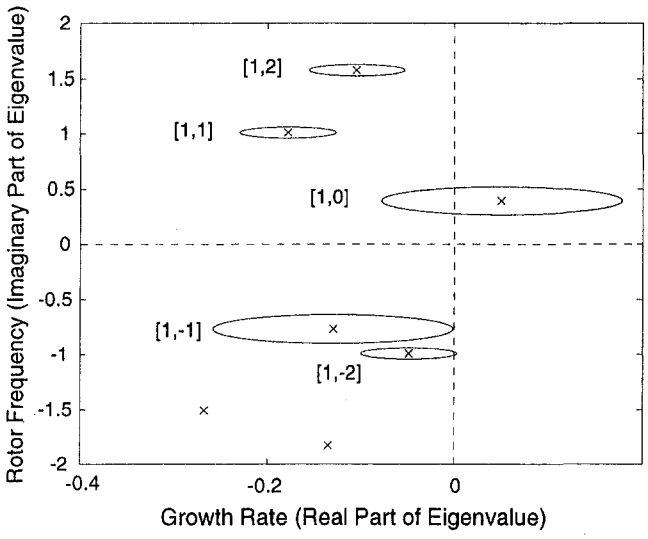

Fig. 7 Eigenvalue perturbations for first harmonic robust control design

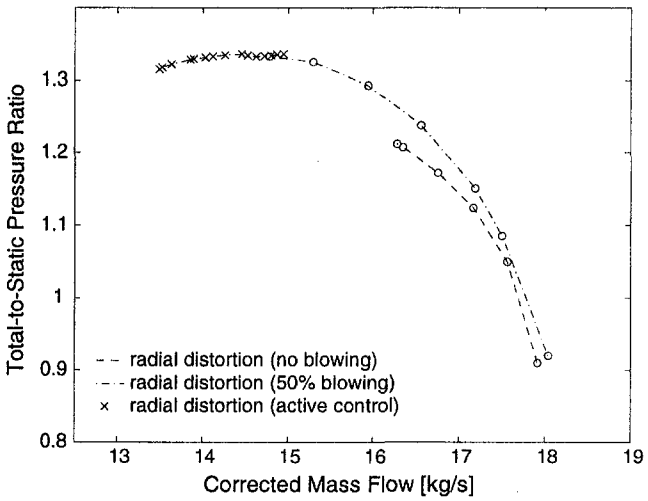

Fig. 9 Speed lines with radial distortion: 50 percent steady blowing and first harmonic active control

extrapolating (from Figs. 4 and 5) the pole associated with the identified stable [1, 0] mode to a lower unstable mass flow. Hence it was assumed that the other modes do not significantly change in growth rate during a throttle ramp; this assumption is consistent with the results in Figs. 4 and 5. Based on the estimated unstable dynamics an H_∞ controller was designed with five eigenvalue perturbation circles as shown in Fig. 7. Note that mode [1, 0] is assumed to be unstable for the control law design. The circles (the scales in Fig. 7 make them appear to be ellipses) represent uncertainty in the eigenvalue location. The controller will stabilize the compressor as long as the first harmonic eigenvalues stay within the boundaries of the uncertainty circles. Also, note that the big circle around mode [1, 0] covers positive (unstable) as well as negative (stable) eigenvalue locations to ensure that the controller does not destabilize the compressor at higher mass flows where mode [1, 0] is stable. All the presented results of the control experiments with radial inlet distortion will be for this controller.

4.2 Closed-Loop Experiments With H_∞ Controller. Figure 8 shows the spectrogram of the first harmonic pressure perturbations for a stall experiment with active control. Mode [1, 0], which was driving the compressor into stall without control (see Fig. 6), is completely damped out (the magnitude of the power density spectrum is small around $0.4\omega_r$). It is now mode [1, 1] that is growing and going unstable at this lower mass flow. The spectrograms of the zeroth and second harmonic perturbations (not shown here) showed little modal activity when the compressor stalled, indicating that the other modes were all well damped.

These results justify the choice of concentrating on a first harmonic controller. Additional zeroth and second harmonic controllers did not result in further reduction of the stalling mass flow. Adding a zeroth harmonic H_∞ controller has no effect since the [1, 1] mode determines the compressor stability. The only way to operate beyond these mass flows is to increase the uncertainty circle around mode [1, 1] in the control law design. However, the eigenvalue perturbations shown in Fig. 7 represent the case with the largest uncertainty that could be obtained within the H_∞ design constraints (Kwakernaak, 1993).

Active control results are summarized in Fig. 9. With 50 percent steady blowing the stalling mass flow could be reduced by 9.7 percent. Applying the first harmonic robust H_∞ controller allowed a further reduction in stalling mass flow of 7.5 percent relative to steady blowing, resulting in a total stalling mass flow reduction of 17.2 percent. Experiments by Weigl et al. (1998) at 100 percent corrected speed without inlet distortion achieved a reduction in stalling mass flow of 4.3 percent with 50 percent steady blowing only and about 7.8 percent using steady blowing plus zeroth, first, and second harmonic active robust control.

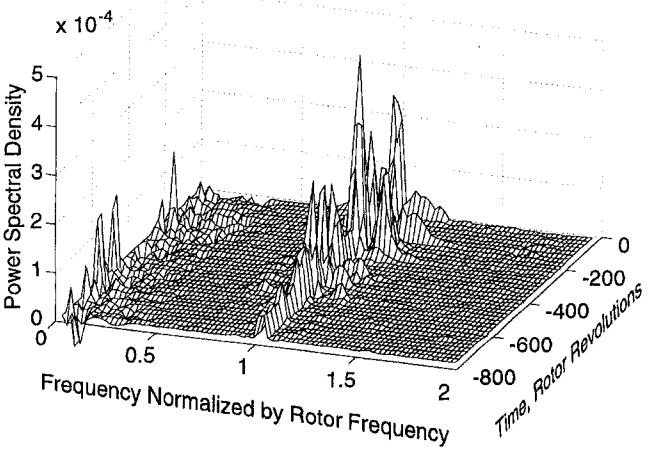

Fig. 8 Spectrogram of the first harmonic during a stall ramp with H_∞ control

5 Stall Patterns in Stage 35 With Radial Inlet Distortion

Previous stall inception studies and experimental work by Camp and Day (1998) have led to the identification of two common flow breakdown processes in low-speed axial flow compressors. According to Camp and Day (1998), stall can be triggered by short length scale disturbances known as spikes, or by longer length scale disturbances known as waves.

A spike may be described as an embryonic stall cell that is created by the local stalling of a particular blade row. Spikes usually start in low velocity troughs and travel quickly around the annulus between 60 to 80 percent of rotor speed. The fewer blade passages a stall cell occupies, the faster the spike will rotate (Camp and Day, 1998). Once a spike is formed, it quickly increases in size, loses rotational speed, and turns into a rotating stall cell. The long length scale waves have been discussed in the preceding sections. Camp and Day (1998) describe the nature and the appearance of these two prestall flow phenomena in several low-speed compressor configurations and explain the mechanism for each case with a simple model. According to Camp and Day

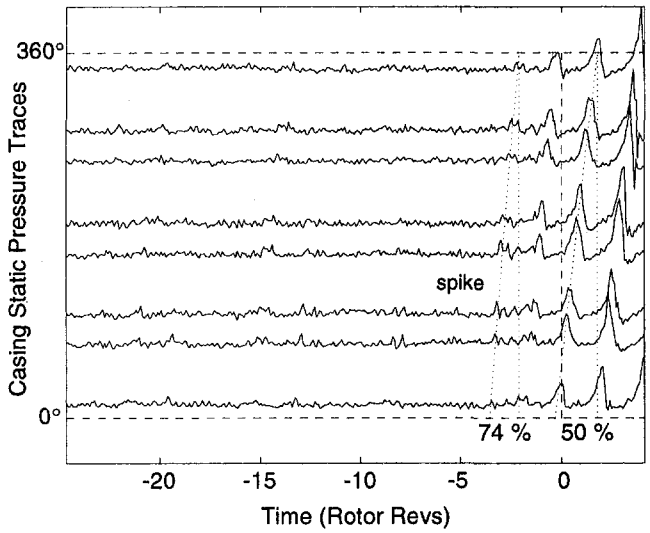

Fig. 10 No blowing: spike speed is 74 percent, initial stall cell speed about 50 percent of rotor speed (position of trace indicates circumferential location)

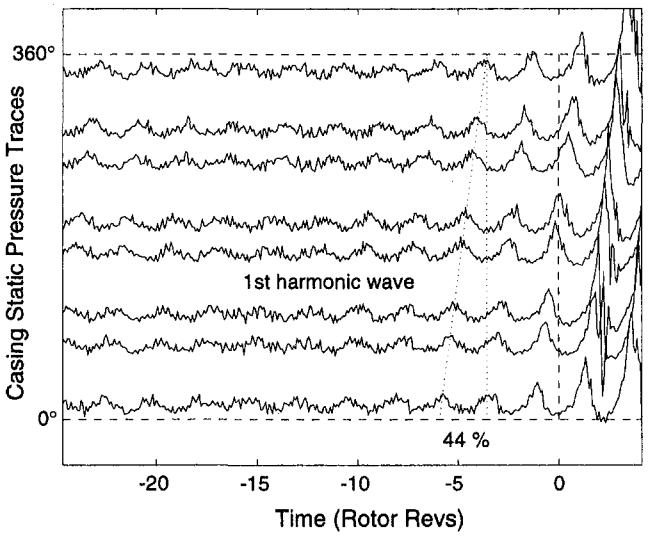

Fig. 11 50 percent steady blowing: dominant first harmonic modal prestall behavior

(1998) spikes occur when the critical incidence at the rotor tip is reached before the slope of the total-to-static pressure rise characteristic changes from negative to positive ($\partial\Psi^{ts}/\partial\phi \leq 0$), and waves are observed when the peak of the total-to-static pressure rise characteristic (neutral stability, $\partial\Psi^{ts}/\partial\phi = 0$) is reached before critical incidence is exceeded. This has been shown experimentally in a multistage low-speed axial compressor where the effects of stage matching and blade row incidence angles were investigated using variable geometry features of the test compressor. The same stall inception behavior has been observed in a low-speed single-stage axial compressor where the tip incidence was changed by artificially skewing the flow toward the casing or the hub (Camp and Day, 1997).

Figure 9 indicates that with inlet distortion and no blowing, the current compressor stalls with $\partial\Psi^{ts}/\partial\phi \leq 0$. However, with steady blowing the compressor stalls with $\partial\Psi^{ts}/\partial\phi = 0$. According to the Camp and Day model, we would therefore expect to find that the path to instability with no blowing is via spikes while the path to instability with blowing is via longer wave length disturbances. The present test results therefore afford us an opportunity to investigate the validity of the Camp and Day model in a transonic compressor.

The first experiment shown in Fig. 10 is an open-loop stall experiment without any injection. Plotted are the eight circumferentially distributed Kulite static pressure traces upstream of the rotor during the event. The pressure perturbations have been scaled by their mean standard deviations. One can see that there is a spike emerging from the pressure traces several rotor revolutions before stall and traveling very fast (about 74 percent of rotor speed) around the annulus. Its size is quickly growing while its speed is slowing down and within a few revolutions the spike forms a stall cell with an initial rotation rate of approximately 50 percent of rotor speed. The fully developed rotating stall cell is then traveling at a rotation rate of about 40 percent of rotor speed. The stall inception mechanism in Stage 35 with radial inlet distortion and no blowing is clearly determined by spikes.

In a second experiment the jet-injectors were turned on to a level of 50 percent steady blowing and the compressor was again throttled into stall. Figure 11 depicts the pressure traces during this event. The pressure traces reveal a very dominant first harmonic wave traveling around the annulus at about 44 percent of rotor speed long before the compressor stalls. The amplitude grows as neutral stability is reached and the modal oscillations turn into a stall cell. Note that the wave speed does not change significantly during the transient into stall. This can also be observed in the growing of mode [1, 0] in Fig. 6.

The reason why the two different stall inceptions depend on the level of blowing can be explained as follows. The radial distortion screen upstream of the rotor leads to a total pressure loss in the tip region and skews the flow toward the hub region as shown in Fig. 2. The axial velocity at the casing drops, the incidence and turning increase, and the blades have a higher loading in the tip region. Critical incidence is therefore exceeded at the blade tip before "system" neutral stability is reached and spikes appear in the prestall flow field. When the injectors are turned on, a high-momentum jet is blown into the rotor tip region. The increase in tip incidence caused by the distortion screen is reduced due to the higher axial velocities with blowing. This suggests that with blowing, the total-to-static characteristic changes in such a way that neutral stability is reached before the critical incidence occurs and therefore waves develop instead of spikes. This verifies the above-described simple model formulated by Camp and Day (1998) for a single-stage transonic axial compressor.

Another interesting result with radial inlet distortion is the pre-stall flow field with active control. Because the controller was designed to stabilize mode [1, 0], that is, dampen the long length scale waves, one would expect to see spikes. Pressure traces taken during an active control experiment are shown in Fig. 12. A spike traveling at approximately 90 percent of rotor speed emerges about 18 rotor revolutions prior to stall. However, this spike dies out and the spike activity restarts a few revolutions later. The spike does not show a continuous growth. Note that at this time the pressure traces are no longer circumferentially uniform. One can see that a first large-sized spike starts to rotate out of a pressure trough but dies again when it hits a region of higher pressures and thus higher velocities.

6 Summary and Conclusions

The experiments discussed in this paper represent the first attempt at active rotating stall control in a transonic compressor with radial inlet distortion using an annular array of jet-injectors. Measurements of the distortion profile showed that the flow is still circumferentially uniform but skewed toward the hub, resulting in a total pressure drop and thus in higher incidence and loading of the blades in the tip region. The peak pressure rise drops and the compressor stalls at higher mass flows. Steady-state injection results in a range extension of 9.7 percent in stalling mass flow relative to the case with inlet distortion and no injection.

Measured compressor transfer functions revealed that the com-

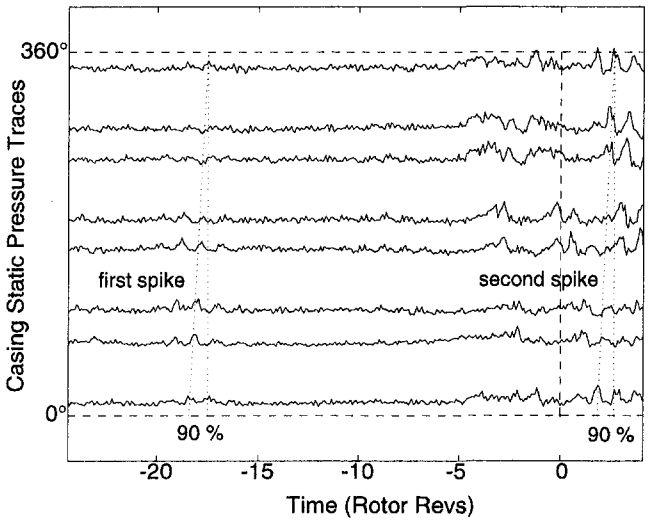

Fig. 12 First harmonic H_∞ control law; spike speed is about 90 percent of rotor speed

pressible stall dynamics with radial distortion are still decoupled. The prestall dynamics were dominated by a Moore–Greitzer-like mode with strong first harmonic content. This allowed the design of SISO control laws to stabilize the compressor. A first harmonic H_∞ robust controller achieved a reduction in stalling mass flow of 7.5 percent relative to steady blowing, yielding a total reduction of 17.2 percent. This result reflects an improvement in stalling mass flow reduction compared to experiments with no inlet distortion (Weigl et al., 1998).

The stall inception pattern with radial inlet distortion showed spikes or waves depending on whether the actuators were turned off or operated at steady blowing. The experiments indicate that the simple model developed by Camp and Day (1998) also holds in a single-stage transonic compressor.

Acknowledgments

This research was conducted under collaboration between the NASA Lewis Research Center and MIT. We would like to thank T. Strazisar for the very useful discussions, D. Williams, R. Brokopp, and B. Piendl at NASA Lewis for their support during compressor testing. Special thanks also to M. Carroll and D. Park for help in preparing this manuscript. This project was conducted under NASA grant NAG3-1457.

References

Berndt, R., Weigl, H., Paduano, J., and Epstein, A., 1995, "Experimental Techniques for Actuation, Sensing, and Measurement of Rotating Stall Dynamics in High Speed Engines," in: J. D. Paduano, ed., *Sensing, Actuation, and Control in Aeropropulsion,* Vol. 2492, SPIE.

Berndt, R. G., 1995, "Actuation for Rotating Stall Control of High Speed Compressors," Master's thesis, Department of Aeronautics and Astronautics, MIT.

Bonnaure, L., 1991, "Modelling High Speed Multistage Compressor Stability," Master's thesis, Department of Aeronautics and Astronautics, MIT.

Camp, T., and Day, I., 1998, "A Study of Spike and Modal Stall Phenomena in a Low-Speed Axial Compressor," ASME JOURNAL OF TURBOMACHINERY, Vol. 120, pp. 393–401.

Day, I., and Freeman, C., 1993, "The Unstable Behavior of Low and High-Speed Compressors," ASME JOURNAL OF TURBOMACHINERY, Vol. 116, pp. 194–201.

Feulner, M., Hendricks, G., and Paduano, J., 1994, "Modeling for Control of Rotating Stall in High Speed Multi-Stage Axial Compressors," ASME Paper No. 94-GT-292.

Hendricks, G., Bonnaure, L., Longley, J., Greitzer, E., and Epstein, A., 1993, "Analysis of Rotating Stall Onset in High Speed Axial Flow Compressors," Paper No. AIAA-93-2233.

Jacques, R., 1994, "On-Line System Identification and Control Design for Flexible Structures," Ph.D. thesis, Department of Aeronautics and Astronautics, MIT.

Koch, C. C., 1970, "Experimental Evaluation of Outer Case Blowing or Bleeding of a Single-Stage Axial Flow Compressor," Tech. Rep. CR-54592, NASA.

Kwakernaak, H., 1993, "Robust Control and H_∞-Optimization: Tutorial Paper," *Automatica,* Vol. 29, No. 3, pp. 255–273.

Moore, F., and Greitzer, E., 1986, "A Theory of Post-Stall Transients in Axial Compressors: Part I—Development of the Equations," ASME *Journal of Engineering for Gas Turbines and Power,* Vol. 108, pp. 68–76.

Paduano, J., Epstein, A., Valavani, L., Longley, J., Greitzer, E., and Guenette, G., 1993, "Active Control of Rotating Stall in a Low-Speed Axial Compressors," ASME JOURNAL OF TURBOMACHINERY, Vol. 115, pp. 48–56.

Reid, L., and Moore, D., 1978a, "Design and Overall Performance of Four Highly Loaded, High Speed Inlet Stages for and Advanced High Pressure Ratio Core Compressor," Tech. Rep. TP-1337, NASA.

Reid, L., and Moore, D., 1978b, "Performance of Single-Stage Axial-Flow Transonic Compressor With Rotor and Stator Aspect Ratios of 1.19 and 1.26, Respectively, and With Design Pressure Ratio 1.82," Tech. Rep. TP-1338, NASA.

Smith, R., 1995, "Technical Notes and Correspondence: Eigenvalue Perturbation Models for Robust Control," *IEEE Transactions on Automatic Control,* Vol. 40, No. 6, pp. 1063–1066.

Spakovszky, Z., 1999, "Active Control of Rotating Stall in a Transonic Compressor Stage With Inlet Distortion," Master's thesis, Department of Aeronautics and Astronautics, MIT.

Spakovszky, Z., Van Schalkwyk, C., Weigl, H., Paduano, J., Suder, K., and Bright, M., 1999, "Rotating Stall Control in a High-Speed Stage With Inlet Distortion: Part II—Circumferential Distortion," ASME JOURNAL OF TURBOMACHINERY, Vol. 121, this issue, pp. 515–522.

Weigl, H., Paduano, J., Fréchette, L., Epstein, A., and Greitzer, E., 1998, "Active Stabilization of Rotating Stall and Surge in a Transonic Single Stage Axial Compressor," ASME JOURNAL OF TURBOMACHINERY, Vol. 120, pp. 625–636.

Weigl, H. J., 1997, "Active Stabilization of Rotating Stall and Surge in a Transonic Single Stage Axial Compressor," Ph.D. thesis, Department of Aeronautics and Astronautics, MIT.

Z. S. Spakovszky
Gas Turbine Laboratory,
Department of Aeronautics and Astronautics,
Massachusetts Institute of Technology,
Cambridge, MA 02139

C. M. van Schalkwyk
Scientific Systems Co., Inc.,
Woburn, MA 01801

H. J. Weigl

J. D. Paduano

Gas Turbine Laboratory,
Department of Aeronautics and Astronautics,
Massachusetts Institute of Technology,
Cambridge, MA 02139

K. L. Suder

M. M. Bright

NASA Lewis Research Center,
Cleveland, OH 44135

Rotating Stall Control in a High-Speed Stage With Inlet Distortion: Part II—Circumferential Distortion

This paper presents the first attempt to stabilize rotating stall in a single-stage transonic axial flow compressor with inlet distortion using active feedback control. The experiments were conducted at the NASA Lewis Research Center on a single-stage transonic core compressor inlet stage. An array of 12 jet injectors located upstream of the compressor was used for forced response testing and feedback stabilization. Results for a circumferential total pressure distortion of about one dynamic head and a 120 deg extent (DC(60) = 0.61) are reported in this paper. Part I (Spakovszky et al., 1999) reports results for radial distortion. Control laws were designed using empirical transfer function estimates determined from forced response results. Distortion introduces coupling between the harmonics of circumferential pressure perturbations, requiring multivariable identification and control design techniques. The compressor response displayed a strong first spatial harmonic, dominated by the well-known incompressible Moore–Greitzer mode. Steady axisymmetric injection of 4 percent of the compressor mass flow resulted in a 6.2 percent reduction of stalling mass flow. Constant gain feedback, using unsteady asymmetric injection, yielded a further range extension of 9 percent. A more sophisticated robust H_∞ controller allowed a reduction in stalling mass flow of 10.2 percent relative to steady injection, yielding a total reduction in stalling mass flow of 16.4 percent.

1 Introduction

For a better understanding of the coupled compressor dynamics, a short overview of *undistorted* flow compressor modeling is given. The classic Moore–Greitzer (1986) formulation considers an incompressible two-dimensional flow field with an axisymmetric, spatially uniform (undistorted) inlet flow, and a linearized approach for the perturbations. The rotating stall dynamics for the nth mode are described by

$$\left(\frac{2}{|n|}+\mu\right)\frac{\partial\delta\phi}{\partial\tau}=\left(\frac{\partial\Psi^{ts}}{\partial\phi}-jn\lambda\right)\delta\phi, \tag{1}$$

where Ψ^{ts} is the total-to-static pressure rise coefficient of the entire compressor and ϕ and $\delta\phi$ are the compressor face flow coefficient and its perturbation, respectively. The inertia parameters are the fluidic inertia in the rotors λ, in the rotors plus stators μ, and in the inlet and exit ducts $2/|n|$, where

$$\lambda=\sum_{\text{rotors}}\frac{c_x/\bar{r}}{\cos^2\xi},\ \mu=\lambda+\sum_{\text{stators}}\frac{c_x/\bar{r}}{\cos^2\xi}. \tag{2}$$

c_x, $\bar{r}$, and ξ are the axial chord, mean radius, and stagger angle, respectively. Solving Eq. (1) with

$$\delta\phi(\theta,t)=\sum_{n=-\infty}^{\infty}\delta\tilde{\phi}_n(t)e^{jn\theta} \tag{3}$$

yields

$$\delta\phi(\theta,t)=\sum_{n=-\infty}^{\infty}a_n e^{(\sigma_n-jn\omega_n)t}e^{jn\theta}, \tag{4}$$

where θ and t are the angle around the annulus and the time, respectively. The growth rate σ_n and rotation rate ω_n are given by

$$\sigma_n=\frac{\partial\Psi^{ts}/\partial\phi}{(2/|n|+\mu)},\ \omega_n=\frac{\lambda}{(2/|n|+\mu)}. \tag{5}$$

This solution describes spatial waves of sinusoidal shape (harmonics) that travel around the annulus at rotation rate ω_n, and grow or decay in time with growth rate σ_n. Compressor stability is determined by the growth rate of these modes. In this model, the axial velocity perturbations $\delta\phi(\theta)$ are axially uniform throughout the compressor. Furthermore, the flow field for the nth mode consists only of the nth spatial harmonic. That is, the harmonics are all *decoupled* (independent of one another).

In the presence of circumferentially nonuniform inlet flow, the pressure rise Ψ^{ts}, and therefore the slope $\partial\Psi^{ts}/\partial\phi$, is no longer a constant but a strong function of θ. This nonlinear coupling between the steady inlet flow field and the compressor map strongly influences the linearized behavior of the flow field perturbations. The mode shapes are no longer purely sinusoidal but have contributions of other harmonics. In other words, distortion introduces *coupling* between the harmonics. Hynes and Greitzer (1987) have extended the Moore–Greitzer model to describe incompressible dynamics with inlet distortion. The accuracy of this model has been verified experimentally by Van Schalkwyk et al. (1998) on a low-speed three-stage compressor.

If an analysis accounting for compressibility is done, acoustic modes with axial structure are introduced. In this case, each compression system mode has both circumferential and axial structure. Modeling of this kind was conducted by Bonnaure (1991), Hendricks et al. (1993), and Feulner et al. (1994). To date,

Contributed by the International Gas Turbine Institute and presented at the 43rd International Gas Turbine and Aeroengine Congress and Exhibition, Stockholm, Sweden, June 2–5, 1998. Manuscript received by the International Gas Turbine Institute February 1998. Paper No. 98-GT-265. Associate Technical Editor: R. E. Kielb.

no control-theoretic compressible model exists that accounts for inlet distortion. Thus it is one of the goals of this paper to investigate the effects of inlet distortion on high-speed compressor prestall behavior.

The other goals of this paper are identification and stabilization of the compression system with inlet distortion. Our framework will be, as in Part I (Spakovszky et al., 1999), a multivariable input–output characterization where measurements and actuation are expressed as complex spatial Fourier coefficients (Paduano et al., 1993). This framework is consistent with the stability analysis of Hynes and Greitzer (1987), except their analysis was homogeneous instead of forced, and a nonlinear steady-state condition was found numerically (ours is achieved experimentally). The frequency domain input–output map, or transfer function matrix, for the first three harmonics is written:

$$\begin{bmatrix} \tilde{y}_0(s) \\ \tilde{y}_1(s) \\ \tilde{y}_2(s) \end{bmatrix} = \begin{bmatrix} G_{00}(s) & G_{01}(s) & G_{02}(s) \\ G_{10}(s) & G_{11}(s) & G_{12}(s) \\ G_{20}(s) & G_{21}(s) & G_{22}(s) \end{bmatrix} \begin{bmatrix} \tilde{u}_0(s) \\ \tilde{u}_1(s) \\ \tilde{u}_2(s) \end{bmatrix}, \quad (6)$$

or, in compact form,

$$\tilde{\mathbf{y}}(s) = \mathbf{G}(s)\tilde{\mathbf{u}}(s), \quad (7)$$

where the output vector $\tilde{\mathbf{y}}$ is a vector containing the system's primary outputs: the complex spatial Fourier coefficients (SFCs) of the pressure perturbations (analogous to Eq. (3)). The input vector $\tilde{\mathbf{u}}$ contains the corresponding SFCs of the injection profile, which is the system input.

Coupling between harmonics due to circumferential distortion is indicated by nonzero off-diagonal elements of $\mathbf{G}(s)$ ($G_{ij}(s) \neq 0$ for all $i \neq j$). The strength of this coupling can be determined by the magnitudes of the off-diagonal transfer functions. The consequence of this coupling is that the individual transfer functions of $\mathbf{G}$ cannot be treated independently; thus controller design becomes a multi-input–multi-output (MIMO) problem. This increases the complexity of the controller and complicates system identification. After describing the steady-state conditions, we will use these concepts to interpret the identification and control results.

2 Experimental Setup

The experiments described in this paper were all conducted at the NASA Lewis Research Center in the single-stage axial compressor test facility. A detailed description of the NASA Stage 35 test compressor and the actuation and instrumentation is given in Part I (Spakovszky et al., 1999), as well as other documents, Reid and Moore (1978), Berndt et al. (1995), Weigl et al. (1998), and will not be repeated here. For our purposes it suffices to say that a set of twelve evenly spaced injectors, blowing high-pressure air in the tip region of the rotor, provide the actuation, and a set of eight static pressure transducers located immediately upstream of the rotor provide sensing. Both the actuation and sensing signals are decomposed into spatial Fourier coefficients, and treated as such in the remainder of the paper.

3 Circumferential Inlet Distortion

An early effort using steady blowing and bleeding devices to determine whether tip boundary layer control was an effective means of increasing the unstalled weight flow range of a transonic single-stage compressor with and without inlet flow distortion was conducted by Koch (1970). The experiments revealed that the blowing device was more effective than the bleed device and that the unstalled range could be improved. Circumferential inlet airflow distortion that is caused by phenomena such as flow separation or nonaxisymmetric intake duct geometry has been studied by installing a circumferential distortion screen: A fine mesh was mounted in the inlet duct, located approximately 2.2 mean radii upstream of the rotor (as in Part I). The screen can be indexed through 350 deg around the annulus to allow more detailed mapping of steady-state compressor performance. The extent of the screen was 120 deg and covered the full blade span.

3.1 Steady-State Experiments. Circumferential total and static pressure and total temperature profiles were measured with probes positioned between the distortion screen and the rotor. In addition, four circumferentially distributed wall static pressure taps at the hub and casing, and a total pressure and total temperature rake provided data on the flow field downstream of the compressor. The steady pressure and temperature probes were geometrically fixed and the screen was rotated in five degree increments to obtain the profiles. Figure 1 shows the total and static pressure profiles at the inlet, approximately 1.1 mean radii upstream of the rotor inlet, and the static pressure profile at the compressor exit. The mean exit static pressure has been subtracted from all these curves to show the relative offset of the pressure profiles. The distortion screen blocked the flow between 120 and 240 deg circumferentially; these angles are marked with the dotted vertical lines in the figure. The total pressure drop generated by the distortion screen was about one dynamic head, that is

$$\frac{\Delta p_t}{\frac{1}{2}\bar{\rho}\bar{v}_x^2} \approx 1. \quad (8)$$

The distortion magnitude can also be described by a parameter commonly used in engine intake aerodynamics called the DC(60) descriptor (Williams, 1991). The DC(60) descriptor is defined by

$$\mathrm{DC}(60) = \frac{\bar{p}_t|_{360°} - \bar{p}_t|_{\text{worst } 60°}}{\frac{1}{2}\rho\bar{v}_x^2}. \quad (9)$$

In the ideal case where the static pressure is uniform, DC(60) = 1 corresponds to zero-velocity flow within the 60 deg sector, giving very poor inlet aerodynamics. The distortion screen designed for Stage 35 with 1 dynamic head distortion magnitude corresponds to DC(60) = 0.61, representing poor inlet conditions, as shown in the velocity profile in Fig. 2.

The inlet static pressure shown in Fig. 1 is approximately uniform around the annulus, while the exit static pressure is circumferentially nonuniform with an increased pressure rise in the range 120 deg $\leq \theta \leq$ 240 deg. This contradicts the basic Hynes–Greitzer (1987) theory, which assumes that the flow angle from the stator vanes is uniform and that the downstream duct has constant area. In a two-dimensional (incompressible) flow field these assumptions imply uniform exit static pressure and nonuniform inlet static pressure. This discrepancy between the theory and measurements can be explained by considering the compressor *plus* down-

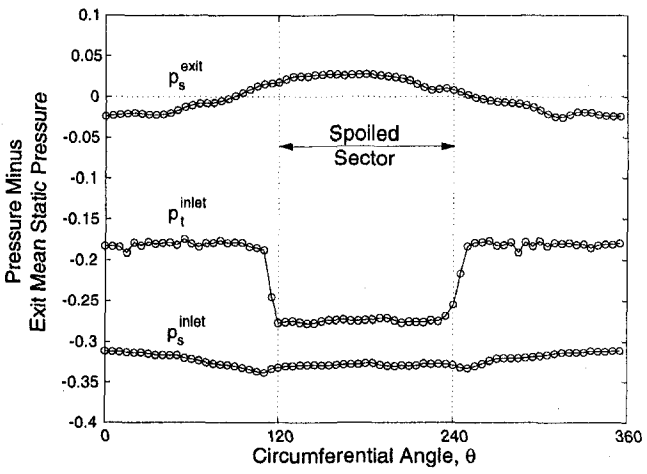

Fig. 1 Total and static pressure at the compressor inlet and static pressure at the compressor exit for one dynamic head distortion at $\dot{m}_{corr}$ = 16.5 kg/s without blowing

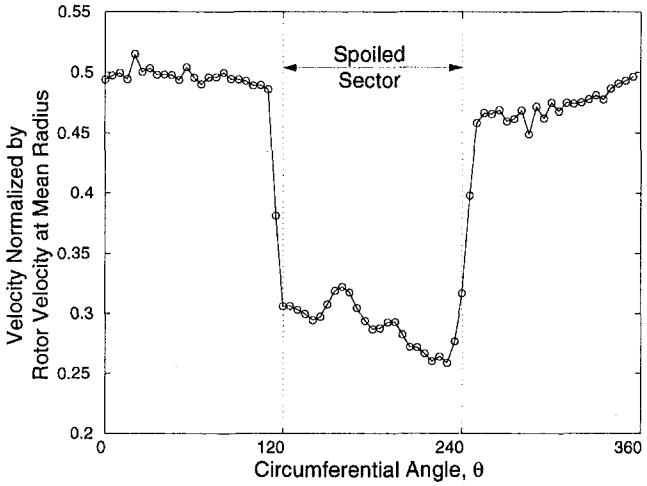

Fig. 2 Measured velocity profile for one dynamic head distortion at $\dot{m}_{corr}$ = 16.5 kg/s without blowing

stream diffuser, and using a parallel compressor type argument as follows (see Longley and Greitzer, 1992): In the spoiled sector the diffuser is operating with low inlet total pressure and thus low velocity, producing a lower pressure rise than the diffuser in the unspoiled sector. Since the static pressure at the diffuser exit must be uniform, the static pressure at the compressor exit must be higher in the spoiled sector than in the unspoiled sector.

Speed lines were measured for undistorted inlet flow as well as with circumferential inlet distortion. The effect of steady blowing (steady valve opening of 50 percent, injected corrected mass flow of 0.65 kg/s) on the pressure ratio was then measured. The speed lines are constructed as described in Part I: Total corrected mass flow is the sum of an upstream orifice mass flow and the injected mass flow, the upstream total pressure is the mass average of total pressure probes between the distortion screen and the actuators, and the downstream pressure is from mass-averaged hub and casing static pressure measurements. In Fig. 3 we see that the circumferential distortion resulted in a peak pressure ratio drop. However, with steady blowing, the peak pressure ratio can be recovered and even a considerable range extension of 6.2 percent in stalling mass flow can be obtained. Although the pressure ratio of the compressor is recovered by blowing, there is no change in the inlet distortion, because the distortion screen is upstream of the compressor, and there is considerable nonuniformity in the compressor face flow field, as evidenced by the system identification results in the next section.

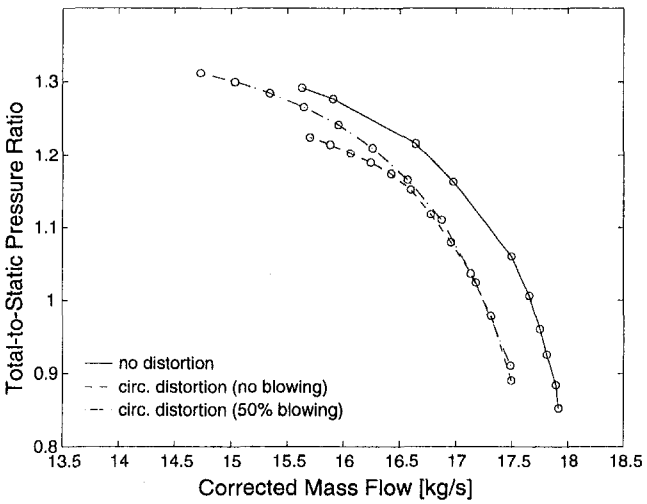

Fig. 3 Speed lines for undistorted inlet (solid), circumferential distortion no blowing (dash), and with 50 percent steady blowing (dash–dot)

4 Open Loop Compressor Dynamics

Having characterized the steady-state behavior, we turn to the dynamic behavior near stall. Using sinusoidal frequency sweeps on each spatial harmonic, we quantify the dominant eigenmodes of the system, their circumferential structure, and the degree of coupling between harmonics that exists in the input–output dynamics. The latter is important for control law design; it is also of interest to determine the degree of coupling between harmonics in *compressible* prestall modes.

Using standard frequency sweep methods (see Ljung, 1987), we measured the transfer function matrix (Eq. (6)). The off-diagonal elements, $G_{ij}(j\omega)$ for $i \neq j$, were found to have magnitudes of about 0.1 to 1.0 times the diagonal elements, indicating strong coupling between some harmonics. A subset of the transfer functions is shown in Fig. 4. The magnitudes of the off-diagonal transfer functions $G_{01}(j\omega)$ and $G_{10}(j\omega)$ are of the same order as the diagonal transfer functions $G_{00}(j\omega)$ and $G_{11}(j\omega)$. To find the eigenvalues, and for control law design, state-space models were identified based on the measured transfer functions using an MIT-developed method called FORSE (Jacques, 1994). The transfer functions of the identified state space model are plotted as dashed lines in Fig. 4.

The peaks in the transfer functions indicate that there are several lightly damped modes in the pressure perturbations. Due to compressibility, several modes with similar circumferential structure can exist, each having different axial structure. Therefore we denote the modes by $[n, m]$, where n is inferred from the circumferential harmonic that is largest in the mode, and m indicates the postulated axial mode number (higher values of m indicate higher frequency, usually associated with more axial mode structure, as in acoustics).[1]

Mode number assignment requires careful data reduction and analysis. First, to visualize the spatial structure of the modes, we reconstruct the mode shapes using the eigenstructure of the identified state-space model (Spakovszky, 1998). Figure 5 shows some of the reconstructed mode shapes, including the harmonic content in each. For these experiments the distortion screen ranged from 180 to 300 deg; this is marked with ×'s in Fig. 5. Next, we assign the number n based on the harmonic that contributes most to the mode shape. The first two modes in Fig. 5 have strong zeroth harmonics, indicating that overall compression system parameters (such as duct lengths and plenum size) will have a strong influence on their stability. The second two modes have strong first harmonics, and we will see that stabilization of these modes can be achieved by controlling the first harmonic of the flow perturbations. Finally, the "acoustic" mode number m is assigned by looking at various factors. Higher frequencies are considered to be more acoustically coupled, and are given larger values of m. We note that the mode shape, and therefore the harmonic contents of each mode, is a function of time. Figure 5 thus portrays the modes at several specific instants in time. Eigenvalues obtained without distortion (Weigl et al., 1997) (also see Weigl, 1997) are compared to those found here, to judge how distortion has altered their frequency, stability, and harmonic content; this also helps to assign the mode numbers. In addition, low-speed modeling (Van Schalkwyk, 1996) is employed to help associate mode numbers with the peaks when strong coupling is present. The results are summarized in Fig. 6, which shows the identified poles and assigned mode numbers.

Several statements can be made based on Fig. 5. First, note that mode [1, 0] has a minimum at approximately 250 deg, which is about in the middle of the distorted region. This behavior is

[1] The mode names used here are primarily for conveying the physical effects involved, and do not affect controller design at all; controllers are based only upon the input–output model.

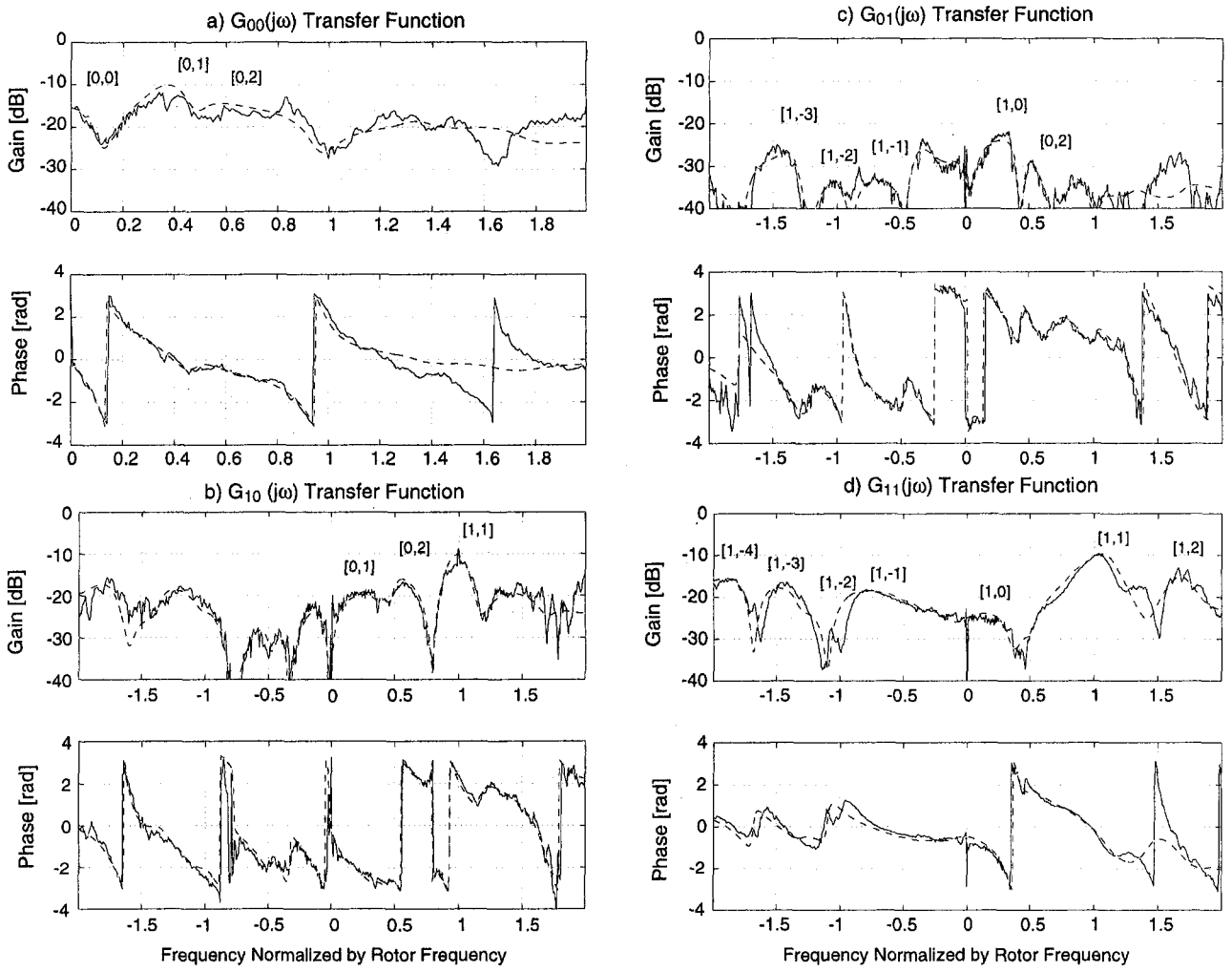

Fig. 4 MIMO transfer functions $G_{00}(j\omega)$, $G_{01}(j\omega)$, $G_{10}(j\omega)$, and $G_{11}(j\omega)$, with circumferential inlet distortion at $\dot{m}_{corr}$ = 16.0 kg/s and 85 percent corrected design speed. — = measured, – – = identified model.

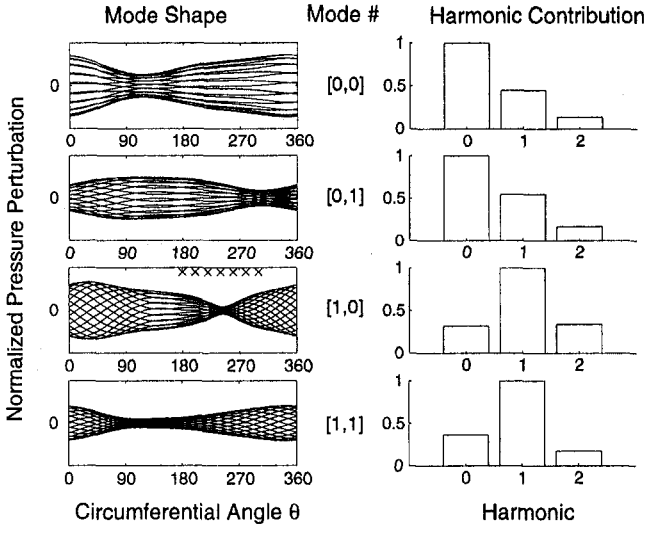

Fig. 5 Left: mode shapes for the four primary modes of the identified dynamics, plotted in several positions as the eigenmode travels around the annulus. Right: amplitude of the harmonic contribution to each mode, indicating which harmonic dominates and the degree of coupling between harmonics. Vertical scales are arbitrary, since only the mode shape is shown.

predicted by the low-speed model and has been observed in a low-speed compressor by Van Schalkwyk et al. (1998). Furthermore, the Fourier decompositions of the mode shapes, shown in the right-hand graphs of Fig. 5, indicate that several harmonics are

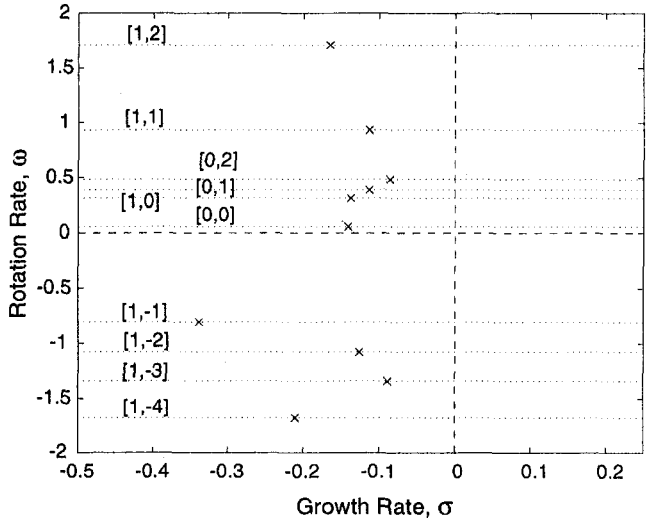

Fig. 6 Identified poles of the multivariable transfer function system at $\dot{m}_{corr}$ = 16.0 kg/s

present in each mode; this is also predicted by incompressible theory. The compressible modes [0, 1] and [1, 1], on the other hand, represent an effect that has not yet been modeled: It appears that these higher frequency, compressible dynamics are also coupled, to an extent very similar to the incompressible dynamics, by inlet distortion. Finally, we note that the richness of the dynamics displayed in Figs. 4 and 5 makes the control problem more complex, but this complexity is mitigated by the fact that some of the high-frequency modes are relatively well damped, and do not tend to go unstable as mass flow is reduced.

To study the relative stability and sensitivity to mass flow of the various compressor modes, we conducted system identification at various mass flows. By comparing all of the transfer functions at all the tested mass flows, it was found that the [1, 0] mode is primarily responsible for system stability. To summarize our conclusion, Fig. 7 shows the magnitude and phase of G_{11} measured at four different mass flows. The [1, 0] mode is particularly visible in this transfer function. Only the positive frequency (forward traveling wave) portion of the transfer functions are shown. As the mass flow is decreased, the magnitude of the peak at $0.4\omega_r$ increases, indicating a lightly damped mode. At the lowest mass flow tested this mode is actually unstable. This can be determined by looking at the corresponding phase plot: For $\dot{m} = 14.0$ kg/s (solid line), the phase increases in the range $0.3 \leq \omega_r \leq 0.6$, indicating that the pole associated with this mode is unstable. For $\dot{m} = 15.0$ kg/s (dash–dot) and 14.7 kg/s (dash) the respective phases decrease in the same frequency range, indicating that at these mass flows the mode is stable. Note that for $\dot{m} = 16.0$ kg/s (dotted) the phase also increases in this frequency range. However, at this high mass flow the mode is stable. The increase in the phase is a result of a zero at $0.35\omega_r$, which is clearly visible as a deep valley in the magnitude of the transfer function.

Note that the compressible modes in Fig. 7 (labeled [1, 1] and [1, 2]) do not change significantly with mass flow. These eigenmodes cause peaks in the transfer function, which change only slightly as the mass flow is decreased, indicating that their degree of stability is not greatly affected by the decrease in mass flow. Similar conclusions were drawn about other prestall modes by looking at the relevant transfer functions and studying eigenvalue migration with mass flow.

Throttle ramps into stall revealed that indeed the [1, 0] mode resonates strongly as the stall point is approached. This mode can be related to the incompressible Moore–Greitzer mode, and has also been observed with radial distortion in Part I (Spakovszky et al., 1999). The spectrogram of the first harmonic of the pressure perturbations during a stall event is plotted in Fig. 8. We note that,

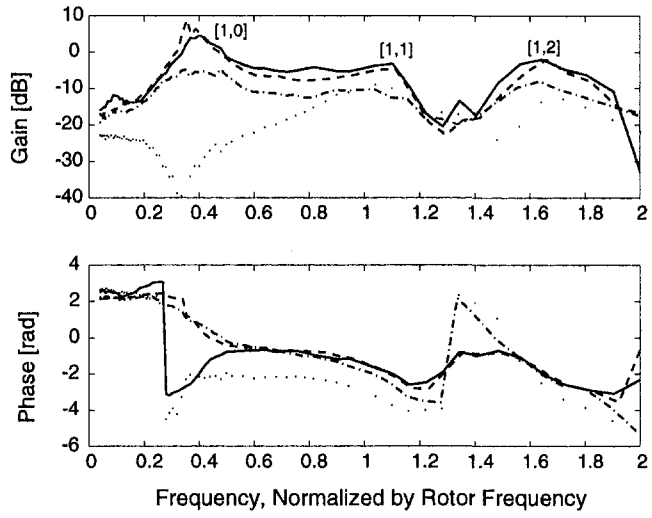

Fig. 7 Measured $G_{11}(j\omega)$ at 16.0 kg/s (dotted), 15.0 kg/s (dash–dot), 14.7 kg/s (dash), and 14.0 kg/s (solid) total corrected mass flow

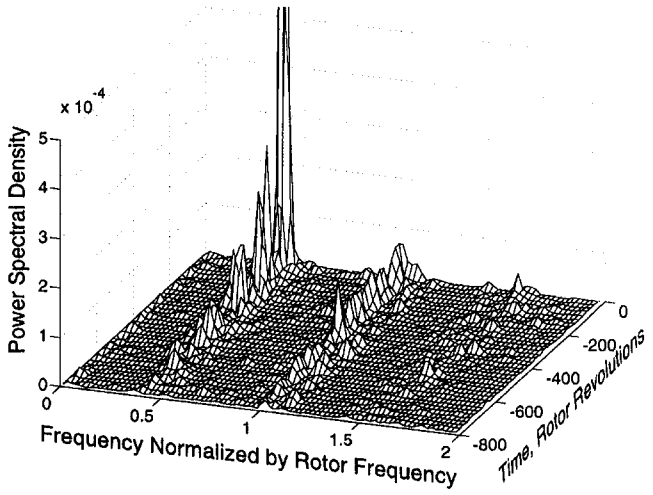

Fig. 8 Spectrogram of the first harmonic perturbations during an open-loop stall ramp

even right up to stall, there is relatively little activity at $1\omega_r$ and $1.6\omega_r$. This indicates the [1, 1] and [1, 2] compressible modes are well damped and that it is the [1, 0] mode that loses stability.

In summary, in the presence of circumferential distortion, the stability of the compression system is determined by the [1, 0] mode. This behavior is analogous to that observed in low-speed compressors. The additional compressible modes were also observed with radial distortion by Spakovszky et al. (1999). Unlike radial distortion, there is strong *coupling* between the harmonics, that is, each mode contains several harmonics. This coupling is considered during design and testing of controllers to stabilize the compression system, discussed in the next section.

5 Active Control Results

In this section we discuss active control of rotating stall in a high-speed single-stage compression system with circumferential distortion. Two different controllers were tested: a constant gain controller, and a dynamic, model based controller. The two controllers are discussed in the following sections.

5.1 Constant Gain Control. Constant gain control has been used successfully by several researchers to stabilize rotating stall in low-speed compressors. Paduano et al. (1993) developed the experimental design procedure on a single-stage compressor, and Haynes et al. (1994) applied it to a three-stage compressor. The same approach was used by Van Schalkwyk et al. (1998) to stabilize a three-stage compressor with circumferential distortion of the inlet total pressure. However, Weigl et al. (1998) showed that constant gain controllers are not effective in high-speed compressors with uniform inlet flow. A similar result was obtained in Part I (Spakovszky et al., 1999) with radial distortion. However, as we will see momentarily, constant gain control was very effective on this machine in the presence of circumferential distortion.

The idea behind constant gain control is as follows. The circumferential pressure perturbation $\delta p(\theta)$ is measured and decomposed in a Fourier series analogous to Eq. (3). The nth harmonic is then spatially rotated by an experimentally optimized angle β_n, multiplied by a constant gain k_n to form the nth harmonic of the control signal. For example, for a sensed first harmonic perturbation $\tilde{y}_1 = \delta\tilde{p}_1$ the constant gain control law is

$$\tilde{u}_1 = -k_1 e^{j\beta_1}\delta\tilde{p}_1 \tag{10}$$

where $\tilde{u}_1$ is the corresponding first harmonic SFC of the injection wave. Finally, the individual actuator commands are reconstructed based on the Fourier coefficients.

A first harmonic constant gain control law was found to be

effective at stabilizing the circumferential distortion case investigated here. When the gain and phase were set to $k_1 = 1$ and $\beta_1 = \pi$, respectively, the stalling mass flow was reduced by 6.8 percent relative to steady blowing. The total-to-static speed lines are plotted in Fig. 9 for undistorted inlet flow (solid), circumferential distortion without blowing (dash), and with 50 percent steady blowing (dash–dot). The stall point with the first harmonic constant gain control law is marked with a + in this figure.

Spectrograms of the first and second harmonics of the pressure perturbations, immediately prior to the control-on stall point, are shown in Figs. 10 and 11, respectively. The [1, 0] mode appears to be relatively well damped during the first 1000 revolutions in Fig. 10, while the [1, 1] mode and the [2, 0] mode (Fig. 11) are resonating strongly during the entire prestall period. Other evidence indicates that the [2, 0] mode goes unstable first, and in fact adding a second harmonic constant gain feedback with $k_2 = 1$ and $\beta_2 = \pi$ damped out the second harmonic mode and achieved a further range extension of 2.2 percent in stalling mass flow relative to the first harmonic constant gain control case. The measured mass flow and pressure ratio is marked with a * in Fig. 9. A zeroth harmonic feedback, with gain $k_0 = 1$, is also in operation during this run.

These results clearly show that constant gain control is effective in the presence of circumferential distortion. Since a compressible, distorted flow, control theoretic model does not exist, it is difficult to explain these phenomena. The system identification experiments indicate that a single mode with dominant first harmonic and incompressible features determines the stability, suggesting the applicability of a constant gain control strategy. This was also qualitatively and quantitatively verified using incompressible modeling methods (Van Schalkwyk, 1996). However, the measurements in Fig. 4 show that there are *compressible* modes that have significant magnitudes in the coupled (off-diagonal) transfer functions (e.g., the [1, 1] mode has the same magnitude in $G_{11}(j\omega)$ as in $G_{10}(j\omega)$). Such coupling is typically detrimental to any control law that does not explicitly take it into account. Even without this coupling, the [1, 1] mode in this compressor has invariably been destabilized by constant gain control without circumferential distortion (Weigl et al., 1998; Spakovszky et al., 1999). Apparently the effect of distortion in this machine is such that the constant gain control law, tuned for mode [1, 0] stabilization, does not destabilize the other lightly damped modes. It is not clear whether this fortuitous effect will exist in other compressors with inlet distortion.

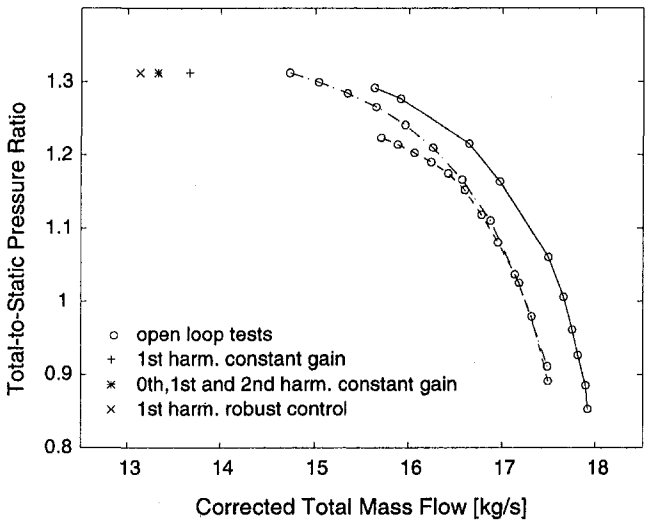

Fig. 9 Speed lines for undistorted inlet flow (solid), circumferential distortion without blowing (dash), and with 50 percent steady blowing (dash–dot). Stall points with control are: first harmonic constant gain control (+), zeroth–first–second harmonic constant gain control (*), and first harmonic H_∞ control (×).

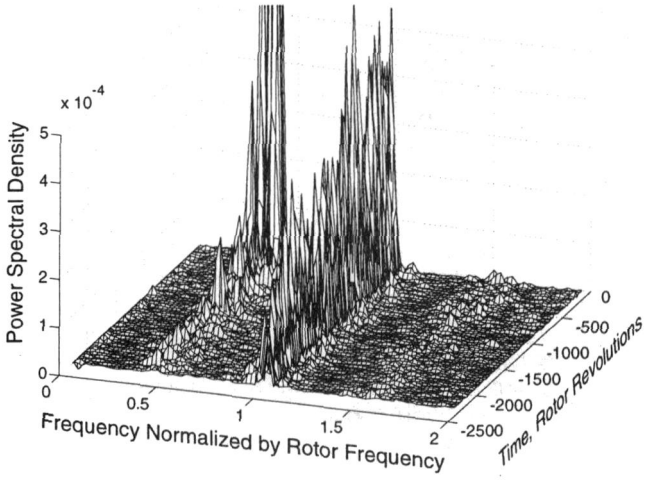

Fig. 10 Spectrogram of the first harmonic pressure perturbations with first harmonic constant gain control

5.2 Robust H_∞ Control. In this section the performance improvement obtained using robust H_∞ control is investigated. As in Part I (Spakovszky et al., 1999), the lack of a theoretical model requires the use of an identified model for the design of these model-based dynamic control laws. This is particularly difficult when circumferential distortion is present, because the compressor becomes a MIMO dynamic system in which one common set of eigenmodes describes the coupled compressor dynamics; in other words, one cannot treat one harmonic at a time. This complicates system identification and significantly increases the order of the controller. Because of this added complexity, initial tests of a MIMO H_∞ controller did not show an improvement in stalling mass flow over constant gain control (Spakovszky, 1998). Although further iteration and improvement of the MIMO controller design should be possible, time did not permit this approach to be pursued. Therefore an alternative method, described below, was investigated.

The dominance of the first harmonic in the [1, 0] mode and the presence of a resonance in the [1, 1] mode in Fig. 10 suggests that a robust controller that ignores coupling, and is designed for the first harmonic only, might yield improvement in performance. Fortunately, such a controller already existed at the time of these tests, because the frequencies associated with the [1, 0] mode for both circumferential and radial distortion are approximately the

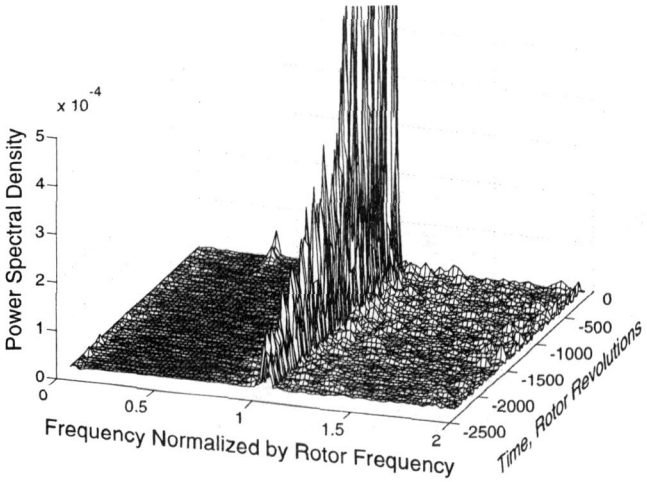

Fig. 11 Spectrogram of the second harmonic pressure perturbations with first harmonic constant gain control

same ($0.4\omega_r$). In fact, the eigenvalue location of the unstable [1, 0] mode used for design of the radial distortion controller was almost identical to the identified eigenvalue location for this mode with distortion. Figure 12 shows the identified eigenvalues with circumferential distortion, together with circles indicating the range of eigenvalues which the first harmonic H_∞ radial distortion controller from Part I (Spakovszky et al., 1998) was designed to stabilize. The [1, 0] mode perturbation circle includes the unstable pole associated with circumferential distortion, indicating that the controller should be able to stabilize this mode. Although the [1, 1] mode with circumferential distortion is more lightly damped than in the design model, the frequency is accurately captured by the design model. This proves to be sufficient for success of the controller, indicating that this pole remains stable for the mass flows of interest.

Based on these arguments, the controller originally designed for radial distortion was tested experimentally and showed a large range extension. The stalling mass flow was reduced by 10.2 percent relative to steady blowing, resulting in a total reduction in stalling mass flow of 16.4 percent. This is indicated in Fig. 9. Of all the methods tested, this first harmonic robust control law achieved the largest reduction in stalling mass flow, which is comparable to the reduction in stalling mass flow with radial inlet distortion shown in Part I (Spakovszky et al., 1999).

6 Concluding Remarks and Summary

This paper presents the first experimental investigation of coupled compressible stall dynamics and it is the first time that a transonic compressor with circumferential inlet distortion was actively stabilized. The distortion magnitude was about one dynamic head, corresponding to DC(60) = 0.61.

Forced response experiments revealed strong coupling between the harmonics of the pressure perturbations. Analysis showed that a single mode of the compression system determines its stability; this behavior is similar to that of low-speed compressors. Constant gain control achieved a large range extension. The dominance of an incompressible mode, together with fortuitous coupling between the harmonics, appears to change the stall dynamics in such a way that (unlike the undistorted flow case) constant gain feedback does not destabilize lightly damped compressible modes. Thus, although the details of the measured dynamics are strongly affected by compressibility, the control strategy applied here was the same as that used in low-speed compressors. The maximum reduction in stalling mass flow with zeroth, first, and second harmonic constant gain controllers was 9.0 percent relative to steady blowing, giving a total reduction in stalling mass flow of 15.2 percent.

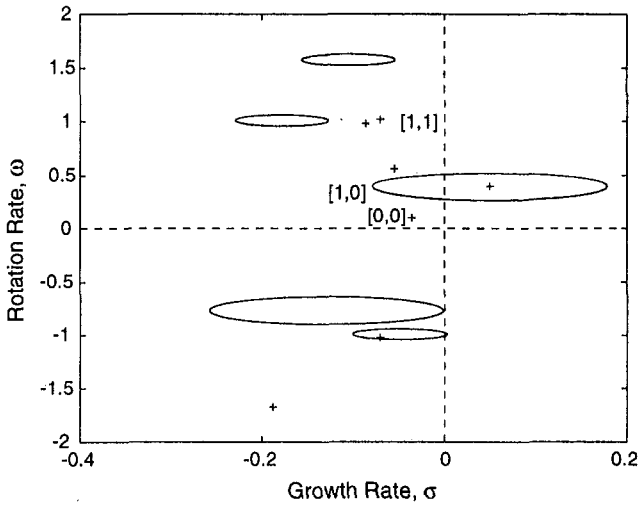

Fig. 12 Identified coupled unstable dynamics at $\dot{m}_{corr}$ = 14.0 kg/s and perturbation circles of H_∞ control law designed for radial distortion

In general, a MIMO control law is indicated when coupled multivariable dynamics are present. In this experiment, however, the dominance of the first harmonic in the destabilizing mode suggested that a SISO H_∞ controller for the first harmonic might work well. This in fact proved to be the case: A controller originally designed for radial distortion achieved a total reduction in stalling mass flow of 16.4 percent, thus demonstrating robustness with respect to a change in inlet flow from radial to circumferential distortion. Time did not permit comparing this performance to a MIMO controller.

These results, together with the results of Part I (Spakovszky et al., 1998), show that active control of rotating stall in a high-speed compressor results in a significant increase in the stable operating range of a compressor operating in the presence of inlet distortion. These results are very promising for future work and applications. Much work remains to be done, however. In particular, the dependence of the dynamics on nonlinear coupling between the compressor and a (typically unknown) inlet distortion add a degree of uncertainty, which is addressed in our approach only to the extent that our control law is robust to modeling errors. More explicitly designing for, and subsequently testing against, unknown distortion scenarios are needed. It is also necessary to investigate and better understand the interplay between distortion and lightly damped compressible dynamics. This interplay was beneficial in these experiments, but may not always be so. Finally, one would like to use as few actuators and as little mass flow as possible to achieve results like those presented here, and do so in a multistage high-speed environment.

Acknowledgments

This project was conducted under collaboration between the NASA Lewis Research Center, Scientific Systems Co., Inc., and MIT. The authors would like to thank T. Strazisar and J. Chi for their very useful input, as well as D. Williams, R. Brokopp, and B. Piendl for their help during compressor testing. Special thanks also to M. Carroll and D. Park for preparing this manuscript. This work was conducted under NASA funding NAG3-1457 and NAS3-97100.

References

Berndt, R., Weigl, H., Paduano, J., and Epstein, A., 1995, "Experimental Techniques for Actuation, Sensing, and Measurement of Rotating Stall Dynamics in High Speed Engines," in: J. D. Paduano, ed., *Sensing, Actuation, and Control in Aeropropulsion,* Vol. 2492, SPIE.

Bonnaure, L., 1991, "Modelling High Speed Multistage Compressor Stability," Master's thesis, Department of Aeronautics and Astronautics, MIT.

Feulner, M., Hendricks, G., and Paduano, J., 1994, "Modeling for Control of Rotating Stall in High Speed Multi-Stage Axial Compressors," ASME Paper No. 94-GT-292.

Haynes, J., Hendricks, G., and Epstein, A., 1994, "Active Stabilization of Rotating Stall in a Three-Stage Axial Compressor," ASME JOURNAL OF TURBOMACHINERY, Vol. 116, pp. 226–239.

Hendricks, G., Bonnaure, L., Longley, J., Greitzer, E., and Epstein, A., 1993, "Analysis of Rotating Stall Onset in High Speed Axial Flow Compressors," Paper No. AIAA-93-2233.

Hynes, T., and Greitzer, E., 1987, "A Method for Assessing Effects of Circumferential Flow Distortion on Compressor Stability," ASME JOURNAL OF TURBOMACHINERY, Vol. 109, pp. 371–379.

Jacques, R., 1994, "On-Line System Identification and Control Design for Flexible Structures," Ph.D. thesis, Department of Aeronautics and Astronautics, MIT.

Koch, C. C., 1970, "Experimental Evaluation of Outer Case Blowing or Bleeding of a Single-Stage Axial Flow Compressor," Tech. Rep. CR-54592, NASA.

Ljung, L., 1987, *System Identification: Theory for the User,* Prentice-Hall, Inc.

Longley, J., and Greitzer, E., 1992, "Inlet Distortion Effects in Aircraft Propulsion System Integration," *Steady and Transient Performance Prediction of Gas Turbine Engines,* AGARD-LS-183, pp. 6-1–6-18.

Moore, F., and Greitzer, E., 1986, "A Theory of Post-Stall Transients in Axial Compressors: Part I—Development of the Equations," ASME *Journal of Engineering for Gas Turbines and Power,* Vol. 108, pp. 68–76.

Paduano, J., Epstein, A., Valavani, L., Longley, J., Greitzer, E., and Guenette, G., 1993, "Active Control of Rotating Stall in a Low-Speed Axial Compressors," ASME JOURNAL OF TURBOMACHINERY, Vol. 115, pp. 48–56.

Reid, L., and Moore, D., 1978, "Performance of Single-Stage Axial-Flow Transonic Compressor With Rotor and Stator Aspect Ratios of 1.19 and 1.26, Respectively, and With Design Pressure Ratio 1.82," Tech. Rep. TP-1338, NASA.

Spakovszky, Z., 1999, "Active Control of Rotating Stall in a Transonic Compressor

Stage With Inlet Distortion," Master's thesis, Department of Aeronautics and Astronautics, MIT.

Spakovszky, Z., Weigl, H., Paduano, J., Van Schalkwyk, C., Suder, K., and Bright, M., 1999, "Rotating Stall Control in a High-Speed Stage With Inlet Distortion, Part I—Radial Distortion," ASME JOURNAL OF TURBOMACHINERY, Vol. 121, this issue, pp. 508–514.

Van Schalkwyk, C., 1996, "Active Control of Rotating Stall With Inlet Distortion," Ph.D. thesis, Department of Aeronautics and Astronautics, MIT; also available as Gas Turbine Lab Report #222.

Van Schalkwyk, C., Paduano, J., Greitzer, E., and Epstein, A., 1998, "Active Stabilization of Axial Compressors With Circumferential Inlet Distortion," ASME JOURNAL OF TURBOMACHINERY, Vol. 120, pp. 431–439.

Weigl, H., Paduano, J., Fréchette, L., Epstein, A., and Greitzer, E., 1998, "Active Stabilization of Rotating Stall and Surge in a Transonic Single Stage Axial Compressor," ASME JOURNAL OF TURBOMACHINERY, Vol. 120, pp. 625–636.

Weigl, H. J., 1997, "Active Stabilization of Rotating Stall and Surge in a Transonic Single Stage Axial Compressor," Ph.D. thesis, Department of Aeronautics and Astronautics, MIT.

Williams, D., 1991, "Engine Compatibility," Tech. rep., Rolls-Royce plc.

External Heat Transfer Predictions in a Highly Loaded Transonic Linear Turbine Guide Vane Cascade Using an Upwind Biased Navier–Stokes Solver

A. Gehrer

H. Jericha

Institute of Thermal Turbomachinery and Machine Dynamics,
Graz University of Technology,
Graz, Austria

External heat transfer predictions are performed for two-dimensional turbine blade cascades. The Reynolds-averaged Navier–Stokes equations with algebraic (Arnone and Pacciani, 1998), one-equation (Spalart and Allmaras, 1994), and two-equation (low-Re k–ϵ, Biswas and Fukuyama, 1994) turbulence closures are solved with a fully implicit time-marching finite volume method. Comparisons with measurements (Arts et al., 1990; Arts, 1994) for a highly loaded transonic turbine nozzle guide vane cascade show good agreement in some cases, but also reveal problems with transition prediction and turbulence modeling. Special attention has been focused on the low-Re k–ϵ model concerning the influence of the inlet boundary condition for the ϵ-equation and problems in the stagnation point region.

Introduction

Numerical prediction methods became an essential tool for the design and analysis of turbomachinery components over the last decade. The continuous increase in turbine inlet pressure and temperature definitely require reliable and accurate predictions of the main stream aero thermal characteristics and of the heat loads imposed to the blades.

A good design from a thermal point of view might allow a higher inlet temperature, less cooling, or a lighter design, thus increasing the performance or efficiency of the machine. A method to predict the heat loads in the design phase of a turbine would be a very valuable engineering tool (e.g., Larsson, 1997).

The interest of the present contribution is specifically directed toward high-pressure turbine wall heat flux predictions for cascade flow; a two-dimensional Navier–Stokes solver, based on an implicit TVD-upwind relaxation scheme (Sanz et al., 1995) has therefore been developed with this objective in mind.

Quite a number of contributions on this topic have been presented in the open literature (e.g., Larson et al., 1995; Larson, 1996, 1997; Lefebvre and Arts, 1997; Migliorini and Michelassi, 1997); listing and comparing them all would definitely be the subject of an interesting review paper.

The originality of the present effort can be found in the application of different turbulence models. The analysis of the results will indicate some guideline about the most suitable choice for turbomachinery flows. The Reynolds-averaged Navier–Stokes equations are solved with an implicit time-marching finite volume method around a two-dimensional blade cascade. The blade is kept at a fixed temperature and the boundary layers are resolved down to the viscous sublayer. The heat transfer is estimated based on the flow in the cells closest to the surface.

Contributed by the International Gas Turbine Institute and presented at the 43rd International Gas Turbine and Aeroengine Congress and Exhibition, Stockholm, Sweden, June 2–5, 1998. Manuscript received by the International Gas Turbine Institute February 1998. Paper No. 98-GT-238. Associate Technical Editor: R. E. Kielb.

Governing Equations

The equations used to model the flow are the compressible, Reynolds-averaged continuity, momentum, and energy equations written in integral form (Eq. (1.1)), where the region of a computational cell is denoted by V and its surface by S:

$$\int_V \frac{\partial \mathbf{Q}}{\partial t}\, dV + \int_S \mathbf{E} dS - \int_S \mathbf{R} dS = 0;$$

$$\mathbf{Q} = [\rho,\ \rho\vec{w},\ e]^T;$$

$$\mathbf{E} = [\rho(\vec{w}\cdot\vec{n}),\ \rho\vec{w}(\vec{w}\cdot\vec{n}) + p\vec{n},\ (e+p)(\vec{w}\cdot\vec{n})]^T;$$

$$\mathbf{R} = [0,\ \vec{\tau}^S,\ \vec{\tau}^S\cdot\vec{w} + \dot{q}^S]^T;\ \tau_i^S = \tau_{ij}\cdot n_j;\ \dot{q}^S = \dot{q}_i\cdot n_i \quad (1.1)$$

Assuming that the fluid is a perfect gas, the pressure p is given by:

$$p = (e - \rho\vec{w}^2/2 - \rho k)(\gamma - 1) \quad (1.2)$$

The shear stresses, τ_{ij}, are divided into a laminar and a turbulent part. The laminar parts, τ_{ij}^{lam}, are given directly by:

$$\tau_{ij}^{\text{lam}} = \mu\left(\frac{\partial u_i}{\partial x_j} + \frac{\partial u_j}{\partial x_i} - \frac{2}{3}\frac{\partial u_k}{\partial x_k}\delta_{ij}\right) \quad (1.3)$$

All turbulence models used in this work rely on Boussinesq's approximation (Boussinesq, 1877) that the principal axes of the turbulent stress tensor are coincident with those of the mean strain-rate tensor (Eq. (1.4)). This assumption makes it possible to close the equations by expressing the turbulent stresses, τ_{ij}^{turb}, with an effective eddy viscosity, μ_t. The eddy viscosity is then calculated using an appropriate turbulence model (see below).

$$\tau_{ij}^{\text{turb}} = -\overline{\rho u_i' u_j'} = \mu_t\left(\frac{\partial u_i}{\partial x_j} + \frac{\partial u_j}{\partial x_i} - \frac{2}{3}\frac{\partial u_k}{\partial x_k}\delta_{ij}\right) - \frac{2}{3}\rho k\delta_{ij} \quad (1.4)$$

Following, e.g., Larsson (1997), the heat flux, q_i, is treated in a similar way according to Reynolds analogy. First the heat flux is divided into a laminar and a turbulent part. The laminar part, q_i^{lam}, is given directly by:

$$\dot{q}_i^{\text{lam}} = \frac{\mu}{\text{Pr}} \frac{\gamma}{\gamma - 1} \frac{\partial (p/\rho)}{\partial x_i} \tag{1.5}$$

To model the turbulent heat flux, q_i^{turb}, a constant turbulent Prandtl number, $\text{Pr}_t = 0.9$, is assumed and Eq. (1.6) then gives an approximation of the heat flux generated by turbulent fluctuations:

$$\dot{q}_i^{\text{turb}} = -c_p \overline{\rho T' u_i'} = \frac{\mu_t}{\text{Pr}_t} \frac{\gamma}{\gamma - 1} \frac{\partial (p/\rho)}{\partial x_i} \tag{1.6}$$

Turbulence Models

Algebraic Turbulence Model. A two-layer algebraic model based on the mixing length concept is used to calculate the eddy viscosity. In the near-wall region the mixing length is computed using the Prandtl–Van Driest formula while in the outer region and in the wake it is kept constant to a fixed fraction of the shear layer thickness δ according to the standard relation (Kwon et al., 1988):

$$L_{m,\text{outer}} = 0.085\ \delta \tag{2.1}$$

In the present work an algebraic criterion, which resembles the features of the Baldwin–Lomax (1978) model, but which implicitly introduces a cut-off criterion for the vorticity field based on the distance from the wall, is used to estimate the boundary layer thickness (Arnone and Pacciani, 1998). If y denotes the distance normal to the wall, the value $y_{\max}$ at which the function

$$G(y) = \frac{1}{y} \int_0^y \bar{y} |\Omega| (1 - e^{-(\bar{y}^+/A^+)}) d\bar{y}$$

$$A^+ = 26,\ y^+ = y \frac{u_\tau \rho_{\text{Wall}}}{\mu_{\text{Wall}}},\ u_\tau = \sqrt{\frac{\tau_{\text{Wall}}}{\rho_{\text{Wall}}}} \tag{2.2}$$

reaches its maximum is assumed as turbulent length scale. The boundary layer thickness is then obtained from the relationship:

$$\delta = 1.145\ y_{\max} \tag{2.3}$$

The effect of transition to turbulence can simulated by setting μ_t equal to zero everywhere in a profile for which the maximum tentatively computed value of μ_t from the foregoing relations is less than a specified value (Baldwin and Lomax, 1978):

$$\mu_t = 0 \quad \text{if} \quad (\mu_t)_{\max}/\mu_0 < 14 \tag{2.4}$$

In cases where the transition onset is forced by an external action (e.g., roughness elements) it can be imposed by setting μ_t equal to zero in laminar regions and switching the laminar boundary layer directly to a fully turbulent boundary layer (user defined). The main drawback of the model is its inability to deal accurately with a complex wake flow.

One-Equation Turbulence Model of Spalart–Allmaras (1994). This model is based on a transport equation written for a variable linked to the eddy viscosity by

$$\mu_t = f_{v1} \tilde{\mu} \quad f_{v1} = \frac{\chi^3}{\chi^3 + c_{v1}^3} \quad \chi = \frac{\tilde{\mu}}{\mu} \tag{3.1}$$

The transport equation is then written in integral form as:

$$\int_V \frac{\partial \tilde{\mu}}{\partial t} dV + \int_S \mathbf{E}^{SA} dS - \int_S \mathbf{R}^{SA} dS = \int_V \mathbf{H}^{SA} dV$$

$$\mathbf{R}^{SA} = \frac{\mu + \tilde{\mu}}{\sigma} \nabla \left(\frac{\tilde{\mu}}{\rho} \right) \cdot \vec{n};\ \mathbf{E}^{SA} = \tilde{\mu} (\vec{w} \cdot \vec{n}) \tag{3.2}$$

This equation is basically of similar form as the equations for conservative flow variables (Eq. (1.1)). The only major difference is that the turbulence equation contains a source term $\mathbf{H}^{SA}$.

$$\mathbf{H}^{SA} = \underbrace{c_{b1}(1 - f_{t2}) \tilde{S} \tilde{\mu}}_{\text{"Production Term"}} - \underbrace{\left(\frac{c_{w1} f_w}{\rho} - \frac{c_{b1}}{\rho \kappa^2} f_{t2} \right) \left(\frac{\tilde{\mu}}{y} \right)^2}_{\text{"Destruction Term"}}$$

$$+ \underbrace{\frac{\rho c_{b2}}{\sigma} \left(\nabla \left(\frac{\tilde{\mu}}{\rho} \right) \right)^2}_{\text{"First Order Diffusion Term"}} + \underbrace{\rho f_{t1} (\Delta V)^2}_{\text{"Ignition Term"}}$$

$$\tilde{S} = |\Omega| + \frac{\tilde{\mu}}{\rho \kappa^2 y^2} f_{v2};\quad f_{v2} = 1 - \frac{\chi}{1 + c_{v1} f_{v1}};$$

$$f_w = g \left(\frac{1 + C_{w3}^6}{g^6 + C_{w3}^6} \right)^{1/6};\quad g = r + c_{w2}(r^6 - r);$$

$$r = \frac{\tilde{\mu}}{\rho \tilde{S} \kappa^2 y^2}; \tag{3.3}$$

To define the laminar/turbulent transitional behavior, the following relations are necessary:

$$f_{t1} = C_{t1} g_t \exp\left(-C_{t2} \frac{\Omega_t}{(\Delta V)^2} (y^2 + (g_t d_t)^2) \right)$$

$$f_{t2} = C_{t3} \exp(-C_{t4} \chi^2);\ g_t = \min \left(0.1, \frac{\Delta V}{\Omega_t \Delta x_t} \right) \tag{3.4}$$

The transition onset location (hereafter called trip) is fixed by the user. d_t is the distance from the grid point to the trip, Ω_t is the vorticity at the trip, Δx_t is the grid spacing along the wall at the trip location, and ΔV is the difference between the velocity

Nomenclature

c = chord length
c_p = specific heat at constant pressure
e = total energy per unit volume
k = turbulent kinetic energy
l_m = mixing length
p = static pressure
P_k = production of turbulent kinetic energy
t = time
T = temperature
T' = temperature fluctuation
u_i = Cartesian velocity components
u_i' = velocity fluctuations
x_i = Cartesian coordinates
y = minimum distance to the wall
δ = shear layer thickness
δ_{ij} = Kronecker delta
ϵ = dissipation of turbulent kinetic energy
γ = ratio of specific heats
μ, μ_t = molecular and turbulent viscosity
ρ = density
Ω = vorticity of the flowfield
$\vec{n}$ = outward unit vector normal to cell interface
$\vec{w}$ = velocity vector
$\vec{\tau}^S$ = cell interface shear stress vector
τ_{ij} = components of the shear stress tensor
$\dot{q}^S$ = cell interface heat flux
q_i = components of the heat flux vector
$\mathbf{E}$, $\mathbf{E}^{SA}$, $\mathbf{E}^{k\epsilon}$ = convective fluxes
$\mathbf{Q}$, $\mathbf{Q}^{k\epsilon}$ = vector of conserved variables
$\mathbf{R}$, $\mathbf{R}^{SA}$, $\mathbf{R}^{k\epsilon}$ = diffusive fluxes

at the grid point and the velocity at the trip. The model coefficients are:

$$c_{b1} = 0.1355; \quad c_{b2} = 0.622; \quad c_{w1} = \frac{c_{b1}}{\kappa^2} + \frac{1 + c_{b2}}{\sigma};$$

$$c_{w2} = 0.3; \quad c_{w3} = 2.0; \quad c_{v1} = 7.1; \quad \sigma = \tfrac{2}{3}; \quad \kappa = 0.41;$$

$$c_{t1} = 1; \quad c_{t2} = 2; \quad c_{t3} = 1.2; \quad c_{t4} = 0.5$$

The boundary conditions are:

- Wall condition: $\tilde{\mu} = 0$
- Inlet condition: Spalart and Allmaras (1994) propose the following value for the turbulent variable which implies a very low value for the actual eddy viscosity: $\tilde{\mu}/\mu = 0.1$.
- Outlet condition: A simple extrapolation is used to transport information from the computational domain to the outside.

Low-Reynolds-Number k–ϵ Model of Biswas and Fukuyama (1994). The main drawback of the two proceeding models is that they do not depend upon turbulence properties, e.g., free stream turbulence. The use of field equations to describe characteristic turbulence scales is therefore at the origin of this third approach.

Various low-Reynolds-number k–ϵ models have been developed so far, which differ through the use of different damping functions, constants, and extra source terms (e.g., Biswas and Fukuyama, 1994). Also boundary conditions vary between some models. The damping functions are only active close to solid walls and make it possible to solve k and ϵ down to the viscous sublayer. However, all models are such that when f_μ, f_1, and f_2 are set to 1, the standard high-Re k–ϵ model is obtained.

The two equations of this model can be written in integral form, similar to Eq. (3.2):

$$\int_V \frac{\partial \mathbf{Q}^{k\epsilon}}{\partial t} dV + \int_S \mathbf{E}^{k\epsilon} dS - \int_S \mathbf{R}^{k\epsilon} dS = \int_V \mathbf{H}^{k\epsilon} dV$$

$$\mathbf{Q}^{k\epsilon} = [\rho k, \rho\epsilon]^T; \quad \mathbf{E}^{k\epsilon} = \mathbf{Q}^{k\epsilon}(\vec{w} \cdot \vec{n});$$

$$\mathbf{R}^{k\epsilon} = \left[\left(\mu + \frac{\mu_t}{\mathrm{Pr}_k} \right) \nabla k \cdot \vec{n}, \left(\mu + \frac{\mu_t}{\mathrm{Pr}_\epsilon} \right) \nabla \epsilon \cdot \vec{n} \right]^T;$$

$$\mathbf{H}^{k\epsilon} = \left[P_k - \rho\epsilon, \frac{\epsilon}{k} (f_1 C_{\epsilon_1} P_k - f_2 C_{\epsilon_2} \rho\epsilon) \right]^T, \qquad (4.1)$$

$$P_k = \tau_{ij}^{\mathrm{turb}} \frac{\partial u_i}{\partial x_j};$$

where the eddy viscosity and turbulent Reynolds numbers are obtained from

$$\mu_t = C_\mu f_\mu \frac{\rho k^2}{\epsilon}; \quad \mathrm{Re}_t = \frac{\rho k^2}{\mu\epsilon}; \quad \mathrm{Re}_y = \frac{\rho y \sqrt{k}}{\mu}; \qquad (4.2)$$

The damping functions and model constants are defined as follows:

$$f_\mu = [1 - \exp(-\mathrm{Re}_t/150)][1 + 18.5/\mathrm{Re}_t]$$

$$f_1 = 1 + 0.3 \exp(-(\mathrm{Re}_t/50)^2)$$

$$f_2 = [1 - 0.3 \exp(-(\mathrm{Re}_t/6.5)^2)][1 - \exp(-\mathrm{Re}_y/10)]$$

$$C_\mu = 0.09; \quad C_{\epsilon_1} = 1.46; \quad C_{\epsilon_2} = 1.9;$$

$$\mathrm{Pr}_k = 1.4; \quad \mathrm{Pr}_\epsilon = 1.3 \qquad (4.3)$$

The boundary conditions are:

- Wall conditions: $k = 0$, $\partial\epsilon/\partial y = 0$
- Inlet conditions:

$$k = 3\ \mathrm{Tu}^2 W_1^2/2, \quad \epsilon = C_\mu^{3/4} k^{3/2}/l_m \qquad (4.4)$$

where W_1 is the inlet velocity, Tu the turbulence intensity, and l_m the mixing length (in the range of 1 percent of the chord length)

Outlet condition: A simple extrapolation is used.

Leading Edge Problems. Most k–ϵ models give overly high levels of turbulent energy in stagnation point regions. This is because the Boussinesq assumption fails in flows with large normal strain, and this results in excessive production of turbulent energy in stagnation flows. These disturbances are convected downstream and can influence the entire boundary layer. One way to overcome these problems is using a modified production term. The modification used was suggested by Kato and Launder (1993) for the simulation of vortex shedding behind square cylinders. The idea is to replace the strain rate with the vorticity in the production. The expression for the new production term is given by

$$P_k = \mu_t \cdot S \cdot \Omega;$$

$$S = \sqrt{\frac{1}{2}\left(\frac{\partial u_i}{\partial x_j} + \frac{\partial u_j}{\partial x_i} \right)^2}; \quad \Omega = \sqrt{\frac{1}{2}\left(\frac{\partial u_i}{\partial x_j} - \frac{\partial u_j}{\partial x_i} \right)^2}; \qquad (4.5)$$

All turbulence models were tested on simple flat-plate benchmark problems and on transonic airfoil test cases to assure a correct implementation before using them in cascade simulations (Artner, 1997).

Numerical Method

The governing equations are treated in conservative form (Eqs. (1.1), (3.2), (4.1)) and discretized in time using the Euler implicit method leading to a set of nonlinear finite difference equations, which is solved using a Newton procedure. In stationary simulations convergence is optimized by using a local time step based on a local stability criterion.

Inviscid Fluxes. The convective (Euler) parts $\mathbf{E}$, $\mathbf{E}^{SA}$, $\mathbf{E}^{k\epsilon}$ are discretized using a third-order-accurate, TVD-upwind, cell-centered finite volume scheme. When solving transport equations for turbulent quantities, a more stable first-order upwind scheme is used. The TVD scheme is based on the MUSCL type of an upwind scheme, which consists of a projection stage and an evolution stage. In the projection stage, left and right states at each cell interface are determined by extrapolating the cell-centered values of the conservative variables toward the cell interface. In the evolution stage, the inviscid flux is evaluated by solving the Riemann problem between left and right states using Roe's approximate Riemann solver (Sanz et al., 1995).

Viscous Fluxes. In order to construct the numerical viscous flux vector at the cell interfaces $\mathbf{R}$, $\mathbf{R}^{SA}$, $\mathbf{R}^{k\epsilon}$, it is necessary to evaluate first-order derivatives of the velocity components, the speed of sound and the turbulent quantities, which is done in a central-differencing manner, using Green's theorem (e.g., Furukawa et al., 1991). The time linearization of the viscous flux vector is performed by applying the thin-layer approximation for the implicit side of the equations.

Source Terms. The source terms $\mathbf{H}^{SA}$, $\mathbf{H}^{k\epsilon}$ are evaluated as cell averages. To estimate the gradients present in the source terms, a cell-centered finite volume scheme is used. This gives a second-order accurate estimation of the gradients. For the implicit side of the equations, a true linearization of the source terms is performed.

Boundary Conditions. In the present cell-centered scheme, phantom cells are used to handle all boundaries. According to the theory of characteristics, flow angle, total pressure, total temperature, and isentropic relations are used at the subsonic axial inlet, whereas all variables are prescribed at the supersonic inlet. At the

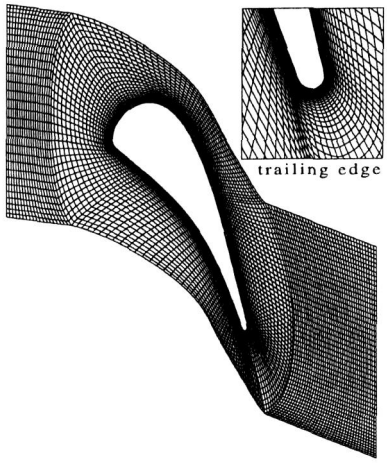

Fig. 1.1 Grid 1: periodic O-type grid with inlet and outlet patches (in total: 12,806 cells)

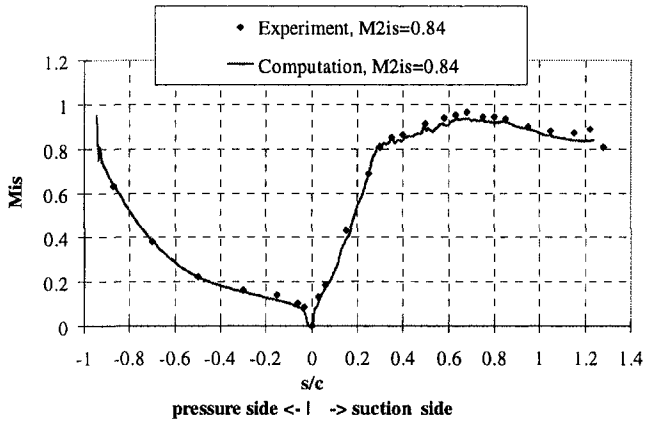

Fig. 2.1 Inviscid computation Mach number distributions

subsonic axial outlet the average value of the static pressure is prescribed, density and velocity components are extrapolated, whereas all variables are extrapolated at supersonic axial outlet. On solid walls, the pressure is extrapolated from the interior points and the nonslip adiabatic or isothermal condition is used to compute density and total energy.

Computational Grids. All meshes are generated with an algebraic multiblock grid generator based on Bézier curves and Bézier surfaces (Gehrer et al., 1996). All results presented here have been verified on different grids (10,000 to 18,000 cells) to ensure grid-independent solutions. Two examples of computational grids can be found in Figs. 1.1 and 1.2.

Grid 1 (Fig. 1.1) consists of three different blocks and avoids strongly skewed cells. The periodic **O**-mesh around the blade enables a good resolution of the leading and trailing edge flow.

Grid 2 (Fig. 1.2) is basically a periodic **H**-type grid with an additional outlet patch and an **O**-grid around the blade. Strongly skewed cells are avoided and the number of cells is 10,101. All meshes allow an easy switch between Euler and Navier–Stokes grids by just refining the inner part of the **O**-grid normal to the blade surface. For heat transfer calculations, the first cell at a solid boundary is placed below approximately $Y^+ = 0.2$–0.4.

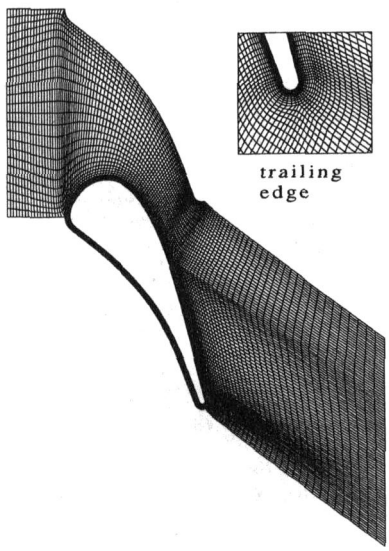

Fig. 1.2 Grid 2: periodic H-type grid with additional outlet patch and O-grid around the blade (in total: 10,101 cells)

Test Case

The test case considered is a highly loaded transonic turbine guide vane designed at the von Karman Institute (VKI). The measurements were performed in the VKI short duration isentropic light piston compression tube facility, allowing a correct simulation of Mach and Reynolds numbers, as well as of the gas to wall temperature ratio compared to the values currently observed in modern aero engines. The experimental program consisted of Schlieren visualizations, blade velocity distribution measurements by means of static pressure trappings and blade convective heat transfer measurements by means of platinum thin films. The wall temperature/wall heat flux conversion was obtained from an electrical analogy, simulating a one dimensional semi-infinite body configuration (Schultz and Jones, 1973).

The blade shape was optimized for a downstream isentropic Mach number equal to 0.9 by means of an inverse method, developed at VKI (Van den Braembussche et al., 1989). The most important geometric characteristics of the blade are:

Chord:	67.647 mm
Pitch/chord:	0.85
Throat/chord:	0.2207
Stagger angle from axial direction:	55 deg

The experimental data have been taken from Arts et al. (1990) and Arts et al. (1994). A rigorous definition of measured quantities is given in the same references.

Simulations

Inviscid Computation. This computation was carried out to validate the inviscid part of the solver. In this case the pressure ratio corresponds to an isentropic exit Mach number of $M_{2is} = 0.84$. The calculated and measured isentropic Mach number distributions on the blade surface are compared in Fig. 2.1. Despite the absence of the boundary layer the agreement is very satisfactory.

Test Case TUC004. The experimental results were obtained by forcing an early transition onset both along suction and pressure side by means of film cooling holes acting as roughness elements (no cooling flow was of course injected). The flow conditions correspond to an isentropic exit Mach number of $M_{2is} = 0.9$, an exit Reynolds number of $Re_2 = 1.06 \times 10^6$, and a free-stream turbulence intensity of Tu = 1 percent.

Numerical results were obtained with the mixing length model and with the Spalart–Allmaras model. For both turbulence models

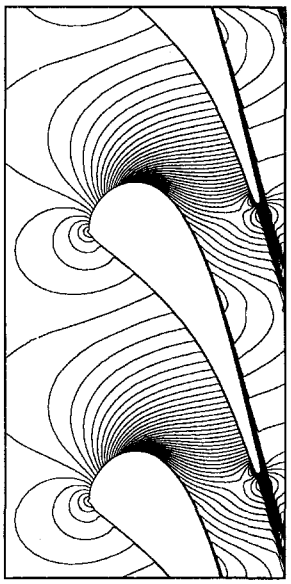

Fig. 3.1 Test case TUC004 Mach number contours

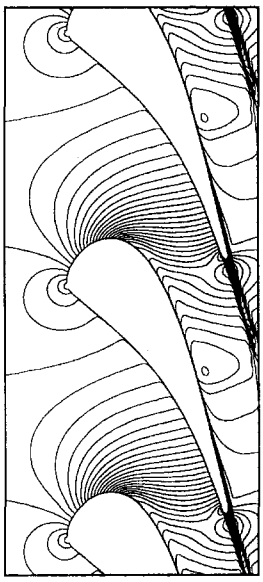

Fig. 4.1 Test case MUR235 Mach number contours

transition was imposed at the position of film cooling holes. As the transition onset was due to a purely external action, there was no reason to run the k–ϵ-model.

Figure 3.1 shows the Mach number distribution for the computed result obtained with the Spalart–Allmaras model. Figure 3.2 contains the respective heat transfer results for both suction and pressure side. Both calculations gave identical results for the laminar part of the boundary layer.

The mixing length model gives rather good results along the suction side in the fully turbulent part of the boundary layer, whereas transition is too abrupt. Here the laminar boundary layer is just switched directly to a fully turbulent boundary layer causing overly high values for the heat flux in the transitional area. Especially along the pressure side, this crude transition modeling leads to an overestimation of the heat transfer rate, as indicated by the sharp increase of the heat transfer coefficient. With a more refined transition region treatment this might be fixed (e.g., Lefebvre and Arts, 1997).

The Spalart–Allmaras model shows very good agreement with the experimental data (as opposed to results obtained with unstructured grids, presented by Lefebvre and Arts, 1997) along suction and pressure side.

Test Case MUR235. The calculations for this test case were performed with all three turbulence models. The flow conditions correspond to an isentropic exit Mach number of $M_{2is} = 0.927$, an exit Reynolds number of $Re_2 = 1.15 \times 10^6$, and a free-stream turbulence intensity of Tu = 6 percent.

The transition onset location based on the measured data was imposed for the Spalart–Allmaras model at $s/c = 0.8$ at the suction side. It was automatically predicted by the mixing length model and by the low-Re k–ϵ model. Figure 4.1 shows the Mach number distribution for the computed result obtained with the low-Re k–ϵ model.

Mixing-Length Model, Spalart–Allmaras Model. This test case is characterized by a higher value of free-stream turbulence. The results obtained with the mixing length model and with the Spalart–Allmaras model (Fig. 4.2) were therefore relatively far from the measured data in the laminar regions (on the whole pressure side and on about the first half of the suction side). They could not take into account the increase of laminar heating due to the increase of free-stream turbulence intensity. On the other hand, both models predict relatively well the heat transfer rates along the fully turbulent part of the boundary layer.

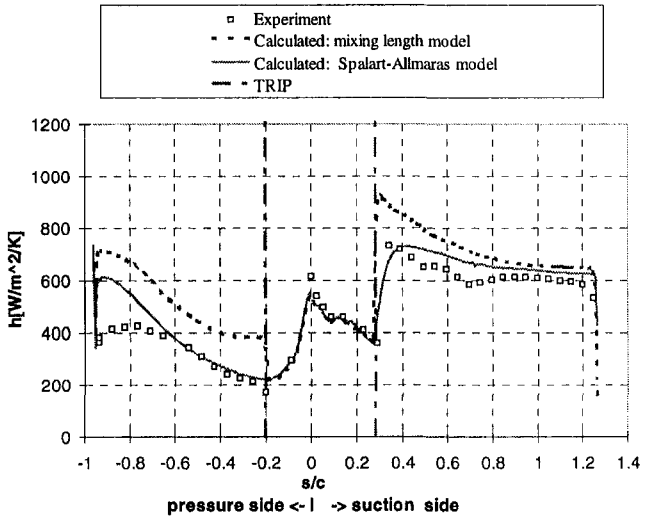

Fig. 3.2 Heat transfer results for test case TUC004

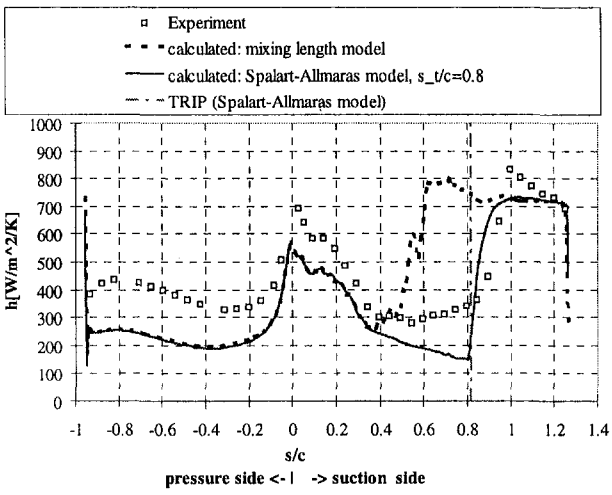

Fig. 4.2 Heat transfer results for test case MUR235 mixing length model and Spalart–Allmaras model

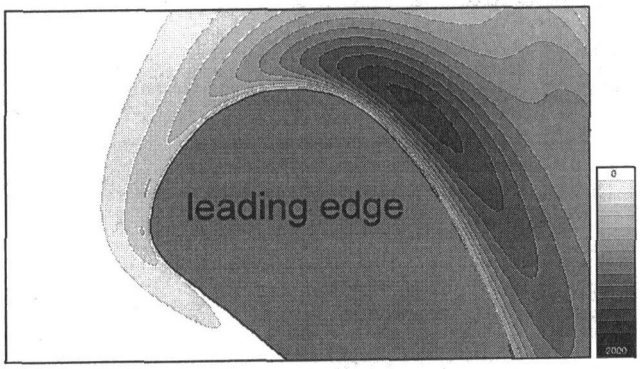

Fig. 4.3 Test case MUR235 turbulent kinetic energy contours k–ϵ model without Kato–Launder modification; $l_{m,\text{inlet}}/c = 0.05$

Transition is predicted too early and too abruptly by the mixing length model in combination with the transition criterion given in Eq. (2.4). The overall behavior in the transitional–turbulent region is captured quite well by the Spalart–Allmaras model.

Low-Re k–ϵ Model—Leading Edge Problems. First calculations with the low-Re k–ϵ model were done without the modified version of the production term suggested by Kato and Launder (1993). The standard formulation for the production (Eq. (4.1)) gave very high levels of turbulent energy in the stagnation point region (Fig. 4.3). These disturbances are convected downstream, causing too early a transition and a large overshot in the heat transfer (Fig. 4.4). In order to avoid these high levels of turbulent kinetic energy in the stagnation point region, the Kato and Launder modification of the production term, which improved the results significantly (see below), was used for all results presented hereafter.

Low-Re k–ϵ Model—Influence of Variation of l_m at the Inlet. When using a k–ϵ turbulence model, the value for l_m at the inflow boundary is often a bit ambiguous. Therefore the influence of l_m at the inflow on the solution has been investigated by varying l_m in the range of $l_m/c = 0.005$ to 0.05 (Fig. 4.5). A value of $l_m/c = 0.05$ at the inlet (together with the Kato–Launder modification) gave rather satisfactory results, especially regarding the laminar part of the boundary layer on the first half of the suction side and the fully turbulent part of the boundary layer. Transition was predicted slightly too early.

Decreasing l_m by a factor of 10 to a value of $l_m/c = 0.005$ (which is equivalent to an increase of ϵ at the inlet, Eq. (4.4)) causes the transition to move downstream and reduces the heat

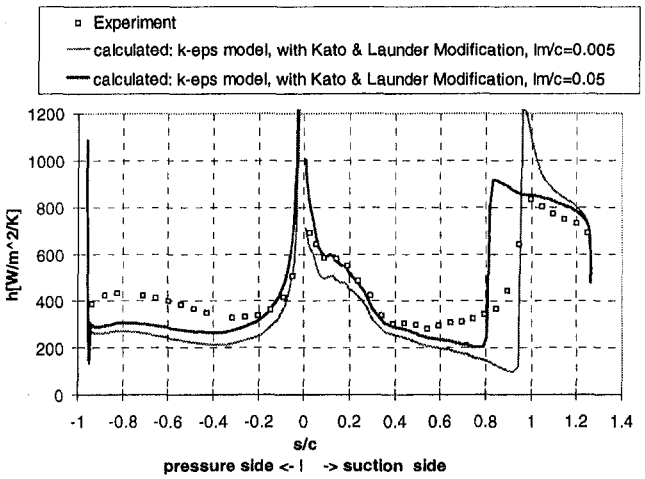

Fig. 4.5 Heat transfer results for test case Mur235 k–ϵ model with Kato–Launder modification influence of variation of l_m at the inlet

transfer rates in the laminar parts of the boundary layer on pressure and suction side. Overall, the results were closer to the measured data, which demonstrates the ability of the model to take into account the free stream turbulence intensity.

Test Case MUR222. The flow conditions for this test case correspond to an isentropic exit Mach number of $M_{2is} = 1.1$, an exit Reynolds number of $Re_2 = 5 \times 10^5$, and a free-stream turbulence intensity of Tu = 6 percent. In this case the boundary layer on the suction side remains in a pseudolaminar state over a large part of the blade. The calculations for this test case were performed with all three turbulence models. The transition onset location based on the measured data was imposed for the Spalart–Allmaras model at $s/c = 1.1$ at the suction side.

Regarding the low-Re k–ϵ model, we used the Kato and Launder modification of the production term in order to avoid leading edge problems and l_m at the inlet was set to $l_m/c = 0.05$, which appeared to be a good choice for the previous test case MUR235.

Figure 5.1 contains the computed Mach number contours showing a pronounced trailing edge shock wave. The results for the heat transfer rate (Fig. 5.2) show that both the algebraic and the one-equation model underpredict the heat flux in the pseudolaminar regions. Similar to test case Mur235, the algebraic model gives transition too early. The result obtained with the low-Re k–ϵ model is closer to the experimental data but the two-equation model still underpredicts the heat flux on the pressure side. How-

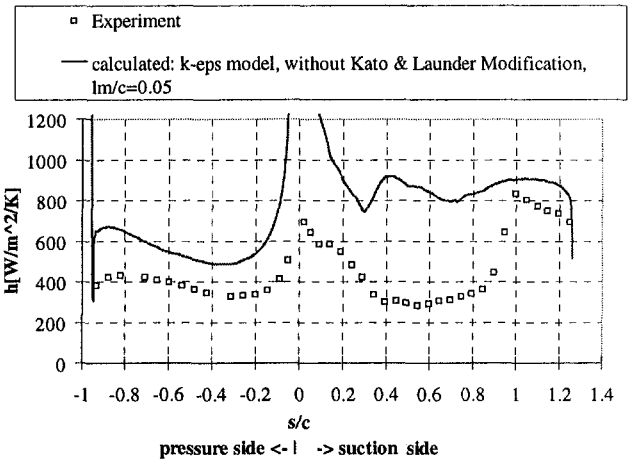

Fig. 4.4 Heat transfer results for test case Mur235 (k–ϵ model without Kato–Launder modification)

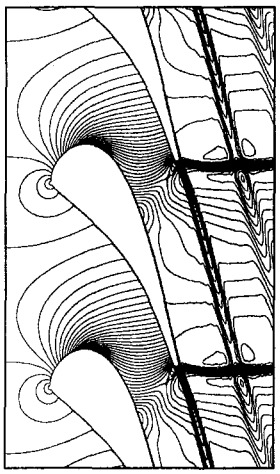

Fig. 5.1 Test case MUR222 Mach number contours, low-Re k–ϵ model

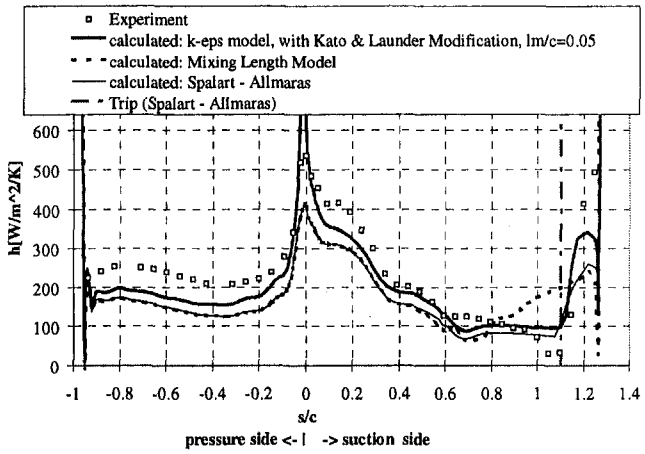

Fig. 5.2 Heat transfer results for test case MUR222

ever, the transition onset location on the suction side was very accurately predicted.

Conclusions

External heat transfer predictions in a highly loaded transonic linear turbine guide vane cascade have been successfully performed by means of an implicit Navier–Stokes solver. Three different turbulence models have been investigated:

The mixing length model gave good heat transfer predictions for cases with low free-stream turbulence levels, especially for the fully turbulent boundary layer, but it needs to be complemented with a more sophisticated transition model, as reported by Migliorini and Michelassi (1997). The main drawback is its lack of generality, which prevents its correct application for complex geometries.

The Spalart–Allmaras model avoids the problems of the mixing length model as it can be applied on any configuration. The heat transfer predictions showed very satisfactory agreement with experimental data regarding flows with low free-stream turbulence levels and with a clearly defined transition onset location. The Spalart–Allmaras model suffers from its inability to predict transition automatically and cannot properly take into account higher levels of free-stream turbulence levels.

Due to the fact that low free-stream turbulence intensity cases seldom exist in real turbines, the application of the mixing length model and the Spalart–Allmaras model to heat transfer calculations in turbomachinery is fairly limited.

The low-Re k–ϵ model of Biswas and Fukuyama appears to be more general. It detected transition onset by itself and took into account the effect of free-stream turbulence intensity. Overly high values of turbulent kinetic energy at the leading edge could be suppressed by combining the model with a modified version of the production term according to Kato and Launder (1993). Moreover, the model appeared to be rather sensitive to the inlet boundary condition for ϵ. For the test cases investigated in this work, a value of $l_m/c = 0.05$ for the mixing length at the inlet gave results, which indicate that the overall behavior of this two-equation model is promising. Nevertheless, further investigations are necessary to meet the desired prediction capability.

Acknowledgments

The authors gratefully acknowledge the support of the Austrian Science Foundation (FWF) of this research as well as of ongoing research in efficiency improvement of thermal energy production.

References

Arnone, A., and Pacciani, R., 1998, "IGV–Rotor Interaction Analysis in a Transonic Compressor Using the Navier–Stokes Equations," ASME JOURNAL OF TURBOMACHINERY, Vol. 120, pp. 147–155.

Artner, W., 1997, "Implementierung eines Eingleichungsmodells in einen 2D Navier Stokes Code," Diploma Thesis, TU-Graz, ITTM.

Arts, T., Lambert de Rouvroit, M., and Rutherford, A. W., 1990, "Aero-thermal Investigation of a Highly Loaded Transonic Linear Turbine Guide Vane Cascade," Technical Note 174, von Karman Institute for Fluid Dynamics, Belgium.

Arts, T., 1994, "Highly Loaded Transonic and Film Cooled Linear Turbine Guide Vane Cascade," in: "Numerical Methods for Flow Calculation in Turbomachines," VKI Lecture Series, 1994-06.

Baldwin, B. S., and Lomax, H., 1978, "Thin layer approximation and algebraic model for separated turbulent flows," AIAA Paper No. 78-257.

Biswas, D., and Fukuyama, Y., 1994, "Calculation of Transitional Boundary Layers With an Improved Low-Reynolds-Number Version of the k–ϵ Turbulence Model," ASME JOURNAL OF TURBOMACHINERY, Vol. 116, pp. 765–773.

Boussinesq, J., 1877, "Essai Sur la Théorie des Eaux Courantes," *Mem. Présentes Acad. Scie.*, Vol. 23, p. 46.

Furukawa, M., Yamasaki, M., and Inoue, M., 1991, "A Zonal Approach for Navier–Stokes Computations of Compressible Cascade Flow Fields Using a TVD Finite Volume Method," ASME JOURNAL OF TURBOMACHINERY, Vol. 113, pp. 573–582.

Gehrer, A., Paßrucker, H., Jericha, H., and Lang, J., 1996, "Blade Design and Grid Generation for Computational Fluid Dynamics (CFD) With Bézier-curves and Bézier-Surfaces," European Conference, Antwerpen, March '97, Paper No. 54.

Kato, M., and Launder, B. E., 1993, "The modeling of turbulent flow around stationary and vibrating square cylinders." in: *Proc. 9th Symposium on Turbulent Shear Flows*, Kyoto, pp. 10.4.1–10.4.6, Aug.

Kwon, O. K., Pletcher, R. H., and Delaney, R. A., 1988, "Calculation of Unsteady Turbulent Boundary Layers," ASME JOURNAL OF TURBOMACHINERY, Vol. 110, pp. 195–201.

Larsson, J., Eriksson, L. E., and Håll, U., 1995, "External Heat Transfer Predictions in Supersonic Turbines Using the Reynolds Averaged Navier–Stokes Equations," *Proc. 12th ISABE Conference*, Melbourne, copies distributed by AIAA.

Larsson, J., 1996, "Numerical Simulation of Turbine Blade Heat Transfer," Thesis for the degree of Licentiate of Engineering, Department of Thermo and Fluid Dynamics Chalmers, University of Technology.

Larsson, J., 1997, "Turbine Blade Heat Transfer Calculations Using Two-Equation Turbulence Models," *IMechE Journal A, Proc Instn Mech Engrs*, Vol. 211, Part A, pp. 253–262; also in *Proc. 2nd European Conference on Turbomachinery Fluid Dynamics and Thermodynamics*, Antwerpen, 1997, pp. 411–420.

Lefebvre, M., and Arts, T., 1997, "Numerical Aero-Thermal Prediction of Laminar/Turbulent Flows in a Two-Dimensional High Pressure Turbine Linear Cascade," European Conference, Antwerpen, Mar.

Migliorini, F., and Michelassi, V., 1997, "Transition and Heat Transfer Modelling in Transonic Linear Cascade," European Conference, Antwerpen, Mar.

Sanz, W., Gehrer, A., and Paßrucker, H., 1995, "An Implicit TVD Upwind Relaxation Scheme for the Unsteady 2D-Euler-Equations" ASME Paper No. 95-CTP-71.

Schultz, D. L., and Jones, T. V., 1973, "Heat Transfer Measurements in Short Duration Hypersonic Facilities," AGARDograph 165.

Spalart, P. R., and Allmaras, S. R., 1994, "A One Equation Turbulence Model for Aerodynamic Flows," *La Recherche Aerospatiale*, No. 1, pp. 5–21.

Van den Braembussche, R. A., Leonard, O., and Nekmouche, L., 1989, "Subsonic and Transonic Blade Design by Means of Analysis Codes," presented at the 64th FDP specialists' meeting on "Computational Methods for Aerodynamic Design (inverse) and Optimization," May 22–23, Loen, Norway.

Physics of Hot Crossflow Ingestion in Film Cooling

E. L. McGrath

J. H. Leylek

Department of Mechanical Engineering,
Clemson University,
Clemson, SC 29634

Computational fluid dynamics (CFD) is used to isolate the flow physics responsible for hot crossflow ingestion, a phenomenon that can cause failure of a film cooled gas turbine component. In the gas turbine industry, new compound-angle shaped hole (CASH) geometries are currently being developed to decrease the heat transfer coefficient and increase the adiabatic effectiveness on film cooled surfaces. These new CASH geometries can have unexpected flow patterns that result in hot crossflow ingestion at the film hole. This investigation examines a 15 deg forward-diffused film hole injected streamwise at 35 deg with a compound angle of 60 deg (FDIFF60) and with a length-to-diameter ratio (L/D) of 4.0. Qualitative and quantitative aspects of computed results agreed well with measurements, thus lending credibility to predictions. The FDIFF60 configuration is a good representative of a typical CASH geometry, and produces flow mechanisms that are characteristic of CASH film cooling. FDIFF60 has been shown to have impressive downstream film cooling performance, while simultaneously having undesirable ingestion at the film hole. In addition to identifying the physical mechanisms driving ingestion, this paper documents the effects on ingestion of the blowing ratio, the density ratio, and the film hole Reynolds number over realistic gas turbine ranges of 0.5 to 1.88, 1.6 to 2.0, and 17,350 to 70,000, respectively. The results of this study show that hot crossflow ingestion is caused by a combination of coolant blockage at the film hole exit plane and of crossflow boundary layer vorticity that has been re-oriented streamwise by the presence of jetting coolant. Ingestion results when this re-oriented vorticity passes over the blocked region of the film hole. The density ratio and the film hole Reynolds number do not have a significant effect on ingestion over the ranges studied, but the blowing ratio has a surprising nonlinear effect. Another important result of this study is that the blockage of coolant hampers convection and allows diffusion to transfer heat into the film hole even when ingestion is not present. This produces both an undesirable temperature gradient and high temperature level on the film hole wall itself. Lessons learned about the physics of ingestion are generalized to arbitrary CASH configurations. The systematic computational methodology currently used has been previously documented and has become a standard for ensuring accurate results. The methodology includes exact modeling of flow physics, proper modeling of the geometry including the crossflow, plenum, and film hole regions, a high quality mesh for grid independent results, second order discretization, and the two-equation $k-\epsilon$ turbulence model with generalized wall functions. The steady, Reynolds-averaged Navier–Stokes equations are solved using a fully elliptic and fully implicit pressure-correction solver with multiblock unstructured and adaptive grid capability and with multigrid convergence acceleration.

1 Introduction

The gas turbine industry is constantly striving to produce more cost-effective and energy-efficient engines. To improve the efficiency of the thermodynamic cycles, designers are increasing turbine inlet temperatures. Already, temperatures of the flow exiting the combustion chamber in today's engines are exceeding the melting temperatures of the metals that comprise the turbine components. To compensate, cooler air is pulled from the high-pressure compressor and is injected through small strategically placed holes on the metal surfaces in the turbine section. This practice is known as "film cooling," and the goal is to form a thin coating of relatively cool air over the metal to protect it from the high temperatures of the crossflow. The drawback is that film cooling reduces the efficiency of the engine. Currently, the drive for high efficiency is pushing crossflow temperatures in the turbine components higher while simultaneously pushing to reduce the amount of coolant used to protect the metal, thus creating a need for innovative film cooling configurations.

The jet-in-crossflow interaction found in film cooling inherently contains complex flow mechanisms that disrupt the layer of coolant on the metal. The challenge to designers is to control the flow mechanisms such that a uniform layer of coolant is produced. Compound-angle shaped hole (CASH) geometries have come to the forefront as a promising way to reduce undesirable flow phenomena, such as jet lift-off. Currently, the flow mechanisms in CASH film cooling are not well understood, which limits the prediction of problems such as hot crossflow ingestion and therefore limits the design capability. Properly validated CFD models of film cooling can be used as an accurate predictive tool in CASH design to save time and money by reducing the number of expensive experimental tests required.

2 Literature Review

The number of papers in the open literature that study CASH configurations is very limited. In addition, there are currently no known papers that study the physics of hot crossflow ingestion for CASH geometries.

Experimental studies that examine a CASH configuration are the companion papers Schmidt et al. (1996) and Sen et al. (1996)

Contributed by the International Gas Turbine Institute and presented at the 43rd International Gas Turbine and Aeroengine Congress and Exhibition, Stockholm, Sweden, June 2–5, 1998. Manuscript received by the International Gas Turbine Institute February 1998. Paper No. 98-GT-191. Associate Technical Editor: R. E. Kielb.

and the thesis by Schmidt (1995). The specific CASH configuration studied was a single row of cylindrical holes with $\alpha = 35$ deg, $\Phi = 60$ deg, $L/D = 4.0$, $P/D = 3.0$, and a $2.1D$ long metering section followed by a 15 deg forward-diffusing section. The blowing ratios studied were 0.63, 1.25, and 1.88. Results of adiabatic effectiveness were reported for a density ratio of 1.6, and results of the heat transfer coefficient were reported for a density ratio of 1.0. No results of flowfield data were reported. The surface results showed excellent lateral spreading of the coolant and better adiabatic effectiveness than cylindrical film hole geometries with streamwise injection.

The only known computational study in the open literature that examines CASH configurations is Brittingham and Leylek (1997), which was part of a four-paper series. The first part of the series, Walters and Leylek (1997b), detailed the flowfield characteristics for streamwise-injected cylindrical film holes. The second part, McGovern and Leylek (1997), studied compound-angle injected cylindrical holes, including a cylindrical hole with $D = 11.1$ mm, $\alpha = 35$ deg, $\Phi = 60$ deg, $L/D = 4.0$, and $P/D = 3.0$. No hot crossflow ingestion was found for this configuration, but blockage of the coolant by the crossflow along the upstream edge of the film hole exit plane (FHEP) was present. The third part, Hyams and Leylek (1997), studied streamwise-injected shaped holes, including a configuration with $D = 11.1$ mm, $\alpha = 35$ deg, $L/D = 4.0$, $P/D = 3.0$, and a metering length of $2.1D$ followed by a 15 deg forward-diffused section. No ingestion or coolant blockage by the crossflow at the FHEP was found. Brittingham and Leylek studied two CASH configurations at blowing ratios of 1.25 and 1.88. The first configuration was studied for a density ratio of 1.60 and is identical to the FDIFF60 geometry studied in this paper and shown in Fig. 2. Hot crossflow ingestion and blockage of the coolant along the upstream edge of the FHEP were found to be present. The conclusions were that the ingestion seemed to be nonlinear with respect to the blowing ratio, and that superposition of the flowfield for the streamwise-aligned forward-diffused geometry (Hyams and Leylek) and of the flowfield for the cylindrical hole with $\Phi = 60$ deg (McGovern and Leylek) does not apply. No conclusions as to the physical mechanisms causing the ingestion were made. The other configuration studied by Brittingham and Leylek was a 12 deg laterally expanded hole with $\Phi = 45$ deg. No crossflow ingestion was present for this configuration.

Several experimental studies in the open literature have observed the presence of hot crossflow ingestion, but none have specifically studied its physics. One paper that indicates the presence of crossflow ingestion is the experimental research by Thole et al. (1998), which studied streamwise-aligned shaped holes. The research included a forward-lateral-expanded hole with 15 deg forward expansion and 14 deg lateral expansion, supplied by a coflowing coolant channel rather than by a plenum. The forward-lateral-expanded hole configuration had some advantages, but also showed crossflow ingestion, which is best summarized by the authors: "The primary disadvantage, however, for the forward-laterally expanded hole is that even though the blowing ratio was quite high, the jet exits primarily from the leeward side of the cooling hole, thereby allowing ingestion of the mainstream fluid into the windward side of the cooling hole."

3 Present Contributions

As discussed in the preceding literature review, a detailed understanding of hot crossflow ingestion has not been documented in the open literature, and studies of CASH geometries are few in number. In light of this, contributions of the present study are:

- documentation of the physics governing hot crossflow ingestion.
- explanation of the effects of blowing ratio, density ratio, and film hole Reynolds number on hot crossflow ingestion.
- identification of coolant blockage at the film hole exit plane as a phenomenon that hampers convection and allows diffusion to transfer heat into the film hole.
- addition to the database and knowledge base for CASH.
- demonstration of CFD's ability to generate accurate and consistent results for jet-in-crossflow interactions, especially as a reliable predictive design tool for CASH film cooling.

Nomenclature

AR = area ratio
CASH = *c*ompound-*a*ngle *s*haped *h*ole
C_p = coefficient of pressure = $P_s/0.5\rho v^2$
D = diameter of metering section of film hole, mm
DR = density ratio = ρ_j/ρ_∞
FDIFF = *f*orward-*diff*used streamwise-aligned configuration
FDIFF60 = *f*orward-*diff*used $\Phi = 60$ deg configuration
FHEP = *f*ilm *h*ole *e*xit *p*lane
L = length of film hole
LE = leading edge of film hole exit plane
L/D = length-to-diameter ratio of film hole
M = mass flux (or blowing) ratio = $(\rho_j v_j)/(\rho_\infty v_\infty)$, where v_j is mean jet velocity defined in hole metering section
P = lateral distance between two adjacent film holes, mm
P_s = static pressure, Pa
P/D = pitch-to-diameter ratio of film hole
Re = Reynolds number
T = local fluid temperature, K
TE = trailing edge of film hole exit plane
tke = turbulent kinetic energy, m^2/s^2
$\bar{v}$ = local fluid velocity vector = $v_x\bar{i} + v_y\bar{j} + v_z\bar{k}$
v = magnitude of local velocity vector = $|\bar{v}|$, m/s
v_x = component of local velocity vector in the x direction, m/s
v_y = component of local velocity vector in the y direction, m/s
v_z = component of local velocity vector in the z direction, m/s
VR = local velocity normalized by mean crossflow velocity = v/v_∞
VR_{YJ} = velocity y component normalized by mean jet velocity = v_y/v_j
x, y, z = Cartesian coordinate system axes
y^+ = nondimensional wall distance = $y\sqrt{|\tau_w|/\rho_w}/\nu_w$
α = injection angle measured from the x–z plane, deg
δ = boundary layer thickness, m
ϵ = dissipation rate of turbulent kinetic energy, m^2/s^3
Φ = compound angle measured from the x–y plane, deg
η = adiabatic effectiveness = $(T_\infty - T_{aw})/(T_\infty - T_j)$
$\bar{\eta}$ = laterally averaged adiabatic effectiveness
θ = nondimensional fluid temperature = $(T - T_j)/(T_\infty - T_j)$
ρ = density, kg/m^3
τ = shear stress, Pa
ν = kinematic viscosity, m^2/s
$\bar{\xi}$ = vorticity vector = $\xi_x\bar{i} + \xi_y\bar{k} + \xi_z\bar{k}$
ξ_x = component of the vorticity vector in the x direction, 1/s
ξ_y = component of the vorticity vector in the y direction, 1/s
ξ_z = component of the vorticity vector in the z direction, 1/s

Subscripts

aw = adiabatic wall
fh = condition inside film hole
j = coolant jet condition
w = condition at wall
∞ = mainstream condition at crossflow inlet plane

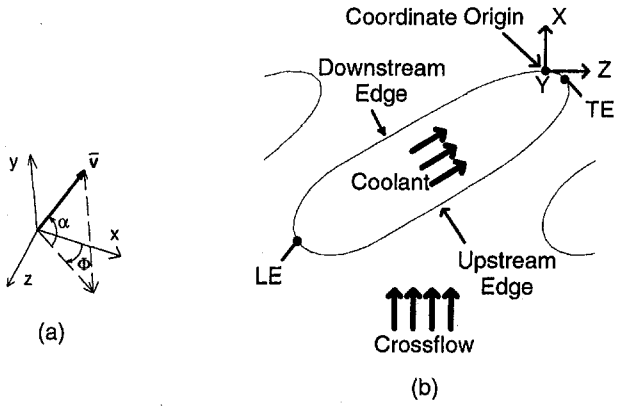

Fig. 1 Definition of terminology for (*a*) angles and (*b*) film hole locations (top-down view)

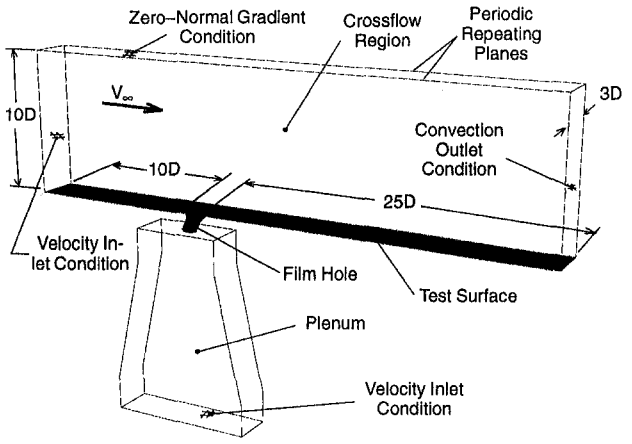

Fig. 3 Computational model utilized in the present study, showing extents of the domain and the boundary conditions

4 Computational Details

A consistent terminology will be used to describe locations in the domain. The definitions of the angles α and Φ are shown in Fig. 1(*a*), and definitions of the leading edge (*LE*), trailing edge (*TE*), upstream edge, and downstream edge of the film hole are shown in Fig. 1(*b*). The viewing angle in Fig. 1(*b*) is an aerial view of the film hole from directly above and will be used extensively throughout the paper. If no crossflow were present the coolant would exit the film hole from the *LE* to the *TE*. The upstream edge is the part of the film hole exit plane (FHEP) that is exposed to the hot crossflow, and the downstream edge is the side facing the test surface. The origin of the coordinate system is located at the point of the film hole edge that is located farthest downstream. Crossflow moves in the $+x$ direction as shown by the coordinate axes in the figure. The current computational geometry is an exact replica of the experimental setup of Schmidt et al. (1996) and Sen et al. (1996), and is detailed in Fig. 2. Film hole diameter is 11.1 mm along a metering length of 2.1 diameters before the start of the 15 deg diffusing section.

The computational domain is displayed in Fig. 3. Turbulent kinetic energy, turbulent dissipation rate, and velocity profile of the crossflow at the inlet plane were set at 10 diameters upstream of the *LE* of the film hole, which is well before the crossflow experiences any influence from the coolant. The plenum velocity inlet, convection outlet, and top zero-normal-gradient slip-plane were all placed well away from the jet-in-crossflow interaction. In order to simulate a row of holes, periodic repeating planes were used on both sides of the film hole to handle the asymmetric nature of the flow at and downstream of the film hole. Therefore, the flow that exits the domain on one side re-enters the domain with the same properties on the other side as if it were coming from the adjacent film hole. Following the same practice as the laboratory experiments, the conditions at both the crossflow and plenum inlets were adjusted as necessary to set the key parameters for each of the seven test cases listed in Table 1. The crossflow temperature was kept constant at 300 K for all the cases, and the coolant temperature was varied to produce the desired density ratio. To set the blowing ratio, the crossflow velocity was varied. The boundary layer thickness at the leading edge of the film hole was held constant at $\delta/D = 0.5$. Inlet turbulence intensity was 0.7 percent, and characteristic length scale was 1/100 of the crossflow inlet height.

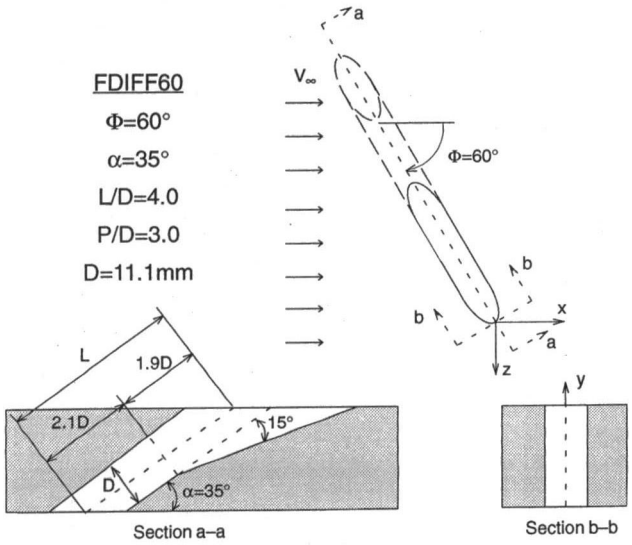

Fig. 2 Dimensions of current FDIFF60 geometry

5 Computational Methodology

The computational methodology utilized has been fully documented by Walters and Leylek (1997a). This methodology ensures accurate and consistent results and is represented by the hierarchy shown in Fig. 4. In summary, the most important step is to create a proper computational model of flow physics. A proper model includes a domain that extends into the film hole and plenum, as emphasized by Leylek and Zerkle (1994), and the application of proper inlet conditions. The next critical step is to create the exact film hole geometry in the computational model. The nonuniform rational *b*-splines (NURBS) based geometry generation in I-DEAS by SDRC, Inc., was utilized. A high-quality background grid was then created with the highest density of finite volumes in the film hole and in the area of the jet-in-crossflow interaction. The background grid consisted of 476,000 unstructured tetrahedrons with minimum skewness to ensure grid quality. In addition, the first layer of tetrahedrons against the walls were sized to result in y^+ values suitable for use with generalized wall functions. The back-

Table 1

Case #	Blowing Ratio	Density Ratio	Film Hole Reynolds Number
1	1.25	1.60	17,350
2	1.25	2.0	17,350
3	1.25	1.60	35,000
4	0.5	1.60	17,350
5	0.5	2.0	17,350
6	0.5	2.0	70,000
7	1.88	1.60	17,350

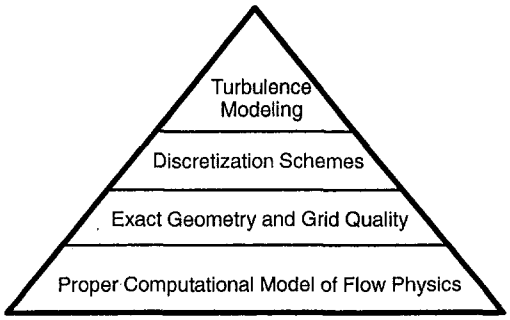

Fig. 4 Hierarchical representation of the computational methodology

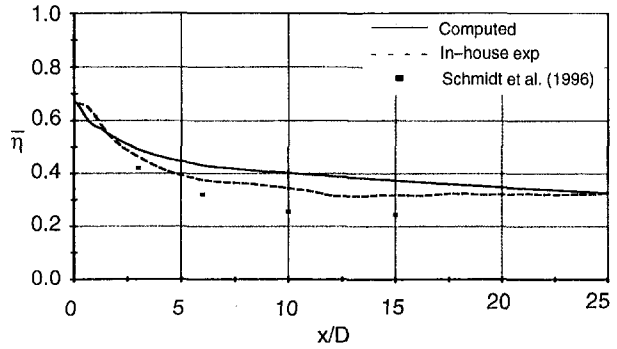

Fig. 5 Comparison of computational and experimental streamwise variations of $\bar{\eta}$ for FDIFF60 at M = 1.25, *DR* = 1.60, and Re_{th} = 17,350 shows good agreement

ground grid was refined in locations of high T, P_s, tke, ϵ, and v gradients using the hanging-node adaption capability of the Fluent/UNS solver by Fluent, Inc., which preserves background grid quality in all subsequent refinement cycles. Convergence was not declared until the overall mass and energy imbalances dropped below 0.01 percent and until the profiles of T, P_s, tke, ϵ, v, and η stopped changing in a number of critical areas. After every grid adaption, the simulation was run until full convergence using an HPC6000 computer from Sun Microsystems with 16 cpu's (250 MHz) and 4 gigabytes of RAM. Grid independence was typically reached at around 800,000 to 900,000 tetrahedrons, when further adaption no longer changed the flow and fluid properties at critical locations in the domain.

A second-order discretization scheme was utilized to reduce numerical viscosity. The turbulence model used was the standard two-equation k–ϵ model with wall functions. In the past, this turbulence model has been criticized for its inability to handle the turbulent anisotropic spreading of the coolant jet in streamwise injected cases. In compound-angle film cooling, as the compound angle increases, one of the counterrotating vortices in the coolant wake gains strength and dominates. The resulting strong lateral convection in the wake dominates spreading of the coolant jet, therefore reducing the importance of the issue of turbulent anisotropy, as demonstrated by McGovern and Leylek (1997) and Brittingham and Leylek (1997). Thus, the standard two-equation k–ϵ model with wall functions does not have difficulty predicting coolant jet spreading for compound-angle hole configurations.

6 Model Validation

The current computational methodology has been proven to produce results that agree well with experimental validation data. In relation to the current CASH geometry, the computational methodology was successfully applied to a streamwise-aligned forward-diffused geometry (FDIFF) by Hyams and Leylek (1997), to a compound-angle (Φ = 60 deg) cylindrical hole by McGovern and Leylek (1997), and to a CASH combination of the first two geometries (FDIFF60) by Brittingham and Leylek (1997). The computational results from these papers were compared to the experimental data of Schmidt et al. (1996) and to in-house experiments. Comparisons showed that the computational results were close to the experimental results and agreed well with the trends of the experimental data. Good agreement of experimental and computational results for FDIFF60 from Brittingham and Leylek are demonstrated by the plot of $\bar{\eta}$ in Fig. 5 and by the plots of lateral variations of η at two downstream locations in Fig. 6(a, b).

The good agreement shown between the experimental validation data and the computational results from Brittingham and Leylek not only validate the results of the computations, but also validate the computational grid, domain, and methodology used to obtain the results. The methodology, geometry, background grid, and boundary layer thickness at the leading edge (δ/D = 0.5) for all seven of the current test cases are identical to the FDIFF60 study by Brittingham and Leylek. Only the crossflow inlet and plenum inlet conditions were changed from case to case to give different combinations of blowing ratio, density ratio, and film hole Reynolds number. Grid independence was established starting from the original background grid for each of the test cases.

7 Results

Only the flow mechanisms relevant to hot crossflow ingestion and to heat diffusion into the film hole are discussed. Downstream surface cooling, including adiabatic effectiveness and heat transfer coefficient, for the FDIFF60 geometry has already been documented by Brittingham and Leylek (1997). The FDIFF60 geometry is a typical CASH configuration, and the physics of ingestion and coolant blockage discussed in this paper are not limited to FDIFF60, but instead apply to CASH configurations in general.

7.1 Influence on Ingestion of Flow Within Film Hole. The mechanisms responsible for hot crossflow ingestion begin inside

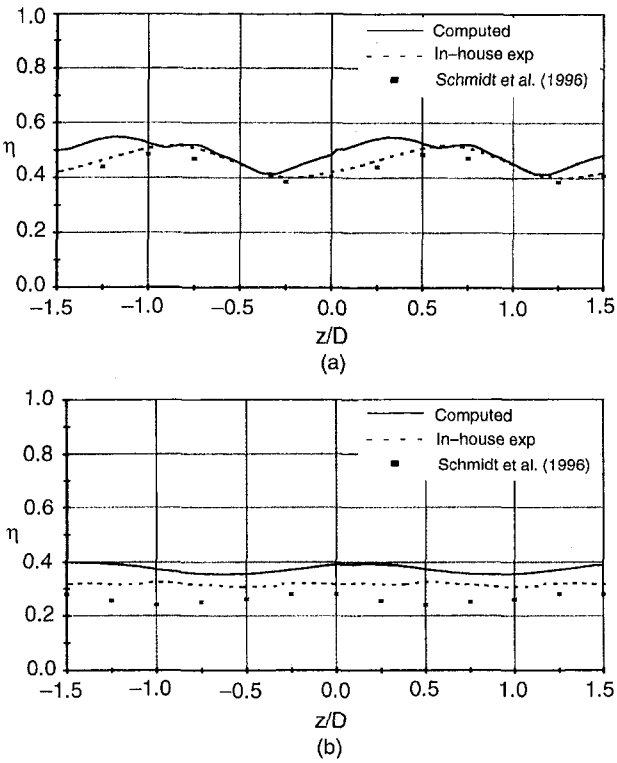

Fig. 6 Comparison of computational and experimental lateral distributions of η for FDIFF60 at M = 1.25, *DR* = 1.60, and Re_{th} = 17,350 at (*a*) *x/D* = 3 and (*b*) *x/D* = 15 shows good agreement

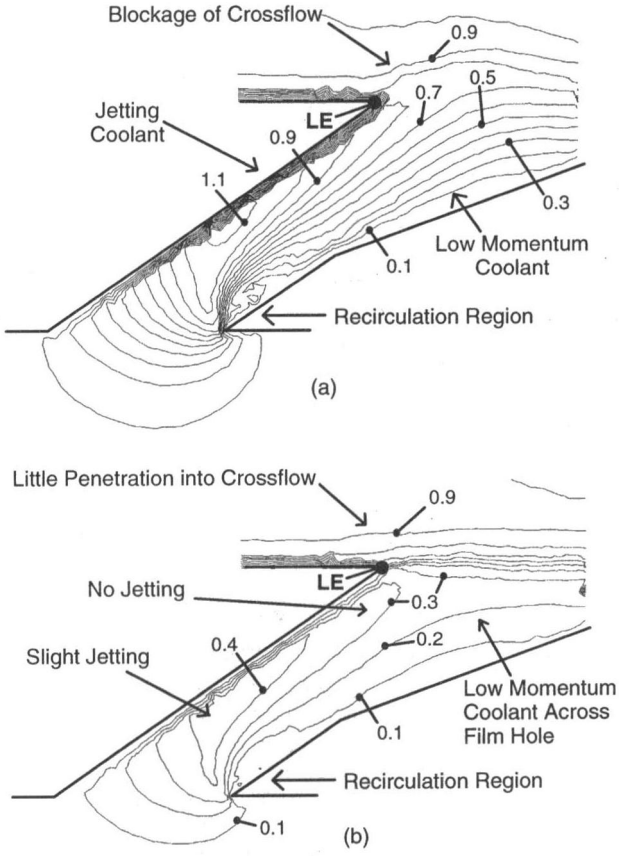

Fig. 7 Contours of *VR* along the film hole centerline show effect of blowing ratio on jetting for *DR* = 1.6, Re_{fh} = 17,350, and (*a*) M = 1.25 and (*b*) M = 0.5

the film hole. Coolant entering the film hole from the plenum is accelerated and is simultaneously turned to the injection angle of the film hole. Some of the coolant undergoes sharp turning of up to 145 deg at the film hole inlet, which produces a recirculation region on the *TE* side of the inlet. This recirculation region is a source of total pressure loss and results in a region of coolant with low momentum on the same side of the film hole as the *TE* (Fig. 7(*a*)). The coolant on the *LE* side of the film hole is not slowed by the recirculation region and "jets" through the film hole. If the film hole were long enough, turbulence and secondary flow would diffuse the momentum of the jetting coolant, and fully developed pipe flow would result. Realistic film cooling geometries have short *L*/*D* ratios, which results in nonuniform velocities at the FHEP. The purpose of the 15 deg diffusing section at the trailing edge is to slow the jetting coolant and reduce penetration of the coolant into the crossflow by increasing the cross-sectional area of the film hole. A measure of the increase in area is the area ratio (AR), which is the ratio of the FHEP area to the cross-sectional area of the metering section of the film hole. For the current FDIFF60 geometry, the AR is 4.15. With respect to ingestion, the problem of this CASH geometry is that the diffusing section is on the same side of the film hole as the low-momentum coolant region. Thus, the already low-momentum coolant flowing through the film hole on the *TE* side is further slowed, as shown in Fig. 7(*a*), while the jetting coolant on the *LE* side of the film hole is relatively unaffected. In comparison, a laterally diffused geometry with an AR of only 3.31 was shown by Hyams and Leylek (1997) and Brittingham and Leylek (1997) to slow the jetting coolant more effectively, because the diffusing area was located next to the jetting coolant. The fact that the diffusing section of the present geometry has no effect on the jetting coolant while further slowing the already low-momentum coolant is a major factor contributing to both hot crossflow ingestion and to the diffusion of heat into the film hole, as described below. In general, any CASH configuration with the diffusing section near the low-momentum coolant region inside the hole will have a similar problem.

Figure 7(*b*) shows contours of *VR* along the film hole centerline for a low blowing ratio of M=0.5. Because the film hole Reynolds number is constant in Fig. 7, the velocities of the coolant inside the film hole are the same at both M = 0.5 and M = 1.25. Since the crossflow velocity is increased at M=0.5, the coolant cannot penetrate or jet into the higher momentum crossflow, which acts like a partial cover over the FHEP. Thus, the presence or absence of jetting coolant is not a function of coolant momentum alone but is a function of the relative coolant-to-crossflow momentum. In the next section coolant jetting will be shown to have a key role in hot crossflow ingestion.

7.2 Flow at the Film Hole Exit Plane Relating to Ingestion. The flow characteristics of the coolant exiting the film hole are greatly affected both by the flow inside the film hole and by the crossflow. The crossflow sees the exiting coolant as an obstacle and attempts to push the coolant from the direction of the injection angle to the streamwise direction. Along the upstream edge of the film hole, the angle of the exiting coolant is changed most by the crossflow, while the coolant along the downstream edge of the film hole is somewhat protected by the coolant along the upstream edge and remains closer to the injection angle. Figure 8(*a*) shows contours of the injection angle (α) at the FHEP for M = 1.25, *DR* = 1.60, and Re_{fh} = 17,350 (Case 1). The contours of $-\alpha$ in the figure show the presence and location of ingestion. If no crossflow was present and if the coolant diffused properly inside the film hole, the coolant would exit at the same injection angle as the film hole metal angle (35 deg at the *LE* and 20 deg at the *TE*).

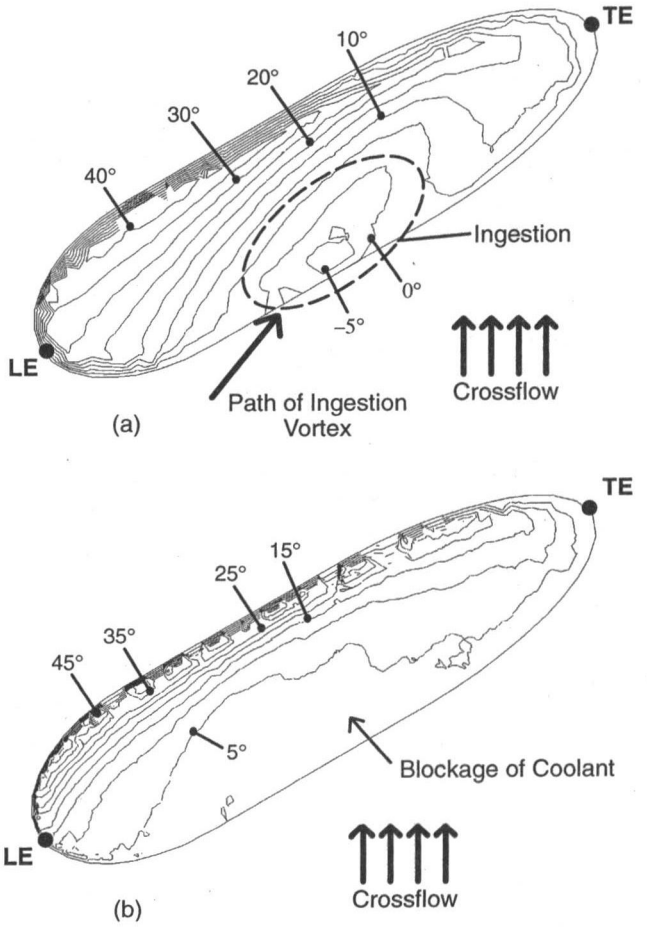

Fig. 8 Contours of α at FHEP show locations of ingestion and coolant blockage for *DR* = 1.60, Re_{fh} = 17,350, and (*a*) M = 1.25 and (*b*) M = 0.5

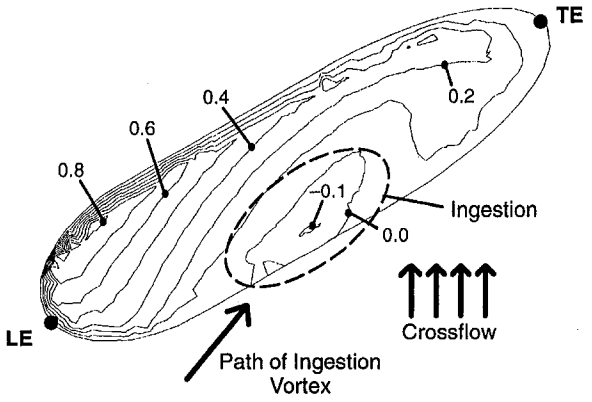

Fig. 9 Contours of VR_{YJ} at FHEP show location of ingestion for M = 1.25, DR = 1.60, and Re_{th} = 17,350

In contrast, the majority of the coolant along the upstream edge exits with $\alpha < 10$ deg. Any low-momentum coolant exiting the film hole is easily turned by the crossflow. Some of the low-momentum coolant along the upstream edge is immediately turned such that it does not even exit the film hole along this edge and thus is essentially blocked. The blocked coolant along the upstream edge must flow just under the FHEP to a location along the downstream edge where it can exit the film hole. In contrast, the jetting coolant near the *LE* offers the greatest resistance to the crossflow and penetrates farther into the crossflow with higher α. Figure 9 shows contours of the y component of velocity at the FHEP normalized by the mean jet velocity (VR_{YJ}) for Case 1. The areas of high and low α in Fig. 8(*a*) correspond to areas of high and low VR_{YJ} in Fig. 9. Contours of $-VR_{YJ}$ in the figure show the presence and location of ingestion. Both contours of α and VR_{YJ} at the FHEP can be used to show jetting, blockage, and ingestion.

Figure 10(*a*) shows contours of C_p along the test surface for Case 1. A high-pressure region is created upstream of the jetting coolant near the *LE*, where the crossflow impinges on the coolant. Since the jetting coolant has greater penetration into the crossflow than the low-momentum coolant and thus creates greater crossflow blockage, the center of the high-pressure region is located in front of the jetting coolant. This high-pressure region in Case 1 is great enough to cause the crossflow boundary layer to separate from the surface and form two legs of opposite rotating vorticity. These vorticity legs are analogous to horseshoe vortices that are formed by the rolling-up of the endwall boundary layer at the leading edge of an airfoil and endwall junction. One of the vorticity legs has positive x-vorticity ($+\zeta_x$) and wraps around the jetting coolant to the left of the *LE* (as viewed from upstream). The other vorticity leg has negative x-vorticity ($-\zeta_x$) and wraps around to the right of the jetting coolant (as viewed from upstream). This is not the first time that a horseshoe vortex structure has been observed in film cooling. Sgarzi and Leboeuf (1997) observed the formation of horseshoe vortices around a normally injected coolant jet. Figure 11 shows contours of ζ_x in a y–z plane at $x/D = -1$. The left vorticity leg ($+\zeta_x$) is squelched by strong $-\zeta_x$ emanating from the film hole boundary layer along the downstream edge near the *LE*. The right vorticity leg ($-\zeta_x$) becomes streamwise aligned, passes over the FHEP, and forms the "ingestion vortex," which is directly responsible for hot crossflow ingestion. The path of the ingestion vortex over the film hole can be tracked by examining contours of ζ_x at the FHEP as shown in Fig. 12. The ingestion vortex is marked by the trail of $-\zeta_x$ crossing the film hole. The $-\zeta_x$ along the downstream edge of the film hole originates in the film hole boundary layer. Any ζ_x originating in the film hole boundary layer along the upstream edge would be $+\zeta_x$. Thus, the $-\zeta_x$ that is identified in Fig. 12 as the ingestion vortex could not have come from the film hole boundary layer. The reason that no vorticity comes from the film hole boundary layer along most of the upstream edge is that the coolant is blocked from exiting the film hole along that edge, as explained above. Thus, the ingestion vortex must be coming from the crossflow boundary layer vorticity. When the ingestion vortex passes over the area of coolant blockage along the upstream side of the FHEP, it causes hot crossflow to dip below the FHEP. The path of the ingestion vortex in Fig. 12 coincides with the region of ingestion marked by values of $-\alpha$ in Fig. 8(*a*) and by values of $-VR_{YJ}$ in Fig. 9. The reason that the ingestion vortex does not cause ingestion along the downstream side of the FHEP is that the ingestion vortex is pushed up away from the FHEP by coolant exiting along the downstream edge. For further visualization of the ingestion vortex, Fig. 13(*a*, *b*) shows two views of the path lines of particles released in the

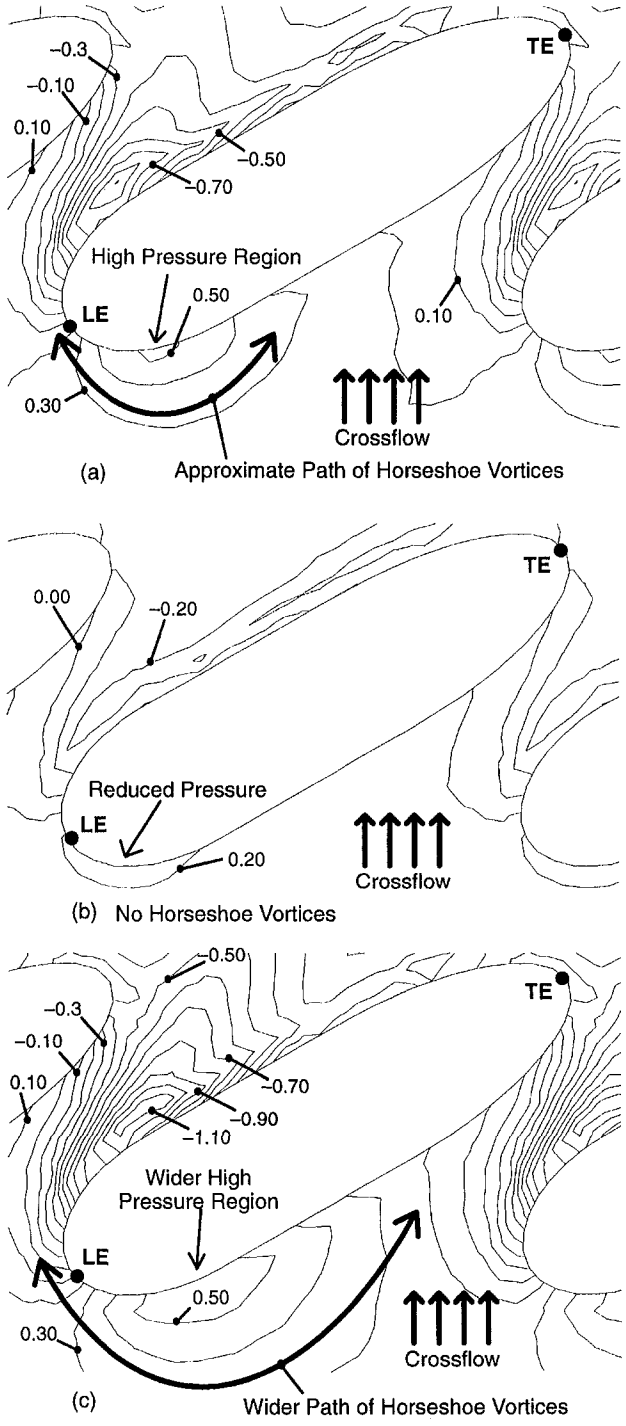

Fig. 10 Contours of C_p on wall outside film hole show effects of pressure for DR = 1.60, Re_{th} = 17,350, and (*a*) M = 1.25, (*b*) M = 0.5, and (*c*) M = 1.88

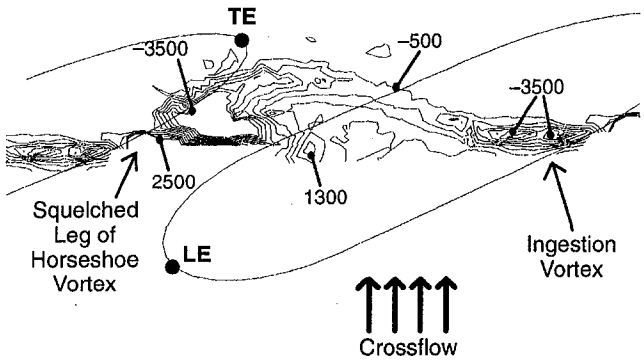

Fig. 11 Contours of ζ_x in y–z plane at $x/D = -1$ show the location of the ingestion vortex for M = 1.25, D = 1.6, Re_{th} = 17,350

crossflow boundary layer just upstream of the film hole. The path lines show the location and presence of the ingestion vortex, which has clockwise rotation ($-\zeta_x$) as viewed from downstream.

When no coolant jets out of the film hole, hot crossflow ingestion does not occur. Contours of α for M = 0.5, DR = 1.60, and Re_{th} = 17,350 (Case 4) in Fig. 8(b) and contours of VR_{YJ} for Case 4 in Fig. 14(c) show that neither jetting coolant at the LE nor hot crossflow ingestion is present. The contours of C_p on the metal surface surrounding the film hole for Case 4 in Fig. 10(b) show that the pressure in front of the LE of the film hole is significantly reduced in the absence of the jetting coolant. As a result, the crossflow boundary layer does not separate and the boundary layer vorticity is not reoriented. In general, any CASH configuration has potential for hot crossflow ingestion if the blowing ratio is large enough to cause strong jetting coolant at the leading edge of the film hole and if blockage of the coolant at the FHEP is found along the upstream edge.

7.3 Diffusion of Heat Inside the Film Hole. The ingested crossflow does not impinge on the metal surface inside the film hole, but nevertheless it causes heating of the surface near the TE. Figure 15(a) shows contours of the nondimensionalized temperature, θ, at the FHEP for Case 1. Inside the plenum, θ equals zero, so the value of θ is expected to be zero across the entire FHEP because of the presence of the coolant. On the contrary, Fig. 15(a) shows that a trail of high θ values, which show heating of the coolant inside the film hole, is associated with the path of the ingestion vortex at the FHEP. Near the TE the film hole becomes very shallow because of the diffusing section. Only a thin layer of low-momentum coolant protects the metal surface inside the film hole from the ingested hot crossflow. The blocked low-momentum coolant absorbs heat from the ingested crossflow while it is flowing just underneath the FHEP from the blocked upstream edge to

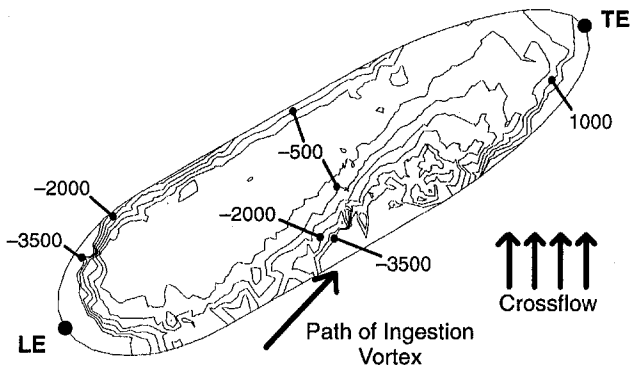

Fig. 12 Contours of ζ_x at FHEP show path of ingestion vortex with $-\zeta_x$ along upstream edge of film hole for M = 1.25, D = 1.60, and Re_{th} = 17,350

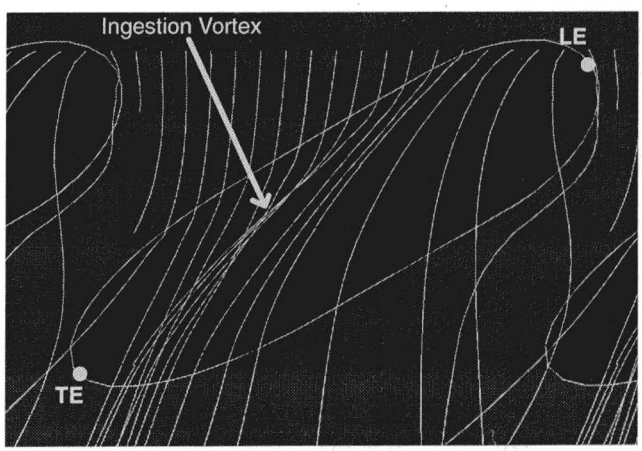

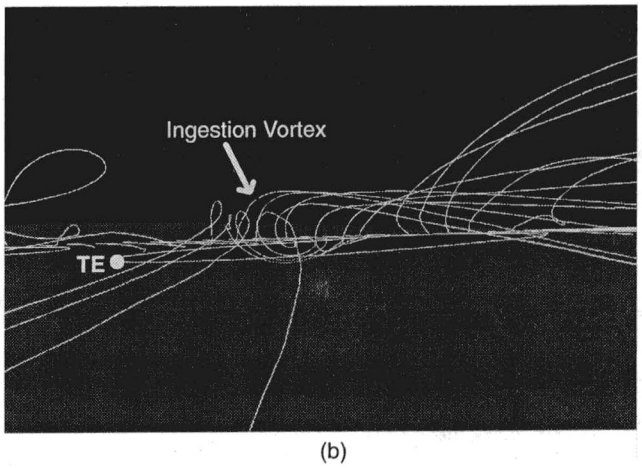

Fig. 13 Path lines of particles released in the crossflow boundary layer just upstream of the film hole for M = 1.25, DR = 1.60, and Re_{th} = 17,350. Viewing angle is (a) from above and (b) from downstream.

the downstream edge where it can exit the film hole. Normally the transfer of heat due to convection dominates the diffusion of heat, but the blockage of the coolant hampers convection out of the film hole. Because the heat absorbed by the blocked coolant is not quickly convected from the film hole, diffusion is able to transfer heat to the shallow bottom surface of the film hole near the TE. Closer to the center of the FHEP, where the bottom surface is much deeper and is separated from the FHEP by a thicker and higher momentum layer of coolant, heat is not able to diffuse down to the surface. Contours of θ on the film hole wall itself for Case 1 are displayed in Fig. 16(a). As shown, there is a significant increase in the temperature of the film hole wall near the TE, with θ reaching almost 0.7. In addition there is a very large and undesirable temperature gradient on the metal surface along the upstream edge inside the film hole.

The heating of the metal surface inside the film hole occurs even when hot crossflow ingestion is absent. Figure 17 shows path lines of coolant starting inside the film hole for Case 4, which has no ingestion. Because of the blockage (shown by VR_{YJ} contours in Fig. 14(c) and by α contours in Fig. 8(b)), the coolant cannot come straight out of the film hole but must flow underneath the FHEP to the downstream edge where it can exit. This blocked coolant coflows with the hot crossflow that is just on top of the FHEP, which allows diffusion to transfer heat from the crossflow to the coolant before it exits the film hole. Contours of θ at the film hole exit plane for Case 4 (Fig. 15(b)) show that the coolant is extensively heated by the crossflow over much of the film hole. As previously discussed, the heat continues to diffuse into the film hole and reaches the shallow bottom surface near the TE. Figure

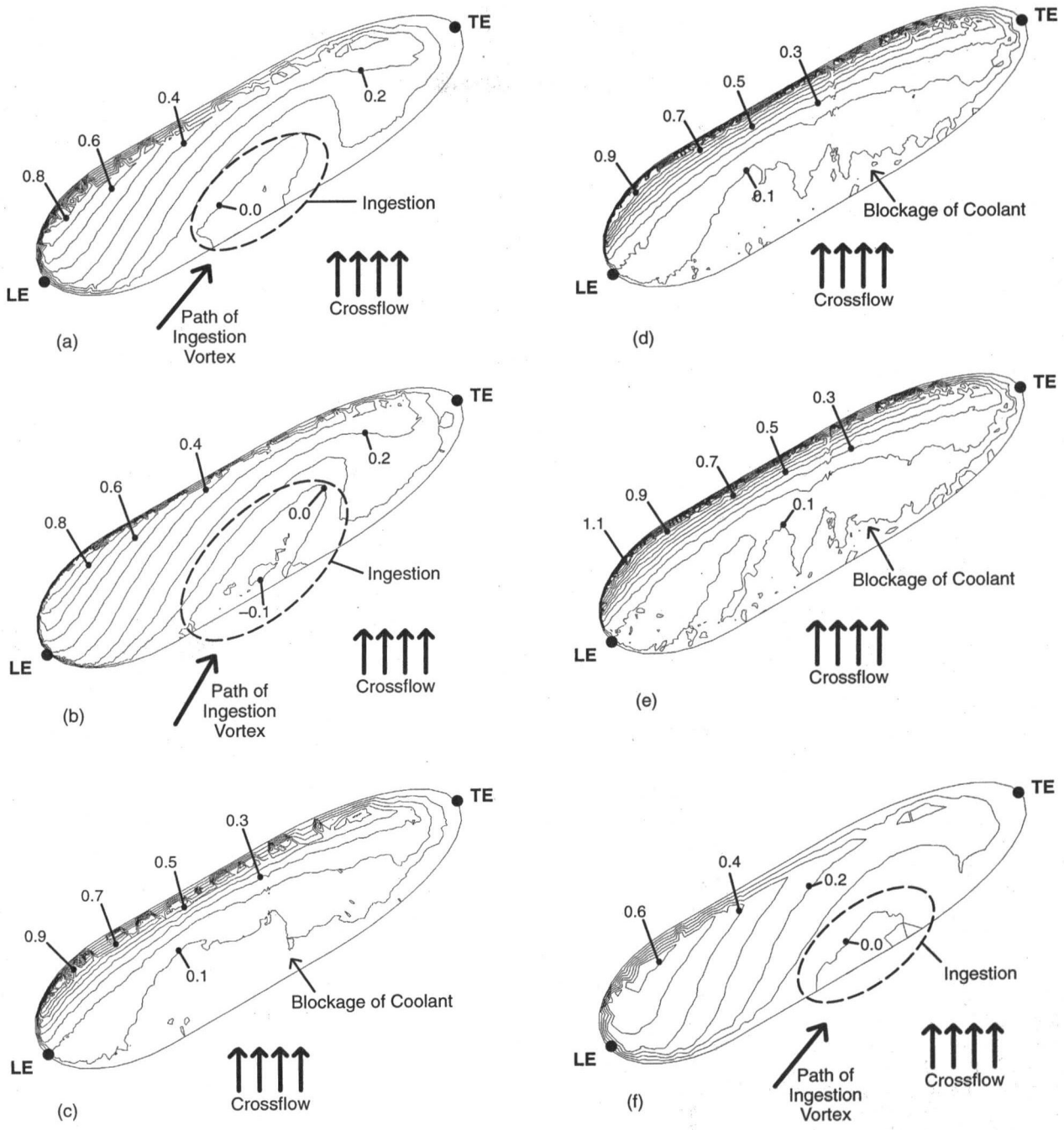

Fig. 14 Contours of VR_{YJ} at FHEP show locations of crossflow ingestion and blockage of coolant for: (*a*) M = 1.25, *D* = 2.0, Re_{th} = 17,350; (*b*) M = 1.25, *D* = 1.60, Re_{th} = 35,000; (*c*) M = 0.5, *DR* = 1.60, Re_{th} = 17,350; (*d*) M = 0.5, *DR* = 2.0, Re_{th} = 17,350; (*e*) M = 0.5, *DR* = 2.0, Re_{th} = 70,000; and (*f*) M = 1.88, *DR* = 1.60, Re_{th} = 17,350

17(*b*) shows path lines of particles released from a vertical line inside the film hole very close to the upstream edge. Same as before, the coolant does not exit along the upstream edge, but instead flows under the FHEP to the downstream edge where it exits. In addition, the path lines show that some of the coolant (marked in Fig. 17(*b*)) travels just under the FHEP for a significant distance along the upstream edge to the *TE*. This coolant experiences extensive exposure to the hot crossflow, and is greatly heated. The heat then easily diffuses through the coolant to the very shallow film hole surface nearby, which is shown by the exceptionally high values and gradients of θ located along the upstream edge in Fig. 16(*b*). This phenomenon poses a threat to the integrity of the metal and is a function of the CASH geometry, occurring regardless of the blowing ratio, density ratio, and film hole Reynolds number. All seven of the present test cases have heating of the metal surface inside the film hole because they all have coolant blockage, as seen by contours of VR_{YJ} in Figs. 9 and 14(*a–f*). The regions of ingestion in Figs. 9, 14(*a*), 14(*b*), and 14(*f*) merely represent blocked coolant regions with an ingestion vortex on top. These observations concerning the diffusion of heat into the film hole are important because most film cooling design is done with the assumption that convection dominates diffusion. This assumption would lead to the oversight of undesirable temperature gradients on the metal surface inside the film hole for a CASH geometry with coolant blockage.

7.4 Effects of Blowing Ratio on Ingestion. In the present research the blowing ratio was varied from 0.5 (Case 4) to 1.25

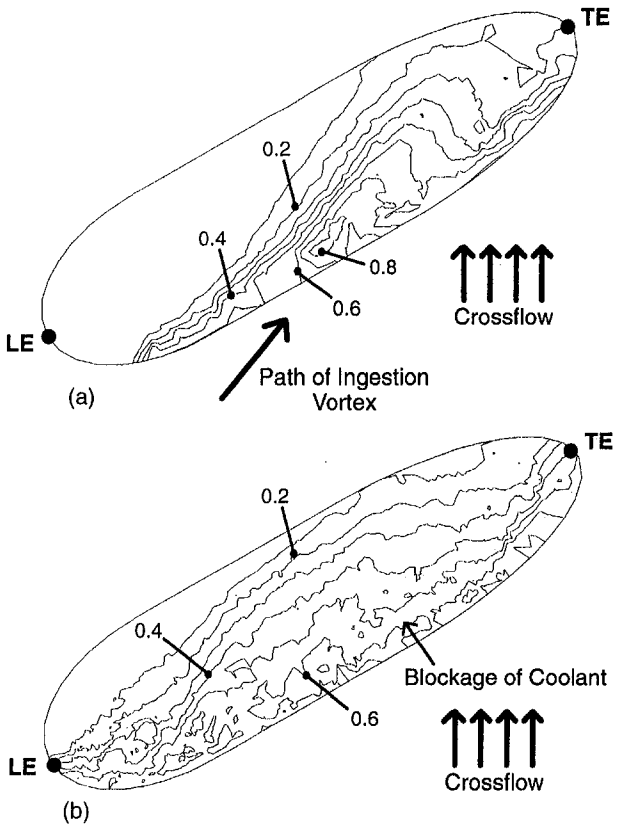

Fig. 15 Contours of θ at the FHEP show heating of coolant inside film hole for DR = 1.60, Re_{fh} = 17,350, (*a*) M = 1.25 and (*b*) M = 0.5

(Case 1) and to 1.88 (Case 7) while all other variables were held constant. Blockage of the low-momentum coolant along the upstream edge is present for all three blowing ratios (Figs. 9, 14(*c*), and 14(*f*)), but the effect on crossflow ingestion for the change in blowing ratio from M = 0.5 to M = 1.25 is significant. The blowing ratio has an effect on ingestion because it controls the strength of the jetting coolant, and at M = 0.5, no jetting coolant is present (Fig. 14(*c*)). The absence of the jetting coolant means that the crossflow boundary layer vorticity is not reoriented at the *LE*, and no ingestion vortex is formed. The fact that the ingestion disappears at the low blowing ratio is counterintuitive, since the relative amount of coolant exiting the film hole is less. At both M = 1.25 (Fig. 9) and M = 1.88 (Fig. 14(*f*)), jetting coolant is present along with crossflow ingestion. When M = 1.25 the VR_{YJ} minimum is approximately −0.2, whereas when M = 1.88 the minimum VR_{YJ} is only −0.1. In addition, the actual area of the ingestion is smaller when M = 1.88 than when M = 1.25. The reason is that the overall area of the jetting coolant is larger when M = 1.88, which from the viewpoint of Fig. 14(*f*), pushes the ingestion vortex farther to the right. The wider area of jetting coolant produces a wider high-pressure region in front of the *LE*, as shown in Fig. 10(*c*), which spreads the vorticity legs farther apart in comparison to the smaller area of jetting coolant when M = 1.25 (Fig. 10(*a*)). Despite the fact that the actual crossflow ingestion seems to be less when M = 1.88 than when M = 1.25, a comparison of the contours of θ on the film hole surface shows no differences. The reason is that the part of the film hole surface next to the *TE* is closest to the FHEP and thus is closest to the ingested crossflow. Therefore, the difference in position of the ingestion for the two blowing ratios does not affect how much heat is able to diffuse to the film hole wall.

7.5 Effects of Density Ratio on Ingestion. The range of density ratios used in gas turbines is fairly narrow. The two density ratios of DR = 1.60 and DR = 2.0, which represent the typical range used in industry, are examined in this paper. The effects of the density ratio are compared at two different blowing ratios. Cases 1 and 2 are used for the purpose of comparing the density ratios when M = 1.25. Cases 4 and 5 are used for the purpose of comparing the density ratios when M = 0.5. The effect of the density ratio on ingestion was found to be negligible. The contours of VR_{YJ} are very similar between Figs. 9 and 14(*a*) (Cases 1 and 2) and between Figs. 14(*c*) and 14(*d*) (Cases 4 and 5). In addition, the density ratio does not have a significant effect on the diffusion of heat to the metal surface inside the film hole, since it does not affect coolant blockage.

7.6 Effects of Film Hole Reynolds Number on Ingestion. The baseline film hole Reynolds number for the current test cases was 17,350. This number was doubled (Re_{fh} = 35,000) in Case 3, which has the same M and DR as Case 1, and was quadrupled (Re_{fh} = 70,000) in Case 6, which has the same M and DR as Case 5. In Case 3, the increased Reynolds number somewhat changes the shape of the ingestion region due to increased crossflow boundary layer vorticity (Fig. 14(*b*)), but the effect on θ on the metal inside the film hole is not noteworthy. Case 6 shows almost no differences when compared to Case 5 in Fig. 14(*d*, *e*). Thus, the effects of the film hole Reynolds number on crossflow ingestion and on diffusion of heat into the film hole seem to be minimal in comparison to the effects of the blowing ratio.

8 Discussion

Coolant blockage is a key issue for CASH configurations. When the coolant exiting any film hole along the upstream edge has low

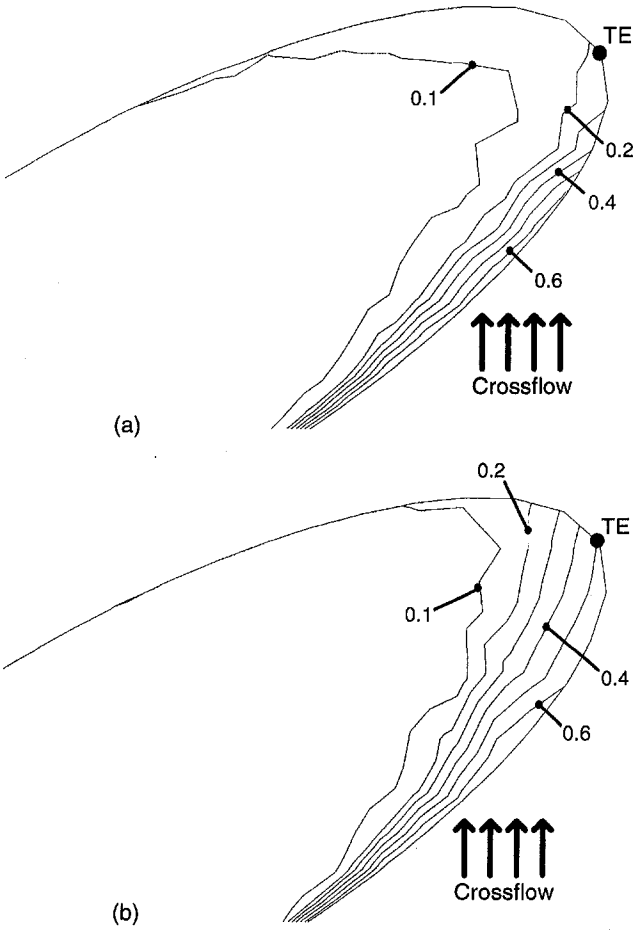

Fig. 16 Contours of θ on metal surface inside film hole show heating of the metal as a result of diffusion for: (*a*) M = 1.25, D = 1.60, Re_{fh} = 17,350; (*b*) M = 0.5, D = 1.60, Re_{fh} = 17,350

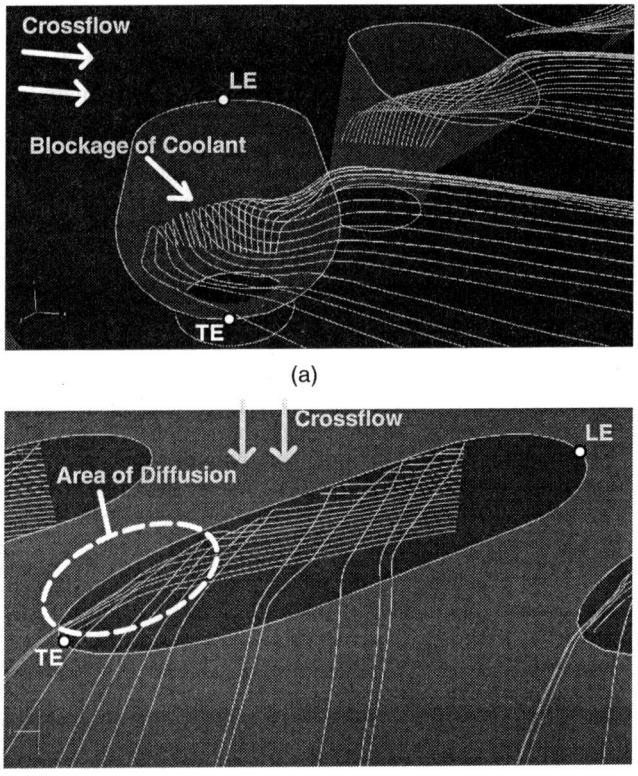

Fig. 17 Pathlines of coolant for M = 0.5, *DR* = 1.60, and Re_{fh} = 17,350, (*a*) released from a horizontal line in the middle of the film hole, and (*b*) released from a vertical line on the upstream side

momentum, blockage of the coolant at the FHEP is likely to occur. In most streamwise-injected configurations, the coolant along the upstream edge has fairly high momentum and is not blocked by the crossflow. A good example is the streamwise-aligned forward-diffused shaped hole (FDIFF) studied by Hyams and Leylek (1997). FDIFF was shown to have coolant with low *VR* exiting near the *TE*, while coolant with higher *VR* exited near the *LE*. Unlike FDIFF60, FDIFF had no coolant blockage, because the low-momentum coolant at the *TE* was protected from the crossflow by the higher momentum coolant at the *LE*. When the compound angle is added to the FDIFF geometry to form the FDIFF60 configuration, the low-momentum coolant at the *TE* is no longer protected from the crossflow. The result is coolant blockage and diffusion of heat into the film hole along the upstream edge. Another problem of coolant blockage is that it allows hot crossflow ingestion. If the FDIFF60 geometry did not have coolant blockage, vorticity exiting the film hole on the upstream side would have been opposite the vorticity that formed the ingestion vortex and most likely would have squelched the vortex just like the $+\zeta_x$ was squelched on the other side of the jetting coolant.

9 Conclusions

- Hot crossflow ingestion is caused by the ingestion vortex, which is formed from upstream crossflow boundary layer vorticity that is reoriented by the presence of jetting coolant at the *LE* of the film hole. Thus, ingestion does not occur when there is no coolant jetting out of the film hole at the *LE*, and the crossflow merely goes over the coolant.
- The blowing ratio has a major effect on ingestion since it affects the presence and size of the jetting coolant and the low-momentum regions within the film hole. Increasing the blowing ratio increases jetting of coolant out of the film hole, which leads to ingestion.
- The density ratio and the film hole Reynolds number have minimal effect on crossflow ingestion.
- The addition of the compound angle to a film hole geometry exposes more of the FHEP to the path of the crossflow, and increases the chance that low-momentum coolant exiting the film hole will be blocked along the upstream edge of the FHEP by the crossflow.
- If a film hole is shallow underneath an area of coolant blockage at the FHEP, heat may diffuse to the metal surface inside the film hole and create undesirable high temperature levels and gradients on the metal.
- The location of hole diffusion is important when a film hole exit is expanded to increase the area ratio. The diffusing location must be placed adjacent to jetting coolant in order for the configuration to become an effective diffuser of coolant momentum.
- Properly validated CFD models offer a powerful predictive tool for CASH configurations. In addition, CFD can be an effective research tool that can be used in conjunction with experiments to understand flow physics.

Acknowledgments

The authors would like to convey special thanks to Robert A. Brittingham for his cooperation in this research.

References

Brittingham, R., and Leylek, J., 1997, "A Detailed Analysis of Film Cooling Physics; Part IV: Compound-Angle Injection With Shaped Holes," ASME Paper No. 97-GT-272.

Hyams, D., and Leylek, J., 1997, "A Detailed Analysis of Film Cooling Physics; Part III: Streamwise Injection With Shaped Holes," ASME Paper No. 97-GT-271.

Leylek, J., and Zerkle, R., 1994, "Discrete-Jet Film Cooling: A Comparison of Computational Results With Experiments," ASME JOURNAL OF TURBOMACHINERY, Vol. 116, pp. 358–368.

McGovern, K., and Leylek, J., 1997, "A Detailed Analysis of Film Cooling Physics; Part II: Compound-Angle Injection With Cylindrical Holes," ASME Paper No. 97-GT-270.

Schmidt, D., 1995, "Effects of Injection Hole Geometry, Surface Roughness, and Freestream Condition on Film Cooling," Ph.D. Dissertation, University of Texas at Austin.

Schmidt, D., Sen, B., and Bogard, D., 1996, "Film Cooling With Compound Angle Holes: Adiabatic Effectiveness," ASME JOURNAL OF TURBOMACHINERY, Vol. 118, pp. 807–813.

Sen, B., Schmidt, D., and Bogard, D., 1996, "Film Cooling With Compound Angle Holes: Heat Transfer," ASME JOURNAL OF TURBOMACHINERY, Vol. 118, pp. 800–806.

Sgarzi, O., and Leboeuf, F., 1997, "Analysis of Vortices in Three-Dimensional Jets Introduced in a Cross-Flow Boundary-Layer," ASME Paper No. 97-GT-517.

Thole, K., Gritsch, M., Schulz, A., and Wittig, S., 1998, "Flowfield Measurements for Film-Cooling Holes With Expanded Exits," ASME JOURNAL OF TURBOMACHINERY, Vol. 120, pp. 327–336.

Walters, D., and Leylek, J., 1997a, "A Systematic Computational Methodology Applied to a Three-Dimensional Film-Cooling Flowfield," ASME JOURNAL OF TURBOMACHINERY, Vol. 119, pp. 777–785.

Walters, D., and Leylek, J., 1997b, "A Detailed Analysis of Film Cooling Physics; Part I: Streamwise Injection With Cylindrical Holes," ASME Paper No. 97-GT-269.

H. J. Seo
Graduate Student.

J. S. Lee
Professor.
Mem. ASME

Turbo and Power Machinery Research Center,
Department of Mechanical Engineering,
Seoul National University,
Seoul 151-742, Korea

P. M. Ligrani
Professor,
Convective Heat Transfer Laboratory,
Department of Mechanical Engineering,
University of Utah,
Salt Lake City, UT 84112
Mem. ASME

Effects of Bulk Flow Pulsations on Film Cooling From Different Length Injection Holes at Different Blowing Ratios

Bulk flow pulsations in the form of sinusoidal variations of velocity and static pressure at injectant Strouhal numbers from 0.8 to 10.0 are investigated as they affect film cooling from a single row of simple angle holes. Similar flow variations are produced by potential flow interactions and passing shock waves near turbine surfaces in gas turbine engines. Time-averaged temperature distributions, phase-averaged temperature distributions, adiabatic film cooling effectiveness values, and iso-energetic Stanton numbers show that important alterations to film cooling protection occur as pulsation frequency, coolant Strouhal number, blowing ratio, and nondimensional injection hole length are changed. Overall, the pulsations affect film performance and behavior more significantly both as L/D decreases, and as blowing ratio decreases.

Introduction

Film cooling flows on turbine surfaces are subject to bulk flow pulsations and other timewise flow variations because of the relative motion of adjacent blade rows and overall arrangement of gas turbine engine components. In transonic turbine passages, such unsteadiness is due to: (*i*) passing families of shock waves, (*ii*) potential flow interactions, (*iii*) passing wakes, and (*iv*) random (and sometimes periodic) free-stream turbulence from the combustion chamber.

Of these different modes of unsteadiness, the dramatic effects of potential flow interactions and passing shock waves in altering the protection nominally provided by film cooling are described by Abhari and Epstein (1994), Abhari (1996), and Ligrani et al. (1996a, b, 1997a, b). Both of these modes of unsteadiness result in important variations of the *static* pressure near turbine airfoil surfaces as blade rows move relative to each other. As a result of such *static* pressure variations at hole exits, the film flow rate and film momentum change instantaneously, which causes film concentrations and film trajectories to move to and from the wall with each imposed bulk flow pulsation (Ligrani et al., 1996a). These then act to alter the time-averaged position of the film and mean-injectant trajectory as the pulsations act to spread the same amount of injectant over a larger volume (Ligrani et al., 1996a). Such changes to *time-averaged* film cooling protection and flow structure have important consequences regarding design of film cooling systems for turbine surfaces. Similar disruptions to instantaneous film flow rates are not produced by the *total* pressure variations (from passing wakes, for example) because changing the total pressure (with constant static pressure) over hole exit planes does not change instantaneous film flow rates.

In an investigation of rotor heat transfer in a short-duration blow-down turbine test facility, Abhari and Epstein (1994) indicate that flow pulsations cause the time-averaged heat transfer rate to increase by 12 percent on the suction surface and to decrease by 5 percent on the pressure surface compared with values measured with no pulsations. Two rows of holes are employed on the suction surface of the rotor blade with blowing ratios from 0.96 to 1.24, and three rows of holes are employed on the pressure surface with blowing ratios from 1.1 to 1.52. Abhari (1996) later predicted time-averaged magnitudes of unsteady surface heat flux on the pressure surface of a similarly cooled rotor blade, which are 230 percent greater than steady-state predictions. This is attributed to reductions of adiabatic film effectiveness by as much as 64 percent.

The present study employs different experimental conditions than the ones investigated by Ligrani et al. (1996a, b, 1997a, b). A higher value of dimensional pulsation frequency (32 Hz) is employed here. In addition, blowing ratios are 0.5 and 1.0, compared to 0.5 in the previous investigations. These values of pulsation frequency and blowing ratio are investigated because they give coolant Strouhal numbers from 0.8 to 10, which covers the range of St_C values employed in many operating engines. Because of their importance to film cooling system design, film cooling performance and behavior, downstream of holes with three different L/D values of 1.6, 4.0, and 10, are investigated. These values are chosen for investigation to illustrate the different effects of pulsations as L/D is changed, and because the smallest two values bracket the range of values used in many current engines. Time-averaged temperature distributions, phase-averaged temperature distributions, adiabatic film cooling effectiveness values, and iso-energetic Stanton numbers are presented. The authors know of no other studies that focus on the combined influences of pulsations, L/D, and blowing ratio. The results are of fundamental importance, of importance to individuals developing numerical models of pulsating film cooling flows, and of importance to designers of film cooling systems.

Experimental Apparatus, Procedures, and Conditions

As in the recent investigations by Ligrani et al. (1996a, b, 1997a, b), the present experiment is conducted on a large-scale, flat plate test section with low speeds and constant properties to allow detailed probing of flow features (which is impossible in an actual engine environment), and to isolate the L/D interactions between the film cooling, imposed pulsations, and boundary layer. Parameters are scaled so that nondimensional forms match turbine operating conditions, including $\bar{m}$, $\bar{U}_c/\bar{U}_\infty$, St_c, St_∞, L/D, x/D, δ/D, Re_c, Re_x, hole angle, hole geometry, and nondimensional spanwise hole spacing.

The wind tunnel is an open circuit and subsonic, with a 6.25:1 contraction ratio nozzle. The nozzle leads to the test section, which

Contributed by the International Gas Turbine Institute and presented at the 43rd International Gas Turbine and Aeroengine Congress and Exhibition, Stockholm, Sweden, June 2–5, 1998. Manuscript received by the International Gas Turbine Institute February 1998. Paper No. 98-GT-192. Associate Technical Editor: R. E. Kielb.

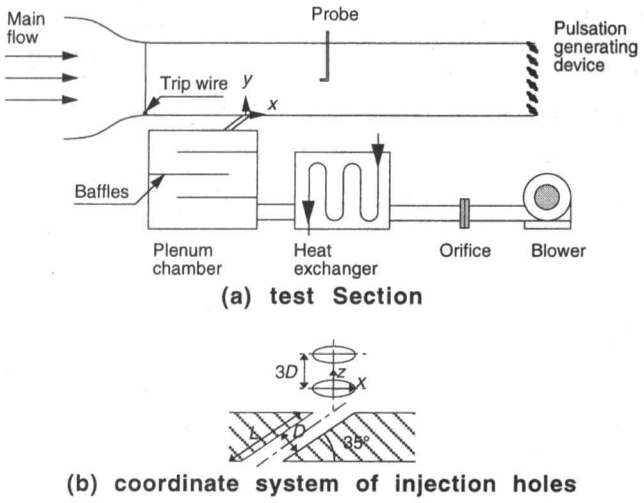

Fig. 1 Schematic drawing of test section and coordinate system

is a rectangular duct 3.0 m long and 0.4 m wide. At a free-stream velocity of 10 m/s, flow at the test section inlet shows excellent spatial uniformity, free-stream streamwise velocity variations less than 0.5 percent, and a free-stream turbulence level less than 0.2 percent. A schematic of the test section, including the coordinate system and injection hole arrangement, is shown in Fig. 1. A boundary layer trip is located on the test plate just downstream of the nozzle exit to trip the boundary layer so that it becomes fully turbulent. The center of the injection holes is located 24 hole diameters downstream of the trip. Hole diameter D is 25 mm. The five film cooling holes are placed in a single row with spanwise spacing of three hole diameters. Each hole is oriented in a streamwise/normal plane (i.e., with a simple angle orientation) inclined at 35 deg angle from the test surface. No trips are used near the hole entrances as they were in the Ligrani et al. (1996a, b, 1997a, b) investigations. The air used for the injectant first flows through an orifice followed by a heat exchanger and a plenum chamber. Pressure drops across the orifice plate are measured to deduce injectant mass flow rates. The heat exchanger provides means to heat the injectant above ambient temperature. The interior dimensions of the plenum chamber, which supplies injectant to the film holes, are 0.58 m by 0.48 m by 0.12 m. Film hole entrances are located on the side of the plenum with the largest surface area, located on the top.

Table 1 Strouhal numbers for nonzero pulsation frequencies

$\bar{m}$	L/D	St_c	St_∞
0.5	1.6	1.6	0.51
	4.0	4.0	
	10.	10.	
1.0	1.6	0.8	
	4.0	2.0	
	10.	5.0	

The Reynolds number, $Re = \bar{U}_\infty X/\nu$, at the hole center is 614,000, where X is measured from the leading edge of the trip. Ratios of boundary layer thickness to hole diameter, displacement thickness to hole diameter, and momentum thickness to hole diameter at the same location are 1.02, 0.12, and 0.08, respectively. The magnitude of the von Karman shape factor at this location is 1.43. Time-averaged blowing ratios $\bar{m}$ of 0.5 and 1.0 are employed. Corresponding injectant Reynolds numbers, $Re_c = \bar{U}_c D/\nu$, are 7800 and 15,600, respectively. The ratio of injectant to free-stream density is approximately 0.93 for the injectant surveys. Injectant and free-stream Strouhal numbers are listed in Table 1. Ratios of injection hole length to hole diameter, L/D, are 1.6, 4.0, and 10. Pulsation frequencies are 0 and 32 Hz. At a pulsation frequency of 32 Hz, the free-stream Strouhal number is 0.51. Injectant Strouhal numbers then range from 0 to 10.0.

A 5-μm-dia single hot-wire probe, operated with a constant-temperature anemometer bridge, is used to measure free-stream velocity pulsations and injectant velocity profiles at the hole exit. The U velocity component is measured in the film cooled boundary layer using a cross-wire probe, also with 5-μm-dia sensing wires, and driven using constant temperature anemometer bridges. These hot-wire probes are calibrated in the wind tunnel free-stream, including yaw calibrations used to determine effective angles of the two sensors in the crossed-wire probe. The frequency response of the electronic components of these constant temperature anemometry systems is about 20 kHz.

A 1-μm-dia cold-wire probe, driven by a constant current anemometer bridge system, is used to measure instantaneous temperature distributions, which are correlated to injectant distributions.

Nomenclature

D = injection hole diameter
f = pulsation frequency
L = injection hole length
$\bar{m}$ = time-averaged blowing ratio = $\rho_c \bar{U}_c/\rho_\infty \bar{U}_\infty$
$\dot{q}''_o$ = surface heat flux with no film cooling
$\dot{q}''$ = spanwise-averaged surface heat flux with film cooling
Re_c = coolant Reynolds number = $\bar{U}_c D/\nu$
Re_x = free-stream Reynolds number = $\bar{U}_\infty X/\nu$
St_c = injectant Strouhal number = $2\pi f L/\bar{U}_c$
St_∞ = free-stream Strouhal number = $2\pi f \delta/\bar{U}_\infty$
$St_{f,c}$ = centerline iso-energetic Stanton number
$St_{f,m}$ = spanwise-averaged iso-energetic Stanton number
St_o = baseline Stanton number with no pulsations and no film cooling
t = time
T = instantaneous temperature
U = instantaneous streamwise velocity
x, X, y, z = coordinate system
δ = boundary layer thickness
η = local adiabatic film cooling effectiveness = $(\bar{T}_{aw} - \bar{T}_\infty)/(\bar{T}_c - \bar{T}_\infty)$
η_c = centerline adiabatic film cooling effectiveness = $(\bar{T}_{aw,c} - \bar{T}_\infty)/(\bar{T}_c - \bar{T}_\infty)$
η_m = spanwise-averaged adiabatic film cooling effectiveness = $(\bar{T}_{aw,m} - \bar{T}_\infty)/(\bar{T}_c - \bar{T}_\infty)$
θ = dimensionless temperature = $(\bar{T} - \bar{T}_\infty)/(\bar{T}_c - \bar{T}_\infty)$
ν = kinematic viscosity
τ = pulsation period

Superscripts

$^-$ = time-averaged
$^\sim$ = phase-averaged
$'$ = fluctuating component

Subscripts

aw = adiabatic wall
c = centerline, or injectant at the exit planes of the holes
m = spanwise-averaged
∞ = free-stream

The frequency response of the electronic components of this constant current system is better than 1 kHz. Steady-state calibrations of the cold wire system are performed using a platinum resistance thermometer (with a relative error of 0.1 percent) as a reference. Time-averaged quantities are obtained using a multimeter with a resolution of 10 nV, which corresponds to a measurement error of ±0.05°C. Time-varying velocities, temperatures, and pressures are recorded using a digital data acquisition system, which includes a multiplexer and an analog-to-digital converter.

Phase-averaged quantities are deduced from instantaneous temperature and velocity time records using a decomposition based on the three different types of timewise variation experienced by the flow. With imposed periodic flow, the instantaneous temperature T is decomposed using an equation of the form

$$T = \bar{T} + \tilde{T} + T' \tag{1}$$

where $\bar{T}$ is the time-averaged temperature, $\tilde{T}$ is the phase-averaged periodic component, and T' is the fluctuating component. A similar approach is used to decompose the instantaneous streamwise velocity. The time period used in the determination of phase-averaged values is based on the angular speed of the encoder of the motor used to drive the rotating shutter blades, which are used to pulsate the flow. One motor rotation corresponds to two flow pulsation periods. Signals from more than 500 flow pulsation periods are ensemble averaged to obtain each phase average. Data are sampled digitally to obtain 500 data points over each flow pulsation period. Individual phase-averaged wave forms are determined at 100 equally spaced times through each flow pulsation period.

Adiabatic film cooling effectiveness distributions are determined from measurements of the free-stream temperature, the injectant temperature and distributions of the surface temperature measured using 96 T-type thermocouples installed along the test surface. Next to the air stream, this test surface is 25 μm thick stainless steel foil. A 12.7 mm thick Lexan plate is attached just beneath the foil. Beneath this, 50 mm of styrofoam is used as an insulator. Injectant temperatures are measured in the injectant plenum chamber near the inlet of one of the injection holes. Each of these tubes is well insulated to minimize heat transfer to or from the injectant, and to minimize temperature changes between the entrance and exit of each tube.

Iso-energetic Stanton numbers are measured when the test surface is heated. The same test surface used to obtain the adiabatic effectiveness measurements is employed and thus, the same 96 thermocouples measure surface temperatures used to compute surface heat transfer coefficients and Stanton numbers. A constant heat flux boundary condition is provided by passing current through the 25-μm-thick stainless steel foil located next to the air stream. To maintain an iso-energetic condition, injectant and freestream temperatures are maintained at the same value for each test. Radiation losses are determined analytically. Energy balances, used to estimate the amount of convection from the test plate to the air stream above, show that conduction losses from beneath the test surface are negligible compared to the power supplied to the foil heater.

Uncertainty estimates are determined based on 95 percent confidence levels using the method described by Kline and McClintock (1953). The temperature measurement error is less than 0.05°C. This gives 5.0 percent of uncertainty in the dimensionless temperature θ, and an uncertainty of the local film cooling effectiveness η of about 7.1 percent. The uncertainty of the iso-energetic heat transfer coefficient (used to determine the iso-energetic Stanton number) is 3.9 percent.

Generation and Characteristics of Flow Pulsations

Static pressure pulsations are produced by an array of six shutter blades, which are driven by a DC motor and a timing belt, and extend across the span of the exit of the wind tunnel test section.

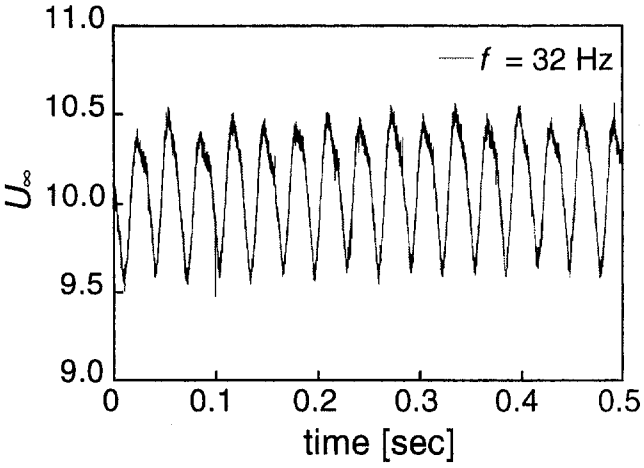

Fig. 2 Typical instantaneous free-stream velocity wave form characteristics for f = 32 Hz

Periodic blockage is produced by the shutter blades as they rotate. Their sizes relative to the cross-sectional area of the test section exit set the amplitudes of the imposed flow pulsations. Each shutter has 25.0 mm width (which, when perpendicular to the flow, gives maximum blockage), and 1.5 mm thickness (for minimum blockage) across the 0.28 m high by 0.4 m wide exit area. This gives a ratio of maximum blockage area to the total open test section area of 0.53. This arrangement produces free-stream pulsation amplitudes, $(\tilde{U}_{\infty,\max} - \tilde{U}_{\infty,\min})/2\bar{U}_\infty$, of about 4.4 percent at a pulsation frequency of 32 Hz. This, and the periodic character of the instantaneous free-stream velocity $\tilde{U}_\infty$ pulsating at 32 Hz, are illustrated in Fig. 2.

Rotating vanes are employed to provide flow pulsations in the present study because: (*i*) The shutters oscillate the static pressure without significant total pressure variations (Karlsson, 1959; Al-Asmi and Castro, 1993); (*ii*) static pressure pulsations produce the most important disruptions to the flow rates, trajectories, and distributions of the film coolant (Abhari and Epstein, 1994; Abhari, 1996; Ligrani et al., 1996a, b, 1997a, b); (*iii*) much higher frequencies of pulsation can be produced than with many other methods (Al-Asmi and Castro, 1993); and (*iv*) deterministic sinusoidal variations of static pressure can be produced at selected frequencies (Karlsson, 1959).

According to Abhari and Epstein (1994), adjustment of coolant flow rates is characterized by the product of coolant flow Mach number M_c and coolant Strouhal number $St_c = 2\pi fL/\bar{U}_c$. These investigators additionally indicate that temporal pressure variations influence the coolant mass flow rate when the disturbance passing frequency is low compared with the time required for the flow to pass through the coolant holes. This occurs if the product of coolant flow Mach number M_c and coolant Strouhal number is about 1 or less ($M_c St_c < 1$). Values range from 0.2 to 0.6 in operating transonic turbines, which gives St_c from 0.2 to 6.0. Results from the present study, wherein St_c ranges from 0 to 10, provide evidence that other parameters also have important effects on film cooling subject to bulk flow pulsations.

Recent experiments by Ligrani et al. (1996a) show two different types of injectant flow behavior whose existence is dependent upon the magnitude of St_c. For the single L/D ratio of 4 employed in that study, magnitudes of St_c less than $1 \sim 2$ correspond to quasi-steady behavior, and magnitudes of St_c greater than $1 \sim 2$ correspond to non-quasi-steady behavior, regardless of the magnitude of the blowing ratio. Quasi-steady film distributions are the same as the steady distribution that would exist at the same instantaneous flow condition. With non-quasi-steady film behavior, multiple pulsations are imposed on the injectant over the time period required for it to pass through a film hole. As a result, portions of the film oscillate in ways different from adjacent

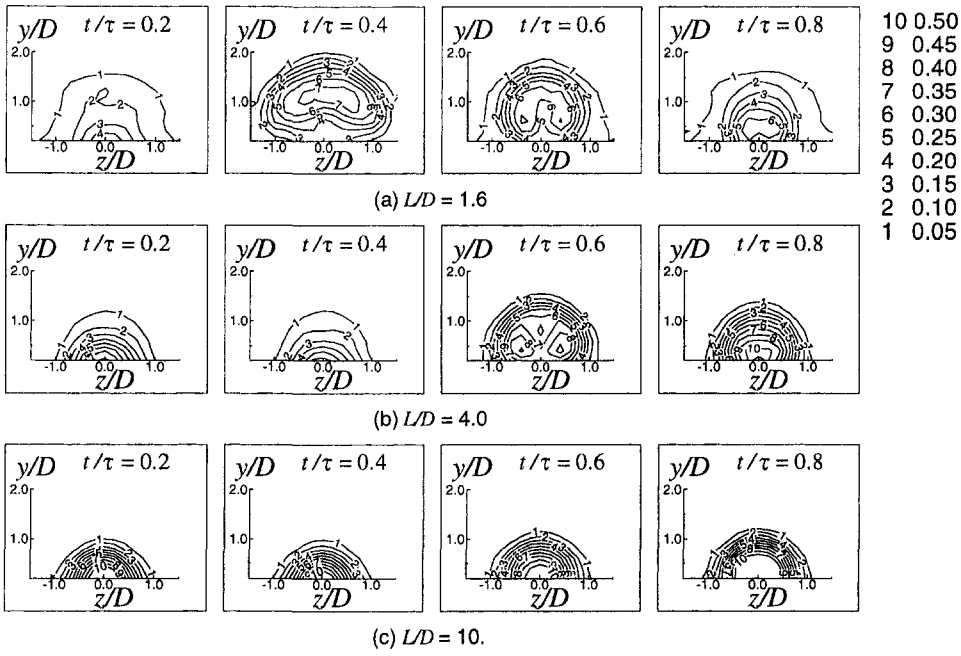

Fig. 3 Phase-averaged injectant concentration distributions θ at $x/D = 5.0$ for $\bar{m} = 0.5$: (*a*) $L/D = 1.6$; (*b*) $L/D = 4$; (*c*) $L/D = 10$

portions, which gives a "wavy" appearance (when viewed from the side) at each instant in time (Ligrani et al., 1996a). Both types of behavior can result in reductions of adiabatic film effectiveness (compared to nonpulsating flows), however, non-quasi-steady film distributions often lead to more important alterations to film effectiveness magnitudes and flow structure (Ligrani et al., 1997a, b).

The freestream Strouhal number, $St_\infty = 2\pi f\delta/\bar{U}_\infty$, is also used to nondimensionalize the pulsation frequency in this study because it characterizes the response time of a boundary layer subject to periodic disturbances (Doorly and Oldfield, 1985). The value employed here is 0.51, compared to a range from 0.01 to 0.60 in operating turbines. In studies in which the film cooling flows (not the bulk flow) are periodically forced, Bons et al. (1995) and Gogineni et al. (1996) use a reduced frequency of the form $\bar{U}_\infty/fD$, which is equivalent to $2\pi\delta/St_\infty D$. According to these authors, magnitudes of $\bar{U}_\infty/fD$ range from 20 to 200 in operating turbines.

Results and Discussion

Bulk Flow Pulsation Characteristics. The instantaneous free-stream velocity trace in Fig. 2 illustrates the character of the pulsation wave form at a frequency of 32 Hz. Some differences from a pure sinusoid are evident. Such deviations become less pronounced at other pulsation frequencies (Ligrani et al., 1996a) because the shape of the free-stream pulsation wave form is affected by the resonance frequency of the wind tunnel (Al-Asmi and Castro, 1993), which is estimated to be about 12 Hz.

Injectant Concentration Distributions. Figures 3 and 4 present phase-averaged injectant surveys measured at $x/D = 5.0$ downstream of holes with L/D values of 1.6, 4.0, and 10.0. The results in these two figures are given for $\bar{m} = 0.5$ and $\bar{m} = 1.0$, respectively, when pulsations are imposed at 32 Hz. Local film-cooled boundary layer temperature distributions in the figures are expressed in nondimensional form using θ. These distributions are obtained using techniques developed by Ligrani and Williams (1990), and by Ligrani et al. (1994) in which the injectant is heated as all other components in the wind tunnel test section are maintained at the free-stream temperature. With this approach, the injectant is the only source of thermal energy relative to the free-stream. Higher magnitudes of θ then indicate greater concentration of injectant, and clear indications of the protection (or lack of protection) provided by the injectant. Near wall values of θ are particularly important because they approach local magnitudes of the surface adiabatic film cooling effectiveness (Ligrani et al., 1994, 1996b).

θ results for $\bar{m} = 0.5$ in Fig. 3 show injectant distributions in a spanwise/normal plane downstream of the center film cooling hole at different times during single pulsation periods. Important changes are evident for the $L/D = 1.6$ holes (top row of plots) during the 32 Hz pulsation as t/τ ranges from 0.2 to 0.8. When the free-stream static pressure is highest during a particular pulsation period, the instantaneous blowing ratio is smallest, and the largest injectant concentrations are located very close to the wall. This is evident at t/τ of 0.2 and 0.8. In the portions of the pulsation in which the free-stream static pressure is lowest, the instantaneous blowing ratio is highest, and the injectant trajectory is located slightly away from the wall, as shown in top row of plots in Fig. 3(*a*) at t/τ of 0.4 and 0.6. These data thus illustrate how pulsations of the static pressure (either from potential flow interactions, passing shock waves, or rotating vanes at the exit of a subsonic wind tunnel) cause the injectant to periodically lift-off of a turbine surface, which often causes the *time-averaged* film cooling effectiveness to decrease.

The $L/D = 4$ results in Fig. 3(*b*), also for $\bar{m} = 0.5$, show some qualitative features which are similar to the $L/D = 1.6$ results. Like the $L/D = 1.6$ results, the largest injectant concentrations with $L/D = 4$ holes are closest to the surface at some t/τ and relatively farther away from the surface at other t/τ. Phase-averaged injectant distributions for the two different L/D holes are dissimilar since different t/τ correspond to injectant positions which are nearest and farthest from the wall. Note that $t/\tau = 0$ refers to the same initial location of the shutter vanes located at the test section exit. This evidences different phase shifts between the free-stream static pressure and the static pressure at the hole exits for the $L/D = 1.6$ and the $L/D = 4$ holes.

The $L/D = 10$ results in Fig. 3(*c*) show different trends. Here, phase-averaged injectant concentrations at different t/τ vary by only very small amounts through each pulsation period. In addition, the largest injectant concentrations with $L/D = 10$ holes are

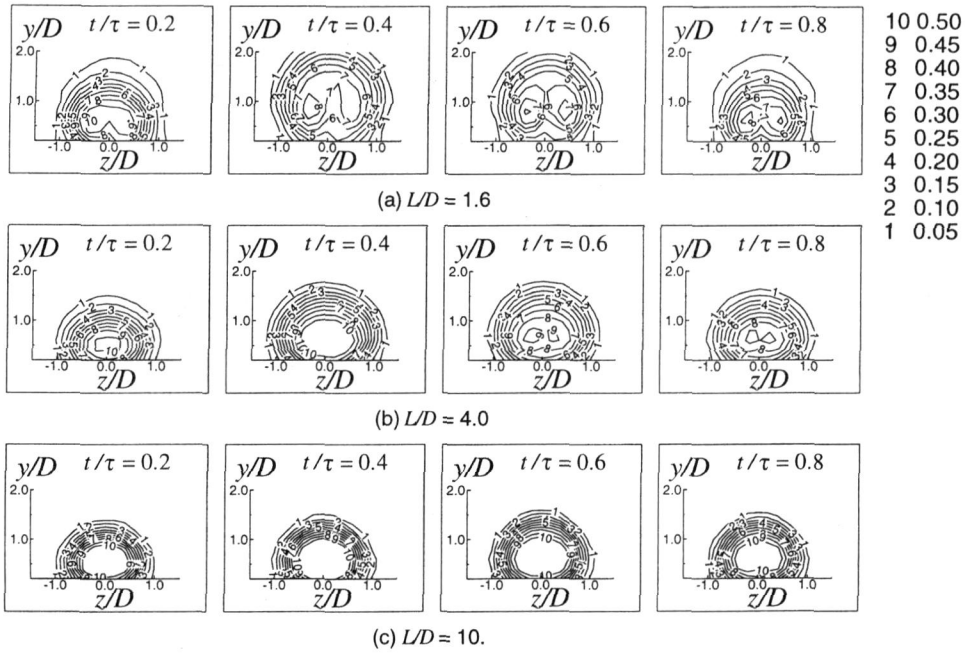

Fig. 4 Phase-averaged injectant concentration distributions θ at $x/D = 5.0$ for $\bar{m} = 1.0$: (*a*) $L/D = 1.6$; (*b*) $L/D = 4$; (*c*) $L/D = 10$

generally located closer to the surface than the concentrations produced with the $L/D = 4$ holes. Similarly, the $L/D = 4$ holes produce distributions that are generally closer to the surface than produced by the $L/D = 1.6$ holes (especially at t/τ when free-stream static pressures are low). Spatial areas corresponding to the highest injectant concentrations in the $x/D = 5.0$ measurement plane also increase considerably as L/D decreases at $\bar{m} = 0.5$. When $L/D = 10$, the region enclosed within $\theta = 0.5$ is enlarged 13.6 percent by the pulsations, whereas this enlargement is 64 percent when $L/D = 1.6$. Such behavior is connected to different flow behavior in the film cooling holes and to different velocity profiles at the hole exists as L/D is changed, and to other phenomena (Ligrani et al., 1996a).

Phase-averaged injectant distributions for $\bar{m} = 1.0$ are presented in Fig. 4. The higher blowing ratio and higher momentum cause the largest injectant concentrations in this latter figure for $\bar{m} = 1.0$ to be generally farther from the surface than the distributions in Fig. 3 for $\bar{m} = 0.5$. At $\bar{m} = 1.0$, more injectant is located farther from the wall as L/D decreases. The data also suggest that phase shifts between the free-stream static pressure and the static pressure at the hole exits are more strongly dependent upon L/D than upon $\bar{m}$. Overall, the results for $f = 32$ Hz in Figs. 3 and 4 show that injectant variations with t/τ through pulsation periods become larger as L/D decreases from 10 to 1.6.

Time averages of injectant distributions subject to bulk flow pulsations imposed at $f = 32$ Hz and time-averaged injectant distributions measured at $f = 0$ Hz are presented in Figs. 5(*a*) and 5(*b*) for $\bar{m} = 0.5$ and $\bar{m} = 1.0$, respectively. At each pulsation

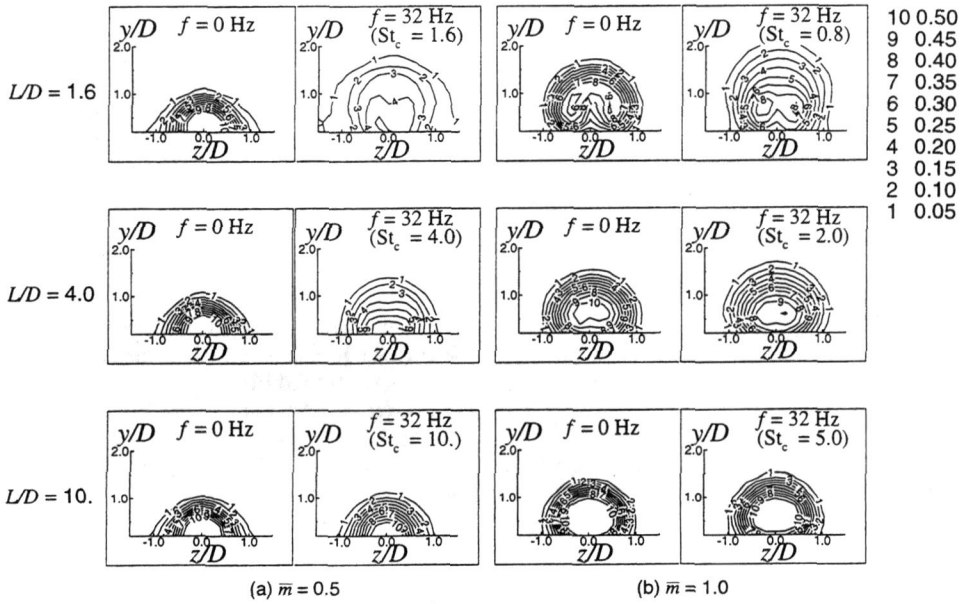

Fig. 5 Time-averaged injectant concentration distributions θ at $x/D = 5.0$: (*a*) $\bar{m} = 0.5$; (*b*) $\bar{m} = 1.0$

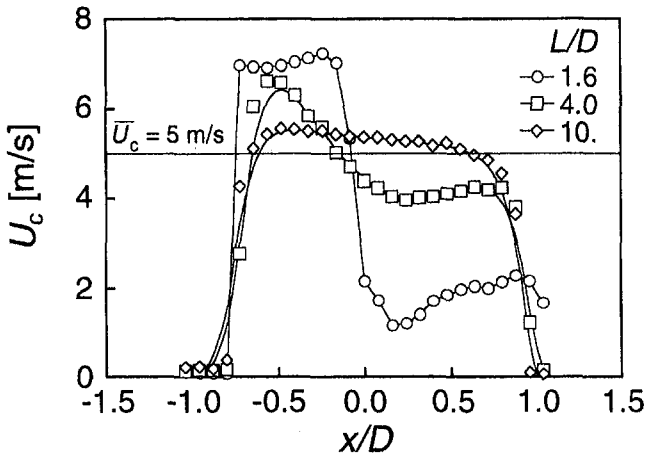

Fig. 6 Injectant velocity profiles at the hole exit in the streamwise direction in the absence of free-stream flow for $\bar{m}$ = 0.5

frequency, the largest disruptions to injectant distributions and coverage are produced by the pulsations when L/D = 1.6 and the smallest result when L/D = 10.0. Figure 5 also shows that pulsation-induced disruptions are greater at $\bar{m}$ = 0.5 than at $\bar{m}$ = 1.0 since the time-averaged distributions are more spread out spatially and less concentrated compared to the f = 0 Hz distributions at the same $\bar{m}$ and L/D.

Injectant Velocity Profiles at Hole Exits and Injection Behavior Within the Film Holes. Streamwise velocity profiles at the exits of the film cooling holes are measured with no free-stream flow (or external boundary layer) present. With or without the free-stream flow, such measurements are a consequence of film behavior within the tubes. Results for L/D of 1.6, 4.0 and 10.0 are presented in Fig. 6 as dependent upon x/D at z/D = 0 for an average injectant velocity of 5.0 m/s. Hole exits at the test surface extend over x/D from −0.9 to +0.9 and over z/D from −0.5 to +0.5.

When L/D = 1.6, Fig. 6 shows that the injectant velocity is higher than mean injectant velocity value ($\bar{U}_c$ = 5 m/s) on the windward side of the hole center ($-0.9 < x/D < 0$) and then abruptly decreases to become less than the mean injectant velocity on the leeward portion of the hole exit ($0 < x/D < 0.9$). (Leeward denotes the side of the injection hole *toward which* the free-stream flow is moving, and windward denotes the side of the injection hole *from which* the free-stream flow is moving.) This nonuniform velocity distribution is present because of flow separation on the leeward side of the injection hole near its entrance (from the plenum chamber). The injectant velocity near the windward side of the hole entrance is thus accelerated because of flow blockage from separation on the opposite side, whereas the flow just downstream of the separated flow is decelerated.

Figure 6 then shows that the injectant velocity profiles become more uniform at hole exits as L/D increases, even though injectant flow separations, and the injectant flow variations that result from such separations are believed to be present near the entrances of all three of the L/D holes investigated. The imposed pulsations are believed further to alter magnitudes of high windward side momentum, especially just away from the holes, where the different trajectories of the injectant are spread over even larger volumes by the pulsations. In addition, the flow separations within the injectant holes are affected by the pulsations (Miller and Pucci, 1971; Krause and Schweitzer, 1990), which happens closer to the hole exits as L/D decreases. In the portion of the pulsation phase where the instantaneous injectant flow rate is lower than the average value, the regions within the holes where the flow is separated and where the flow direction is reversed become larger. Such physics is consistent with the results in Figs. 3–5, which overall indicate that the injectant at L/D = 1.6 is much more sensitive to the influences of imposed bulk flow pulsations than injectant from holes with larger values of L/D.

Adiabatic Film Cooling Effectiveness Distributions. Figures 7(*a*) and 7(*b*) show local adiabatic film cooling effectiveness η_c variations with streamwise distance along the centerline of the central injection hole for $\bar{m}$ = 0.5 and $\bar{m}$ = 1.0, respectively. Figures 8 and 9 show variations of spanwise-averaged adiabatic film cooling effectiveness η_m with streamwise distance for the same respective time-averaged blowing ratios.

With no imposed pulsations (f = 0 Hz), Figs. 7(*a*) and 7(*b*) show that the centerline film cooling effectiveness increases at each x/D as L/D increases, and that the rate of increase is significantly greater with $\bar{m}$ = 1.0 than with $\bar{m}$ = 0.5. Responsible are different injectant velocity distributions and different effective injection angles for the three different values of L/D. When compared at the same L/D and x/D, centerline adiabatic film cooling effectiveness values (with no pulsations) are also consistently greater with $\bar{m}$ = 0.5 than for $\bar{m}$ = 1.0 because of greater film lift-off from the surface at the higher blowing ratio.

Figure 7(*a*) shows that centerline effectiveness values are reduced considerably (when compared at the same x/D) at L/D of 1.6 and 4.0 when $\bar{m}$ = 0.5 and pulsations are imposed at f = 32 Hz. In contrast, Fig. 7(*b*) shows that changes due to 32 Hz pulsations are much smaller when the blowing ratio $\bar{m}$ is 1.0.

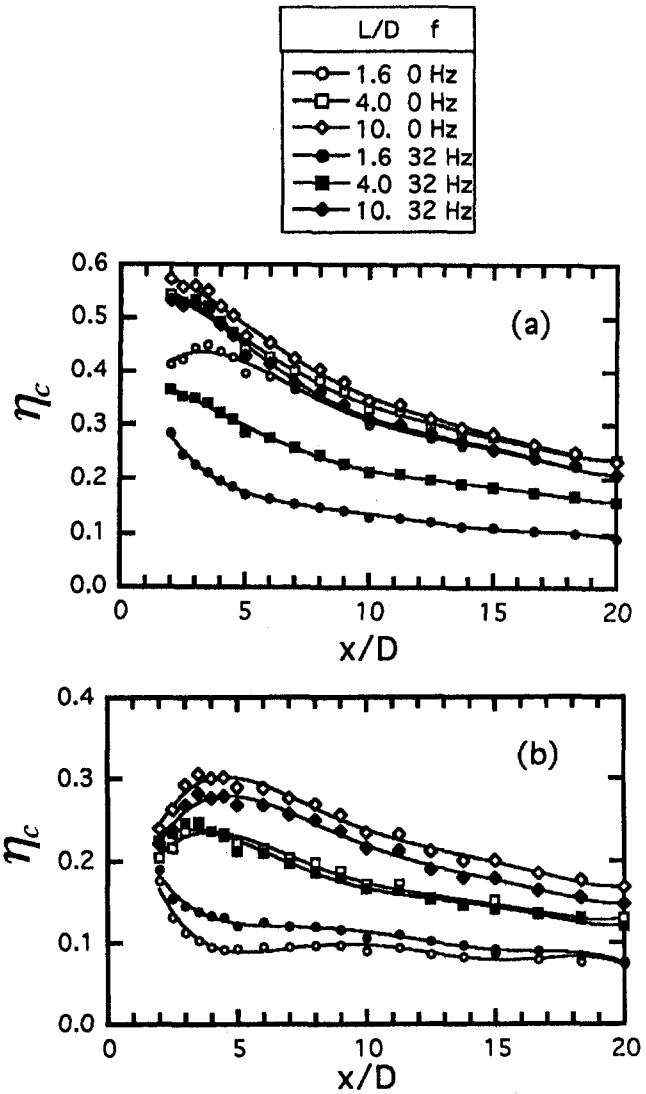

Fig. 7 Centerline adiabatic film cooling effectiveness for f = 0 Hz and f = 32 Hz: (*a*) $\bar{m}$ = 0.5; (*b*) $\bar{m}$ = 1.0

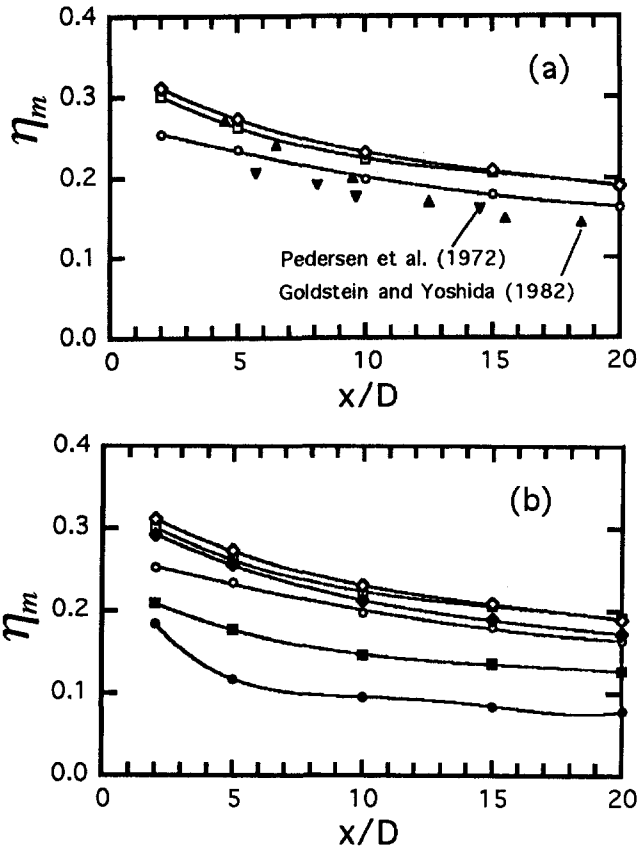

Fig. 8 Spanwise-averaged adiabatic film cooling effectiveness for $\bar{m}$ = 0.5. Symbols are identified on Fig. 7. (*a*) Comparison of f = 0 Hz data with data from Pedersen et al. (1977) and Goldstein and Yoshida (1982); (*b*) f = 0 Hz and f = 32 Hz data.

Alterations to time-averaged injectant distributions with imposed pulsations relative to injectant distributions measured with no pulsations are responsible. This is illustrated by results in Fig. 5(*a*), which shows marked differences between f = 32 Hz and f = 0 Hz injectant distributions measured at x/D = 5.0 and $\bar{m}$ = 0.5, especially when L/D is 1.6 and 4.0. In these two cases, the largest injectant concentrations in the pulsating flows are much less concentrated and spread much further from the wall compared to injectant distributions measured with f = 0 Hz. Results in Fig. 5(*b*) for $\bar{m}$ = 1.0, on the other hand, show much less spreading and that the locations of highest injectant concentrations are not altered significantly by imposed pulsations.

Adiabatic effectiveness values in Figs. 8 and 9 are determined from averages of local values over z/D from −1.5 to 1.5. The data of Pedersen et al. (1977) and Goldstein and Yoshida (1982) are compared to our L/D = 10 data in Figs. 8(*a*) and 9(*a*) because their injection hole lengths are long enough to produce velocity profiles that are nearly fully developed at their hole exits. Present steady effectiveness values (for f = 0 Hz) at $\bar{m}$ of 0.5 (in Fig. 8(*a*)) and 1.0 (in Fig. 9(*a*)) are larger than theirs because of different experimental conditions. Their ratio of displacement thickness to the hole length is less and their blowing ratio is slightly higher than present values, which causes their injectant to penetrate further into the boundary layer and free stream. As a result, their effectiveness distributions are somewhat lower than ours when compared at the same x/D and $\bar{m}$.

Spanwise-averaged effectiveness values (for f = 0 Hz) in Figs. 8(*a*) and 9(*a*) are smaller than centerline values in Figs. 7(*a*) and 7(*b*) because the region between the adjacent holes is not fully covered by the injectant. Qualitative trends show some similarity since effectiveness values in both cases are higher at particular values of x/D when L/D is larger. The effects of film lift-off from the surface are also evident in the spanwise-averaged data since effectiveness values are consistently greater with $\bar{m}$ = 0.5 than for $\bar{m}$ = 1.0 when compared at the same L/D and x/D. As for the centerline data, the effects of pulsations on spanwise-averaged effectiveness values in Figs. 8(*b*) and 9(*b*) are most important at $\bar{m}$ = 0.5 when L/D is 1.6 and 4.0. Alterations resulting from the 32 Hz pulsations are somewhat less at $\bar{m}$ = 0.5 when L/D is 10, and at $\bar{m}$ = 1.0 when L/D is 1.6, 4.0, and 10.

Iso-Energetic Stanton Number Ratio Distributions. Spanwise-averaged iso-energetic Stanton number ratios are presented in Fig. 10(*a*) for $\bar{m}$ = 0.5 and in Fig. 10(*b*) for $\bar{m}$ = 1.0. Comparisons of $St_{f,m}/St_o$ results corresponding to f = 0 Hz and $\bar{m}$ = 0.5 show that values generally increase with L/D when compared at the same x/D. The f = 0 Hz data for $\bar{m}$ = 1.0 in Fig. 10(*b*) show similar trends at $x/D < 7$–10. Opposite $St_{f,m}/St_o$ trends with L/D are evident in this figure at x/D larger than 7–10. Such changes are largely due to different amounts of mixing and turbulence in the injectant as it leaves the holes. These are tied to varying L/D, which result in different distances between hole exits and the leeward side separations near hole entrances.

As for the effectiveness distributions, the largest $St_{f,m}/St_o$ variations with f occur for L/D = 1.6 in Figs. 10(*a*) and 10(*b*). With the exception of data corresponding to x/D = 5, L/D = 4, and $\bar{m}$ = 0.5 in Fig. 10(*a*), almost no change with pulsation frequency f are evident at each x/D for L/D = 4 and L/D = 10. The change of $St_{f,m}/St_o$ with f for L/D = 1.6 at particular values of x/D at $\bar{m}$ = 0.5 is opposite to the change at $\bar{m}$ = 1.0. Spanwise-averaged $St_{f,m}/St_o$ distributions in Fig. 10(*a*) for $\bar{m}$ = 0.5 increase as the pulsation frequency increases from 0 Hz to 32 Hz. In contrast, spanwise-averaged $St_{f,m}/St_o$ distributions in Fig. 10(*b*) for $\bar{m}$ = 1.0 decrease as the pulsation frequency increases from 0 Hz to 32 Hz. The pulsations thus seem to alter Stanton number ratios in different ways at these two different blowing ratios because of different amounts of injectant lift-off.

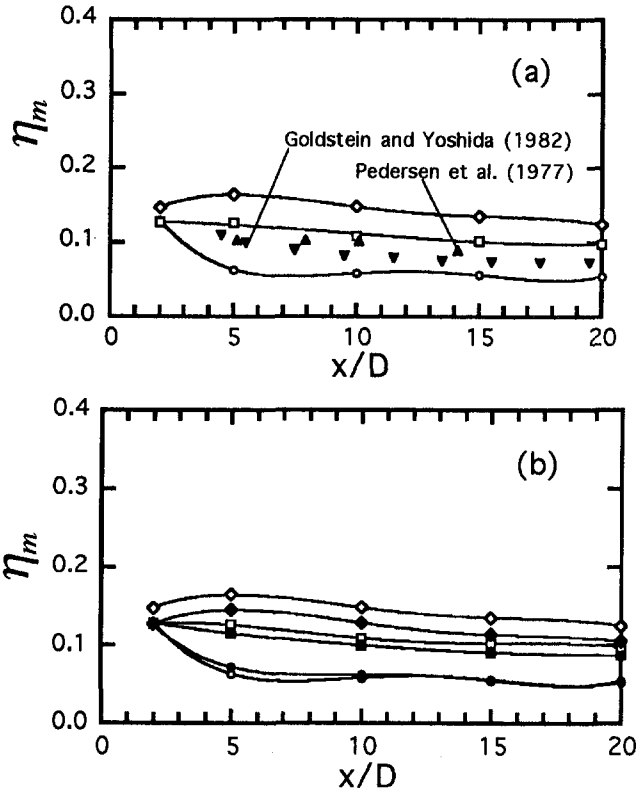

Fig. 9 Spanwise-averaged adiabatic film cooling effectiveness for $\bar{m}$ = 1.0. Symbols are identified on Fig. 7: (*a*) Comparison of f = 0 Hz data with data from Pedersen et al. (1977) and Goldstein and Yoshida (1982); (*b*) f = 0 Hz and f = 32 Hz data.

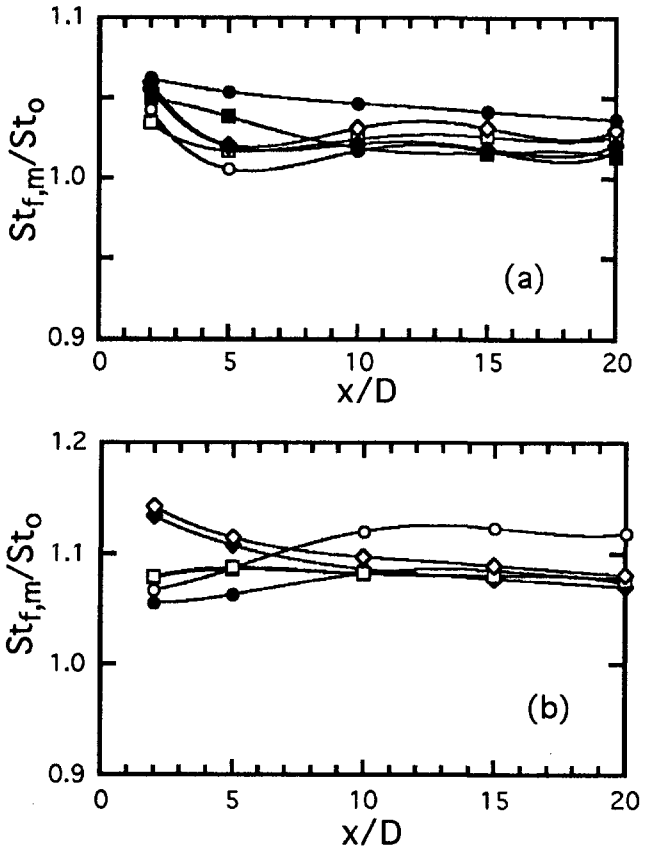

Fig. 10 Spanwise-averaged iso-energetic Stanton number ratio for $f = 0$ Hz and $f = 32$ Hz. Symbols are identified on Fig. 7: (*a*) = 0.5; (*b*) $\bar{m} = 1.0$.

Overall Film Cooling Performance Parameter Distributions. Spanwise-averaged magnitudes of the overall film cooling performance parameter, $\dot{q}''/\dot{q}''_o$, are presented in Fig. 11(*a*) for $\bar{m} = 0.5$ and in Fig. 11(*b*) for $\bar{m} = 1.0$. Values of $\dot{q}''/\dot{q}''_0$ are determined using the spanwise-averaged effectiveness data in Figs. 8 and 9, the spanwise-averaged iso-energetic Stanton number ratio data in Fig. 10, and a θ value at the surface of 1.75.

The largest differences in $\dot{q}''/\dot{q}''_o$ data for $f = 0$ Hz and $f = 32$ Hz (when compared at the same x/D) are present for $\bar{m} = 0.5$ with $L/D = 1.6$ and $L/D = 4.0$ in Fig. 11(*a*). In these cases, the best overall film cooling protection (and the lowest $\dot{q}''/\dot{q}''_o$ distribution), for each L/D, are present when no pulsations are imposed. When $L/D = 10.0$, effects of the pulsations are minimal in Fig. 11(*a*) since $\dot{q}''/\dot{q}''_o$ distributions for $f = 0$ Hz and $f = 32$ Hz are very similar to each other.

In Fig. 11(*b*), $\dot{q}''/\dot{q}''_0$ distributions are nearly the same or increase slightly at each x/D as f increases from 0 Hz to 32 Hz when $\bar{m} = 1.0$ and L/D is either 4.0 or 10.0. The $L/D = 1.6$ results, also in Fig. 11(*b*) for the same $\bar{m}$, however, show interesting behavior with different trends compared to other $\dot{q}''/\dot{q}''_o$ distributions described in this paper. At this L/D, the $f = 32$ Hz distribution is generally lower than the $f = 0$ Hz distribution when compared at the same x/D. This is interesting because it indicates that the protection provided by film cooling is *improved* by the pulsations. According to Abhari (1996), unsteady pressure fluctuations can either increase or decrease the time-averaged coolant fluxes downstream of the film cooling holes, depending upon the details of the film cooling hole design, hole placement, and turbine operating conditions. Protection is improved by 32 Hz pulsations in the present study when $\bar{m} = 1.0$ because the pulsations act to periodically oscillate injectant locations with time (Ligrani et al., 1996a). As a result, injectant that is nominally continuously lifted off of the surface without pulsations is rearranged when pulsations are present so that it is *periodically* located near the surface during a portion of each pulsation period. This results in better time-averaged film coverage on the surface, which is consistent with $f = 0$ Hz and $f = 32$ Hz injectant distributions for $L/D = 1.6$ in Fig. 5(*b*) for $\bar{m} = 1.0$. There, the time-averaged injectant distribution measured with $f = 32$ Hz shows larger concentrations closer to the surface than the distribution measured with $f = 0$ Hz.

Summary and Conclusions

The alterations to film cooling (from a single row of simple angle holes) produced by pulsations imposed at 32 Hz become greater as the hole length-to-diameter ratio decreases from 10 to 4 to 1.6. Important changes to injectant distributions by the pulsations occur at both time-averaged blowing ratios investigated, 0.5 and 1.0, but they are more significant at the lower blowing ratio. The largest alterations thus occur using $L/D = 1.6$ holes with $\bar{m} = 0.5$ subject to pulsations at 32 Hz (which corresponds to a coolant Strouhal number of 1.6), and are in the form of spreading of injectant concentrations over larger volumes compared to steady distributions.

This results in diminished film cooling protection, as evidenced by the overall film cooling performance parameter, which is reduced significantly by pulsations imposed at 32 Hz when $\bar{m} = 0.5$ and L/D is 1.6 or 4.0. When compared at particular x/D and L/D, the most important reductions to centerline and spanwise-averaged adiabatic film cooling effectiveness magnitudes, and the largest increases of spanwise-averaged iso-energetic Stanton number ratios from the pulsations occur for the same $\bar{m}$ and L/D. In contrast, the overall film cooling performance parameter is improved by pulsations imposed at 32 Hz when $\bar{m} = 1.0$ and L/D is 1.6.

Phase-averaged injectant temperature distributions, measured in the spanwise/normal plane at $x/D = 5.0$, show periodic variations due to instantaneous changes of both the injectant flow rate and

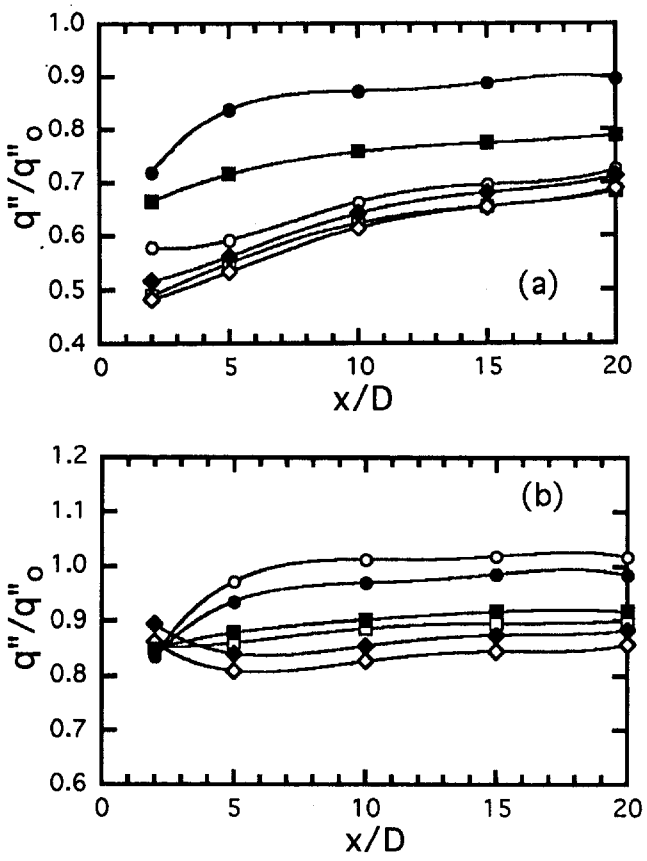

Fig. 11 Spanwise-averaged overall film cooling performance parameter for $f = 0$ Hz and $f = 32$ Hz. Symbols are identified on Fig. 7: (*a*) $\bar{m} = 0.5$; (*b*) $\bar{m} = 1.0$.

injectant flow characteristics within the holes. Different injectant flow characteristics within holes are evidenced by velocity distributions at hole exits, which are highly nonuniform at smaller length-to-diameter ratios. The imposed bulk flow pulsations influence the behavior of the separation region producing this nonuniformity as well as the film distribution as it leaves the holes and is advected downstream. As a result, changes to film protection which occur at a pulsation frequency of 32 Hz (at coolant Strouhal numbers from 0.8 to 10.0) for a particular film injection hole cross-section geometry are not characterized by a single value of injectant Strouhal number (Ligrani et al., 1996a) as L/D and $\bar{m}$ are varied. Instead, the decrease in film protection is dependent upon a number of characteristics, including the injectant Strouhal number St_c, the free-stream Strouhal number St_∞, the length-to-diameter ratio of the holes L/D, the behavior of the film injectant as it passes through the holes, the design of the injectant supply plenum, and the time-averaged blowing ratio $\bar{m}$.

Acknowledgments

The portions of this effort conducted at the University of Utah were sponsored by the National Science Foundation, Grant number CTS-9615196.

References

Abhari, R. S., 1996, "Impact of Rotor–Stator Interaction on Turbine Blade Film Cooling," ASME JOURNAL OF TURBOMACHINERY, Vol. 118, pp. 123–133.

Abhari, R. S., and Epstein, A. H., 1994, "An Experimental Study of Film Cooling in a Rotating Transonic Turbine," ASME JOURNAL OF TURBOMACHINERY, Vol. 116, pp. 63–70.

Al-Asmi, K., and Castro, I. P., 1993, "Production of Oscillatory Flow in Wind Tunnels," *Experiments in Fluids,* Vol. 15, pp. 33–41.

Bons, J. P., Rivir, R. B., MacArthur, C. D., and Pestian, D. J., 1995, "The Effect of Unsteadiness on Film Cooling Effectiveness," AIAA Paper No. 95-0306.

Doorly, D. J., and Oldfield, M. L. J., 1985, "Simulation of the Effects of Shock Wave Passing on a Turbine Rotor Blade," ASME *Journal of Engineering for Gas Turbines and Power,* Vol. 107, pp. 998–1006.

Gogineni, S. P., Trump, D. D., Rivir, R. B., and Pestian, D. J., 1996, "PIV Measurements of Periodically Forced Flat Plate Film Cooling Flows With High Free Stream Turbulence," ASME Paper No. 96-GT-236.

Goldstein, R. J., and Yoshida, T., 1982, "The Influence of a Laminar Boundary Layer and Laminar Injection on Film Cooling Performance," ASME *Journal of Heat Transfer,* Vol. 104, pp. 355–362.

Karlsson, S. K., 1959, "An Unsteady Turbulent Boundary Layer," *Journal of Fluid Mechanics,* Vol. 14, pp. 622–636.

Kline, S. J., and McClintock, F. A., 1953, "Describing Uncertainties in Single Sample Experiments," *Experiments in Fluids,* Vol. 9, pp. 159–166.

Krause, E., and Schweitzer, W. B., 1990, "The Effect of an Oscillatory Freestream-Flow on a NACA-4412 Profile at Large Relative Amplitudes and Low Reynolds Numbers," *Experiments in Fluids,* Vol. 9, pp. 159–166.

Ligrani, P. M., Gong, R., Cuthrell, J. M., and Lee, J. S., 1996a, "Bulk Flow Pulsations and Film Cooling: Part 1, Injectant Behavior," *Int. J. Heat Mass Transfer,* Vol. 39, pp. 2271–2282.

Ligrani, P. M., Gong, R., Cuthrell, J. M., and Lee, J. S., 1996b, "Bulk Flow Pulsations and Film Cooling: Part 2, Flow Structure and Film Effectiveness," *Int. J. Heat Mass Transfer,* Vol. 39, pp. 2283–2292.

Ligrani, P. M., Gong, R., and Cuthrell, J. M., 1997a, "Bulk Flow Pulsations and Film Cooling: Flow Structure Just Downstream of the Holes," ASME JOURNAL OF TURBOMACHINERY, Vol. 119, pp. 568–573.

Ligrani, P. M., Gong, R., Cuthrell, J. M., and Lee, J. S., 1997b, "Effects of Bulk Flow Pulsations on Film-Cooled Boundary Layer Structure," ASME *Journal of Fluids Engineering,* Vol. 119, pp. 56–66.

Ligrani, P. M., Wigle, J. M., Ciriello, S., and Jackson, S. W., 1994, "Film-Cooling From Holes With Compound Angle Orientations: Part 1—Results Downstream of Two Staggered Rows of Holes With 3D Spanwise Spacing," ASME *Journal of Heat Transfer,* Vol. 116, pp. 341–352.

Ligrani, P. M., and Williams, W. W., 1990, "Effects of an Embedded Vortex on Injectant From a Single Film-Cooling Hole in a Turbulent Boundary Layer," ASME JOURNAL OF TURBOMACHINERY, Vol. 112, pp. 428–436.

Miller, J. A., and Pucci, P. F., 1971, "Heat Transfer to an Airfoil in Oscillating Flow," ASME *Journal of Engineering for Power,* Vol. 93, pp. 461–468.

Pedersen, D. R., Eckert, E. R. G., and Goldstein, R. J., 1977, "Film Cooling With Large Density Differences Between the Mainstream and the Secondary Fluid Measured by the Heat–Mass Transfer Analogy," ASME *Journal of Heat Transfer,* Vol. 99, pp. 620–627.

Turbulence Spectra and Length Scales Measured in Film Coolant Flows Emerging From Discrete Holes

S. W. Burd
Combustor Module Center,
Pratt and Whitney Florida,
West Palm Beach, FL 33410-9600

T. W. Simon
Heat Transfer Laboratory,
University of Minnesota,
Minneapolis, MN 55455

To date, very little attention has been devoted to the scales and turbulence energy spectra of coolant exiting from film cooling holes. Length-scale documentation and spectral measurements have primarily been concerned with the free-stream flow with which the coolant interacts. Documentation of scales and energy decomposition of the coolant flow leads to more complete understanding of this important flow and the mechanisms by which it disperses and mixes with the free stream. CFD modeling of the emerging flow can use these data as verification that flow computations are accurate. To address this need, spectral measurements were taken with single-sensor, hot-wire anemometry at the exit plane of film cooling holes. Energy spectral distributions and length scales calculated from these distributions are presented for film cooling holes of different lengths and for coolant supply plenums of different geometries. Measurements are presented on the hole streamwise centerline at the center of the hole, one-half diameter upstream of center, and one-half diameter downstream of center. The data highlight some fundamental differences in energy content, dominant frequencies, and scales with changes in the hole and plenum geometries. Coolant flowing through long holes exhibits smoothly distributed spectra as might be anticipated in fully developed tube flows. Spectra from short-hole flows, however, show dominant frequencies.

Introduction

To date, measurement of spectral distributions and length scales in film cooling studies has primarily focused on the free stream. It is common, for instance, to see film cooling studies that document the integral length scales calculated from spectral measurements taken in the free stream. Although the precise influence that free-stream scales have on film cooling performance has not been discerned, such documentation has been considered necessary for complete documentation and for proper starting of computational studies. The effect of length scales on cooling performance can only be inferred from data taken in film cooling studies performed at different turbulence levels that were generated by a variety of means.

To complete the documentation and the boundary conditions for computation, details of the scales, energy distribution, and dissipation rates in the coolant flow are needed. Early studies in the literature were primarily with long-hole delivery and, thus, the turbulence was that of fully developed turbulent pipe flow. As we realize the importance of the hole L/D, and investigate with shorter holes, we raise the need for documenting the influence of the hole and supply plenum geometries on coolant flow velocity distributions, turbulence levels, and scales.

Spectral measurements have been documented in considerable detail over the years for fully developed turbulent pipe flow, including the studies of Laufer (1953), Lawn (1971), Bremhorst and Walker (1973), and Berman and Dunning (1973). In general, fully developed pipe flow studies have documented low energy content at low frequencies, a universal $-\frac{5}{3}$ equilibrium range in the high frequencies, and a majority of the energy containing eddies in a midfrequency range. Depending upon radial location, integral length scales of 25–75 percent of the pipe diameter have been determined. The larger scales are measured along the hole centerline while the smaller scales are found nearer the wall. Peak energies were found at $0.3 < \mathrm{St_D} < 1.2$. Spectra in developing pipe flows have been documented by Azad et al. (1978).

Cylinders in crossflows exhibit some similarities to film cooling flows. Like a cylinder in crossflow, the coolant jet is subjected to a free-stream cross flow and sheds vortices in its wake. For flow past a solid cylinder, the Strouhal number for $300 < \mathrm{Re} < 100{,}000$ is nearly constant and equal to 0.21.

Spectral measurements in film cooling flows are few. Coherent frequencies in deflected jets are in the range $\mathrm{St_D} = 0.08-0.085$ (McMahon et al., 1971). For an $L/D = 4.0$, Kohli and Bogard (1998) documented spectra of temperature fluctuations along the hole centerline at $y/D = 0.1$ and at different streamwise locations. The characteristic length scale was the hole diameter.

In this paper, spectral energy distributions based on effective velocity are given and corresponding length scales and turbulence parameters are calculated. This is done for film cooling holes of different lengths and coolant supply plenum geometries. The data highlight some fundamental differences from case to case.

Experimental Test Facility

The test facility has two major sections: mainstream and coolant supply systems. The mainstream flow is supplied via a high-turbulence wind tunnel constructed by Wang (1996). The tunnel is a combustor simulator that produces turbulence levels characteristic of those found downstream from the combustor in an actual engine. For reference, the mean velocity and turbulence level in the free stream above the holes are nominally 10.8 m/s and 11.5 percent, respectively. The boundary layer thicknesses at the film cooling holes are $\delta_{99}/D = 1.13$, $\theta/D = 0.082$, and $\delta^*/D = 0.105$. Some details of the free stream are given in Fig. 3 and Table 1. The coolant flow is delivered by a blower to a large plenum (37.5 cm × 66 cm × 17.8 cm) and then to the film cooling test plate. Mass flow to the film cooling holes is monitored with

Contributed by the International Gas Turbine Institute and presented at the 43rd International Gas Turbine and Aeroengine Congress and Exhibition, Stockholm, Sweden, June 2–5, 1998. Manuscript received by the International Gas Turbine Institute February 1998. Paper No. 98-GT-190. Associate Technical Editor: R. E. Kielb.

Table 1 Turbulence parameters and scales

Case, Flow	VR	x/D	U_{eff}/U_{hole}	k (m^2/s^2)	ε (m^2/s^3)	L_u/D	η/D (x10^3)
2.3, Sink	0.5	-0.5	1.40	0.186			
		0.0	1.47	1.034	271.8	0.166	3.30
		0.5	1.18	1.788	662.3	0.154	2.64
	1.0	-0.5	1.32	0.306			
		0.0	1.09	8.712	4451	0.248	1.61
		0.5	0.83	5.184	4710	0.107	1.59
4.6, Sink	0.5	0.0	1.24	1.212	295.9	0.193	3.15
	1.0	-0.5	1.20	3.952	1267	0.266	2.18
		0.0	1.00	4.128	1910	0.189	1.97
		0.5	1.01	2.542	1360	0.127	2.14
6.6, Sink	0.5	0.0	1.28	0.724	163.1	0.162	3.74
	1.0	0.0	1.06	2.794	969.6	0.207	2.41
7.0, Sink	0.5	-0.5	1.16	1.108	292.9	0.171	3.18
		0.0	1.33	0.418	25.37	0.456	5.85
		0.5	1.47	0.284	23.63	0.274	5.96
	1.0	-0.5	1.08	1.626	346.0	0.257	3.08
		0.0	1.11	1.402	277.2	0.256	3.25
		0.5	1.32	0.764	225.1	0.127	3.43
2.3, Co-Flow	0.5	0.0	1.30	1.622	401.3	0.220	2.95
	1.0	-0.5	1.21	0.766	211.5	0.136	3.47
		0.0	1.02	10.01	3950	0.344	1.67
		0.5	0.94	5.910	3755	0.164	1.69
2.3, Counter-Flow	0.5	0.0	1.51	0.944	197.1	0.199	3.51
	1.0	-0.5	1.38	1.148			
		0.0	1.27	9.004	3760	0.308	1.68
		0.5	1.16	8.284	8732	0.117	1.36
Freestream	N/A	0.0	N/A	2.124	154.0	0.857	3.77

laminar flow meters ($\Delta\dot{m} = \pm 2.3$ percent). Engine-representative film coolant-to-free-stream velocity ratios of 0.5 (Re_D = 6,500) and 1.0 (Re_D = 13,000) are documented. The nominal density ratio between the two streams is unity. Compressibility effects are not captured in this experiment. Further details of the facility are provided in Burd and Simon (1997) and Burd et al. (1998).

Film Cooling Geometries

One row of eleven, streamwise-oriented film cooling holes (Fig. 1(*A*)) is machined in a 2.54-cm-thick phenolic laminate plate to form the film cooling test section. The holes, 19.05 mm diameter and with 35 deg inclination, have a hole length-to-diameter ratio of 2.3 and a hole pitch-to-diameter ratio of 3.

To investigate the influence of hole length-to-diameter ratio, several sets of tubes of different lengths were connected to the supply plenum side of the film cooling test plate. The tubes have t/D equal to 0.18. In engines, of course, this ratio would be very large. Entrance loss data of Fried and Idelchik (1989) indicate that the t/D used in this study is large enough that t influences are insignificant. With the tubes, hole length-to-diameter ratios of 4.6, 6.6, and 7.0 are created. The L/D = 7.0 tube geometry is machined with its entrance normal to the tube centerline (Fig. 1(*B*)). The entrance is parallel to the hole exit plane with the L/D = 4.6 and 6.6 tubes.

Two additional geometries (Figs. 1(*C*) and 1(*D*)), which introduce approach flow momentum, are also investigated. For these geometries, a baffle was placed along the plenum side of the film cooling test plate to restrict the coolant supply flow and force it to enter with a counterflow (parallel but in the opposite direction, Fig. 1(*C*)) or coflow (parallel and in the same direction, Fig. 1(*D*)) relative to the mainstream. Both have L/D = 2.3. Actual engine L/D's range over $1 < L/D < 10$. The total baffle length is 25.3 cm (13.3D) with the entrance to the channel located 10.5 cm (5.5D) upstream from the leading edge of the holes. The delivery channel height is 2D. The film cooling hole-to-channel cross-sectional area ratio is 0.125.

Measurements

Single-sensor, hot-wire anemometry (TSI Model 1218-T1.5 connected to a TSI IFA-100 anemometer bridge) is used to measure instantaneous velocity over the exit plane of the film cooling holes. Measurements were with a 3.81-μm-dia hot wire, with an

Nomenclature

D = film cooling hole, pipe, or cylinder diameter, m
$E(\kappa)$ = wave number based power spectral density, m^3/s^2
$E(f)$ = frequency based power spectral density, m^2/s
f = frequency, Hz
k = turbulence kinetic energy, m^2/s^2
L = film cooling hole length, m
L_u = energy or dissipation turbulent length scale, m
I = coolant-to-mainstream momentum flux ratio
P = frequency-weighted spectra = $E(f) \times f/(u_{eff})^2$
Re = Reynolds number based on U_∞ and D
Re_D = Reynolds number based on U_{hole} and D
St = Strouhal number = fD/U_{eff}
St_D = Strouhal number = fD/U_{hole}
t = wall thickness of hole extension tube, m
U_{eff} = mean effective velocity, m/s
U_{hole} = bulk mean film cooling hole (pipe) velocity, m/s
U_∞ = free-stream velocity, m/s
VR = coolant-to-mainstream velocity ratio
u_{eff} = rms fluctuation about U_{eff}, m/s
x = streamwise distance from hole center, m
y = wall-normal distance, m
z = lateral distance from hole center, m
δ^* = boundary layer displacement thickness, m
δ_{99} = boundary layer thickness (99%), m
$\Delta\dot{m}$ = mass flow uncertainty (95% confidence), kg/s
ϵ = dissipation rate, m^2/s^3
η = Kolmogorov or microscale of turbulence, m
θ = boundary layer momentum thickness, m
κ = wave number, m^{-1}
Λ = integral length scale, m
ν = kinematic viscosity, m^2/s

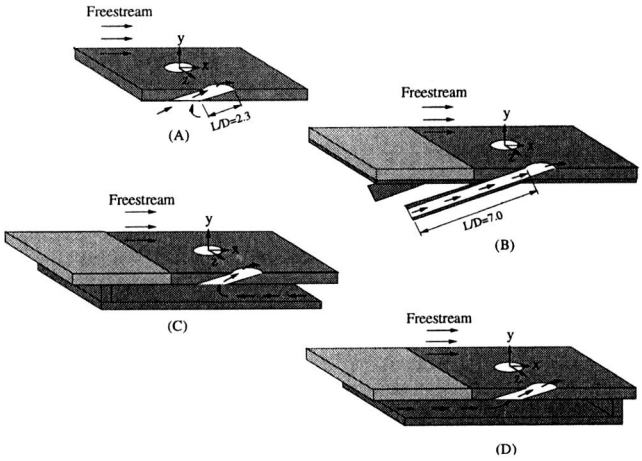

Fig. 1 Film cooling geometries

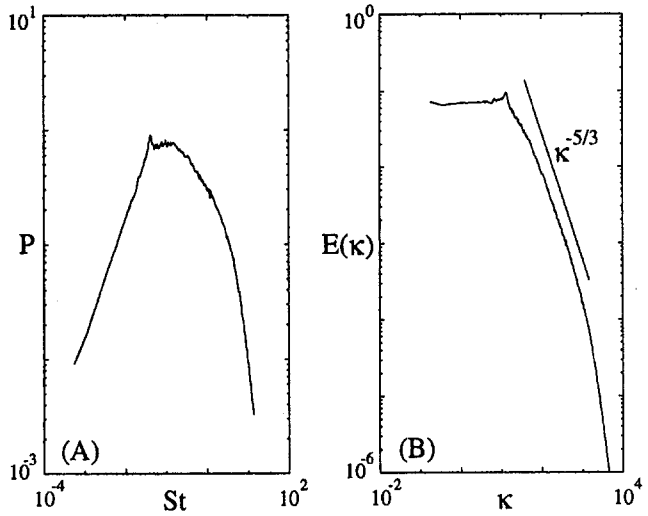

Fig. 3 Spectra of free stream

active length-to-diameter ratio of 300, positioned normal to the free stream and parallel to the film-cooled surface (Fig. 2). Thus, the measured velocities are effective cooling velocities to the hot-wire sensor, U_{eff}. Spectral distributions were measured along the streamwise hole centerline at $x/D = -0.5$, $x/D = 0.0$, and $x/D = 0.5$ of a single hole, of the eleven-hole array, as shown in Fig. 2. Surveys of velocities over all the holes show hole-to-hole uniformity to within 2 percent.

For brevity, hole-exit velocity, U_{eff}, and rms turbulence level, u_{eff}, distributions are not presented in this paper. Readers are referred to Burd and Simon (1997, 1999) for such measurements. In general, both L/D and flow entry geometry influence hole exit velocity profiles. Short holes exhibit high momentum or "jetting" toward the windward (upstream relative to the free stream) portion of the exit plane whereas longer lengths result in more uniform velocity profiles or slight skewing toward the leeward portion of the exit plane. With short holes, changes in supply plenum geometry influence the location and size of the separation zones that form at the entrance of the film cooling holes. With coflow, coolant momentum is higher in the leeward portion of the exit plane and with counterflow, there is substantial "jetting" toward the windward portion of the exit plane.

Film Cooling Spectra. The hot-wire voltage was sampled using a 16-bit analog-to-digital converter (IOTECH Model #ADC 488/8SA) in batch sizes of 262,144. Low-pass filtering was performed using a dual-channel filter (Stanford Research Systems, Inc., Model SR650).

After acquiring data, a fast Fourier transform was performed using Matlab software (The Math Works, Inc.) yielding the power spectral distribution (Hinze, 1975):

$$E(f) = \frac{[u_{\text{eff}}(f, df)]^2}{df} \quad \text{and} \quad E(f) = \frac{2\pi}{U_{\text{eff}}} E(\kappa) \qquad (1)$$

Spectral measurements were recorded in four segments, then pieced together during post-processing to yield a total of 1.05 million points for each spectral distribution. The sampling frequencies associated with these segments were 20 kHz, 2 kHz, 200 Hz, and 20 Hz. Low-pass filtering for these cases was at 10 kHz, 1 kHz, 100 Hz, and 10 Hz, respectively. This just satisfies the Nyquist sampling criterion. It was not aggressive enough to remove all alias error from the sampled data records. The use of four segments, however, produced large bands of overlap between spectra gathered at different sampling frequencies. Thus, aliases were removed by joining individual segments to produce a single continuous spectrum from the four segments, with only the highest frequency band containing a small amount of alias error. As a check, the sampling frequency was doubled and no appreciable differences were noted. Without smoothing, the spectra distributions would exhibit substantial scatter. Smoothing was employed using Hanning windowing.

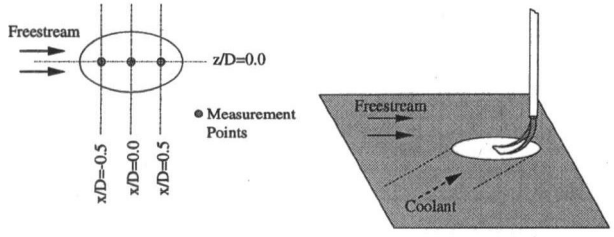

Fig. 2 Measurement locations

The spectral distribution in this paper are presented in two plot formats. The first details P (the product of the power spectral density, $E(f)$, and the local frequency, f, normalized on u_{eff}^2) versus St (e.g., Fig. 3(A)). This type of figure is useful for determining the proportional energy content of the flow at particular frequencies for, in this form, the area under the curve in any frequency band is proportional to the energy in that frequency band. The second type of plot details the power spectral density, $E(\kappa)$, versus the wave number, κ (e.g., Fig. 3(B)). This plot is useful in determining the dissipation rate and scales within the coolant flow. Examples of the spectra are given in Fig. 3. This figure highlights spectra measured in the free stream. On Fig. 3(B), the various regimes of the spectra can be easily distinguished. At low frequencies, the energy is associated with the largest eddies in the flow and whatever unsteadiness may exist at those frequencies. At high frequencies, the spectra denote the inertial subrange (identified by the $\kappa^{-5/3}$ relationship) and, for higher κ, the dissipation range. At midfrequencies, the spectra distribution is related to the energy-containing eddies in the flow (e.g., peak in Fig. 3(A)). Very low-frequency ($f < 10$ Hz) spectral data are not representative of turbulence and merely highlight some low-frequency unsteadiness of the film cooling and mainstream flows.

The single-sample uncertainties involved in single-sensor measurements of velocity are typically larger at smaller velocities. Bias errors result from items such as changes in fluid properties between calibration and measurement, instantaneous flow reversal over the sensor, and sensor drift. A standard propagation, as detailed by Kline and McClintock (1953), of uncertainty contributions assigned for these various effects yields a combined uncertainty on time-mean and rms velocity fluctuations of 5–7 percent. Due to the large sample sizes and long sampling times associated with the hot-wire calibration and measurements, sto-

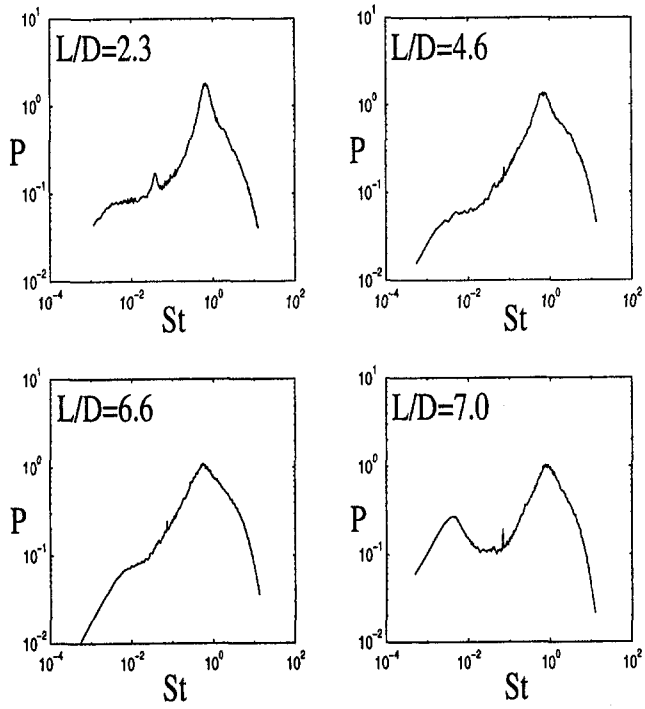

Fig. 4 Spectral distributions at *x/D* = 0 for *L/D*'s at *VR* = 1.0

chastic errors fall well below the deterministic errors and are negligible in comparison. Comparisons of mean velocity and turbulence intensity to data by Laufer (1953), Lawn (1971), Bremhorst and Walker (1973), and Berman and Dunning (1973) in a fully developed pipe flow are used to corroborate these uncertainty values. Per these data, uncertainty values on the order of 5 percent of mean values are reasonable under the conditions of the bulk of the present data, so long as velocity fluctuation rms levels remain below 25 percent of the local measured velocity. Flow reversal over the sensor would be rectified, causing error in both fluctuation magnitude and the indicated frequency. Analyses by Russ and Simon (1990) indicate that such errors become significant for turbulence intensities in excess of 25 percent. Spectra measurements were taken in flows that did not violate the 25 percent criterion. These uncertainties are consistent with previous experience with such measurements and with Yavuzkurt (1984).

Spectra With Varying *L/D*. Four film cooling hole geometries having L/D = 2.3, 4.6, 6.6, and 7.0 with a large, open plenum ("sink" flow delivery, Figs. 1(*A*) and 1(*B*)) were investigated to document the effects of hole length.

Figures 4 and 5 show such data (P versus St) at the hole center ($x = y = z = 0$) with VR = 1.0 and 0.5, respectively. It is evident that all the coolant flows exhibit the same dominant frequencies, centered on St = 0.8, suggesting turbulent scales on the order of $0.8D$. This is similar to the range of scales of temperature fluctuations found by Kohli and Bogard (1998). For the VR = 1.0 case, Fig. 4, data from short holes exhibit concentration in a narrower part of that frequency range. Data from long holes are more typical of fully developed flows, like those given for the free stream in Fig. 3. Also, peak values are higher with small L/D than with large L/D, suggesting attenuation of some energy with increased hole length. Although not presented, spectral measurements were also taken without the free stream flow. These spectra still exhibit the same range of dominant frequencies, $0.5 < \text{St} < 0.9$, for all cases and show that the peak dies off as the hole length is increased. It is speculated that this dominant frequency corresponds to the frequency of unsteady separation at the hole entrance and is not associated with any processes in the coolant–mainstream mixing zone.

Recall that the free-stream turbulence is centered around St = 0.05 (Fig. 3). Noteworthy is that the influence of this low-frequency free-stream turbulence ($0.02 < \text{St} < 0.07$) is small. In the spectra, some low-frequency unsteadiness ($\text{St} < 0.01$) is visible. It is most evident for the L/D = 7.0 cases, primarily focused at the windward and center measurement locations, and is measured with and without the external free-stream flow. Since this unsteadiness is substantial for L/D = 7.0 and minor for L/D = 6.6, it is attributed to differences in inlet geometries and the associated separation zones at inlet. Unlike the other cases, L/D = 7.0 has no strong preference for the separation location at the inlet. This may make this geometry more susceptible to low-cycle unsteadiness within the coolant supply flow. It is likely that this separation oscillates or precesses.

For VR = 0.5 (Fig. 5), trends similar to the VR = 1.0 case are observed. With the lower coolant momentum, differences between L/D cases are lessened. The shorter L/D's cases exhibit more peaking of energy, but not to the extent found in Fig. 4. Also, all the peak magnitudes are below those for the VR = 1.0 flow. Finally, the VR = 0.5 flow cases appear to be more influenced by the free stream than for VR = 1.0 case, since more distinct energy is visible in the $0.02 < \text{St} < 0.08$ range.

Given the distinctly different distributions of exit velocity with different L/D (Burd and Simon, 1997, 1999), it is also likely that spectra may change from one position to another within the emerging jet. To document this, data at $y = z = 0$ were also taken at $x/D = -0.5$ (upstream of hole center) and x/D = 0.5 (downstream of hole center). Figures 6 and 8 highlight these measurements for L/D's of 2.3, 4.6, and 7.0 and VR = 1.0.

Upstream, $x/D = -0.5$ (Fig. 6), there are very distinct differences for different L/D's. Dominant frequencies are visible in each of the coolant flows, but they center about St = 0.6 for the short lengths and St = 1.0 for L/D = 7.0. With such inclined holes, L/D = 2.3 and L/D = 4.6 cases would be expected to have substantial separation zones and associated shearing at the inlet to the delivery hole, whereas the L/D = 7.0 case would have a smoother entrance, a smaller vena contracta, and more decay of the effect of this region over the longer delivery length. A sketch of the expected separation zones is shown in Fig. 7. It is apparent from Fig. 6 that the peaks are more defined and larger for L/D = 2.3,

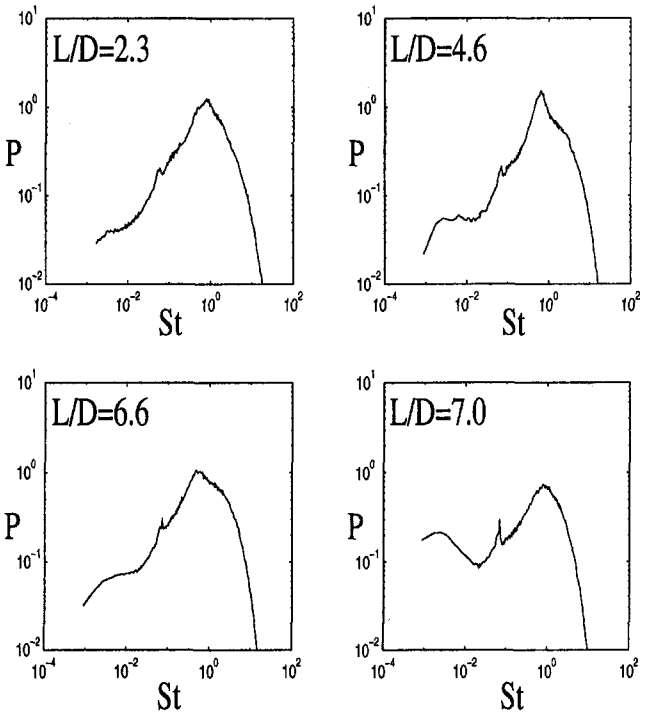

Fig. 5 Spectral distributions at *x/D* = 0 for *L/D*'s at *VR* = 0.5

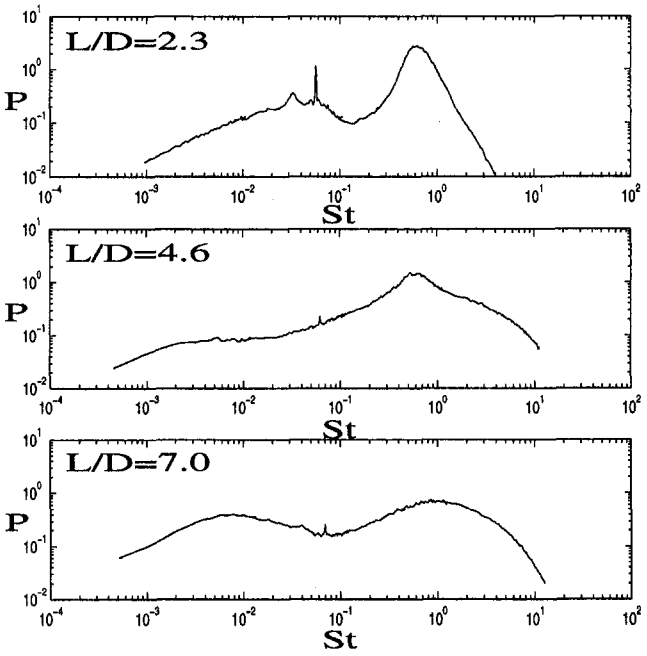

Fig. 6 Spectral distributions at $x/D = -0.5$ for $L/D = 2.3$, 4.6, and 7.0 and $VR = 1.0$

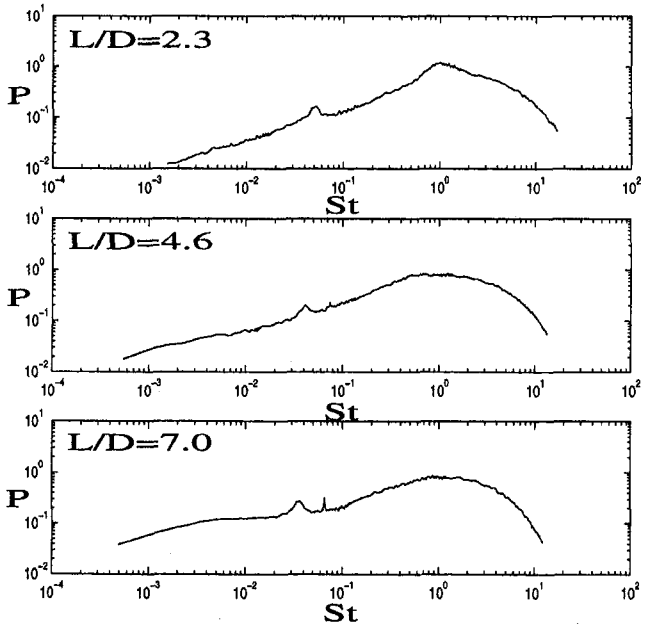

Fig. 8 Spectral distributions at $x/D = 0.5$ for $L/D = 2.3$, 4.6, and 7.0 and $VR = 1.0$

decreasing as L/D increases. As discussed by Burd and Simon (1997), the shorter L/D cases are more susceptible to "jetting" or having higher velocities in the windward portion of the hole exit plane (see Fig. 7(*A*)), yielding significantly more coolant mass and turbulence energy in that region. Perhaps the most intriguing aspect of Fig. 6 is found in looking for frequencies that may be associated with the free stream. Both $L/D = 4.6$ and $L/D = 7.0$ cases show very little energy at the free-stream frequencies ($0.02 < St < 0.07$) in their spectral distributions. The $L/D = 2.3$ case has more prominent jetting toward the windward side of the hole (see Fig. 7(*B*)) and is expected to have more momentum exchange with the free stream in the upstream portion of hole exit plane. Indeed, more influence of the free stream is being "felt" at this upstream location with the short hole, as evidenced by more energy in the $0.02 < St < 0.07$ range (Fig. 6, $L/D = 2.3$). The interaction is probably not influential, however, for the coolant-energy and free-stream-induced-energy peaks remain separated in frequency and the fraction of energy at the free-stream-dominant frequency is relatively low.

Measurements leeward of hole center are presented in Fig. 8. Unlike in the upstream measurements, the distributions for all L/D's are similar; all exhibit the majority of their energy content in the frequency band $0.3 < St < 3.0$ and show little influence of free-stream frequencies. Peak energies are centered about $St = 1.0$, suggesting a turbulence scale equal to one hole diameter. As in Figs. 4 and 6, the short L/D cases exhibit more concentrated peak energy. Though a modest contribution, the free-stream frequency influence ($0.02 < St < 0.07$) appears to increase mildly with L/D.

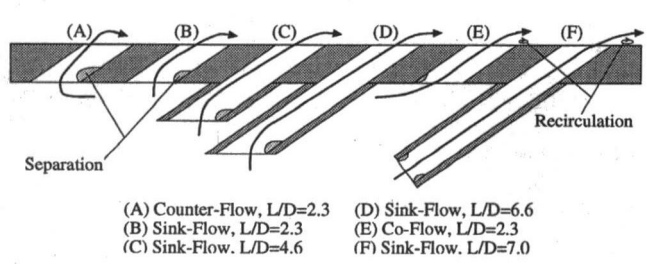

Fig. 7 Expected flow patterns of coolant through various hole geometries

Spectra With Modified Entrance Flow. Spectral distributions (Figs. 9–11) were also taken for film cooling with $L/D = 2.3$ and modified entrance flow (Figs. 1(*C*) and 1(*D*)). Corresponding hole-exit velocity distributions for these configurations were presented by Burd and Simon (1997, 1999).

In general, the spectra for counterflow and coflow are similar to one another at all measurement locations. Contrary to the short-hole, sink-flow configuration, these flows have coolant flow delivered to the holes through a closed channel. As this coolant flow approaches the entrance to the holes, a turbulent boundary layer develops within the channel. This boundary layer is eventually ingested into the hole, contributing midfrequency energy ($St \sim 0.1$) to the coolant flow. The net effect is a broader-band spectra for counter- and coflow, with additional energy in the frequency range $0.005 < St < 0.4$.

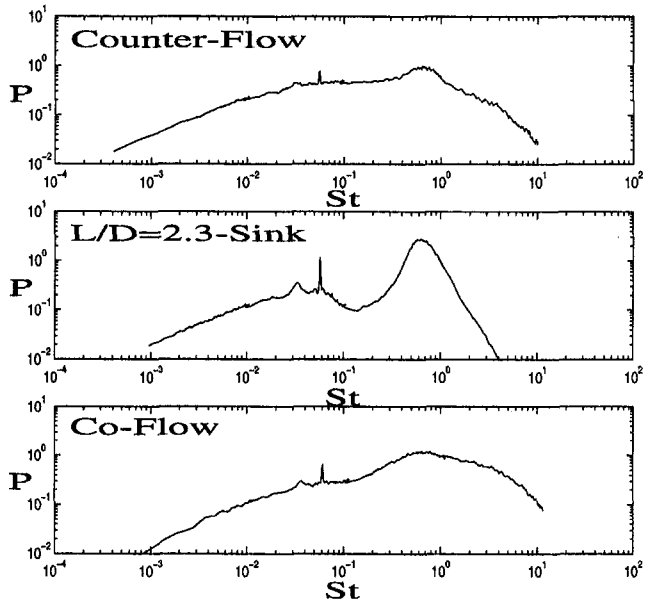

Fig. 9 Spectra distributions with $L/D = 2.3$ and modified entrance flow at $x/D = -0.5$ and $VR = 1.0$

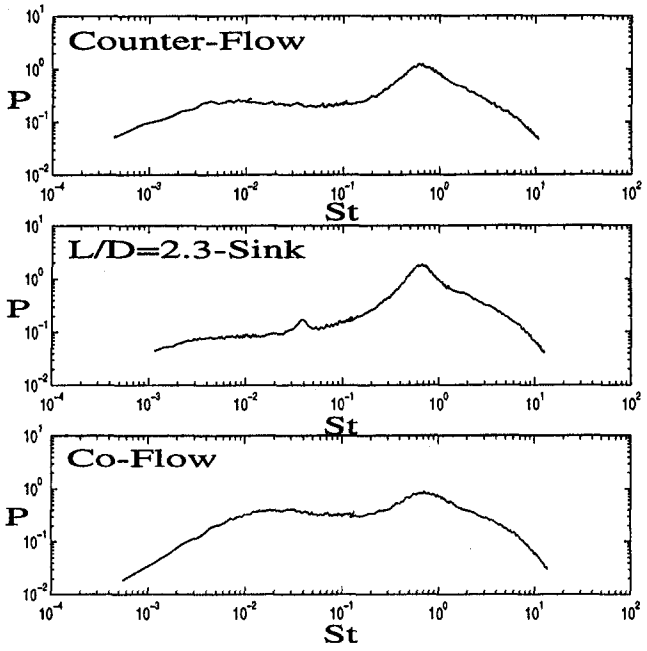

Fig. 10 Spectra distributions with *L/D* = 2.3 and modified entrance flow at *x/D* = 0.0 and *VR* = 1.0

Figure 9 highlights the spectral distributions for $x/D = -0.5$. All cases show a energy peak at St = 0.6–0.7. This was previously attributed to unsteady separation at the hole inlet. The peak is less well defined for counter- and coflow. The counterflow case has the most prominent "jetting," or skewing of the exit velocity distribution toward the windward portion of the hole, and, thus, is expected to have the highest momentum exchange with the free stream in the upstream portion of hole exit plane (see Fig. 7). Unlike the "sink flow" case, this interaction is strong enough that the free stream ($0.02 < St < 0.07$) and coolant peak ($St \sim 0.6$) energies have merged. With coflow, the extent of jetting is reduced

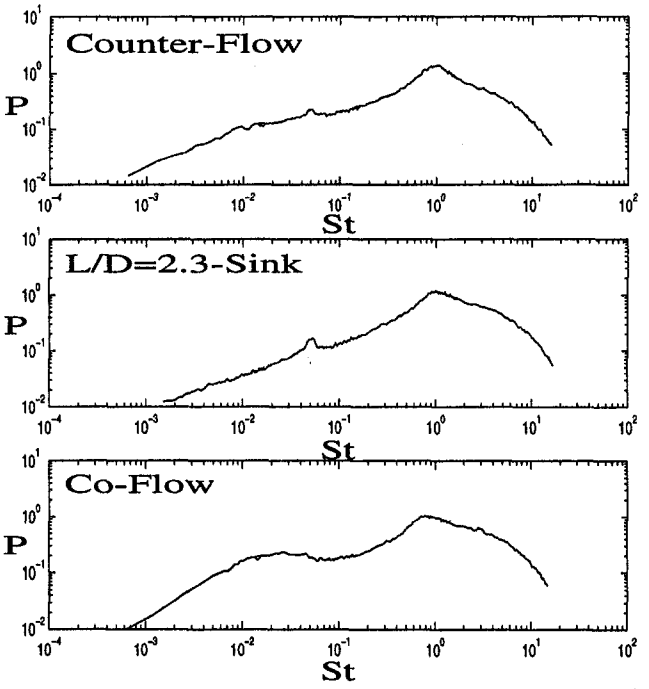

Fig. 11 Spectra distributions with *L/D* = 2.3 and modified entrance flow at *x/D* = 0.5 and *VR* = 1.0

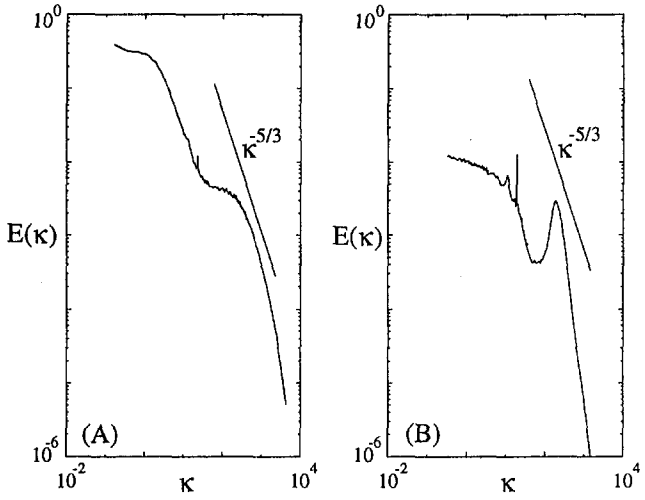

Fig. 12 Examples of spectra for short and long holes: (*A*) *L/D* = 7.0, *x/D* = −0.5, *VR* = 1.0; (*B*) *L/D* = 2.3, *x/D* = −0.5, *VR* = 1.0

significantly (Burd and Simon, 1997); thus, coolant–free-stream interaction is weaker. As a result, the free-stream influence ($0.02 < St < 0.07$) is reduced.

Distributions at the hole center ($x = y = z = 0$) are in Fig. 10. All configurations still have an energy peak about $0.6 < St < 0.7$, with the "sink flow" configuration being most pronounced. Again, with the channel delivery, counter- and coflow have more significant energy for $St < 0.3$. Since the coolant jetting and interaction with the free stream is at the windward portion of the hole exit, the energy at the free-stream frequencies, $0.02 < St < 0.07$, is reduced at this location.

At $x/D = -0.5$ (Fig. 11), distributions for all the configurations are again similar to one another. Well-defined peak energies are common to all the cases while counter- and coflow continue to exhibit the broader spectrum. Coflow exhibits slightly higher energy levels for $0.02 < St < 0.05$. This suggests that coflow unsteadiness may be more influenced in the leeward portion of the hole, primarily due to more downstream interaction with the free stream.

Turbulence Parameters and Scales. Thus far, normalization has been with the hole diameter. For better understanding and complete documentation, more characterization of the turbulent scales, local turbulent kinetic energy (k), and local dissipation rates (ϵ) is needed. These quantities are particularly useful in computational modeling using k–ϵ or large eddy simulation (LES) models.

A common methodology for characterizing length scales in turbulent flows is the integral length scale (Hinze, 1975), a measure of the largest eddies in the flow:

$$\Lambda = \lim_{f \to 0} \left[E(f) \times \frac{U_{\text{eff}}}{4(u_{\text{eff}})^2} \right] = \lim_{\kappa \to 0} \left[E(\kappa) \times \frac{2\pi}{4(u_{\text{eff}})^2} \right] \quad (2)$$

As $f \to 0$, $E(f)$ typically plateaus.

For long film cooling holes, spectral distributions similar to those shown in Fig. 3(*B*) are found. Unlike free-stream spectra, though, coolant spectra have two regions in which $E(\kappa)$ tend to plateau (Fig. 12). One corresponds to low-frequency unsteadiness ($f \to 0$) and the other is considered to correspond to the larger scales of turbulence. Length scales computed from Eq. (2) using $E(\kappa)$ at this second plateau are generally about 0.1–$0.5D$, characteristic of values found for developing and near-fully developed pipe flows.

Power spectral density distributions can also be used to determine energy dissipation rates when a $-\frac{5}{3}$ equilibrium inertial subrange exists (Hinze, 1975). This is done using Eq. (3) below, in

which the dissipation rate is calculated by locating points, (κ, $E(\kappa)$), on the spectral distributions that are tangent to a $\kappa^{-5/3}$ line:

$$E(\kappa) = \tfrac{18}{55} \times 1.62 \times \epsilon^{2/3}\kappa^{-5/3} \quad (3)$$

The selection of the coefficient 1.62 is consistent with Hinze. Other results may suggest the use of a different empirical value. In using this type of analysis, an assumption of isotropy must be employed. These flows are not expected to be isotropic in the larger scales, but in the inertial subrange, the turbulence is anticipated to be reasonably isotropic. Thus, this model is considered to give a suitable estimate of dissipation when a $-\frac{5}{3}$ relationship is visible in the power spectra. Dissipation rates are not calculated for several cases with a shorter delivery length, however, as they tended to not follow this relationship. The dissipation rates calculated are listed in Table 1 and are generally observed to be smallest for (1) low *VR*'s, and (2) longer film cooling hole lengths. It was previously speculated that these cases have less interaction with the free-stream. This speculation is supported by the spectra in Figs. 4, 5, 6, and 8. Also, dissipation values tend to be lowest in the region of highest coolant velocity and lowest turbulence kinetic energy. This generally corresponds to regions in coolant flows where shear is low.

The local turbulence kinetic energy is calculated using the measured rms velocity fluctuations (Table 1). To determine the local turbulence kinetic energy, k, a formulation that again assumes that the turbulence was isotropic (i.e., that rms components perpendicular to U_{eff} were also equal to u_{eff}) was used:

$$k = 1.5(u_{\text{eff}})^2 \quad (4)$$

Observations regarding turbulence kinetic energy are that: (1) k magnitudes are largest for short film cooling hole lengths and decrease monotonically as *L/D* is increased, (2) k scales on *VR*, and (3) locations of highest coolant momentum tend to have lowest k values.

Knowledge of the turbulence kinetic energy and the dissipation rate provides a means of calculating the energy or dissipation length scale (Hancock and Bradshaw, 1983). Calculated L_u are also provided in Table 1.

$$L_u = \frac{1.5(u_{\text{eff}})^3}{\epsilon} = \frac{0.817(k)^{3/2}}{\epsilon} \quad (5)$$

A final scale that is deduced from the measurements is the Kolmogorov or microscale of turbulence (Table 1):

$$\eta = \left(\frac{\nu^3}{\epsilon}\right)^{1/4} \quad (6)$$

Several trends are apparent. Energy length scales for all cases tend to fall into the range $0.1 < L_u/D < 0.45$. No correlation with parameters emerges. In general, microscales of turbulence are largest for low *VR*'s. No other correlations are clear.

Conclusions

Spectral distributions have been measured for a variety of film cooling configurations of differing film cooling hole lengths and coolant supply flow orientations. The results highlight some of the fundamental differences. Where possible, physical explanations of the trends were given. The distributions of turbulence energy were dependent on the film cooling design and the measurement location over the exit plane.

In general, coolant flows through long and short holes exhibit nominally the same ranges of peak-energy frequencies. The range of dominant frequencies is $0.5 < \text{St} < 0.9$ for measurements over the upstream portion and center of the hole exit-plane. Slightly larger peak frequencies are evident for flows over the downstream portion of the hole-exit plane ($0.8 < \text{St} < 1.0$). Such dominant frequencies suggest dominant turbulence scales of 0.5–$1.0D$ for coolant flows.

Documentation of additional turbulence parameters, including dissipation rates, and integral, energy, and Kolmogorov length scales, is also presented. In general, these data highlight the fact that short holes have higher dissipation values. Length scales for all geometries tend to be nominally of the same order of magnitude.

Useful for CFD and turbulence modeling is that though energy at the free-stream turbulence length scales is visible in the spectra (some spectra show it to be more prominent than others), it never seems to dominate the spectra. This implies that computation of the coolant flow and the free-stream-mixing zone could be separated so long as the appropriate velocity distribution of the coolant flow was imposed.

Acknowledgments

This work is part of a combined study of film cooling with short film cooling holes and lateral injection sponsored by the NASA-Lewis Research Center and Department of Energy, respectively. The NASA project manager is Douglas Thurman. The DOE project is managed by Dr. Daniel Fant of the South Carolina R&D Center.

References

Azad, R. S., Arora, S. C., and Reichert, J. K., 1978, "Spectra of Reynolds Stresses in a Developing Pipe Flow," *Proc. 1978 Heat Transfer and Fluid Mech. Inst.*, Pullman, WA, June 26–28, pp. 281–295.

Berman, N. S., and Dunning, J. W., 1973, "Pipe Flow Measurements of Turbulence and Ambiguity Using Laser-Doppler Velocimetry," *J. Fluid Mech.*, Vol. 61, Part 2, pp. 289–299.

Bremhorst, K., and Walker, T. B., 1973, "Spectral Measurements of Turbulent Momentum Transfer in Fully Developed Pipe Flow," *J. Fluid Mech.*, Vol. 61, Part 1, pp. 173–186.

Burd, S. W., and Simon, T. W., 1997, "The Influence on Film Cooling Supply Geometry on Film Coolant Exit and Surface Adiabatic Effectiveness," ASME Paper No. 97-GT-25.

Burd, S. W., Kaszeta, R. W., and Simon, T. W., 1998, "Measurements in Film Cooling Flows: Hole *L/D* and Turbulence Intensity Effects," ASME JOURNAL OF TURBOMACHINERY, Vol. 120, pp. 791–798.

Burd, S. W., and Simon, T. W., 1999, "Measurements of Discharge Coefficients in Film Cooling," ASME JOURNAL OF TURBOMACHINERY, Vol. 121, pp. 243–248.

Fried, E., and Idelchik, I. E., 1989, *Flow Resistance: A Design Guide for Engineers*, Hemisphere Publishing Corp., New York.

Hancock, P. E., and Bradshaw, P., 1983, "The Effect of Free-Stream Turbulence on Turbulent Boundary Layers," ASME *Journal of Fluids Engineering*, Vol. 105, pp. 284–289.

Hinze, J. O., 1975, *Turbulence*, McGraw-Hill, New York.

Kline, S. J., and McClintock, F. A., 1953, "Describing Uncertainties in Single-Sample Experiments," *Mech. Eng.*, Jan., pp. 3–8.

Kohli, A., and Bogard, D. G., 1998, "Effects of Very High Free-Stream Turbulence on the Jet-Mainstream Interaction in a Film Cooling Flow," ASME JOURNAL OF TURBOMACHINERY, Vol. 120, pp. 785–790.

Laufer, J., 1953, "The Structure of Turbulence in Fully Developed Pipe Flow," NACA Report 1174.

Lawn, C. J., 1971, "The Determination of the Rate of Dissipation in Turbulent Pipe Flow," *J. Fluid Mech.*, Vol. 48, Part 3, pp. 477–505.

McMahon, H. M., Hester, D. D., and Palfrey, J. G., 1971, "Vortex Shedding From a Turbulent Jet in Crosswind," *J. Fluid Mech.*, Vol. 48, pp. 73–80.

Russ, S., and Simon, T. W., 1990, "Signal Processing using the Orthogonal Triple-Wire Equations," *Flow Lines*, The TSI Quarterly Magazine, Winter.

Walters, D. K., and Leylek, J. H., 1997, "A Detailed Analysis of Film-Cooling Physics: Part 1—Streamwise Injection With Cylindrical Holes," ASME Paper No. 97-GT-269.

Wang, L., 1996, "A Study of Gas Turbine Flows, Turbulence Generation, and Film Cooling Flow Measurement," M.S. Thesis, Department of Mechanical Engineering, University of Minnesota.

Yavuzkurt, S., 1984, "A Guide to Uncertainty Analysis of Hot-Wire Data," ASME *Journal of Fluids Engineering*, Vol. 106, pp. 181–186.

Heat Transfer and Flowfield Measurements in the Leading Edge Region of a Stator Vane Endwall

M. B. Kang

A. Kohli[1]

K. A. Thole

Mechanical Engineering Department,
University of Wisconsin,
Madison, WI 53706

The leading edge region of a first-stage stator vane experiences high heat transfer rates, especially near the endwall, making it very important to get a better understanding of the formation of the leading edge vortex. In order to improve numerical predictions of the complex endwall flow, benchmark quality experimental data are required. To this purpose, this study documents the endwall heat transfer and static pressure coefficient distribution of a modern stator vane for two different exit Reynolds numbers ($Re_{ex} = 6 \times 10^5$ and 1.2×10^6). In addition, laser-Doppler velocimeter measurements of all three components of the mean and fluctuating velocities are presented for a plane in the leading edge region. Results indicate that the endwall heat transfer, pressure distribution, and flowfield characteristics change with Reynolds number. The endwall pressure distributions show that lower pressure coefficients occur at higher Reynolds numbers due to secondary flows. The stronger secondary flows cause enhanced heat transfer near the trailing edge of the vane at the higher Reynolds number. On the other hand, the mean velocity, turbulent kinetic energy, and vorticity results indicate that leading edge vortex is stronger and more turbulent at the lower Reynolds number. The Reynolds number also has an effect on the location of the separation point, which moves closer to the stator vane at lower Reynolds numbers.

Introduction

Increasing exiting combustor temperatures for future gas turbine designs lead to high heat load demands on downstream turbine vanes. One of the regions having the highest heat transfer is where the leading edge of the vane meets the endwall. As the endwall boundary layer approaches the stagnation location of the protruding turbine vane, it experiences an increase in pressure, causing a stronger deceleration for the higher speed fluid than the lower speed fluid in the boundary layer. As a result of these differences in the deceleration, a transverse pressure gradient occurs along the vane, causing the higher speed fluid to turn toward the endwall plate. Subsequently, the formation of a horseshoe vortex occurs just upstream of the turbine vane. One of the legs of the horseshoe vortex wraps around the pressure side of the vane and the other around the suction side of the vane.

There have been quite a few studies documenting endwall characteristics for rotors, but fewer stator vane studies, which typically have less of a turning angle and higher flow accelerations than rotors where both effects are believed to influence the secondary flows. Based on previously reported studies, there is still a need for a better understanding of the endwall flow, particularly in the leading edge region where the leading edge horseshoe vortex is formed and its relationship with secondary flows in the passage. Before computational efforts can expect to simulate the complex flowfield in the vane passage, it is imperative that the leading edge horseshoe vortex be correctly predicted. This study involves quantifying the surface heat transfer as well as the horseshoe vortex that occurs in the leading edge endwall region of a modern turbine vane geometry. Highly resolved surface heat transfer measurements, made through the use of an infrared camera, will be reported for two different Reynolds numbers. In addition to surface heat transfer measurements, flow field measurements of the leading edge vortex and a comparison of measured and CFD predicted endwall static pressure will be discussed.

Past Studies

As mentioned earlier, many of the endwall investigations presented in the open literature have used airfoil geometries that have high turning angles, which are more representative of rotor geometries. Sieverding (1985) presents a summary of endwall flowfield models for rotor passages including one of the first models as presented by Langston et al. (1977). All of these studies imply the formation of the horseshoe vortex at the leading edge–endwall intersection with a pressure-side leg and suction-side leg.

Since the blade curvature is an important effect in setting up the secondary flows, it is difficult to apply these same results to a stator vane that has a smaller turning angle. This fact is illustrated by Bailey (1980) in which he compared vane flowfield measurements by Marchal and Sieverding (1977) to rotor flowfield measurements by Langston et al. (1977). This comparison was made near the exits of the vane and rotor passages, which showed that the extent of the passage vortex was much greater for the vane than for the rotor. In addition, while the passage vortex was centered halfway between the suction and pressure surfaces for the vane, it was located nearer to the suction surface in the rotor. Bailey himself presented flowfield measurements for the endwall of a turbine vane in which his results concurred with Marchal and Sierverding's (1977), but was complicated by the fact that his test facility did not simulate the leading edge vortex.

[1] Present address: Pratt & Whitney, 400 Main Street, MS 169-02, East Hartford, CT 06108.

Contributed by the International Gas Turbine Institute and presented at the 43rd International Gas Turbine and Aeroengine Congress and Exhibition, Stockholm, Sweden, June 2–5, 1998. Manuscript received by the International Gas Turbine Institute February 1998. Paper No. 98-GT-173. Associate Technical Editor: R. E. Kielb.

Graziani et al. (1980), who used the same rotor geometry as Langston et al. (1977), compared differences between a boundary layer that was thick (15 percent of the span) and thin (2 percent of the span) at the same inlet Reynolds numbers. One could, however, consider these two cases to be a high Re_θ for the thick boundary layer and a low Re_θ for the thin boundary layer, where θ is the momentum thickness. This is in contrast to the results that will be discussed for our paper (in Table 2), whereby the higher Re_θ occurs for the thinner boundary layer. This difference in the relations between thick and thin boundary layers and momentum thicknesses occurs because of how the experiments were conducted. While we maintained the same upstream endwall plate length and only changed the free-stream velocity to vary the Reynolds number, Graziani et al. (1980) maintained the same inlet velocity and shortened their upstream endwall length.

Graziani et al. (1980) showed for their surface streakline visualization at the low Re_θ case (thin boundary layer), there was less cross-over of the ink traces toward the suction side of the airfoil. Although the traces on the blade indicated that for both Re_θ cases there was a movement of the traces toward the midspan of the blade, the high Re_θ case had traces that crawled farther toward the midspan of the blade as compared with the low Re_θ case. As stated by Graziani et al. (1980), both of these results indicate that for the higher Re_θ the passage vortex occupies more of the passage in this region, which would then subject the suction side of the adjacent airfoil to be affected greater by secondary flow effects. The Stanton numbers are also consistent with this in that the contours for the high Re_θ case was more affected by the path of the vortex. Their endwall static pressure measurements, however, indicate lower pressure coefficients for the low Re_θ case, whereby a lower pressure coefficient would be more consistent with a lift-off of the passage vortex. This can be explained, however, by the fact that Graziani et al. (1980) maintained the same inlet velocity and changed the boundary layer by changing the approach plate length. In this case, the actual mass flow rate going through the passage would be more for the thinner boundary layer case and one would expect a larger decrease in the static pressure.

Although the previous data indicate a stronger passage vortex at higher Reynolds number, the data of Graziani et al. (1980) were presented for a rotor. Boyle and Russell (1990) performed experiments for a large Reynolds number range for a stator vane geometry. At low Reynolds numbers, they found that Stanton number contours closely followed the inviscid streamlines from the pressure side to the suction side of the airfoil, while at higher Reynolds numbers the surface heat transfer correlates closely with the free-stream velocity and thereby looks more similar to the static pressure contours.

Because the leading edge-endwall location typically has high heat transfer, particular attention has been paid to that region. On the endwall, one of the regions having the highest heat transfer coefficient is near where the airfoil leading edge meets the endwall. In relating information from the flow visualization to the heat transfer data, Gaugler and Russell (1984) combined two studies, their own and that of York et al. (1984), for a large-scale turbine vane in which they found the peak Stanton number to coincide with the region having the most intense vortex action. They also found near the suction surface a secondary peak in Stanton number, which coincided with the region where the endwall separation line contacts the suction surface at the point where the flow started to climb the suction surface.

Comparisons made by Boyle and Russell (1990) for endwall leading edge heat transfer for various Reynolds numbers and approach plate lengths indicated that heat transfer augmentation was higher at lower Reynolds numbers. Based on their heat transfer measurements for the thick and thin boundary layer cases, Graziani et al. (1980) postulated that the boundary layer separation due to the horseshoe vortex for the thinner inlet boundary layer was closer to the airfoil than for the thicker inlet boundary layer. In comparing two independent studies where the momentum thickness was the same, including the studies of Goldstein and Spores (1988) and Graziani et al. (1980), the Stanton number values and trends in the leading edge region were similar even though the Reynolds number was four times greater for Graziani et al. These results would indicate that for a rotor there is only a weak dependence on Reynolds number.

One study in which the leading edge vortex has been measured is that presented by Pierce and Harsh (1988) who used a streamlined cylinder normal to a flat plate where the $Re_D = 1.7 \times 10^5$, based on the inlet velocity, and having a boundary layer thickness-to-cylinder diameter ratio of $\delta_{99}/D = 0.63$. These results indicated a single vortex where the center of that vortex is located approximately $0.8D$ upstream of the cylinder. Heat transfer data reported by Goldstein and Spores (1988), however, had two peaks that near the leading edge indicated the presence of a corner vortex, causing an intense spike in the mass transfer coefficients, and the presence of the horseshoe vortex, causing a slight rise in the mass transfer coefficients. The flowfield data of Pierce and Harsh (1988) indicate only a single vortex but, as pointed out by Pierce and Harsh, this may be due to the resolution of the grid. In addition, because the data were acquired with a pitot probe, there was no information

Nomenclature

C = true chord of stator vane
C_p = pressure coefficient = $(p - p_{in})/\frac{1}{2}\rho U_{in}^2$
D = diameter of vane leading edge = $2R$
H = shape factor = δ^*/θ
k = turbulent kinetic energy = $\frac{1}{2}(u_{rms}^2 + v_{rms}^2 + w_{rms}^2)$
p = static pressure
R = radius of vane leading edge
Re_{ex} = Reynolds number defined as $Re_{ex} = CU_{ex}/\nu$
Re_2 = Reynolds number defined as $Re_2 = 2RU_{in}/\nu$
Re_θ = Reynolds number defined as $Re_\theta = U_{in}\theta/\nu$
s = distance along streamline
S = half-span height of stator vane
St = Stanton number defined as $St = h/\rho CpU_{in}$
U, u = streamwise mean and fluctuating velocities
U^+ = mean velocity in wall coordinates = $U/\sqrt{\tau_w/\rho}$
U_{in} = averaged inlet velocity over two vane pitches
V, v = pitchwise mean and fluctuating velocities
W, w = spanwise mean and fluctuating velocities
x = streamwise distance from stagnation point
y = pitchwise distance from stagnation point
z = spanwise distance measured from endwall surface
z^+ = spanwise distance in inner coordinates, $z^+ = z\sqrt{\tau_w/\rho}/\nu$
δ_{99} = boundary layer thickness
δ^* = displacement thickness
ϵ = dissipation
θ = momentum thickness
ν = viscosity
ρ = density
τ_w = wall shear stress
ω_y = vorticity in the pitchwise direction = $(\partial U/\partial z) - (\partial W/\partial x)$

Subscripts

avg = average
in = inlet
ex = exit
rms = root mean square

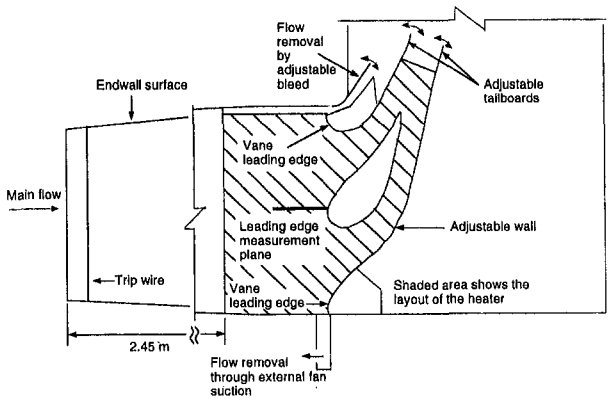

Fig. 1 View of the corner turbine vane test section

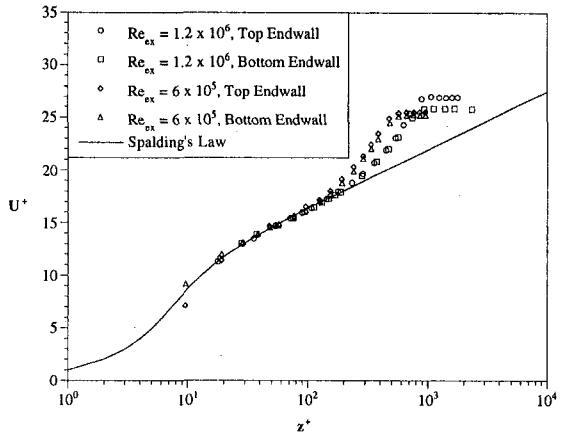

Fig. 2(*a*) Inlet boundary layers measured one chord upstream for two Reynolds numbers on top and bottom endwalls

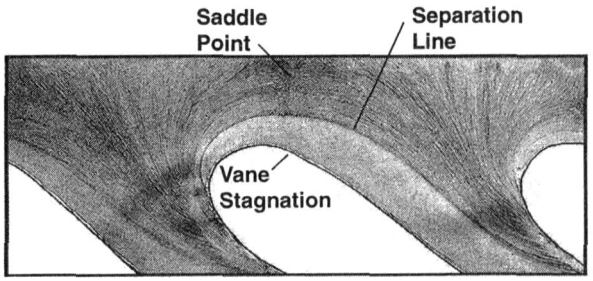

Fig. 2(*b*) Endwall streakline visualization for $Re_{ex} = 1.2 \times 10^6$

regarding the turbulence field associated with the horseshoe vortex region itself.

Based on past studies, there is a clear need to investigate further the heat transfer characteristics of the endwall of a commercial stator vane. Although there has been a link between flowfield visualization and surface heat transfer measurements, a link between measured flowfields and measured heat transfer is still needed. In particular, it is clear that the formation of the leading edge horseshoe vortex still needs to be understood and that there is still a need to provide benchmark data for computational studies.

Experimental Design

A modern stator vane, scaled up by a factor of nine, was placed in a large-scale wind tunnel for this study. The construction and the development of the scaled-up stator turbine vane and the test section have been documented by Bangert et al. (1997). Some modifications were made to the facility described in the above-mentioned study and these will be addressed in this paper. The wind tunnel used in this study is a large recirculating wind tunnel that contains a square test section and a corner test section. Figure 1 shows the corner test section, which contains a scaled-up central turbine vane and two leading edges, representing the two adjacent vanes, which are attached to flexible side walls. The adjacent leading edges were included to insure that the passage vortex was correctly simulated in these experiments. The side wall boundary layers were removed by an adjustable bleed on one side and a suction box on the other to insure that the stagnation point was positioned correctly on the outer leading edges. This allowed for a periodic flow in both passages around the central airfoil. A heat flux plate was placed on the bottom endwall while various lids were placed on the top endwall depending upon the type of measurements that were needed, as will be described later. The flow was prevented from going from the pressure to the suction sides under the vane by applying a sealant at the base of the vane. A description of the turbine vane itself is given by Table 1.

The major modification to the test section of Bangert et al. for this study was the use of both the top and bottom endwalls.

Table 1 Geometric and flow conditions for stator vane

Actual chord length	6.60 cm
Scaling factor	9
Scaled-up chord length	59.4 cm
Pitch/chord	0.77
Span/chord	0.93
Exit Reynolds number	1.2×10^6
Flow inlet angle	0°
Flow exit angle	78°
Approach length/chord	4.1

The heat transfer measurements were made on the bottom endwall while the static pressure and flowfield measurements were made on the top endwall. For this reason, it was important to match the inlet boundary layer for the top and bottom endwalls. Boundary layer growth was controlled using splitter plates of length 2.7 m (or 4.6 vane chords) installed upstream of the stator vane leading edge. The flow approaching the stator vane test section is decelerated by the diffuser only in the lateral direction, while the distance across the span of the turbine vane is held fixed from the start of the splitter plates to the turbine vane. The splitter plates allow flow from the top and the bottom of the diffuser to be diverted; it is then redirected into the wind tunnel downstream of the stator vane test section. This diverted airflow was controlled using valves to insure that the same boundary layer conditions are met on both the top and bottom walls. The flow was tripped at the start of the splitter plates to obtain fully turbulent boundary layers at the inlet to the stator vane test section. The endwall heat transfer and flowfield was investigated for two Reynolds numbers of $Re_{ex} = 6 \times 10^5$ and 1.2×10^6.

Inlet Boundary Layer and Streakline Visualization. Inlet boundary layer measurements using the laser-Doppler velocimeter were done one chord upstream of the stator vane test section on the top and bottom endwalls. These are shown in Fig. 2(*a*) for both the high and low Reynolds number cases and the corresponding boundary layer parameters are listed in Table 2. Note that the incident turbulence level upstream of the vane was 0.6 percent. The results show that there is very good agreement between the boundary layers on the top and bottom endwalls. The ratio of boundary layer thickness to half-span height is $\delta_{99}/S = 0.21$ and $\delta_{99}/S = 0.18$ for the low and high-Reynolds-number cases, respectively. The shape factors for these boundary layers are higher than those predicted by a zero-pressure gradient correlation, but this is expected as the boundary layers experience an adverse pressure gradient in the diffuser section of the wind tunnel. The decrease in boundary layer

Table 2 Inlet boundary layer characteristics

	$Re_{ex} = 6 \times 10^5$		$Re_{ex} = 1.2 \times 10^6$	
	Top	Bottom	Top	Bottom
δ_{99} (cm)	5.8	5.8	5.0	4.8
δ^* (cm)	1.20	1.21	1.06	0.92
θ (mm)	7.8	7.9	7.1	6.2
H	1.55	1.52	1.50	1.48
Re_θ	1870	1900	3340	2960
U (m/s)	3.73	3.70	7.33	7.45

thickness as the Reynolds number is increased between the two cases can be predicted based on a flat plate turbulent boundary layer correlation to be an decrease of 87 percent, which is consistent with the data presented in Table 2. Note that for these endwall studies the Reynolds number, based on the incident velocity and chord length are different by a factor of two, but the boundary layer thickness itself is only a factor of 15 percent different.

Figure 2(*b*) shows the surface streakline patterns on the endwall for the high Reynolds number case, $Re_{ex} = 1.2 \times 10^6$. These streaklines were obtained by painting a mixture of black paint, kerosene, and machine oil on shelf paper that was placed on the endwall. After the mixture was painted on the endwall, the wind tunnel was turned on and after about two hours a steady-state pattern was achieved. This pattern is very similar to those previously reported in the literature. A saddle point is clearly seen upstream of the stagnation location of the vane. The separation line is also clearly seen starting from the suction side of the vane and intersecting with the adjacent vane. This separation line occurs at a streamwise distance upstream of the stagnation location that is $x/R = -0.76$ for $Re_{ex} = 1.2 \times 10^6$ and slightly closer to the vane at $x/R = -0.69$ for $Re_{ex} = 6 \times 10^5$ (not shown here). This location of the separation line occurs at a position near where the flowfield measurements indicate a reverse flow direction (as will be discussed later in the text for Figs. 9(*a*) and 9(*b*)).

Static Pressure Measurements. As mentioned earlier, a different top endwall was designed and installed for the static pressure measurements. Static pressure taps were made using brass tubes with an inside diameter of 0.79 mm. These taps were 9.5 mm long which resulted in a length-to-diameter ratio of 12. The measuring end of the tube was chamfered using a 82 deg countersink. These parameters were chosen to give the most accurate static pressure measurements based on the recommendations of Mattingly (1996). The pressure taps were connected using flexible vinyl hose to two scanivalves (Scanivalve W0602/1P-24T Fluid Switch Wafer), which were connected to two differential pressure transducers (Omega PX 653) with pressure ranges of 0–0.5 and 0–2.0 in. of water. Voltage data from the pressure transducers were acquired using a National Instruments A/D board (AT-MIO-16E-2) and controlled using National Instrument's LabVIEW, software.

A total of 93 pressure taps were installed for the endwall static pressure measurements and are shown in Fig. 3. The locations of these taps were determined using CFD predictions of the endwall pressure coefficient, *Cp*, distribution. The CFD solution was sampled at selected locations and the static pressure contours were plotted using just those locations. Pressure locations were added until the pressure gradients were resolved sufficiently and the contours looked smooth. This resulted in a highly nonuniform distribution of the pressure taps as can be seen clearly in Fig. 3. For these pressure measurements 5000 samples were acquired at every location at a sampling frequency of 1 kHz. The uncertainty in the pressure measurements from repeatability and run-to-run variations was estimated to be $\pm 0.05Cp$. The total uncertainty in the pressure coefficient results including a 1 percent uncertainty in the inlet velocity was estimated to be $\pm 0.25Cp$.

Heat Transfer Measurements. Heat transfer measurements were made on the bottom endwall of the test section. A constant heat flux plate, manufactured by Electrofilm Manufacturing, was designed to surround the styrofoam stator vane. The heater itself consists of a 50-μm-thick copper layer on top of a 75-μm-thick kapton layer within which 25-μm-thick inconel heating elements were embedded in a serpentine pattern. The heater was then attached to the bottom endwall using double-sided tape. The total area of the heat flux plate was 0.549 m^2. Using a variac, the heat flux was varied between 400 and 800 W/m^2 for the two Reynolds numbers investigated in this study. The bottom endwall was made of 1.9-cm-thick plywood and insulated below by a 2.54-cm-thick R-5 extruded styrofoam. Lateral conduction in the copper layer was estimated to be less than 1 percent when considering the spot size over which the infrared camera averages the surface temperatures. On the top surface of the heater, where measurements were made, four E-type ribbon thermocouples were placed using electrically insulating epoxy for calibration of the infrared camera. The top surface of the heater plate and the thermocouples were painted black. The free-stream temperature for these cases was nominally 21°C.

An infrared camera (Inframetrics Model 760) was used to collect the surface temperature information from the constant heat flux plate on the bottom endwall. The camera was calibrated in situ using a thermocouple placed on the heater surface. The correct plate emissivity and background temperature were determined over the required measurement temperature range, thereby giving a linear relationship between the thermocouple reading and infrared camera measurement. For these measurements, the top endwall was replaced with one that had 13 viewing ports 11.43 cm in diameter, in which a lexan insert or a crystal fluoride window was placed. These viewing ports are shown in Fig. 3. The crystal fluoride window is 98 percent transmissive over the 8 to 12 μm wavelength range, which is the operating range of the camera. The crystal fluoride window was moved to each of the 13 viewing ports and an image was recorded. Each image was an average of 16 images and, based on an uncertainty analysis, it was determined that five of these 16-averaged images were enough to get a good average of the endwall temperatures. Some of the images from the 13 viewing ports overlapped spatially and, in those cases, the temperatures were averaged to get a final temperature for those endwall positions.

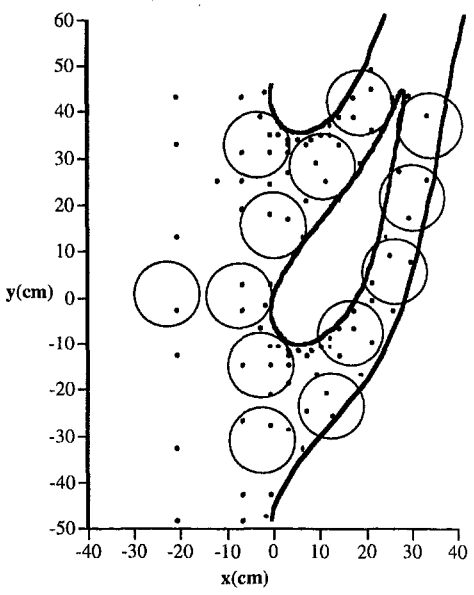

Fig. 3 Schematic of pressure tap locations and viewing ports for the infrared camera measurements

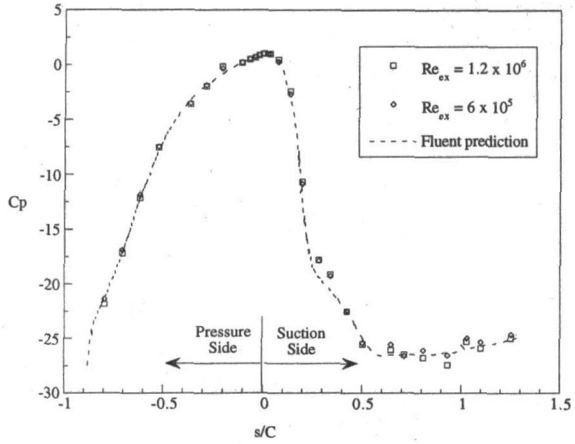

Fig. 4(*a*) Static pressure distribution at the vane midspan

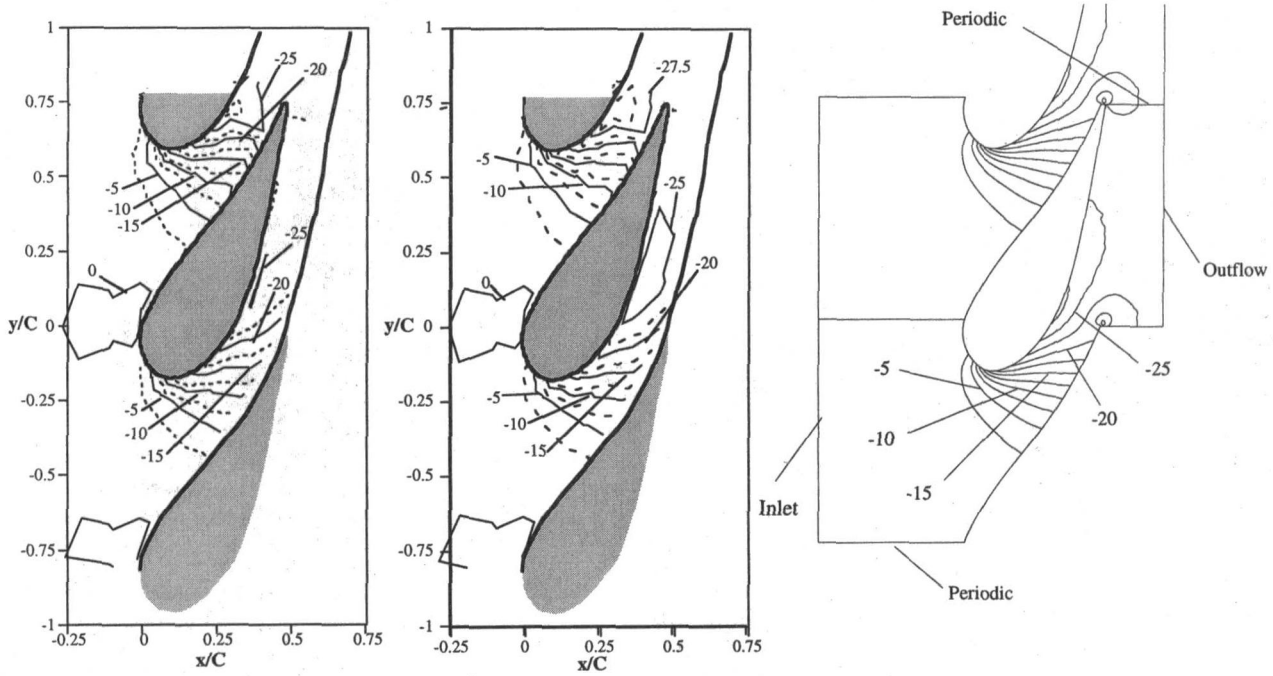

Fig. 4(*b, c, d*) Pressure coefficient contours on the endwall measured for $Re_{ex} = 6 \times 10^5$ (left) and for $Re_{ex} = 1.2 \times 10^6$ (middle) and computed for $Re_{ex} = 1 \times 10^6$ (right)

The camera was operated at its maximum viewing area of 21.5 cm × 16 cm, which it digitized onto 255 × 206 pixels. The spot size over which the infrared camera performed a spatial integration was 0.37 cm or, for comparison with the dimensions in terms of vane chords, $0.0062C$. Small positioning crosses were placed on the endwall to identify where each of the pictures were taken. Temperature data from the camera were processed using ThermoMonitor Lite software, manufactured by Thermoteknix Systems Ltd, which gave the temperature data at each pixel. For each picture, the positioning crosses were used to scale and transform data at each pixel to its corresponding position on the endwall. A processing routine was written in-house to assemble all the pictures into one complete picture of the endwall temperature distribution.

The input heat flux was corrected for radiation losses, which amounted to 4–23 percent of the input power, and conduction losses, which amounted to 1.7–3.5 percent of the input power. No correction was necessary regarding heat losses from conduction to the turbine vane itself because the vane was constructed using styrofoam (Bangert et al., 1997). Using the measured temperatures and the remaining convective heat flux, the heat transfer coefficients were computed and put in terms of a Stanton number based on the inlet velocity of 3.2 m/s for $Re_{ex} = 6 \times 10^5$ and 6.4 m/s for $Re_{ex} = 1.2 \times 10^6$. The uncertainty in the Stanton number for a temperature difference of 5°C is ±3.5 and 3 percent for the low and high Reynolds number cases, respectively. This uncertainty was dictated by the uncertainty in measuring the temperature and therefore is highest at the lowest temperature difference (5°C).

Flowfield Measurements. All three components of velocity were measured using a two-component LDV on the stagnation plane to quantify the leading edge vortex at the two different Reynolds numbers. Since this is a plane of symmetry, V, the pitchwise velocity component was very small. This component, however, was measured such that a total turbulent kinetic energy approaching the vane could be computed. The two-component backscatter fiberoptic LDV system used in this study consists of a 5 W Coherent laser used in conjunction with a TSI model 9201 Colorburst beam separator. Velocity data were processed using TSI model IFA 755 Digital Burst Correlator controlled using TSI's FIND software. Two different focusing lenses (350 and 750 mm) were used for these measurements. The 350 mm focusing lens was used to make measurements of the streamwise

and pitchwise components through the top endwall. The spanwise component was measured from the side using the 750 mm focusing lens.

The velocity measurement plane was over a region 7.6 cm $\times$ 7.6 cm in area. Velocity profiles were measured at 15 streamwise locations with 14 points each in the spanwise direction for a total of 210 measurement locations. Distance between the profiles in the streamwise direction was kept fixed at $0.0085C$ while the measurement locations in the spanwise direction were concentrated near the endwall to discern the leading edge vortex. At each measurement location for each component of velocity 10,000 data points were used to compute the mean and turbulence quantities. The data were corrected for velocity bias effects by applying the residence time weighting. Uncertainties in the mean velocity is estimated to be ± 1 percent while the precision uncertainties, based on a 95 percent confidence interval, for the rms of the velocity fluctuations were 3.0 percent in the highly turbulent regions.

Results

Results for the two Reynolds numbers investigated in this study are presented first in terms of pressure coefficient and Stanton number contours on the endwall. Next, the flowfield results on the stagnation plane are presented in terms of mean velocity vectors and contours of the turbulent kinetic energy and vorticity.

Endwall Static Pressure. Before the endwall static pressure results are discussed, it is useful to study the pressure distribution along the midspan of the vane. This allows us to separate the effect of secondary flows from the bulk motion. Figure $4(a)$ gives the static pressure measurements, in terms of the pressure coefficient for the low and high Reynolds number cases at a spanwise location that is 40 percent up from the bottom endwall. The results have been presented as normalized distance along the vane surface, with the pressure side on the left and the suction side on the right. The strong acceleration on the suction side of the vane is clear from the rapidly decreasing value of Cp through $s/C = 0.3$. The flow continues to accelerate at a smaller rate until $s/C = 0.5$ after which the velocity stays relatively constant with $Cp \sim -27$. Note that there are slightly lower values of Cp for the high-Reynolds-number case. The flow slows down slightly beyond $s/C = 1$ near the trailing edge of the vane. Unlike the suction side of the vane, flow on the pressure side of the vane accelerates monotonically.

The pressure coefficient results for $\mathrm{Re}_{ex} = 6 \times 10^5$ and 1.2×10^6 on the endwall are shown in Figs. $4(b)$ and $4(c)$. Note that the measurements indicate good periodicity between the two passages surrounding the airfoil. On the endwall, the largest difference between the two Reynolds numbers is a larger low-pressure region on the endwall for the high-Reynolds-number case where there is a contour level of $Cp = -27.5$ as compared with the low-Reynolds-number case where there is just a small region having a minimum value of $Cp = -25$. This is due to the secondary flow, which is much stronger at the high-Reynolds-number case. As the secondary flow separates from the endwall, one would expect a low-pressure region to occur, resulting in a lower Cp value. This was also evident beyond $s/C = 0.5$, on the suction side of the vane at the midspan as discussed already.

Surface oil visualization studies along the vane span and in the passage endwall were done for this turbine vane at both the high and low Reynolds numbers. There were two primary differences between the low and high-Reynolds-number cases. First, the boundary layer separation point moved farther upstream from the stagnation point for the higher Reynolds number case, as discussed earlier. The second and probably the more interesting result was the fact that at the high Reynolds number, oil from the endwall was carried up onto the suction side of the vane surface, starting at approximately $s/C = 0.5$. The location at which the paint/oil mixture was found on the vane occurs where the decrease in the static pressure levels off. The oil/paint mixture propagated to a spanwise position of $z/S = 0.14$. In contrast, there was no oil/paint mixture that propagated onto the vane for the low-Reynolds-number case. These results are consistent with the fact that there was a larger low-pressure region on the endwall for the higher Reynolds number case.

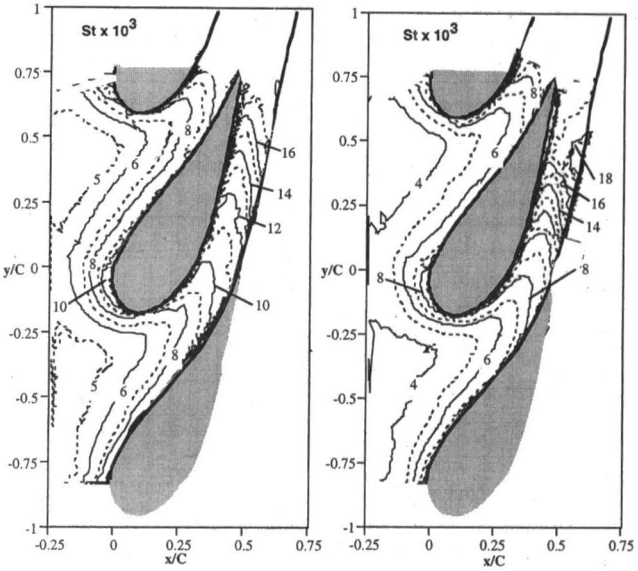

Fig. 5(*a, b*) Stanton contours for $\mathrm{Re}_{ex} = 6 \times 10^5$ (left) and 1.2×10^6 (right)

In order to benchmark these experimental results CFD predictions of the endwall pressure distribution were done using FLUENT/UNS for $\mathrm{Re}_{ex} = 1 \times 10^6$. As mentioned earlier, these CFD predictions were also used to design the static pressure endwall with the pressure taps. As these simulations are not the focus of this study, only a brief description is given here. The computational domain modeled just one passage with the suction side and pressure side of the vane as boundary walls. This along with periodic boundaries at the stagnation plane and the trailing edge made the domain periodic in the pitchwise direction. An inlet boundary layer thickness of 5 cm was used for these simulations and inlet velocity, k and ϵ profiles were generated using the boundary layer code TEXSTAN (Crawford, 1986). An outflow boundary condition was imposed after the trailing edge of the domain and a symmetry boundary condition was applied at the midspan height. Some of these boundary conditions are identified in Fig. $4(d)$, which shows the pressure coefficient contours on the endwall. The comparisons for the high Reynolds number show that there is a good agreement between the predicted and measured Cp values. The location and peak value of Cp agree quite well. The contours do not agree near the trailing edge of the vane because the flexible wall was not simulated in order to make the domain periodic. This was necessary to limit the number of cells, which was 360,000 for these simulations. These CFD calculations served as a good benchmark for our measurements.

Endwall Heat Transfer. The heat transfer results in terms of Stanton numbers based on inlet velocity for the two Reynolds numbers are given in Figs. $5(a)$ and $5(b)$. In the region upstream of the vanes, the Stanton numbers are higher for the lower Reynolds number, which can be expected from a turbulent boundary layer prediction. In both cases, there is a high heat transfer region that occurs between the stagnation point and the reattachment of the flow on the suction side of the airfoil. This

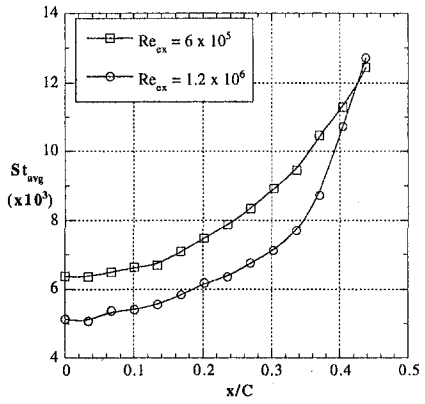

Fig. 6 Pitchwise-averaged Stanton numbers in the passage

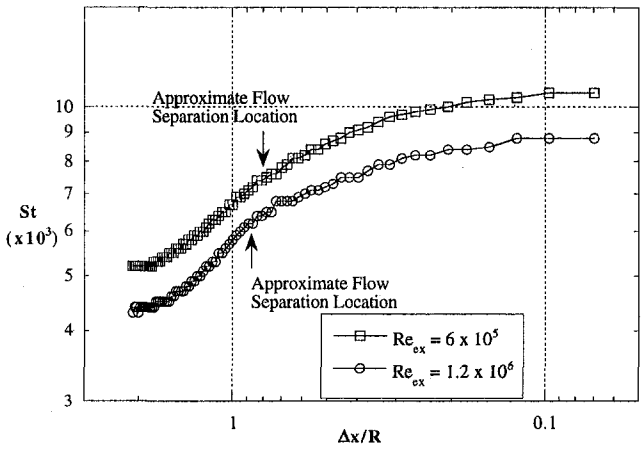

Fig. 7(*a*) Stanton numbers upstream of turbine vane stagnation point

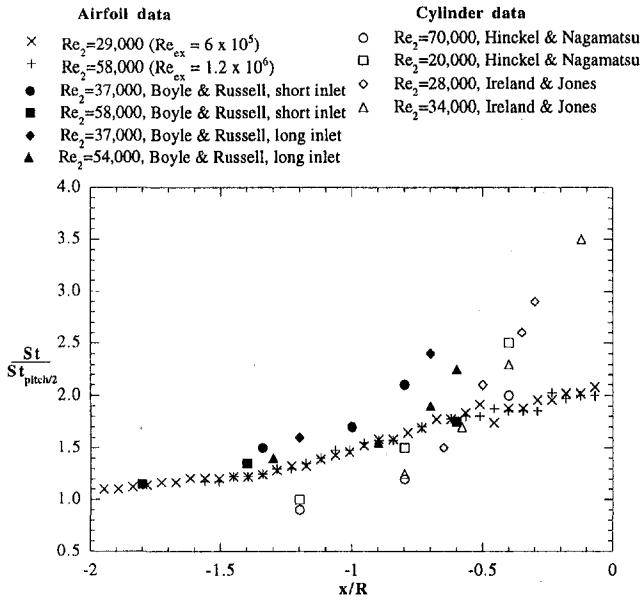

Fig. 7(*b*) Comparison of augmentation on the endwall at the stagnation line (St) normalized by midpitch value ($St_{pitch/2}$) with that given in the literature

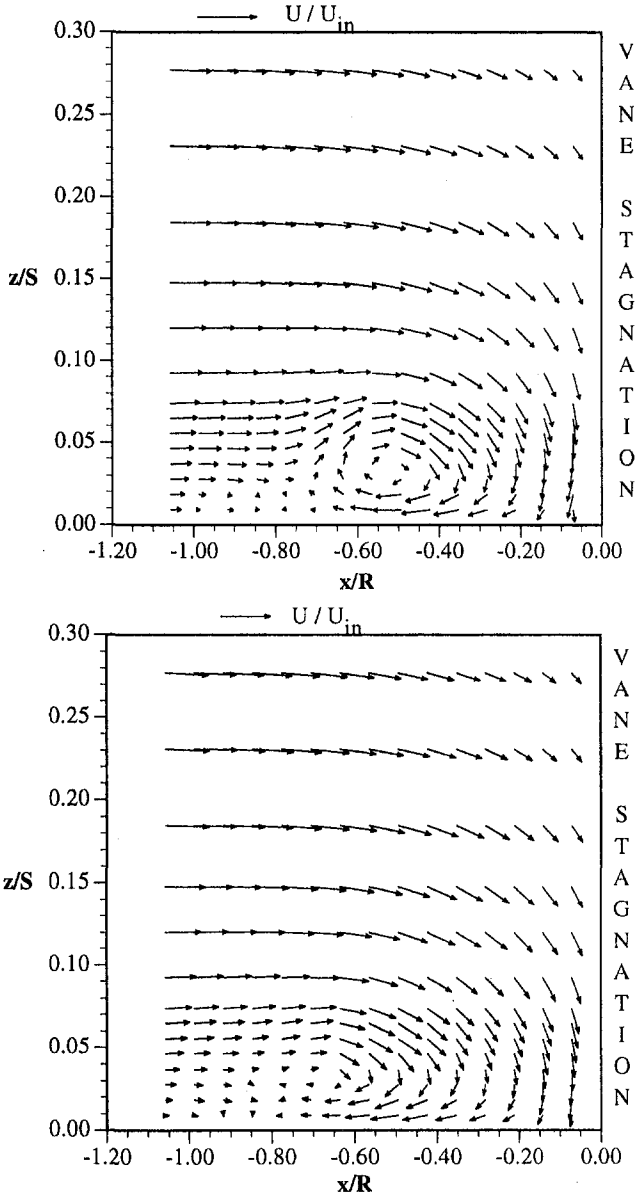

Fig. 8(*a, b*) Mean velocity vectors on the stagnation plane for $Re_{ex} = 6 \times 10^5$ (top) and 1.2×10^6 (bottom)

is the area that experiences very high acceleration, as described earlier. As the flow moves through the passage, it is apparent that the locations of the peak Stanton numbers are being swept from the outer pressure surface toward the suction side of the central vane. But in the case of the high Reynolds number, the peak local Stanton number occurs at the suction surface–endwall intersection, whereas for the low Reynolds number the peak occurred slightly farther into the passage and away from the suction surface of the vane. This is consistent with the fact that at the high Reynolds number there is a higher transverse pressure gradient across the passage causing a stronger secondary flow.

The heat transfer distribution near the trailing edge of the central vane is also affected by the flexible tailboard, which simulates the pressure side of the adjacent vane because this wall extends beyond where the trailing edge of an adjacent vane would end. Since the goal of this facility was to match engine Reynolds numbers and allow detailed boundary layer measurements on the central vane, the facility was designed to have the smallest number of vanes in order to scale up as much as possible. The flow in the front part of the vane passage is not affected by the tailboard, and this can be seen clearly from the good periodicity of the Stanton number and pressure coefficient contours between the two vane passages. Before more flowfield measurements are made inside the vane passage, the effect of

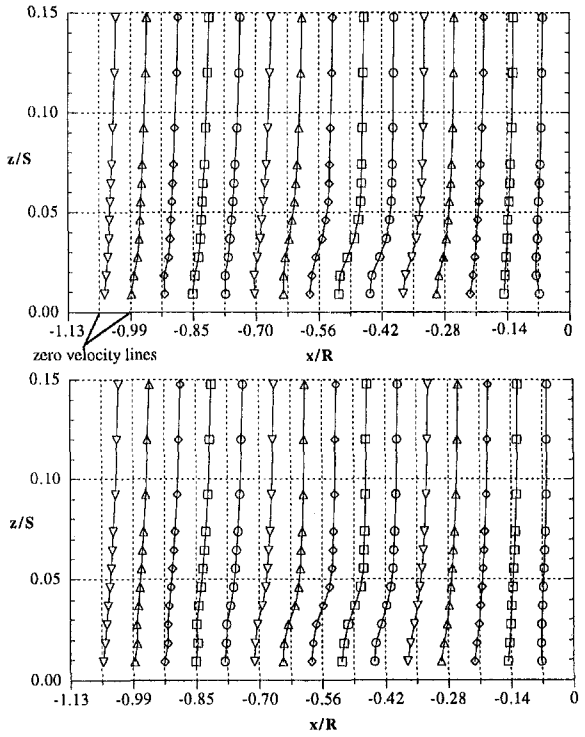

Fig. 9(*a*, *b*) Streamwise velocity profiles at the stagnation plane for $Re_{ex} = 6 \times 10^5$ (top) and 1.2×10^6 (bottom)

the tailboard on the central vane will be quantified using CFD simulations.

Figure 6 shows the pitchwise-averaged Stanton numbers for the two Reynolds number cases. As expected there is a higher average at the lower Reynolds number. Using flat plate turbulent boundary layer correlations, one would predict a 15 percent increase in the Stanton number based on the change in Reynolds number. These results, however, indicate a larger 25 percent increase for the lower Reynolds number case. This may be due to an unheated starting length effect, which would give slightly larger differences for the two Reynolds number cases. Both the low and high Reynolds number cases, however, show the same trend with just a shift until $x/C = 0.35$, whereby there is a strong increase for the high-Reynolds-number case. One plausible explanation for the strong increase is that this is approximately the location where the flow separated off of the endwall, which would be caused by the passage vortex. This location is consistent with the location at which the oil/kerosene mixture was being brought up onto the base of the turbine vane.

Figures 7(*a*) and 7(*b*) investigate the endwall upstream stagnation region of the vane. Figure 7(*a*) shows the Stanton numbers along a line parallel with the flow direction directly in front of the stagnation position. This line corresponds to the surface that is affected by the flowfield plane that was measured upstream of the stagnation, which will be discussed in the next section. Figure 7(*b*) indicate that for both cases, the Stanton number starts to increase dramatically upstream of the stagnation between $x/R = -1.6$ and -1.7 (equivalent to $\Delta x/R = 1.6$ in Fig. 7(*a*)). As will be shown in the flowfield measurements, this location corresponds to a position upstream of the boundary layer separation point.

Figure 7(*b*) gives the augmentation of the heat transfer caused by the leading edge of the turbine vane for the two different Reynolds numbers as compared with those results presented by Boyle and Russell (1990), Hinckel and Nagamatsu (1986), and Ireland and Jones (1986). This augmentation is calculated using the Stanton numbers approaching the stagnation position of the vane divided by the Stanton numbers on the midpitch line. Our data indicate that there is no effect of the Reynolds number on the augmentation. Only very close to the stagnation location is there a large discrepancy between our data and those of Ireland and Jones (1986) who used a cylinder as opposed to an airfoil. Although there is some scatter in the data, the agreement farther away from the stagnation position is fairly good. Data from Goldstein and Spores (1988) indicated two peaks for their mass transfer Stanton numbers approaching their rotor blade leading edge. They attributed the peak further away from the blade to the leading edge horseshoe vortex, which is similar to the peak shown in Fig. 7(*b*), and the peak closest to the blade stagnation to a corner vortex. Our flowfield measurements, which are discussed in the next section, did not show a corner vortex in our measurement plane, which is consistent with the heat transfer measurements. That is to say, there may be a corner vortex but, if so, it is very small. This also indicates that the existence of a large corner vortex seems to be geometry dependent.

Leading Edge Flowfield. As mentioned earlier, all three components of velocity were measured on the stagnation plane at the leading edge region of the stator vane. Figure 8(*a*) and 8(*b*) show the $U-W$ vectors in this plane. Note that the streamwise distance has been normalized by the vane radius (R) while the spanwise has been normalized using the vane half-span (S). In each figure, the velocity vectors have been scaled by the respective inlet velocity. It is clear from these results that the

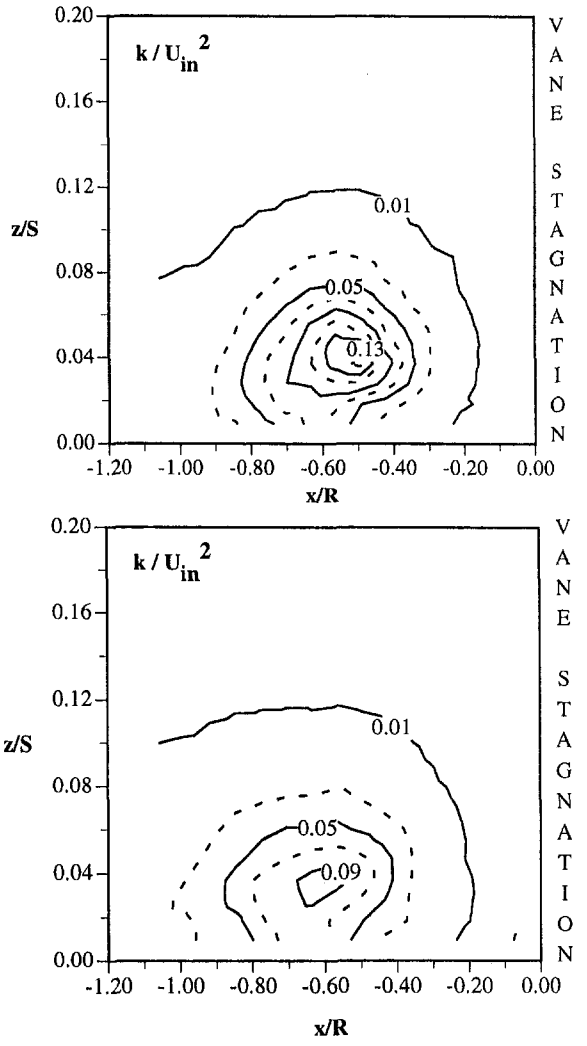

Fig. 10(*a*, *b*) Turbulent kinetic energy (k/U_{in}^2) at the stagnation plane for $Re_{ex} = 6 \times 10^5$ (top) and 1.2×10^6 (bottom)

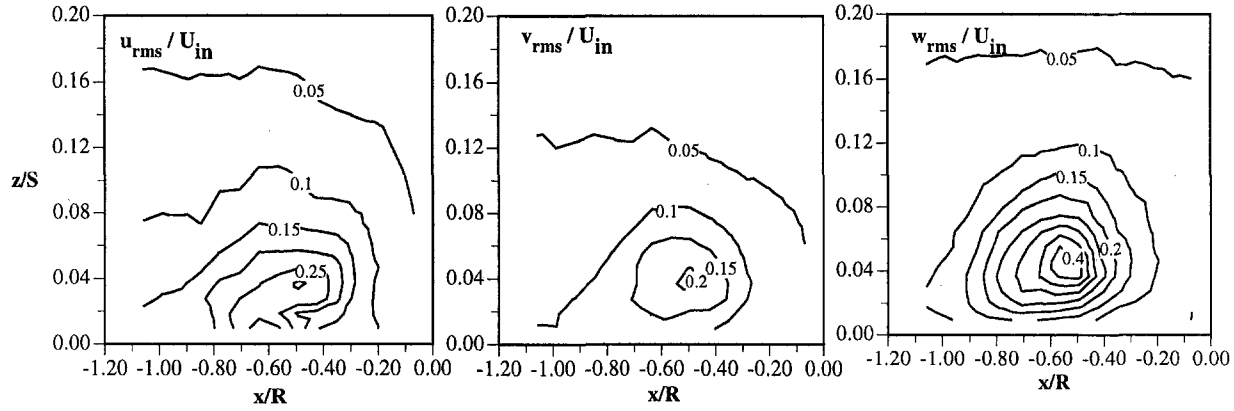

Fig. 11(*a, b, c*) Normalized fluctuating velocities at the stagnation plane for $Re_{ex} = 6 \times 10^5$

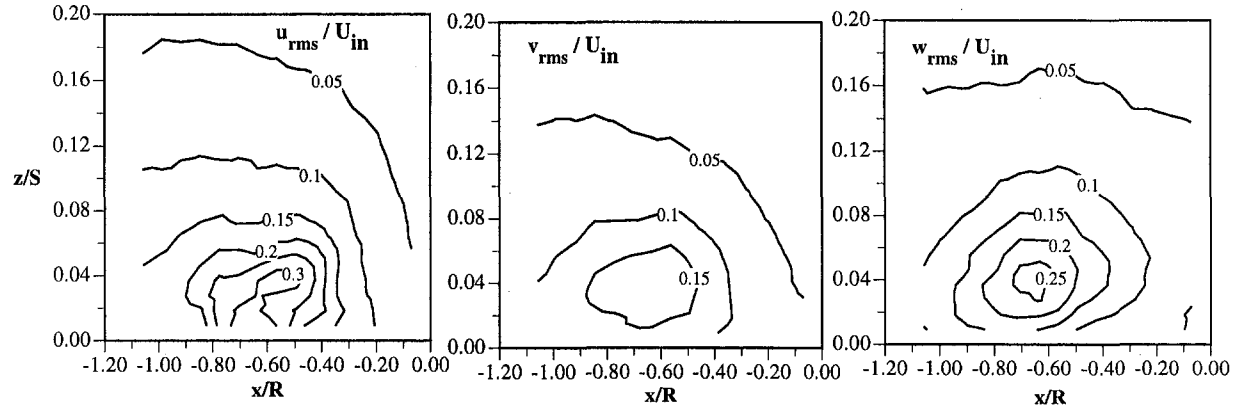

Fig. 12(*a, b, c*) Normalized fluctuating velocities at the stagnation plane for $Re_{ex} = 1.2 \times 10^6$

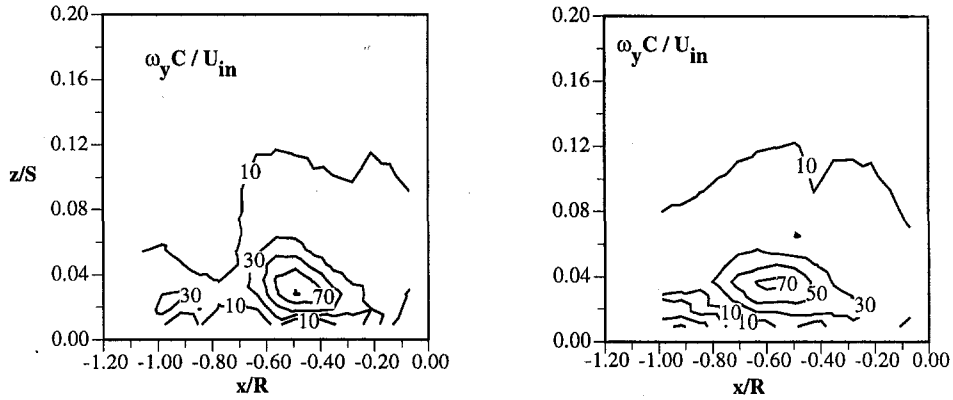

Fig. 13(*a, b*) Normalized vorticity on the stagnation plane for $Re_{ex} = 6 \times 10^5$ (left) and 1.2×10^6 (right)

density of the measurement locations is sufficient to document the leading edge vortex flowfield. For both Reynolds numbers, the inlet boundary layer separates as it approaches the stator vane and rolls up into a vortex motion, which is accompanied by a downward movement of free-stream fluid. The amount of this downward movement of fluid toward the endwall increases as the flow approaches the stator vane. As the gases away from the endwall are usually hotter in an actual turbine, this downwash would bring hot fluid into contact with the endwall and explains why the endwall-leading edge junction is a critical area from a design perspective.

Although the overall flow features are quite similar, there are key differences between the two Reynolds number cases. At the high Reynolds number, the vortex is not as pronounced and does not extend as far into the span (z direction) as compared with the low Reynolds number. For the low-Reynolds-number case, the vectors indicate a more complete roll up of the leading edge vortex. This may be the consequence of the larger momentum that the flow carries at the high Reynolds number that the vortex motion is unable to overcome. Another difference is the location of the separation point, which is closer to the stator vane for the low Reynolds number case. This can be seen in more detail by focusing on the streamwise velocity profiles as shown in Figs. 9(a) and 9(b). In order to see the separation better, only the region near the wall ($z/S < 0.15$) has been plotted.

Note that zero velocity lines associated with each profile are indicated as dashed vertical lines in these figures. Away from the wall, the velocity profiles flatten out as they approach the stator vane. Near the wall, the reverse flow becomes stronger going away from the stator vane and then decreases until the separation point is reached. This happens at about $x/R = -0.82$ at low Reynolds number and at $x/R = -0.99$ for the high Reynolds number. These profiles also identify the strong velocity gradients that mainly exist near the core of the leading edge vortex. The lower-Reynolds-number case shows larger velocity gradients, especially near the core of the vortex. The velocity gradients are much smaller near the stator vane and upstream of the separation point. These gradients dictate the amount of turbulent kinetic energy in the flowfield and is discussed below.

Velocity fluctuations for all three components were combined to calculate the turbulent kinetic energy for the two Reynolds number cases. These results normalized by the inlet velocity are shown in Figs. $10(a)$ and $10(b)$. Both contours show maximum values centered about the core of the leading edge vortex. As the vortex core was formed closer to the stator vane for the low-Reynolds-number case, the peak k values are also closer to the stator vane as compared to the high-Reynolds-number case. In the streamwise direction, the turbulent kinetic energy levels decrease as one goes closer to the stator vane or further upstream. This is consistent with the location of the high-velocity gradients as discussed above. The peak value of k is higher for the lower-Reynolds-number case because of a more complete roll up and the presence of stronger velocity gradients.

Figures $11(a-c)$ and $12(a-c)$ give contours of the rms levels of each of the fluctuating velocity components for the low and high-Reynolds-number cases normalized by the inlet velocity. In general, the peak values for all of the fluctuations occur at the same location which is at the center of the vortex core. For both the low and high-Reynolds-number cases, the u_{rms}/U_{in} and v_{rms}/U_{in} have similar contour patterns and have nominally the same levels. However, the vertical fluctuations, w_{rms}/U_{in}, are noticeably larger for the low Reynolds number as compared with the high Reynolds number. In addition, at the low Reynolds number the contours are asymmetrically skewed with higher gradients closer to the turbine vane. These higher levels can be attributed to the fact that for the low Reynolds number there is a complete turning of the vortex, where there is a stronger vertical motion. The large gradients in the w_{rms}/U_{in} contours occur at the upstream edge of the vortex.

Another measure of the strength of the leading edge vortex can be obtained from the vorticity magnitude. By using a three-point second-order-accurate differencing scheme for unequally spaced data the vorticity component normal to the stagnation plane, ω_y, was calculated. The results, normalized using the vane chord and inlet velocity, are shown in Figs. $13(a)$ and $13(b)$. The peak value for the vorticity magnitude is the same at both Reynolds numbers, but for the vortex at low Reynolds number it is spread over a bigger region. This indicates a slightly stronger vortex motion at the low Reynolds number and is consistent with the results discussed earlier.

Conclusions

This study has focused on determining the effects of Reynolds numbers on the static pressure and surface heat transfer distributions as well as the leading edge vortex for a modern, scaled-up turbine vane geometry. The test facility included a central airfoil with two leading edges representing the adjacent airfoils, such that the passage vortex would be correctly simulated. All of the data, including endwall oil streakline visualizations, indicated that for the higher Reynolds number the passage vortex lifted off of the endwall onto the turbine vane, thereby decreasing the endwall static pressure and causing a different surface heat transfer pattern. The heat transfer pattern was such that the peak Stanton number occurred at the suction surface for the high-Reynolds-number case as opposed to occurring more toward the center of the passage for the low-Reynolds-number case. The increase in the average Stanton numbers for the two Reynolds numbers could not be predicted using a flat plate turbulent boundary layer correlation. The peak heat transfer augmentation that occurred on the endwall nearest the stagnation position of the leading edge was a maximum of two times the heat transfer that occurred in the midspan of the passage.

In the leading edge region, there were some clear differences in the flowfield characteristics of the leading edge vortices for the two different Reynolds numbers. While the separation of the boundary layer occurred slightly farther upstream of the stagnation position for the higher Reynolds number, the vortex itself did not have a complete rotation for the higher Reynolds number. The lack of a complete rotation was attributed to the fact that at the higher Reynolds number there were too many inertial effects to overcome such that the upturn was not evident. Higher turbulent kinetic energy levels and a larger vorticity region were all consistent with the fact that the lower Reynolds number case had a stronger upturning vortex than the higher Reynolds number case.

Acknowledgments

The authors would like to thank Pratt & Whitney, W. Palm Beach, Florida, for their support of this work. In particular, thanks go to William Kvasnak and Fred Soechting for being the contract monitors.

References

Bailey, D. A., 1980, "Study of Mean- and Turbulent-Velocity Fields in a Large-Scale Turbine-Vane Passage," ASME *Journal of Engineering for Power,* Vol. 102, pp. 88–95.

Bangert, B. A., Kohli, A., Sauer, J. H., and Thole, K. A., 1997, "High Freestream Turbulence Simulation in a Scaled-up Turbine Vane Passage," ASME Paper No. 97-GT-51.

Boyle, R. J., and Russell, L. M., 1990, "Experimental Determination of Stator Endwall Heat Transfer," ASME JOURNAL OF TURBOMACHINERY, Vol. 112, pp. 547–558.

Crawford, M. E., 1986, "Simulation Codes for Calculation of Heat Transfer to Convectively-Cooled Turbine Blades," 130 pp., a set of four lectures in Convective Heat Transfer and Film Cooling in Turbomachinery, T. Arts, ed., Lecture Series 1986-06, von Karman Institute for Fluid Dynamics, Rhode-Saint-Genese, Belgium.

Gaugler, R. E., and Russell, L. M., 1984, "Comparison of Visualized Turbine Endwall Secondary Flows and Measured Heat Transfer Patterns," ASME *Journal of Engineering for Gas Turbines and Power,* Vol. 106, pp. 168–172.

Goldstein, R. J., and Spores, R. A., 1988, "Turbulent Transport on the Endwall in the Region Between Adjacent Turbine Blades," ASME *Journal of Heat Transfer,* Vol. 110, pp. 862–869.

Graziani, R. A., Blair, M. F., Taylor, J. R., and Mayle, R. E., 1980, "An Experimental Study of Endwall and Airfoil Surface Heat Transfer in a Large Scale Turbine Blade Cascade," ASME *Journal of Engineering for Power,* Vol. 102, pp. 257–267.

Hinckel, J. N., and Nagamatsu, H. T., 1986, "Heat Transfer in the Stagnation Region of the Junction of a Circular Cylinder Perpendicular to a Flat Plate," *International Journal of Heat and Mass Transfer,* Vol. 29, pp. 999–1005.

Ireland, P. T., and Jones, T. V., 1986, "Detailed Measurements of Heat Transfer On and Around a Pedestal in Fully Developed Passage Flow," *Proc. 8th International Heat Transfer Conference,* San Francisco, Vol. 3, Hemisphere Publishing Corporation, pp. 975–980.

Langston, L. S., Nice, M. L., and Hooper, R. M., 1977, "Three-Dimensional Flow Within a Turbine Cascade Passage," ASME *Journal of Engineering for Power,* Vol. 99, pp. 21–28.

Marchal, P., and Sieverding, C. H., 1977, "Secondary Flows Within Turbomachinery Bladings," *Secondary Flows in Turbomachines,* AGARD CP 214.

Mattingly, G. E., 1996, "Volume Flow Measurements," *Fluid Mechanics Measurements,* 2nd ed., R. J. Goldstein, ed., Taylor and Francis: New York.

Pierce, F. J., and Harsh, M. D., 1988, "The Mean Flow Structure Around and Within a Turbulent Junction or Horseshoe Vortex—Part II. The Separated and Junction Vortex Flow," ASME *Journal of Fluids Engineering,* Vol. 110, pp. 415–423.

Sieverding, C. H., 1985, "Recent Progress in the Understanding of Basic Aspects of Secondary Flows in Turbine Blade Passages," ASME *Journal of Engineering for Gas Turbines and Power,* Vol. 107, pp. 248–257.

York, R. E., Hylton, L. D., and Mihelc, M. S., 1984, "An Experimental Investigation of Endwall Heat Transfer and Aerodynamics in a Linear Vane Cascade," ASME Paper No. 84-GT-51.

DISCUSSION

L. S. Langston[2]

This paper presents data that validates and compliments the earlier work of Boyle and Russell (1990) on stator endwall heat transfer. In addition, the authors present fluid flow field measurements (e.g., Figs. 8 and 9), which give insight to the endwall convective heat results in their work and in that of others. Their results provide further validation of the endwall flow model that has emerged from the research of investigators over the last twenty years or more.

I would like comment on three aspects of the paper, all concerning the fluid flow results reported:

1 The authors discuss the existence of an endwall "separation line," labeled as such in Fig. 2(*b*). I doubt that it is a "separation line," for it lacks evidence of a singular point (such lines begin and end at a saddle point or a separation point (see Lighthill, 1963)). Also, the velocity data presented in Fig. 8(*b*) show no evidence of separation at the "line." In addition, their "saddle point" (shown in Fig. 2(*b*)), formed by the intersection of a true separation line (where the incoming endwall boundary layer does separate) and an attachment line, is some distance upstream. I offer the explanation that their "line of separation" is an artifact of the oil-film flow visualization technique used. This artifact is described by Langston (1990) as a "line of accumulation."

2 The authors present their velocity data on a "stagnation plane" (Figs. 8–13), which they claim is a plane of symmetry. This plane appears to be defined by $y = 0$. (They do not explicitly define its location.) What is a "stagnation plane"? Did they indeed find a plane of symmetry, defined by actual measurements showing that the planar pitchwise velocity V was zero everywhere in the plane? In the symmetric flow around an endwall-mounted cylinder there is indeed such a plane of symmetry. However, it is not apparent to me that such a *plane* of symmetry exists in the asymmetric flow field entering a cascade of turning vanes, with its streamlines curved in the main flow and twisted near the endwalls.

3 The authors observed strong vortex motion in their plane of velocity measurement for the low-Reynolds-number case (0.6×10^6) and little vortex motion for the larger Reynolds number case (1.2×10^6). For the boundary layer flow around an endwall-mounted cylinder, Eckerle and Awad (1991) measured two types of endwall separation, identified by the nondimensional parameter $E = (\mathrm{Re_D})^{1/3} D/\delta^*$ where $\mathrm{Re_D}$ is the Reynolds number based on cylinder diameter D, and δ^* is the boundary layer momentum thickness. For $E > 1000$, little or no vortex motion occurred in or near the cylinder flow plane of symmetry, while for $E < 1000$ there was strong vortex motion. Assume that the authors' single vane is approximated by a cylinder of diameter equal to the axial chord of the vane. (As concluded by Langston et al. (1977) and later by Moore and Ransmayr (1984), the leading edge radius has little effect on the endwall flow.) From the authors' Fig. 4 it can be estimated that the axial chord-to-chord ratio is about 0.5. (The authors do not give values for the axial chord, the leading edge radius, or the stator airfoil coordinates.) For their smaller Reynolds number case (0.6×10^6) the value of the Eckerle–Anwar parameter is about $E = 980$ (based on axial chord) and for the larger Reynolds number case (1.2×10^6), $E = 1484$.

Thus the authors' results concerning horseshoe vortex motion near the saddle point are in agreement with the Eckerle–Anwar endwall cylinder results, if one uses the axial chord as an equivalent cylinder diameter.

[2] Mechanical Engineering Department, University of Connecticut, Storrs, CT 06269.

References

Boyle, R. J., and Russell, L. M., 1990, "Experimental Determination of Stator Endwall Heat Transfer," ASME JOURNAL OF TURBOMACHINERY, Vol. 112, pp. 547–558.

Eckerle, W. A., and Awad, J. K., 1991, "Effect of Freestream Velocity on the Three-Dimensional Separation Flow Region in Front of a Cylinder," ASME *Journal of Fluid Engineering,* Vol. 113, pp. 37–44.

Langston, L. S., Nice, M. L., and Hooper, R. M., 1977, "Three-Dimensional Flow Within a Turbine Cascade Passage," ASME *Journal of Engineering for Power,* Vol. 99, pp. 21–28.

Langston, L. S., 1990, "Research in Cascade Secondary and Tip Clearance Flows-Periodicity and Surface Flow Visualization," NATO AGARD-CPP-468/469, pp. 19-1–19-15.

Lighthill, M. J., 1963, *Laminar Boundary Layers,* L. Rosenhead, ed., Oxford UP, pp. 60–88.

Moore, J., and Ransmayr, A., 1984, "Flow in a Turbine Cascade: Part I—Losses and Leading-Edge Effects," ASME *Journal of Engineering for Gas Turbines and Power,* Vol. 106, pp. 400–408.

Authors' Closure

The authors would like to thank Professor Langston for his comments regarding our paper. The following information is given in response to the three aspects on which he commented.

Professor Langston has corrently pointed out that the line given in Fig. 2(*b*) indicated as a separation line from the endwall visualization is rather an accumulation line where the pressure gradients cause a deceleration of the reverse flow. The streamwise velocity data given in Fig. 9(*b*) for $\mathrm{Re_{cx}} = 1.2 \times 10^6$ indicate a flat profile at $x/R = -0.85$ where, closer to the vane, negative streamwise velocities occur. The zero velocity gradient at the wall followed by negative velocities was interpreted by the authors to indicate a flow separation. This $x/R = -0.85$ location, however, is farther upstream than the line of accumulation shown in Fig. 2(*b*), which is located at $x/R = -0.76$. The location of the zero velocity gradient occurs closer to the saddle point region given in Fig. 2(*b*), which is in agreement with the analysis presented by Eckerle and Langston (1987).

We have in fact called the plane of data presented in Figs. 8–13 a "stagnation plane" but have not stated that it is a plane of symmetry. Our measurement plane is located out from the flow stagnation point in a direction parallel with the upstream incoming flow direction, as was shown in Fig. 1. Our results indicate that for this measurement plane, there is a v-component to the velocity, as one would expect based on the streamline curvature approaching the vane.

It is clear that there are two different vortex structures given in Figs. 8(*a*) and 8(*b*) with only the lower Reynolds number indicating a complete roll-up of the vortex. In calculating a Reynolds number based on the inlet velocity and an effective cylinder diameter of 16.9 cm, the high and low Reynolds numbers would be 470 and 775, respectively. Note that this effective cylinder diameter was calculated based on a curve fit of the measured approach velocity to the theoretical, inviscid equation for the approach flow to a cylinder in crossflow. Both Reynolds numbers are clearly below $\mathrm{Re_D}$ of 1000. If, however, one uses the axial chord length of 29.2 cm (close to what Professor Langston used in his approximations) the $\mathrm{Re_{AC}}$ numbers would be 990 and 1640. As pointed out by Professor Langston, this is in agreement with the Reynolds number constraints of Eckerle and Anwad (1991).

References

Eckerle, W. A., and Langston, L. S., 1987, "Horseshoe Vortex Formation around a Cylinder," ASME JOURNAL OF TURBOMACHINERY, Vol. 109, pp. 278–284.

Eckerle, W. A., and Awad, J. K., 1991, "Effect of Freestream Velocity on the Three-Dimensional Separated Flow Region in Front of a Cylinder," ASME *Journal of Fluids Engineering,* Vol. 113, pp. 37–44.

Sieverding, C. H., 1985, "Recent Progress in the Understanding of Basic Aspects of Secondary Flows in Turbine Blade Passages," ASME *Journal of Engineering for Gas Turbines and Power,* Vol. 107, pp. 248–257.

York, R. E., Hylton, L. D., and Mihelc, M. S., 1984, "An Experimental Investigation of Endwall Heat Transfer and Aerodynamics in a Linear Vane Cascade," ASME Paper No. 84-GT-51.

DISCUSSION

L. S. Langston[2]

This paper presents data that validates and compliments the earlier work of Boyle and Russell (1990) on stator endwall heat transfer. In addition, the authors present fluid flow field measurements (e.g., Figs. 8 and 9), which give insight to the endwall convective heat results in their work and in that of others. Their results provide further validation of the endwall flow model that has emerged from the research of investigators over the last twenty years or more.

I would like comment on three aspects of the paper, all concerning the fluid flow results reported:

1 The authors discuss the existence of an endwall "separation line," labeled as such in Fig. 2(*b*). I doubt that it is a "separation line," for it lacks evidence of a singular point (such lines begin and end at a saddle point or a separation point (see Lighthill, 1963)). Also, the velocity data presented in Fig. 8(*b*) show no evidence of separation at the "line." In addition, their "saddle point" (shown in Fig. 2(*b*)), formed by the intersection of a true separation line (where the incoming endwall boundary layer does separate) and an attachment line, is some distance upstream. I offer the explanation that their "line of separation" is an artifact of the oil-film flow visualization technique used. This artifact is described by Langston (1990) as a "line of accumulation."

2 The authors present their velocity data on a "stagnation plane" (Figs. 8–13), which they claim is a plane of symmetry. This plane appears to be defined by $y = 0$. (They do not explicitly define its location.) What is a "stagnation plane"? Did they indeed find a plane of symmetry, defined by actual measurements showing that the planar pitchwise velocity V was zero everywhere in the plane? In the symmetric flow around an endwall-mounted cylinder there is indeed such a plane of symmetry. However, it is not apparent to me that such a *plane* of symmetry exists in the asymmetric flow field entering a cascade of turning vanes, with its streamlines curved in the main flow and twisted near the endwalls.

3 The authors observed strong vortex motion in their plane of velocity measurement for the low-Reynolds-number case (0.6×10^6) and little vortex motion for the larger Reynolds number case (1.2×10^6). For the boundary layer flow around an endwall-mounted cylinder, Eckerle and Awad (1991) measured two types of endwall separation, identified by the nondimensional parameter $E = (\mathrm{Re_D})^{1/3} D/\delta^*$ where $\mathrm{Re_D}$ is the Reynolds number based on cylinder diameter D, and δ^* is the boundary layer momentum thickness. For $E > 1000$, little or no vortex motion occurred in or near the cylinder flow plane of symmetry, while for $E < 1000$ there was strong vortex motion. Assume that the authors' single vane is approximated by a cylinder of diameter equal to the axial chord of the vane. (As concluded by Langston et al. (1977) and later by Moore and Ransmayr (1984), the leading edge radius has little effect on the endwall flow.) From the authors' Fig. 4 it can be estimated that the axial chord-to-chord ratio is about 0.5. (The authors do not give values for the axial chord, the leading edge radius, or the stator airfoil coordinates.) For their smaller Reynolds number case (0.6×10^6) the value of the Eckerle–Anwar parameter is about $E = 980$ (based on axial chord) and for the larger Reynolds number case (1.2×10^6), $E = 1484$.

[2] Mechanical Engineering Department, University of Connecticut, Storrs, CT 06269.

Thus the authors' results concerning horseshoe vortex motion near the saddle point are in agreement with the Eckerle–Anwar endwall cylinder results, if one uses the axial chord as an equivalent cylinder diameter.

References

Boyle, R. J., and Russell, L. M., 1990, "Experimental Determination of Stator Endwall Heat Transfer," ASME JOURNAL OF TURBOMACHINERY, Vol. 112, pp. 547–558.

Eckerle, W. A., and Awad, J. K., 1991, "Effect of Freestream Velocity on the Three-Dimensional Separation Flow Region in Front of a Cylinder," ASME *Journal of Fluid Engineering,* Vol. 113, pp. 37–44.

Langston, L. S., Nice, M. L., and Hooper, R. M., 1977, "Three-Dimensional Flow Within a Turbine Cascade Passage," ASME *Journal of Engineering for Power,* Vol. 99, pp. 21–28.

Langston, L. S., 1990, "Research in Cascade Secondary and Tip Clearance Flows-Periodicity and Surface Flow Visualization," NATO AGARD-CPP-468/469, pp. 19-1–19-15.

Lighthill, M. J., 1963, *Laminar Boundary Layers,* L. Rosenhead, ed., Oxford UP, pp. 60–88.

Moore, J., and Ransmayr, A., 1984, "Flow in a Turbine Cascade: Part I—Losses and Leading-Edge Effects," ASME *Journal of Engineering for Gas Turbines and Power,* Vol. 106, pp. 400–408.

Authors' Closure

The authors would like to thank Professor Langston for his comments regarding our paper. The following information is given in response to the three aspects on which he commented.

Professor Langston has correctly pointed out that the line given in Fig. 2(*b*) indicated as a separation line from the endwall visualization is rather an accumulation line where the pressure gradients cause a deceleration of the reverse flow. The streamwise velocity data given in Fig. 9(*b*) for $\mathrm{Re_{cx}} = 1.2 \times 10^6$ indicate a flat profile at $x/R = -0.85$ where, closer to the vane, negative streamwise velocities occur. The zero velocity gradient at the wall followed by negative velocities was interpreted by the authors to indicate a flow separation. This $x/R = -0.85$ location, however, is farther upstream than the line of accumulation shown in Fig. 2(*b*), which is located at $x/R = -0.76$. The location of the zero velocity gradient occurs closer to the saddle point region given in Fig. 2(*b*), which is in agreement with the analysis presented by Eckerle and Langston (1987).

We have in fact called the plane of data presented in Figs. 8–13 a "stagnation plane" but have not stated that it is a plane of symmetry. Our measurement plane is located out from the flow stagnation point in a direction parallel with the upstream incoming flow direction, as was shown in Fig. 1. Our results indicate that for this measurement plane, there is a v-component to the velocity, as one would expect based on the streamline curvature approaching the vane.

It is clear that there are two different vortex structures given in Figs. 8(*a*) and 8(*b*) with only the lower Reynolds number indicating a complete roll-up of the vortex. In calculating a Reynolds number based on the inlet velocity and an effective cylinder diameter of 16.9 cm, the high and low Reynolds numbers would be 470 and 775, respectively. Note that this effective cylinder diameter was calculated based on a curve fit of the measured approach velocity to the theoretical, inviscid equation for the approach flow to a cylinder in crossflow. Both Reynolds numbers are clearly below $\mathrm{Re_D}$ of 1000. If, however, one uses the axial chord length of 29.2 cm (close to what Professor Langston used in his approximations) the $\mathrm{Re_{AC}}$ numbers would be 990 and 1640. As pointed out by Professor Langston, this is in agreement with the Reynolds number constraints of Eckerle and Anwad (1991).

References

Eckerle, W. A., and Langston, L. S., 1987, "Horseshoe Vortex Formation around a Cylinder," ASME JOURNAL OF TURBOMACHINERY, Vol. 109, pp. 278–284.

Eckerle, W. A., and Awad, J. K., 1991, "Effect of Freestream Velocity on the Three-Dimensional Separated Flow Region in Front of a Cylinder," ASME *Journal of Fluids Engineering,* Vol. 113, pp. 37–44.

Fluid Flow in a 180 deg Sharp Turning Duct With Different Divider Thicknesses

Tong-Miin Liou
email: tmliou@tmp.nthu.edu.tw

Yaw-Yng Tzeng

Chung-Chu Chen

Department of Power Mechanical Engineering,
National Tsing Hua University,
Hsinchu, Taiwan 30043

The effect of divider thickness on fluid flows in a two-pass smooth square duct with a 180 deg straight-corner turn is an important issue to the turbine blade internal cooling but has not been explored in the past. Laser-Doppler velocimetry measurements are thus presented for such a study at a Reynolds number of 1.2 × 10⁴ and dimensionless divider thicknesses (W_d^*) of 0.10, 0.25, 0.50. Results are presented in terms of various mean velocity components in two orthogonal streamwise planes and three cross-sectional planes, the local and regional averaged turbulent kinetic energy and resultant mean velocity distributions, and complemented by the liquid crystal measured heat transfer coefficient contours. The measured velocity data are able reasonably to explain published and present measured heat transfer results. W_d^* is found to have profound effects on the flow features inside and immediately after the turn. The turbulence level and uniformity in the region immediately after the turn respectively decrease and increase with increasing W_d^*.

Introduction

In some applications, such as ventilation piping system, the internal coolant pass of advanced gas turbine blades, and the hot gas manifold of the space shuttle main engine power head, the space constraints dictate a small radius of curvature (Rc) for the 180 deg turn, often smaller than the duct hydraulic diameter (D_H) (Fig. 1). For $Rc/D_H < 1$, the sharp turning geometry-induced secondary flow in the duct cross-sectional plane and streamwise flow separation, recirculation, and reattachment lead to noticeable effects on the pressure loss and nonuniformity of heat transfer distribution (Metzger et al., 1984). The flow characteristics in such a case are affected by the turning configuration and divider-wall thickness W_d (Fig. 1). The present study focuses on examining the effect of the latter, which receives little attention in the open literature.

Most prior studies relevant to 180 deg turning flows without duct rotation, both laminar (Cheng et al., 1977; Fairbank and So, 1987) and turbulent (Chang et al., 1983; Johnson, 1988; Choi et al., 1989; Besserman and Tanrikut, 1991), are limited to turning geometries with $Rc/D_H > 1$. In such configurations, streamwise flow separation is either mild or absent. For $Rc/D_H < 1$, Metzger et al. (1984, 1986) performed surface ink-streakline visualizations, pressure measurements, and heat transfer coefficient measurements based on thermocouple measured segment temperatures. The parameters examined included the ratio of inlet-to-outlet channel width, the divider tip-to-wall clearance, and the Reynolds number ranging from 1 × 10⁴ to 6 × 10⁴. A large separation bubble along the downstream side of the divider was observed in their study. Considerable nonuniformity in heat transfer distribution was attributed to the observed flow separation and reattachment. Han et al. (1988) studied the detailed mass transfer distributions around the sharp 180 deg turns in two-pass, square, smooth, and rib-roughened channels. For the smooth channel, the mass transfer after the turn was found to be higher than that before the turn. The mass transfer in the turn was also high compared with that before the turn except at the first outside corner of the turn. In addition, the average Sherwood number around the sharp turn decreased slightly with increasing Reynolds number for Re ranging from 1.5 × 10⁴ to 6 × 10⁴. Chyu (1991) investigated both two- and three-pass channels with rectangular turns using an analogous naphthalene mass transfer technique for Reynolds numbers of 2 × 10⁴ to 7.4 × 10⁴. He concluded that heat transfer at the first turn has already reached the thermally periodic condition. Ekkad and Han (1995) measured local heat transfer distributions near a sharp 180 deg turn of a two-pass smooth square channel using a transient liquid crystal image technique for Reynolds numbers of 1.0 × 10⁴, 2.5 × 10⁴, and 5.0 × 10⁴. The heat transfer results were broadly consistent with the aforementioned mass transfer results reported by Han et al. (1988), except for Reynolds number dependence. They showed an increase of the Nusselt number with increasing Reynolds number, which is opposite to the slight decrease of the Sherwood number with increasing Reynolds number reported from the mass transfer experiment of Han et al. (1988). Mochizuki et al. (1997) investigated the effects of ten different rib arrangements on pressure drop and heat transfer in a square channel with a sharp 180 deg turn. The smooth-wall case was used as a reference one for comparison.

The observation of the secondary flow patterns in a square duct with a 180 deg sharp turn was first reported by Cheng et al. (1992) using the smoke injection method for three different divider tip-to-wall clearances and Reynolds numbers of 200, 500, and 800. It was found that the secondary flow patterns, featuring one to four pairs of vortices, were distorted, and the flow became turbulent in the region two to three duct hydraulic diameters after the turn for Re = 500 and 800. Subsequently, Wang and Chyu (1994) presented computational results of mean secondary flow patterns and heat transfer distribution in a two-pass, square duct with 180 deg sharp straight-corner turn, rounded-corner turn, and circular turn. The inlet conditions were assumed fully developed and a modified version of κ–ϵ model was adopted. Results indicated that spatial variation in the local heat transfer was very significant and depended greatly on the turn geometry. The straight-corner turn was found to yield the highest heat transfer augmentation relative to the fully developed straight channel flow. In view of the lack of turbulent velocity measurements in the preceding literature, Liou and Chen (1999) recently performed detailed laser-Doppler velocimetry (LDV) measurements of developing flows through a smooth two-pass duct without duct rotation. The Reynolds number was 1.4 × 10⁴ and the divider tip had sharp corners. Quantitative results, such as the upstream and downstream extents of the

Contributed by the International Gas Turbine Institute and presented at the 43rd International Gas Turbine and Aeroengine Congress and Exhibition, Stockholm, Sweden, June 2–5, 1998. Manuscript received by the International Gas Turbine Institute February 1998. Paper No. 98-GT-189. Associate Technical Editor: R. E. Kielb.

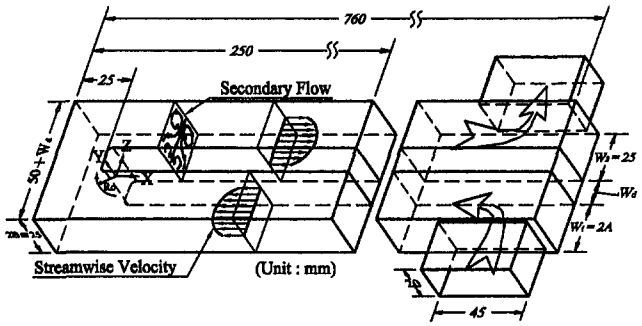

Fig. 1 Sketch of configuration, coordinate system, and dimensions of test section

Table 1 A list of W_d^* studied by various researcher groups

Authors	Year	Geometries	W_d^*	Authors	Year	Geometries	W_d^*
Metzger	1984 1986		0.10	Wang & Chyu	1994		0.25
Han et al.	1988		0.125				
Chyu	1991		0.25	Ekkad & Han	1995		0.125
Cheng et al.	1992		0.25	Liou & Chen	1997		0.06
Prakash & Zerkle	1992		0.50	Present study	1997		0.10
Zhang et al.	1993		0.228				0.25
Mochizuki et al.	1994		0.50				0.50

sharp-turn effect on the main flow profile, curvature-induced Dean vortices inside the turn, turning geometry-induced separation bubble, double-peak mean velocity profiles in the second pass, and high turbulence levels and nonuniformity in the front part of the second pass, were presented in detail to complement the previous heat and mass transfer results measured by others.

The present study aims at performing detailed measurements of the turbulent flowfields in a straight-corner turn two-pass square duct with three different divider thicknesses (Fig. 1) covering the W_d^* range adopted by other researchers (Table 1) using nonintrusive LDV. The straight-corner (or square-corner) turn is used to simulate actual turbine blade cooling passages (North, 1997), and is the most common case when a 180 deg sharp turn is molded in the laboratory and adopted virtually in all of the previous studies (Wang and Chyu, 1994). Moreover, a rounded-corner divider tip that is more practical than sharp-corner divider tip adopted in our previous work (Liou and Chen, 1999) is used in the present work. LDV is chosen since flow reversals and large turbulence fluctuations associated with the sharp turn are expected. It is hoped that the data obtained herein lead to insight to the effect of W_d^* on the complex flows examined and can be used for verifying ongoing computational predictions.

Experimental Apparatus and Conditions

Test Apparatus. Figure 2 schematically depicts the LDV experimental setup and flow circuit. The fluid flow was driven by a 2.2 kW turbo blower located at downstream end of the flow circuit and operated in the suction mode. Air was the working medium, which was drawn into a rectangular duct with an aspect ratio of 2.25:1, and subsequently turned 90 deg into the two-pass test duct with a square cross section. A length of 500 mm in front of the test section functions as flow development region to reduce the 90 deg entry turning effect. Downstream of the test section with a 180 deg sharp turn, the air flowed through a flowmeter, a bellows, and then exhausted by the turbo blower.

The LDV optics is a two-color four-beam two-component system (Liou et al., 1997). A 4-W argon-ion laser with 488 nm (blue) and 514.5 nm (green) lines provided the coherent light sources. Both forward and off-axis scattering configurations were used in the experiment; the former provided a probe volume of about 1.69 mm in length and 0.164 mm in diameter and the latter 0.74 mm in length and 0.164 mm in diameter inside the test section, based on $1/e^2$ extent of light intensity. The entire LDV system was mounted on a milling machine with four vibration-isolation mounts, allowing the probe volume to be positioned with 0.01 mm resolution. The light scattered from salt particles with a nominal size of 0.8 μm was collected into the photomultiplier and subsequently downmixed to the appropriate frequency shift of 0.1 to 10 MHz. The two counterprocessors with 1 ns resolution were used to process the Doppler signals and feed the digital outputs into a PC-486 for storage and analysis.

Test Section and Conditions. Figure 1 shows the configuration, coordinate system, and dimensions of the test section, which was made of 3-mm-thick acrylic sheets for optical access. The flow

Nomenclature

A = half-width of duct = 12.5 mm, 0.5 W_1 or 0.5 W_2
B = half-height of duct = 12.5 mm, Fig. 1
D_H = hydraulic diameter = $4AB/(A + B)$ = 25 mm
Nu = local Nusselt number
Nu_o = Nusselt number in fully developed tube flow
Nu_{rg} = regional averaged Nusselt number
R_c = radius of curvature = 2.5 mm, Fig. 1
Re = Reynolds number = $\rho U D_H/\mu$
U = streamwise mean velocity, m/s
U_b = duct bulk mean velocity, m/s
u = streamwise velocity fluctuation, m/s
V = transverse mean velocity, m/s
v = transverse velocity fluctuation, m/s
W = spanwise mean velocity, m/s
W_1 = width of first-pass duct = 25 mm, Fig. 1
W_2 = width of second-pass duct = 25 mm, Fig. 1
W_d = divider thickness, mm, Fig. 1
W_d^* = dimensionless divider thickness = $W_d/(W_1 + W_2)$
X = streamwise coordinate, mm, Fig. 1
X^* = normalized streamwise coordinate = X/D_H
Y = transverse coordinate, mm, Fig. 1
Y^* = normalized transverse coordinate = Y/B
Z = spanwise coordinate, mm, Fig. 1
Z^*, Z^{**} = normalized spanwise coordinate:
(*i*) $X < 0$, $Z^{**} = Z/(2A + W_d)$ (in the turn)
(*ii*) $X \geqq 0$, $Z < 0$, $Z^* = (Z + W_d/2)/2A$ (in the first pass)
(*iii*) $X \geqq 0$, $Z > 0$, $Z^* = (Z - W_d/2)/2A$ (in the second pass)
μ = air absolute viscosity (kg/m-s)
ρ = air density (kg/m^3)

Subscripts

b = bulk
rg = regional averaged

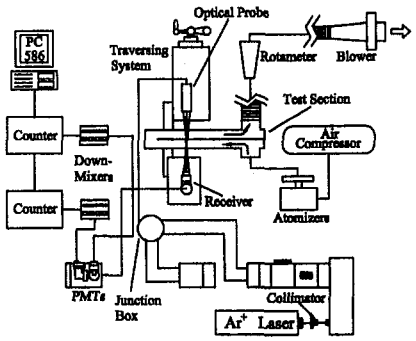

Fig. 2 Schematic drawing of overall experimental system

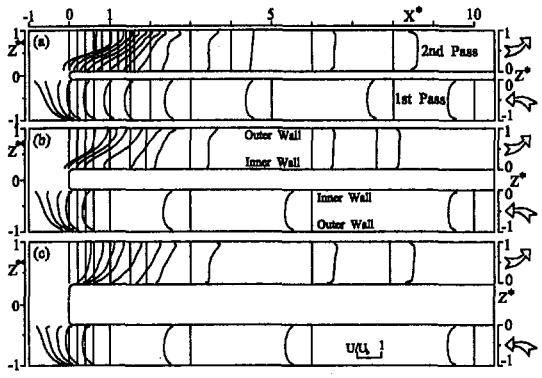

Fig. 3 Evolution of streamwise mean velocity profile in $Y^* = 0$ plane of the first and second passes for Re = 1.2×10^4: (*a*) $W_d^* = 0.10$; (*b*) $W_d^* = 0.25$; and (*c*) $W_d^* = 0.50$

path has a cross section of 25 mm × 25 mm with a corresponding hydraulic diameter of $D_H = 25$ mm. The lengths of the first pass, sharp turn, and second pass are 30.4 D_H, 1 W_d, and 30.4 D_H, respectively. At the turn, the clearance between the tip of the divider wall and the duct outer wall is kept equal to 1 D_H (or 25 mm). The three divider-wall thicknesses W_d examined are 0.2 D_H, 0.5 D_H, and 1 D_H or $W_d^* = 0.10$, 0.25, and 0.50. R_c, the radius of curvature of the divider tip's rounded corners, is 2.5 mm. The coordinate origin is chosen at the tip center of the partition wall (Fig. 2) such that the X coordinates upstream and downstream of the turn are all positive, whereas they are negative in the turn.

The Reynolds number, based on the bulk mean velocity of U_b = 7.3 m/s and hydraulic diameter, was fixed at 1.2×10^4. The velocity measurements were made at 8 to 11 and 10 to 14 X^* stations for the first and second flow passes, respectively. In each station the streamwise velocity was made along two orthogonal lines, ($Y^* = -1$ to 1, $Z^* = 0.5$) and ($Y^* = 0$, $Z^* = -1$ to 1). The secondary-flow velocity vector mappings were performed over three cross-sectional planes. Moreover, detailed velocity vector mappings for the region from 1 D_H upstream of the turn to 2 D_H downstream of the turn in the $Y^* = 0$ plane were made, i.e., 9, 11, and 21 X^* stations for the pre-turn, intra-turn, and post-turn regions, respectively. The inlet reference cross section was chosen at $X^* = 10$ of the first pass.

The mean velocity and turbulence data presented below were calculated from the probability distribution function of the measurements. Typically, 2000–4000 realizations were ensemble averaged at each measuring location. Additional measurements of higher realizations (8000) in the high fluctuation regions were also taken to be sure statistical convergence was attained. The corresponding statistical errors in the ensemble averaged mean velocity and turbulence intensity were less than 0.018 U_b and 0.031 U_b, respectively, for a 95 percent confidence level. Other sources of error were documented in detail in our previous work (Liou and Chen, 1999).

Results and Discussion

Flow Evolution in $Y^* = 0$ Plane. Figure 3 depicts the streamwise development of the X component of the mean velocity profile along $Y^* = 0$ plane for the three divider-wall thicknesses examined. The nearly symmetric top-hat streamwise mean velocity profiles at $X^* = 10$ of the first pass for all three W_d^* indicate that the mean flow patterns here are practically independent of the upstream entry turn ($X^* = 28.5$, Fig. 1) and downstream 180-deg sharp turn ($X^* < 0$). $X^* = 10$ is thus a good choice for the inlet reference plane. Before the turn, the divider-wall thickness seems to have little effect on the evolution of the streamwise mean velocity profile. A near-wall LDV scan along lines at a distance 1 mm from the inner and outer walls reveals that downstream of $X^* = 1.5$ in the first pass the flow has sensed the existence of the sharp turn and, hence, displays an acceleration and a deceleration near the inner and outer walls, respectively, as shown in Fig. 4. In general, before a curved turn a flow undergoes favorable and adverse pressure gradients along the inner and outer walls, respectively, whereas the trend is reversed after the turn (Liou and Liao, 1995). Within the measured locations of the first pass, the streamwise mean velocities near the inner wall for $W_d^* = 0.10$, 0.25, and 0.50, respectively, can be accelerated up to values as high as 1.45 U_b, 1.42 U_b, and 1.33 U_b at $X^* = 0$ whereas near the outer wall they can be decelerated to values as low as 0.24 U_b, 0.26 U_b, and 0.30 U_b at $X^* = 0$. This trend is because the thinner the divider wall, the sharper the turning. Consequently, the smaller the W_d^*, the larger the maximum acceleration and deceleration near the inner and outer walls, respectively. However, the quantitative differences in the maximum acceleration and deceleration of mean velocities are small for the range of W_d^* examined.

Immediately after the turn Fig. 4 shows the reversed trend in the streamwise mean velocity evolution; the acceleration now occurs along the region near the outer wall (open circle) of the second pass. Depending on the location of the sharp-turn-induced separation bubble, as depicted in Fig. 5, Fig. 4 shows the acceleration can be up to 1.60 U_b, 1.50 U_b, and 1.31 U_b occurring at $X^* = 0.8$,

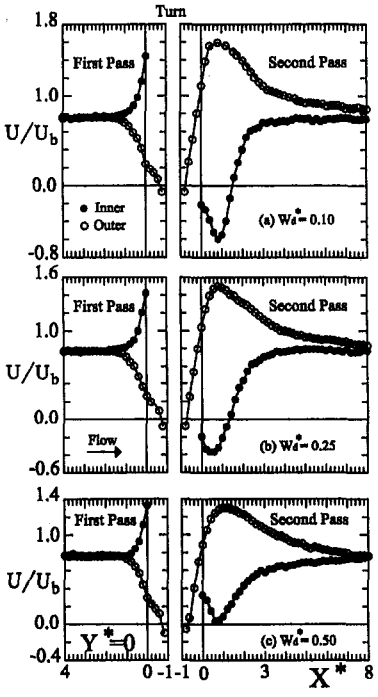

Fig. 4 Variations of streamwise mean velocity along lines at a distance 1 mm from the inner and outer walls, respectively, in $Y^* = 0$ plane

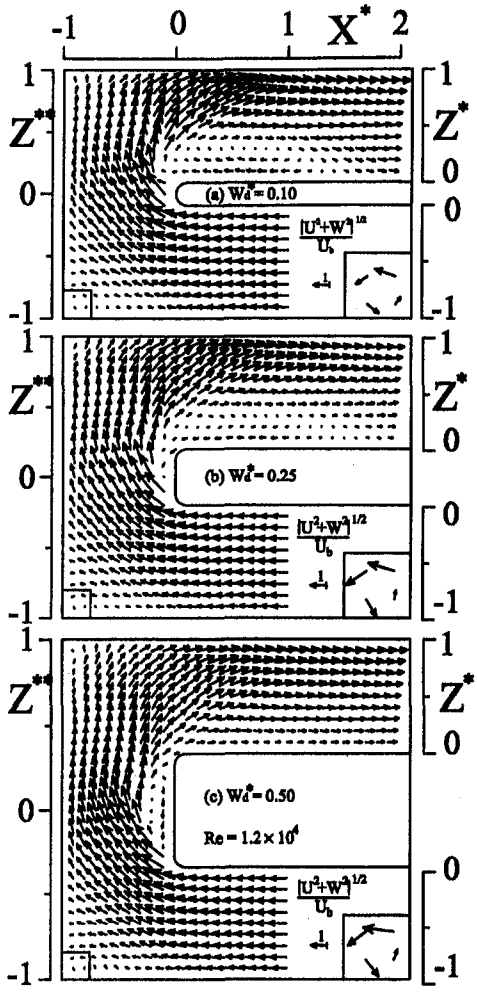

Fig. 5 Vector plot of the flow patterns near and inside the sharp turn in $Y^* = 0$ plane for Re = 1.2×10^4: (*a*) $W_d^* = 0.10$; (*b*) $W_d^* = 0.25$; and (*c*) $W_d^* = 0.50$ (note: For clarity data within 1 mm from the wall are not included in the figure)

0.8, and 1.0 for $W_d^* = 0.10$, 0.25, and 0.50, respectively. Notice that the peak U/U_b all occur at about 0.5 to 1.0 D_H downstream of the sharp turn. In this region, the gap formed by the outer wall and the sharp-turn-induced separation bubble for the cases of $W_d^* = 0.10$ and 0.25 or low-velocity zone on the inner-wall side for the case of $W_d^* = 0.50$ (Fig. 5) is the smallest. As the flow proceeds farther downstream, the influence of the 180 deg sharp turn gradually diminishes and the streamwise mean velocities, both near the outer and inner walls of the second pass, gradually redevelop (Fig. 4). Beyond $X^* = 8$ of the second pass, Figs. 4 and 5 show that U/U_b recover to the values close to those at $X^* \geqq 1.5$ of the first pass. In other words, the influential range of the 180 deg sharp turn on the streamwise mean flow profile extends from 1.5 D_H upstream to 8 D_H downstream of it.

Figure 5 depicts the mean velocity vector plots of the flow patterns near and inside the sharp turn in $Y^* = 0$ plane for the three W_d^* studied. Notice that for the sake of clarity and space limitation, the vector data presented in Fig. 5 are limited to 2.5 mm away from the solid wall. For $W_d^* = 0.10$ (Fig. 5(*a*)) the inability of the flow to follow the sharp turn and the thin divider tip cause a large separation bubble prevailing after the turn and adjacent to the divider tip. A similar observation was visualized by Metzger et al. (1984) for the same $W_d^* = 0.10$ (Table 1). The separation bubble has a maximum negative U/U_b of 0.60 occurring at $X^* = 0.8$ (second pass in Fig. 4) and a reattachment length of about 1.5 D_H away from the divider tip, as located by $U = 0$ in Fig. 4 where the measurements were brought to as close as 1 mm from the wall. The maximum height of the separation bubble is about one-half of the second-pass width W_2. For $W_d^* = 0.25$ (Fig. 5(*b*)) the separation bubble has a maximum negative U/U_b of 0.37 occurring at $X^* = 0.6$ (Fig. 4) and a size similar to that of $W_d^* = 0.10$; however, the flow reversal extends upstream into the top of divider tip, a phenomenon lacking in the case of $W_d^* = 0.10$. Owing to the thick divider wall in the case of $W_d^* = 0.50$, the fluid flow separated at the upstream corner of the divider tip is able to reattach onto the divider tip, as shown in Fig. 5(*c*), with a maximum height of about one-third of the clearance between the divider tip and duct outer wall and a maximum negative streamwise mean velocity of 0.42 U_b at $Z^{**} = 0$. The separation bubble in this case has a length slightly less than the divider wall thickness and the fluid is able to flow smoothly around the divider tip's downstream rounded corner without separation but resulting in a low velocity zone after the turn on the inner wall side (Fig. 5(*c*)). The foregoing comparison suggests the significant effect of the divider wall thickness on the flow characteristics inside and immediately after the sharp turn.

Inside the sharp turn, the negative U/U_b around $X^* = -1$ in Fig. 4 and the negative mean velocity vector around ($X^* = -1$, $Z^{**} = \pm 1$) in Fig. 5 indicate the presence of the corner vortices near the two outer wall corners for all three W_d^*. It should be pointed out that in the numerical calculation of Wang and Chyu (1994), W_d^* was 0.25 and the corner vortex was also found to exist near the upstream outer corner ($X^* = -1$, $Z^{**} = -1$) for both straight-corner and rounded-corner turns but not for the case of the U-bend. For the straight-corner turn they found a rather weak corner vortex appearing in the downstream outer corner ($X^* = -1$, $Z^{**} = 1$), which is consistent with our measured results depicted in Fig. 4(*b*). Conversely, their calculation showed that the turn-induced main separation recirculation zone in $Y^* = 0$ plane was only confined to the region adjacent to the top of divider tip without extending further into the post-turn region immediately adjacent to the divider wall for both straight-corner and rounded-corner turns, which is different from our measured results shown in Fig. 5(*b*).

Cross-Stream Flow Patterns. It is well known that Dean-type secondary flow typically exists for a flow through a turn due to the imbalance of centrifugal force and pressure gradient. Figure 6 shows the evolution of the secondary-flow pattern at three selected cross sections: pre-turn ($X^* = 0.2$), midturn ($Z^{**} = 0$), and postturn ($X^* = 0.2$), for $W_d^* = 0.10$, 0.25, and 0.50. As addressed in the preceding section, the fluid flow at $X^* = 1.5$ of the first pass has sensed the sharp turning. Hence, at the preturn location $X^* = 0.2$ or $X = 0.2$ D_H upstream of the turn, the mainstream is ready for turning with a skew streamwise mean velocity profile (Fig. 3), higher velocities near the inner wall ($Z^* = 0$), and the secondary flow in the cross-sectional plane thus moves from the outer wall ($Z^* = -1$) toward the inner wall ($Z^* = 0$). Note that the secondary-flow mean-velocity vector fields are plotted facing the downstream direction. It is also observed from Fig. 6 that at the preturn location, secondary flow pattern is relatively insensitive to the difference in W_d^*. The maximum magnitude of cross-stream velocity vectors is only about 0.49 U_b, 0.41 U_b, and 0.32 U_b for $W_d^* = 0.10$, 0.25, and 0.50, respectively, at the selected preturn cross section $X^* = 0.2$.

As the fluid flow proceeds to the midplane of turning, the counterrotating Dean vortex pair appears. Figure 6 clearly reveals that the difference in W_d^* does affect the cross-stream flow pattern inside the turn. For $W_d^* = 0.10$ the streamwise separation recirculation zone mainly occurs in the second pass, a pair of well-organized Dean vortices prevails in the midturn plane with the dominant cross-stream mean velocities occurring near the divider tip, i.e., along Y^* at $X^* = -0.1$ (Fig. 6(*a*)). However, as W_d^* is increased, the main part of the separation recirculation zone gradually shifts from the second pass to the divider tip inside the turn. As a result, for $W_d^* = 0.25$ (Fig. 6(*b*)) and 0.50 (Fig. 6(*c*)) the locations where dominant cross-stream mean velocities occur are

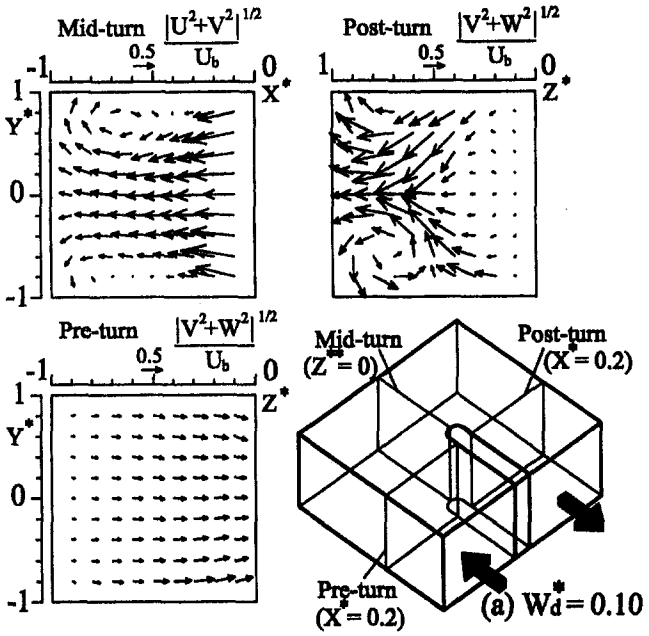

Fig. 6 Secondary flow patterns at selected preturn, midturn, postturn cross sections for Re = 1.2 × 10⁴: (*a*) $W_d^* = 0.10$; (*b*) $W_d^* = 0.25$; and (*c*) $W_d^* = 0.50$

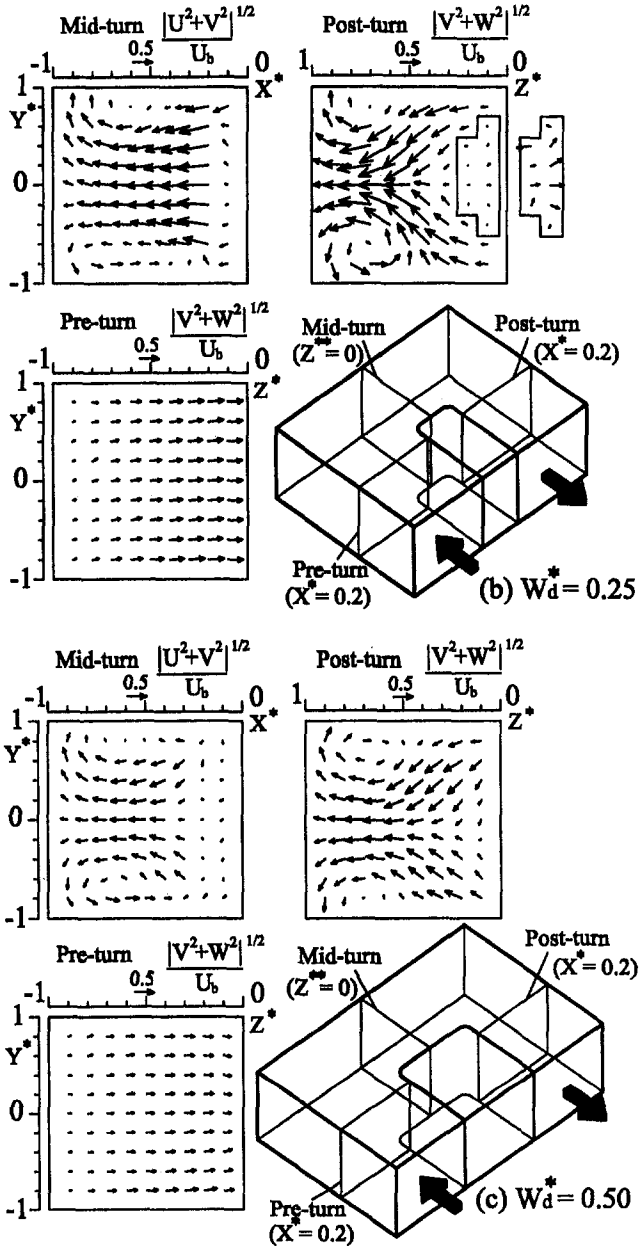

Fig. 6 (Continued)

respectively shifted 0.1 D_H and 0.4 D_H toward the outer wall (relative to the $W_d^* = 0.10$ case), i.e., the dominant cross-stream mean velocities occur along Y^* at $X^* = -0.2$ and $X^* = -0.5$, respectively. The shift of the streamwise separation bubble's main body to the divider tip leads to the formation of a rather low-speed cross-stream zone adjacent to the divider tip, which lowers the dominant cross-stream velocities. Figure 6 shows that the size of the low-speed cross-stream zone near the divider tip increases with increasing W_d^* and the sizes of Dean vortex pairs thus occupy about 100, 80, and 70 percent of the midturn cross section for $W_d^* = 0.10$, 0.25, and 0.50, respectively. The resultant mean velocities in the low-speed cross-stream zone near the divider tip are as low as 0.07 U_b and 0.03 U_b, respectively, for $W_d^* = 0.25$ and 0.50. Also the dominant cross-stream resultant mean velocities decreases with increasing W_d^*, approximately 1.10 U_b, 0.80 U_b, and 0.42 U_b for $W_d^* = 0.10$, 0.25, and 0.50, respectively.

Immediately after the turn, $X^* = 0.2$ (Fig. 6), the effect of W_d^* on the Dean vortex pair still persists; nevertheless, the size of Dean vortex pair and its distortion due to the existence of the turning curvature-induced separation recirculation zone is just opposite to that occurred in the aforementioned midturn plane. It is interesting to note that the size of the low-velocity zone (i.e., a cross section of the streamwise separation bubble) for $W_d^* = 0.25$ (dotted box in Fig. 6(*b*)) happens to facilitate the formation of a second pair of counterrotating vortices driven by the main pair of Dean vortices.

Flow Evolution in $Z^* = \pm 0.5$ Planes. It should be mentioned here that the streamwise flow development in $Z^* = \pm 0.5$ planes (Fig. 2) of a two-pass duct with a sharp turn has seldom been reported in the open literature and is therefore depicted in Fig. 7. Because the $Z^* = \pm 0.5$ planes are normal to the 180 deg sharp turning plane, the streamwise mean velocity profiles in the $Z^* = -0.5$ plane of the first pass are almost unaffected by the turning curvature and divider wall thickness W_d^*, and hence more symmetric than the counterparts in the $Y^* = 0$ plane (Fig. 3), particularly around $X^* = 0$ just before the turn. In the $Z^* = 0.5$ plane of the post-turn region, however, the combined effect of the sharp-turn-induced separation recirculation flow and the turning-curvature-induced cross section secondary flow leads to concave streamwise mean velocity profiles (lower velocity around $Y^* = 0$) within the region of about 6 D_H after the turn. The concavity in the streamwise mean velocity profiles will augment the heat transfer through the duct walls ($Y^* = \pm 1$) and is found to decrease with increasing W_d^* due to the shift of the separation recirculation zone from the postturn region to the midturn region. For $X^* > 6$, the streamwise mean velocity profiles become top-hat shaped for all three W_d^* studied.

Turbulent Kinetic Energy Distribution. In view of the fact that mean-velocity profiles for all three W_d^* are greatly distorted near the divider tip and in the region within the short distance after the turn, as shown by Figs. 3, 5, and 7, the turbulence is expected to prevail in these regions. Figure 8 thus depicts the dimensionless turbulent kinetic energy (TKE) distribution in these corresponding regions. It is seen that the uniformity of TKE increases with increasing W_d^*; a more solid and quantitative comparison will be shown in the next section in terms of the regional averaged values. The major local TKE peaks are associated with the separation bubble's shear layer and its reattachment. For each W_d^* there exist, therefore, two peak values. The peak value associated with the

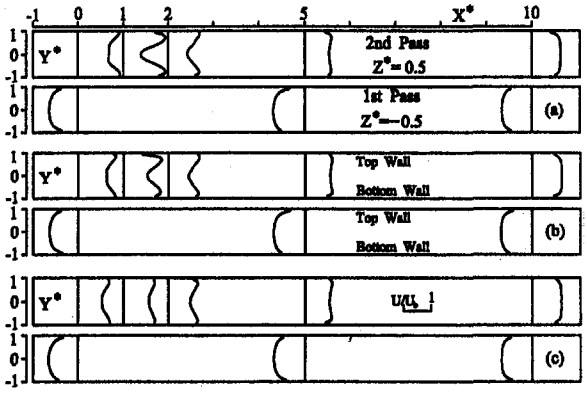

Fig. 7 Evolution of streamwise mean velocity profile in $Z^* = \pm 0.5$ plane of the first and second passes for Re = 1.2×10^4: (*a*) $W_d^* = 0.10$; (*b*) $W_d^* = 0.25$; and (*c*) $W_d^* = 0.50$

front shear layer of the main separation bubble increases with increasing W_d^* since its location moves closer to the separation point as W_d^* increases. These TKE peaks have values of 11, 13, and 15 percent and occur at ($X^* = 0$, $Z^{**} = 0.4$), ($X^* = -0.2$, $Z^{**} = 0.2$), and ($X^* = -0.2$, $Z^{**} = -0.15$) for $W_d^* = 0.10$, 0.25, and 0.50, respectively. Conversely, the peak value associated with the reattachment point decreases as W_d^* increases since the strength of the main separation recirculation zone decreases with increasing W_d^*. The magnitudes of these TKE peaks are 19, 12, and 11 percent and appear at ($X^* = 1.3$, $Z^{**} = 0.4$), ($X^* = 1.5$, $Z^{**} = 0.45$), and ($X^* = -0.2$, $Z^{**} = 0.2$) for $W_d^* = 0.10$, 0.25, and 0.50, respectively.

Relation Between Fluid Flow and Heat Transfer Results. From Figs. 5 and 8, the dimensionless regional averaged turbulent kinetic energy $[(\overline{u^2} + \overline{w^2})/2U_b^2]_{rg}$ and magnitude of convective mean-velocity vector $(U^2 + W^2)_{rg}^{0.5}/U_b$ around the turn region of the two-pass duct for $W_d^* = 0.10$, 0.25, and 0.50 are calculated according to the region index layout shown in Fig. 9(*a*) and the results are presented in Fig. 9(*b*). A preliminary result of heat transfer coefficient contours obtained using a transient liquid crystal image technique for $W_d^* = 0.06$ adopted in our previous work (Liou and Chen, 1999) are shown in Fig. 10. From Fig. 10 the regional averaged Nusselt number nondimensionalized with the fully developed Nusselt number, $Nu_o = 37.5$, is calculated and plotted in Fig. 9(*b*). The present measured Nu_{rg}/Nu_o are also compared with published results from Chyu (1991) using mass transfer analysis and Ekkad and Han (1995) using liquid crystal analysis.

It is observed from Fig. 9(*b*) that the regional averaged Nusselt number distribution obtained from Fig. 10 compares reasonably well with the results reported by Chyu (1991) and Ekkad and Han (1995) in terms of the trend although the inlet conditions and values of Re and W_d^* are different among these studies. All the results indicate that the heat transfer augmentation is higher in the second pass than in the first pass. The maximum heat transfer augmentation occurs in the regions of 1 to 3 (or $X^* = -1$ to 2) after the turn and Nu can be up to 1.9 ~ 2.4 times Nu_o. Moreover, the streamwise variation of the reported heat transfer coefficient in the two-pass duct can be illustrated by the present measured flowfield results. As shown in Fig. 9, in general, the regional averaged turbulent kinetic energy increases toward the downstream direction from region −2 in the first pass to region 3 in the second pass; it is expected to drop farther downstream. This general trend of $[(\overline{u^2} + \overline{w^2})/2U_b^2]_{rg}$ parallels that of Nu_{rg}/Nu_o with the increasing rate modified by the convective velocity. In region −2 before the turn, the regional averaged turbulent kinetic energy is very low and the increase of Nu_{rg} from Nu_o is attributed to the high regional averaged convective mean velocity. For region −1 inside the turn, the increase of Nu_{rg}/Nu_o is mainly due to increased

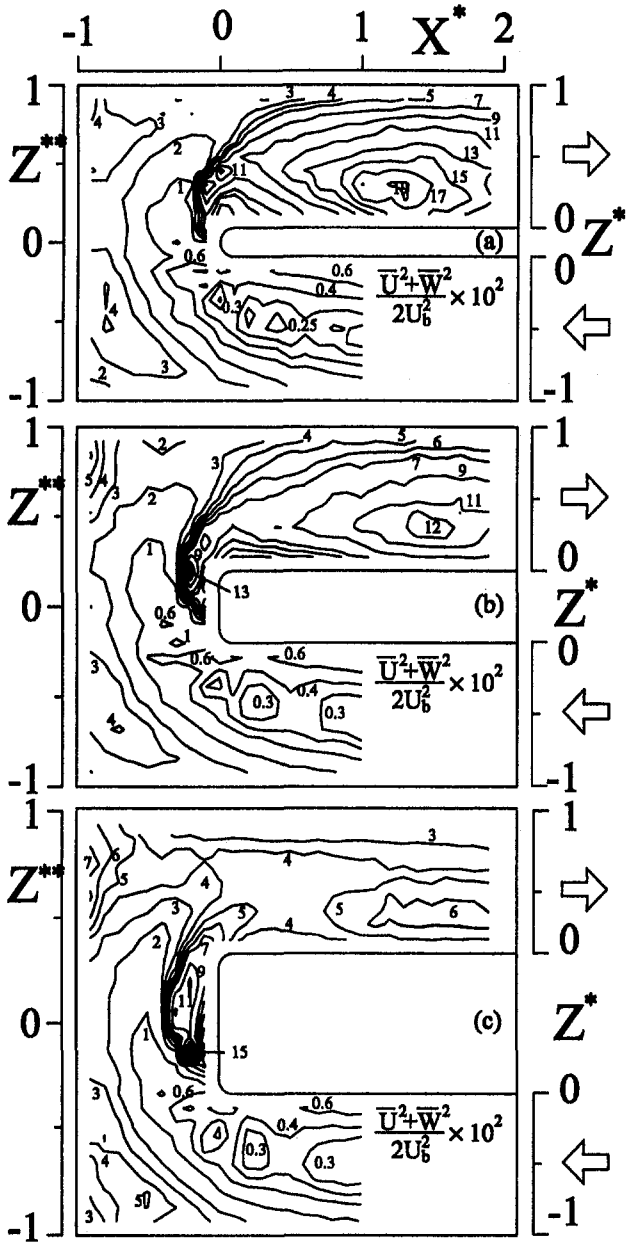

Fig. 8 Turbulent kinetic energy contours around the sharp turn in $Y^* = 0$ plane for Re = 1.2×10^4: (*a*) $W_d^* = 0.10$; (*b*) $W_d^* = 0.25$; and (*c*) $W_d^* = 0.50$

regional averaged turbulent kinetic energy since the regional averaged resultant convective mean velocity decreases. As the flow proceeds from region −1 to the midturn region 0, $[(\overline{u^2} + \overline{w^2})/2U_b^2]_{rg}$ decreases slightly but $(U^2 + W^2)_{rg}^{0.5}/U_b$ increases steeply for $W_d^* = 0.10$ and 0.25, resulting in a further increase in Nu_{rg}/Nu_o. For region 1 inside the turn, Nu_{rg}/Nu_o increases persistently since the regional averaged turbulent kinetic energy increases although the regional averaged resultant convective mean velocity decreases slightly. After the turn in regions 1 to 3, the regional averaged turbulent kinetic energy and resultant convective mean velocity respectively increase and decrease sharply for $W_d^* = 0.10$ and 0.25. As a result, Nu_{rg}/Nu_o distribution reveals a plateau in these regions. Farther downstream from region 3, the turning effect gradually diminishes, leading to a weak variation in the regional averaged resultant convective mean velocity, and a gradual decrease in the regional averaged turbulent kinetic energy and, in turn, in Nu_{rg}/Nu_o.

For a fixed Re, Fig. 9 shows that the difference in W_d^* has almost

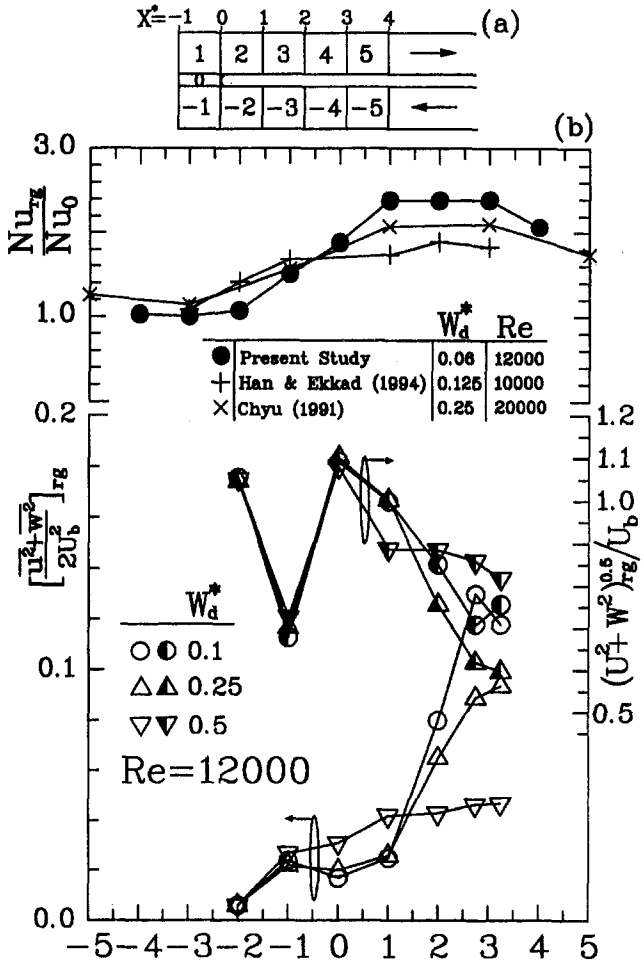

Fig. 9 (*a*) **Region index layout for performing region average;** (*b*) **dimensionless regional averaged turbulent kinetic energy, magnitude of convective mean-velocity vector, and Nusselt number versus region index**

no influence on both the regional averaged turbulent kinetic energy and resultant convective mean velocity in the first pass. It is therefore expected that W_d^* has a weak influence on Nu_{rg}/Nu_o in the first pass. Inside the turn and in the second pass, W_d^* is found to have significant effects on both regional averaged turbulent kinetic energy and resultant convective mean velocity. At a fixed Re = 12,000, the present data indicate that the levels of $[(\overline{u^2} + \overline{w^2})/2U_b^2]_{rg}$ and $(U^2 + W^2)_{rg}^{0.5}/U_b$ in the second pass are higher for $W_d^* = 0.10$ than for $W_d^* = 0.25$. In addition, as mentioned in the introduction, for a fixed $W_d^* = 0.125$ the results published by Ekkad and Han (1995) for Re = 1.0×10^4 to 5.0×10^4 showed that the higher the Reynolds number, the higher the Nusselt number. These two results provide a possible explanation for the higher Nu_{rg}/Nu_o in the second pass measured by the present authors than by Ekkad and Han (1995), as shown in Fig. 9. The competition in raising Nu_{rg}/Nu_o between smaller W_d^* and higher Re is encountered by comparing the present case of $W_d^* = 0.06$ and Re = 1.2×10^4 with Chyu's case of $W_d^* = 0.25$ and Re = 2.0×10^4 (Chyu, 1991). Apparently, W_d^* is the dominant factor in this special competition (also recall that the mass transfer study of Han et al. (1988) concluded a slight decrease of the average Sherwood number with increasing Re) and a higher Nu_{rg}/Nu_o in the second pass is attained for the present case. More extensive studies should be made to gain insight into the relative effect of W_d^* and Re. A complementary heat transfer study using a liquid crystal technique on the relation between W_d^* and Nu is being performed. There is one more aspect regarding the effect of W_d^* worthy of address. Figure 9 clearly reveals that the uniformity of $[(\overline{u^2} + \overline{w^2})/2U_b^2]_{rg}$ increases with increasing W_d^*, as mentioned in the preceding section based on the broad observation from Fig. 8.

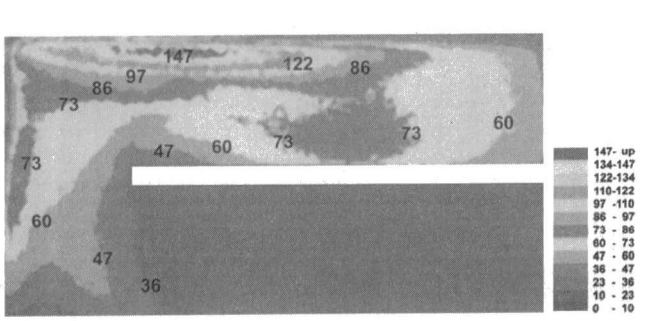

Fig. 10 Liquid crystal measured heat transfer coefficient contours for $W_d^* = 0.06$ and Re = 1.2×10^4

Conclusions

The effect of divider thickness W_d^* on flow characteristics near a 180 deg straight-corner turn for a two-pass, smooth, square duct was explored using LDV. The conclusions drawn based on the data presented are:

1 W_d^* has little effect on fluid flow, both streamwise and cross-stream secondary flows, before the turn. In contrast, the location of the sharp-turn-induced separation recirculation zone is shifted from immediately after the turn to inside the turn and on the top of the divider tip when W_d^* is increased from 0.10 to 0.50.

2 The local turbulent kinetic energy peaks associated with the shear layer and reattachment of the aforementioned separation recirculation zone thus also undergo the same shift as W_d^* is increased from 0.10 to 0.50. As a result of the above-mentioned shift, the uniformity and level of the regional averaged turbulent kinetic energy increases and decreases with increasing W_d^*, respectively, especially for the region immediately after the turn.

3 Near and in the turn, the maximum cross-stream mean velocity decreases with increasing W_d^*. Inside the turn, the percentage area of the cross section prevailed by the curvature-induced Dean-type vortex pair decreases with increasing W_d^*. The trend is reversed immediately after the turn.

4 The regional averaged turbulent kinetic energy and convective mean velocity can complementarily provide the rationale for published and present measured distributions of the regional averaged heat transfer coefficient and, especially, their relative levels in the region immediately after the turn.

5 For all W_d^* examined, in general, near and in the turn, the regional averaged turbulent kinetic energy increases with increasing streamwise distance. The regional averaged Nusselt number follows this trend with its increasing rate modified by the evolution of the convective mean velocity. The maximum regional averaged turbulent kinetic energy and heat transfer coefficient occur therefore in the region immediately downstream of the turn and are approximately 0.09 ~ 0.24 times U_b^2 and 1.9 ~ 2.4 times Nu_o, respectively.

Acknowledgments

Support for this work was partially provided by the National Science Council of the Republic of China under contract No. SC-85-2212-E007-056.

References

Besserman, D. L., and Tanrikut, S., 1991, "Comparison of Heat Transfer Measurements With Computations for Turbulent Flow Around a 180 Degree Bend," ASME Paper No. 91-GT-2; published in the ASME JOURNAL OF TURBOMACHINERY, Vol. 114, 1992, pp. 865–871.

Chang, S. M., Humphrey, J. A. C., and Modavi, A., 1983, "Turbulent Flow in a Strongly Curved U-Bend and Downstream Tangent of Square Cross-Sections," *Physico Chemical Hydrodynamics*, Vol. 4, No. 3, pp. 243–269.

Cheng, K. C., Nakayama, J., and Akiyama, M., 1977, "Effect of Finite and Infinite

Aspect Ratios on Flow Patterns in Curved Rectangular Channels," *Proc. International Symposium on Flow Visualization,* Oct., Tokyo, Japan, pp. 640–645.

Cheng, K. C., Shi, L., Kurokawa, M., and Chyu, M. K., 1992, "Visualization of Flow Patterns in a 180 Deg Sharp Turn of a Square Duct," *Fourth International Symposium on Transport Phenomena and Dynamics of Rotating Machinery,* Honolulu, HI, USA, Apr.

Choi, Y. D., Iacovides, H., and Launder, B. E., 1989, "Numerical Computation of Turbulent Flow in a Square-Sectioned 180 Deg Bend," ASME *Journal of Fluids Engineering,* Vol. 111, pp. 59–68.

Chyu, M. K., 1991, "Regional Heat Transfer in Two-Pass and Three-Pass Passages With 180 Deg Sharp Turns," ASME *Journal of Heat Transfer,* Vol. 113, pp. 63–70.

Ekkad, S. V., and Han, J. C., 1995, "Local Heat Transfer Distributions Near a Sharp 180 Deg Turn of a Two-Pass Smooth Square Channel Using a Transient Liquid Crystal Image Technique," *Journal of Flow Visualization and Image Processing,* Vol. 2, pp. 285–297.

Fairbank, J. A., and So, R. M. C., 1987, "Upstream and Downstream Influence of Pipe Curvature on the Flow Through a Bend," *International Journal of Heat and Fluid Flow,* pp. 211–217.

Han, J. C., Chandra, P. R., and Lau, S. C., 1988, "Local Heat/Mass Transfer Distributions Around Sharp 180 deg Turns in Two-Pass Smooth and Rib-Roughened Channels," ASME *Journal of Heat Transfer,* Vol. 110, pp. 91–98.

Johnson, R. W., 1988, "Numerical Simulation of Local Nusselt Number for Turbulent Flow in a Square Duct With a 180 Deg Bend," *Numerical Heat Transfer,* Vol. 13, pp. 205–228.

Liou, T. M., and Chen, C. C., 1999, "LDV Study of Developing Flows Through a Smooth Duct With 180 deg Straight-Corner Turn," ASME JOURNAL OF TURBOMACHINERY, Vol. 121, pp. 167–174.

Liou, T. M., and Liao, C. C., 1995, "Flows in Curved Combustor Inlet With and Without a Guide Vane," *AIAA Journal of Propulsion and Power,* Vol. 11, No. 3, pp. 464–472.

Liou, T. M., Yang, G. P., and Lee, H. L., 1997, "LDV Measurements of Spatially Periodic Flow Over a Detached Solid-Rib Array," ASME *Journal of Fluids Engineering,* Vol. 119, pp. 383–389.

Metzger, D. E., Plevich, C. W., and Fan, C. S., 1984, "Pressure Loss Through Sharp 180 Deg Turns in Smooth Rectangular Channels," ASME *Journal of Engineering for Gas Turbines and Power,* Vol. 106, pp. 677–681.

Metzger, D. E., and Sahm, M. K., 1986, "Heat Transfer Around Sharp 180 Deg Turns in Smooth Rectangular Channels," ASME *Journal of Heat Transfer,* Vol. 108, pp. 500–506.

Mochizuki, S., Takamura, J., Yamawaki, S., and Yang, W. J., 1994, "Heat Transfer in Serpentine Flow Passages With Rotation," ASME JOURNAL OF TURBOMACHINERY, Vol. 116, pp. 133–140.

Mochizuki, S., Murata, A., and Fukunaga, M., 1997, "Effects of Rib Arrangements on Pressure Drop and Heat Transfer in a Rib-Roughened Channel With a Sharp 180 deg Turn," ASME JOURNAL OF TURBOMACHINERY, Vol. 119, pp. 610–616.

North, E., 1997, private communication.

Prakash, C., and Zerkle, R., 1992, "Prediction of Turbulent Flow and Heat Transfer in a Radially Rotating Square Duct," ASME JOURNAL OF TURBOMACHINERY, Vol. 114, pp. 835–846.

Wang, T. S., and Chyu, M. K., 1994, "Heat Convection in a 180-Deg Turning Duct With Different Turn Configuration," *Journal of Thermophysics and Heat Transfer,* Vol. 8, No. 3, pp. 595–601.

Zhang, N., Chiou, J., Fann, S., and Yang, W. J., 1993, "Local Heat Transfer Distribution in a Rotating Serpentine Rib-Roughened Flow Passage," ASME *Journal of Heat Transfer,* Vol. 115, pp. 560–567.

Dynamics of Large-Scale Structures for Jets in a Crossflow

F. Muldoon
Graduate student.

S. Acharya[1]
Professor.

Mechanical Engineering Department,
Louisiana State University,
Baton Rouge, LA 70803

Results of a three-dimensional unsteady computational study of a row of jets injected normal to a crossflow are presented with the aim of understanding the dynamics of the large-scale structures in the region near the jet. The jet to crossflow velocity ratio is 0.5. A modified version of the computer program (INS3D), which utilizes the method of artificial compressibility, is used for the computations. Results obtained clearly indicate that the near-field large-scale structures are extremely dynamic in nature, and undergo breakup and reconnection processes. The dynamic near-field structures identified include the counterrotating vortex pair (CVP), the horseshoe vortex, wake vortex, wall vortex, and shear layer vortex. The dynamic features of these vortices are presented in this paper. The CVP is observed to be a convoluted structure interacting with the wall and horseshoe vortices. The shear layer vortices are stripped by the crossflow, and undergo pairing and stretching events in the leeward side of the jet. The wall vortex is reoriented into the upright wake system. Comparison of the predictions with mean velocity measurements is made. Reasonable agreement is observed.

Introduction

Jets in crossflow have been studied extensively due to potential applications in gas turbine blade cooling, control of pollutant discharges, roll-control of missiles, etc. The majority of these studies dealing with the details of the flow structure have been on single jets issuing into a crossflow. Early experimental studies dealt with experimental efforts to determine the mean flow behavior and pressure distributions (see, for example, Kamotani and Gerber, 1972; Andreopoulos, 1985; Andreopolous and Rodi, 1984). Flow visualization studies have revealed the existence of several vortical structures, and have indicated the importance of their dynamic nature. The counterrotating vortex pair (commonly referred to as the CVP) is reported to be the most dominant structure persisting far downstream of the jet injection. This is believed to be due to the vortex street exiting the injection hole and its reorientation by the crossflow (Foss, 1980; Andreopoulos, 1985; Kelso et al., 1996). In addition, shear layer or ring vortices, driven by Kelvin–Helmholtz instability, are generated in the near field of the jet. The adverse pressure gradient introduced by the jet blockage produces the horseshoe vortices (with spanwise vorticity), which are deflected and stretched by the crossflow, and these travel downstream (with streamwise vorticity) rotating in a direction opposite to the CVP. Finally upright wake vortices between the surface and the jet have been observed (see Fric and Roshko, 1994), and these have been attributed to the separation of the entrained crossflow boundary layer due to spanwise pressure gradients.

Computational studies aimed at examining the details of the flow structure have been relatively limited. The majority of the reported studies have primarily solved the Reynolds-Averaged-Navier–Stokes (RANS) equations, and due to the intrinsic time-averaging that is associated with these equations, the dynamic nature of the vortical structures cannot be predicted. Further, turbulence models have to be introduced, and the accuracies of even the time-averaged calculations are themselves compromised by the validity of the model. Examples of RANS calculations are those of Patankar et al. (1977), Sykes et al. (1986), Kim and Benson (1992), and Demuren (1993). More recently, Jones and Wille (1996) and Yuan and Street (1999) presented Large Eddy Simulations (LES) that resolve the dynamics of the large scales and model the small scales, and observed some of the reported phenomena in the experiments.

The application of interest in the present paper is the film cooling of gas turbine blades. In this configuration, a row of coolant jets is injected into a hot crossflow. The coolant jets are usually injected at an angle to the main crossflow direction. The goal of the jets is to provide a wide coverage of the blade surface. This problem differs from the single-jet-in-crossflow studies, in that the spanwise boundaries are no longer free-stream boundaries. They are either periodic or symmetry (for a time-averaged variable) boundary conditions. Further, the length-to-diameter ratio of the injection hole is usually small (in the range of 1.5–5), and therefore the flow development in the injection hole is affected by the crossflow leading to a highly nonuniform jet-exit profile. This is in contrast to the single-jet studies, where the hole exit profile has been assumed to be or is symmetric. Since the vorticity exiting the hole has a very strong influence of the downstream development of the dynamic structures, appropriate specification of the jet-exit conditions is necessary.

In the near field of the film cooling jet, the dynamic large-scale structures are likely to control the mixing process, as has been shown in free jet studies (see, for example, the review by Ho and Huerre, 1984) and it is this mixing that dictates the normal and transverse penetration of the jet. To predict the heat transfer or the adiabatic effectiveness accurately from the surface, it is important to predict the jet penetration and reattachment correctly, and for this the dynamics of the near-field structures must be accurately simulated. This necessitates a time-and space-accurate calculation of the flow field, i.e., direct numerical simulation (DNS) or LES. However, while there are many computational studies dealing with film cooling predictions (see Garg and Gaugler, 1994, 1997), they are primarily limited to RANS-based calculations and

[1] Corresponding author.

Contributed by the International Gas Turbine Institute and presented at the 43rd International Gas Turbine and Aeroengine Congress and Exhibition, Stockholm, Sweden, June 2–5, 1998. Manuscript received by the International Gas Turbine Institute February 1998. Paper No. 98-GT-19. Associate Technical Editor: R. E. Kielb.

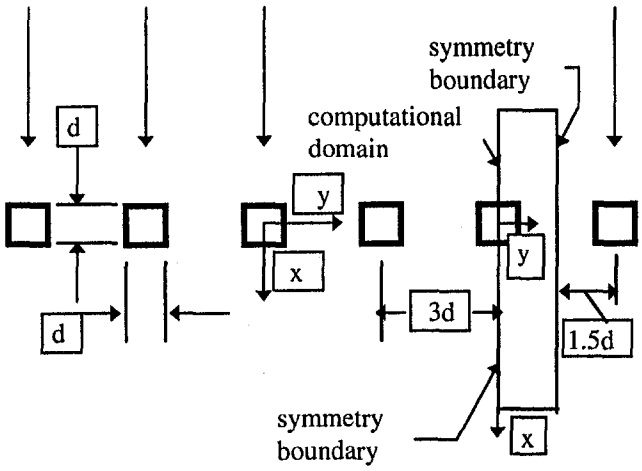

Fig. 1 Diagram of the physical problem

are therefore unable to predict the near-field evolution of the jet ($x/d < 5$) very well. In this paper, we present time and space-accurate calculations for a typical film cooling configuration, with the specific intent of understanding the dynamics of the various vortical structures in the near-field. To the authors' knowledge, DNS or LES for the film cooling configuration have not been reported.

Problem Description

The physical configuration (Fig. 1) chosen corresponds to an experimental study reported by Ajersch et al. (1997). The coolant jets are injected at 90 deg (vertically upward) from a square-cross-section duct with an average velocity of 5.5 m/s. The width of the square jet exit hole is $d = 12.7$ mm. The free-stream value of the crossflow velocity is 11 m/s. The measurements of Ajersch et al. (1997) are used for boundary conditions at both the crossflow inlet and the jet exit. In the experiments of Ajersch et al. (1997) the crossflow boundary layer approaching the jet was tripped by a thin rod to ensure a turbulent boundary layer. Both the jet and crossflow air are at the same (room) temperature. The Reynolds number based on the jet hydraulic diameter (d) and average jet velocity is 4700.

Since the primary goal of the present study is to examine the *dynamics* of the large-scale vortical structures in the near field, only a modest number of grid points (nearly 277,000) have been used in the present study. It is recognized that this mesh will be unable to resolve the dynamics of the small-scale structures, nor the interaction between the small and large scales. With this in mind, no statistics, except mean velocity, are presented in this paper, and the discussion is focused on the dynamics of the near-field large-scale structures. The experimental studies referenced earlier (Foss, 1980; Fric and Roshko, 1994; Kelso et al., 1996) clearly indicate that the near-field vortical structures are large-scale events, controlled largely by inviscid phenomena, and that the small-scale turbulence has little influence in this region. Therefore, it is expected that with the mesh used in the present calculations, the near-field dynamics would be correctly predicted.

Figures 1 and 2 show the computational domain. The computational domain extended from $x/d = -6.3$ to 12, $y/d = 0$ to 1.5, $z/d = 0$ to 4. A stretched Cartesian grid with 191 points in the x direction, 29 in the y, and 50 in the z direction was used. The grid was stretched in the x direction so that grid points were clustered in the jet region. Grid points were also clustered near the wall boundary in the z direction. In wall coordinates $\Delta x^+((x/\nu)\sqrt{\tau_w/\rho})$ (where τ_w is the wall shear stress) ranged from 20 near the jet to 60 well downstream, Δy^+ is nearly 20 across the whole spanwise direction, and Δz^+ ranged from about 8 near the wall to about 60 far away from the wall.

At $y/d = 0$ and $y/d = 1.5$, symmetry boundary conditions were used at each time step. In order to represent the inlet boundary conditions accurately, perturbations were introduced at both the jet and crossflow inlet. This was accomplished by adding a fluctuating component of velocity to the mean velocity data of Ajersch et al. (1997). The fluctuating component $F(j, k, t)$ is specified by Eq. (1) and is composed of 10 frequencies ($f(n)$). The numbers a and b are generated randomly between 0 and 1, where j and k represent the indices of the inlet planes. The term a is used to provide a slightly different frequency for each real time step. The effect of b, which is a function only of the gridpoints, is to provide a different phase shift for every spatial location. The term A was chosen to control the amplitude of the perturbations to match that of the experimental data of Ajersch et al. (1997).

$$F(j, k, t) = A(j, k) \sum_{n=1}^{10} \sin [f(n)*[1 + .015*(a(j, k, t) - .5)]*t + b(j, k)] \quad (1)$$

The frequencies at which the flow was perturbed ranged from 1.2 to 36 Hz. The computed dominant frequencies of the flow were in the range 100–200 Hz (see section on Dynamics of the Large-Scale Structures). This indicates that the natural instabilities were established in the flow, and were not the result of the frequencies introduced at the boundaries.

Solution Method

The three-dimensional unsteady incompressible Navier–Stokes equations are solved by the method of artificial compressibility, which was first suggested by Chorin (1968). In this method the incompressible Navier–Stokes equations are modified by the addition of a derivative of pressure (times a constant) with respect to a psuedo-time to the continuity equation. This creates a situation similar to that of the compressible Navier–Stokes equations in which the effect of pressure appears in the continuity equation due to the presence of a derivative of density with respect to time. This enables the incompressible Navier–Stokes equations to be solved using methods derived for the compressible Navier–Stokes equations. When steady state is reached in psuedo-time, the added term in the continuity equation becomes zero and the incompressible continuity equation is satisfied. Real-time solutions are obtained by adding the appropriate terms to the steady-state incompressible Navier–Stokes equations and obtaining a steady-state solution in psuedo-time for each real time step. A code called INS3D, which was developed at NASA Ames Research Center by Rogers and Kwak (1991), was used. This code incorporates a third and a fifth-order upwind representation for the convective terms along with a second-order central difference representation for

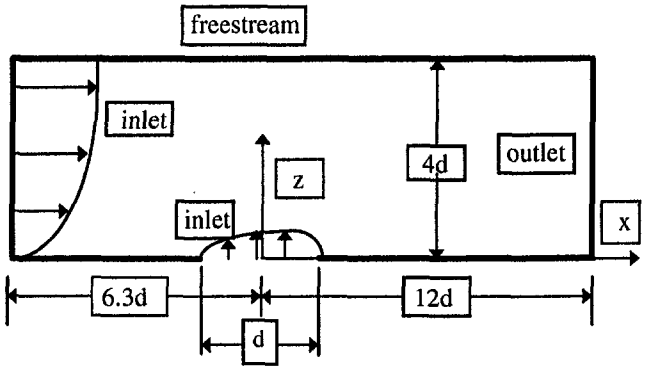

Fig. 2 Diagram of the computational domain

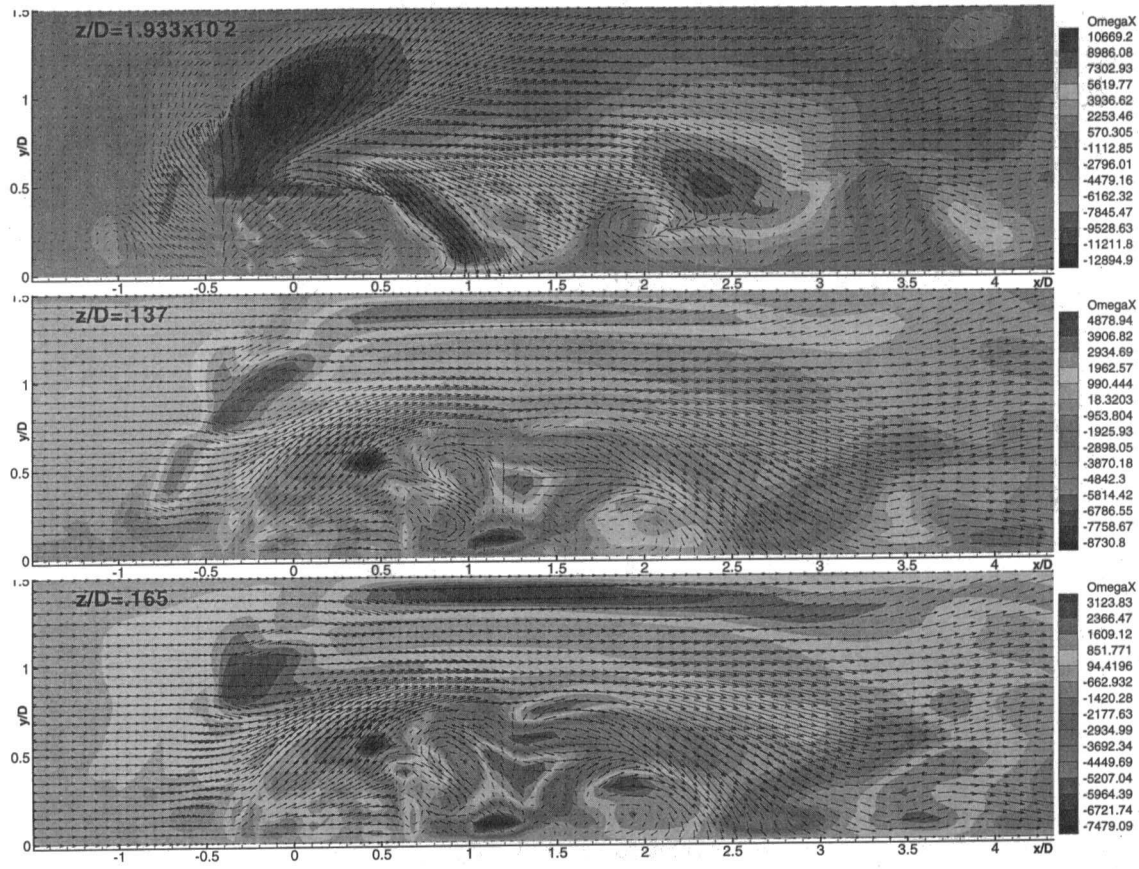

Fig. 3 The x component of vorticity in the x–y plane at one instant in time

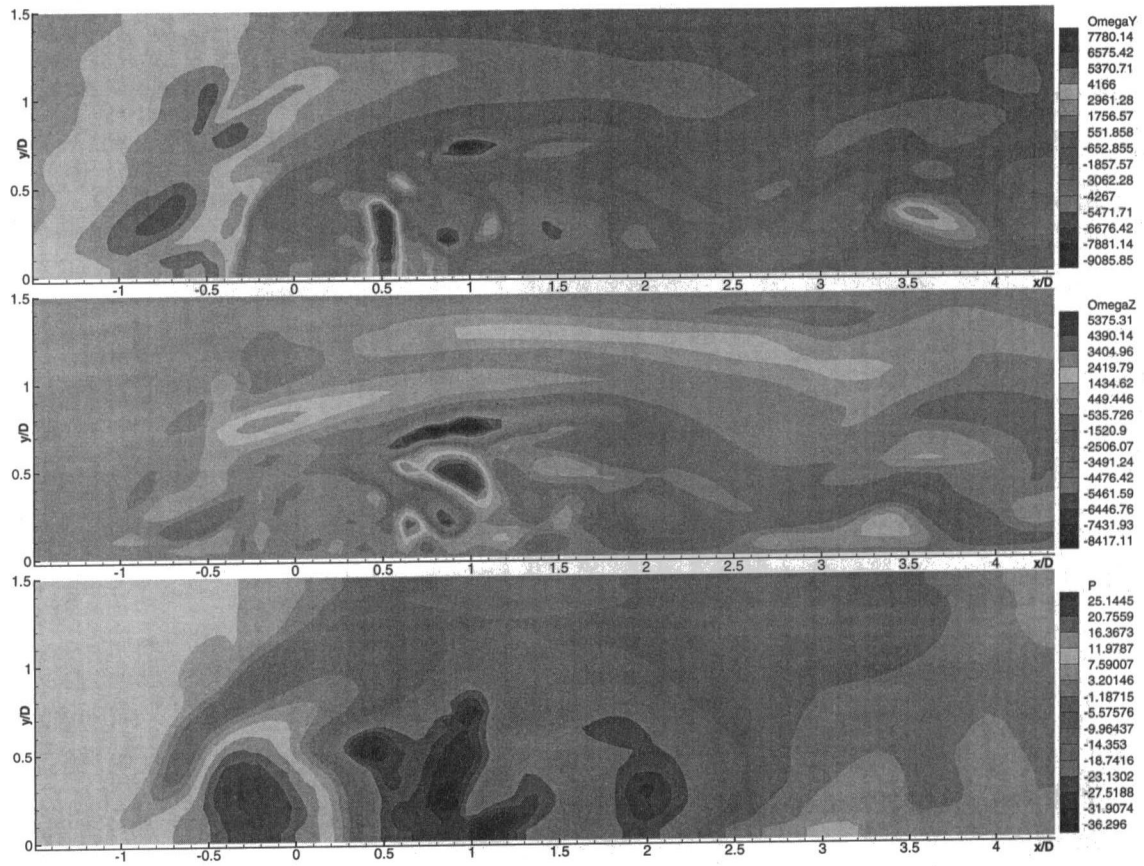

Fig. 4 The y and z components of vorticity and pressure in the x–y plane at the same instant in time at $z/d = 0.137$

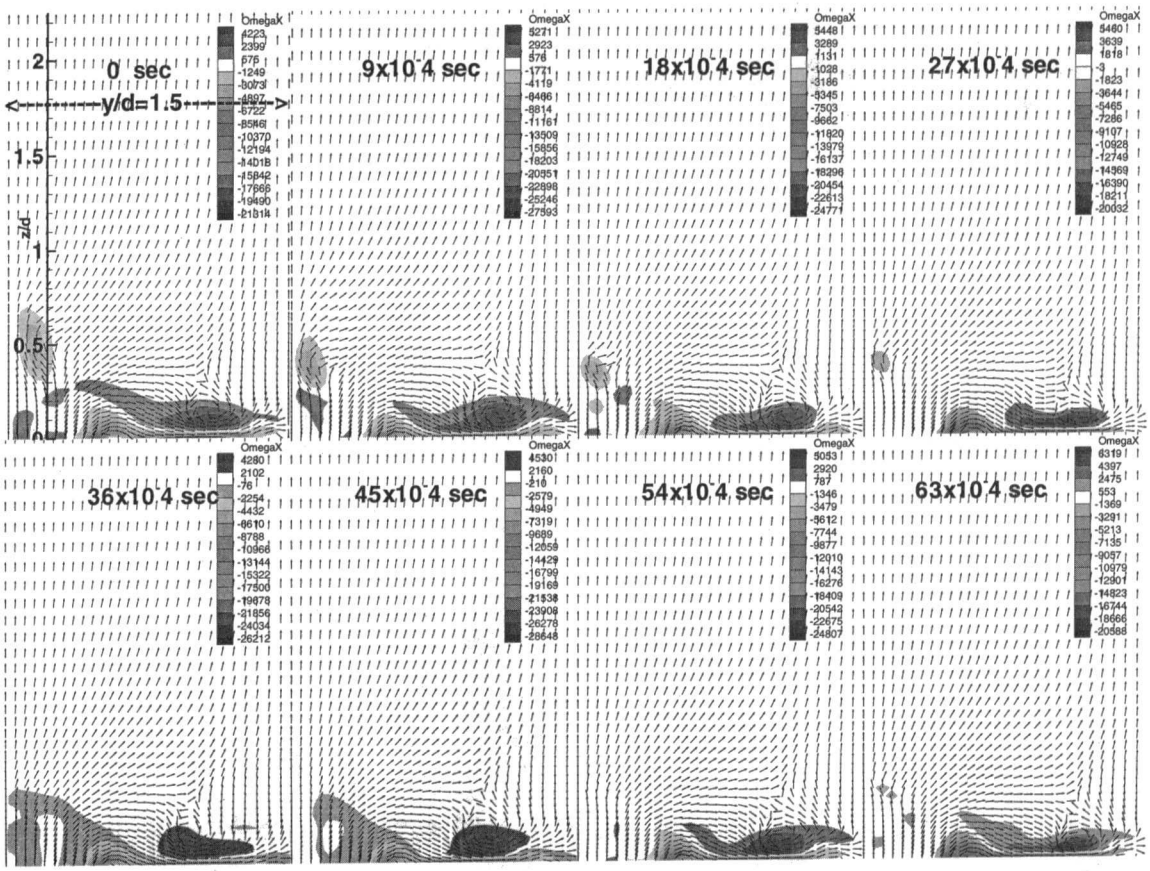

Fig. 5 The x component of vorticity and velocity vectors in the $y-z$ plane at $x/d = 0$

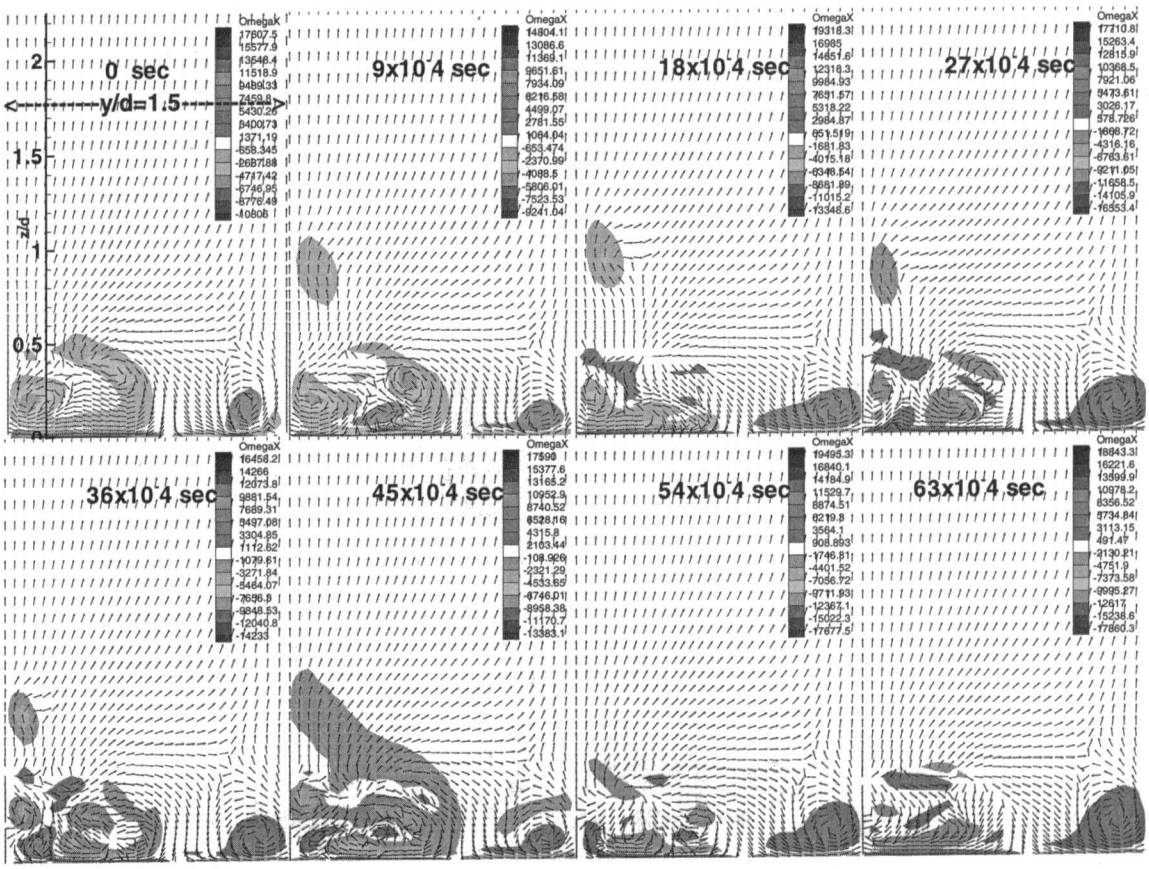

Fig. 6 The x component of vorticity and velocity vectors in the yz plane, at $x/d = 0.979$

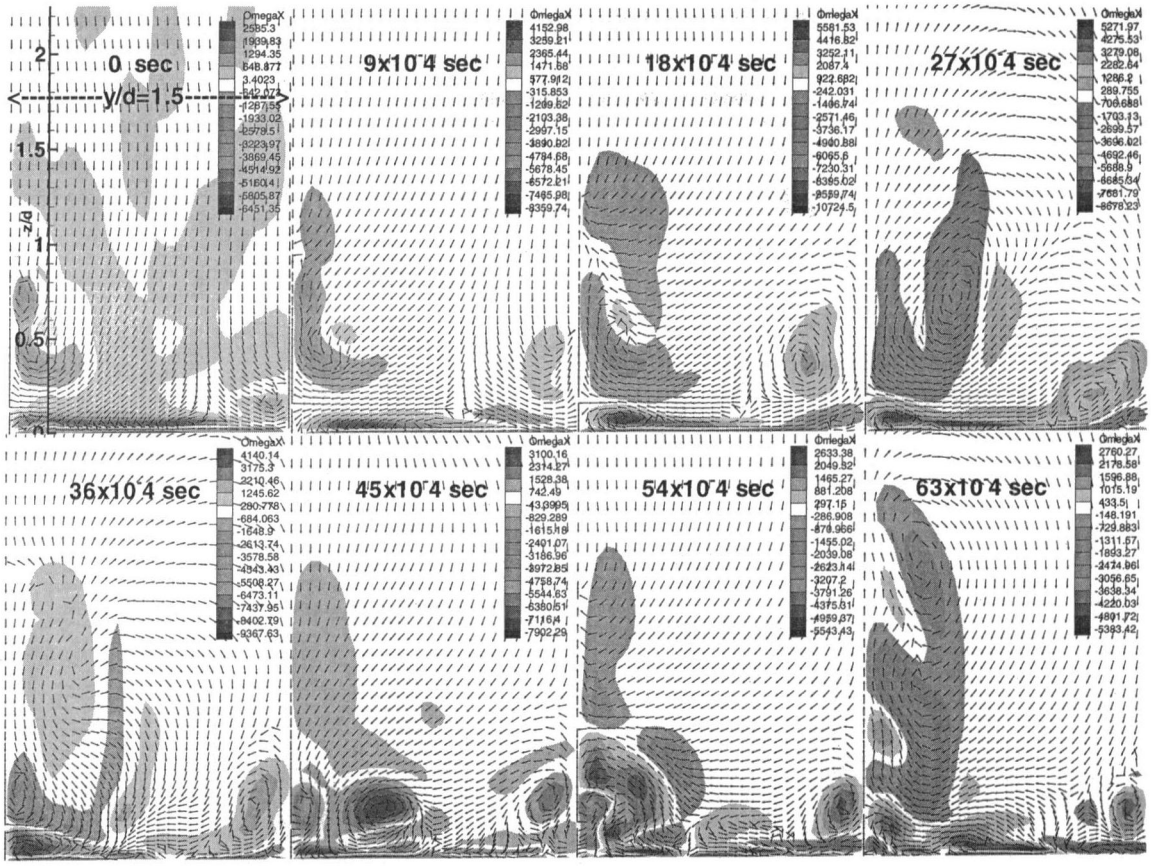

Fig. 7 The x component of vorticity and velocity vectors in the y–z plane, at $x/d = 4.0$

the diffusion terms. All calculations presented in this paper were done using the 3rd order upwind representation for the convective terms. The code was modified to use a fourth-order central difference representation for the diffusion terms. A second-order representation is used for the temporal terms. Although a Cartesian grid was used, the code is capable of handling generalized curvilinear coordinates. We have changed the differencing of the metric terms from second-order accuracy to a user-defined arbitrary order of accuracy utilizing Fornberg's algorithm (1988). In our calculations we use fourth-order accurate representations for the metric terms. Between 40 and 45 subiterations were needed to move one real time step. Eight hours on a Cray C90 were required to move approximately 68 time steps. The solution was advanced over 1700 time steps. This corresponds to a particle passing through the computational domain 12 times based on the jet velocity, and is long enough for the effect of the initial conditions to be "washed out."

Results and Discussions

Main Features at One Time Instance. Figure 3 shows the instantaneous values of the x vorticity at three different x–y planes above the surface. Above the surface, the dominant features of the flow field are the horseshoe vortex (positive vorticity) and the CVP (negative vorticity). The horseshoe vortex system grows in both the spanwise and vertical directions as it develops downstream. At a vertical location corresponding to $z/d = 0.137$, two legs of the horseshoe vortex system are noted, with one leg traveling downstream along the symmetry boundary, and the other being partly entrained into the wake of the jet (by $x/d = 2$). This process repeats itself farther downstream (by $x/d = 4$, see Fig. 7 and again by $x/d = 6$). In the near field ($x/d = 2$), the entrained positive vorticity convolutes the CVP, and as a consequence, the instantaneous flow field consists of a highly stretched and distorted CVP (negative vorticity) with pockets of positive vorticity. The positive vorticity, particularly close to the wall, is also caused by the wall vortex, as discussed in the next paragraph.

Very close to the surface, $z/d = 0.01933$ (Fig. 3), negative vorticity is noted directly below the footprint of the horseshoe vortex, while positive vorticity is noted on the leeward side of the injection hole. The low pressure in the wake region produces the pressure defect responsible for driving the crossflow in the spanwise direction. Examination of the instantaneous pressure contours at the same time instance (Fig. 4) indicates both axial and spanwise pressure gradients along the transverse edge of the jet, which are responsible for a thin flow-stream from the transverse edge of the jet, with positive vorticity, to be directed toward the jet symmetry plane. This is akin to the wall-vortex behavior observed by Kelso et al. (1996) where the flow bifurcates toward the jet center plane from a saddle point on the transverse side and encounters an adverse pressure gradient near the centerline, causing flow separation and a wall vortex system. Contours of the x vorticity in cross-stream planes, shown later, will show time instances in which this positive vorticity associated with the wall vortex will link up with positive vorticity in the horseshoe vortex.

Figure 4 presents the y and z components of vorticity and pressure, at a given instance in time in the x–y plane corresponding to $z/d = 0.137$. The corresponding x component of vorticity was provided in Fig. 3. The y component of vorticity shows the signature of the horseshoe vortex beginning roughly one diameter upstream of the jet exit, but diminishes rapidly downstream of $x/d = 0$, implying the reorientation of the vortex

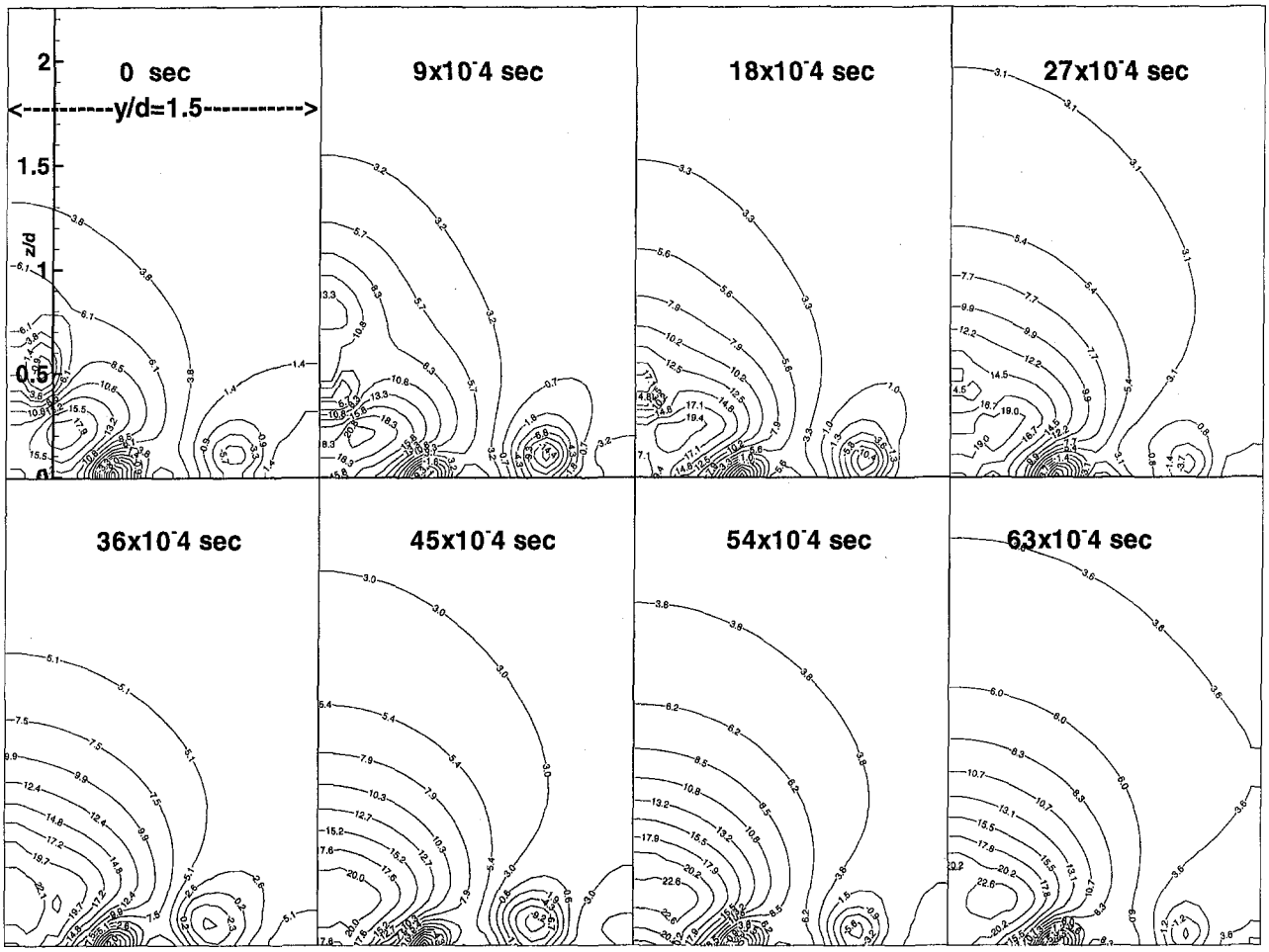

Fig. 8 Pressure in the y–z plane, at $x/d = 0$

by the crossflow. The large positive vorticity values from the trailing edge of the hole ($x/d = 0.5$) are also evident and are associated with the boundary layer on the trailing wall of the jet exit. The corresponding negative vorticity along the leading edge of the jet hole is considerably smaller due to the distortion of the jet-hole exit profile by the crossflow (as obtained from measurements), which diminishes the velocity gradients along the leading edge and accentuates them along the trailing edge. Downstream from the hole, patches of negative vorticity can be observed. These are presumably associated with the jet-shear-layer or ring vortices associated with Kelvin–Helmholtz rollup.

The z-vorticity contour shows two distinctive features. First, the horseshoe vortex is associated with positive z vorticity downstream of the leading edge of the injection hole. This is presumably induced by the periodic splitting and transverse entrainment of the vortex into the wake region. The second distinctive feature is associated with the wake region where patches of strong positive and negative z vorticity are noted. The negative vorticity is associated with the wake vortex, and Kelso et al. (1996) and Fric and Roshko (1994) have concluded that this is caused by the entrainment of the crossflow boundary layer into the wake, and its reorientation by the vertical upflow. Further evidence and clarification on this will be provided in Figs. 6 and 7. Three mechanisms for the positive vorticity are possible. First, an examination of the jet-hole-exit profile shows strong pockets of z vorticity, and these could be transported downstream into the wake region. Second, the periodic entrainment of the horseshoe vortex (discussed in reference to Fig. 3), associated with positive z vorticity as noted above, can lead to pockets of positive z vorticity in the wake. Third, Kelso et al. (1996) have postulated a mechanism for wake vortices, where the "upright vortices are formed by vortex loops on either side of the wake," and is "composed of vorticity from one or the other side of the wake." Such a mechanism would lead to alternate positive and negative pockets of vorticity. While, at the $z/d = 0.137$ location, the wake vortices appear to be contiguous, at a higher z/d location ($z/d = 0.42$), the vortices are more distinct and separate from each other (see Fig. 11). The visualization pictures of Fric and Roshko (1994) and Kelso et al. (1996) appear to indicate that such behavior is also borne out in the experiments.

The pressure contours show the stagnation region upstream of the jet centerline, and the region of low pressure just downstream of the leeward side of the jet. Because of the low blowing ratio (0.5), the stagnation region extends into the jet-exithole. The lower pressures in the horseshoe vortex and its trajectory are clearly evident. The excursions of the crossflow boundary layer or the horseshoe vortex into the low-pressure wake region are also noticeable in the form of spanwise fingering of the pressure contours originating from the crossflow regions. The adverse pressure gradient regions near the jet center plane that lead to the wall vortex system can also be seen in the pressure contours.

Dynamics of the Large-Scale Structures. In the discussion below we will focus attention on the vorticity and pressure contours at different streamwise (x–y and x–z) and cross-stream (y–z) planes. Of interest are the dynamics of the structures, and therefore,

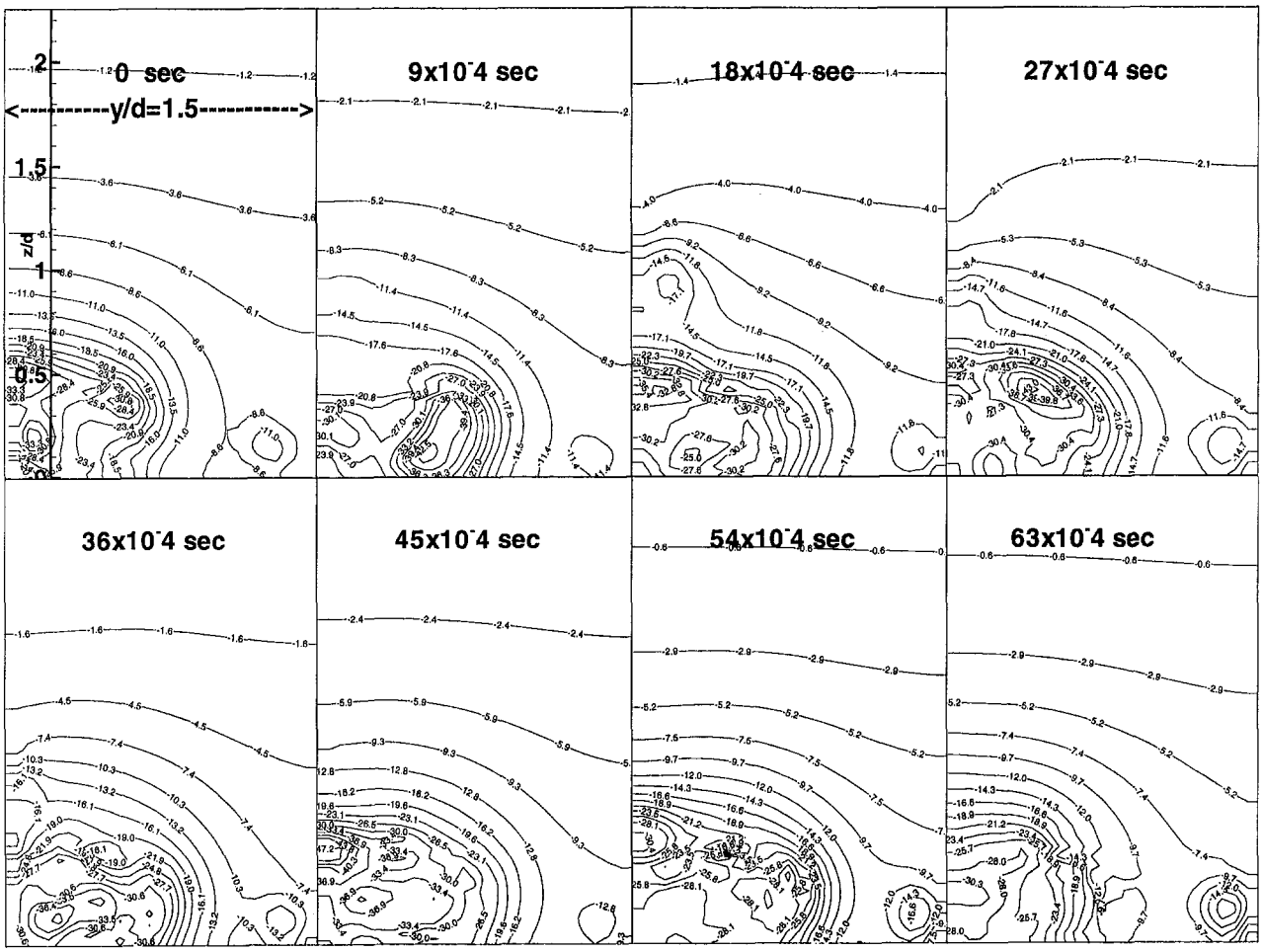

Fig. 9 Pressure in the y–z plane, at $x/d = 0.979$

results are presented for successive times. In picking the time increments and the time interval over which the data are to be presented, a sampling of a few locations downstream of the jet was made, and a Fast Fourier Transform of the time trace of the velocity variables at that location was performed. A range of frequencies was obtained, representing different scales in the flow. The dominant mode was then determined, and the time period of this mode was used to make a decision on the time interval over which the data are to be presented. A representative increment in time of 9×10^{-4} or 18×10^{-4} seconds over this interval was then picked to illustrate the temporal evolution.

Figures 5, 6, and 7 show the x vorticity together with the superimposed velocity vectors in three streamwise locations, corresponding to $x/d = 0$ (jet center plane), $x/d = 0.979$ (near-wake region), and $x/d = 4$ (far-wake region). Figures 8, 9, and 10 show the corresponding pressure contours.

At the low blowing ratio value of 0.5, the jet begins to bend immediately. Therefore, the CVP is established early in the jet development. At $x/d = 0$, the velocity vectors indicate the stretching of the core jet by the crossflow and by the bound vorticity in the jet-exit profile. Early evidence of the development of the CVP can be seen in the region directly above the jet associated with a pocket of negative vorticity. The negative vorticity exiting the transverse edge of the jet hole is seen to be primarily transported in the transverse direction directly below the horseshoe vortex system, and serves to strengthen the horseshoe vortex. This was also observed at the $z/d = 0$ plane in Fig. 3, and as noted earlier is associated with the pressure defect established between the high-pressure region in the middle of the hole (associated with the stagnation region created when the jet encounters the crossflow) and the lower-pressure regions in the crossflow. The cross-stream pressure profile in Fig. 8 shows that there are two regions of low pressure in the transverse direction, one associated with the jet-exit-flow boundary layer, and the other associated with the horseshoe vortex. In between there is a region of adverse pressure gradient, but no instantaneous flow reversals were noted. With time, the low-pressure region associated with the horseshoe vortex (Fig. 8) and the eye of the vortex (Fig. 5) meanders somewhat in the transverse direction, first moving toward the jet center plane and then away from it. As seen in Fig. 3 and also in Fig. 5, the horseshoe vortex is a dominant feature in this flow, and at certain time instances, the positive vorticity associated with this system extends all the way to the transverse edge of the jet.

At $x/d = 0.979$ (Figs. 6 and 9), corresponding to the near-wake region, the CVP (negative vorticity) is more well defined. However, as noted in Fig. 3, it is convoluted with patches of positive vorticity, which are a consequence of the entrainment of the crossflow boundary layer and fluid from the horseshoe vortex system into the wake. This is clearly evident at time instances marked as 27×10^{-4}, 36×10^{-4}, 45×10^{-4}, and 54×10^{-4} seconds. The flow is entrained into the wake along a thin stream adjoining the plate surface, and separates near the jet center plane, forming a recirculation or wall vortex with positive vorticity just below the CVP. As can be seen clearly at 27×10^{-4}, 36×10^{-4}, and 45×10^{-4} seconds, this wall vortex is entrained by the upflow into the CVP. As the z vorticity contours will show later, the entrained wall vortices (with x

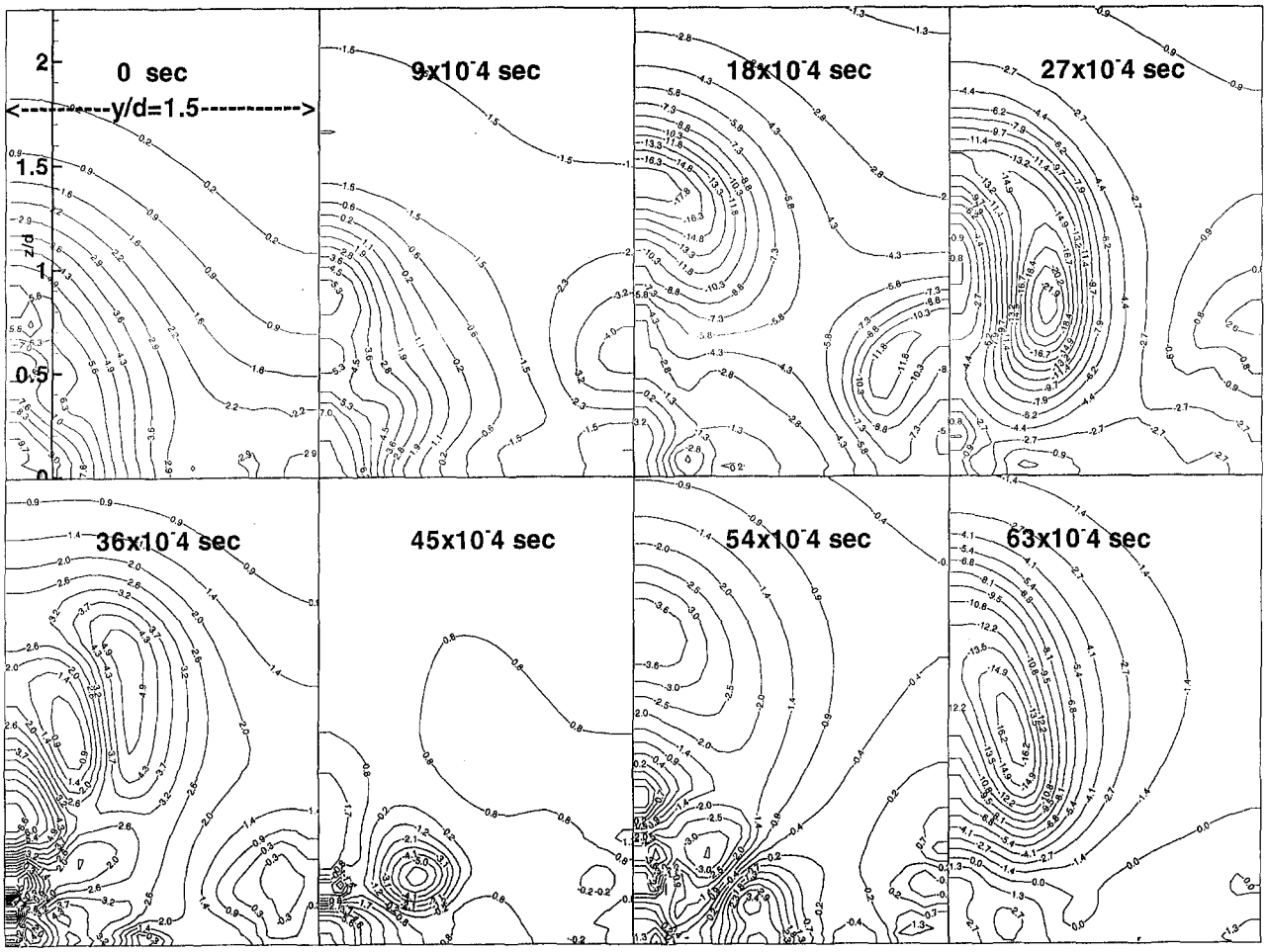

Fig. 10 Pressure in the y–z plane, at $x/d = 4.047$

vorticity) are reoriented into upright wake vortices (with z vorticity). Note that unlike the high-blowing-ratio (in the range of 2 to 10) cases considered by Fric and Roshko (1994) and Kelso et al. (1996), at the low blowing ratio considered in this study, the CVP is close to the surface, and therefore the upflow entrainment of the wall vortices significantly convolutes the CVP. Another important observation is that at certain time instances, part of the fluid in the horseshoe vortex system is entrained along with the crossflow into the wake. This can be even more clearly observed at $x/d = 4$.

The CVP can also be observed to go through a sequence of being pinched off at the top, resulting in a separate region of negative vorticity above the CVP (see the contours at 18×10^{-4} seconds), and then reconnecting later (see the contours at $t = 45 \times 10^{-4}$). In examining the pressure contours (Fig. 8), this pinch off is associated with the development of a local pressure excursion near the top of the CVP. In the vicinity of the jet center plane, adverse pressure gradients in the transverse direction can clearly be seen, which as discussed above, leads to the development of the wall vortex. Associated with this, favorable pressure gradients can be seen in the vertical direction leading to the upward entrainment of the wall vortex.

At $x/d = 4$, the CVP has grown in size considerably, and its various dynamic features are illustrated in Fig. 7. At $t = 0$, the CVP has two regions of concentrated vorticity, and there is significant entrainment of the crossflow into the region directly below the CVP leading to a wall vortex. However, over more than half the transverse direction along the wall, there is an adverse pressure gradient (Fig. 10) leading to a thin, elongated wall vortex, much unlike that seen in the near wake region. Further, the entrainment and reorientation of the wall vortex are much more complex. At certain time instances (18×10^{-4} in Fig. 7), the crossflow is directly entrained into the midregions of the CVP (at z/d nearly equal to 0.5) made possible by mildly favorable pressure gradients in the transverse direction (see pressure contour at $t = 18 \times 10^{-4}$) at this level. However, close to the jet center plane, the pressure gradient becomes adverse, leading to the formation of a small midspan vortex with positive vorticity. This midspan vortex splits the primary CVP into two halves. As the midspan vortex is entrained upward, the two halves of the CVP reconnect behind it. At 36×10^{-4} seconds, the pressure contours show a strong pressure deficit associated with the positive vorticity vortex, with high-pressure regions on either side. A fairly large positive vorticity eddy is therefore obtained, centered near $z/d = 1$, and appears nestled between the two legs of the CVP (each driven by the high-pressure region on either side of the pressure deficit). The right lobe of the CVP then diminishes (as does the high-pressure region driving it), the positive vorticity eddy (and the associated low-pressure region) descends to take its place connecting with the wall vortex, and the left lobe of the CVP is accentuated. The CVP continues to develop around the positive vorticity eddy as it is entrained upwards. At 63×10^{-4} seconds, pieces of the positive vorticity eddy are entrained into the CVP, which takes on an inverted "E" shape.

The horseshoe vortex can be seen to be lifted off the surface, and at specific time instances (see 27×10^{-4} seconds) develops a tail that connects with the wall vortex along the jet center plane.

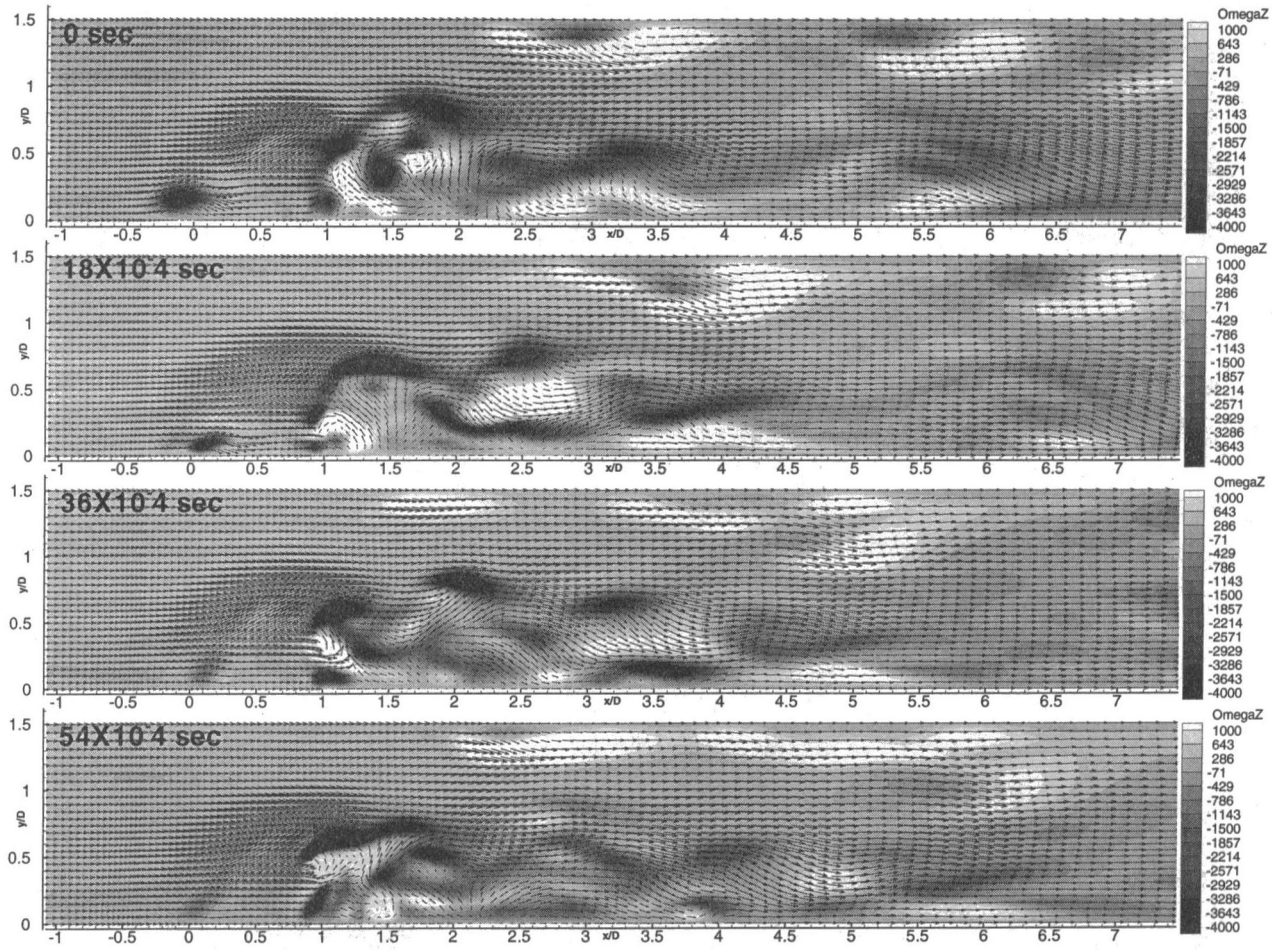

Fig. 11 The z component of vorticity in the x–y plane at $z/d = 0.42$

In this instance the wall vortex is fed both by the crossflow boundary layer and by the horseshoe vortex. The eye of the horseshoe vortex bobs up and down along the right symmetry plane, and as it moves up the crossflow is entrained beneath it. However, in a manner similar to that along the jet center plane, the entrained fluid encounters an adverse pressure gradient, and a wall vortex is also obtained directly beneath the horseshoe vortex. To the authors' knowledge, observations of a wall vortex on the horseshoe side have not been reported in the literature.

Figure 11 shows the z vorticity in an x–y plane at $z/d = 0.42$. Also shown are superimposed velocity vectors. The footprint of the horseshoe vortex near its evolution upstream of the exit-hole center and in the far-wake regions can be quite clearly seen. Near the stagnation region associated with the evolution of the vortex, pressure decreases away from the jet center plane, and leads to negative vorticity of the horseshoe vortex. Near the opposite transverse boundary, pressure decreases as one moves away from that boundary, leading to a positive z vorticity of the horseshoe vortex. In the wake, both positive and negative vorticity eddies are observed, with the negative vorticities associated with the upright vortices arising either from a reorientation of the wall vortices or from a reorientation of the midspan vortices. Three possible reasons for the positive vorticity eddies were mentioned earlier. It should be noted that contiguous pockets of negative upright vortices are possible, as shown at $t = 36 \times 10^{-4}$. A careful examination of frame-by-frame evolution indicates that vortex stretching and breakup, and compression and coalescence are occurring at several time instances. The velocity vectors show not only significant entrainment of the crossflow into the wake region, but also stagnation regions. These are associated with the reorientation of the wall or midspan vortex into an upright vortex. Note also the existence of neighboring eddies rotating in the same direction.

Figure 12 shows the y-vorticity contours in an x–z plane corresponding to $y/d = 0.45$. The positive vorticity along the downstream edge of the coolant hole, and the negative vorticity along the upstream edge, are evident, and are associated with the jet-hole exit velocity profiles. Clear evidence of shear-layer vortices can be seen on the leeward side of the jet. These vortices are shed from both sides of the jet, but convect downstream at different velocities, with the windward vortices (negative vorticity) accelerated by the high-speed crossflow. Vortex pairs of positive vorticity and negative vorticity can be seen at $t = 0$. One vortex is along the wall, and the other is along the underside of the deflected jet. These vortex pairs can clearly be seen to undergo pairing events. For example, at $t = 0$, between x/d of 1.25 and 2.5, four vortex pairs can be distinctly observed. These four pairs can be clearly observed to have paired at $t = 18 \times 10^{-4}$, and have convected downstream to the region between x/d of 1.25 and 2.75. With time, these vortices are stretched and grow downstream. It is anticipated that some reorientation of these vortices in the streamwise direction is achieved by the crossflow. This reorientation, depending on the initial vorticity direction, can either enhance or detract from the CVP.

The superimposed velocity vectors clearly show the positive vorticity near the wall directing the fluid downward in a sweep-type motion, and the negative vorticity near the wall ejecting

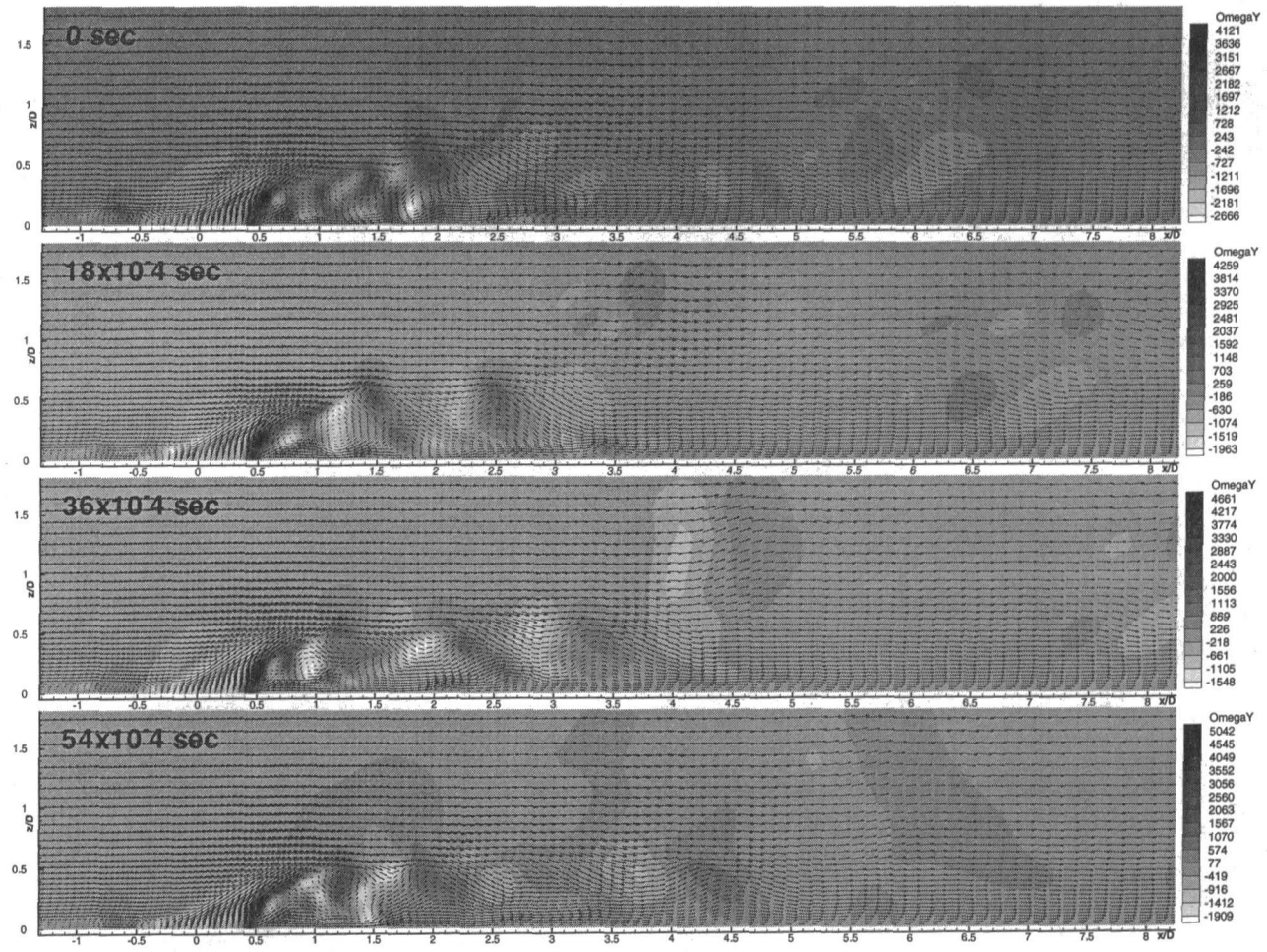

Fig. 12 The y component of vorticity and velocity vectors in the x–z plane at $y/d = 0.45$

the fluid upward from the surface. Thus the wall is subject to alternate sweep and ejection events, which can lead to high levels of wall shear.

Comparison With Experiments. The time averaged x and y components of velocity at various locations are shown in Fig. 13. It is compared to the experimental data of Ajersch et al. (1997). Agreement with Ajersch et al. (1997) is quite good in the near-jet region but deteriorates somewhat as one moves downstream away from the jet. One possible reason for this is the grid spacing, which becomes progressively coarser as one moves downstream away from the jet and the increasing importance of the small scales farther downstream. At $x/d = 0.979$, flow separation is still present in the predicted profiles, and a distinct wake-type profile is observed. Note that at $x/d = 2.977$, the predicted profile accurately reproduces the measured wake-defect region.

Concluding Remarks

A time and space-accurate computational study is performed to understand the dynamics of the large-scale structures in the near field of a film cooling jet injected normal to a crossflow. The following are the major conclusions of this study:

1 The near field is characterized by several fairly dominant dynamic large-scale structures. These include the CVP, shear-layer vortices, horseshoe vortices, wall vortices, and wake vortices.

2 The CVP appears to be a dynamically convoluting structure with patches of positive and negative vorticity. The convolution appears to stem from the low blowing ratio, due to which the CVP is constrained to the near-wall region. The crossflow is entrained periodically into the CVP and leads to the convolution.

3 The crossflow and flow from the horseshoe vortex system are both observed to be entrained into the wake region. The entrained near-wall crossflow-boundary layer experiences an adverse pressure gradient near the jet symmetry plane and separates to form a wall vortex. This wall vortex is then stretched and reoriented into the upright wake vortices.

4 Direct entrainment of the midspan crossflow into the wake region is also observed for $x/d = 4$. This midspan vortex (with x vorticity) dynamically interacts with the CVP, the wall vortices, and also the horseshoe vortex system. The CVP is seen to undergo a process of breakup and reconnection.

5 The horseshoe vortex appears to be a dominant feature for a normal jet in crossflow. Entrainment of the horseshoe vortex into the wake region is clearly evident.

6 The wake vortices (z vorticity) are an outcome of the reorientation of the wall vortices and the midspan vortices by the wake upflow.

7 The shear layer vortices (y vorticity) appear primarily on the leeward side of the jet. This is attributed to the low blowing ratio case being studied here. The crossflow appears to strip the y vorticity from the windward and leeward sides for the jet into the wake region. Vortex pairs are clearly observed to undergo pairing and stretching events.

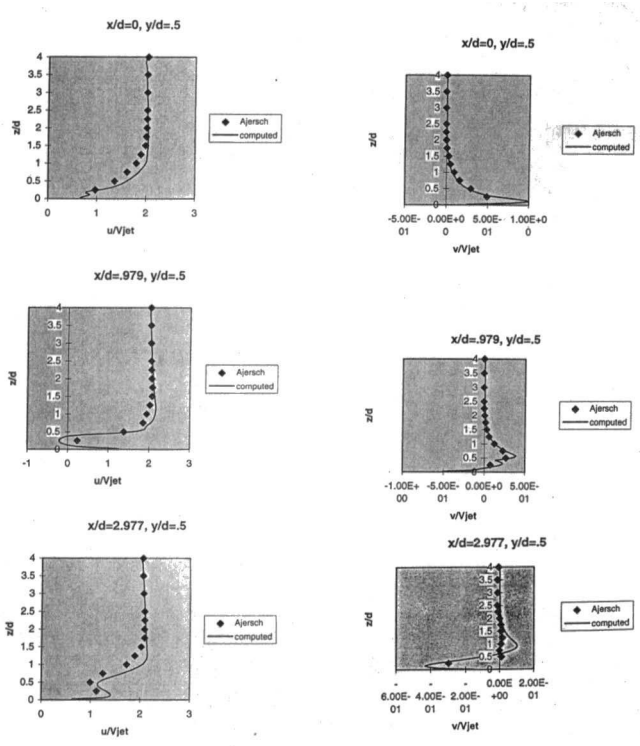

Fig. 13 Time-averaged *x* and *y* components of velocity

8 Comparisons of the current predictions with the mean velocity measurements are in good agreement.

Acknowledgments

This work was supported by a grant from the Turbomachinery Physics Group at NASA-Lewis. Dr. Chi Wang and Dr. Ray Gaugler served as the technical monitors for the project. Their support is gratefully acknowledged. Computing support for the project was received from NASA-Ames Computing Center and also through NASA-Lewis. This support is also acknowledged. The assistance of Dr. Albert Harvey III and Raymond Jones at Dow Chemical Company is gratefully acknowledged.

References

Ajersch, P., Zhou, J. M., Ketler, S., Salcudean, M., and Gartshore, I. S., 1997, "Multiple Jets in a Crossflow: Detailed Measurements and Numerical Simulations," ASME JOURNAL OF TURBOMACHINERY, Vol. 119, pp. 330–342.

Andreopoulos, J., 1985, "On the structure of jets in a crossflow," *J. Fluid Mech.*, Vol. 157, pp. 163–197.

Andreopoulos, J., and Rodi, W., 1984, "Experimental investigation of jets in a crossflow," *J. Fluid Mech.*, Vol. 138, pp. 93–127.

Chorin, A. J., 1968, "Numerical Solution of the Navier–Stokes Equations," *Math. Comput.*, Vol. 22, pp. 745–762.

Crabb, D., Durao, D. F. G., and Whitelaw, J. H., 1981, "A round jet normal to a crossflow," ASME *Journal of Fluids Engineering*, Vol. 103, pp. 142–153.

Demuren, A. O., 1993, "Characteristics of three-dimensional jets in crossflow," *Int. J. Engng. Sci.*, Vol. 31, No. 6, pp. 899–913.

Fornberg, B. G., 1988, "Generation of finite difference formulas on arbitrarily spaced grids," *Mathematics of Computations*, Vol. 31, No. 184, pp. 699–706.

Foss, J., 1980, "Interaction region phenomena for the jet in a crossflow problem," Rep. SFB 80/E/161, Univ. Karlsruhe, Germany.

Fric, T. F., and Roshko, A., 1994, "Vortical structure in the wake of a transverse jet," *J. Fluid Mech.*, Vol. 279, pp. 1–47.

Garg, V. K., and Gaugler, R. E., 1994, "Prediction of film cooling on gas turbine airfoils," ASME Paper No. 94-GT-16.

Garg, V. K., and Gaugler, R. E., 1997, "Effect of velocity and temperature distribution at the hole exit on film cooling of turbine blades," ASME JOURNAL OF TURBOMACHINERY, Vol. 119, pp. 343–351.

Ho, C. M., and Huerre, P., 1984, "Perturbed Shear Layers," *Ann. Rev. Fluid Mech.*, Vol. 16, pp. 365–424.

Hyams, D. G., and Leylek, J. H., 1997, "A detailed analysis of film-cooling physics: Part III—streamwise injection with shaped holes," ASME Paper No. 97-GT-271.

Jones, W. P., and Wille, M., 1996, "Large eddy simulation of a round jet in crossflow," *Engineering Turbulence Modeling and Experiments 3*, Rodi, W., and Bergeles, G., eds., pp. 199–209.

Kamotani, Y., and Gerber, I., 1972, "Experiments on a turbulent jet in crossflow," *J. Fluid Mech.*, Vol. 306, pp. 111–114.

Kelso, R. M., Lim, T. T., and Perry, A. E., 1996, "An Experimental Study of Round Jets in Cross-Flow," *J. Fluid Mech.*, Vol. 306, pp. 111–144.

Kim, S. W., and Benson, T. J., 1992, "Calculation of a circular jet in crossflow with a multiple-time-scale turbulence model," *Int. J. Comp. Phys.*, Vol. 59, p. 308.

McGovern, T. K., and Leylek, J. H., 1997, "A detailed analysis of film-cooling physics, Part II: compound-angle injection with cylindrical holes," ASME Paper No. 97-GT-270.

Moussa Z. M., Trischka, J. W., and Eskinazi, S., 1977, "The near field in the mixing of a round jet with a cross-stream," *J. Fluid Mech.*, Vol. 80, pp. 49–80.

Patankar, S. V., Basu, D. K., and Alpay, S. A., 1977, "Prediction of the three-dimensional velocity field of a deflected turbulent jet," *Trans. SME I: J. Fluids Engng. 99*, pp. 758–762.

Rogers, S., and Kwak, D., 1991, "Steady and Unsteady Solutions of the Incompressible Navier–Stokes Equations," *AIAA Journal*, Vol. 29, No. 4, pp. 603–610.

Singer, B. A., 1994, "Metamorphosis of a hairpin vortex into a young turbulent spot," *Phys. Fluids*, Vol. 6, No. 11, pp. 3724–3736.

Sykes, R. I., Lewellen, W. S., and Parker, S. F., 1986, "On the vorticity dynamics of a turbulent jet in a crossflow," *J. Fluid Mech.*, Vol. 80, pp. 49–80.

Walters, D. K., and Leylek, J. H., 1997, "A detailed analysis of film-cooling physics: Part I—streamwise injection with cylindrical holes," ASME Paper No. 97-GT-269.

Yuan, L. L., and Street, R. L., 1999, "Large Eddy Simulation of a Round Jet in Crossflow," *J. Fluid Mech.*, Vol. 379, pp. 71–104.

A Theory for Predicting the Turbulent-Spot Production Rate

R. E. Mayle
Professor Emeritus of Mechanical Engineering,
Rensselaer Polytechnic Institute,
Troy, NY 12180
Fellow ASME

A theory is presented for predicting the production rate of turbulent spots. The theory, based on that by Mayle–Schulz for bypass transition, leads to a new correlation for the spot production rate in boundary layer flows with a zero pressure gradient. The correlation, which agrees reasonably well with data, clearly shows the effects of both free-stream turbulence level and length scale. In addition, the theory provides an estimate for the lowest level of free-stream turbulence causing bypass transition.

Introduction

When designing airfoils for gas turbine engines, the designer is usually faced with a decision of how to calculate laminar-to-turbulent transitional flow. Since the aerodynamic loss of these airfoils, their off-design performance, and their heat load in the hot section depend critically on transition, this decision must be made carefully.

Presently, the flow around gas turbine airfoils is usually computed using the well-known k–ε equations of motion modified according to each manufacturer's experience. Some of these computation methods are rather sophisticated and use low-Reynolds-number "correlations" to calculate transition. As shown by Savill (1991) and later by Sieger et al. (1993), however, these methods are somewhat unreliable when used to "predict" new data. Briefly, the problems with them are that: (*a*) the low-Reynolds-number correlations can't account for all of the effects, and (*b*) none properly account for the inherent unsteady, three-dimensional nature of transitional flow. Accordingly, these methods should now be considered "old."

A "new" method, which actually dates back to 1951 when Emmons discovered the turbulent spots now named after him, was described more recently by the author (Mayle, 1991). Briefly, the method requires one to: (*a*) calculate a separate set of flow-conditioned, time-averaged equations for both the laminar and turbulent portions of the flow, and (*b*) combine the results at every location according to the probability that the flow is either laminar or turbulent. In the past, this method simply involved combining laminar and turbulent solutions for the various mean-flow quantities (such as skin friction) according to Emmons' superposition model. Now, two sets of flow-conditioned k–ε equations are being used that not only account for both the three-dimensional nature of transition, but also the large eddy interaction[1] between the laminar and turbulent portions. The success of this approach has recently been shown by Steelant and Dick (1994, 1996). It depends, however, on predicting the flow's probability distribution.

The probability that the flow passing over any portion of a surface is turbulent was first introduced by Emmons (1951). It is now called "intermittency." When the intermittency is zero, the flow is completely laminar, and when it is one the flow is completely turbulent. For intermediate values, the flow at any position is part of the time laminar and the rest of the time turbulent, i.e., transitional. Currently, the accepted expression for intermittency in unaccelerating, two-dimensional flow is

$$\gamma(x) = 1 - \exp\{-\hat{n}\sigma\,(\mathrm{Re}_x - \mathrm{Re}_{xt})^2\}; \quad \mathrm{Re}_x \geq \mathrm{Re}_{xt} \qquad (1)$$

where Re_x is the Reynolds number based on the streamwise distance x, Re_{xt} is the Reynolds number where turbulent spots in the laminar boundary layer first appear and transition begins, $\hat{n}$ is a dimensionless turbulent spot production rate (the subject of this paper), and σ is Emmons' spot propagation parameter. Measurements by Schubauer and Klebanoff (1955) in a flow with a zero pressure gradient indicate that σ, which in general depends on the shape and velocity of the spot, is constant and equal to 0.27. Therefore, once Re_{xt} and $\hat{n}$ are known,[2] the intermittency distribution can be calculated, and transition can be predicted. The intermittency distribution for $\mathrm{Re}_{xt} = 9(10)^4$ and $\hat{n}\sigma = 10^{-10}$ is shown in Fig. 1. This distribution corresponds roughly to that for bypass transition with a free-stream turbulence level of 3 percent. As the turbulence level increases, Re_{xt} decreases, $\hat{n}\sigma$ increases, and the transition length Re_{LT} decreases.

Presently, Re_{xt} and $\hat{n}$ are obtained from correlations that generally relate them to the free-stream turbulence level, pressure gradient, and sometimes Mach number. One example from several for the onset of transition is shown in Fig. 2. This correlation (obtained by the author, 1991) is good for zero-pressure-gradient flows and, rather than Re_{xt}, relates the momentum thickness Reynolds number at onset to the turbulence level. For zero-pressure-gradient flows, Blasius' solution (Schlichting, 1979) provides $\mathrm{Re}_{xt} = 2.27\,\mathrm{Re}_{\theta 1}^2$. Recently, a new theory for pretransitional flow was proposed by Dr.-Ing. Schulz and myself (Mayle and Schulz, 1997) which is not only the basis for the present work, but may also replace correlations of the type shown in Fig. 2.

Several correlations for the production rate are also available. While Emmons and Bryson (1951) made the earliest attempt at correlating the spot production rate with free-stream turbulence, it wasn't until Narasimha (1957) formulated Eq. (1) that Dhawan and Narasimha (1958) provided a more appropriate one. This was later revised by Narasimha himself in 1985. Twenty years after Emmons' work, Chen and Thyson (1971) obtained a correlation for compressible flow and later, Walker and Gostelow (1990) presented one using Walker's (1987) result based on laminar instability theory. Last of all, the author (1991) presented another based only on intermittency measurements.

These correlations are given in Table 1. For the purpose of comparison, all are presented in terms of the free-stream turbulence level. To accomplish this, those that were originally formulated in terms of the momentum thickness Reynolds number at onset were reformulated using the correlation shown in Fig. 2, and those originally formulated in terms of the transition length (see Fig. 1) were reformulated in terms of the spot production rate using

$$\hat{n}\sigma = 4.61/\mathrm{Re}_{LT}^2 \qquad (2)$$

[1] The implications of this interaction on the equations for the mean-flow quantities have previously been discussed by Paxson (1989) and myself (1991), and for the turbulence quantities by Steelant and Dick (1994).

[2] There are some other considerations, such as the spot-formation distribution function and spot growth rate in flows with pressure gradients (Narasimha, 1985), but Re_{xt} and $\hat{n}$ are the primary independent parameters for zero pressure gradient flows.

Contributed by the International Gas Turbine Institute and presented at the 43rd International Gas Turbine and Aeroengine Congress and Exhibition, Stockholm, Sweden, June 2–5, 1998. Manuscript received by the International Gas Turbine Institute February 1998. Paper No. 98-GT-256. Associate Technical Editor: R. E. Kielb.

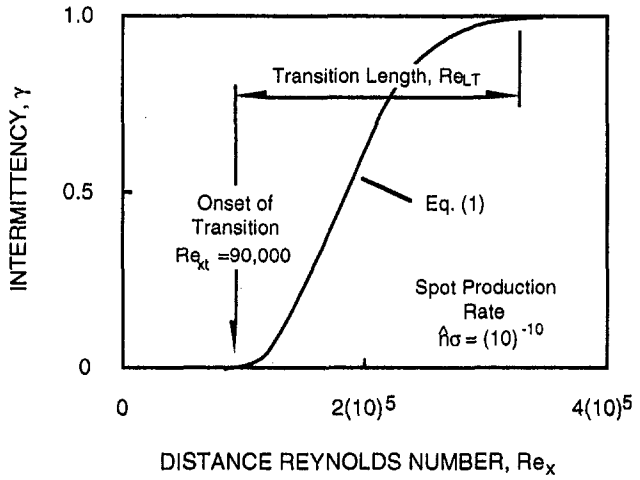

Fig. 1 Intermittency distribution for bypass transition with a 3 percent free-stream turbulence level

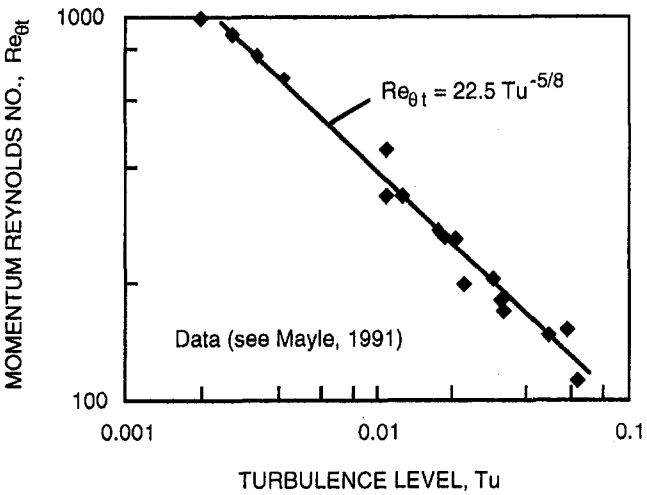

Fig. 2 Onset of transition for zero pressure gradient flows

This relation is acquired by setting $Re_x - Re_{xt} = Re_{LT}$ in Eq. (1) assuming transition ends when $\gamma = 0.99$. Since both the correlation in Fig. 2 and the relation in Eq. (2) are for zero-pressure-gradient, low-speed flow, the correlations as presented in Table 1 are only good for this flow. The correlations are plotted and compared with data in Fig. 3. Three of them are virtually the same, while all have about the same slope and could be made to more or less fit the data for $Tu \geq 0.01$ by simply changing their coefficients. Since the author's correlation was based on these data, it should agree.

The aim of this paper is to present a theory for the production rate of turbulent spots in flows undergoing bypass transition. As mentioned above it is not the first theory, but in contrast to that presented by Walker (1987), which is based on Tollmien–Schlichting's theory for "natural" transition, the present is based on that by Mayle and Schulz (1997) for "bypass" transition. As we will see, the theory not only provides a new correlation for the turbulent-spot production rate, but implicitly accounts for the separate influences of free-stream-turbulence level and length scale.

The paper is divided into four sections. First, we will consider the concept of intermittency and formally introduce the spot production rate. Second, we will very briefly review Mayle and Schulz' theory and introduce the latest results of Mayle et al. (1998). Third, we will develop a new spot production theory and obtain a new correlation for the production rate. Finally, we will conclude and offer some suggestions for further work.

Intermittency and Spot Production

A statistical theory for transitional flow was first developed by Emmons (1951), who showed that the probability of finding a turbulent spot passing over the position (x, z) on the surface is

$$\gamma(x, z, t) = 1 - \exp\left\{ \int\int\int_{R^*} g(x^*, z^*, t^*) dx^* dz^* dt^* \right\} \quad (3)$$

where g is the production rate of turbulent spots at the position (x^*, z^*) at time t^*, and R^* is the volume defined by all points that are sources of turbulent spots that will pass over the position (x, z) at time t. Assuming the production rate is constant, Emmons integrated Eq. (3) and obtained an expression for γ that is not too different from that presently accepted.

The currently accepted expression was obtained by Narasimha (1957) and Dhawan and Narasimha (1958) who compared their intermittency measurements with the expression obtained from Eq. (3) by substituting a Gaussian distribution for g. They concluded that the production rate for two-dimensional flow is best represented by a Gaussian distribution with a zero standard deviation, namely,

$$g(x^*, z^*, t^*) = n\delta(x^* - x_t)$$

where n is the turbulent spot production rate per unit distance in the z direction, $\delta(x)$ is the Dirac delta function of x, and x_t is the

Nomenclature

f = circular frequency, Hz
f_{eff} = effective frequency of free-stream turbulence, Hz
k = kinetic energy of laminar fluctuations, m^2/s^2
l_{eff} = effective wavelength of free-stream turbulence, m
n = production rate of turbulent spots, $m^{-1}\ s^{-1}$
Re = Reynolds number; $Re_x = Ux/\nu$
Re_λ = turbulence Reynolds number = $\sqrt{\overline{u'^2_{fs}}}\lambda/\nu$
t = time, s
Tu = free-stream turbulence level = $\sqrt{\overline{u'^2_{fs}}}/U$
u = velocity component in the x-direction, m/s
U = free-stream velocity, m/s
v = velocity component in the y direction, m/s
x = coordinate along the surface in the free-stream direction, m
y = coordinate normal to the surface, m
z = coordinate along the surface normal to the flow, m
δ = boundary layer thickness, m
ε = dissipation of turbulent kinetic energy, m^2/s^3
ε_ν = dissipation of laminar kinetic energy, m^2/s^3
η = Kolmogorov's length scale, m
θ = momentum thickness, m
λ = Taylor's microscale of turbulence, m
ν = kinematic viscosity, m^2/s
ρ = density, kg/m^3
υ = Kolmogorov's velocity scale, m/s

Subscripts

fs = free stream
t = evaluated at the onset of transition

Symbols

$\bar{q}$ = time average of quantity q
q' = fluctuating component of q, $\overline{q'} = 0$

Table 1 Spot production rate correlations (zero-pressure-gradient flow)

INVESTIGATOR(S)	CORRELATION
Dhawan & Narasimha (1958)	$\hat{n}\sigma = 2.11(10)^{-7} Tu^2$
Chen & Thyson (1971)	$\hat{n}\sigma = 1.02(10)^{-7} Tu^{1.68}$
Narasimha (1985)	$\hat{n}\sigma = 1.32(10)^{-7} Tu^{1.88}$
Walker & Gostelow (1990)	$\hat{n}\sigma = 1.16(10)^{-7} Tu^{1.88}$
Mayle (1991)	$\hat{n}\sigma = 4.74(10)^{-8} Tu^{1.75}$

Table 2 Effective frequencies and length scales

TEST CASE	$f_{eff}\nu/U^2$	f_{eff}, [Hz]	l_{eff}/δ_{xt}
Rolls-Royce (1%)	$1.7(10)^{-4}$	4350	0.9
Westin et al. (1.5%)	$2.5(10)^{-4}$	1070	1.5
Dyban & Epik (2%)	$3.8(10)^{-4}$	2530	1.0
Rolls-Royce (3%)	$4.7(10)^{-4}$	850	1.6
Rolls-Royce (6%)	$5.6(10)^{-4}$	3440	1.7
Tollmien-Schlichting	$0.5(10)^{-4}$	—	6

location where turbulent spots are produced, i.e., the beginning of transition. Substituting this into Eq. (3) and considering only flows with a zero pressure gradient, one obtains

$$\gamma(x) = 1 - \exp\left\{ -\frac{n\sigma}{U}(x - x_t)^2 \right\}; \quad x \geq x_t$$

where U is the free-stream velocity and σ, as mentioned before, is Emmons' spot propagation parameter. This may be arranged into the dimensionless form given in Eq. (1), namely,

$$\gamma = 1 - \exp\{-\hat{n}\sigma\,(\mathrm{Re}_x - \mathrm{Re}_{xt})^2\}; \quad \mathrm{Re}_x \geq \mathrm{Re}_{xt}$$

by introducing a dimensionless spot production rate

$$\hat{n} = n\nu^2/U^3 \tag{4}$$

where ν is the kinematic viscosity.

If it isn't already clear, n is a kinematic quantity—the number of spots produced per unit time per unit distance in the z direction. In other words, n is the frequency of spot production per unit span. Since it is likely that this frequency is related to the frequency within the free-stream turbulence which is amplified in the laminar boundary layer, we need to review the results of that theory briefly.

Pretransitional Flow Theory

A theory for unsteady flow in a laminar boundary layer preceding transition was recently presented by Mayle and Schulz (1997). As they showed, the appropriate equation for the kinetic energy of pretransitional fluctuations, called the laminar kinetic energy (LKE) equation, is

$$\bar{u}\frac{\partial k}{\partial x} + \bar{v}\frac{\partial k}{\partial y} = \overline{u'\frac{\partial u'_{fs}}{\partial t}} + \nu\frac{\partial^2 k}{\partial y^2} - \varepsilon_\nu \tag{5}$$

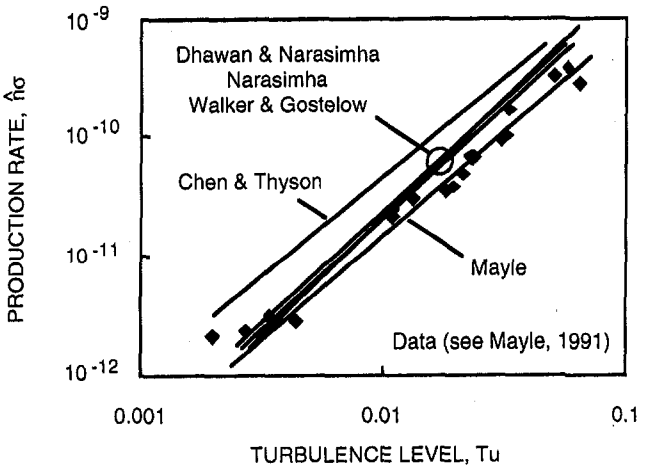

Fig. 3 Spot production rate for zero pressure gradient flows

where k is the kinetic energy, u'_{fs} is the free-stream velocity fluctuation, and ε_ν is the dissipation of laminar kinetic energy. The rest of the notation is standard, including the overbars, which refer to time-averaged quantities. The terms on the right-hand side correspond to the production, diffusion, and dissipation of LKE, respectively. The production term, shown as the time average of the product of the velocity fluctuations in the boundary layer and the temporal derivative of those in the free stream, represents the work done on the fluctuations by the imposed fluctuating pressure forces.

From dimensional considerations guided by the form of the production term, Mayle and Schulz reasoned that the production of LKE must be proportional to $f_{\mathrm{eff}}\sqrt{u'^2_{\mathrm{eff}}}\sqrt{k}$, where, according to the ideas of Dullenkopf and Mayle (1995), f_{eff} is the frequency of free-stream turbulence most effective in producing the fluctuations and $\sqrt{u'_{eff}}$ is the turbulence intensity at that frequency. Consequently, the maximum production of k occurs for the frequency of free-stream turbulence that maximizes $f_{\mathrm{eff}}\sqrt{u'^2_{\mathrm{eff}}}$. Reasoning that this frequency is near the dissipative range of the turbulence spectrum, Mayle and Schulz were able to obtained estimates for f_{eff} and $\sqrt{u'^2_{\mathrm{eff}}}$. Presently, however, it is better to use the more recent and accurate results of Mayle et al. (1998).

Using a unified expression for the spectrum of isotropic turbulence, Mayle et al. evaluated $f_{\mathrm{eff}}\sqrt{u'^2_{\mathrm{eff}}}$ for various turbulence Reynolds numbers and showed that its maximum always occurs near the frequency $f = 0.3U/2\pi\eta$, where η is Kolmogorov's length scale (Hinze, 1975) defined by

$$\eta = (\nu^3/\varepsilon)^{1/4} \tag{6}$$

Here, ε is the dissipation of free-stream turbulent kinetic energy, which should not be confused with the dissipation of laminar kinetic energy ε_ν in Eq. (5). Therefore, the frequency of turbulence most effective in producing pretransitional boundary-layer fluctuations is

$$f_{\mathrm{eff}} = 0.3U/2\pi\eta \tag{7}$$

Since Kolmogorov's length scale is normally considered "very small," and therefore f_{eff} expected to be "very high," it is enlightening to calculate some numbers.

Forming the dimensionless frequency $f_{\mathrm{eff}}\nu/U^2$, one can show from Eqs. (6) and (7) that $f_{\mathrm{eff}}\nu/U^2 = 0.048\upsilon/U$ where $\upsilon = (\varepsilon\nu)^{1/4}$ is Kolmogorov's velocity scale. Values of υ/U were calculated by Mayle and Schulz (1997) for the experiments of Dyban and Epik (1985) and Rolls-Royce (1993). In addition, a value for the data of Westin et al. (1994), which Mayle and Schulz were unaware of at the time, is also included. These were used to provide the first five values of $f_{\mathrm{eff}}\nu/U^2$ shown in Table 2. In all cases, they are shown for the position corresponding to the plate's leading edge. Downstream, they are somewhat smaller. In the test of Westin et al., for example, the value downstream where turbulent spots were first observed is about $1.9(10)^{-4}$. The value listed in the table for Tollmien–Schlichting is at the point of instability, which is always upstream of where natural transition begins.

Since forced pretransitional fluctuations begin to grow where $\mathrm{Re}_x \approx (f_{\mathrm{eff}}\nu/U^2)^{-1}$ and initially grow linearly (see Mayle and Schulz), and since Tollmien–Schlichting instabilities initially grow

exponentially, it is important that the smallest value of $f_{\text{eff}}\nu/U^2$ listed in Table 2 is that for Tollmien–Schlichting. Otherwise transition in each test would have occurred via the "natural" rather than "bypass" mode as observed. The actual values of the effective frequency are given in the second column of the table and, as seen, are neither outrageously high nor have any relation to the free-stream turbulence level.

An "effective" wavelength can be defined as $l_{\text{eff}} = U/f_{\text{eff}}$. Substituting Eq. (7) for f_{eff} yields

$$l_{\text{eff}} = 2\pi\eta/0.3 \approx 21\eta \tag{8}$$

which may also be expressed as $l_{\text{eff}} \approx 21\nu/v$. For zero-pressure-gradient flows, it is then not too difficult to show that the ratio of this to the boundary layer thickness at the onset of transition is given by $l_{\text{eff}}/\delta_t = 4.2[v/U\sqrt{\text{Re}_{xt}}]^{-1}$. Evaluating this ratio for each test in Table 2 provides the values given in its last column. That given for Tollmien–Schlichting, however, corresponds to the wavelength of the most amplified instability. Clearly, the wavelength of turbulence that affects the velocity fluctuations in pre-transitional flow is roughly equal to the boundary layer thickness at transition. One might also expect the "initial size" of a turbulent spot to be about the same.

A Spot Production Theory for Bypass Transition

Supposition and Theory. If f_{eff} is the turbulence frequency in the free stream that most affects the velocity fluctuations in a laminar boundary layer preceding the onset of transition, it seems reasonable to suppose, unless there is an unproportional transfer of energy to another frequency, that one spot can be produced every $1/f_{\text{eff}}$ seconds. If this is true, then the maximum number of spots that can form across the span of the flow during the time $1/f_{\text{eff}}$ is the span divided by the initial size of a turbulent spot. This would imply that the flow at the onset of transition during this time would be fully turbulent and, while certainly statistically possible, it is not probable. The most probable situation, of course, since the flow at onset is still nearly laminar, is that the number of spots formed across the span must be some very small fraction of this. Recalling that the production rate of turbulent spots is the number of spots formed at the onset of transition per unit time per unit span, it is reasonable to consider then that

$$n \propto \frac{(\text{span/spot size})}{(1/f_{\text{eff}}) \times (\text{span})} = \frac{f_{\text{eff}}}{(\text{spot size})}$$

For now, and without any data indicating otherwise, it is also reasonable to consider the initial spot size proportional to one of the important length scales of the flow. As we have already seen, η, or what amounts to the same, l_{eff}, is one and δ is another. Other length scales of the flow are ν/U, all of the integral boundary layer thicknesses, which for zero-pressure-gradient flow are all proportional to δ, and all the other turbulence length scales, both micro and macro, which as shown by Mayle et al. (1998) are all related by the turbulence Reynolds number to η. Data are presently available, however, only to determine whether η, δ, or ν/U is the important scale, and of these it was found that the boundary layer thickness at the onset of transition provided the best correlation.

Substituting the boundary layer thickness at onset into the above expression, Eq. (4) yields

$$\hat{n} \propto \left(\frac{f_{\text{eff}}\nu}{U^2}\right)\left(\frac{\nu}{U\delta_t}\right) \propto \left(\frac{f_{\text{eff}}\nu}{U^2}\right)\frac{1}{\text{Re}_{\theta t}}$$

where the proportionality between the boundary layer thicknesses δ_t and θ_t for zero-pressure-gradient flow has been used. Substituting Eq. (7), using Eq. (6), and introducing Kolmogorov's velocity scale $v = (\varepsilon\nu)^{1/4}$, one obtains

$$\hat{n} = C(v/U)\ \text{Re}_{\theta t}^{-1} \tag{9}$$

where C is a proportionality constant.

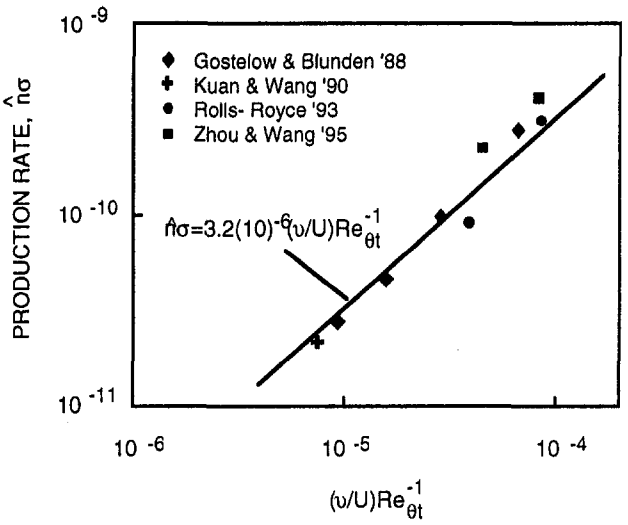

Fig. 4 A correlation for the spot production rate

A New Production Rate Correlation. In general, it would be best to compare Eq. (9) with data obtained from experiments in which both the streamwise distributions of intermittency and free-stream turbulence were measured. It would also be best if the turbulence was isotropic. Then the spot production rate, actually $\hat{n}\sigma$, and Re_{xt} could be determined by fitting[3] the intermittency data using Eq. (1), and for isotropic turbulence (see Hinze) v/U could be evaluated from

$$(v/U)^4 = \left(\frac{\varepsilon\nu}{U^4}\right) = -\frac{3}{2}\frac{d(Tu^2)}{d\ \text{Re}_x} \tag{10}$$

In addition, it would be good to have measurements of Re_θ to check those obtained from Blasius' solution.

Experiments providing at least an intermittency or free-stream turbulence distribution were conducted by Gostelow and Blunden (1989), Kuan and Wang (1990), Rolls-Royce (1993), and Zhou and Wang (1995). In each case, values of $\text{Re}_{\theta t}$ were either reported or previously determined (Mayle, 1991). A plot of $\hat{n}\sigma$ versus $(v/U)\text{Re}_{\theta t}^{-1}$ for these data is shown in Fig. 4. Since none of these investigators measured both intermittency and free-stream turbulence distributions, the data shown in the figure are "best" determined for only one of the coordinates. However, each of these investigators did report enough data to reasonably calculate the other. Since Gostelow and Blunden measured intermittency distributions, $\hat{n}\sigma$ was obtained by fitting Eq. (1). The spot production rate for the others was obtained using Eq. (2) by equating the transition length to 1.27 times the distance between the minimum and maximum values of either the skin friction or heat transfer distributions. The 1.27 value was determined previously by Narasimha (1985). The free-stream turbulence for the Rolls-Royce data is well documented by Roach (1987), and the values of v/U have already been used for Table 2. Since Kuan and Wang and Zhou and Wang measured the free-stream turbulence distributions, v/U was obtained using Eq. (10) for their data. For Zhou and Wang's tests, however, only data for Grids 1 and 3 were used, since the data for their other grids exhibited a significant departure from being isotropic. Gostelow and Blunden, on the other hand, only reported free-stream turbulence levels at the leading edge of their plate. It was found, however, that their turbulence data could be fitted by Baines and Pederson's (1951) correlation using a somewhat smaller coefficient than the one suggested. The values of v/U for Gostelow and Blunden's data were then obtained from Eq. (10) using this fit.

[3] The best method of doing this was first presented by Narasimha (1957). It is also presented in Appendix B of the author's 1991 review paper.

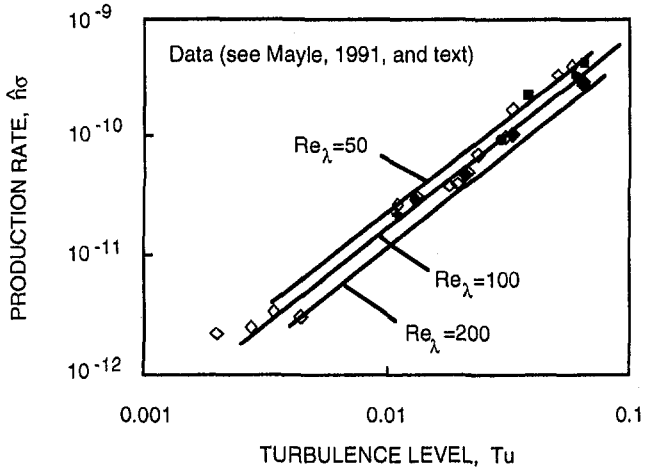

Fig. 5 A comparison with a previous correlation based on turbulence level

The theoretical result given in Eq. (9) is also shown in Fig. 4. Considering the difficulties in evaluating either $\hat{n}\sigma$ or $(\nu/U)\mathrm{Re}_{\theta t}^{-1}$, the agreement is quite reasonable although the data (which is for Tu greater than 1 percent) exhibit a slightly larger slope. The best fit to the data is given by

$$\hat{n}\sigma = 3.2(10)^{-6}(\nu/U)\ \mathrm{Re}_{\theta t}^{-1} \tag{11}$$

This expression can be rearranged in terms of the free-stream-turbulence level and length scale if one is willing to accept the correlation shown in Fig. 2. Using $\nu = (\varepsilon\nu)^{1/4}$ and $\varepsilon = 15\nu\overline{u'^2_{fs}}/\lambda^2$, where λ is Taylor's microscale of turbulence (Hinze, 1975), together with the correlation yields

$$\hat{n}\sigma = 2.8(10)^{-7}Tu^{1.62}/\sqrt{\mathrm{Re}_\lambda} \tag{12}$$

where $\mathrm{Re}_\lambda = \sqrt{\overline{u'^2_{fs}}}\lambda/\nu$ is the turbulence Reynolds number. This relation is plotted in Fig. 5 for Re_λ = 50, 100, and 200, which should cover the Reynolds number range for grid-generated turbulence. Except for the data of Rolls-Royce and Zhou and Wang, the data in this figure are the same as those given in Fig. 3. The data used to establish Eq. (11) have been highlighted with filled symbols. While this comparison shows that the data scatter could be an effect of turbulence length scale, it should be remembered that Eq. (12) depends on the correlation given in Fig. 2 and therefore should not be used until experimentally verified.

Conclusions

A theory has been presented for predicting the production rate of turbulent spots in bypass transition. The theory depends on the concept of an effective frequency previously developed in a series of papers by Dr.-Ings. Dullenkopf and Schulz and the author (Dullenkopf and Mayle, 1995; Mayle and Schulz, 1997; Mayle et al., 1998), by relating the frequency of spot formation to the effective frequency of the free-stream turbulence for fluctuations in pretransitional flow. In particular, we found

$$\hat{n}\sigma = C(\nu/U)\ \mathrm{Re}_{\theta t}^{-1}$$

which correlates spot production rate data quite well when $C = 3.2(10)^{-6}$. The weakest link in the theory has to do with the initial spot size. Without any data indicating otherwise, it was taken proportional to the boundary layer thickness at the onset of transition.

Although the theory was developed for zero-pressure-gradient flow, it should be compared to data for other pressure gradients. A quick look into Schlichting (1979) will show that the ratio of momentum thickness to boundary layer thickness is nearly constant for flows over a wide range of pressure gradients. Therefore, if the initial spot size is indeed proportional to the boundary layer thickness, the theory and the correlation given by Eq. (11) just might be more generally valid.

An interesting by-product of this work is that a lower limit for the turbulence level causing bypass transition can now be established. Referring back to the discussion of Table 2, if the Tollmien–Schlichting frequency is the lowest effective frequency for bypass transition, then bypass transition occurs when

$$(f_{\mathrm{eff}}\nu/U^2)_{\mathrm{Bypass}} \geq (f_{\mathrm{eff}}\nu/U^2)_{TS} = 5(10)^{-5}$$

where the numerical value has been taken from Table 2. Using Eqs. (6) and (7) and the relation $\varepsilon = 15\nu\overline{u'^2_{fs}}/\lambda^2$, this may be rewritten as

$$(Tu)_{\mathrm{Bypass}} \geq 5.3(10)^{-4}\sqrt{\mathrm{Re}_\lambda} \tag{13}$$

Considering Re_λ = 50, which is a reasonable value for the lower free-stream-turbulence levels generated by grids (see Fig. 5), Eq. (13) provides the very plausible value of $(Tu)_{\mathrm{Bypass}} \geq 0.4$ percent.

Acknowledgments

I wish to thank my colleagues Dr.-Ings. K. Dullenkopf and A. Schulz at the Institut für Thermische Strömungsmaschinen, Universität Karlsruhe, for all the good times we've had discussing turbulence and transition. These times and all the fun times spent talking about a lot of other things have led to this paper.

References

Baines, W. D., and Pederson, E. G., 1951, "An Investigation of Flow Through Screens," *Trans. ASME,* Vol. 73, pp. 467–480.

Chen, K. K., and Thyson, N. A., 1971, "Extension of Emmons' Spot Theory to Flows on Blunt Bodies," *AIAA Journal,* Vol. 9, pp. 821–825.

Dhawan, S., and Narasimha, R., 1958, "Some Properties of Boundary Layer Flow During Transition From Laminar to Turbulent Motion," *J. Fluid Mech.,* Vol. 3, pp. 418–436.

Dullenkopf, K., and Mayle, R. E., 1995, "An Account of Free-Stream-Turbulence Length Scale on Laminar Heat Transfer," ASME JOURNAL OF TURBOMACHINERY, Vol. 117, pp. 401–406.

Dyban, E., and Epik, E., 1985, *Thermal/Mass Transport and Hydrodynamics of Turbulent Flows,* Kiev [in Russian].

Emmons, H. W., 1951, "The Laminar–Turbulent Transition in a Boundary Layer—Part I," *J. Aero. Sci.,* Vol. 18, pp. 490–498.

Emmons, H. W., and Bryson, A. E., 1951, "The Laminar–Turbulent Transition in a Boundary Layer—Part II," *Proc. 1st U.S. Nat. Cong. Theoretical and Appl. Mech.,* pp. 859–868.

Gostelow, J. P., and Blunden, A. R., 1989, "Investigations of Boundary Layer Transition in Adverse Pressure Gradient," ASME JOURNAL OF TURBOMACHINERY, Vol. 111, pp. 366–375.

Hinze, J. O., 1975, *Turbulence,* McGraw-Hill, New York.

Kuan, C., and Wang, T., 1990, "Some Intermittent Behavior of Transitional Boundary Layers," *Exp. Thermal & Fluid Sci.,* Vol. 3, pp. 157–170.

Mayle, R. E., 1991, "The Role of Laminar–Turbulent Transition in Gas Turbine Engines," ASME JOURNAL OF TURBOMACHINERY, Vol. 113, pp. 509–537.

Mayle, R. E., Dullenkopf, K., and Schulz, A., 1998, "The Turbulence That Matters," ASME JOURNAL OF TURBOMACHINERY, Vol. 120, pp. 402–409.

Mayle, R. E., and Schulz, A., 1997, "The Path to Predicting Bypass Transition," ASME JOURNAL OF TURBOMACHINERY, Vol. 119, pp. 405–411.

Narasimha, R., 1957, "On the Distribution of Intermittency in the Transition Region of a Boundary Layer," *J. Aero. Science,* Vol. 24, pp. 711–712.

Narasimha, R., 1985, "The Laminar–Turbulent Transition Zone in the Boundary Layer," *Prog. Aerospace Science,* Vol. 22, pp. 29–80.

Paxson, D. E., 1989, "An Investigation of the Steady and Unsteady Near Wake and Its Effect on a Laminar Boundary Layer," Ph.D. Thesis, Rensselaer Polytechnic Institute, Troy, NY.

Roach, P. E., 1987, "The Generation of Nearly Isotropic Turbulence by Means of Grids," *Int. J. Heat & Fluid Flow,* Vol. 8, pp. 82–92.

Rolls-Royce, 1993, Data transmitted by J. Coupland from Rolls-Royce Applied Science Laboratory.

Savill, A. M., 1991, "Synthesis of T3 Test Case Computations," *Proc. 1st ER-COFTAC Workshop on Numerical Simulation of Unsteady Flows, Transition to Turbulence and Combustion,* Lausanne.

Schlichting, H., 1979, *Boundary-Layer Theory,* McGraw-Hill, New York.

Schubauer, G. B., and Klebanoff, P. S., 1955, "Contribution to the Mechanism of Boundary-Layer Transition," NACA TN 3489.

Sieger, K., Schulz, A., Wittig, S., and Crawford, M. E., 1993, "An Evaluation of Low-Reynolds-Number k–ε Turbulence Models for Predicting Transition Under the

Influence of Free-Stream Turbulence and Pressure Gradient," *Proc. 2nd Int. Sym. Engng. Turb. Modeling & Measurements,* Florence, Italy, pp. 593–602.

Steelant, J., and Dick, E., 1994, "Modelling of By-Pass Transition With Conditioned Navier–Stokes Equations and *K–E* Model Adapted for Intermittency," ASME Paper No. 94-GT-12.

Steelant, J., and Dick, E., 1996, "Modelling of By-Pass Transition With Conditioned Navier–Stokes Equations Coupled to an Intermittency Transport Equation," *Intern. J. Num. Methods in Fluids,* Vol. 23, pp. 193–220.

Walker, G. J., 1987, "Transitional Flow on Axial Turbomachine Blading," AIAA Paper No. 87-0010.

Walker, G. J., and Gostelow, J. P., 1990, "Effects of Adverse Pressure Gradients on the Nature and Length of Boundary Layer Transition," ASME JOURNAL OF TURBOMACHINERY, Vol. 112, pp. 196–205.

Westin, K. J. A., Boiko, A. V., Klingmann, B. G. B., Kozlov, V. V., and Alfredsson, P. H., 1994, "Experiments in a Boundary Layer Subjected to Free Stream Turbulence. Part 1. Boundary Layer Structure and Receptivity," *J. Fluid Mech.,* Vol. 281, pp. 193–218.

Zhou, D., and Wang, T., 1995, "Effects of Elevated Free-Stream Turbulence on Flow and Thermal Structures in Transitional Boundary Layers," ASME JOURNAL OF TURBOMACHINERY, Vol. 117, pp. 407–417.

A Prediction Model for Separated-Flow Transition

A. Hatman

T. Wang

Department of Mechanical Engineering,
Clemson University,
Clemson, SC 29634-0921

The present study formulates an improved approach for analyzing separated-flow transition that differentiates between the transition process in boundary layers that are laminar at separation and those that are already transitional at separation. The paper introduces new parameters that are necessary in classifying separated-flow transition modes and in accounting for the concomitant evolution of transition in separated shear layer and the average effect of periodic separation bubble build-up and vortex shedding. At least three separated-flow transition modes are positively distinguished: (a) transitional separation, with the transition starting upstream of the separation point and developing mostly as natural transition, (b) laminar separation/short bubble mode, with the onset of transition induced downstream of the separation point by inflexional instability and with a quick transition completion, and (c) laminar separation/long bubble mode, with the onset of transition also induced downstream of the separation point by inflexional instability, and with the transition completion delayed. Passing from one mode to another takes place continuously through a succession of intermediate stages. The location of maximum bubble elevation has been proved to be the controlling parameter for the separated flow behavior. It was found that, downstream of the separation point, the experimental data expressed in terms of distance Reynolds number Re_x can be correlated better than momentum or displacement thickness Reynolds number. For each mode of separated-flow transition, the onset of transition, the transition length, and separated flow general characteristic are determined. This prediction model is developed mainly on low free-stream turbulence flat plate data and limited airfoil data. Extension to airfoils and high turbulence environment requires additional study.

Introduction

The typical structure of a two-dimensional laminar boundary layer separation bubble, as described by Horton (1968), consists of an initial "dead" air region containing slow-moving fluid, followed by a reverse flow vortex. The extent of the recirculation region is bounded by a separation streamline, which rises away from the surface at separation (x_S) and rejoins the wall after the boundary layer undergoes laminar-to-turbulent transition. Downstream of the separation location, due to the inherent instability of the separation velocity profile, a hydrodynamically unstable, laminar free shear layer develops. The free shear layer undergoes transition to turbulence from x_t to x_T. The turbulent part of the shear layer entrains higher momentum fluid from the free stream at a higher rate than the laminar shear layer and the turbulent shear layer reattaches at x_R. On an airfoil, at high Reynolds numbers and small attack angles, the extent of a laminar separation bubble, if it exists, is typically small, of the order of 1 percent of the airfoil chord (Tani, 1964). The slight change in the pressure distribution due to the separation bubble existence has a negligible effect on the forces acting on the surface. With an increase of incidence angle or a reduction in speed, the shear layer may fail to reattach and the short bubble may "burst" to form either a closed long bubble, or an unattached free shear layer. The pressure distribution associated with a "long" bubble is different from that of the inviscid flow, and the forces acting on the airfoil are therefore changed. Bubble bursting creates a significant increase in drag and an undesirable change in pitching moment.

Recent studies (Malkiel and Mayle, 1996; Hazarika and Hirsch, 1997) have provided basic information about how transition originates and develops in separated boundary layers. It is commonly accepted that the detached laminar shear layer is inherently unstable and promotes the growth of disturbances, leading to an earlier laminar-to-turbulent transition. The separated-flow transition may or may not involve linear instability of the Tollmien–Schlichting (TS) type.

Critical studies of transitional phenomena in compressors and gas turbine engines were presented in the review papers of Mayle (1991) and Walker (1993). They have given an overview of the recent developments, prediction methods, and their applications to the design of engine components. The papers have identified the limitations of the actual predictions for separated-flow transition and emphasized the necessity of improving the modeling of transition in separated flow to allow the full application in modern numerical codes. They have shown that there is no complete model to describe the overall process without contradicting some of the frequently observed features. For example, most of the models predict a monotonic decrease in separated-flow transition length with an increase of the adverse pressure gradient, which is not always true. The current level of understanding does not allow for precise prediction of the transition onset and transition length and does not explain how the bubble existence mode is related to the transition mechanism in the separated shear layer. The prediction schemes used in numerical codes that are based either on empirical correlations or on the e^n amplification model are not generally applicable for all separated flow transition modes and they can give misleading results. A fully satisfactory method for predicting the characteristics of separation bubbles and the bubble bursting process is still in development. As long as the fundamental physical mechanisms associated with transition in separated boundary layers are not well understood, one is facing the difficulty of identifying the bubble type and distinguishing the separated-flow transition modes.

The conventional definitions for long and short bubble are ambiguous; they have been based either on the physical length of the bubble or on their effect on the main flow inviscid pressure distribution. It has never been clear how long the extent of a bubble

Contributed by the International Gas Turbine Institute and presented at the 43rd International Gas Turbine and Aeroengine Congress and Exhibition, Stockholm, Sweden, June 2–5, 1998. Manuscript received by the International Gas Turbine Institute February 1998. Paper No. 98-GT-237. Associate Technical Editor: R. E. Kielb.

length must be or how much the pressure distribution must deviate from the prescribed one in order to characterize a bubble as "long." Contrary to the conventional methods, this study proposes to distinguish short and long bubbles based on the separated flow structure and vortex dynamics.

Glossary

A thorough description of the separated-flow transition requires specific notations that are necessary for identifying the effects of different phenomena involved. The notations and the terminology used in the following analysis are defined below.

- The *onset of transition* (x_t) is defined as the location where the intermittency factor $\Gamma > 0$; the global flow structure of the boundary layer, or of the separated shear layer, deviates from the laminar behavior, and the dissipation spectrum shows an increase in magnitude at selective frequencies (Hatman, 1997).
- The *early transition* region represents the early portion of the transition process, characterized by strong turbulence production in the mean flow direction and cross-stream Reynolds transports, and by drastic changes in all variables.
- The *midtransition point* ($x_{u'\max}$) establishes the border between early and late transition, and is identified as the location of maximum rms streamwise fluctuations in the boundary layer. Kuan and Wang (1990) determined that it corresponds to an intermittency factor of about 0.7.
- The *late transition* region is the late portion of the transition process, characterized by weaker turbulence production, stronger dissipation, and redistribution of turbulence energy toward equilibrium and isotropic turbulence. In this region, (u') decreases asymptotically toward the fully turbulent flow value.
- The *end of transition* (x_T) is defined as the location where the intermittency factor $\Gamma = 1$; the global behavior of the boundary layer or of the separated shear layer matches that of a fully turbulent flow.
- The *separation point* (x_S) represents the location where the boundary layer detaches from the wall.
- The *maximum displacement location* (x_{MD}) is the location where the time-averaged height of the separation bubble attains for the first time a maximum value. It is believed to coincide with the averaged location of reverse flow vortex shedding.
- The *first reattachment point* (x_{R1}) is defined only for long bubbles as the unsteady region in which the periodic inflow toward the wall between two shedding vortices locally modifies the mean velocity profile into a reattached-like flow.
- The *reattachment point* (x_R) is the time-averaged location where flow rejoins the surface.

The separation *bubble types* are defined by the flow regime at the separation location. A *laminar separation bubble* is defined as a separation that occurs in the laminar or pretransitional flow, $x_S < x_t$. A *transitional separation bubble* is defined as a separation that occurs downstream of the onset of transition, $x_S > x_t$.

Separated-Flow Transition Primary Modes

The proposed approach in modeling separated-flow transition is based on the assumption that the transition to turbulence in separated boundary layers is a result of the superposition of the effects of two different types of instability: Kelvin–Helmholtz (KH) instability and Tollmien–Schlichting (TS) instability.

The first type of instability can be associated with the separated laminar shear layer and the near-wall low-speed flow, which can be regarded as an antisymmetric mixing layer and is inflectional unstable (Morkovin, 1991), and can be identified with Kelvin–Helmholtz instability. It occurs and develops at a specific location downstream of the separation point, and is traceable to the presence of a maximum of mean vorticity within the shear layer. The mechanism of vortex evolution is primarily inviscid, even if the viscosity acts to diffuse zones of concentrated vorticity.

For relatively large Reynolds numbers and mild adverse pressure gradients, the start of transition is likely to precede separation, being induced by the Tollmien–Schlichting instability mechanism. For this second type of instability, any initial disturbance is advected by the flow as it is amplified and interacts with the inflectional instability.

The predominance of one type of instability or another determines the modes of separated-flow transition. The proposed classification of the separated-flow transition modes considers the location of separation relative to the onset of transition, the succession of instabilities, and their mutual interactions.

The analysis of the low free-stream turbulence intensity (Tu = 0.3 to 0.6 percent) data of Hatman (1997) and partially presented by Hatman and Wang (1998a, b, c) led to the observation that the location of maximum bubble elevation (x_{MD}) is the key parameter for correlating the separated-flow transition. Using this parameter, specific regions were delineated for each mode of the separated-flow transition. It was observed that the boundary layers, that separate in a laminar state behave differently from those that are already transitional or highly unstable (pretransitional) at separation. At least three primary separated-flow *transition modes* were positively distinguished. In this study, they are defined as *transitional separation* mode, *laminar separation/short bubble* mode, and *laminar separation/long bubble* mode.

A detailed description of each primary mode is given below. The vortex dynamics associated with the three primary modes is presented by Hatman and Wang (1998c).

Transitional Separation. The *transitional separation mode* occurs when the boundary layer separation takes place at relatively high Reynolds numbers and low adverse pressure gradient strength. The onset of transition takes place prior to boundary layer separation and the early transition is similar to the natural transition in attached boundary layers. The late transition is affected by the addition of KH instability and near-wall fluid ejection (see Hatman and Wang, 1998c). The transitional separation bubble can be accompanied by vortex shedding.

The characteristic regions of the transitional separation mode

Nomenclature

$K = (\nu/U_\infty^2)(dU_\infty/dx)$ = pressure gradient parameter
$\mathrm{Re}_x = U_\infty x/\nu$ = local Reynolds number
$\mathrm{Re}_{\delta 2} = U_\infty \delta_2/\nu$ = momentum thickness Reynolds number
Tu = free-stream turbulence intensity
U = mean velocity in streamwise direction
x, y = coordinates in streamwise and cross-stream directions
Γ = turbulent intermittency
δ = boundary layer thickness
δ_1 = displacement thickness
δ_2 = momentum thickness
ν = kinematic viscosity
$\Lambda_{\delta 2} = (\delta_2^2/\nu)(dU_\infty/dx)$ = pressure gradient parameter

Subscripts

att = attached flow
cr = critical value, from linear instability
LT $= (x_T - x_t)$ = transition length
MD = maximum displacement
R = reattachment
R_1, R_2 = first and second reattachments (long bubbles)
S = separation
t = onset of transition
T = end of transition
$u'_{\max}$ = mid-transition point, where u' reaches maximum
∞ = free stream

are presented in Fig. 1. The first region [0, x_t], characterized by attached, stable, laminar flow is followed by natural transition, which starts in the attached boundary layer. Between (x_t) and (x_S), the two-dimensional Tollmien–Schlichting (TS) instability waves develop, the spanwise three-dimensional waves evolve, break down, and eventually turbulent wave packets form. In the third region, [x_S, x_{MD}] or [x_S, $x_{u'max}$], the turbulent wave packets spread within the detached shear layer. The early transition takes place more slowly than would be expected for the overall adverse pressure gradient flow condition, due to the reduction of adverse pressure gradient induced by the deflection of the shear layer. Downstream of x_S, the Kelvin–Helmholtz (KH) instability also sets in; the roll-up vortex periodically forms, grows, pairs, and finally interacts with the wall. Due to the vortex–wall interaction process, the near-wall fluid is ejected into the free stream and large eddies are released into the shear layer. The entire detached shear layer oscillates due to the periodic bubble "breathing." The ejection-shedding process takes place at the average maximum displacement location. For transitional separation mode, the maximum displacement location (x_{MD}) was observed to be coincidental with the midtransition point, ($x_{u'max}$). In the fourth region, [$x_{u'max}$, x_T] or [x_{MD}, x_R], the interactions between the transitional shear layer and the periodically ejected turbulent fluid accelerate the coalescence into turbulence, resulting in a short late transition region. Besides the increased turbulent mixing, the periodic ejections and subsequent sweeping of upstream flow forces the shear layer to reattach. In general, the x_T occurs downstream of reattachment in the immediate neighborhood of x_R.

For relatively moderate adverse pressure gradients of this mode, the shear layer remains attached and a nonequilibrium turbulent boundary layer results downstream of the reattachment point (x_R). The location for the end of transition varies from case to case; however, (x_T) is always situated relatively close to the reattachment point.

Laminar Separation/Short Bubble Mode. The *laminar separation/short bubble mode* occurs at moderate Reynolds numbers and mild adverse pressure gradients with the onset of transition induced downstream of the separation point by inflexional instability at a location coincidental with that of the maximum displacement of the shear layer. It is characterized by a quick transition completion due to a complex interaction between the separated shear layer and the reverse flow vortex. The laminar separation/short bubble mode is characterized by distinctive vortex shedding. For laminar separation, (both short and long bubble modes, Figs. 2 and 3) the first region, [0, x_S], characterized by attached laminar flow, is followed by detached laminar shear layer, [x_S, x_t] or [x_S, x_{MD}]. Close to the separation location, low-frequency oscillations, mainly induced by the downstream periodic bubble "breathing," which are not subject to amplification, are dominant. Instability waves of the TS type, initiated upstream of the separation point, may still be present within the detached shear layer. The data of Hatman (1997) have shown that in some laminar

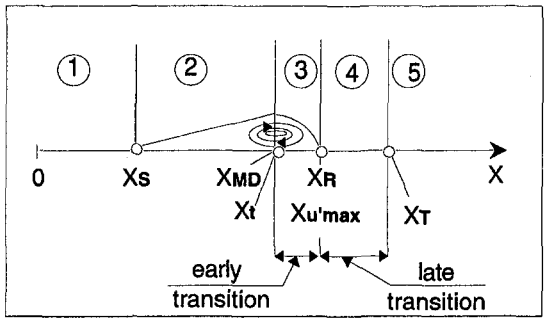

Fig. 2 Time-averaged representation of laminar separation/short bubble mode

separation cases the TS instability waves are damped out, whereas in other cases they continue to be amplified. This suggests a continuous succession of stages between the transitional separation mode and the laminar separation mode.

After the laminar shear layer detaches, the KH instability sets in. The onset of transition (x_t) is observed to be situated close to the location of the maximum bubble elevation (x_{MD}) where the ejection-shedding process takes place. The transition in laminar separated boundary layers is characterized by a short early transition region, [x_t, $x_{u'max}$] or [x_{MD}, x_R]. This early transition is shortened by the periodic ejection of turbulent fluid from the recirculating region into the detached shear layer. For a bubble in the short mode, characterized by relatively moderate adverse pressure gradient, the vigorous mixing in the region of maximum (u') leads to reattachment.

In other words, since the adverse pressure gradient is not strong in the laminar separation/short bubble mode, the high rate of turbulence production and the ejection-shedding process are sufficient to bring in more momentum to overcome the adverse pressure gradient and force the reattachment of the shear layer. The coalescence into turbulence takes place within the reattaching boundary layer, resulting in a short late transition region.

The laminar short-bubble mode is the only mode that can be reasonably well predicted by the "instantaneous transition" models (Horton, 1968; Roberts, 1980; Mayle, 1991). Many previous studies did not distinguish transitional separation from the laminar separation/short bubble mode. Their global configuration is similar but the turbulent flow structures are very different. This lack of understanding has caused confusion in interpreting data and hindered progress in developing an effective prediction model.

Laminar Separation/Long Bubble Mode. When the laminar boundary layer separation takes place at low Reynolds numbers due to strong adverse pressure gradients, the shear layer may fail to remain reattach and the *laminar separation/long bubble mode* is likely to occur. The first part, up to start of transition ($x_t = x_{MD}$), of a long bubble is identical to that of a short bubble. The onset of transition is

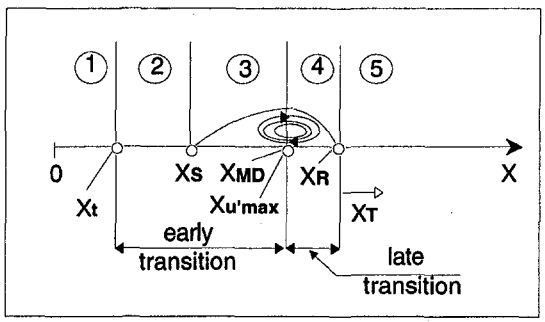

Fig. 1 Time-averaged representation of the transitional separation mode

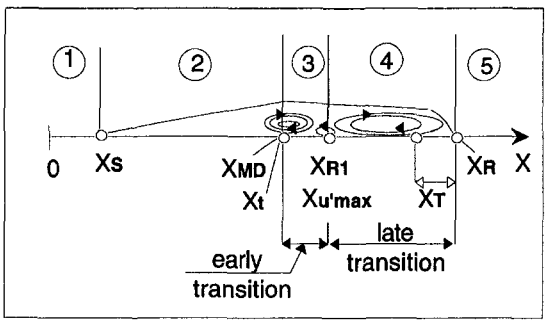

Fig. 3 Time-averaged representation of laminar separation/long bubble mode

also induced downstream the separation point by inflexional instability and ejection process. However, the laminar separation/long bubble is no longer accompanied by vortex shedding.

The mixing in the region of maximum u' and the high rate of momentum transport inward and toward the wall leads to the first "reattachment" type behavior (x_{R1}). Due to the relatively lower local Reynolds number and stronger adverse pressure gradient (compared to a bubble in the short mode), the mixing is reduced and the shear layer fails to remain attached; the bubble then *"bursts"* and a *"long bubble"* results. Due to the low-Reynolds-number effect, the transition completion is delayed, resulting in a long late transition region. Finally, the coalescence into turbulence forces the turbulent reattachment and a closed long bubble results. For very strong adverse pressure gradients, the bubble may never close.

The passage from the transitional separation mode to the laminar separation modes take place gradually through a succession of intermediate stages dominated by one mode of transition or another. The separation bubble's type and structure are mainly determined by the conditions at separation. Downstream of separation, conditions (e.g., abrupt variations in pressure gradient distribution) may alter some features of the primary modes, leading to some confusion in determining the bubble type.

For example, a laminar bubble in the long mode can be "forced" short in terms of the physical length by suppressing the adverse pressure gradient downstream of the first reattachment. A shorter separation region will result, but the absence of the vortex shedding nullifies the classification of this separation bubble as short since the flow structure characteristic for a bubble in the long mode is preserved (see Hatman, 1997, and Hatman and Wang, 1998b, for details).

Prediction Model

In the following analysis, besides the authors' data, other groups' experimental data sets were considered. A difficulty arose in attempting to use data coming from a variety of sources because not only the reported final results were to be used, the information had also to be derived from the velocity profiles and pressure distributions in a consistent manner for all the analyzed cases. This was a tedious process, which was also susceptible to uncertainties resulting from data interpretation.

Data for boundary layer separation over flat plates (the present data and Gaster's Series I and II) represent the core of the present model; however, several other data sets for airfoils have also been considered. Except otherwise noted, the correlations developed are mainly based on flat plate data. The cited data of Hoheisel et al. (1984) and Brendel and Mueller (1987) were adopted from what was presented by Walker (1989).

To investigate the effects of the streamwise pressure gradients on transition, the following analysis considers the *local* value of the nondimensional pressure gradient parameter K.

The K parameter is more convenient to use than the Pohlhausen pressure gradient parameter: $\Lambda_{\delta 2} = (\delta_2^2/\nu)(dU_\infty/dx)$. The main inconvenience in using the Pohlhausen parameter as separation and transition indicator resides in the difficulty of accurately evaluating the growth of the momentum thickness for the separated boundary layers. The boundary layer growth depends on the actual pressure distribution, which can be altered by the separation in an undetermined fashion.

The velocity profile inside the recirculating region is highly uncertain; therefore, the integral parameters are usually determined in the assumption of zero mass flux across the dividing streamline. Due to the high uncertainty in determining δ_1 and δ_2 (see Hatman and Wang, 1998a), the analysis will be mainly conducted in terms of length Reynolds numbers, Re_x.

The usage of Re_x as correlating parameter is further justified by the inviscid nature of KH instability, which requires a certain length of the separated shear layer to develop, regardless of the presence of the wall. Therefore, the KH instability triggered phenomenon can be correlated with the streamwise distance, x, but not necessarily strongly correlated with δ_1 and δ_2, which are produced by the wall viscous effect.

Separation Reynolds Number. The prediction of a precise location for the onset of separation frequently presents difficulty unless separation occurs at a discontinuity in surface slope. In the boundary layer theory, the laminar boundary layer is amenable to mathematical treatment and the characteristics of laminar flow can be predicted to a high degree of accuracy. The zero wall shear stress condition has been adopted as an unambiguous laminar separation criterion; however, it becomes more difficult to use in more complex flows, or in dealing with experimental data, when the separation point is unsteady and the average velocity profile does not have zero gradient at the wall. Several simple approaches exist for determining the location of laminar separation. Mayle (1991) recommended the Thwaites value: $\Lambda_{\delta 2S} = \mathrm{Re}_{\delta 2S}^2 K_S = -0.082$. The method for determining the separation point location for the present experimental data was described by Hatman and Wang (1998a).

In Fig. 4, besides the present data, the two series of experimental results of Gaster (1967) were considered. Gaster's results were reported in terms of $\Lambda_{\delta 2S}$, which provided an indirect evaluation for the velocity gradient at separation $(dU_\infty/dx)_S$, as it was determined by Gaster. The velocity gradient at separation was also checked using Gaster's pressure distribution results, and subsequently used to calculate the local pressure parameter K_S. This procedure provided consistency in evaluating K_S for all different sets of experimental data considered. A new correlation, in terms of K_S and Re_{xs}, valid for all separated-flow transition modes, was generated by fitting the experimental results for separation on a flat surface:

$$\mathrm{Re}_{xs} = 5750 - 215{,}000/(K_S \times 10^6) - 45{,}500/(K_S \times 10^6)^2 - 5750/(K_S \times 10^6)^3 - 250/(K_S \times 10^6)^4. \quad (1)$$

Analyzing each case, all the data that can be defined as laminar separation/long bubble mode (including the bubbles "forced" short) lie in the strong adverse pressure gradient region defined by $K_S < -1.3 \times 10^{-6}$ and $\mathrm{Re}_{xs} < 2.05 \times 10^5$. The data for the transitional separation mode lie in the region of mild adverse pressure gradient defined by $K_S > -0.3 \times 10^{-6}$ and $\mathrm{Re}_{xs} > 4.5 \times 10^5$. It must be noted that the characteristic ($K_S - \mathrm{Re}_{xs}$) domains for the laminar separation with dominant transitional behavior ($x_S < x_t < x_{MD}$, see Hatman and Wang,

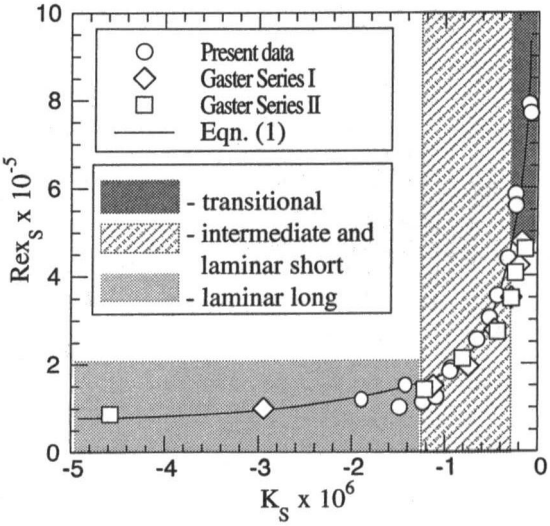

Fig. 4 Correlation between separation Reynolds number and pressure gradient parameter at separation: $\mathrm{Re}_{xS} = f(K_S)$

1998a, b) and laminar separation/short bubble mode can not be strictly delineated.

The data for laminar separation/short bubble mode cases and for the bubbles in the intermediate stages are apparently randomly distributed in the region defined by $2.05 \times 10^5 < \mathrm{Re}_{xS} < 4.5 \times 10^5$ and $-1.3 \times 10^{-6} < K_S < -0.3 \times 10^{-6}$. There is an ambiguous region in which both the inviscid inflexional mode instability and the TS originated instability may equally affect the start of transition. The overlapping band comprises the intermediate stages, from the transitional separation, which originates very close to the separation point, to the laminar separation, for which the effect of TS instability waves is still significant.

If $\mathrm{Re}_{\delta 2S}$ is used as a criterion (see Fig. 5), the laminar separation cases (both long and short modes) are characterized by $\mathrm{Re}_{\delta 2S} < 320$.

The transitional separation mode cases and the laminar separation cases with dominant transitional behavior are characterized by $\mathrm{Re}_{\delta 2S} > 320$.

Note that both Re_x and $\mathrm{Re}_{\delta 2}$ correlate well the data at the separation point. However, in Fig. 4 the K_S–Re_{xS} domains for the laminar short bubble mode and for the intermediate stages can not be distinguished, while in Fig. 5 $\mathrm{Re}_{\delta 2S}$ shows a clear delineation between them. For locations downstream of the separation point, after that the KH instability has set in, $\mathrm{Re}_{\delta 2S}$ no longer correlated the data well. Therefore, all the correlations in the rest of this paper were developed in terms of Re_x.

Maximum Displacement Location Reynolds Number. As shown in Fig. 6, for all separated-flow transition modes, the Reynolds number based on the local free-stream velocity and the streamwise location of the maximum bubble elevation, can be empirically determined by a linear correlation which relates $\mathrm{Re}_{x\mathrm{MD}}$ to the Reynolds number at separation, Re_{xS}:

$$\mathrm{Re}_{x_{\mathrm{MD}}} = 1.0816\ \mathrm{Re}_{x_S} + 26{,}805. \qquad (2)$$

It was explained by Hatman and Wang (1998b, c) that the maximum displacement was caused by fluid ejection from the near-wall region due to the viscid–inviscid interaction between the wall and the shear layer roll-up vortices originated from KH instability.

The correlation (2) is independent of the local pressure gradient strength and satisfies not only the data obtained on flat surfaces but also data for leading edge separation on airfoil surfaces. The pressure gradient effect seems implicitly absorbed in the $U_\infty x$ product. A plausible explanation would be that the rate of growth of the KH instability is related to the cross-stream velocity gradient, which in turn is related to the development of the shear layer as a function of the distance from the origin. The streamwise pressure gradient affects the growth rate and affects the local cross-stream velocity gradient, which is scaled with the shear layer width and the local velocity. Therefore, it seems that Re_x proves to be a good scaling parameter.

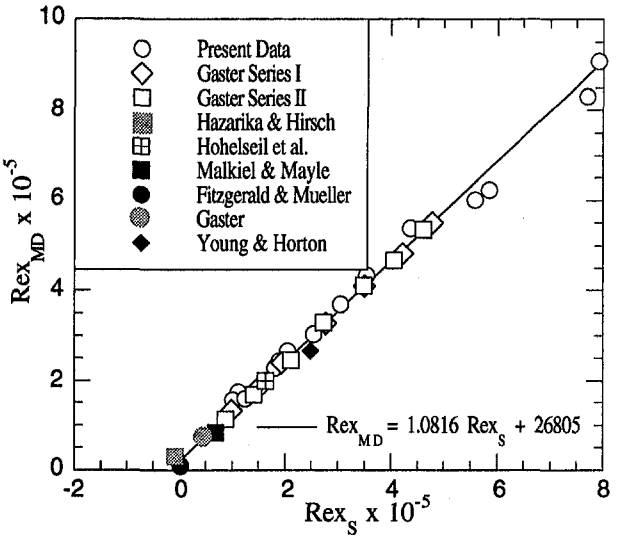

Fig. 6 Correlation for the maximum displacement location Reynolds number for both flat plate and airfoil surfaces

Reattachment Location Reynolds Number. Determining the reattachment location is essential in distinguishing between long and short bubbles.

The second reattachment of a long bubble can be evaluated easily from the pressure distribution data. Determining the location of the first reattachment is not an easy task without detailed boundary layer measurements and cross-checking with other flow characteristics such as mean and rms velocity profiles, as detailed by Hatman and Wang (1998a). Knowing the location of the first reattachment is of practical interest because it is characterized by very high velocity fluctuations in the near-wall region and increased local mixing.

The evolution of Re_{xR}, Re_{xR1}, and Re_{xR2} versus Re_{xS} is shown in

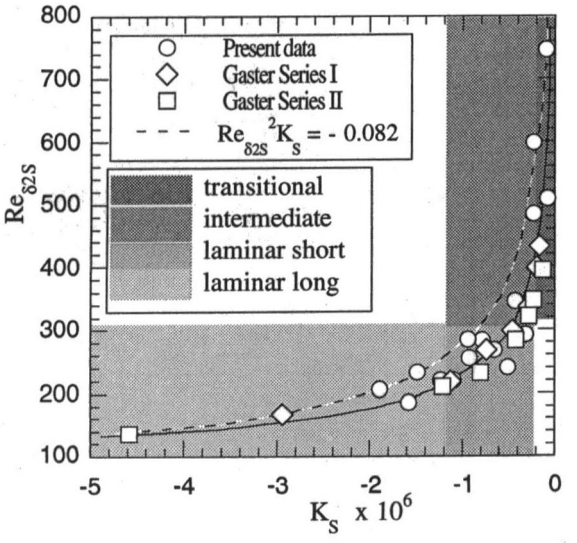

Fig. 5 Momentum thickness Reynolds number and pressure gradient parameter at separation

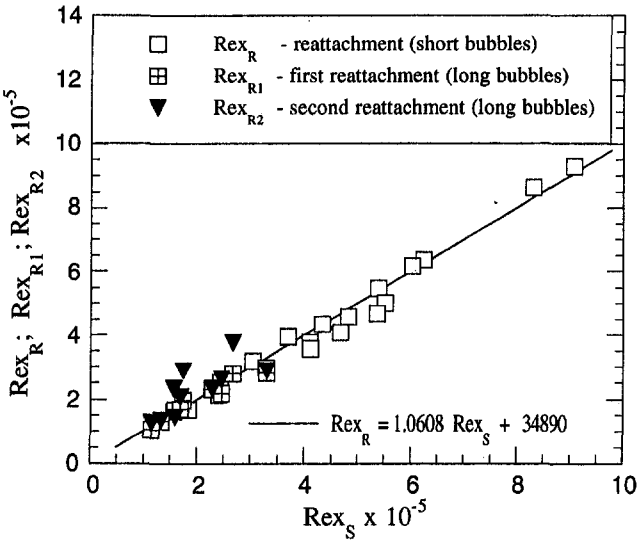

Fig. 7 Correlation for reattachment Reynolds number: Re_{xR}, Re_{xR1}, Re_{xR2} versus Re_{xS}

Fig. 7. The data for the second reattachment of long bubbles Re_{xR2} show a large scatter, while the short bubbles' reattachment Re_{xR} and the long bubbles' first reattachment Re_{xR1} seem to have similar behaviors and correlate well by a linear relation:

$$Re_{x_{R,R1}} = 1.0608\ Re_{x_S} + 34{,}890 \quad (3)$$

This correlation cannot be applied for the (second) reattachment Re_{xR2} of the long bubbles. The amount of documented Re_{xR2} data was insufficient for an attempt to correlate them.

Another linear empirical correlation for $Re_{x_{R,R1}}$ can be also determined in terms of Reynolds number at the maximum displacement location by fitting the actual data (see Fig. 8):

$$Re_{x_{R,R1}} = 1.0005\ Re_{x_{MD}} - 7535 \quad (4)$$

Equation (4) represents well flat plate data as well as the available $Re_{xR,R1}$ airfoil data from the set considered in this study. Equation (4) is slightly different from the equation (not shown) that can be obtained by combining Eqs. (2) and (3). It fits the data better, especially in the high-Reynolds-number range, $Re_{xMD} > 6 \times 10^5$.

The separation bubble in transitional separation mode is characterized by a *local* steep decrease in the free-stream velocity between (x_{MD}) and (x_R). Thus, for the transitional separation mode, the Reynolds number at maximum displacement location (Re_{xMD}) or even the Reynolds number at separation (Re_{xS}) may have a higher value than that of the Reynolds number at reattachment (Re_{xR}), which is obviously located downstream. This situation is possible when the rate of increase in x is lower than the rate of decrease in velocity over the same length, such that there is a local maximum in the Reynolds number distribution. Figure 9 shows three different flow configurations with simple pressure gradient distributions, (*b*) and (*c*) having $Re_{xR} < Re_{xS}$.

For a constant-K flow, as shown in Fig. 9(*a*), Re_x monotonically increases with x and always $Re_{xR} > Re_{xS}$. When the constant-K flow region is preceded by a zero pressure gradient starting length, as in Fig. 9(*b*), the situation of $Re_{xR} > Re_{xS}$ may occur.

The present data were taken in conditions similar to Fig. 9(*b*). An example of flow with continuous Reynolds number distribution, which shows a maximum value is shown in Fig. 9(*c*). A flow with linear velocity drop leads to a parabolic Reynolds number distribution, which makes the $Re_{xR} > Re_{xS}$ condition possible.

As the separation Reynolds number is reduced and the *overall* adverse pressure gradient increases, the potential of having $Re_{xR} < Re_{xMD}$ diminishes for laminar separation bubbles. The experimental

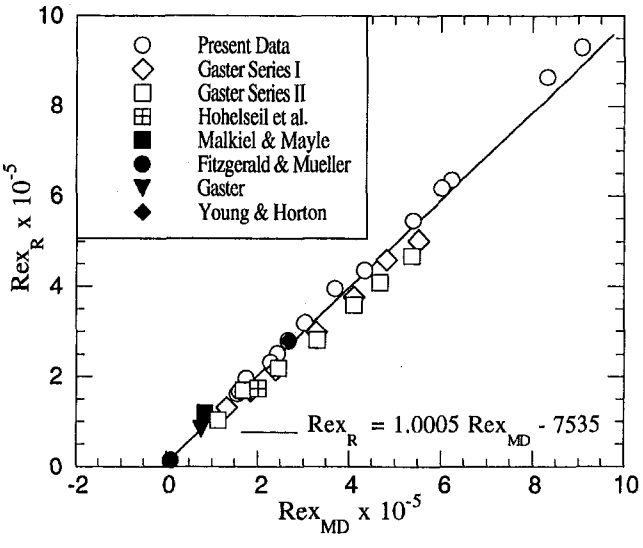

Fig. 8 Correlation for reattachment Reynolds number: Re_{xR} versus Re_{xMD} for both flat plate and airfoil surfaces

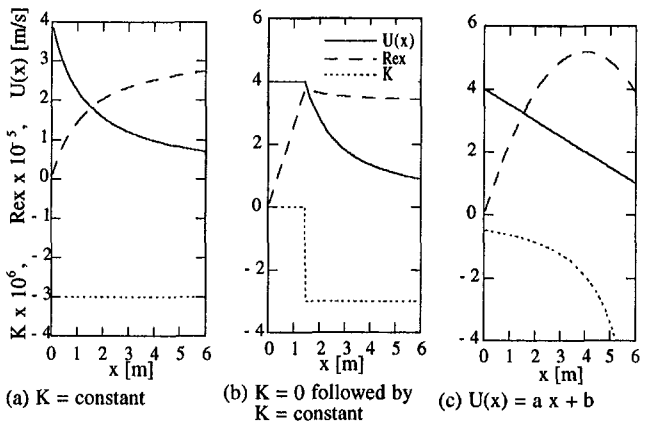

Fig. 9 Reynolds number distribution for various pressure gradient distributions showing the possibility of $Re_{xR} < Re_{xS}$ for $x_R > x_S$

data for laminar long bubbles, with the highest adverse pressure gradients and lower separation Reynolds numbers, show a different behavior, with $Re_{xR} \gg Re_{xS}$ and $Re_{xR} \gg Re_{xMD}$.

Prediction of the Onset of Transition. The main difficulty in predicting separated-flow transition lies in accurately determining the onset of transition, because there is no general valid relation for all separated-flow transition modes.

One way to handle the situation is to use different correlations for each mode of transition. One could predict reasonably well the onset of transition in the transitional separation mode independent of the conditions at separation by using one of the existing models for transition in attached adverse pressure gradient flows.

Based on Hatman and Wang's data (1998a, b), the onset of transition for laminar separation modes coincides with the location of maximum displacement, $Re_{xt} = Re_{xMD}$.

Thus, for laminar separation, both short and long bubble modes, the onset of transition depends only on conditions at the separation location and can be determined using Eq. (2) for $Re_{xMD} = f(Re_{xS})$.

Prediction of the Midtransition Point. Figure 10 presents the available experimental results for the midtransition point (defined as the location where maximum u' occurs) in separated-flow transition as $Re_{x(u')max}$ versus Re_{xt}. They can be correlated by a linear relationship:

$$Re_{x_{(u')max}} = 1.3633\ Re_{x_t} - 65846 \quad (5)$$

Prediction of the End of Transition. Once the onset of transition is determined, the end of transition can be calculated

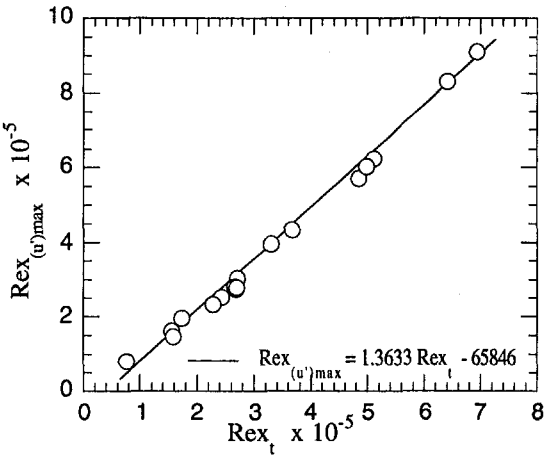

Fig. 10 Correlation for the midtransition point

using the Cebeci correlation for the transition length (based on Chen–Thyson intermittency formula and presented by Walker, 1989):

$$\mathrm{Re}_{\mathrm{LT}} = C\,\mathrm{Re}_{x_t}^{0.67};\quad C^2 = 213[\log \mathrm{Re}_{x_t} - 4.7323] \qquad (6)$$

As a result of interpolating the experimental data analyzed in the present study, and presented in Fig. 11, an alternative, simpler, linear relation is proposed:

$$\mathrm{Re}_{x_T} = 1.193\ \mathrm{Re}_{x_t} - 393 \qquad (7)$$

The differences between the Re_{x_T} values predicted by Eqs. (6) and (7) are within 3 percent. Both correlations predict the end of transition reasonably well for all the separated-flow transition modes. The correlation (7) satisfies the data obtained on flat surfaces, as well as on airfoils.

With the onset and end of transition predicted, the transition length can be determined. Most of the existing models predict a monotonic decrease in separated-flow transition length with an increase of the adverse pressure gradient, which is not consistently supported by the experimental data. It can be seen in Fig. 12 that there is an increase in transition length for the bubbles in the laminar separation/long mode in the low-Reynolds-number region when the high adverse pressure gradient effect is seemingly overcome by the low-Reynolds-number effect.

Procedure for Predicting Separated-Flow Transition. Based on this analysis, a summary of the observed features for each mode of separated-flow transition is presented in Table 1, and a new approach for predicting the separated-flow transition is proposed below:

(*i*) For a specific flow configuration, determine the separation location using Eq. (1) or the separation criterion given by Mayle (1991): $\Lambda_{\delta 2S} = \mathrm{Re}^2_{\delta 2S}\,K_S = -0.082$. One may also apply any other established model for calculating the laminar separation bubbles in two-dimensional incompressible flows.

(*ii*) Based on the conditions at separation Re_{xs} and K_S:
- evaluate the transition mode using the conditions in Table 1;
- determine the maximum displacement location Reynolds number $\mathrm{Re}_{x\mathrm{MD}}$ using Eq. (2);
- evaluate the reattachment Reynolds number (Re_{xR}) or, for the long bubbles, the first reattachment Reynolds number (Re_{xR1}) using Eq. (3) or (4).

(*iii*) Determine the onset of transition ($\mathrm{Re}_{x_t,\mathrm{att}}$) using any established model for attached flows in adverse pressure gradient conditions (for example, Walker, 1989, 1993).

(*iv*) Compare ($\mathrm{Re}_{x_t,\mathrm{att}}$) to ($\mathrm{Re}_{x\mathrm{MD}}$):

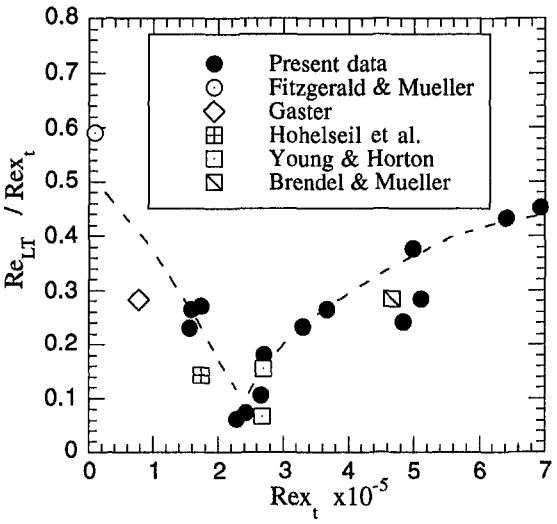

Fig. 12 Transition length Reynolds number

- if ($\mathrm{Re}_{x_t,\mathrm{att}}$) < ($\mathrm{Re}_{x\mathrm{MD}}$), assume transitional separation mode and let (Re_{x_t}) = ($\mathrm{Re}_{x,\mathrm{att}}$);
- if ($\mathrm{Re}_{x_t,\mathrm{att}}$) > ($\mathrm{Re}_{x\mathrm{MD}}$), assume laminar separation mode and let (Re_{x_t}) = ($\mathrm{Re}_{x\mathrm{MD}}$).

(*v*) Determine the midtransition point using Eq. (5) and the end of transition using Eq. (7) or Cebeci correlation, Eq. (6).

General Discussion of Separated-Flow Transition in Constant-*K* Flow Configuration. The study of separated-flow transition cannot be easily handled in a general manner as long as it involves a large number of variables. When the simplified case of constant-K flow is considered, an analysis of the separated-flow transition, the phenomena involved and their mutual interactions can be more easily realized, although decelerating constant-K flow is not common in real applications except in straight-wall diffusers.

For a constant-K flow, Eqs. (2) and (3) can be modified in terms of K, by using relation (1) in the assumption that the local pressure gradient parameter K at the separation point is the same with the overall pressure gradient for the entire flow ($K_S \sim K$). (Note that the local K value will be modified by the separation.)

The curves $\mathrm{Re}_{xS} = f(K)$, $\mathrm{Re}_{x\mathrm{MD}} = f(K)$, and $\mathrm{Re}_{xR} = f(K)$ are presented in Fig. 13. In addition, Fig. 13 includes: (*a*) the curve for the critical Reynolds number, $\mathrm{Re}_{x\mathrm{cr}} = f(K)$, from linear instability analysis in adverse pressure gradient, (*b*) the empirical curves for the onset and end of transition Reynolds numbers $\mathrm{Re}_{x_t} = f(K)$ and

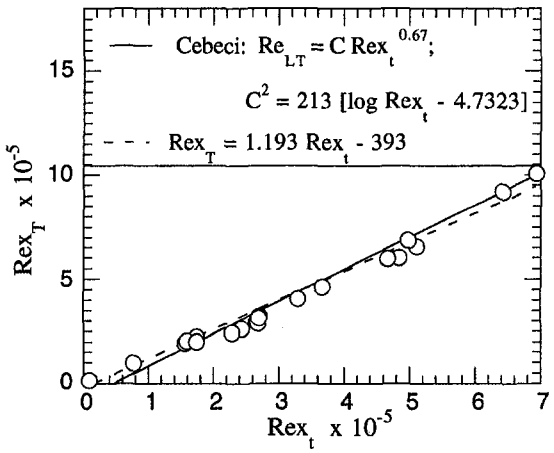

Fig. 11 Correlation for the end of transition

Table 1 Criteria for separated-flow transition

LAMINAR SEPARATION $\mathrm{Re}_{\delta 2s} < 320$		TRANSITIONAL SEPARATION $\mathrm{Re}_{\delta 2s} > 320$
laminar separation long bubble mode	intermediate stages	transitional separation mode
$K_S < -1.3\times10^{-6}$ $\mathrm{Rex}_S < 2.05\times10^5$ $\mathrm{Re}_{\delta 1t}/\mathrm{Re}_{\delta 1s} > 2$	$-1.3\times10^{-6} < K_S < -0.3\times10^{-6}$ $2.05\times10^5 < \mathrm{Rex}_S < 4.5\times10^5$ $\mathrm{Re}_{\delta 1t}/\mathrm{Re}_{\delta 1s} = O(1)$	$K_S > -0.3\times10^{-6}$ $\mathrm{Rex}_S > 4.5\times10^5$ $\mathrm{Re}_{\delta 1t}/\mathrm{Re}_{\delta 1s} < 1$
	laminar separation short bubble mode	laminar separation dominant transitional mode	
$\mathrm{Rex}_S < \mathrm{Rex}_t$ $\mathrm{Rex}_t = \mathrm{Rex}_{\mathrm{MD}}$ $\mathrm{Re}_{\delta 2s} < 240$	$\mathrm{Rex}_S < \mathrm{Rex}_t$ $\mathrm{Rex}_t = \mathrm{Rex}_{\mathrm{MD}}$ $240 < \mathrm{Re}_{\delta 2s} < 320$	$\mathrm{Rex}_S < \mathrm{Rex}_t$ $\mathrm{Rex}_t < \mathrm{Rex}_{\mathrm{MD}}$ $\mathrm{Re}_{\delta 2s} > 320$	$\mathrm{Rex}_t < \mathrm{Rex}_S$ $\mathrm{Re}_{\delta 2s} > 320$

$Re_{xT} = f(K)$ in attached flows as presented by Mayle (1991), and (*c*) the curves for the onset and end of transition in separated flow determined from the correlations developed in this study.

Considering a straight wall diffuser, with a fixed K-value, the boundary layer flow evolution along the wall can be represented in Fig. 13 by a vertical line at that specific K-value. It can be seen that two conditions are present for a constant-K flow configuration. First, the laminar separation does not occur for low adverse pressure gradients because, in terms of local Reynolds numbers, the transition is likely to be completed before the laminar boundary layer separates. This aspect can be seen on the right of point 1 where the end of transition curve for attached flow occurs upstream of the separation curve Re_{xS}. Recall that in a constant-K flow Reynolds number increases monotonically, so that if $Re_{xS} > Re_{xt,att}$ it implies that $x_S > x_t$. The dotted curve of Re_{xS} should not exist above the $Re_{xt,att}$ curve because in turbulent flow the condition for separation given by Eq. (1) is not applicable.

Second, the laminar separation/short bubble mode is not achievable in a constant-K flow. Only the intermediate stages with a significant contribution of the TS instability may take place. The laminar separation/short bubble mode can be generated only in flows with variable K distribution, in which the laminar separation can be induced upstream of the transition onset.

In many previous experimental studies it was reported that the bubble "bursting" process was characterized by a sudden drastic change in the separated flow behavior with a relatively small increase in the adverse pressure gradient. In Fig. 13, the only apparent "discontinuity," which may correspond to a sudden change in separated flow behavior, occurs when the curve for the onset of transition in attached flow (induced by TS instability) intersects the separation curve (point number 2 on the diagram). Within a narrow range of K values, $-1.7 \times 10^{-6} < K < -1.3 \times 10^{-6}$, the onset of transition shifts to the maximum displacement curve (point number 3), which corresponds to the onset of transition in the laminar separation mode. The bubble "bursting" process is more likely to be caused by the change in the dominant type of instability and transition mode rather than by a change in the separation bubble physical size. The end of transition switches from point 1 on the curve corresponding to the attached flow to point 4 on the curve corresponding to the separated flow. This implies a change of the dominant instability mode that induces the onset of transition from the TS instability to the KH instability.

Based on the correlations developed above, Fig. 14 presents the

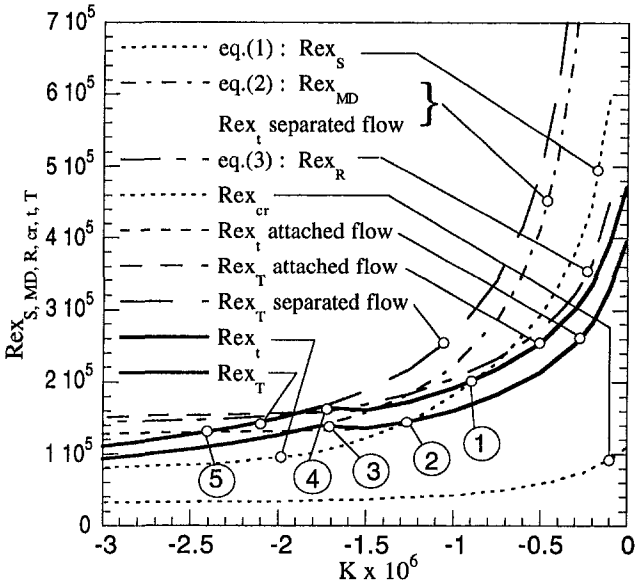

Fig. 13 Hypothetical separated-flow transition process in constant-K flow

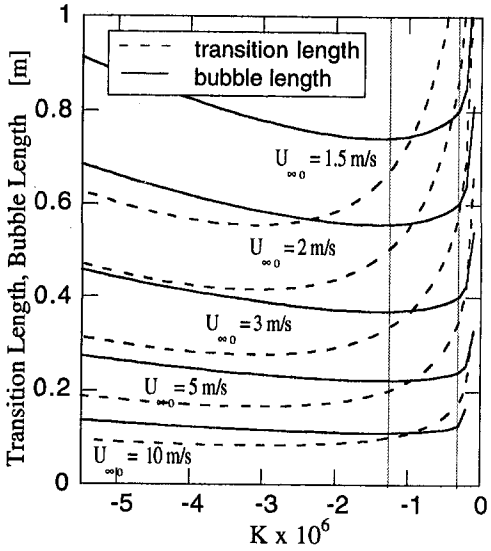

Fig. 14 Separation bubble length and separated flow transition length for various inlet free-stream velocities in constant-K flow conditions

dependence of the separation bubble length and of the transition length on the adverse pressure gradient and the inlet free-stream velocity, $U_{\infty 0}$, for a constant-K flow. For a given K and $U_{\infty 0}$, the separation point x_S can be determined from Eq. (1): $x_S = \nu Re_{xS}/U_\infty$; and x_R can be determined using Eq. (3) as $x_R = \nu Re_{xR}/U_\infty$. The bubble length $(x_R - x_S)$ in the transitional separation mode decreases until the conditions for laminar separation mode are met ($Re_{xS} < 4.5 \times 10^5$; $K_S < -0.3 \times 10^{-6}$).

When the flow is laminar at separation, the rate of decrease in bubble length diminishes. Once the conditions for laminar separation/long bubble mode are satisfied ($Re_{xS} < 2.05 \times 10^5$; $K_S < -1.3 \times 10^{-6}$) there is a steady increase in the bubble length as the adverse pressure gradient increases or the free-stream velocity reduces. A K value of about -1.3×10^{-6} can be associated with the bursting phenomenon.

For transitional separation, the transition length monotonically decreases as the adverse pressure gradient increases. However, for the laminar short bubbles and incipient long bubbles, there is a milder decrease of transition length with increasing the adverse pressure gradient. As shown in Fig. 14, the transition length increases for the laminar separation long bubbles when K becomes less (or more negative) than -2.5×10^{-6}.

This trend is confirmed by the experimental observations; however, the previous models predict only a monotonic decrease with the increase of the adverse pressure gradient. For very strong adverse pressure gradients, the rate of growth for bubble length is higher than the rate of growth of transition length, so, for long bubbles the transition will end in the detached shear layer. This aspect can also be seen to the left of point 5 in Fig. 13.

Conclusions

This paper presented an improved approach for analyzing the transition process in separated boundary layer. New parameters that are necessary in describing and classifying the various modes of separated-flow transition were introduced. Three primary separated-flow transition modes were positively distinguished.

(*a*) The transitional *separation mode* has the start of transition upstream of the separation point ($Re_{xt} < Re_{xS}$) and develops mostly as natural transition; the addition of inflectional KH instability and the near-wall fluid ejection shortens the transition length.

Besides the typical ejection of the secondary vortex, the shedding of the primary vortex usually occurs. In this mode, the maximum rms velocity fluctuation occurs in the separated shear layer at the maximum displacement location ($Re_{xu'max} = Re_{xMD}$).

The transitional separation mode takes place at high separation Reynolds number and low adverse pressure gradient: $K_S > -0.3 \times 10^{-6}$; $Re_{xS} > 4.5 \times 10^5$ and $Re_{\delta 2S} > 320$.

(*b*) The *laminar separation/short bubble mode* of transition has the onset of transition induced downstream of the separation point ($Re_{xt} = Re_{xMD} > Re_{xS}$) by inflectional instability and near-wall fluid ejection. The strong shedding of the primary vortex is the dominant feature of this mode of transition. The laminar short bubble mode is characterized by a quick transition completion and the maximum rms velocity fluctuation occurs in the reattachment region ($Re_{xu'max} = Re_{xR}$). It occurs at moderate separation Reynolds number and mild adverse pressure gradient, and $240 < Re_{\delta 2S} < 320$.

(*c*) The *laminar separation/long bubble mode* of transition has the onset of transition also induced downstream of the separation point ($Re_{xt} = Re_{xMD} > Re_{xS}$) by inflectional instability and near-wall fluid ejection. The primary vortex remains in place, developing in a second extended near-wall region of slow moving fluid. The maximum rms velocity fluctuation occurs in the first reattachment region ($Re_{xu'max} = Re_{xR1}$), the transition completion is delayed and no vortex shedding is observed. The laminar long bubble mode occurs at low separation Reynolds number and strong adverse pressure gradient: $K_S < -1.3 \times 10^{-6}$; $Re_{xS} < 2.05 \times 10^5$ and $Re_{\delta 2S} < 240$. Passing from one mode to another ($Re_{xS} < Re_{xt} < Re_{xMD}$) takes place continuously through a succession of intermediate stages.

A new empirical prediction model capable of determining the general separated flow characteristics, the separated-flow transition mode, the onset and length of transition was developed. The location of maximum bubble elevation (x_{MD}) has been discovered to be the key parameter in correlating the separated flow behavior to the transition process. Correlations for maximum displacement and reattachment locations in terms of conditions at separation were developed. At separation both Re_x and $Re_{\delta 2}$ experimental data correlated well however, downstream of the separation point, the data were better correlated by K and the distance Reynolds number Re_x than by $\Lambda_{\delta 2}$ and $Re_{\delta 2}$ or $Re_{\delta 1}$. This was explained not only by the reduced uncertainty in determining Re_x but also by the inviscid nature of KH instability, which requires a certain length of the separated shear layer ($x_{MD} - x_S$) to develop, regardless of the presence of the wall. The integral length scales δ_1 and δ_2 are direct results of the viscous effects; therefore, they are less appropriate length scales for correlating separated flows downstream of the separation point, when KH instability sets in.

A methodology for predicting the separated-flow transition and the separated flow parameters was proposed. The onset of transition must be determined differently for transition modes because they are induced by different instability mechanisms. The conditions at separation can be used to describe the separated flow behavior but they are inappropriate for predicting transition, especially when transition starts upstream of the separation point. The simple semiempirical method developed in the present study is appropriate for predicting some of the separated-flow transition properties over flat plates. Extension to airfoils requires caution.

Acknowledgments

The research was partially sponsored by the Air Force Office of Scientific Research (Grant No. F49620-94-1-0126).

References

Brendel, M., and Mueller, T. J., 1987, "Boundary Layer Measurements on an Airfoil at Low Reynolds Numbers," AIAA Paper No. 87-0495.

Fitzgerald, E. G., and Mueller, T. J., 1989, "Measurements in a Separation Bubble on an Airfoil Using Laser Velocimetry," *AIAA J.*, 28 (4), 584–592.

Gaster, M., 1967, "The Structure and Behavior of Separation Bubble," NPL Reports and Memoranda No. 3595.

Gleyzes, C., Cousteix, J., and Bonnet, J. L., 1980, "Flow Visualization of Leading Edge Separation Bubbles," *International Symposium of Flow Visualization*, Bochum, 1979, pp. 198–203.

Hatman, A., 1997, "Laminar–Turbulent Transition in Separated Boundary Layers," Ph.D. Dissertation, Department of Mechanical Engineering, Clemson University, Clemson, SC.

Hatman, A., and Wang, T., 1998a, "Separated-Flow Transition, Part 1—Experimental Methodology," ASME Paper No. 98-GT-461.

Hatman, A., and Wang, T., 1998b, "Separated-Flow Transition, Part 2—Experimental Results," ASME Paper No. 98-GT-462.

Hatman, A., and Wang, T., 1998c, "Separated-Flow Transition, Part 3—Primary Modes and Vortex Dynamics," ASME Paper No. 98-GT-463.

Hazarika, B. K., and Hirsch, C., 1997, "Transition Over C4 Leading Edge and Measurement of Intermittency Factor Using PDF of Hot-Wire Signal," ASME JOURNAL OF TURBOMACHINERY, Vol. 119, pp. 412–425.

Hoheisel, H., et al., 1984, "A Comparison of Laser-Doppler Anemometry and Probe Measurements Within the Boundary Layer of an Airfoil at Subsonic Flow," *Laser Anemometry in Fluid Mechanics—II, Selected Papers from 2nd International Symposium on Applications of Laser Anemometry to Fluid Mechanics*, Lisbon, Portugal.

Horton, H. P., 1968, "A Semi-Empirical Theory for the Growth and Bursting of Laminar Separation Bubbles," Aeronautical Research Council, CP-1073.

Kuan, C. L., and Wang, T., 1990, "Investigation of the Intermittent Behavior of Transitional Boundary Layer Using a Conditional Averaging technique," *Experimental Thermal and Fluid Science*, Vol. 3, pp. 157–173.

Kwon, O. K., and Pletcher, R. H., 1979, "Prediction of Incompressible Separated Boundary Layers Including Viscous-Inviscid Interaction," ASME *Journal of Fluids Engineering*, Vol. 101, pp. 466–472.

Malkiel, E., and Mayle, R. E., 1996, "Transition in a Separation Bubble," ASME JOURNAL OF TURBOMACHINERY, Vol. 118, pp. 752–759.

Mayle, R. E., 1991, "The Role of Laminar–Turbulent Transition in Gas Turbine Engines," ASME JOURNAL OF TURBOMACHINERY, Vol. 113, pp. 509–537.

Mislevy, S. P., and Wang, T., 1996, "The Effects of Adverse Pressure Gradients on Momentum and Thermal Structures in Transitional Boundary Layers; Part 1—Mean Quantities, Part 2; Fluctuating Quantities," ASME JOURNAL OF TURBOMACHINERY, Vol. 118, pp. 717–736.

Morkovin, M. V., 1991, "Panoramic view of changes in vorticity distribution in transition instabilities and turbulence," *Instability, Transition and Turbulence*, Hussaini & Kumar, eds., pp. 1–12.

Roberts, W. B., 1980, "Calculation of Laminar Separation Bubbles and Their Effect on Airfoil Performance," *AIAA J.*, Vol. 18.

Schmidt, G. S., and Mueller, T. J., 1989, "Analysis of Low Reynolds Number Separation Bubbles Using Semi-empirical Methods," *AIAA J.*, 27 (8), 993–1001.

Tani, I., 1964, "Low Speed Flows Involving Bubble Separations," *Progress in Aeronautical Sciences*, Vol. 5, pp. 70–104.

van Ingen, J. L., 1977, "On the Calculation of Laminar Separation Bubbles in Two Dimensional Incompressible Flow," AGARD, CP 168, No. 11.

Walker, G. J., Subroto, P. H., and Platzer, M. F., 1988, "Transition Modeling Effects and Viscous/Inviscid Interaction Analysis of Low Reynolds Number Airfoil Flows Involving Laminar Separation Bubbles," ASME Paper No. 88-GT-32.

Walker, G. J., 1989, "Modeling of Transitional Flow in Laminar Separation Bubbles," *Proc. 9th International Symposium on Air Breathing Engines*, Athens, pp. 539–548.

Walker, G. J., 1993, "The Role of Laminar–Turbulent Transition in Gas Turbine Engines: A Discussion," ASME JOURNAL OF TURBOMACHINERY, Vol. 115, pp. 207–217.

Young, A. D., and Horton, H. P., 1966, "Some Results of Investigations of Separation Bubbles," AGARD CP 4, pp. 779–811.

Zhou, D., and Wang, T., 1992, "Laminar Boundary Layer Flow and Heat Transfer With Favorable Pressure Gradient at Constant K Values," ASME Paper No. 92-GT-246.

Numerical Simulation of Impeller–Volute Interaction in Centrifugal Compressors

K. Hillewaert

R. A. Van den Braembussche

von Karman Institute for Fluid Dynamics, St-Genesius-Rode, Belgium

A numerical procedure to predict the impeller–volute interaction in a single-stage centrifugal compressor is presented. The method couples a three-dimensional unsteady flow calculation in the impeller with a three-dimensional time-averaged flow calculation in the volute through an iterative updating of the boundary conditions on the interface of both calculation domains. The method has been used to calculate the flow in a compressor with an external volute at off-design operation. Computed circumferential variations of flow angles, total temperature, and pressure are shown and compared with measurements. The good agreement between the predictions and measurements confirms the validity of the approach.

Introduction

The flow leaving the impeller of a single-stage centrifugal compressor is often collected by a volute (Fig. 1). The nonaxisymmetry of this component results in a circumferential distortion of the impeller-outlet/volute-inlet flow of which the amplitude increases with increasing deviation of the volute inlet flow angle from the design value.

Any circumferential variation of the flow conditions at volute inlet constitutes time-varying outlet conditions for the rotating impeller. It results in unsteady impeller flow, which in turn modifies the volute inlet flow conditions. Nonuniformities in the impeller outlet relative flow are at the origin of time-dependent variations of the volute flow.

A correct simulation of this strong interaction therefore requires the simultaneous solution of the three-dimensional unsteady Navier–Stokes equations in both the impeller and volute. This, however, is not feasible at present because of the excessive storage and computing time required. Simplifying assumptions cannot be avoided.

Models that have been proposed up to now make two-dimensional quasi-steady calculations in both the impeller and volute (Miner et al., 1992), or two-dimensional unsteady potential flow calculations (Morfiadakis et al., 1991; Badie et al., 1994), three-dimensional but quasi-steady Navier–Stokes calculations (Chen and Liaw, 1997; Flathers and Bache, 1996) or unsteady but two-dimensional Navier–Stokes calculations (Croba, 1993).

Previous experiments and calculations (Sideris and Van den Braembussche, 1989; Fatsis et al., 1997) have shown that this type of interaction is strongly influenced by wave propagation in the impeller. The three-dimensional unsteady impeller flow is mainly dominated by inertial forces and to a lesser extent by viscous forces. This justifies our preference for an unsteady inviscid solver over a steady viscous solver. This simplification results in an affordable computer time and gives relevant results for most industrial compressors of which the impeller is not heavily loaded and flow separation is limited.

The unsteadiness of the flow in the volute is a consequence of the pitchwise variation of the flow at the outlet of the rotating impeller. This unsteadiness, however, is confined to the vicinity of the impeller exit because of the rapid mixing of the blade to blade flow variations in the vaneless diffuser (Dean and Senoo, 1960). Furthermore, this distortion decreases with increasing number of blades, and disappears even completely in the hypothetical case of an impeller with an infinite number of blades. Because of these arguments, it was concluded that only a small error was made by neglecting the flow unsteadiness in the volute. This resulted in a further reduction of computation time so that it becomes feasible to use this model also for industrial applications.

The present model combines a three-dimensional inviscid but unsteady solver for the impeller with a three-dimensional steady (or time-averaged) volute flow solver. The purpose is not to predict performance, but the circumferential distortion of the volute flow, the unsteady periodic blade loading, and the resulting radial force on the impeller shaft.

The first part of this paper describes the procedure to couple the unsteady three-dimensional impeller flow calculation with the time-averaged three-dimensional volute flow calculation such that the calculated time-averaged impeller and volute flow match one another on the interface between the calculation domains.

The second part shows the results that have been obtained on an impeller–volute combination, typical for geared compressors. The convergence and accuracy of the method are discussed and illustrated by comparisons of the calculated distributions of P, P^o, T^o, and α with measured values.

Numerical Procedure

Volute and impeller computations are alternated and coupled on a common boundary halfway between the impeller outlet and volute inlet. The boundary conditions on the outlet of the impeller and inlet of the volute computational domain are updated iteratively until the local time-averaged quantities are the same in both calculations.

Volute Solver. The volute solver used in present study is the one developed by Ayder et al. (1994) and calculates the three-dimensional steady flow in a vaneless diffuser and volute. The effects of friction are accounted for by extra forces on the diffuser and volute walls and correction terms for the energy equation. The discretization is central on a cell-vertex mesh with second and fourth-order dissipation. A sufficient amount of second-order dissipation is required to guarantee a correct description of the vortices. The update of the unknown in a given mesh point is calculated from the flux balance on a super-cell composed of all mesh cells surrounding the point.

Calculations are normally made for prescribed inlet conditions ($P_2^0(\theta)$, $T_2^0(\theta)$, $V_u(\theta)$, $V_z(\theta)$). The outlet static pressure is fixed in one point of the outlet section and calculated in the other points by extrapolation of the values computed on the next-to-last section.

Contributed by the International gas Turbine Institute and presented at the 43rd International Gas Turbine and Aeroengine Congress and Exhibition, Stockholm, Sweden, June 2–5, 1998. Manuscript received by the International Gas Turbine Institute February 1998. Paper No. 98-GT-244. Associate Technical Editor: R. E. Kielb.

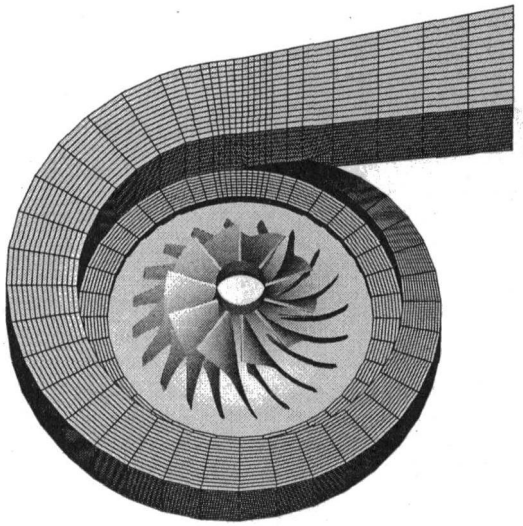

Fig. 1 Compressor geometry

Impeller Solver. The unsteady impeller solver is the one developed by Fatsis et al. (1997). It calculates the three-dimensional inviscid time-dependent flow in the impeller. The flow variables are stored in the center of the cell faces perpendicular to the streamwise direction. The flux balance is expressed on a super-cell, composed of the two mesh cells adjacent to the storage point. As in the volute calculations, the time integration is done by a simplified four-step Runge–Kutta scheme, which allows for a minimal storage, good stability, and a second-order accuracy in time.

Only average values of P^o, T^o, and flow angles are prescribed at the inlet. Nonreflecting boundary conditions allow for circumferential and time-dependent flow variations due to upstream propagation of disturbances.

The outlet boundary is placed sufficiently far from the blades so that the flow on that plane can be assumed to be time-independent in the absolute frame of reference.

In order to limit the memory and CPU required to perform the calculations, the calculation domain of the impeller is restricted to one or two blade passages. As the outlet pressure of such a passage changes with circumferential position, the classical periodicity conditions can no longer be applied. They have been replaced by phase-lagged periodicity conditions in which the flow quantities near the "periodic" boundaries are stored at each time step and applied as a boundary condition for the opposite side, taking the appropriate time delay into account.

The maximum allowable time step from stability considerations, as defined by the CFL number, is very small and the number of time steps needed for a full impeller rotation ($\tau/\Delta t$) is very large. Storing the flow parameters on the periodic boundaries at every circumferential position corresponding to each time step, would take too much memory. The boundary conditions are therefore kept constant during the number of timesteps corresponding to the rotation of the impeller over one grid spacing.

Interface Boundary Conditions. Assuming that the flow in the diffuser is subsonic and radially outward, one has to impose one boundary condition at the impeller outlet and four at the volute inlet. They do not need to be the same as the ones used in the uncoupled solvers as long as they are independent and comply with the characteristic theory.

At the impeller outlet boundary, the circumferential and spanwise variation of the static pressure resulting from the volute calculation is imposed. The volute calculation method predicts the pressure in the vertices of the volute grid, so that an interpolation is required to define the pressure in the center of the cell faces as required by the scheme of the impeller calculations.

On the volute inlet boundary, the spatial variation of four time-averaged flow quantities must be imposed. It has been decided to impose mass flux, tangential and axial momentum flux and energy flux locally through the impeller outlet plane (common boundary) because these quantities can be time averaged in a consistent and conservative way. Together with static pressure (imposed on the same plane as an outlet boundary condition for the impeller calculation) these fluxes fully determine the flow variables.

The variables used in following calculation are explained in Figs. 2 and 3, together with a schematic presentation of the impeller and volute grid. Only the region near the tongue is shown for the volute grid, and both grids have been separated radially for reasons of clarity. In reality, they are adjacent to one another and their boundaries are sliding over each other at the interface where the boundary conditions are imposed.

Because of the periodicity of the impeller flow, the time-averaging can be limited to a period τ/N corresponding to the passing of one blade passage at a given point in the volute. The four time-averaged fluxes F through each cell face k of the volute inlet plane (between θ_k and θ_{k+1} in Fig. 2) are defined by

$$\frac{N}{\tau}\int_0^{\tau/N}\int_{\theta_k}^{\theta_{k+1}} F(\theta, t)\,d\theta dt \tag{1}$$

The flux $F(\theta, t)$ is related to the flux $\tilde{F}(\tilde{\theta}, t)$, at the position $\tilde{\theta}$ at the impeller exit, by means of the impeller rotational speed ω (Fig. 2):

$$F(\theta, t) = \tilde{F}(\tilde{\theta}, t) = \tilde{F}(\theta - \omega t, t) \tag{2}$$

Nomenclature

a = speed of sound
f = frequency of pressure perturbation
F = general flux function
J = number of grid spacings along the impeller circumference
L = channel length
m = mass flow
N = number of impeller full blades
P = pressure
r = radial position
S_r = acoustic Strouhal number
T = temperature
t = time
V = velocity
α = absolute flow angle
β = relative flow angle
θ = angular position
τ = period of rotation
ω = speed of rotation

Subscripts

av = average value
des = design value
j = circumferential position on the impeller grid
k = circumferential position on the volute grid
max = maximum value
min = minimum value
r = radial component
ref = reference value
u = tangential component
z = axial component

Superscripts

n = value after the rotation over n grid spacings
o = stagnation values
$\tilde{}$ = relative to impeller

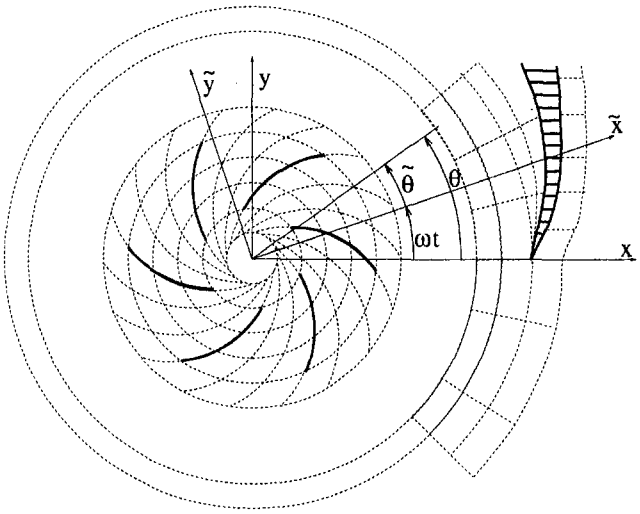

Fig. 2 Definition of circumferential position in the impeller and volute

When calculating the integral (1) one assumes that the flux $\tilde{F}(\tilde{\theta}, t)$ is constant over each boundary cell face j of the impeller (defined by $\tilde{\theta}_j$ and $\tilde{\theta}_{j+1}$) during the time t^n to t^{n+1} needed to rotate the impeller over one grid spacing (Fig. 3). Its value is calculated as the average flux $\bar{F}_j^n$ over the intermediate time steps.

The flux function $\tilde{F}(\tilde{\theta}, t)$ is then approximated by:

$$\tilde{F}^n(\tilde{\theta}) = \sum_{j=1}^{J} \bar{F}_j^n A_j(\tilde{\theta}) \tag{3}$$

for $t \in [t^n, t^{n+1}]$, where $A_j(\tilde{\theta}) = 1$ if $\tilde{\theta}_j \le \tilde{\theta} \le \tilde{\theta}_{j+1}$ and zero for all other values of $\tilde{\theta}$.

This simplified flux function corresponds to a rotating block wave and can be integrated analytically. Its shape changes from time step to time step.

Once the fluxes through the cell faces of the impeller exit are known, they can be updated at the cell vertices of the volute grid. This is done by a linear redistribution of the fluxes through the neighboring cells. It results in flux smoothing and is conservative only for fluxes that are linearly dependent on the flow variables. However, as will be shown later, the corresponding error is negligible.

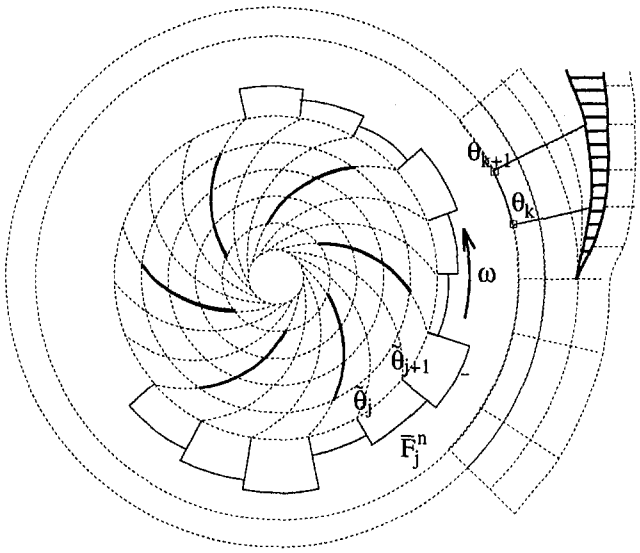

Fig. 3 Simplified flux function $\tilde{F}_n(\tilde{\theta})$

Iterative Coupling Procedure. The coupling procedure starts with a steady impeller calculation for a circumferentially constant outlet static pressure, which is adjusted until the desired mass flow is obtained. The resulting values of average P^o, T^o, tangential and axial velocity at the outlet boundary are imposed as inlet conditions for a first volute calculation in which the outlet pressure is adjusted until the mass flow equals the one in the impeller.

At off-design mass flow, the volute predicts a circumferential variation of the inlet static pressure, which is then imposed as outlet condition for a first approximation of the distorted flow in the impeller. In order to avoid divergence of the impeller calculation, this pressure distortion is underrelaxed. Experience has shown that about six impeller rotations are needed before a periodic impeller flow corresponding to the imposed pressure distortion is obtained.

This calculation provides a first guess of the circumferential variation of the fluxes at impeller exit, which are then imposed as new inlet boundary conditions for a next approximation of the flow in the volute. This in turn provides an update of the volute inlet (impeller outlet) static pressure distortion. The boundary conditions at the impeller inlet and the volute outlet are kept constant during the whole procedure.

This sequence of impeller and volute calculations, with an update of the outlet and inlet conditions, is repeated until the static pressure distribution on the interface remains unchanged. As a consequence also the other time-averaged flow variables will be the same.

However, the static pressure rise over the impeller or volute can be influenced by the circumferential pressure distortion. This means that the average pressure on the interface can be different from the one at the first iteration. For the same reasons it is possible that the mass flow at a given overall pressure ratio has changed during the iterative procedure and the mass flow at convergence can therefore be different from the initial one. This makes it difficult to make calculations exactly at a prescribed mass flow. The boundary conditions on the interface, however, guarantee the same mass flow in the compressor as in the volute.

Results

This procedure has been tested by analyzing the flow in an impeller/volute combination typical for industrial geared compressors and comparing the results with experimental data. The impeller has 10 full and 10 splitter blades (Fig. 1) with 30 deg backward lean at the exit. The vaneless diffuser has a radius ratio of 1.5 and an outlet over inlet width ratio of 0.84. It is followed by an external volute designed for zero pressure distortion at impeller optimum mass flow.

Overall performance (Fig. 4) and detailed flow measurements have been made at the "Institut für Strömungsmaschinen" of the University of Hannover. A more detailed description of the com-

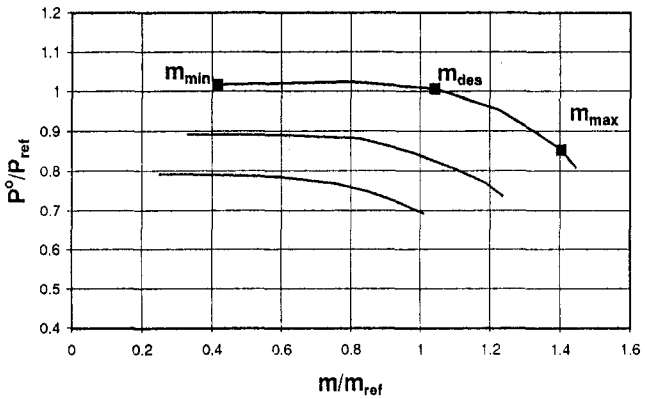

Fig. 4 Compressor overall performances and measurement points

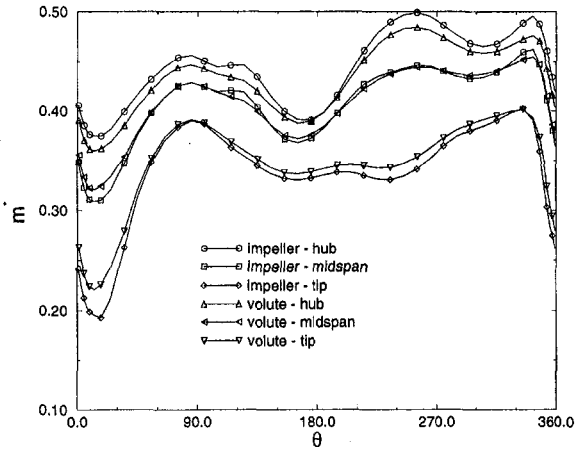

Fig. 5 Mass flux at hub, midspan, and tip of the vaneless diffuser outlet

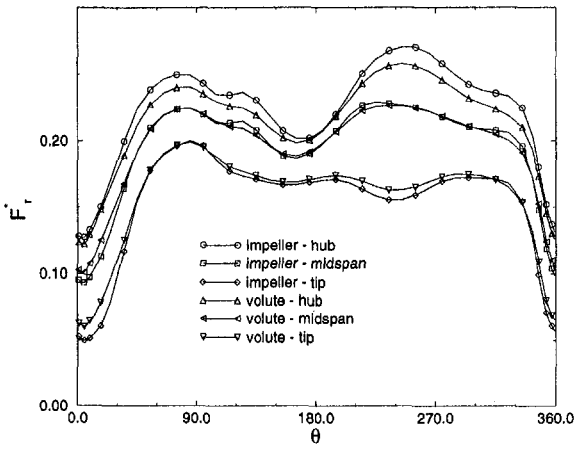

Fig. 6 Radial momentum flux at hub, midspan, and tip of the vaneless diffuser outlet

pressor geometry and performance is given by Hagelstein et al. (1997).

The circumferential static pressure distribution at the vaneless diffuser inlet and outlet has been measured at 14,000 rpm for nine different mass flows ranging from surge to choking. In addition, the circumferential and spanwise variation of the total pressure, total temperature, and flow angles at vaneless diffuser outlet are measured at m_{max}, m_{des}, and m_{min} indicated on Fig. 4. The circumferential distortion is almost zero at m_{des}, confirming the correct layout of the geometry by means of the volute flow solver. Combined impeller–volute calculations have been made for a mass flow near m_{max} where the circumferential flow distortion is larger than at m_{min}.

Because of stability problems in the volute calculations, related to a large separation of the flow at the volute tongue, it was not possible to do the calculations at exactly m_{max} for which detailed flow measurements are available. They have been made for a 6 percent lower mass flow where only the circumferential static pressure distortion is available. One will therefore compare the amplitude of the variations and not the absolute values of T^o, P^o, and α.

The whole calculation procedure, using 35,000 grid points per impeller passage and 25,000 grid points in the diffuser and volute takes about 48 hr of CPU on an Alpha dec 500 5/500.

Convergence of the Method. Figure 5 shows a comparison between the circumferential distribution of nondimensionalized mass flux m^* at three spanwise positions on the interface boundary as they result from the impeller and volute calculation after full convergence of the procedure.

One observes an almost perfect agreement between both calculations at midspan, indicating a good convergence of the procedure. As the mass flux is one of the four fluxes imposed at the volute inlet, the differences between the distributions calculated by impeller and volute near the hub and tip wall can only be due to the interpolation procedure described in the previous section. This small error, resulting from the redistribution of fluxes in case of a nonnegligible hub-to-tip flow variation, could be further decreased by an increase of the number of grid points over the span. However, it is felt that this will increase the required computer time without any substantial increase in accuracy.

Figure 6 shows the nondimensional radial momentum flux F_r computed by the impeller and the volute solver as a function of the local primitive variables at the interface. Since the radial momentum flux was not imposed as a boundary condition, one can conclude that the coupling procedure assures the correct conservation of other fluxes also when it is not explicitly imposed.

Circumferential Variation of Flow Variables in the Diffuser. The instantaneous pressure field on the impeller hub surface together with the steady pressure field on the volute hub wall is shown in Fig. 7. One does not see any change of the pressure contours when going from the impeller to the volute calculation domain. Large variations, however, are observed at the diffuser outlet because of the sudden increase of the width at the volute inlet. The largest pressure distortion is at the volute tongue because of a very large incidence. This creates a separation-type flow on the tongue suction side, which is, however, strongly influenced by the vortical flow in the volute, as illustrated by the streamlines on the hub wall (Fig. 8) and over a cross section downstream of the throat (Fig. 9).

Figures 10, 11, 12, and 13 show a comparison between the calculated and measured circumferential variation of P, P^o, T^o, and α at midspan. Open symbols show calculated values, respectively, at diffuser inlet (squares) and diffuser outlet (triangles). Measured values are depicted by the corresponding filled symbols.

The static pressure distribution shown on Fig. 10 is measured at vaneless diffuser inlet and outlet. Besides a slight overestimation of the impeller of the circumferential variation, the method correctly predicts the shape of the variation and the pressure rise from diffuser inlet to outlet. Of interest is also the very small phase shift between the inlet and outlet distribution. This results from the fact that the static pressure is mainly determined by the radial equilibrium of pressure and forces.

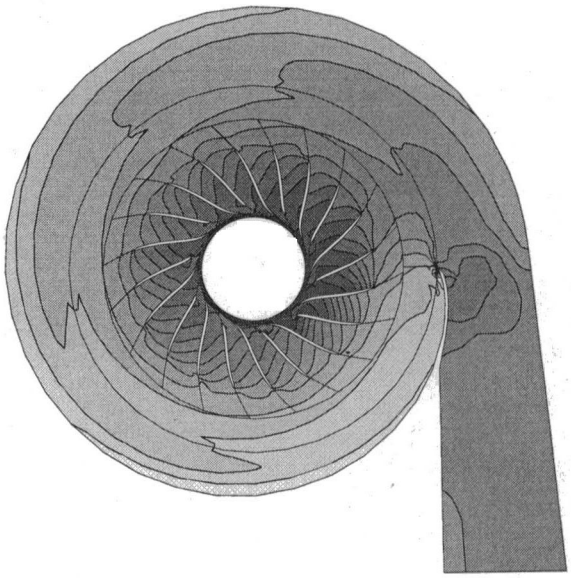

Fig. 7 Instantaneous pressure distribution on impeller, vaneless diffuser, and volute hub wall

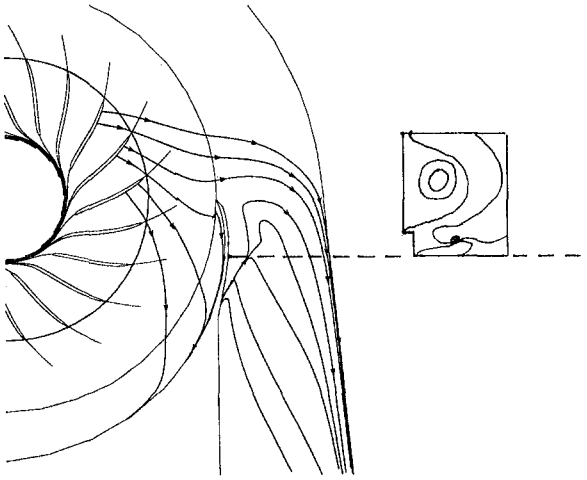

Fig. 8 Stream traces near volute tongue

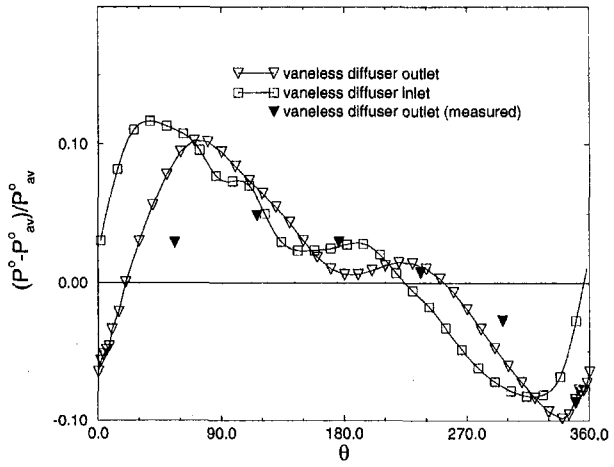

Fig. 11 Total pressure variation

The total pressure and temperature (Figs. 11 and 12) show a much more wavy variation with two periods along the circumference and a smoother variation toward the vaneless diffuser outlet where a good agreement with all measurements is observed. A more detailed comparison requires measurements in more circumferential positions which unfortunately are not available.

The wavy variations are very similar to those observed also in Figs. 5 and 6. The waves are very strong at the hub side where a longer blade length corresponds to an acoustic Strouhal number $S_r \approx 0.25$ ($S_r = f \cdot L/a$). It has been shown (Fatsis et al., 1997) that these variations are due to pressure waves generated in the impeller by the sudden pressure rise at the volute tongue and reflected at the impeller inlet. Acoustic Strouhal number of 0.25 allow waves traveling twice back and forth during each rotation, which explains the two wave variation of P^o and T^o per rotation. It also means that

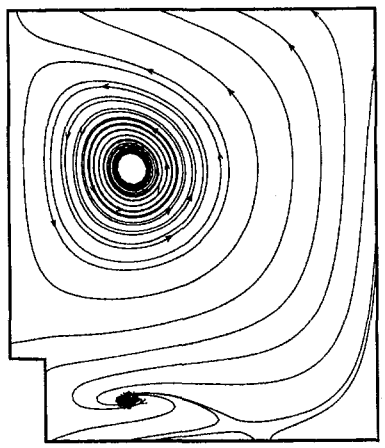

Fig. 9 Streamtraces in a cross section downstream of the volute tongue

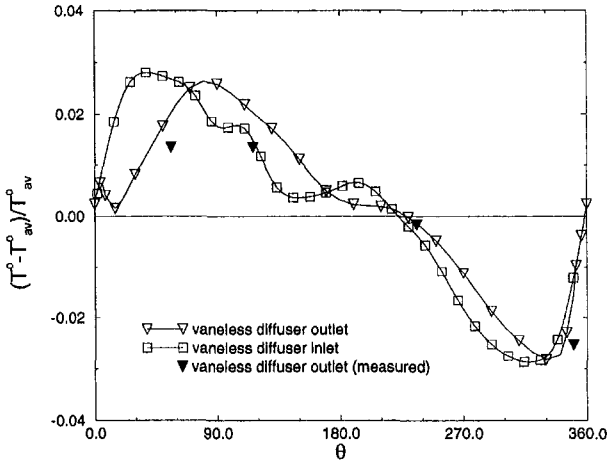

Fig. 12 Total temperature variation

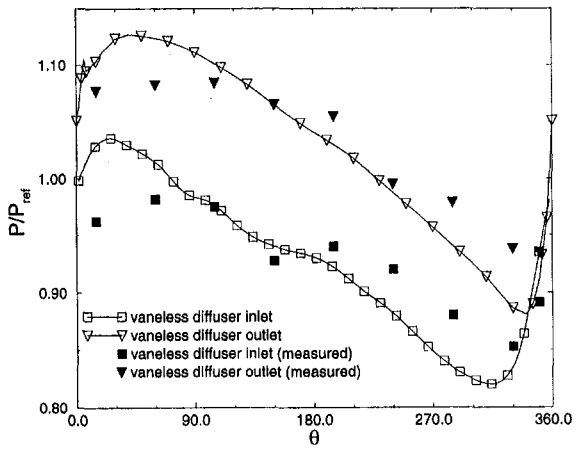

Fig. 10 Static pressure variation

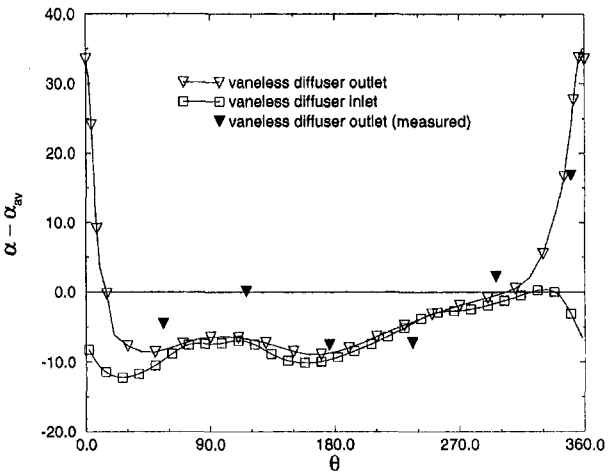

Fig. 13 Absolute flow angle variation

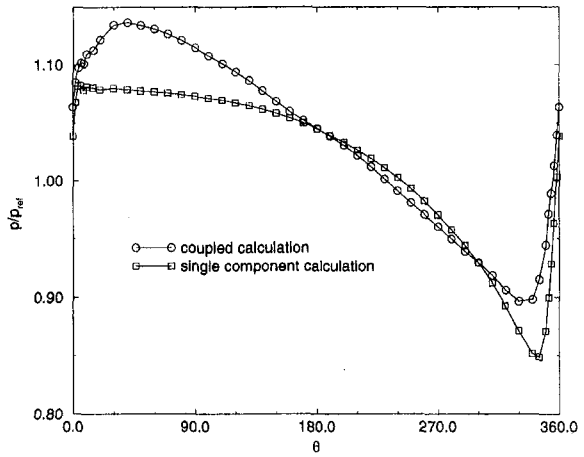

Fig. 14 Comparison of calculated pressure distortions

the blade forces change twice during each rotation. This important characteristic of the interaction cannot be predicted by quasi-steady flow calculations in the impeller.

The much weaker wave with four periods per rotation, visible only at the diffuser inlet, results from the reflection of pressure waves on the leading edge plane of the splitter vanes.

One also notices a phase shift of the maximum and minimum value between the diffuser inlet and outlet. This is the consequence of the nonzero tangential velocity component because P^o and T^o are flow properties that are convected with the flow. Except for a reduction of the average total pressure, because of diffuser losses, one observes no reduction in distortion amplitude from diffuser outlet to inlet. This allows the conclusion that this steady distortion does not mix out in the diffuser, contrarily to the rapid mixing of the rotating distortions at the impeller exit.

The calculated absolute flow angle at diffuser inlet and outlet are shown on Fig. 13. The flow pattern, shown in Fig. 8, gives rise to very large velocity variations with strong pressure gradients near the volute tongue. Large local variations of the flow angle do not spread upstream in the diffuser and the calculated variations at the impeller exit are rather small. The predicted values at diffuser exit show the same trend as the measured ones. Because of the large attenuation of the distortion between inlet and outlet, it is not possible to make any conclusion about the circumferential phase shift.

Impeller–Volute Interaction. The influence of the impeller–volute interaction on the circumferential distortion of the static pressure is evaluated by comparing the results of a coupled calculation with those obtained from a simple volute calculation with constant P^o, T^o, and flow angles at the inlet. The circumferential static pressure variation resulting from both calculations are compared in Fig. 14.

For reasons explained previously, the average static pressure of the coupled calculation is slightly higher than the one obtained from the simple calculation.

The smoother pressure variation, observed in the coupled calculation is due to:

- the delay between the static pressure rise at the impeller exit and the subsequent total pressure rise resulting from impeller reaction. This can be deduced from a comparison between Figs. 10 and 11.
- a phase shift between diffuser inlet and outlet total pressure due to the convection of the stagnation quantities with the flow as shown in Figs. 11 and 12.

Any change in total pressure has a direct effect on the static pressure. The wavy variation of the total pressure over the circumference also results in a more linear variation of the static pressure in the coupled calculation.

Conclusions

One can conclude that the numerical procedure presented in this paper is a valuable tool to study the strong interaction between a radial impeller and volute.

In spite of the simplifications introduced in the model, needed to reach an affordable computer time, the basic features of the interaction are correctly predicted, as can be concluded from the good agreement between measured and predicted flow variations.

The methods allows a better understanding of:

- the waviness of the circumferential distributions of total pressure and temperature and its relation to the unsteady impeller flow.
- the circumferential phase shift between diffuser inlet and outlet of the total pressure and temperature variation and the small phase shift of the static pressure distribution.

It also explains the more gradual static pressure rise near the tongue as compared to the one obtained from a single volute calculation.

Results of these calculations could further be used to calculate the time-varying pressure forces on the blades and the extra radial force on the shaft.

Acknowledgments

The authors want to thank the working group "Spiralenströmung" of the "Forschungsverein für Verbrennungskraftmaschinen" (FVV) for making the experimental data available for this study.

References

Ayder, E., Van den Braembussche, R. A., and Brasz, J. J., 1994, "Numerical analysis of the three-dimensional swirling flow in centrifugal compressor volutes," ASME JOURNAL OF TURBOMACHINERY, Vol. 116, pp. 462–468.

Badie, R., Jonker, J. B., and Van den Braembussche, R., 1994, "Finite element calculations and experimental verification of the unsteady potential flow in a centrifugal pump," *International Journal for Numerical Methods in Fluids*, Vol. 19, No. 12, pp. 1083–1102.

Chen, S. H., and Liaw, L.-F., 1997, "The flowfield calculations of a centrifugal pump with volute," ASME Paper No. 97-GT-49.

Croba, D., 1993, "Modélisation de l'écoulement instationaire dans les pompes centrifuges, intéraction roue-volute," PhD. Thesis, Institut National Polytechnique de Grenoble, France.

Dean, R., and Senoo, Y., 1960, "Rotating wakes in vaneless diffusers," ASME *Journal of Basic Engineering*, Vol. 82, No. 3, pp. 563–570.

Fatsis, A., Pierret, S., and Van den Braembussche, R., 1997, "Three-dimensional unsteady flow and forces in centrifugal impellers with circumferential distortion of the outlet static pressure," ASME JOURNAL OF TURBOMACHINERY, Vol. 119, pp. 94–102.

Flathers, B., and Bache, G. E., 1996, "Aerodynamically induced radial forces in a centrifugal gas compressor: Part 2—Computational investigation," ASME Paper No. 96-GT-352.

Hagelstein, D., Van den Braembussche, R., Keiper, R., and Rautenberg, M., 1997, "Experimental investigation of the circumferential static pressure distortion in centrifugal compressor stages," ASME Paper No. 97-GT-50.

Miner, S. M., Flack, R. D., and Allaire, P. E., 1992, "Two-dimensional flow analysis of a laboratory centrifugal pump," ASME JOURNAL OF TURBOMACHINERY, Vol. 114, pp. 333–339.

Morfiadakis, E. E., Voutsinas, S. G., and Papantonis, D. E., 1991, "Unsteady flow calculation in a radial flow centrifugal pump with spiral casing," *International Journal for Numerical Methods in Fluids*, Vol. 12, pp. 895–908.

Sideris, M., and Van den Braembussche, R. A., 1989, "Unsteady flow in centrifugal compressors due to downstream circumferential distortions," ISABE Paper No. 89-7098.

Comparison of Measurement Data at the Impeller Exit of a Centrifugal Compressor Measured With Both Pneumatic and Fast-Response Probes

C. Roduner

P. Köppel

P. Kupferschmied

G. Gyarmathy

Turbomachinery Laboratory,
Institute of Energy Technology,
ETH-Swiss Federal Institute of Technology,
8092 Zurich, Switzerland
http://www.lsm.ethz.ch/

The main goal of these investigations was the refined measurement of unsteady high-speed flow in a centrifugal compressor using the advanced FRAP® fast-response aerodynamic probe system. The present contribution focuses on the impeller exit region and shows critical comparisons between fast-response (time-resolving) and conventional pneumatic probe measurement results. Three probes of identical external geometry (one fast and two pneumatic) were used to perform wall-to-wall traverses close to the impeller exit. The data shown refer to a single running condition near the best point of the stage. The mass flow obtained from different probe measurements and from the standard orifice measurement were compared. Stage work obtained from temperature rise measured with a FRAP® probe and from impeller outlet velocity vectors fields by using Euler's turbine equation are presented. The comparison in terms of velocity magnitude and angle distribution is quite satisfactory, indicating the superior DC measurement capabilities of the fast-response probe system.

Introduction

An extensive measurement campaign in a single-stage centrifugal compressor was performed by using different probe measuring techniques. The campaign focused on the following objectives:

- Test of the in-house developed fast-response aerodynamic probe technology (FRAP®) in a turbomachinery application.
- Time-resolved measurement of the impeller flow at the outlet and at different other positions downstream in a vaned diffuser channel.
- To provide experimental boundary conditions for steady CFD calculations in the vaned diffuser (Casartelli et al., 1999), using in-house developed pneumatic probes.

As reported by several authors (e.g., Traupel, 1958, 1988; Dean and Senoo, 1960; Eckardt, 1975) the flow at the outlet of the impeller is very complex and highly fluctuating. Hot-wire techniques became the standard tool for such investigations (e.g., Dean and Senoo, 1960; Jansen, 1964; Bammert and Rautenberg, 1974) but their use was mostly limited to low-speed compressors. Optical methods (L2F and LDV) proved to be very fruitful in investigating the rotating impeller channels as well as the diffusers (Runstadler and Dolan, 1975; Eckardt, 1976; Krain, 1981). Pressure fluctuations were measured by wall transducers (e.g., Bammert and Rautenberg, 1974; Kämmer and Rautenberg, 1982; Inoue and Cumpsty, 1984), but pressure probes took quite some time to become available (e.g., Eckardt, 1975).

In the centrifugal compressor of the Turbomachinery Laboratory of the ETH, the highly fluctuating flow field caused by a blade passing frequency of 6.5 kHz gives the opportunity for further tests and improvements of both the FRAP® system and the associated measurement concepts. The results of a measurement campaign and the possible interpretation are strongly dependent on the measurement concepts applied. For this reason great care was spent on preparing the campaign. The experience from measurement, data evaluation, and data interpretation influences the measurement concepts.

High accuracy is required not only for the AC part but also for the DC part of the fast-response signal to measure, for example, distributions of the flow quantities at the impeller outlet in both circumferential and axial direction, or the mixing out of *jet and wake* patterns.

In this paper investigations aimed at quantifying the accuracy of the DC part of the fast-response signal are presented. Comparisons of pneumatic with fast-response probes of identical external geometry and with standard orifice measurements are presented and discussed. The investigations presented herein set the basis for further evaluations and interpretations of this extensive campaign.

Test Rig and Instrumentation

The experiments described were performed on a closed-loop test rig using air; see Fig. 1. The centrifugal compressor is a standard industrial stage and is driven by a 440 kW DC motor coupled to a two-stage gear box. The maximum rotational speed of the shaft is limited to 22,000 rpm by the oil seal. The present measurements were made at the near-optimum shaft speed of 17,720 rpm corresponding to Mu = 0.75, where dynamic velocity head values were readily measurable, but the temperature increase was too low to allow accurate efficiency measurements. The flow rate is controlled by a throttle and it is measured by a standard orifice (DIN 1952, 1982). A flow straightener mounted in the suction pipe ensures axial flow at the stage inlet.

During measurements the inlet temperature was held at 24°C and the pressure in the suction pipe was set to 960 mbar.

Figure 2 shows the impeller and diffuser of the opened compressor. It is the configuration used for all measurements described in this paper.

Contributed by the International Gas Turbine Institute and presented at the 43rd International Gas Turbine and Aeroengine Congress and Exhibition, Stockholm, Sweden, June 2–5, 1998. Manuscript received by the International Gas Turbine Institute February 1998. Paper No. 98-GT-241. Associate Technical Editor: R. E. Kielb.

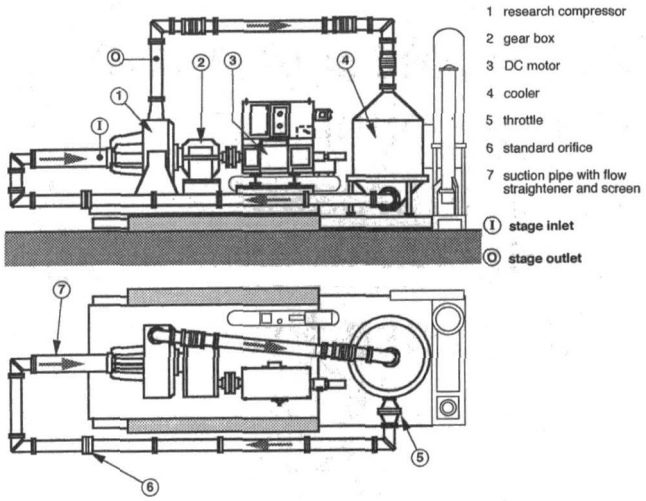

Fig. 1 General view of the centrifugal compressor test rig

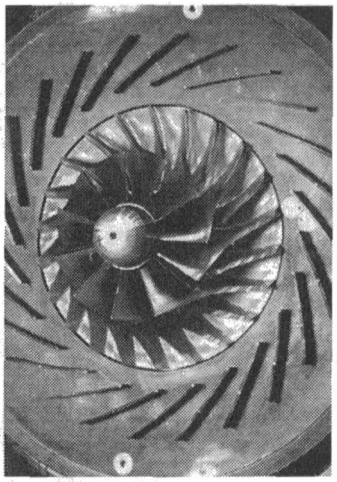

Fig. 2 View of unshrouded impeller and diffuser (configuration: 24 vanes, blade angle 25 deg)

The main data of the unshrouded impeller were:

impeller tip diameter ($2r_2$)	280 mm
full/splitter blades	11/11 (total 22)
exit blade angle	30 deg back lean
exit width b	16.8 mm

The diffuser configuration used for the measurements consists of two parallel walls and 24 prismatical, circular-arc vanes. The leading edge blade angle $\alpha_{B\,\text{vane}}$ of the vanes was set to 25 deg. Additional geometric data of the diffuser are given in Fig. 3.

The radial diffuser is followed by a large toroidal collecting chamber (Fig. 8) providing a virtually uniform circumferential pressure distribution at the impeller outlet (Hunziker, 1993).

The overall performance of the compressor was determined by conventional wall pressure taps and temperature probes in the suction pipe and in the outlet tube. A large number of wall pressure taps are located along the casing contour as well as in the front and the rear diffuser wall. These wall-tap pressure data are measured with a 256-channel pressure data acquisition system. All these data were collected by a μVAX computer.

Measurement System

Aerodynamic Probes. The probes used for these investigations are part of a research project dedicated to the development of a fast-response aerodynamic probe measurement system for turbomachines and other turbulent flows (Gossweiler et al., 1995).

Both pneumatic and fast-response pressure probes used have a similar external geometry. Great care was taken to minimize the probe size. Several probes accommodating one or three piezoresistive pressure sensor chips have been developed, featuring a tip diameter of only 1.8 mm. Due to the size of the miniature sensor chips of only $1.7 \times 0.6 \times 0.15$ mm^3, these are located directly behind the pressure taps (see Fig. 4, and Kupferschmied et al., 1994).

This miniature size reduces static errors due to probe blockage and limits the errors due to dynamic flow effects around the probe tip, which are known to be directly proportional to the probe size (Humm et al., 1995). Also to avoid large errors due to dynamic effects, a circular cylinder geometry has been chosen for the probe tip instead of the wedge shape widely used for conventional pneumatic measurements. All probes have been designed and fabricated in-house.

The miniature piezoresistive pressure sensor chips encapsulated in the probe tip exhibit a pressure sensitivity above 60 mV/bar for an excitation current I_e of only 1 mA. Since the Wheatstone bridge on each chip diaphragm is supplied with constant current, a low-frequency measurement of the diaphragm temperature and thus of the flow temperature is also possible through the temperature sensitivity of the supply voltage U_e.

Nomenclature

A = area
a_a = stage work
b = diffuser width (axial)
C = specific speed
c = velocity
c_p = specific heat at constant pressure
h = enthalpy
I = current
L = length of diffuser vane
M = Mach number
Mu = impeller tip speed Mach number
$\dot{m}$ = mass flow
p_{tot} = total pressure
p_{stat} = static pressure
R = gas constant
r = radius
r = recovery coefficient
T = temperature
T_{stat} = static temperature
T_s = sensor temperature
t = diffuser vane thickness
U = voltage
u = circumferential speed
$\dot{V}$ = flow rate
W = specific speed in the relative frame
z = axial coordinate
α = flow angle (diffuser coordinates)
$\alpha_{B\,\text{vane}}$ = diffuser vane leading edge blade angle
β = flow angle in the relative frame
κ = isentropic coefficient
η° = isentropic efficiency (total-to-total)
ρ = density
φ = flow angle (probe coordinates)
φ = specific flow rate = $\dot{V}_1/(D_2^2 \cdot u_2)$

Subscripts

1 = impeller inlet
2 = impeller outlet
3 = diffuser outlet
A = measurement position in the diffuser
B = diffuser vane leading edge
E = measurement position in the diffuser
e = excitation
I = stage inlet
K = curvature

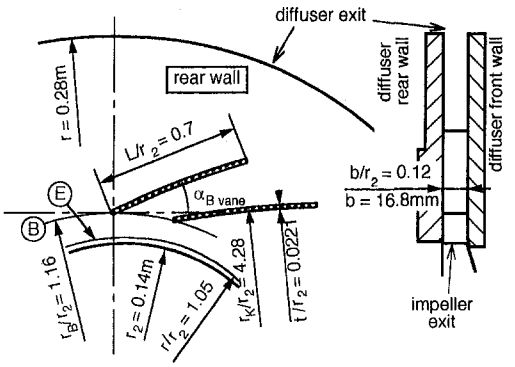

Fig. 3 Sketch of the vaned diffuser

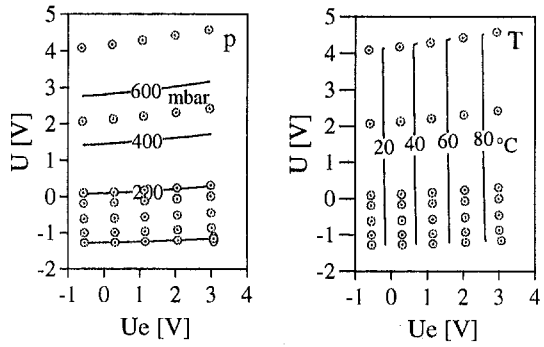

Fig. 5 Sensor pressure and temperature as functions of excitation voltage U_e and signal voltage U shown after signal amplification (sensor operated at constant excitation current)

Due to semi-conductor noise (p-n-junction), the monocrystalline silicon material used for the sensor chip sets a temperature limit for the measurements at about 140°C, which is beyond the level of the application in the test rig.

The sensors are working in a differential pressure mode: A controlled reference pressure is supplied through the probe shaft, and can be varied to more or less match the common pressure level in the turbomachine. The pressure difference can be maintained within a small range (approximately 200 to 500 mbar) so that sensor types with a high-pressure sensitivity can be used. By this means, the pressure signal offset and the gain can be readjusted while the turbomachine is running. This is of great advantage for the accuracy of the DC signal measurement.

Probe Sensor Calibration. Prior to the aerodynamic probe calibration in a reference flow, the sensors of the fast-response probe are calibrated in an automatic facility. The probes are placed in an environmental chamber. The well-controlled static conditions are varied by computer control according to a temperature cycle and at pressure steps suited for the flow conditions expected in the experiment to come. A typical temperature step in the cycle lasts a few hours, and several pressure calibrations take place during this time.

The data collected from each sensor during the cycle comprise the excitation and signal voltages as well as the temperature and pressure levels from a reference equipment. This information is used to model the static behavior of each sensor numerically with pressure and temperature outputs as functions of the excitation and signal voltages as represented in Fig. 5.

This approach renders unnecessary any electronic circuitry otherwise needed to compensate for the thermal shift of the zero-pressure voltage and of the pressure sensitivity of the sensors. It enhances the accuracy by one order of magnitude. All sensor data are stored as second or third-degree polynomial coefficients for the flow data evaluation process.

The sensor calibration facility is also used to characterize the sensor's measurement errors for pressure and temperature, such as thermal drift, hysteresis, and creep. These investigations also provide a feed-back to improve the sensor packaging technique (Gossweiler et al., 1992).

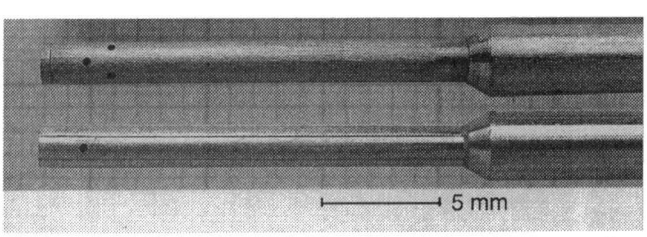

Fig. 4 Tip of a three- and a one-sensor probe C3LS18 and -C1LS18 (tip: ϕ1.8 mm; prismatic shaft: ϕ3, then 6 mm for the rear part)

The dynamic response of the pressure measurement has been investigated in a shock tube. Different geometries of the pneumatic cavity between the flow and the sensor diaphragm have been tested and revealed an eigenfrequency above 90 kHz for this type of probes. This limits the bandwidth to 0–45 kHz.

Aerodynamic Probe Calibration. Both the conventional, pneumatic probes and the fast-response probes have been calibrated under steady flow conditions in a computer-controlled jet calibration facility. The flow angles have been varied between ±30 deg (yaw) and ±10 deg (pitch) in 2 deg steps for Mach numbers ranging from 0.2 to 0.6. The large angular range in yaw is necessary for the data evaluation to cover the fluctuating flow field. Although blockage effects are low in the 100-mm-dia jet, the raw calibration data have been corrected for static pressure influence according to Wyler (1975).

As described in Kupferschmied and Gossweiler (1992), the calibration data have then been transformed into sets of nondimensional coefficients and modeled as coefficients of bivariate polynomials of higher degree to allow an accurate and efficient evaluation of flow measurement data.

Temperature Measurements. Ng and Epstein (1985) and Ruck (1989) reported that the tip of their probes was heating up due to the relatively high current necessary to exploit the built-in sensors. This was detrimental to the sensor's stability, thus making the DC pressure measurement less accurate and a flow temperature measurement impossible. Compared to those miniature probes, the excitation current supplied to each sensor in the FRAP® probes is very low. The self-heating of the probe tip (1.6 K beyond room temperature under still air conditions, and 0.3 K at 4 m/s) can be corrected during the sensor calibration process to have an uncertainty for the absolute temperature level below 0.5°C at low steady flow velocities.

In order to enhance the temperature measurement accuracy for flow velocities corresponding to the application, the recovery coefficient r in

$$T_{\text{stat}} = T_s - r \cdot \frac{c^2}{2c_p} \tag{1}$$

for each probe has been calibrated in the jet facility prior to the experiment. The coefficient of a probe is shown in Fig. 6.

Probe Control and Data Acquisition. To achieve a high accuracy including the DC part of measurement with fast-response probes (e.g., pressure uncertainties below 1 percent of dynamic head), special measurement concepts have to be followed. For this purpose, a fully computerized probe control unit (FRAP®-PCS) has been developed (Fig. 7), consisting of a Macintosh PowerPC with LabView™ software driving special measurement equipment, a high-precision probe actuator, a probe pressure unit for pressure

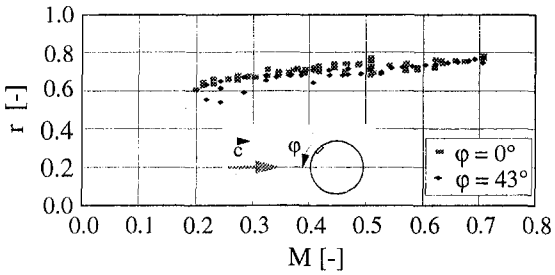

Fig. 6 Typical recovery coefficient r of a C1LS18 probe (Kupferschmied, 1998)

adjustments (PPU) and a high-speed data acquisition system (12 bit, 8 channels, sampling rate 200 kHz/channel).

Experimental Setup and Measurement Procedure

The probe actuator (Fig. 7) can be mounted (Fig. 8) on the front wall of the diffuser in seven different positions (Fig. 9). In the following, the measurements taken at position I will be discussed.

Two different setups have to be distinguished: The experimental setup for the fast-response type probes and a setup for measurements with pneumatic probes. The same probe actuator is used for both types of probes. The measurement system used for fast-response probes is shown in Fig. 7. For measurements of the pneumatic probe a multichannel pressure acquisition system is used instead of the high-speed data acquisition system.

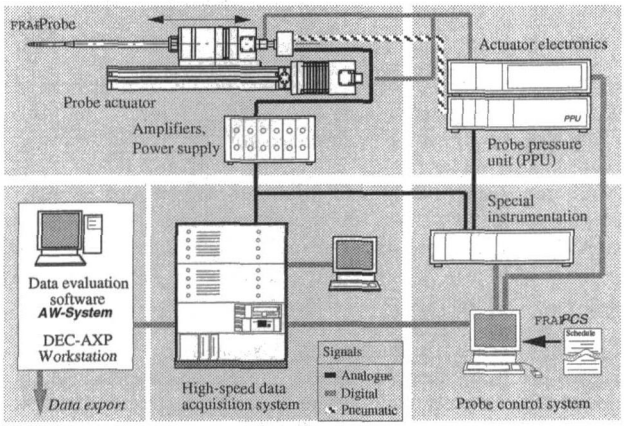

Fig. 7 Probe control system and data acquisition

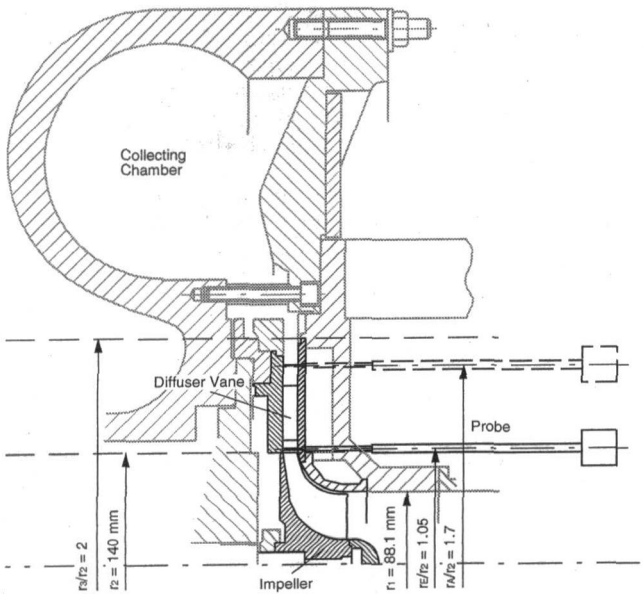

Fig. 8 Cross-sectional view of the centrifugal compressor with probe locations

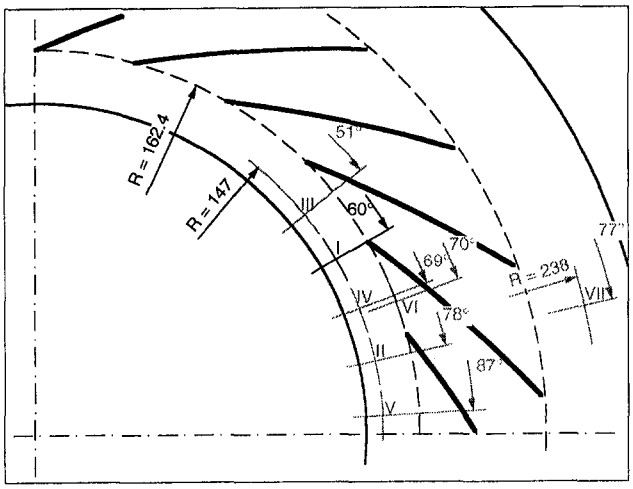

Fig. 9 Top view of the diffuser with probe positions I to VII

In the diffuser the probes have been traversed in axial direction from the rear to the front wall in 13 positions.

The height b of the diffuser channel is 16.8 mm. LDV measurements performed in this test rig (Stahlecker and Gyarmathy, 1998) have shown that the axial component of the velocity vector is at least one order of magnitude smaller than the other two components. In such, i.e., essentially two-dimensional flows, three-hole probes are sufficient to measure the two main velocity components.

To avoid the flow being forced around the tip of the probe and causing three-dimensional effects and secondary flows, the auxiliary device shown in Fig. 10 by Type A was developed. A cylinder of the same diameter as the probe is mounted in the rear wall of the diffuser. The cylinder is kept in touch with the moving probe tip pneumatically. Thus all end effects are eliminated. This arrangement has the great advantage that no mechanical stresses due to fixing are applied to the probe sensors.

Measurement Procedure for the One-Sensor Fast-Response Pressure Probe (C1LS18). To measure the systematic fluctuations, a one-sensor fast-response probe is used providing two-dimensional velocity, total and static pressure in steady or reproducibly unsteady flows. The probe was used in a *pseudo-3-sensor* mode: At every traverse position the fluctuating flow was measured time-resolved under three angular positions of the probe shaft. The middle of the three angle positions was set to the time-averaged flow direction. For the other two angle positions the probe was rotated (in yaw) by 43 deg to the left and the right, respectively. A once per revolution signal from a trigger on the

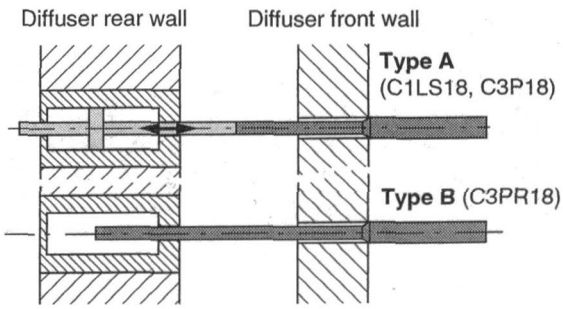

Fig. 10 Schematic of the two different setups

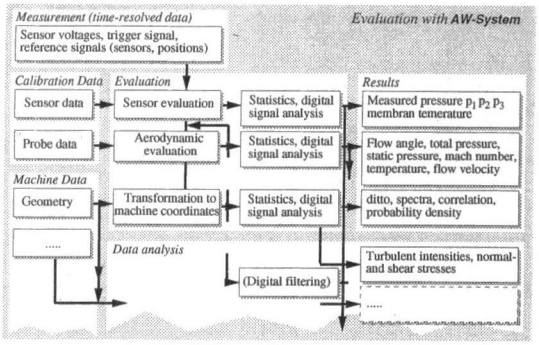

Fig. 11 Steps of the evaluation of measured data

impeller shaft allows us to fit the sensor signal data together to a *pseudo-3-sensor* probe (Kupferschmied, 1998). This involves an ensemble averaging of the time-resolved measured pressure fluctuations. The averaged results represent the systematic pressure fluctuations of each of the three sensors for one rotation of the impeller.

The aerodynamic calibration-based data evaluation of the pressure fluctuations thus obtained provides the time-resolved flow values at a given traverse position. By taking these data traverse-point by traverse-point, the circumferential systematic flow fluctuations over the diffuser channel height can be plotted.

The advantages of this method as compared to a three-sensor fast-response probe are:

- Systematic errors reduced to a minimum since one single sensor operating in difference-pressure mode is used to collect all data.

Disadvantages of the method:

- Stochastic parts of the signal like turbulence getting lost due to the ensemble-averaging.
- The measuring time is trebled (not significant).

Measurement Procedure for the Three-Hole Pneumatic Probe (C3P18, C3PR18). The middle hole has 1 mm offset in the shaft direction to the two side holes of the probe (see Fig. 4). The following procedure is performed to achieve measurements in one diffuser channel plane. The probe is set to the designated traverse position. With a fuzzy controller (Biswas, 1994) the direction of the mean flow is evaluated automatically by minimizing the pressure difference between the two side holes of the probe. In this position a first pressure measurement will be taken. Then the probe is moved by 1 mm in axial direction so that the middle hole is in the same plane as the side holes were before. The angle of the probe shaft is kept unchanged. A second pressure measurement is performed. Finally, the pressure of the side holes taken in the first step and the pressure of the middle hole taken in the second step are combined to get a three-hole measurement.

Method of Evaluation and Analysis

Data Evaluation. In this measurement campaign more than 280 million data points were recorded. The processing of the FRAP® data has to consider such requirements as handling of an enormous quantity of measured data, the transformation of the signal from voltage to pressure and temperature, the connection of the single measured positions to a traverse, or the meaningful presentation of the results.

From Probe Signals to Flow Quantities. The steps required to convert probe measurement data into flow quantities are described in Fig. 11. The sensor voltages have been converted into pressure and temperature signals with a model-based reconstruction where the sensor calibration data are used. The flow angle φ is determined via the yaw sensitive coefficient. The total pressure and the static pressure are calculated by using the flow angle φ. The other quantities such as flow velocity or temperature are computed later on. More detailed information can be found in Kupferschmied and Gossweiler (1992).

For efficient data processing, a dedicated software package has been developed. This performs the data evaluation for an entire traverse and prints the results in a variety of preselected digrams. The program is based on the AW System that was developed as an interactive environment for the evaluation of large time series (Herter et al., 1992). Through further automation of the data acquisition and evaluation, the time a standard evaluation requires is reduced from two or three months to three or four days. The program is organized into three parts. In the first part the required specifications and control orders can be fed into the computer as file hierarchy adapted to the measurement campaign. In the second part the measured data are read and processed (Fig. 11). In the third part of the standard evaluation program the results of the single traverse positions are assembled and printed in suitable diagrams.

Averaging Methods. Averaging methods are used to statistically connect the time-resolved data measured in any one traverse position at different times and to assemble the ensemble-averaged data over one traverse. The actual measurements made in the test rig were performed by using the one-sensor probe. It is necessary to perform measurements at three yaw angles per traverse position to get the static pressure and the flow angle, as described above. To link these three nonsynchronous pressure measurements, the ensemble-average per revolution has to be formed.

The ensemble-averaged pressure values $\tilde{p}_1(t)$, $\tilde{p}_2(t)$, $\tilde{p}_3(t)$ are determined from the time-dependent pressure values $p_1(t)$, $p_2(t)$, $p_3(t)$ by Eq. (2), where x_i is the measured value and m is the number of revolutions. The time index n is set to zero after each rotor revolution:

$$\tilde{x}(t_n) = \frac{1}{m} \sum_{i=1}^{m} x_i(t_n) \tag{2}$$

In order to have an acceptable interval of confidence, 250 rotations of the impeller per traverse position were measured within 0.82 s. This sums up to 12.8 million data points collected per traverse. With the ensemble-average it is possible to separate the systematic fluctuations from the stochastic fluctuations of the signal. The systematic fluctuations are dependent on the frequency of the rotor or multiples of this frequency. All other frequencies (even if they are systematic) are separated from the rotor-based systematic fluctuations. The stochastic fluctuations in themselves can be quantified by the ensemble standard deviation, shown by:

$$\tilde{\sigma}(t_n) = \sqrt{\frac{1}{m} \cdot \sum_{i=1}^{m} (x_i(t_n) - \tilde{x}(t_n))^2} \tag{3}$$

Finally, in order to compare the time-mean pneumatic measurements with the corresponding FRAP® measurements, it is necessary to calculate the time average of the data row:

$$\bar{x} = \frac{1}{N} \cdot \sum_{n=1}^{N} x(t_n) \tag{4}$$

where N is the total number of data readings at any one sensor position.

Results

Test Rig Measurements

Circumferential Pressure Uniformity at the Diffuser Inlet. This ensures that traverses performed at one single circumferential position (Φ = 60 deg, Fig. 9) are sufficient to calculate the entire

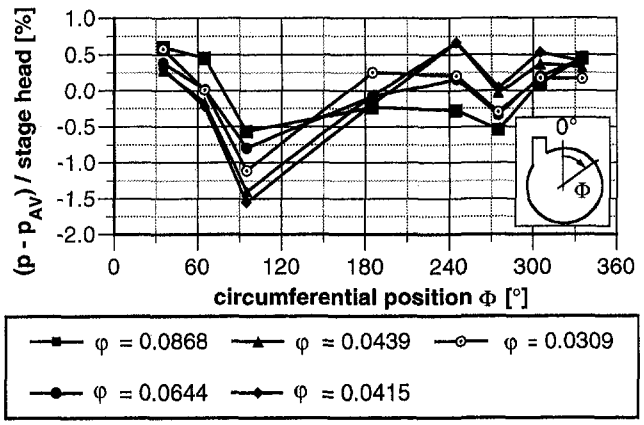

Fig. 12 Circumferential static pressure distribution at the diffuser front wall at $r_E/r_2 = 1.05$

mass flow. Uniformity within +0.6 and −1.5 percent is confirmed by the circumferential static front wall pressure plotted in Fig. 12. The pressure taps are located at a diameter ratio to the impeller tip diameter of 1.05.

Running Conditions and Performance Map. All measurements discussed below were made in the "Best Point" (BP) of the performance map shown in Fig. 13. (Mu = 0.75, $\dot{V}_I = 1.55$ m^3/s, giving $\varphi = 0.0767$, $\eta° = 0.82$). At this point the flow conditions in the diffuser are in the high subsonic regime.

Standard Orifice Measurements. Mass flow measurement with a standard orifice (Fig. 1) were performed according to DIN 1952 (1982). Following this standard, the maximum deviation of the measured mass flow within the orifice can be calculated. At the above-mentioned running conditions, the mass flow measurement uncertainty remains below 0.87 percent.

Measurements With a Pneumatic Three-Hole Probe (C3P18). Figure 14 gives an overview of the flow quantities calculated via the aerodynamic data evaluation procedure. Traverses were performed in diffuser position I (Fig. 9) from hub to shroud (diameter ratio $r_E/r_2 = 1.05 = \text{const}$, $z/b = 0.18 \ldots 0.99$). In order to calculate the local velocity, temperature traverses were performed with the C1LS18 fast-response sensor probe.

Plotted over traverse position in Fig. 14 are C_E, α_E, p_{tot}/p_i, p_{stat}/p_i and local Mach number. C_E is the absolute value of the flow velocity vector in the absolute frame, nondimensionalized by the impeller tip speed u_2. "Flow angle" indicates the angle α_E of the flow velocity vector to the tangent. Both static (p_{stat}) and total pressure (p_{tot}) are normalized by the absolute static inlet pressure (p_i) of the stage.

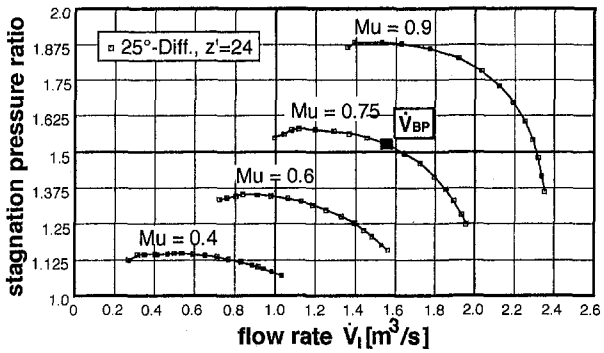

Fig. 13 Performance map of the measured stage configuration

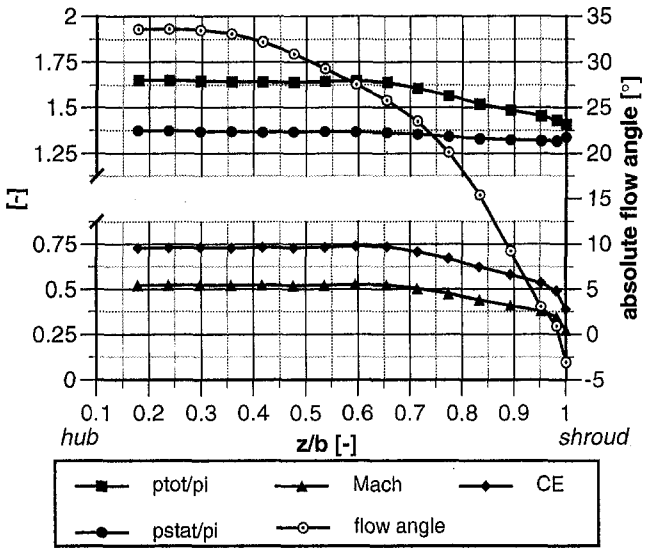

Fig. 14 Traverse through the diffuser channel at Mu = 0.75, $\varphi = 0.0767$ (C3P18, pneumatic probe)

Measurements With a One-Sensor Probe (C1LS18). In Figs. 15 to 18 ensemble-averaged measurements (according to Eq. (2)) made with the one-sensor probe (C1LS18) at position I (Fig. 9) are plotted over traverse position and time. Results are shown in both the absolute and the relative (co-rotating) frame. Only the first three blade passages of the impeller are plotted. Time runs from right to left. Starting at 0 ms (trigger signal), the events caused by the passing of the three blades (splitter, full, splitter) are seen. The sharp velocity peaks seen near the hub pertain to the trailing-edge wakes. Near the casing the velocity is low and the fluctuations are moderate.

Figures 15 and 16 show the absolute velocity and the flow angle distribution. By transforming the velocity vectors into the relative frame, the distribution of the nondimensionalized relative velocity W_E and the distribution of the relative flow angle β_E can be plotted as shown in Figs. 17 and 18 respectively.

The velocity vector distribution in the relative frame (Fig. 17) shows the following:

- The trailing-edge wakes appear as sharp dips in the sound near-hub flow.

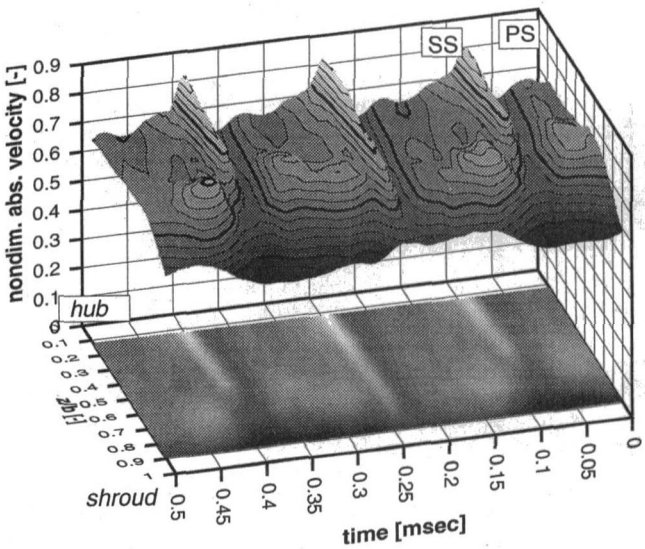

Fig. 15 Ensemble-averaged absolute velocity C_E distribution at $r_E/r_2 = 1.05$

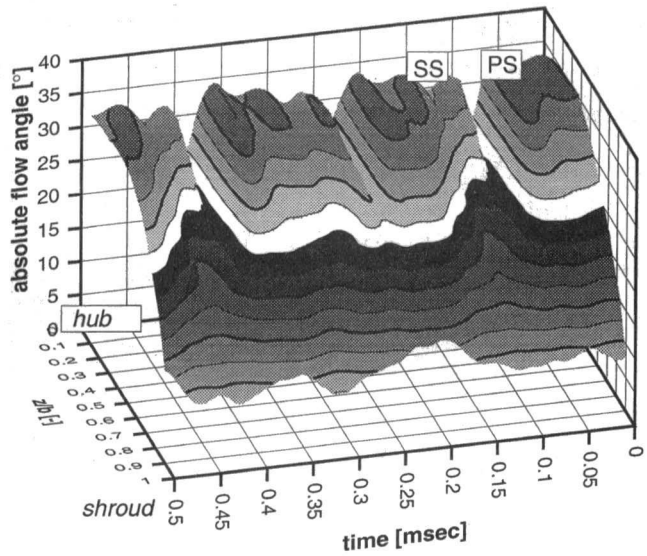

Fig. 16 Ensemble-averaged absolute flow angle α_E distribution at r_E/r_2 = 1.05

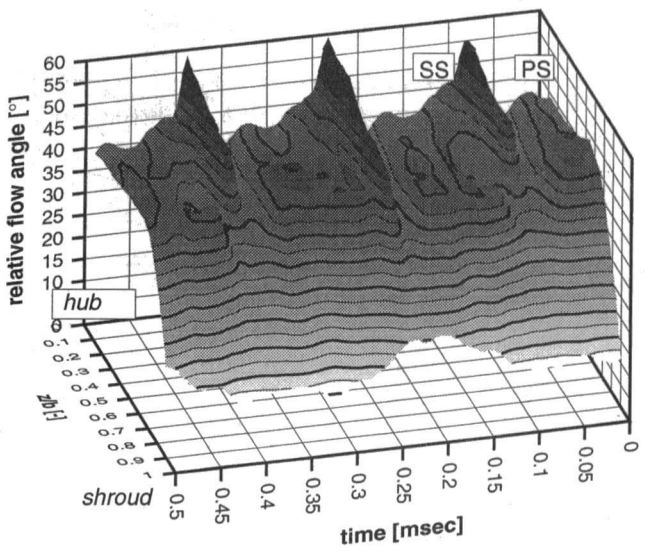

Fig. 18 Ensemble-averaged relative-frame flow angle β_E distribution at r_E/r_2 = 1.05

- In the shroud/suction side corner of the impeller an area of low momentum can be observed. This so-called *"jet/wake" distribution* of the flow was observed and described by Dean and Senoo (1960) and Eckardt (1975). This behavior of the flow is characteristic for impellers without backsweep but can be observed in backsweapt impellers like the present one, too.
- The blade metal angle of the impeller at the tip amounts to 60 deg to the tangent. Obviously all measured flow angles are below the above indicated value (Fig. 18). This is an effect of Coriolis acceleration or, spoken in centrifugal impeller terms, of the slip factor. Wiesner (1967) gives a review of various methods proposed to estimate this factor. In interpreting Fig. 18 one should keep in mind that the position where the measurements were taken is not right at the impeller tip at r_2 but rather at r_E/r_2 = 1.05, tending to exaggerate the slip effect.

As already mentioned, the one-sensor probe is not only capable of measuring pressures but mean flow (not time-resolved) temperatures, too. Figure 19 shows the increase of the static temperature of the flow through the impeller plotted over the traverse position.

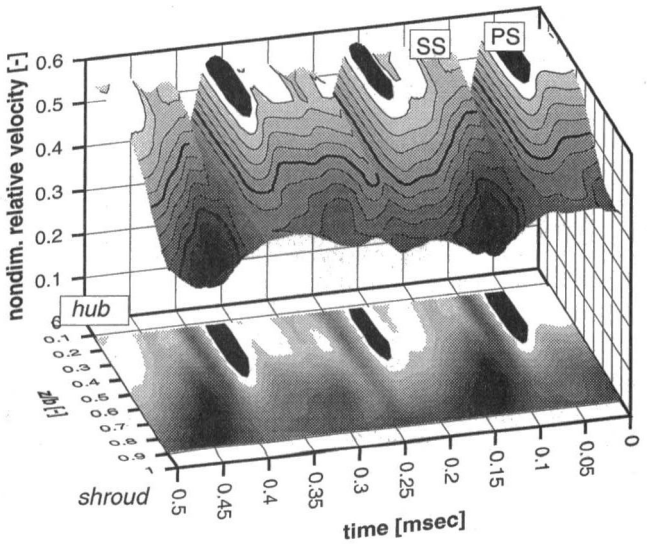

Fig. 17 Ensemble-averaged value of the relative velocity W_E distribution at r_E/r_2 = 1.05

Comparisons

Mass Flow

Motivation. The main incentive for using probes is certainly not the measurement of global mass flow. But this calculation and its comparison with the standard orifice measurement is interesting in order to get an idea of the overall performance and accuracy of the probe traverses made.

Mass Flow Sensitivity Analysis for Probe Measurements. The mass flow is defined as follows:

$$\dot{m} = c_\perp \cdot \rho \cdot A \tag{5}$$

With the parametric model, based on the aerodynamic calibration, the flow angle α_E, static and total pressure are calculated from the measured pressures. The flow temperature is calculated with the model of the sensor calibration. In order to investigate the sensitivity of the mass flow calculation, Eq. (5) is put into a form where $\dot{m}$ is a function of the measured values:

$$\dot{m} = f(p_{\text{stat}}, p_{\text{tot}}, T_{\text{stat}}, \alpha_E) \tag{6}$$

$$\dot{m} = \sum_0^b \sqrt{\kappa R T_{\text{stat}}(z)} \cdot \sqrt{\frac{2}{\kappa - 1} \cdot \left[\left(\frac{p_{\text{tot}}(z)}{p_{\text{stat}}(z)} \right)^{(\kappa-1)/\kappa} - 1 \right]} \times \sin \alpha_E(z) \cdot \frac{p_{\text{stat}}(z)}{R T_{\text{stat}}(z)} \cdot 2 \cdot \pi \cdot r_E \cdot \Delta z \tag{7}$$

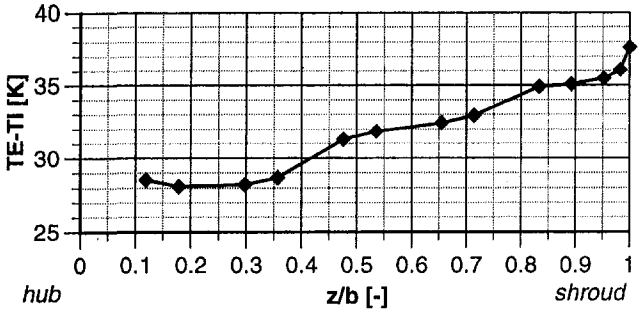

Fig. 19 Difference of the static flow temperature rise between impeller outlet and inlet (not time-resolved)

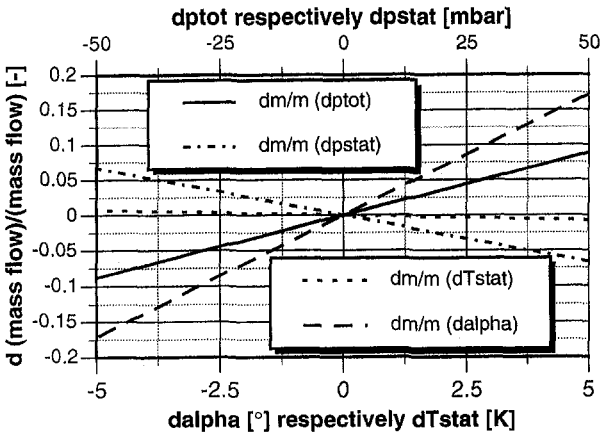

Fig. 20 Effect of measurement errors of mass flow calculation

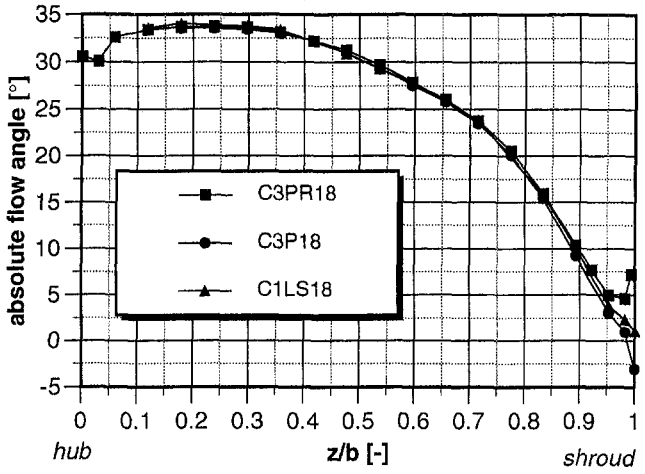

Fig. 21 Flow angle α_E at $r_E/r_2 = 1.05$

In order to distinguish the influence of each variable in Eq. (6) on the mass flow calculation, we compute the total differential of Eq. (7):

$$d\dot{m} = \frac{\partial \dot{m}}{\partial p_{stat}} dp_{stat} + \frac{\partial \dot{m}}{\partial p_{tot}} dp_{tot} + \frac{\partial \dot{m}}{\partial T_{stat}} dT_{stat} + \frac{\partial \dot{m}}{\partial \alpha_E} d\alpha_E \quad (8)$$

where each partial differential $(\partial f/\partial x) = g_x$ is a function of the variables and can be determined from Eq. (6) as:

$$\frac{\partial \dot{m}}{\partial x} = g_x(p_{stat}, p_{tot}, T_{stat}, \alpha_E) \quad (9)$$

These influence coefficients g_x have been numerically determined for the running conditions *BP* of the stage. Figure 20 summarizes the relative effect $d\dot{m}/\dot{m}$ of changes (or errors) in the independent variables.

The mass flow measurements with probe traverses is highly sensitive to uncertainties of the flow angle. A deviation of 1 deg of the flow angle α_E leads to a misestimation of the mass flow of roughly 3.5 percent. An error in static and/or total pressure measurement leads to an error in the flow velocity. An offset error of 10 mbar at the given running conditions and the associated flow rate of the rig results in a mismatch of the mass flow of about 1.5 percent. Compared to these errors, the effect of temperature errors can be neglected, since an offset of 5 K accounts only for 0.8 percent of mass flow error.

It can be concluded that very high accuracy with respect to flow angle, static and total pressure would be required to calculate the mass flow with a acceptable accuracy. Certainly, measuring the mass flow with a standard orifice is a more suitable method.

Comparison of Probe Traverse Mass Flow Measurements and Standard Orifice Measurements. Table 1 lists the orifice (SDO) mass flow data actually measured during the tests using different probe types. The SDO error estimate is based on the DIN 1952 (1982) directives. The last column compares the probe mass flow integrals to the SDO value. It is seen the C3PR18 pneumatic probe and C1LS18 FRAP® probe give excellent agreement. The 2 percent error of the C3P18 pneumatic probe is due to an uncertainty in one single near-wall angle value.

Table 1 Comparison of mass flow calculated from probe measurements and standard orifice measurements

	mass flow measurements		
Probe type	SDO* (kg/sec)	accuracy of SDO meas.	$\frac{\dot{m}_{probe} - \dot{m}_{SDO}}{\dot{m}_{SDO}}$
C3PR18	1.77	0.87%	0.6%
C3P18	1.79	0.87%	2.0%
C1LS18	1.75	0.87%	-0.2%

* SDO: standard orifice measurement

Concerning these results the following remarks shall be added:

- For the measurements the test rig was run at "Best Point"; this means stable flow conditions and relatively small fluctuations.
- Of course, the uniformity of the circumferential pressure distribution in Fig. 12 allows us to calculate the mass flow out of a single traverse taken in the vaneless space at the diffuser inlet only if the probe measurements is not disturbed by the presence of vanes. In order to quantify such effects, probe traverses were made with the C3PR18 probe at different circumferential positions (Fig. 9, positions I–V). These showed that the upstream impact of the diffuser vanes at $r_E/r_2 = 1.05$ is negligible.
- The most delicate value for the mass flow calculation is the flow angle α_E. The standard deviation of the aerodynamic probe model for C3PR18 is 0.02 deg and for C1LS18 is 0.05 deg. The maximum deviation of the modeled data amounts to 0.06 deg for C3PR18 and 0.17 deg for C1LS18, respectively. In addition to this, the uncertainty of the angle measurements in the calibration facility amounts to a maximum of 0.05 deg (Kupferschmied, 1998). For measurements under steady flow conditions as provided in the above-mentioned calibration facility, maximum mass flow miscalculations of 0.4 percent or 0.8 percent, respectively, would result.

Velocity Vector Measurements (Absolute Frame)

Comparison of the Flow Angle. Probe C3P18 and C3PR18 are pneumatic three-hole probes of identical external geometry. These probes measure the pressure through a long tube leading to the pressure measuring system. Fluctuations are damped out. C1LS18 is a fast-response one-sensor probe of identical external geometry capable of measuring time-resolved pressure fluctuations. In Figs. 21–23 time-averaged data of the C1LS18 fast-response probe are presented.

Figure 21 shows the flow angle measurement of all three probes. For traverse positions of chief interest (z/b = 0.1 to 0.9) the differences are below 0.5 deg. Measurements above $z/b = 0.9$ are uncertain due to the horseshoe vortex created by the probe at the probe shroud–wall intersection. The differences in flow angle are not systematic with respect to the pressure measurement technique used, the time-resolving probe data lying halfway between the two pneumatic results. Therefore, no significant difference between the

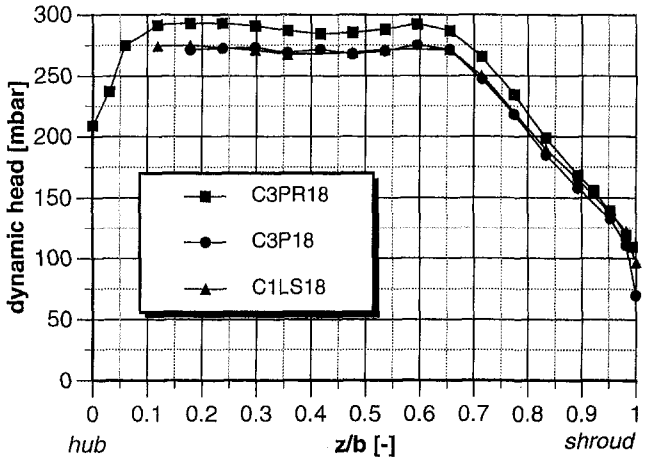

Fig. 22 Dynamic head at $r_E/r_2 = 1.05$

two measuring techniques regarding the time-mean flow angle at the impeller outlet can be identified.

Comparison of the Dynamic Head. The dynamic head profiles yielded by the three probes are presented in Fig. 22. The general character over the channel with z/b is identical for all three probes. C1LS18 and C3P18 gave also the identical values of dynamic head. Therefore, one can conclude, as for the steady flow angle measurements, that no clear difference between the two measuring techniques regarding the measurement of time-mean dynamic pressures can be observed.

Concerning the offset of the extended-tip C3PR18 probe, the following has to be considered: For this the setup in the test rig is of type B (Fig. 10), whereas C1LS18 and C3P18 were of type A (Fig. 10). That means that C1LS18 and C3P18 were free ending probes. In contrast to these, C3PR18 had an extra long tip extension to enter a hole in the back wall of the diffuser. Thus in the test rig the external geometry is exactly identical for all three probes.

The discrepancy of the dynamic head results is rooted in the calibration procedure. Due to the displacement of the free jet in the calibration facility by the probe shaft, a correction to the jet static pressure was applied following Wyler (1975). The way the shaft diameter increase was accounted for probably has caused an overcorrection for the C3P18 and C1LS18 probes, while the slender C3PR18 probe was correctly evaluated.

Stage Work. To evaluate the time-averaged temperature measurement of the fast-response probe the rise of total enthalpy over the impeller is determined both from: Euler's turbine equation and from the enthalpy calculated using the temperature measurements.

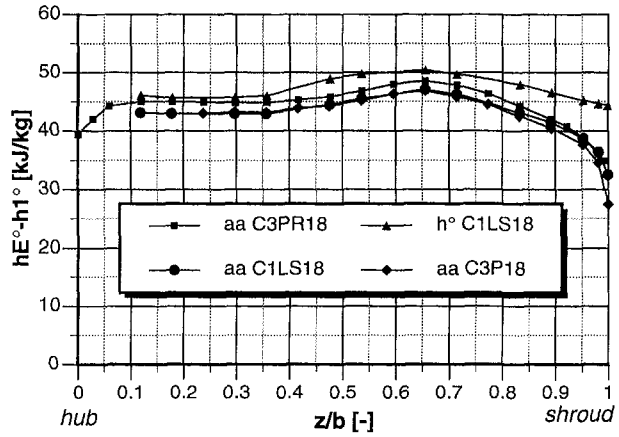

Fig. 23 Stage work and rise of total enthalpy

The flow at the impeller inlet was assumed to be of uniform state. Furthermore it was assumed that no inlet swirl existed. This results in the assumption that c_{u1} is negligible.

Euler's turbine equation for the specific aerodynamic work

$$a_a = u_E c_{uE} - u_1 c_{u1} \tag{10}$$

becomes, with the above-mentioned assumptions,

$$a_a = u_E c_{uE} \tag{11}$$

The rise of total enthalpy can be determined as follows:

$$\Delta h^\circ_{1E} = (T_E c_p + c_E^2/2) - h^\circ_1 \tag{12}$$

where T_E and c_E follow from traverses.

The work input distribution over the diffuser channel (z/b) has been calculated from data collected with different probe types based on the values of Figs. 21 and 22 and compared in Fig. 23. The difference in dynamic head between C1LS18 and C3P18 on one hand and C3PR18 on the other hand, as an expression of the velocity (Fig. 22), is responsible for the differences between the three a_a curves.

In addition to the comparison of a_a of the three probes, a comparison of a_a and the temperature-based Δh°_{1E} of the same measurement with probe C1LS18 is also shown in Fig. 23. Both are expressions of the stage work and should be identical for steady adiabatic flow. The following can be stated:

The characteristics of the curves over the diffuser channel are roughly equal, with the exception of the measuring points at the front wall (shroud) of the diffuser. In the level of the curves an offset of about 3 kJ/kg can be observed. Assuming that the velocity measurement on which a_a is based is correct, the offset is caused by a misestimation of the static flow temperature used to calculate Δh°_{1E}. The static temperature is calculated using the recovery coefficient r (Eq. (1)). The recovery coefficient is calibrated in terms of Mach number and flow angle for each fast-response probe in the jet calibration facility as

$$r = 1 - \frac{2c_p}{c_j^2}(T_{\text{tot},j} - T_s) \tag{13}$$

The total temperature of the jet ($T_{\text{tot},j}$), the sensor temperature T_s, and the flow velocity c_j of the jet are measured. The small temperature difference $T_{\text{tot},j} - T_s$ requires good accuracy of T_s to provide a satisfying recovery coefficient for the calculation of the static flow temperature. Further reducing of the errors in the sensor temperature determination is the objective of an ongoing investigation.

A final remark to the mismatching of the two curve characteristics at the shroud: The rise of the difference between Δh°_{1E} and a_a near the shroud has to be considered as a result of heat transfer from the diffuser front wall. Temperature measurements at the back wall (hub) would be of high interest. But with the actual probe geometry of C1LS18 this was not possible.

Summary and Conclusions

- The comparisons presented in this paper were made for a single running condition of a centrifugal compressor. The rig was operated in a stable range of the operating line. All probes used were of cylindrical external shape.
- A general sensitivity analysis of the mass flow calculation from wall-to-wall traverses with probes showed significant sensitivity to errors of static pressure, total pressure, and flow angle. Consequently mass flow comparisons are a suitable and sensitive method to investigate the accuracy of probe measurements.
- Both probe measuring techniques used, fast-response (FRAP®) and conventional pneumatic, showed good agreement with the standard orifice measurement. A high accuracy of the probes can be attested. The DC levels of the

fast-response probe signals are found to be reliable. They can be used for the quantitative interpretation of fluctuating flows where not only fluctuation amplitudes but also the absolute level of the quantities is of interest.

- No significant differences of the two probe measuring techniques can be observed in terms of stage work calculated from Euler's turbine equation.
- Temperature traverses made with FRAP® probes gave up to 9 percent higher work input than the velocity traverses; this discrepancy requires further investigation.
- Flow angle and dynamic head measured with the two probe techniques are in good agreement. Under the given impeller outlet flow conditions with a high fluctuating component, conventional pneumatic probe measurements are sufficiently accurate to measure time-mean flow quantities. These measurements are sufficient for applications such as for example the determination of CFD boundary conditions.
- The huge amount of data collected with the FRAP® system requires specific concepts for the measurement campaign. Not only the goal of the measurements has to be defined, but also the planning of the campaign, the possibilities of the standard evaluation, and the desired presentation of the results have to be considered in advance in order to get the optimum of information.

These investigations and considerations set the basis for the evaluation and interpretation of the huge amount of data taken with the fast-response one-sensor probe in this campaign. It includes measurements at the diffuser positions I, VI, and VII (Fig. 9) at three running conditions for each measurement position.

Acknowledgments

The authors would like to thank the Swiss Commission for Technology and Innovation (CTI), ABB Turbo Systems Ltd., Sulzer Innotec Ltd., and Sulzer Turbo Ltd. for their financial support. They also wish to thank all the technical staff of the laboratory for their support.

References

Bammert, K., and Rautenberg, M., 1974, "On the Energy Transfer in Centrifugal Compressors," ASME Paper No. 74-GT-121.

Biswas, R., 1994, "A Fuzzy Controller to Balance Pneumatic Multi-hole Probes," *Proc. 12th Symposium on Measuring Techniques for Transonic and Supersonic Flows in Cascades and Turbomachines,* Prague, Czech Republic.

Casartelli, E., Saxer, A. P., and Gyarmathy, G., 1999, "Numerical Flow Analysis in a Subsonic Vaned Radial Diffuser With Leading Edge Redesign," ASME JOURNAL OF TURBOMACHINERY, Vol. 121, pp. 119–126.

Dean, R. C., Jr., and Senoo, Y., 1960, "Rotating Wakes in Vaneless Diffusers," ASME *Journal of Basic Engineering,* Vol. 82, Sept.

DIN 1952, 1982, "Durchflussmessung mit Blenden, Düsen und Venturirohren in voll durchströmten Rohren mit Kresisquerschnitt," Beuth Verlag GmbH, Berlin, Germany.

Eckardt, D., 1975, "Instantaneous Measurements in the Jet-Wake Discharge Flow of a Centrifugal Compressor Impeller," ASME *Journal of Engineering for Power,* Vol. 97, July.

Eckardt, D., 1976, "Detailed Flow Investigations Within a High-Speed Centrifugal Compressor Impeller," ASME *Journal of Fluids Engineering,* Vol. 98, Sept.

Gossweiler, C., Humm, H. J., and Kupferschmied, P., 1992, "Development of a System for Aerodynamic Fast-Response Probe Measurements," *Proc. 18th Congress of Int. Council of the Aeronautic Sciences (ICAS),* Beijing.

Gossweiler, C., Kupferschmied, P., and Gyarmathy, G., 1995, "On Fast-Response Probes, Part 1: Technology, Calibration and Application to Turbomachinery," ASME JOURNAL OF TURBOMACHINERY, Vol. 117, No. 4.

Herter, D., Chrisander, O., and Gossweiler, C., 1992, "AW-System—An Interactive Environment for the Evaluation of Large Time Series," *Proc. 11th Symposium on Measuring Techniques for Transonic Flows in Cascades and Turbomachines,* Munich, Germany.

Humm, H. J., Gossweiler, C., and Gyarmathy, G., 1995, "On Fast-Response Probes, Part 2: Aerodynamic Design Studies," ASME JOURNAL OF TURBOMACHINERY, Vol. 117, No. 4.

Hunziker, R., 1993, "Einfluss der Diffusorgeometrie auf die Instabilitätsgrenze des Radialverdichters," PhD thesis No. 10252, ETH Zürich, Switzerland.

Inoue, M., and Cumpsty, N. A., 1984, "Experimental Study of Centrifugal Impeller Discharge Flow in Vaneless and Vaned Diffusers," ASME *Journal of Engineering for Gas Turbines and Power,* Vol. 106, Ap.

Jansen, W., 1964, "Rotating Stall in a Radial Vaneless Diffuser," ASME *Journal of Basic Engineering,* Vol. 86, Dec.

Kämmer, N., and Rautenberg, M., 1982, "An Experimental Investigation of Rotating Stall Flow in a Centrifugal Compressor," ASME Paper No. 82-GT-82.

Krain, H., 1981, "A Study on Centrifugal Impeller and Diffuser Flow," ASME *Journal of Engineering for Power,* Vol. 103, No. 4.

Kupferschmied, P., and Gossweiler, C., 1992, "Calibration, Modelling and Data Evaluation Procedures for Aerodynamic Multihole Pressure Probes on the Example of a Four Hole Probe," *Proc. 11th Symposium on Measuring Techniques for Transonic and Supersonic Flows in Cascades and Turbomachines,* Munich, Germany.

Kupferschmied, P., Gossweiler, C., and Gyarmathy, G., 1994, "Aerodynamic Fast-Response Probe Measurement Systems: State of Development, Limitation and Future Trends," *Proc. 12th Symposium on Measuring Techniques for Transonic and Supersonic Flows in Cascades and Turbomachines,* Prague, Czech Republic.

Kupferschmied, P., 1998, "Zur Methodik zeitaufgelöster Strömungssondenmessungen in Verdichtern und Turbinen," PhD thesis No. 12774, ETH Zürich, Switzerland.

Ng, W. F., and Epstein, A. H., 1985, "Unsteady Losses in Transonic Compressors," ASME *Journal of Engineering for Gas Turbines and Power,* Vol. 107, pp. 345–353.

Ruck, G., 1989, "Verfahren zur instationären Geschwindigkeitsund Turbulenzmessung mit einer pneumatisch messenden Keilsonde," *Mitteilungen des Institutes No. 33,* Institut für Thermische Strömungsmaschinen und Maschinenlaboratorium der Universität Stuttgart, Stuttgart, Germany.

Runstadler, P. W., Jr., and Dolan, F. X., 1975, "Design, Development, and Test of a Laser Velocimeter for High Speed Turbomachinery," *Proc. LDA Symposium Copenhagen 1975.*

Stahlecker, D., and Gyarmathy, G., 1998, "Investigations of Turbulent Flow in a Centrifugal Compressor Vaned Diffuser by 3-Component Laser Velocimetry," ASME Paper No. 98-GT-300.

Traupel, W., 1958, 1988, *Thermische Turbomaschinen I,* Springer-Verlag, Berlin, p. 307.

Wiesner, F. J., 1967, "A Review of Slip Factors for Centrifugal Impellers," ASME *Journal of Engineering for Power,* Vol. 89, Oct.

Wyler, J. S., 1975, "Probe Blockage Effects in Free Jets and Closed Tunnels," ASME *Journal of Engineering for Power,* Vol. 97, Oct.

R. A. Van den Braembussche

E. Ayder[1]

von Karmen Institute for Fluid Dynamics,
Sint-Genesius-Rode, Belgium

D. Hagelstein

M. Rautenberg

Institute of Turbomachinery,
University of Hannover,
Hannover, Germany

R. Keiper
Kühnle, Kopp, & Kausch AG,
Frankenthal, Germany

Improved Model for the Design and Analysis of Centrifugal Compressor Volutes

This paper describes a new model for the analysis of the flow in volutes of centrifugal compressors. It explicitly takes into account the vortical structure of the flow that has been observed during detailed three-dimensional flow measurements. It makes use of an impeller and diffuser response model to predict the nonuniformity of the volute inlet flow due, to the circumferential variation of the pressure at the volute inlet, and is therefore applicable also at off-design operation of the volute. Predicted total pressure loss and static pressure rise coefficients at design and off-design operation have been compared with experimental data for different volute geometries but only one test case is presented here. Good agreement in terms of losses and pressure rise is observed at most operating points and confirms the validity of the impeller and diffuser response model.

Introduction

Compactness, efficiency, and the absence of circumferential pressure distortion are the main design targets for compressor volutes. The compactness, required for low cost and weight, often has a negative effect on efficiency and up to now no reliable prediction methods have been available to decide on a compromise. The main problems are the swirling flow in a complex three-dimensional geometry and the nonuniformity of the inlet flow, resulting from the unsteady interaction between the impeller and volute flow.

A reliable prediction of the volute static pressure rise and losses are a prerequisite for an accurate prediction of the compressor performance. Most of the analytical models, proposed up to now, assume uniform flow over each volute cross section (Japikse, 1982; Weber and Koronowski, 1986). Detailed measurements by Ayder et al. (1991, 1993), however, indicate a very complex three-dimensional flow. They also showed that these one-dimensional models are unable to predict the losses and pressure rise except by introducing unrealistic and tailored loss and pressure rise coefficients. The first target of the model described in this paper is to relate the losses and static pressure rise to the vortical flow in volutes, as a function of inlet conditions and geometry.

A second major problem is the circumferential pressure distortion resulting from the off-design operation of the volute. This is of major importance for the prediction of the unsteady impeller forces, noise and radial forces on the shaft. Its prediction requires the modeling of the strong interaction between the volute and the impeller. In the context of the present approach a simple one-dimensional quasi-steady model is proposed. The alternative is a three-dimensional unsteady impeller flow prediction with prescribed outlet pressure distortion (Fatsis et al., 1997).

The present paper presents a new analytical model for performance and flow prediction and evaluates its accuracy through a detailed comparison between predicted and experimental results obtained on volutes of different shapes. It is a more elaborate version of the model proposed by Van den Braembussche and Haende, (1990) to account also for the crosswise swirl velocity and total pressure losses.

Theoretical Model

The flow inside a volute and the resulting circumferential static pressure distortion and total pressure losses are calculated by an iterative procedure. The model consists of following components:

- **Rotor response calculation:** to define the circumferential velocity distribution (V_{R2} and V_{T2}) resulting from a circumferential variation of the outlet static pressure distribution. At the first iteration, the static pressure is assumed to be constant and the diffuser inlet velocity is defined by the circumferentially averaged value.
- **Diffuser flow calculation:** to predict the diffuser outlet flow velocity components, total and static pressure distribution by calculating the diffuser static pressure rise and losses at different circumferential positions as a function of the inlet conditions.
- **Volute flow calculation:** to approximate the three-dimensional flow in the volute. Starting from the nonuniform diffuser outlet flow, it defines the volute losses and static pressure rise, and updates the circumferential static pressure distortion at the diffuser outlet.
- **Impeller outlet pressure calculation:** to predict the rotor outlet circumferential static pressure variation as a function of the diffuser outlet pressure distortion.
- **Exit diffuser flow calculation:** to define the mixed-out conditions at the outlet of the exit diffuser downstream of the tongue.

With the exception of the last one, used only once for the overall performance calculations, these components are combined in an iterative procedure in which the flow conditions at impeller and diffuser outlet are adjusted. The static pressure distortion, resulting from the volute calculations, is imposed at the diffuser outlet and transferred to the impeller exit where it is an input for the impeller response model. The latter provides the circumferential variation of the total pressure and tangential and radial velocity variation at the impeller exit. The diffuser calculation transfers them to the diffuser exit where they provide the volute inlet conditions. The iterative procedure is stopped when the new diffuser outlet pressure distribution equals the previous one.

[1] Current address: Istanbul Technical University, Turkey.

Contributed by the International Gas Turbine Institute and presented at the 43rd International Gas Turbine and Aeroengine Congress and Exhibition, Stockholm, Sweden, June 2–5, 1998. Manuscript received by the International Gas Turbine Institute February 1998. Paper No. 98-GT-187. Associate Technical Editor: R. E. Kielb.

Each of these components will be explained in more detail in the following sections.

Rotor Response

For the operating point under consideration, defined by a given mass flow and rotational speed, only the inlet total temperature and the average total pressure and temperature at the impeller exit are required. The last ones are easily obtained from one-dimensional impeller predictions or from measurements.

The total temperature rise between the impeller inlet and outlet allows the calculation of the average tangential velocity at the impeller exit.

$$\bar{V}_{T2} = CP(\overline{T_2^o} - T_1^o)/U_2 \tag{1}$$

The circumferentially averaged radial velocity at the impeller exit is calculated from the mass conservation

$$\bar{V}_{R2} = \frac{\bar{m}}{\bar{\rho}_2 2\pi R_2 b_2} \tag{2}$$

The static temperature, defined by

$$\overline{T_2} = \overline{T_2^o} - .5(\overline{V_{T2}^2} + \overline{V_{R2}^2})/CP \tag{3}$$

is calculated in an iterative way, with $\bar{V}_{R2}$ defined by Eq. (2) as a function of $\bar{\rho}_2$. The static pressure required to calculate the density is given by the isentropic relation.

$$\overline{P_2} = \overline{P_2^o}\left(\frac{\overline{T_2}}{\overline{T_2^o}}\right)^{\gamma/(\gamma-1)} \tag{4}$$

At off-design operation of the volute, the difference between the local and average impeller exit static pressure $(P_2(\theta) - \bar{P}_2)$ results in a circumferential variation of the impeller outlet velocity components and total pressure. In the present method they are determined by local linearization of the average impeller performance curve.

The slope of the pressure rise characteristics $\overline{dP_2}/dm$ and $\overline{dP_2^o}/dm$ at the mass flow $\bar{m}$ are used to calculate the local radial velocity component and outlet total pressure when the local static pressure is different from the average value.

$$V_{R2}(\theta) = \overline{V_{R2}} + (P_2(\theta) - \bar{P}_2)\Big/\frac{\overline{dP_2}}{dm}$$

$$P_2^o(\theta) = \overline{P_2^o} + (V_{R2}(\theta) - \overline{V_{R2}})\frac{\overline{dP_2^o}}{dm}$$

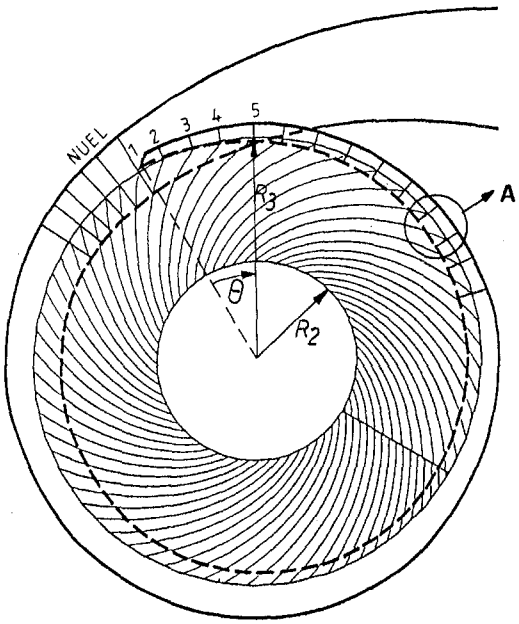

Fig. 1 Definitions and diffuser flow calculations

Based on experimental observations by Sideris and Van den Braembussche (1987), the impeller outlet tangential velocity is assumed to be constant along the impeller circumference and equal to the average value defined in Eq. (1). As a consequence also the outlet total temperature T_2^o equals the average value.

Diffuser Calculations

The method used in the present work for vaneless diffuser calculations is the one proposed by Traupel (1977) and similar to the one of Stanitz (1952). This well-known method integrates the spanwise-averaged continuity, tangential momentum, and energy equation from diffuser inlet to outlet, taking into account the friction on the diffuser walls and the conservation of total enthalpy. It is applied at NUEL circumferential positions in the vaneless diffuser using the local impeller outlet flow conditions as starting conditions (Fig. 1). The friction coefficient is defined as a function of the Reynolds number and roughness.

The circumferential extent of the streamlines in the diffuser depends on the inlet flow angle and is likely to be different at the different circumferential positions. This results in an interaction between neighboring streamlines and a different shift in the circumferential location between inlet and outlet. However, the exact

Nomenclature

A = area
C_P = static pressure rise coefficient
CP = specific heat coefficient
m = mass flow
NUEL = number of circumferential positions (Fig. 1)
P = pressure
R = radius measured from the impeller center of rotation
r = radius measured from the volute cross-sectional center
T = temperature
U = peripheral velocity
V = fluid velocity
α = absolute flow angle measured from tangential
γ = isentropic exponent
ρ = density
θ = angle of the circumferential position (measured from the tongue)
ω = total pressure loss coefficient

Subscripts

1 = at the impeller inlet
2 = at the impeller outlet
3 = at the vaneless diffuser outlet
C = at the volute cross-section center
i = at the inlet
INV = inviscid
iw = at the inner wall
o = at the outlet
ow = at the outer wall
R = radial component
S = swirl component
T = tangential or throughflow component
W = at the wall

Superscripts

o = stagnation condition
$-$ = circumferentially averaged value
$'$ = position at the diffuser outlet
$''$ = at the cross section

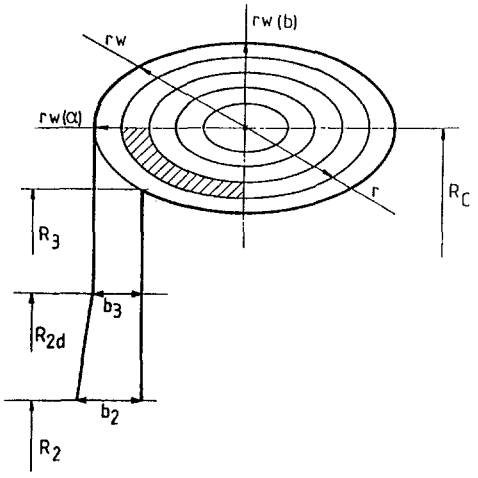

Fig. 2 Diffuser and volute cross section

circumferential position of the inlet distortion is irrelevant in the present context as we are only interested in the amplitude of the impeller flow distortion and not in the direction of the net radial force on the impeller resulting from it. The interaction between neighboring streamlines is neglected.

Volute Calculations

The volute channel is divided into a number of segments by means of NUEL (typically 36) radial planes located at equidistant angular positions (Fig. 1). Each cross section is supposed to be composed of four identical quadrants of ellipses defined by two radii as shown in Fig. 2. Rectangular volutes are replaced by elliptical ones of equal area and height-to-width ratio. The flow quantities are defined at a number of equidistant points along each axis. The integration of the flow quantities over the cross sections uses the average values over the finite surfaces defined by these points.

Conservation of mass and angular momentum for each of the NUEL segments allows the calculation of the outlet conditions (position o) as a function of the inlet flow (position i) and diffuser outlet (position 3) (Fig. 3).

Comparisons of existing prediction methods and experimental results (Ayder et al., 1993) have shown that the losses and static pressure variation depend strongly on the velocity variations over the cross sections. Great attention has therefore been given to the correct estimation of the crosswise flow variations as a function of the volute geometry and inlet flow conditions. The volute flow calculation has the following components which are used in an iterative procedure until all equations are satisfied.

Swirl Velocity and Total Pressure Distribution. According to the flow model developed by Van den Braembussche and Haende (1990) and confirmed by Ayder and Van den Braembussche (1994), the fluid entering the volute at the position close to the tongue remains at the center of the volute cross section. The fluid entering farther downstream wraps around the previous one. The inviscid variation of the total pressure and swirl velocity over the cross sections can therefore be related to the total pressure and radial velocity at the volute inlet and the change in radial position.

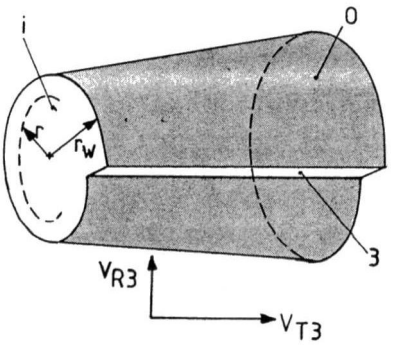

Fig. 3 Control volume for volute calculation (detail A of Fig. 1)

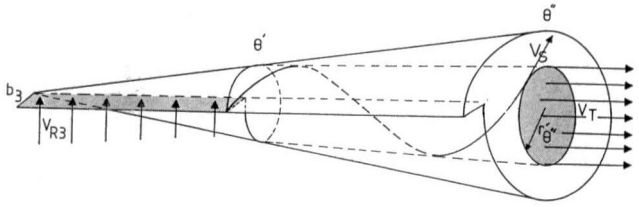

Fig. 4 Flow path between volute inlet, at θ', and cross section at θ''

The radial position in a cross section, at θ'', of the fluid that entered the volute at an upstream circumferential position θ' (Fig. 4), is determined from continuity. Comparing the amount of the fluid entering the volute between the volute tongue and position θ', with the mass flow integrated up to $r'(\theta'')$ over the cross section under consideration:

$$m(\theta') = \int_0^{\theta'} \rho_3(\theta) b_3 R_3 V_{R3}(\theta) d\theta = \int_0^{r'(\theta'')} 2\pi\rho V_T r dr$$

provides the radial position $r'(\theta'')$ where the fluid entering the volute at position θ' is located.

The inviscid swirl velocity at this radial location ($V_{S_{INV}}$) of the cross section can then be defined by means of the conservation of the swirl momentum, taking into account the difference in radius between the point where the fluid has entered the volute ($r_W(\theta')$) and the radius at which the fluid is now located $r'(\theta'')$:

$$V_{S_{INV}}(\theta'', r') = V_{R3}(\theta') r_W(\theta') / r'(\theta'') \quad (5)$$

This also allows the inviscid total pressure to be defined as a function of the local total pressure at the vaneless diffuser outlet:

$$P^o_{INV}(\theta'', r') = P^o_3(\theta') \quad (6)$$

Figure 5 shows the typical inviscid swirl distributions over a cross section of a volute operating at low mass flow. The large swirl velocity in the center results from the large radial velocity component of the fluid entering near the tongue (and remaining in the center). The smaller swirl velocity component near the walls results from the smaller radial velocity component of the fluid entering further downstream in the volute.

Experimental observations (Elholm et al., 1992; Ayder and Van

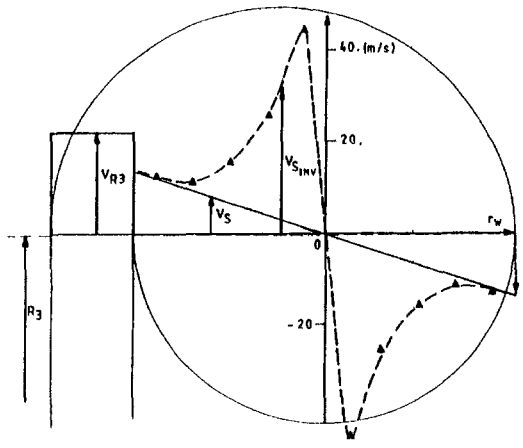

Fig. 5 Comparison of the inviscid (– – –) and real (—) swirl distributions over two volute cross sections at low mass flow

den Braembussche, 1991; Ayder et al., 1993) all indicate a forced-vortex type of swirl velocity variation resulting from the internal shear in the center of the vortex. The real total pressure is therefore lower than the inviscid one by the difference between the inviscid and viscous swirl kinetic energy:

$$P^o(\theta'', r) = P^o_{\text{INV}}(\theta'', r) - 0.5\rho(\theta'', r)(V^2_{S_{\text{INV}}}(\theta'', r) - V^2_S(\theta'', r)) \quad (7)$$

The variation of the real swirl velocity over the cross section is determined by

$$V_S(\theta'', r) = \frac{V_S(\theta'', r_w)}{r_W(\theta'')} * r \quad (8)$$

and shown by the full lines in Fig. 5. The large difference between the inviscid and forced vortex swirl velocity gives rise to high losses in the center of the volute.

At the first approximation, the magnitude of the viscous swirl velocity on the volute wall near the diffuser exit is assumed to be

$$V_S(\theta'', r_W) = V_{R3}(\theta'')$$

The value of $V_S(\theta'', r_W)$ will be modified during the iterative procedure until Eq. (11) is satisfied. This difference between V_S and V_{R3} results from a deceleration or acceleration of the fluid when coming out of the diffuser.

Static Pressure. The variation of the static pressure over the cross section is determined by the radial equilibrium between the static pressure gradient and the centrifugal forces due to the swirling flow:

$$\frac{dP}{dr} = \rho \frac{V^2_S(\theta'', r)}{r(\theta'')} \quad (9)$$

One should keep in mind that a change in swirl velocity at the wall influences only the radial static pressure gradient. The static pressure itself is defined later as a function of the wall static pressure.

Throughflow Velocity. The throughflow velocity variation over the section is calculated by means of the following relation:

$$\frac{\rho(\theta'', r)V^2_T(\theta'', r)}{2} = P^o(\theta'', r) - P(\theta'', r) - \frac{\rho(\theta'', r)V^2_S(\theta'', r)}{2} \quad (10)$$

The value of V_S, defined in Eq. (8), is modified by changing $V_S(\theta'', r_W)$ until the throughflow velocity at the wall equals the one calculated from the conservation of the angular momentum:

$$V_T(\theta'', r_W) = V_{T3}(\theta'')R_3/R_C(\theta'') \quad (11)$$

where R_C is the location of the volute cross section center as shown on Fig. 6.

The value of the wall static pressure ($P(\theta'', r_W)$) is assumed to be equal to the volute inlet static pressure only in the first iteration and will be modified later to increase or decrease V_T and density until the mass conservation over the control segment is also satisfied.

Circumferential Variation of the Static Pressure. Continuity alone cannot explain the origin of the static pressure distortion in the volute and conservation of the tangential momentum in the volute is also needed to predict correctly the new circumferential static pressure distribution. The following form of the conservation of the angular momentum in tangential direction, between θ_i and θ_o (Fig. 6) accounts also for the important influence of the radial position of the volute channel on the volute characteristics:

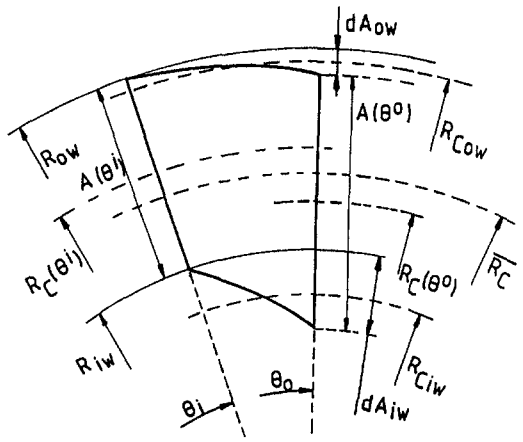

Fig. 6 Cross section of a volute element and definition of unknown

$$R_C(\theta_i)A(\theta_i)(P(\theta_i) + \rho(\theta_i)V^2_T(\theta_i)) + dA_{iw}\left(\bar{P} - \bar{\rho}\overline{V^2_T}\frac{\overline{R_C} - R_{Ciw}}{R_{Ciw}}\right)R_{Ciw} + dA_{ow}\left(\bar{P} - \bar{\rho}\overline{V^2_T}\frac{\overline{R_C} - R_{Cow}}{R_{Cow}}\right)R_{Cow} = R_C(\theta_o)A(\theta_o)(P(\theta_o) + \rho(\theta_o)V^2_T(\theta_o)) \quad (12)$$

where the throughflow velocity V_T is calculated by mass-averaging the previously defined value at the inlet and outlet section.

The tangential projections of the volute surface wall, dA_{iw} and dA_{ow}, are functions of the divergence between the outer and inner wall and the change of the radial position of the volute center R_C. The latter is decreasing for internal volutes and increasing for external volutes.

The static pressure on dA_{ow} and dA_{iw} is calculated as a function of the average pressure at a cross section, increased or decreased by the influence of the centrifugal forces between R_C and R_{Ciw} or R_{Cow} in the curved volute. (This correction drops in a straight convergent or divergent channel.)

The static pressure at the diffuser outlet equals the average static pressure at the center of the downstream cross section, corrected by the pressure difference between R_C and R_3 due to the centrifugal forces in the curved volute channel:

$$P_3(\theta_o) = P_C(\theta_o) - 2.\rho(\theta_o)\frac{V^2_T(\theta_o)}{R_C(\theta_o) + R_3}(R_3 - R_C(\theta_o)) \quad (13)$$

This equation is used to update the diffuser exit static pressure as a function of the volute distortion.

Solution Procedure. These components of the volute calculation are linked in an iterative procedure described by the flowchart shown in Fig. 7.

The inviscid swirl velocity and total pressure distribution are calculated as a function of the volute inlet conditions (Eqs. (5) and (6)) [RADMATCH, INVVSPOTO]. This procedure (loop 1) is repeated three times to account for the influence of the later changes of the throughflow velocity distribution on the inviscid swirl and inviscid total pressure distribution.

The viscous swirl velocity and total pressure distribution are fully defined by Eqs. (7) and (8) as a function of the swirl velocity at the wall [VISVSPOTO]. The last one is modified until the throughflow velocity at the wall equals the one defined by Eq. (11) as a function of the the local diffuser outlet tangential velocity. Loop 2 is repeated until DIFFV < 0.01.

Integrating the radial pressure gradient, Eq. (9), allows the calculation of the static pressure distribution over the cross section as a function of the wall static pressure [NISRE]. The local value

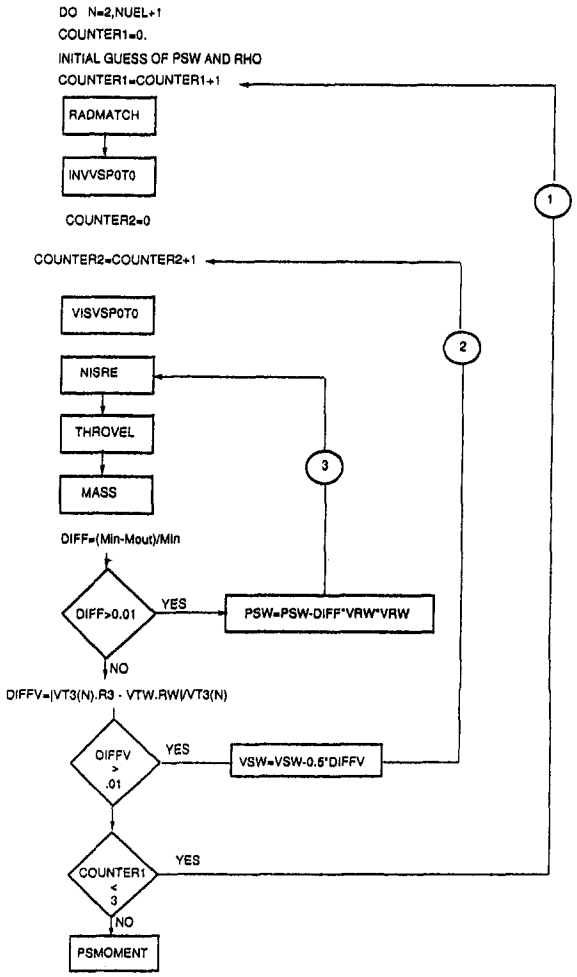

Fig. 7 Flow chart of volute calculation model

of the throughflow velocity being calculated as a function of the local total and static pressures (10) [TROVEL], the wall static pressure is updated until the outlet mass flow equals the incoming one [MASS]. This is done by repeating loop 3 until DIFF < 0.01. Applying the momentum equations (12) and (13) [PSMOMENT] provides an update of the $P_3(\theta)$ distribution at the diffuser exit resulting from the volute flow, taking into account the nonuniform inlet flow conditions.

Impeller Outlet Pressure Calculation

The impeller outlet static pressure calculation is based on the assumption that the amplitude of the circumferential pressure variation is the same at the vaneless diffuser inlet and outlet, which, for compressible flow, is confirmed by experimental evidence (Sideris and Van den Braembussche, 1987; Ayder and Van den Braembussche, 1991).

The local value of P_2 is therefore a function of the diffuser outlet pressure distortion and the average value $\overline{P_2}$ defined by the performance curve:

$$P_2 = \bar{P}_2 + (P_3 - \bar{P}_3)$$

Exit Diffuser Flow Calculation

The pressure rise in the exit diffuser is calculated by expressing the conservation of the momentum between inlet and outlet section. It accounts for the predicted nonuniform flow at the volute outlet and assumes a uniform flow at the exit diffuser outlet:

$$\overline{P_o}A_o = \int_{r=0}^{r=rw} (\rho V_T^2 + P)_i dA_i - (\overline{\rho V_T^2})_o A_o$$

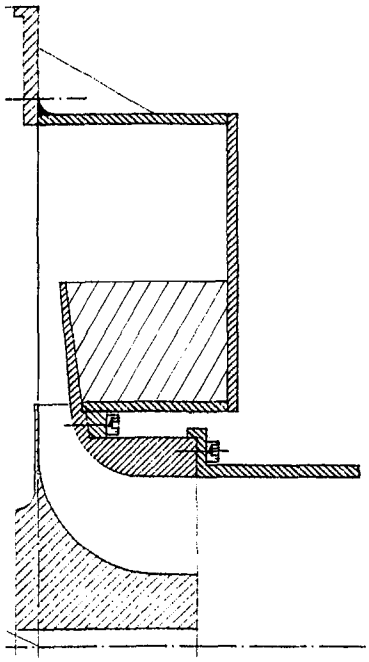

Fig. 8 Impeller and volute cross section

The average outlet velocity is calculated from continuity whereby the value of $\overline{\rho_o}$ is iteratively adjusted as a function of the calculated outlet pressure and temperature. The outlet temperature is defined from the total temperature and the local velocity components, Eq. (3), where the swirl is assumed to be sufficiently small to be neglected. The average total pressure at the outlet of the exit diffuser can then be defined by the isentropic relation (4).

Evaluation of the Model

The model has been evaluated by recalculating the flow in different compressors with overhung volutes of different cross section (elliptic and rectangular) at different radial positions (internal, central, and external volutes). The following comparison, however, is restricted to a compressor with an external volute of rectangular cross section of which a cross section is shown on Fig. 8. The flow in the vaneless diffuser and volute has been measured in detail on the compressor test rig of IFS at the University of Hannover. A more detailed description of the compressor and performance is given by Hagelstein et al. (1997).

The following definition of static pressure rise and loss coefficient is used:

$$C_P = \frac{\overline{P_o} - \overline{P_3}}{\overline{P_3^o} - \overline{P_3}} \quad \omega = \frac{\overline{P_3^o} - \overline{P_o^o}}{\overline{P_3^o} - \overline{P_3}} \tag{14}$$

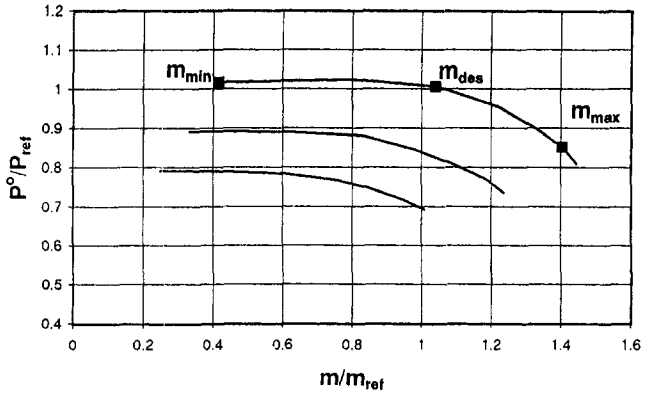

Fig. 9 Compressor performance map

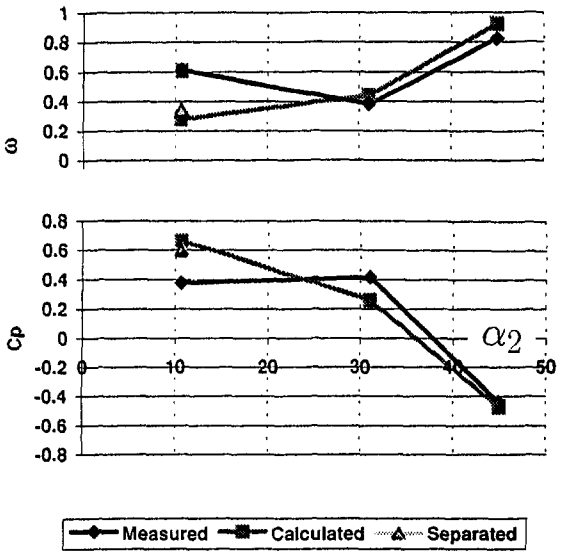

Fig. 10 Loss and static pressure rise coefficient for the external volute as a function of the inlet flow angle

where the subscript o stands for the outlet of the exit diffuser.

Figure 10 shows the measured and predicted loss and static pressure rise coefficient at maximum, design and minimum mass flow, defined on the performance curve shown in Fig. 9. Taking into account the complexity of the geometry and flow, one can conclude that the new prediction model is quite accurate.

One observes almost a doubling of the losses at maximum mass flow, resulting from the dissipation of the large swirl in the volute. This confirms the assumption that the outlet swirl is lost. The losses at minimum mass flow are underestimated because the prediction model does not account for the flow separation that has been observed in the exit diffuser.

Flow separation reduces the static pressure rise and increases the losses. Unfortunately, there are no separation criteria in the model and they are not easily introduced because of the complexity of the three-dimensional flow with large velocity variations at the volute inlet and over the cross section.

From the definition of the static pressure rise and loss coefficients one can derive following expression:

$$C_P + \omega + \frac{\overline{P_o^o} - \overline{P_o}}{\overline{P_3^o} - \overline{P_3}} = 1. \tag{15}$$

The third term is a measure of the outlet kinetic energy. As one assumes a fully mixed-out uniform flow at the outlet section, it should be a function of mass flow only. Any error in the loss prediction should therefore result in an opposite error in the static pressure rise.

Repeating the one-dimensional calculations at minimum mass flow, assuming that no diffusion takes place in the exit diffuser because of flow separation, results in a decrease of C_P and according to Eq. (15) in a corresponding increase of the losses. This prediction agrees better with the measurements but the remaining discrepancy suggests (and this will be confirmed later) that separation already starts in the volute.

Circumferential Flow Distortion

The circumferential variation of the static pressure depends mainly on the volute flow. The circumferential variation of total pressure, temperature, and diffuser flow angle is mainly a consequence of the impeller and diffuser response to an outlet static pressure distortion. The following comparison therefore evaluates both the volute flow and the impeller-response models.

Figures 11–14 compare the measured and predicted pressure

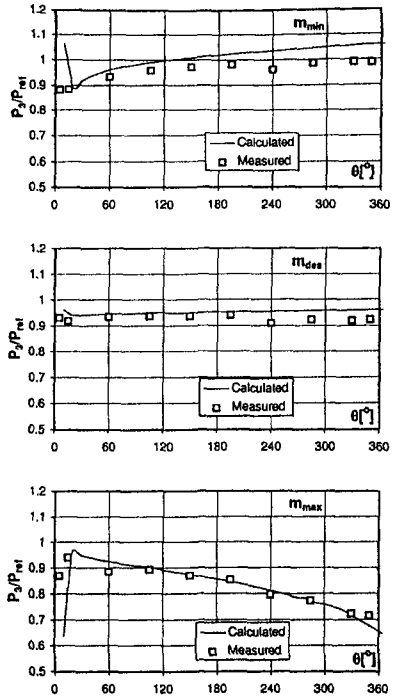

Fig. 11 Circumferential static pressure distribution at the three operating points

and flow variation at the vaneless diffuser exit ($R/R_2 = 1.45$) for the external volute at the three operating points indicated in Fig. 9. The static and total pressure distortion (Figs. 11 and 12) is very well predicted at maximum mass flow. The constant pressure at design mass flow confirms that the volute is well designed. The circumferential variation of the static pressure is slightly overestimated at minimum mass flow. The main discrepancy is a zone of constant pressure, observed for 200 deg $< \theta <$ 360 deg, suggest-

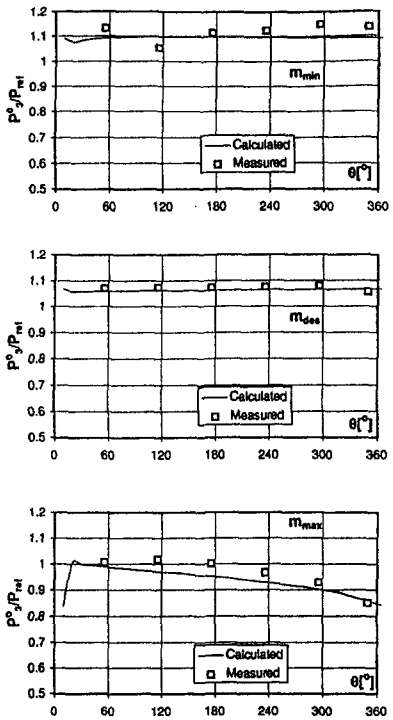

Fig. 12 Circumferential total pressure distribution at the three operating points

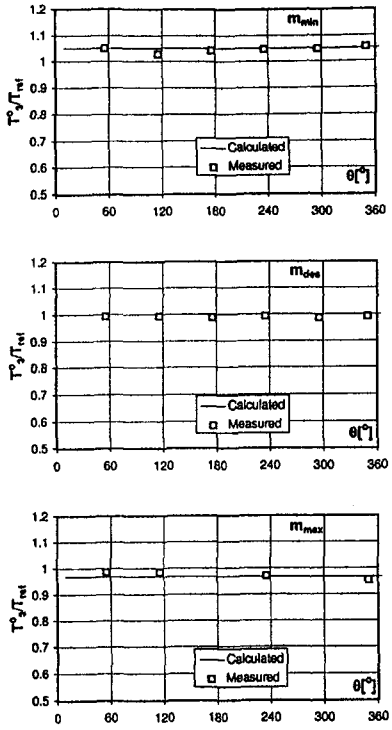

Fig. 13 Circumferential total temperature distribution at the three operating points

ing that the flow separation is not restricted to the exit diffuser but already starts inside the volute.

The small variation in total temperature at all operational points confirms the assumption of constant work (Fig. 13).

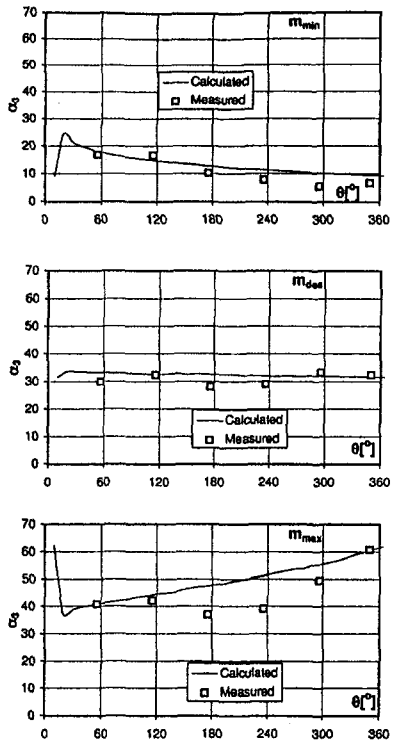

Fig. 14 Circumferential absolute flow angle distribution at the three operating points

The model predicts an almost linear variation of the flow angle along the volute length whereas the measured one shows a wavy variation with two periods over one circumference (Fig. 14). The last one agrees well with the results of a combined three-dimensional volute/unsteady impeller flow calculation (Hillewaert et al., 1999). The waviness is generated by the compression waves traveling back and forth inside the impeller (Fatsis et al., 1997) and cannot be predicted by the simple impeller response model used in the present calculations. However, this discrepancy has no large effect on the circumferential pressure distortion, which is a major result of these calculations.

Conclusions

It has been shown how the three-dimensional structure of the flow in volutes, as revealed by detailed measurements, can be described by an improved one-dimensional model and how the main losses are related to it.

Loss and pressure rise predictions by this model have shown to be sufficiently accurate for overall performance predictions except when the flow separates in the volute or exit diffuser at very low mass flows. The weak point of the prediction model is its inability to predict flow separation in the volute.

As a result of the impeller response model, the method also allows a good prediction of the circumferential pressure and flow distortion at off-design operation and can be used to define a distortion-free volute at design conditions.

Acknowledgments

The research described in this paper was funded by the Forschungsvereinigung für Verbrennungskraftmaschinen e.V. (FVV) and the authors wish to thank them for their support. The authors also wish to thank the industrial members of the working group "Spiralenströmung" ("Flow in Volutes") for their stimulating discussions and comments.

References

Ayder, E., and Van den Braembussche, R. A., 1991, "Experimental Study of the Swirling Flow in the Internal Volute of a Centrifugal Compressor," ASME Paper No. 91-GT-7.

Ayder, E., Van den Braembussche, R. A., and Brasz, J., 1993, "Experimental and Theoretical Analysis of the Flow in a Centrifugal Compressor Volute," ASME JOURNAL OF TURBOMACHINERY, Vol. 115, pp. 582–589.

Ayder, E., and Van den Braembussche, R. A., 1994, "Numerical Analysis of the Three-Dimensional Swirling Flow in a Centrifugal Compressor Volute," ASME JOURNAL OF TURBOMACHINERY, Vol. 116, pp. 462–468.

Elholm, T., Ayder, E., and Van den Braembussche, R. A., 1992, "Experimental Study of the Swirling Flow in the Volute of a Centrifugal Pump," ASME JOURNAL OF TURBOMACHINERY, Vol. 114, pp. 366–372.

Fatsis, A., Pierret, S., and Van den Braembussche, R. A., 1997, "Three-Dimensional Unsteady Flow and Forces in Centrifugal Impellers With Circumferential Distortion of the Outlet Static Pressure," ASME JOURNAL OF TURBOMACHINERY, Vol. 119, pp. 94–100.

Hagelstein, D., Van den Braembussche, R. A., Keiper, R., and Rautenberg, M., 1997, "Experimental Investigation of the Circumferential Static Pressure Distortion in Centrifugal Compressor Stages," ASME Paper No. 97-GT-50.

Hillewaert, K., and Van den Braembussche, R. A., 1999, "Numerical Simulation of the Impeller–Volute Interaction in Centrifugal Compressors," ASME JOURNAL OF TURBOMACHINERY, Vol. 121, this issue, pp. 601–606.

Japikse, D., 1982, "Advanced Diffusion Levels in Turbocharger Compressors and Component Matching," *Proc. Int. Conf. on Turbocharging and Turbochargers*, London, IMechE., pp. 143–155.

Sideris, M., and Van den Braembussche, R. A., 1987, "Influence of a Circumferential Exit Pressure Distortion on the Flow in an Impeller and Vaneless Diffuser," ASME JOURNAL OF TURBOMACHINERY, Vol. 109, pp. 48–54.

Stanitz, J., 1952, "One Dimensional Compressible Flow in Vaneless Diffusers of Radial and Mixed Flow Compressors Including Effects of Friction, Heat Transfer and Area Change," NACA TN 2610.

Traupel, W., 1977, *Die Theorie der Strömung durch Radialmaschinen*, Verlag Braun, Karlsruhe, Germany.

Van den Braembussche, R. A., and Haende, B. M., 1990, "Experimental and Theoretical Study of the Swirling Flow in Centrifugal Compressor Volutes," ASME JOURNAL OF TURBOMACHINERY, Vol. 112, pp. 38–43.

Weber, C. R., and Koronowski, M. E., 1986, "Meanline Performance Prediction of Volutes in Centrifugal Compressors," ASME Paper No. 86-GT-216.

The Effect of Inlet Boundary Layer Thickness on the Flow Within an Annular S-Shaped Duct

T. Sonoda

T. Arima

M. Oana

Honda R&D Co., Ltd.,
Wako Research Center,
Saitama 351-0193, Japan

Experimental and numerical investigations were carried out to gain a better understanding of the flow characteristics within an annular S-shaped duct, including the effect of the inlet boundary layer (IBL) on the flow. A duct with six struts and the same geometry as that used to connect compressor spools on our experimental small two-spool turbofan engine was investigated. A curved downstream annular passage with a similar meridional flow path geometry to that of the centrifugal compressor has been fitted at the exit of S-shaped duct. Two types of the IBL (i.e., thin and thick IBL) were used. Results showed that large differences of flow pattern were observed at the S-shaped duct exit between two types of the IBL, though the value of "net" total pressure loss has not been remarkably changed. According to "overall" total pressure loss, which includes the IBL loss, the total pressure loss was greatly increased near the hub as compared to that for a thin one. For the thick IBL, a vortex pair related to the hub-side horseshoe vortex and the separated flow found at the strut trailing edge has been clearly captured in the form of the total pressure loss contours and secondary flow vectors, experimentally and numerically. The high-pressure loss regions on either side of the strut wake near the hub may act on a downstream compressor as a large inlet distortion, and strongly affect the downstream compressor performance. There is a much-distorted three-dimensional flow pattern at the exit of S-shaped duct. This means that the aerodynamic sensitivity of S-shaped duct to the IBL thickness is very high. Therefore, sufficient care is needed to design not only downstream aerodynamic components (for example, centrifugal impeller) but also upstream aerodynamic components (LPC OGV).

Introduction

A swan-neck duct is used to connect the low- and high-pressure compressors of aircraft gas turbine engines. In a small gas turbine, a centrifugal high-pressure compressor is often used. In this case, the swan-neck duct is **S**-shaped due to the aerodynamic design restriction of the centrifugal compressor. Within this duct, flow separation must be avoided to minimize the total pressure loss within the duct. In addition, a uniform flow field at the duct exit must also be achieved. However, it is very difficult to satisfy these various requirements in practice. The **S**-shaped duct also contains struts to support loads and passages for engine accessories and other systems, resulting in a highly complex flow field pattern due to interaction of the duct passage with the struts. Furthermore, the requirements must be fulfilled for a short axial length.

Recently, some studies have been reported on **S**-shaped ducts (Britchford et al., 1994; Bailey et al., 1997; Bailey and Carrotte, 1996). Their long-term objective is to apply CFD methods to enable the optimum design of **S**-shaped ducts. Therefore, comprehensive measurements were done using an LDV system under ideal and typical actual engine inlet conditions. However, the **S**-shaped duct inlet velocity was relatively low and the duct itself was of constant-flow area. Only one radial strut was used in order to assess the effect on performance of placing radial struts within the duct. On the other hand, Sonoda et al. (1998) studied the flow within an **S**-shaped duct with a more practical configuration and high-speed condition, experimentally and numerically. The emphasis of the earlier paper was to investigate the influence on the flow of downstream passage located at the exit of the **S**-shaped duct. They showed that the total pressure loss is greatly increased near the hub in the case of the curved annular downstream passage when compared to the straight annular passage. Furthermore, a vortex related to casing-side horseshoe vortex was observed in the form of high-loss region adjacent to the casing, experimentally. However, they could not detect a vortex related to hub-side horseshoe vortex as a spatial concentrated total pressure loss (as a vortex core). According to their numerical simulation results of the effect of IBL thickness, they qualitatively predicted the existence of a much higher loss region due to the hub-side horseshoe vortex, as the IBL thickness was thicker. However, these numerical results are not still acceptable for aerodynamic engineer as a design data, due to the uncertainty of simulation technique or the lack of quantitative estimation.

In this stage of progress in research, it would be worthwhile to investigate not only the effect of the IBL thickness on the flow within an **S**-shaped duct but also the limitation of in-house-developed density-based Navier–Stokes code.

The motivation of our study is that, according to performance test of our centrifugal compressor with an **S**-shaped duct, the decrease in efficiency was much greater than expected. Therefore, a project team was organized last year to investigate the flow mechanism within the **S**-shaped duct, and to clear the cause of efficiency drop on centrifugal compressor test.

The objectives of this investigation are: (1) to study the aerodynamic sensitivity of the flow within an **S**-shaped duct to the IBL thickness, experimentally and numerically, and (2) to evaluate the reliability of the three-dimensional density based Navier–Stokes time marching code, in more detail.

Contributed by the International Gas Turbine Institute and presented at the 43rd International Gas Turbine and Aeroengine Congress and Exhibition, Stockholm, Sweden, June 2–5, 1998. Manuscript received by the International Gas Turbine Institute February 1998. Paper No. 98-GT-260. Associate Technical Editor: R. E. Kielb.

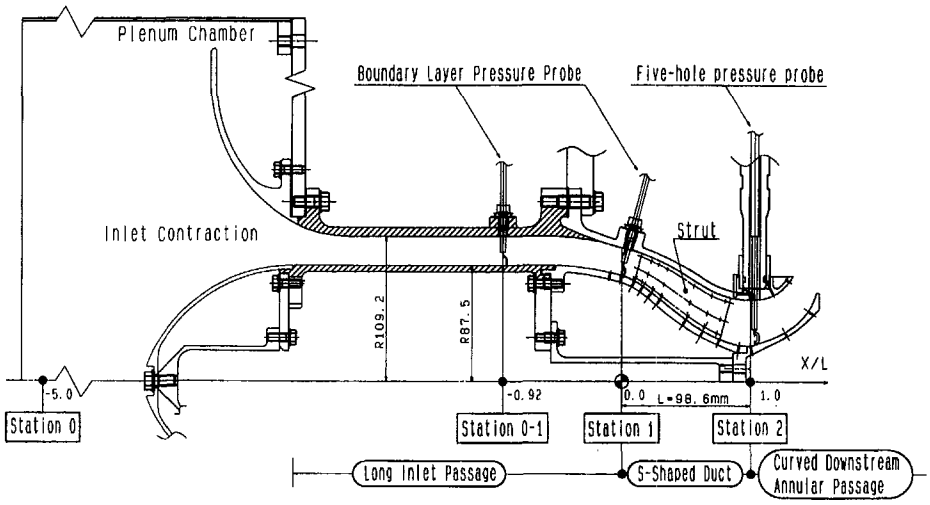

Fig. 1 Experimental apparatus for thick inlet boundary layer

Experimental Methods

Experimental Facility. An experimental apparatus of the S-shaped duct test rig is shown in Fig. 1. This is for the case of the thick inlet boundary layer (IBL). Air is supplied by laboratory compressors into a plenum chamber prior to passing through the S-shaped duct, and is exhausted to atmospheric pressure via an exhaust diffuser system set up in the test cell. A curved downstream annular passage, which is a similar meridional flow path geometry to that of the centrifugal compressor on our experimental small two-spool turbofan engine, has been fitted at the exit of S-shaped duct.

A long inlet passage with about 200 mm length has been newly fitted between the inlet contraction and the S-shaped duct to investigate the effect of the IBL thickness on the flow within the S-shaped duct. A test rig shown in our earlier paper is for the thin IBL. That is, the long inlet passage is removed in the test for the thin IBL. The detailed configuration of the S-shaped duct and the curved downstream annular passage was described in our earlier paper. A passage (from about $X/L = -0.2$ to about $+0.1$) upstream of the S-shaped duct leading edge has the same geometry as that of the LPC OGV. In Fig. 1, Station 1 ($X/L = 0.0$) corresponds to the trailing edge position of the LPC OGV, and Station 2 ($X/L = 1.0$) corresponds to a leading edge of centrifugal impeller. The inlet Mach number, used in the case of the thick IBL, is 0.386 ± 0.03, based on the inlet total pressure (Station 0) and the mean value of the hub and casing static pressures at Station 1. This Mach number is the same as that of the thin IBL.

Static pressure taps are located at various streamwise positions on the hub and the casing, which allow for the estimation of the flow characteristic and the effect of the IBL thickness. The circumferential position of these taps corresponds to midpoint between the struts. In addition, on the strut surface, static pressure taps are located at 11, 44, and 89 percent of the strut span. The area ratio ($A1/A2$) of the S-shaped duct is about 1.2. The S-shaped duct has six struts with NACA 0021-profile geometry.

Instrumentation. Inlet total pressure and temperature are measured at the center of the plenum chamber (at Station 0 in Fig. 1). At the outlet, using the three-axis traverse mechanism, traverse measurements of pressure were made using a miniature five-hole pressure probe with an overall diameter of 1.5 mm, which was calibrated in advance. The axial position of these measurements ($X/L = 1.03$) nearly corresponds to the centrifugal impeller leading edge (Station 2). The outer ring of curved annular passage moves in the circumferential direction by the three-axis traverse mechanism. The data are mainly obtained at eight radial positions traversed along 20 circumferential points. The area traversed corresponds to half of the strut pitch. The measurements of the two types of the IBL profile (i.e., the thin and the thick IBL) are done at Station 1 using a miniature boundary layer pressure probe 0.4 mm (height) × 0.85 mm (width). Furthermore, additional boundary layer measurements are done at Stations 0–1 in order to get inlet boundary pressure conditions for CFD in the case of the thick IBL. The flows on the strut and the hub/casing surfaces have been visualized using a mixture of titanium dioxide and oleic acid.

Data Reduction. Static pressures along the hub, the casing, and the strut surface are given in terms of the pressure recovery coefficient (Cp); while the total pressure loss coefficient between the S-shaped duct inlet (Station 1: $X/L = 0.0$) and the duct exit ($X/L = 1.03$: near Station 2) is defined as λ:

$$C_p \equiv \frac{P_{s,w} - \overline{P_{s,1}}}{P_{t,1} - \overline{P_{s,1}}}; \quad \lambda \equiv \frac{P_{t,1} - P_{t,2}}{P_{t,1} - \overline{P_{s,1}}}$$

Nomenclature

A = local cross-sectional area
Cp = static pressure recovery coefficient
L = representative axial length of S-shaped duct = 98.6 mm (see Fig. 1)
Pt = total pressure, kPa
Ps = static pressure, kPa
R = radius, mm
Tt = total temperature, K
V = flow velocity
X = axial distance, mm
δ^* = displacement thickness, mm
H = shape factor
θ = momentum thickness, mm
λ = total pressure loss coefficient

Superscripts and Subscripts

$-$ = time average
hub = inner casing wall
casing = outer casing wall
max = maximum
w = wall
0, 1, 2 = streamwise position (see Figs. 1 and 2)

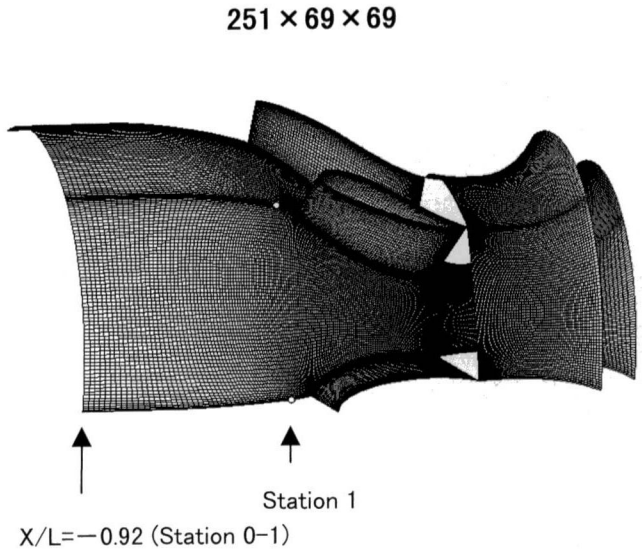

Fig. 2 Computational grid of S-shaped duct for thick IBL

$$\overline{P_{s,1}} \equiv \tfrac{1}{2}\,(P_{s,1,\text{casing}} + P_{s,1,\text{hub}})$$

Here, the total pressure at Station 1 ($Pt_{,1}$) has been assumed the same as the pressure at Station 0 ($Pt_{,0}$) in the plenum chamber. The total pressure loss coefficient obtained from this assumption is called "overall" total pressure loss, which includes the loss of the IBL.

On the other hand, total pressure loss that does not include the loss of the IBL is called "net" total pressure loss. The "net" loss is obtained using the measured mass-averaged total pressure at Station 1 ($Pt_{,1}$) instead of $Pt_{,0}$.

The five-hole pressure probe provides information on total and static pressure as well as flow direction (pitch and yaw angles) and velocity is calculated from these data.

Estimate of Experimental Error. The inlet total pressure probe, the boundary layer pressure probe, the static taps, and the five-hole pressure probe discussed above were connected to a precalibrated differential pressure transducer, which had a range of ±98 kPa. The output was read automatically from an integrating digital voltmeter. Total and static pressure measurements were reproducible to within ±10 mm of water. Based on these values, it was estimated that the static pressure recovery and the total pressure loss coefficient were reproducible to within ±0.02 and ±0.01, respectively.

Computational Methods

A three-dimensional compressible density based Navier–Stokes code with a low-Reynolds number k–ϵ turbulent model (Arima et al., 1997), has been applied to the flow within the **S**-shaped duct. The computational body-fitted grid, for example, used for the thick IBL is shown in Fig. 2. Part of the casing grid is omitted to allow a better view of the **S**-shaped duct with struts. The grid consists of 69 nodes in the strut-to-strut direction, 69 nodes in the spanwise direction, and 251 nodes in the streamwise direction. High grid density has been used because of the increase of computational accuracy. That is, the change of total pressure between **S**-shaped duct inlet and outlet is a very small fraction of the inlet total pressure.

A grid sensitivity study had been performed by focusing on the distribution of total pressure loss coefficient obtained from different grid systems. The coarse grid sometimes gave a local numerical error, such as a negative loss coefficient. With the increasing of grid points (in especially radial direction), the unreasonable physical phenomena had disappeared. Therefore, such a high-density grid, as used in this work (251 × 69 × 69), has been adopted. For proper resolution of the boundary layer, a typical value less than 5 should be required. In this work, except in the immediate vicinity of the leading and trailing edges, the strut, hub, and casing surface boundary layers had at least 11 grid points with values of $y^+ < 20$. This yielded values of $y^+ \cong 1$ at grid points adjacent to the walls; and then its average value of whole grid points adjacent to the walls had become $y^+ < 2$.

Calculations have been performed for two types of IBL thickness. For the case of the thick IBL, as inlet boundary conditions, the measured pressure and temperature at Station 0–1 were used, and inlet flow direction was along the hub and the casing without swirling.

On the other hand, for the case of the thin IBL, the grid was partially changed. That is, a grid with short inlet passage (from $X/L = -0.62$ to 0.0 (Station 1)) was used instead of the long inlet passage (from $X/L = -0.92$ to 0.0 (Station 1)). This is because the experimental data as inlet boundary conditions for the thin IBL could not be gotten due to restrictions on the test rig layout. Therefore, the calculation for the thin IBL was repeated until the calculated IBL thickness of Station 1 was in good agreement with that of the measurement, by changing the IBL thickness at $X/L = -0.62$.

The initial total pressure profile in the IBL was calculated automatically using a $\frac{1}{7}$-power velocity profile law and was used as an inlet total pressure boundary condition. Downstream back pressure was fixed at hub and casing due to no swirling and adjusted to coincide with the corrected mass flow of Station 1.

Results and Discussion

Inlet Boundary Layer. In order to estimate the characteristic of the IBL at Station 1 for the thin and thick IBL, the IBL measurements were done using the miniature boundary layer pressure probe. The obtained total pressure data were transformed to velocity profile using static pressure values measured on the hub and the casing. Figures 3(*a*) and 3(*b*) show the total pressure profile and the velocity profile at Station 1, respectively. In both cases (the thin and the thick IBL), as the flow is affected by a curvature effect in this station, the velocity-shear flow field is generated. The thickness of IBL on the hub and casing is of the same order, and it is about 5 percent and about 30 percent of passage height for the "thin" and the "thick" IBL, respectively. Calculated results are also shown in Fig. 3. When contrasting both results (experiments and calculations), there is a difference regarding the boundary layer profile. This is due to the use of the $\frac{1}{7}$-power velocity profile as an inlet boundary condition at Station 0–1, instead of the measured boundary layer total pressure profile. However, the tendency between measurements and calculations is quite the same, though there is a little deficit of inlet total pressure from about 30 to 60 percent span height.

The boundary layer parameters (δ^*, θ, H) were obtained under the extrapolation of the main flow velocity (i.e., the velocity of no pressure loss region), as shown in the form of "straight lines" in Fig. 3(*b*). Table 1 shows the measured boundary layer parameters. It is apparent that the IBL at Station 1 is turbulent flow, because the shape factor $H \equiv \delta^*/\theta$ is sufficiently small as compared to 2.59 (laminar flow along a plate) or 1.30 (turbulent flow along a plate).

$$\delta^* = \int_0^{\delta} \left(1 - \frac{V}{V_{\max}}\right) dR$$

$$\theta = \int_0^{\delta} \left(1 - \frac{V}{V_{\max}}\right) \frac{V}{V_{\max}}\, dR$$

Flow Visualization. Flow has been visualized experimentally and numerically to gain a qualitative understanding of the flow pattern within the **S**-shaped duct. The representative results are

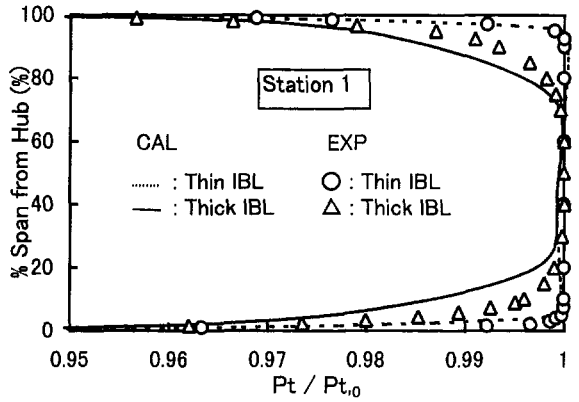

(a) Total Pressure Profile

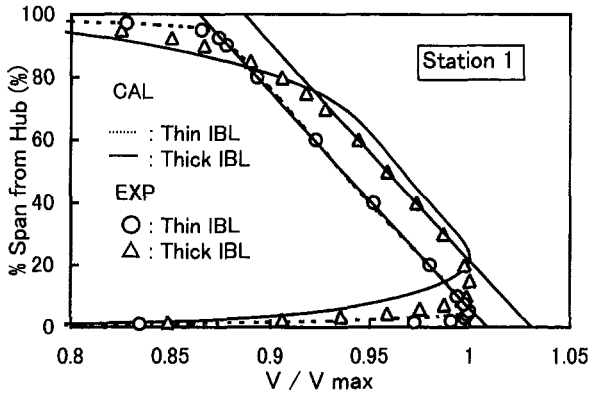

(b) Velocity Profile

Fig. 3 Boundary layer profiles for thin and thick IBL at Station 1

shown in Fig. 4. Figure 4(*a*) shows the flow pattern along the strut and hub surface. A typical horseshoe vortex that forms ahead of the blunt-strut leading edge with a saddle point is observed. From this point, two limiting streamlines emerge and wrap around the strut. As the limiting streamline is traced downstream, it is seen to move toward the strut surface and to be migrating in the spanwise direction on the strut surface. A small separation region is observed on the strut surface at the hub corner of the trailing edge, experimentally and numerically.

When contrasting the two IBL (i.e., the thin and the thick IBL), the difference of each saddle point's position is not so large. In the case of the thick IBL, the migration levels of low-momentum fluid on the strut surface are smaller than that of the thin IBL, experimentally and numerically. This may be due to a developed counterclockwise hub-side horseshoe vortex (see Figs. 5 and 9) and due to a decreased radial pressure gradient (see Fig. 6). The calculated flow pattern on the hub surface has very small shear stress in the both cases, as compared to that for a straight downstream passage (Sonoda et al., 1998). This is mainly due to a high positive streamwise pressure gradient on the hub in the latter half of the S-shaped duct. The pressure gradient measured for the straight downstream passage in our earlier paper is the limitation for the separation on the hub.

Table 1 Measured boundary layer parameters for thin and thick IBL at Station 1

– IBL	– SIDE	δ^*(mm)	θ (mm)	H
Thin	CASING	0.184	0.172	1.07
	HUB	0.138	0.133	1.04
Thick	CASING	0.383	0.344	1.11
	HUB	0.314	0.300	1.05

The horseshoe vortex observed on the hub can also be seen on the casing as shown in Fig. 4(*b*). The strut has been removed. This feature is, however, very different from that of the hub. That is, the distance between the limiting streamline and the strut surface is almost constant within the S-shaped duct, while at the trailing edge, two-wake limiting streamlines form. In the two types of IBL, the feature of the flow pattern for the thick IBL is somewhat different from that for the thin IBL. First, the saddle point is moved toward the upstream direction as the IBL thickness is increased. Second, though the shape of the wake-limiting streamline is almost same for the two types of IBL, the distance between the limiting streamline related the horseshoe vortex and the wake limiting streamline is significantly increased. On the whole, the calculated results are in good agreement with the experimental results, qualitatively.

Figure 5 numerically shows the relation between the oil flow pattern and the hub-side horseshoe vortex. This is in the case of the thick IBL. As already described, though the limiting streamline is seen to be migrating in the spanwise direction on the strut surface (in Fig. 4(*a*)), the hub-side horseshoe vortex keeps a constant distance from the strut surface. The spatial development of the hub-side horseshoe vortex becomes noticeable from the latter half of the strut, due to a positive pressure gradient on the hub, as shown in Fig. 6.

Hub, Casing, and Strut Static Pressure. The hub and casing wall pressure coefficient, Cp, is presented in Fig. 6 for two cases of the IBL. As the flow follows a curved path within the S-shaped duct, a modification to the static pressure field occurs due to the balance between centrifugal force and radial pressure gradient. Across the first bend (≈Station 1), the pressure close to the casing is higher than that adjacent to the hub. However, this situation is reversed at the second bend since the flow follows the downstream curved passage fitted at the exit of S-shaped duct. The flow experiences a significant positive streamwise pressure gradient in the latter half of the duct on the hub surface. In contrast, the pressure gradient is almost negative adjacent to the casing where Cp decreases along approximately 80 percent of the duct length. When contracting both cases (i.e., the thin and thick IBL), Cp profiles show significant, though not dramatic, differences in the latter half of the S-shaped duct. Radial pressure gradient from hub to casing is decreased adjacent to the S-shaped duct exit in the case of the thick IBL. The cause is the less curvature effect due to the thick boundary layer. As shown in Fig. 6, the calculated results are in good agreement with experimental results.

The strut wall static pressure coefficient, Cp, is presented in Fig. 7 at 11, 44, and 89 percent of the strut span. There is not a noticeable effect of the IBL thickness on the strut surface static pressure. The tendency between the measurement and the calculation is quite the same.

Total Pressure Loss Coefficient. Experimental and calculated contours of the total pressure loss coefficient are shown in Fig. 8 for thin IBL (left) and the thick IBL (right), obtained at the S-shaped duct exit (X/L = 1.03). The calculated contours have an increment of 5 percent. According to the experimental results in both cases (i.e., the thin and the thick IBL), the boundary layer near the hub at the midpoint between the struts is thicker than that near the casing. This is due to the streamwise positive pressure gradient along the hub in the latter half of the duct, as already shown in Fig. 6. When contrasting both cases (i.e., thin and thick IBL), the boundary layer thickness near the hub and casing region is greatly increased in the case of the thick IBL. At the same time, the higher loss region is observed, as a large total pressure hole, on either side of the strut wake near the hub in the case of the thick IBL. This "hole" seems to be related to the inlet hub-side horseshoe vortex. The calculated total pressure losses in Fig. 8 are much larger than indicated in the experimental contours, especially for the thick IBL. This is probably due to the difference of inlet

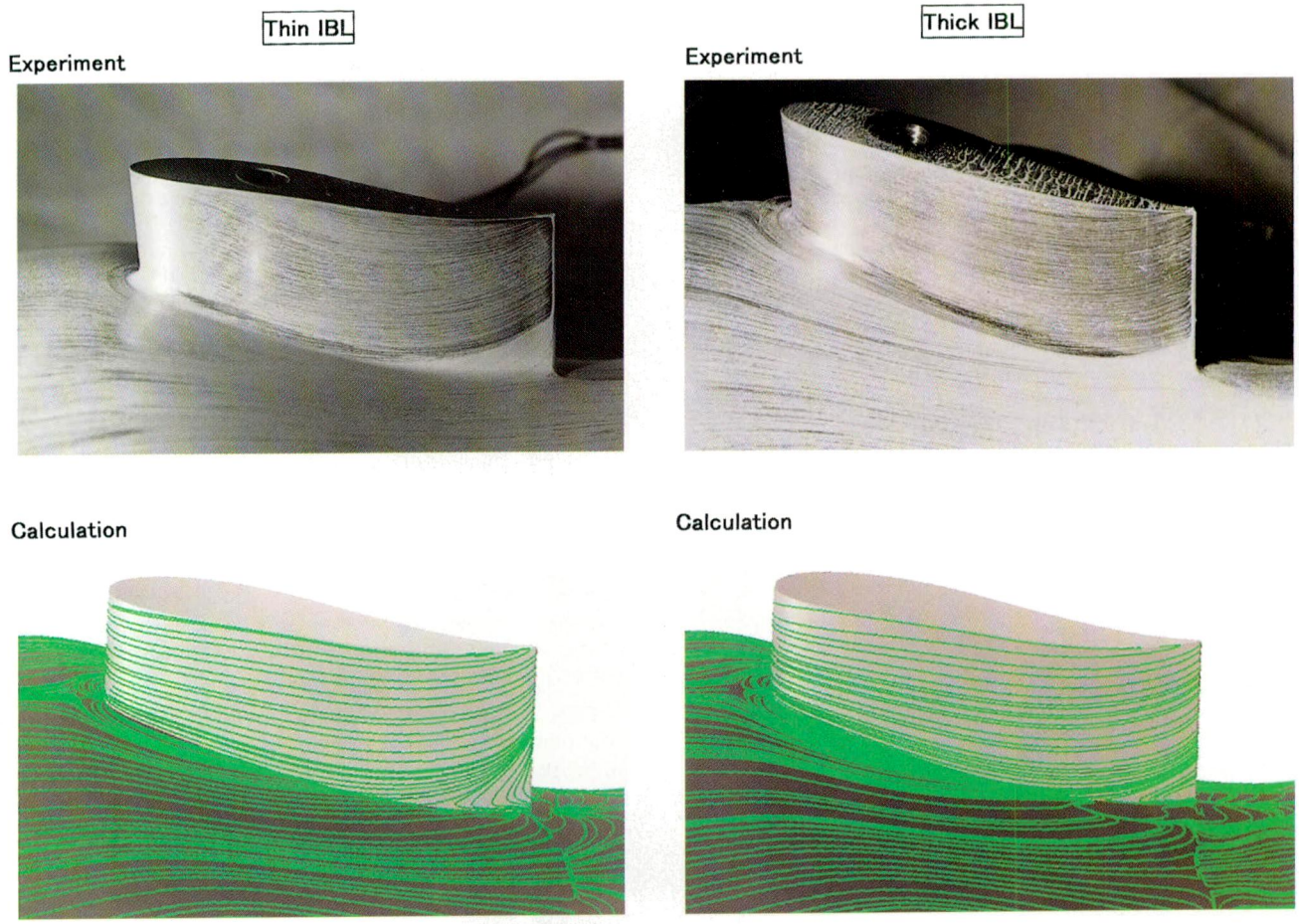

(a) Flow Pattern along Strut and Hub Surfaces

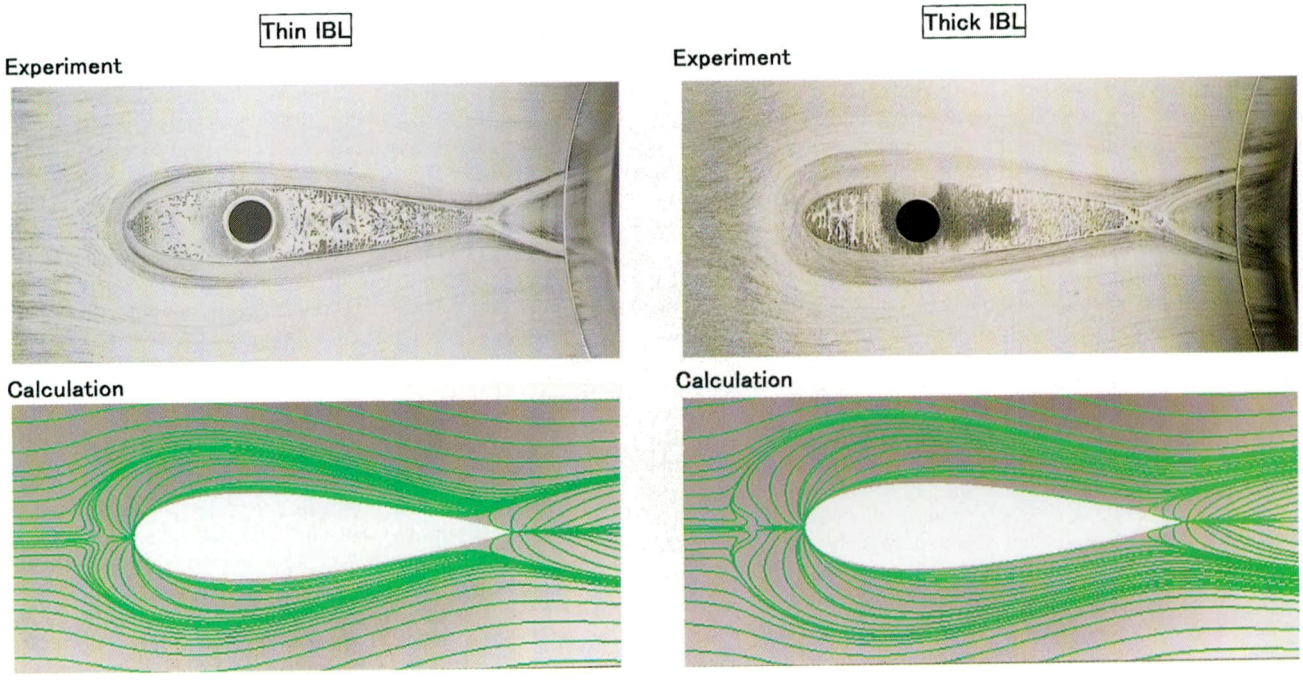

(b) Flow Pattern along Casing Surface

Fig. 4 Experimental and numerical flow visualization results for thin and thick IBL

boundary layer total pressure profile at Station 1 between experiment and CFD (see Fig. 3(*a*)). That is, total pressure loss in CFD is larger than that of the experiment. In our CFD calculation, the boundary layer thickness is adjusted to be the same value of the experiment, using a $\frac{1}{7}$-power velocity profile law. Furthermore, in the case of the thick IBL, the circumferential variation region of

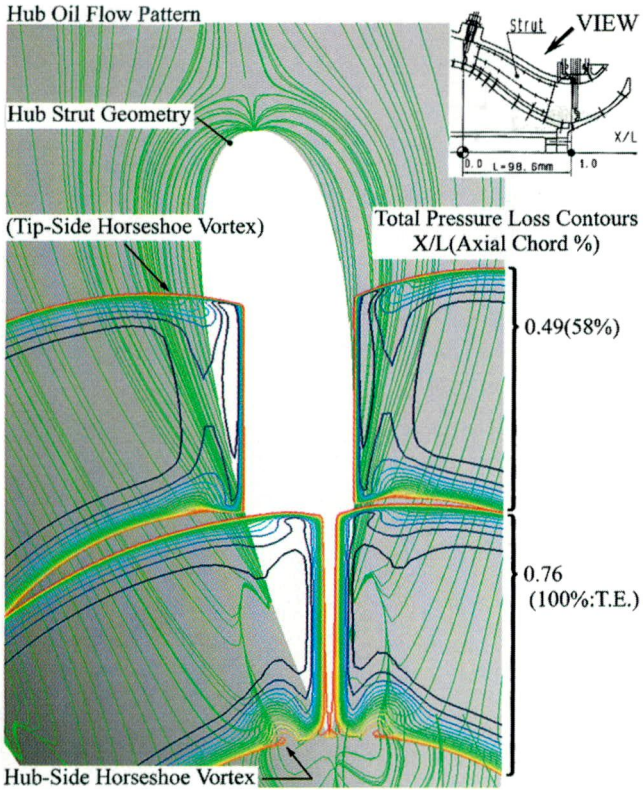

Fig. 5 Comparison of hub-side oil flow pattern with hub-side horseshoe vortex

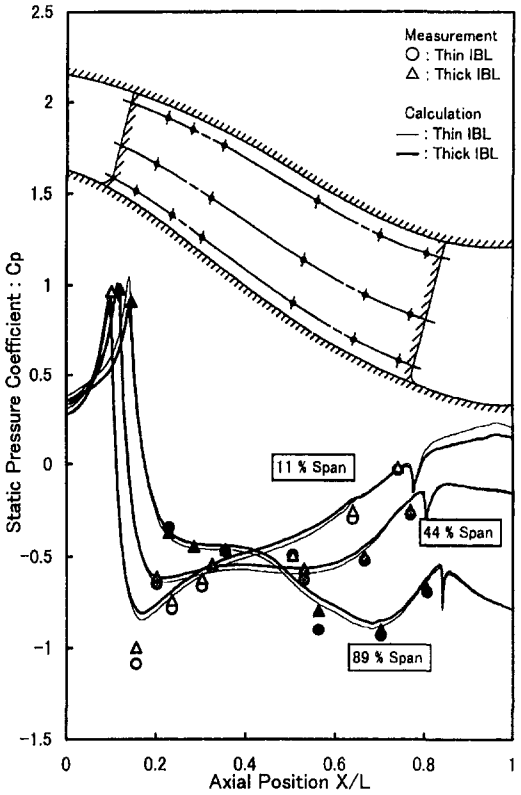

Fig. 7 Static pressure distribution on strut surface for thin and thick IBL

the total pressure loss adjacent to the casing is more extended radially inward. The maximum of total pressure loss at about 5 deg corresponds to the "wake limiting streamline," as already shown in Fig. 4(*b*). This deformation of the total pressure loss is due to the casing-side horseshoe vortex.

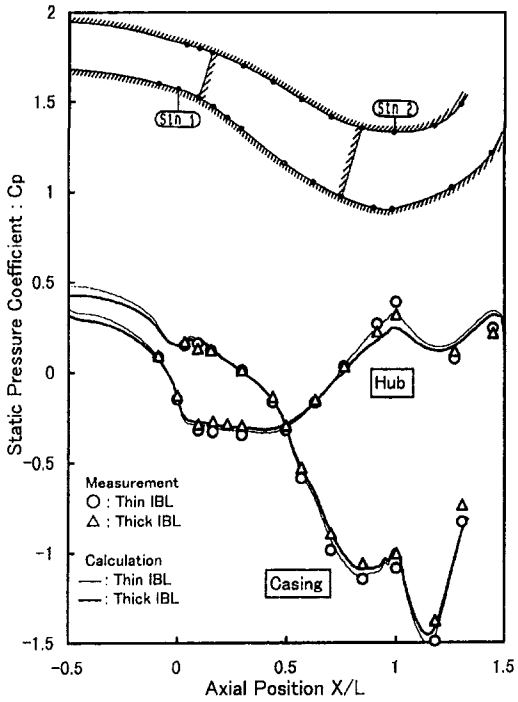

Fig. 6 Static pressure distribution on hub and casing for thin and thick IBL

Secondary Flow Vectors. As already reported in our earlier paper, the secondary flow vectors indicated radially outward flow due to the hub passage curvature at the S-shaped duct exit (at about Station 2: $X/L = 1.03$). Therefore, the flow features are not clear due to the high radially outward flow. In this study, the radial velocity vectors at the various spatial points have been subtracted from that of each radial position at the midposition in order to clear the flow feature. Figure 9 shows the experimental and calculated secondary flow vectors at the S-shaped duct exit. The flow features are very clear, especially for the thick IBL. A vortex related to a casing-side horseshoe vortex has been clearly captured for both thin and thick IBL in the form of velocity vectors, experimentally and numerically. Furthermore, a single vortex (clockwise) has been observed near the hub wall for the thin IBL. The hub-side single vortex is induced in the separated flow found at the strut trailing edge. On the other hand, in the case of the thick IBL, a vortex pair is noticeable in both experimental and numerical velocity vector results. Counterclockwise vortical motion corresponds to the hub-side horseshoe vortex. It is the counterrotating action of the two vortices that is pumping the low total pressure fluid from the near-hub wall boundary layer into the passage that causes the "hole." On the whole, the experimental and calculated results show good qualitative agreement.

It is very clear that the effect of the IBL thickness on the flow within an S-shaped duct is very high. In other words, the aerodynamic sensitivity of the S-shaped duct to the IBL thickness is very high. Especially, the hub-side horseshoe vortex may have an adverse effect on the downstream centrifugal compressor performance, such as a large inlet distortion. Since, in a real engine, the inlet flow upstream of the S-shaped duct may be much distorted and occupied with a poor IBL than our "thick" IBL used in this study. Therefore, sufficient carefulness is needed to design not only downstream aerodynamic component (for example, centrifugal impeller) but also upstream aerodynamic component (for example, LPC OGV).

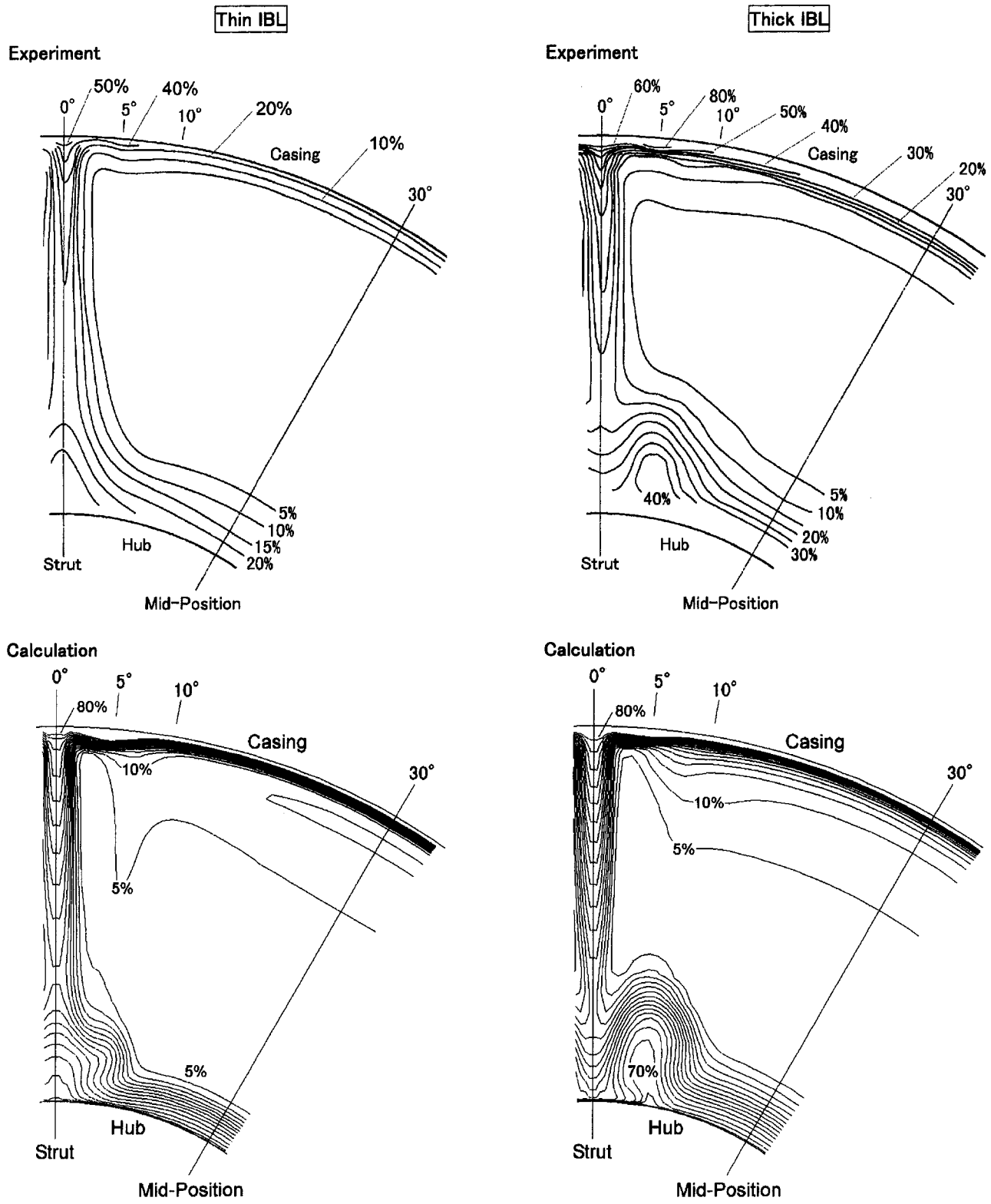

Fig. 8 Total pressure loss contours at S-shaped duct exit (≈Station 2) for thin and thick IBL

Overall and Net Total Pressure Loss. Figure 10 shows the spanwise distribution of mass-averaged "overall" total pressure loss coefficient. The total pressure loss near the hub is greatly increased in the case of the thick IBL, experimentally and numerically.

As already described in "Data Reduction," the overall total pressure loss coefficient includes the pressure loss within the IBL developed along the inlet upstream passage. Therefore, it is worthwhile to subtract the upstream IBL total pressure loss from the results in Fig. 10. Table 2 shows not only the overall mass-averaged total pressure loss coefficient but also the net total pressure loss coefficient for the thin and the thick IBL. The measurement neglects the high loss regions in the annulus boundary layer. Therefore, the calculations had been processed in the same way as the experiments. The "overall" loss of the measurements increases from 6.4 to 11.8 percent as the IBL thickness

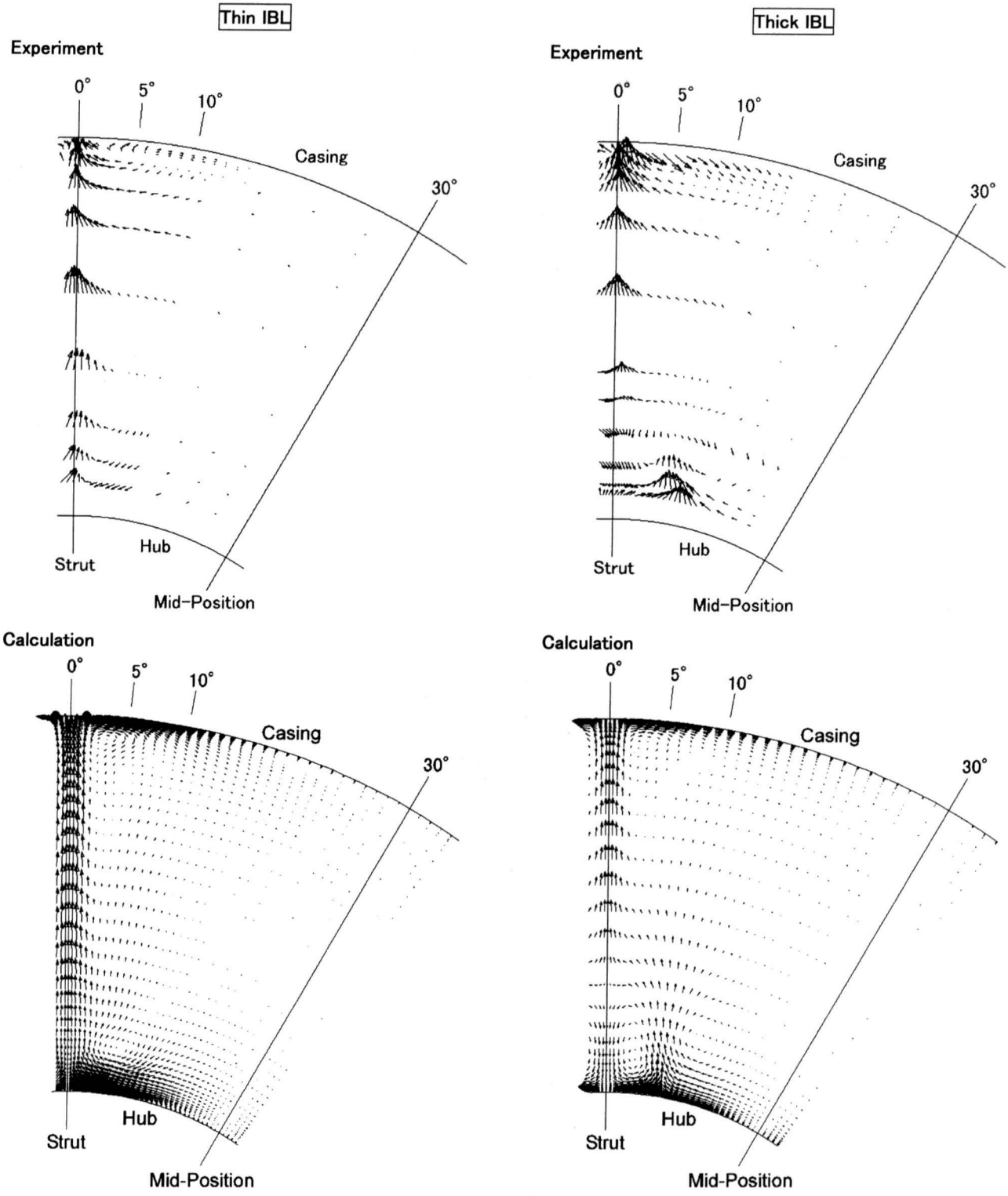

Fig. 9 Secondary flow vectors at S-shaped duct exit (≈Station 2) for thin and thick IBL

increases; while the "net" total pressure loss increases from 5.4 to 7.2 percent. The rate of increase for the net loss is about 33 percent. Although there is no dramatic difference for the "net" pressure loss between the thin and thick IBL, it is apparent that the flow pattern within the S-shaped duct is significantly affected by the IBL thickness. In comparing the experimental and calculated results, there are discrepancies in the spanwise distribution of overall total pressure loss and in the "net" total pressure loss values for the thin and the thick IBL. Both results, however, indicate the same overall behavior.

Concluding Remarks

Experimental and numerical investigations were carried out to gain a better understanding of the flow characteristics within an annular S-shaped duct with the curved annular downstream passage, including the effect of the inlet boundary layer (IBL) thickness on the flow. The following conclusions were drawn:

1 A vortex related to a casing-side horseshoe vortex has been clearly captured for both thin and thick IBL in the form of velocity vectors, experimentally and numerically. Further-

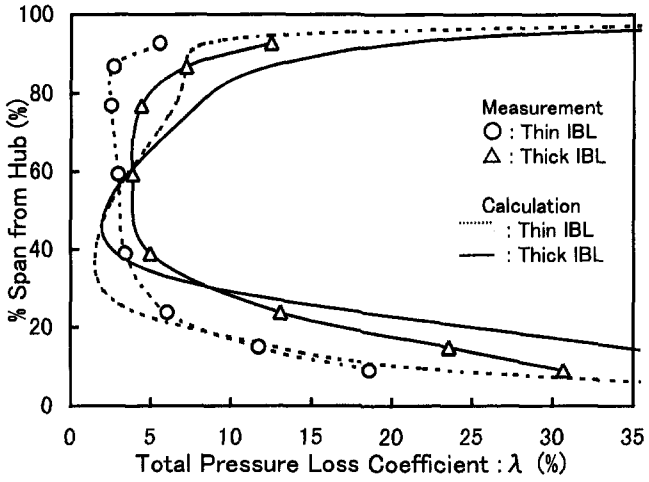

Fig. 10 Spanwise distribution of overall total pressure loss coefficient at S-shaped duct exit (≈Station 2)

more, a single vortex has been observed near the hub wall for the thin IBL. The hub-side single vortex is induced in the separated flow found at the strut trailing edge.

2 When contrasting both cases (thin and thick IBL), the spatial concentrated high loss region (i.e., the large total pressure "hole") has been generated near the hub wall for the thick IBL. This is due to a vortex pair. It is the counterrotating action of the two vortices that is pumping the low total pressure fluid from the near-hub wall boundary layer into the passage that causes the "hole." At the same time, high total pressure loss region near the casing has been extended radially inward.

3 Large differences of flow pattern have been observed at the S-shaped duct exit between two types of the IBL, though the value of "net" total pressure loss has not been significantly increased. Aerodynamic characteristic of the flow within an S-shaped duct is greatly affected by the IBL thickness.

4 A vortex pair near the hub wall may have an adverse effect on the downstream centrifugal compressor performance, such as a large inlet distortion. Since, in a real engine, the inlet flow upstream of S-shaped duct may be much distorted and occupied with a poor IBL than our "thick" IBL used in this study. Therefore, sufficient carefulness is needed to design not only downstream aerodynamic component (for example, centrifugal impeller) but also upstream aerodynamic component (for example, LPC OGV).

5 Calculated results using the three-dimensional Navier–Stokes code with a low-Reynolds-number k–ϵ turbulent model are in good agreement with experimental results. However, quantitative discrepancies are still observed in the wake region.

Table 2 Comparison between mass-averaged overall and net total pressure loss coefficient

λ (%)		Thin IBL	Thick IBL
Overall	Measurement	6.4	11.8
	Calculation	8.6	16.5
Net	Measurement	5.4	7.2
	Calculation	6.4	7.9

Acknowledgments

The authors would like to acknowledge Dr. Jon Carrotte of Loughborough University of Technology for useful discussions. We also thank Mr. Junji Takado and Mr. Yasuyoshi Oke of Honda R&D for their excellent support in obtaining the data presented here.

References

Arima, T., Sonoda, T., Shirotori, M., Tamura, A., and Kikuti, K., 1999, "A Numerical Investigation of Transonic Axial Compressor Rotor Flow Using a Low-Reynolds-Number k–ϵ Turbulence Model," ASME JOURNAL OF TURBOMACHINERY, Vol. 121, pp. 44–58.

Bailey, D. W., and Carrotte, J. F., 1996, "The Influence of Inlet Swirl on the Flow Within an Annular S-Shaped Duct," ASME Paper No. 96-GT-60.

Bailey, D. W., Britchford, J. F., Carrotte, J. F., and Stevens, S. J., 1997, "Performance Assessment of an Annular S-Shaped Duct," ASME JOURNAL OF TURBOMACHINERY, Vol. 119, pp. 149–156.

Britchford, K. M., Carrotte, J. F., Stevens, S. J., and McGuirk, J. J., 1994, "The Development of the Mean Flow and Turbulence Structure in an Annular S-Shaped Duct," ASME Paper No. 94-GT-457.

Sonoda, T., Arima, T., and Oana, M., 1998, "The Influence of Downstream Passage on the Flow Within an S-Shaped Duct," ASME JOURNAL OF TURBOMACHINERY, Vol. 120, pp. 714–722.